

ISBN 978-86-7031-244-9



26<sup>th</sup> Summer School and International  
Symposium on the **Physics of Ionized Gases**

August 27<sup>th</sup> -31<sup>st</sup>, 2012, Zrenjanin Serbia

**CONTRIBUTED  
PAPERS  
&  
ABSTRACTS OF INVITED LECTURES  
AND  
PROGRESS REPORTS**



**Editors**

**M. Kuraica, Z. Mijatović**

**University of Novi Sad, Faculty of Sciences  
Department of Physics  
Novi Sad, Serbia**

ISBN 978-86-7031-242-5

CONTRIBUTED PAPERS & ABSTRACTS  
OF INVITED LECTURES AND PROGRESS REPORTS  
of the  
26<sup>th</sup> SUMMER SCHOOL AND INTERNATIONAL  
SYMPOSIUM ON THE PHYSICS OF IONIZED GASES

August 27<sup>th</sup> - 31<sup>st</sup>, Zrenjanin, Serbia

Editors: Milorad Kuraica  
Zoran Mijatović

Publisher:

University of Novi Sad  
Faculty of Sciences  
Department of Physics  
Trg Dositeja Obradovića 3  
21000 Novi Sad, Serbia

© **2012 Department of Physics, Novi Sad**

All rights reserved.

No part of this publication may be reproduced, stored in retrieval systems,  
in any form or any means, electronic, mechanical, photocopying or otherwise,  
without the prior permission of the copyright owner.

**Printed by:**  
**Štamparija "Stojkov", Novi Sad, Serbia**

## PREFACE

This publication of Department of Physics, Faculty of Sciences, University of Novi Sad contains the Contribution Papers and the abstracts of Invited Lectures (General/Topical and Progress Reports) to be presented at the 26<sup>th</sup> Summer School and Symposium on the Physics of Ionized Gases – SPIG 2012. The symposium shall be held in Zrenjanin, Serbia, from August 27<sup>th</sup> – 31<sup>st</sup>, 2012. It is organized by Department of Physics, Faculty of Sciences, University of Novi Sad under the auspices and with support of Provincial Secretariat for Science and Technological development, Autonomous Province of Vojvodina, Ministry of Education and Science, Republic of Serbia, Institute Français Serbia and with sponsorship of European Physical Society (EPS).

The Invited Lectures and Contributed Papers are related to the following research fields: (i) Atomic Collision Processes (Electron and Photon Interactions with Atomic Particles, Heavy Particles Collisions, Swarms and Transport Phenomena); (ii) Particle and Laser Beam Interactions with Solids (Atomic Collisions in Solids, Sputtering and Deposition, Laser and Plasma Interaction with Surfaces); (iii) Low Temperature Plasmas (Plasma Spectroscopy and Other Diagnostics Methods, Gas Discharges, Plasma Applications and Devices); (iv) General Plasmas (Fusion Plasmas, Astrophysical Plasmas and Collective Phenomena). These four disciplines have strong interaction in numerous applications, however, due to the development of specialized international conferences, it has become increasingly rare that such a wide range of topics are covered at a single conference. Except the abstracts of invited lectures this book includes 78 contributed papers from which one can have impression about state-of-art of investigations in these four research fields.

The Editors would like to thank to the members of the Scientific and Advisory Committees of SPIG 2012 for their efforts in proposing the invited lectures and review of the contributed papers. Especially we acknowledge the support of all of the members of the Organizing Committee for a huge work in organization of the Conference.

Editors

Milorad M. Kuraica and Zoran Mijatović

## **ACKNOWLEDGEMENTS**

26<sup>th</sup> Summer School and International  
Symposium on the **Physics of Ionized Gases**

<http://spig2012.pmf.uns.ac.rs>

**was organized by**



**Department of Physics, Faculty of Sciences, University of Novi Sad**  
**Trg Dositeja Obradovića 4, 21000 Novi Sad, Serbia**  
<http://www.df.uns.ac.rs>

**under the auspices and with support of**

**Provincial Secretariat for Science and Technological development,  
Autonomous Province of Vojvodina**

**Ministry of Education and Science, Republic of Serbia**

**and also supported by the sponsors**

**Institute Français Serbia**

**European Physical Society**

**Editors**

**M. Kuraica, Z. Mijatović**

**University of Novi Sad, Faculty of Sciences**  
**Department of Physics**  
**Novi Sad, Serbia**

# 26<sup>th</sup> SPIG

## Scientific Committee

**M. Kuraica (Chairmen) Serbia**

**S. Buckman, Australia**

**J. Burgdoerfer, Austria**

**Z. Donko, Hungary**

**V. Guerra, Portugal**

**D. Jovanović, Serbia**

**K. Lieb, Germany**

**G. Malović, Serbia**

**I. Mančev, Serbia**

**A. Milosavljević, Serbia**

**N. J. Mason, USA**

**M. Danezis, Greece**

**Z. Mijatović, Serbia**

**K. Mima, Japan**

**Z. Mišković, USA**

**G. Poparić, Serbia**

**L. Č. Popović, Serbia**

**Z. Rakočević, Serbia**

**Y. Serruys, France**

**N. Simonović, Serbia**

**M. Škorić, Serbia**

## Advisory Committee

**D. Belić**

**N. Konjević**

**J. Labat**

**B. P. Marinković**

**S. Đurović**

**M. S. Dimitrijević**

**N. Bibić**

**M. Milosavljević**

**Z. Lj. Petrović**

**J. Purić**

**B. Stanić**

## Organizing Committee

**Z. Mijatović (Chairmen)**

**I. Savić (Secretary)**

**S. Đurović**

**N. Cvetanović**

**R. Kobilarov**

**T. Gajo**

**Z. Nađ**

**L. Gavanski**

## CONFERENCE TOPICS

### **Section 1. ATOMIC COLLISION PROCESSES**

- 1.1. Electron and Photon Interactions with Atomic Particles
- 1.2. Heavy Particle Collisions
- 1.3. Swarms and Transport Phenomena

### **Section 2. PARTICLE AND LASER BEAM INTERACTION WITH SOLIDS**

- 2.1. Atomic Collisions in Solids
- 2.2. Sputtering and Deposition
- 2.3. Laser and Plasma Interaction with Surfaces

### **Section 3. LOW TEMPERATURE PLASMAS**

- 3.1. Plasma Spectroscopy and Other Diagnostic Methods
- 3.2. Gas Discharges
- 3.3. Plasma Applications and Devices

### **Section 4. GENERAL PLASMAS**

- 4.1. Fusion Plasmas
- 4.2. Astrophysical Plasmas
- 4.3. Collective Phenomena

# CONTENT

## SECTION 1.

### Invited Lectures

<i>GI.1</i> Dieter Gerlich <b>EXPERIMENTAL STUDIES ON <math>HnDm^+</math> COLLISION SYSTEMS <math>n+m \leq 5</math></b> .....	3
<i>GI.2</i> M. Charlton <b>TRANSPORT AND COLLISION PHENOMENA INVOLVING ANTIPARTICLES AND ANTIHYDROGEN</b> .....	4
<i>GI.3</i> M. Stockli <b>PLASMA-WALL INTERACTIONS IN CESIATED H-ION SOURCES</b> .....	5
<i>TI.1</i> Jean-Marc Bizau <b>PHOTOIONIZATION OF ATOMIC AND MOLECULAR POSITIVELY CHARGED IONS</b> .....	6
<i>TI.2</i> R. Čurik <b>VIBRATIONALLY INELASTIC COLLISIONS OF SLOW ELECTRONS WITH MOLECULES</b> .....	8
<i>TI.3</i> F. Penent, P. Lablanquie, J. Palaudoux, L. Andric, P. Selles, S. Carniato, M. Žitnik, T.P. Grozdanov, E. Shigemasa, K. Soejima, Y. Hikosaka, I. H. Suzuki, M. Nakano and K. Ito <b>SINGLE PHOTON DOUBLE K-SHELL IONIZATION OF SMALL MOLECULES</b> .....	9
<i>PI.1</i> Marcello Coreno <b>CITIUS AND LDM@FERMI: VUV LIGHT SOURCES FOR ULTRAFAST SPECTROSCOPY ON ATOMS AND MOLECULES</b> .....	11
<i>PI.2</i> M. M. Ristić, G. B. Poparić and D. S. Belić <b>DIFFERENTIAL CROSS SECTIONS AT <math>0^\circ</math> AND <math>180^\circ</math> FOR ELECTRON IMPACT EXCITATION OF <math>H_2</math> AND CO</b> .....	12
<i>PI.3</i> S. D. Tošić <b>MEASUREMENTS OF DIFFERENTIAL CROSS SECTIONS FOR ELASTIC ELECTRON SCATTERING AND ELECTRONIC EXCITATION OF SILVER AND LEAD ATOMS</b> .....	13
<i>PI.4</i> Dušan Kubala, Olivier May and Michael Allan <b>DISSOCIATIVE ELECTRON ATTACHMENT TO SMALL MODEL MOLECULES</b> .....	14

### Contributed papers

<i>SI.1</i> I. Mančev and N. Milojević <b>CHARGE EXCHANGE IN FAST <math>Li^{3+}</math>-He COLLISIONS</b> .....	19
---	----

<i>SI.2</i> Tasko P. Grozdanov and Ronald McCarroll <b>MODIFIED STATISTICAL MODEL FOR CH<sup>+</sup>+H→C<sup>+</sup> +H<sub>2</sub> REACTION</b> .....	23
<i>SI.3</i> M. Vojnović, M. Popović, M. M. Ristić, M. Vičić and G. Poparić <b>RATE COEFFICIENTS IN CROSSED E AND B FIELDS IN CO</b> .....	27
<i>SI.4</i> Nenad Simonović <b>ANALYSIS OF ADIABATIC POTENTIAL CURVES OF HELIUM IN TERMS OF CLASSICAL CONFIGURATION</b> .....	31
<i>SI.5</i> V. Stojanović, J. Sivoš, D. Marić, N. Škoro and Z. Lj. Petrović <b>MONTE CARLO SIMULATION OF ELECTRON TRANSPORT IN H<sub>2</sub>O VAPOUR</b> .....	35
<i>SI.6</i> J. Jose, H. R. Varma, P. C. Deshmukh, S. T. Manson and V. Radojević <b>CORE CORRELATION EFFECTS IN THE VALENCE PHOTODETACHMENT OF Cu<sup>-</sup></b> .....	39
<i>SI.7</i> M. P. Popović, M. M. Vojnović, M. M. Ristić, M. Vičić and G. B. Poparić <b>RATE COEFFICIENTS FOR ELECTRON IMPACT IONIZATION IN RF ELECTRIC FIELD IN NITROGEN</b> .....	43
<i>SI.8</i> J. J. Jureta, A. R. Milosavljević and B. P. Marinković <b>ELECTRON IMPACT STUDY OF AUTOIONIZING STATES IN NEON</b> .....	47
<i>SI.9</i> V. M. Ristić, M. M. Radulović, T.M. Miladinović and J.S. Stefanović <b>A NEW TESTING OF THE NOETHER'S THEOREM COROLLARY</b> .....	51
<i>SI.10</i> A. R. Milosavljević, F. Canon, J. B. Maljković, L. Nahon and A. Giuliani <b>PHOTODISSOCIATION OF PURE AND NANO- SOLVATED PROTONATED LEUCINEENKE- PHALIN PEPTIDE</b> .....	55

## SECTION 2.

### Invited Lectures

<i>G2.1</i> Dimitri Batani <b>PRELIMINARY RESULTS FROM RECENT EXPERIMENTS AND FUTURE ROADMAP TO SHOCK IGNITION FOR INERTIAL CONFINEMENT FUSION</b> .....	61
<i>G2.2</i> Uroš Cvelbar <b>THE ORIGIN OF THE PLASMA GROWN</b>	

<b>NANOSTRUCTURES AT THE SOLID-SOLID INTERFACE</b>	63
<i>G2.3</i> J. Hermann, L. Mercadier, S. Noël, E. Axente, S. Beldjilali, M. Ćirišan, E. Mothe and W. L. Yip	
<b>PROPERTIES OF PLASMAS PRODUCED BY LASER ABLATION WITH SINGLE AND DOUBLE PULSES</b>	64
<i>T2.1</i> T. Ikeda	
<b>GUIDING OF SLOW HIGHLY CHARGED IONS THROUGH TAPERED GLASS CAPILLARIES</b>	65
<i>T2.3</i> V. Milosavljević	
<b>COMPREHENSIVE PLASMA DIAGNOSTICS FOR AN ECR ETCHER</b>	66
<i>T2.4</i> J. L. Gervasoni	
<b>ON PLASMON PROPERTIES OF NANOMETRIC SYSTEMS EXPOSED TO ION BOMBARDMENT</b>	67
<i>P2.1</i> S. M. D. Galijaš, N. N. Nedeljković, M. D. Majkić and M. A. Mirković	
<b>THE NON-REZONANT NEUTRALIZATION DYNAMICS OF THE MULTIPLY CHARGED RYDBERG IONS ESCAPING SOLID SURFACES</b>	69
<i>P2.2</i> M. D. Majkić, N. N. Nedeljković and S. M.D. Galijaš	
<b>INTERMEDIATE STAGES OF THE NEUTRALIZATION OF MULTIPLE CHARGED IONS INTERACTING WITH SOLID SURFACES</b>	70
<i>P2.3</i> Suzana Petrović	
<b>COMPOSITION AND STRUCTURE MODIFICATION OF A WTi/Si SYSTEM BY NANOSECOND AND PICOSECOND LASER PULSES</b>	71
<i>P2.4</i> M. Radović	
<b>LOW DIMENSIONAL TI-OXIDE BASED STRUCTURE: FROM SrTiO<sub>3</sub> TO TiO<sub>2</sub></b>	73
<i>P2.5</i> G. Wachter, C. Lemell and J. Burgdörfer	
<b>ELECTROM EMISSION FROM A METAL NANOTIPE BY ULTRASHORT LASER PULSES</b>	74
<i>P2.6</i> M. Zlatar, O. May, M. Gruden-Pavlović and M. Allan	
<b>DISSOCIATIVE ELECTRON ATTACHMENT MEASUREMENTS AND TDDFT CALCULATIONS OF THE EXCITATION ENERGIES IN Pt(PF<sub>3</sub>)<sub>4</sub>: SYNERGY BETWEEN THE EXPERIMENT AND THEORY</b>	75
<b>Contributed papers</b>	
<i>S2.1</i> A. R. Milosavljević, R. J. Berezky, M. Kovačević, K. Tőkési and B. P. Marinković	79
<b>ENERGY AND ANGULAR DISTRIBUTION OF ELECTRONS TRANSMITTED THROUGH A SINGLE GLASS MICROCAPILLARY</b>	
<i>S2.2</i> M. Nenadović, J. Potočnik, S. Štrbac and Z. Rakočević	
<b>SURFACE MODIFICATION OF HIGH DENSITY</b>	

<b>POLYETHYLENE BY GOLD ION IMPLANTATION</b> .....	83
<i>S2.3</i> I. Radović, D. Borka and Z. L. Mišković	
<b>ENERGY LOSS OF CHARGED PARTICLES MOVING OVER MULTILAYER GRAPHENE</b> .....	87
<i>S2.4</i> N. N. Nedeljković, M. D. Majkić, S. M. D. Galijaš and M. A. Mirković	
<b>POPULATION PROBABILITIES OF MULTIPLY CHARGED IONS INTERACTING WITH SOLID SURFACE: PARALLEL VELOCITY EFFECT</b> .....	91
<i>S2.5</i> S. M. D. Galijaš, N. N. Nedeljković, M. D. Majkić and I. P. Prlina	
<b>POPULATION OF THE RYDBERG STATES OF THE ArVIII, KrVIII AND XeVIII IONS AT SOLID SURFACE FOR GRAZING INCIDENCE</b> .....	95
<i>S2.6</i> M. D. Majkić, N. N. Nedeljković, R. J. Dojčilović and M. B. Obradović	
<b>TVM v.s. KINETIC ENERGY GAIN FOR MULTIPLY CHARGED IONS INTERACTING WITH SOLID SURFACES</b> .....	99
<i>S2.7</i> J. Pajović, R. J. Dojčilović, D. K. Božanić, F. G. Kilibarda and N. N. Nedeljković	
<b>ANALYSIS OF SIGNAL BROADENING IN CHARGE TRANSFER PROCESSES BETWEEN RYDBERG ATOMS AND METAL SURFACE</b> .....	103
<i>S2.8</i> V. Borka Jovanović and D. Borka	
<b>SPATIAL DISTRIBUTION S OF BODIES IN HENON-HÉILES INTERACTION POTENTIAL</b> .....	107
<i>S2.9</i> M. Novaković, A. Traverse, M. Popović, K.P. Lieb, K. Zhang and N. Bibić	
<b>EFFECTS OF VANADIUM IONS IRRADIATION ON THE MICROSTRUCTURE OF CrN LAYERS</b> .....	111
<i>S2.10</i> M. Popović , M. Novaković , M. Šiljegović and N. Bibić	
<b>MICROSTRUCTURAL CHANGES OF TiN FILMS INDUCED BY 200 keV ARGON IONS</b> .....	115

### SECTION 3.

#### Invited Lectures

<i>G3.1</i> A. Bogaerts, M. Yusupov, W. Van Gaens, R. Aerts, M. Mao, W. Somers and E. Neyts	
<b>MODELING OF PLASMA AND PLASMA SURFACE INTERACTIONS FOR ENVIRONMENTAL, MEDICAL AND NANO APPLICATIONS</b> .....	121
<i>G3.2</i> U. Ebert	
<b>EXTREMELY FAR FROM EQUILIBRIUM: THE MULTISCALE DYNAMICS OF STREAMER</b> .....	122
<i>G3.3</i> M. Kushner	
<b>MODEL BASED DESIGN OF LOW TEMPERATURE</b>	

<b>PLASMA REACTORS</b>	123
<i>G3.4</i> J-M. Pouvesle	
<b>ANTITUMORAL EFFECT OF NON THERMAL PLASMAS ALONE OR IN COMBINATION WITH CHEMOTHERAPY</b>	124
<i>G3.5</i> H-E. Wagner	
<b>THE COMPLEX DIAGNOSTICS OF BARRIER DISCHARGES - AN EXPERIMENTAL CHALLENGE</b>	125
<i>T3.1</i> J. A. Aparicio, M. T. Belmonte, R. J. Peláez, S. Djurović and S. Mar	
<b>EXPERIMENTAL TRANSITION PROBABILITY MEASUREMENTS IN PULSED LAMPS: CRITICAL POINTS</b>	127
<i>T3.2</i> A. Bultel, J. Annaloro and V. Morel	
<b>PHYSICO-CHEMISTRY OF PLANETARY ATMOSPHERIC ENTRY PLASMAS</b>	128
<i>T3.4</i> E. Kovacevic, J. Berndt, H. Acid, Th. Maho and L. Boufendi	
<b>THE PLASMA BASED FORMATION AND FUNCTIONALIZATION OF NANOPARTICLES AND NANOCOMPOSITE MATERIALS</b>	130
<i>T3.5</i> Djordje Spasojevic	
<b>CATHODE SHEATH AND HYDROGEN BALMER LINES MODELING IN A MICRO-HOLLOW GAS DISCHARGES</b>	131
<i>P3.1</i> N. Cvetanović	
<b>INVESTIGATION OF ENERGETIC HYDROGEN ATOMS IN GLOW DISCHARGES</b>	132
<i>P3.2</i> Saša Lazović	
<b>DIAGNOSTICS AND BIOMEDICAL APPLICATIONS OF RADIOFREQUENCY PLASMAS</b>	133
<i>P3.3</i> Andrej Mihelič	
<b>STUDIES OF MULTIPHOTON PROCESSES IN NOBLE GAS ATOMS</b>	134
<i>P3.4</i> N. M. Šišović	
<b>SPECTROSCOPIC STUDY OF HYDROGEN BALMER LINE SHAPES IN A HOLLOW CATHODE GLOW DISCHARGE IN NH<sub>3</sub> AND Ar/NH<sub>3</sub>, Ar/CH<sub>4</sub> AND Ar/C<sub>2</sub>H<sub>2</sub> MIXTURES</b>	135
<i>P3.5</i> Nikola Škoro	
<b>BREAKDOWN AND DISCHARGE REGIMES IN STANDARD AND MICROMETER SIZE DC DISCHARGES</b>	136

#### Contributed Papers

<i>S3.1</i> M. Bartlova, V. Aubrecht, N. Bogatyreva	
<b>CALCULATION OF RADIATION TRANSFER IN</b>	

<b>SF6 ARC PLASMAS USING THE P1- APPROXIMATION</b>	139
<i>S3.2</i> M. T. Belmonte, J. A. Ap aricio, R. J. Peláez, S. Djurović and S. Mar	
<b>TRANSITION PROBABILITIES MEASUREMENTS OF SEVERALXE II LINES</b>	143
<i>S3.3</i> A. Bojarov, M. Radmilović-Radjenović and Zoran Lj. Petrović	
<b>EFFECTS OF THE SECONDARY ELECTRON EMISSION INDUCED BY ARGON IONS AND FAST NEUTRALS</b>	147
<i>S3.4</i> M. Ćirisan, M. Cvejić, J. Hermann, S. Jovićević and N. Konjević	
<b>STUDY OF THE OPTICAL THICKNESS OF LASER-INDUCED PLASMA FOR IMPROVED CALIBRATION-FREE LIBS ANALYSIS</b>	151
<i>S3.5</i> M. Cvejić, M. Gavrilović and S. Jovićević	
<b>PROCEDURE FOR PROCESSING SPECTRAL IMAGES AND SELFABSORPTION CORRECTION</b>	155
<i>S3.6</i> J. Cvetić, R. Djuric, M. Ponjavic, D. Sumarac and Z. Trifkovic	
<b>GENERALIZED LIGHTNING TCS MODEL WITH CURRENT REFLECTIONS</b>	159
<i>S3.7</i> J. Cvetić, R. Djuric, M. Ponjavic, D. Sumarac and Z. Trifkovic	
<b>MODIFIED LIGHTNING TRAVELING CURRENT SOURCE RETURN STROKE MODEL</b>	163
<i>S3.8</i> S. Djurović, Z. Mijatović, Z. Nađ, L. Gavanski and R. Kobilarov	
<b>INCIDENT SHOCK FRONT VELOCITY MEASUREMENTS IN AT-TUBE</b>	167
<i>S3.9</i> S. Djurović, Z. Mijatović, R. Kobilarov and I. Savić	
<b>LIGHT INTENSITY OSCILLATIONS IN WALL STA BILIZED ARC DURING HIGH CURRENT PULSES</b>	171
<i>S3.10</i> M. Gavrilović, M. Cvejić, S. Jovićević and N. Konjević	
<b>CHARACTERIZATION OF LASER-INDUCED PLASMA BY OPTICAL EMISSION SPECTROSCOPY</b>	175
<i>S3.11</i> M. Gavrilović, S. Jovićević and N. Konjević	
<b>SPECTROSCOPIC CHARACTERISATION OF MICRO APGD IN HELIUM</b>	179
<i>S3.12</i> M. Ivković, M. Á. González, N. Lara, M. A. Gigosos and N. Konjević	
<b>THE STARK BROADENING OF THE HE I 492.1 NM LINE WITH FORBIDDEN COMPONENTS IN DENSE COOL PLASMA</b>	183
<i>S3.13</i> J. Jovović, S. Stojadinović, N. M. Šišović and N. Konjević	
<b>EMISSION SPECTROSCOPY OF PLASMA DURING</b>	

<b>ELECTROLYTIC OXIDATION (PEO) OF Mg- AND Al-ALLOY</b>	187
<i>S3.14</i> J. Jovović, I. L. Epstein, N. Konjević, Yu. A. Lebedev, N. M. Šišović and A.V. Tatarinov	
<b>SPECTROSCOPIC AND 2D MODELING STUDY OF THE INFLUENCE OF SMALL HYDROGEN ADDITION IN NONUNIFORM NITROGEN MICROWAVE DISCHARGE</b>	191
<i>S3.15</i> V. V. Kovačević, R. Brandenburg, B. M. Obradović, G. B. Sretenović and M. M. Kuraica	
<b>CHARACTERISTICS OF TOLUENE DEGRADA- TION BY WATER FALLING FILM DBD REACTOR</b>	195
<i>S3.16</i> F. Krcma, V. Mazan kova and I. Teslikova	
<b>MEASUREMENT OF N<sub>2</sub>(X, v=19) METASTABLES DURING THE NITROGEN POST-DISCHARGE BY MERCURY VAPOR TITRATION</b>	199
<i>S3.17</i> I. Filatova, V. Azharonok, S. Goncharik, G. Gadzhieva and A. Zhukovsky	
<b>LOW-TEMPERATURE AIR PLASMA PRESOWING SEEDS TREATMENT AGAINST PHYTO- PATHOGENIC FUNGI AND BACTERIA</b>	203
<i>S3.18</i> I. B. Krstić, G. B. Sretenović, V. V. Kovačević, B. M. Obradović and M. M. Kuraica	
<b>ELECTRICAL AND SPECTRAL CHARACTERISTICS OF DBD PLASMA JET</b>	207
<i>S3.19</i> G. Lj. Majstorović and N. M. Šišović	
<b>SPECTROSCOPIC TEMPERATURE MEASURE- MENTS IN DEUTERIUM HOLLOW CATHODE GLOW DISCHARGE</b>	211
<i>S3.20</i> M. M. Martinović, I. P. Dojčinović and J. Purić	
<b>QUASISTATIONARY PLASMA FLOW AND EXTERNAL MAGNETIC FIELD ACTION ON THE SILICON SURFACE</b>	215
<i>S3.21</i> V. Morel, A. Bultel, G. Godard	
<b>IMPORTANCE OF MULTIPHOTON IONIZATION DURING THE CREATION OF ALUMINUM PLASMA PRODUCED BY LASER WITH MODERATE FLUENCE</b>	219
<i>S3.22</i> Ž. Nikitović, V. Stojanović and Z. Lj. Petrović	
<b>MONTE CARLO SIMULATIONS IN Ar/H<sub>2</sub> MIXTURES</b>	223
<i>S3.23</i> D. Šević, M. Rabasović and B. Marinković	
<b>DETECTING LEAD USING LASER INDUCED BREAKDOWN SPECTROSCOPY</b>	227
<i>S3.24</i> N. Škoro and E. Gogolides	
<b>CHARACTERIZATION OF HYDROGEN BASED RF PLASMAS SUITABLE FOR REMOVAL OF CARBON LAYERS</b>	231
<i>S3.25</i> G. B. Sretenović, I. B. Krstić, V. V. Kovačević, B. M. Obradović and M. M. Kuraica	

<b>SPECTROSCOPIC MEASUREMENTS OF ELECTRIC FIELD IN LOW FREQUENCY DBD PLASMA JET</b> .....	235
<i>S3.26</i> D. Zhechev and V. Steflekova	
<b>ON MAGNETO-INDUCED PROPERTIES OF HOLLOW CATHODE DISCHARGE</b> .....	239
<i>S3.27</i> D. Jevtić, I. P. Dojčinović, I. Tapalaga and J. Purić	
<b>STARK BROADENING REGULARITIES WITHIN NEUTRAL SODIUM SPECTRAL LINES</b> .....	245
<i>S3.28</i> I. P. Dojčinović, I. Tapalaga, M. Šćepanović and J. Purić	
<b>STARK BROADENING WITHIN 3s-np AND 3d-np SPECTRAL LINES OF NEUTRAL LITHIUM</b> .....	249
<i>S3.29</i> V. Lj. Marković, S. N. Stamenković, S. R. Gocić, A. P. Jovanović and M. N. Stankov	
<b>TRANSIENT REGIMES OF DC GLOW DISCHARGE IN ARGON AT LOW PRESSURE: EXPERIMENT AND MODELLING</b> .....	253
<i>S3.30</i> A. P. Jovanović, V. Lj. Marković, M. N. Stankov and S. N. Stamenković	
<b>STOCHASTICS OF ELECTRICAL BREAKDOWNS IN SYNTHETIC AIR</b> .....	257
<i>S3.31</i> M. Šćepanović, I. P. Dojčinović, I. Tapalaga, M. K. Milosavljević and J. Purić	
<b>STARK PARAMETERS REGULARITIES WITHIN TRANSITION ARRAYS OF MULTIPLY CHARGED IONS</b> .....	261
<i>S3.32</i> D. Bošnjaković, S. Dujko and Z. Lj. Petrović	
<b>ELECTRON TRANSPORT COEFFICIENTS IN GASES FOR RESISTIVE PLATE CHAMBERS</b> .....	265
<i>S3.33</i> V. Mihailov, R. Djulgerova, J. Koperski and Z. Lj. Petrović,	
<b>OPTOGALVANIC SIGNALS FROM IRON POSITIVE IONS IN HOLLOW CATHODE DISCHARGE</b> .....	269
<i>S3.34</i> J. Sivoš, N. Škoro, D. Marić, G. Malović and Z. Lj. Petrović	
<b>VOLT-AMPERE CHARACTERISTICS OF LOW PRESSURE DC DISCHARGES IN WATER VAPOR</b> .....	273
<i>S3.35</i> S. Vučić	
<b>ELECTRONIC DENSITIES OF ATOMS IN A LASER FIELD</b> .....	277
<i>S3.36</i> M. Burger, M. Skočić, Z. Nikolić, S. Bukvić and S. Djeniže	
<b>ON THE POPULATION PROCESSES IN THE In III</b> .....	281
<i>S3.37</i> M. Skočić, M. Burger, S. Bukvić and S. Djeniže	
<b>STARK BROADENING IN THE In III SPECTRUM</b> .....	285
<i>S3.38</i> M. Cvejić, S. Jovićević and N. Konjević	
<b>SPECTROSCOPIC CHARACTERISATION OF ATMOSPHERIC PRESSURE GLOW DISCHARGE</b> .....	289

<b>S3.39</b> S. Mijović, M. Vučeljić and M. Šćepanović <b>THE OPTICAL EMISSION SPECTROSCOPY EXPERIMENT OF OPEN AIR PLASMAS</b>	..... 293
<b>S3.40</b> M. Šćepanović, M. Vučeljić and S. Mijović, <b>SPECTROSCOPIC TEMPERATURE MEASURE- MENTS IN A FREE-BURNING ZINCVAPOR ELECTRIC ARC</b>	..... 297
<b>S3.41</b> S. N. Stamenković, V. Lj. Marković, S. R. Gocić, A. P. Jovanović, M. N. Stankov and N. D. Nikolić <b>INFLUENCE OF SURFACE CHARGES ON DC GLOW DISCHARGE IN NEON WITH Au-Ni CATHODE SPOTS</b>	..... 301
<b>S3.42</b> K. Spasić, S. Lazović, N. Puač, Z. Lj. Petrović, G. Malović, M. Mozetič and Uroš Cvelbar <b>CATALYTIC PROBE MEASUREMENTS OF ATOMIC OXYGEN CONCENTRATION IN LARGE VOLUME OXYGEN CCP</b>	..... 305
<b>S3.43</b> N. Selaković, D. Maletić, N. Puač, S. Lazović, G. Malović, A. Djordjević and Z. Lj. Petrović <b>AXIAL PROFILES OF PLASMA BULLET WITH DIFFERENT ELECTRODE GAPS</b>	..... 309
<b>S3.44</b> T. Gajo, I. Savić, R. Kobilarov and Z. Mijatović <b>STARK WIDTHS OF SEVERAL Ar II SPECTRAL LINES EMITTED FROM PULSED ARC PLASMAS</b>	..... 313
<b>S3.45</b> I. Savić, L. Gavanski, S. Djurović, Z. Mijatović and R. Kobilarov <b>ICCD SPECTROMETER – CHARACTERIZATION OF INSTRUMENTAL LINE PROFILES AND SATURATION LEVEL DETERMINATION</b>	..... 317
<b>S3.46</b> A. A. Kirillov, Y. A. Safronau, L. V. Simonchik, N. V. Dudchik and O. E. Nezhvinskaya <b>DC ATMOSPHERIC PRESSURE GLOW DISCHARGE COLD PLASMA FOR BACTERIA INACTIVATION</b>	..... 321
<b>S3.47</b> M. Savić, M. Radmilović-Radjenović, B. Radjenović <b>THEORETICAL PREDICTIONS OF THE MICROWAVE BREAKDOWN FIELD</b>	..... 325
<b>S3.48</b> M. Savić, M. Radmilović-Radjenović, D. Marić, M. Šuvakov, Z. Lj. Petrović <b>MONTE CARLO SIMULATIONS OF RF BREAKDOWN</b>	..... 329
<b>S3.49</b> S. Marjanović, A. Banković, M. Šuvakov, T. Mor- tensen, A. Deller, C. A. Isaac, D. P. van der Werf, M. Charlton, Z. Lj. Petrović <b>COLLISION-DRIVEN POSITRON CLOUD EXPANSION – EXPERIMENT AND SIMULATION</b>	..... 333
<b>S3.50</b> S. Marjanović, M. Šuvakov and Z. Lj. Petrović <b>MONTE CARLO SIMULATION OF POSITRON TRAPPING EFFICIENCY</b>	..... 337

<i>S3.51</i> V. Stojanović, Z. Raspopović, J. Jovanović, Ž. Nikitović, Z. Lj. Petrović <b>TRANSPORT OF F- IONS IN F2</b>	341
<i>S3.52</i> S. Dujko, A. Markosyan, R. D. White, U. Ebert <b>HIGH ORDER FLUID MODEL FOR STREAMER DISCHARGES</b>	345
<i>S3.53</i> M. S. Dimitrijević, S. Sahal-Bréchet, D. Jevremović, V. Vujčić and A. Kovačević <b>PROGRESS OF STARK-B DATABASE AND SERBIAN VIRTUAL OBSERVATORY</b>	349

## SECTION 4.

### Invited Lectures

<i>G4.1</i> V. M. Astashinski <b>ION-DRIFT ACCELERATION OF MAGNETIZED PLASMA IN QUASI-STATIONARY PLASMA ACCELERATORS</b>	355
<i>G4.2</i> G. Ferland <b>PLASMA SIMULATIONS FOR LASER FUSION</b>	356
<i>T4.1</i> H. Nagatomo <b>INTGRATED SIMULATIONS FOR LASER FUSION</b>	357
<i>T4.2</i> Laurence Campbell and Michael J. Brunger <b>ELECTRON IMPACT EXCITATION IN PLANETARY AND COMETARY ATMOSPHERES</b>	358
<i>T4.3</i> N. B. Nassib <b>AB INITIO DETERMINATION OF STARK BROADENING PARAMETERS AND APPLICATION IN ASTROPHYSICS</b>	359
<i>T4.4</i> Tsv. K. Popov, M. Dimitrova, P. Ivanova, J. Horacek, J. Stöckel, R. Dejarnac and COMPASS tokamak team <b>EVALUATION OF PLASMA POTENTIAL AND ELECTRON ENERGY DISTRIBUTION FUNCTION BY LANGMUIR PROBES IN MAGNETIZED PLASMA</b>	360
<i>T4.5</i> J. Rosato, Y. Marandet, V. Kotov, D. Reiter, H. Capes, L. Godbert-Mouret, R. Hammami, M. Koubiti and R. Stamm <b>PLASMA SPECTROSCOPY IN THE CONDITIONS OF THE ITER TOKAMAK</b>	362
<i>T4.6</i> T.-H.Watanabe, H. Sugama, M. Nunami and A. Ishizawa <b>KINETIC TRANSPORT SIMULATION STUDIES FOR NON-AXISYMMETRIC HELICAL PLASMA CONFINEMENT</b>	363
<i>P4.1</i> A. Antoniou, E. Danezis, E. Lyratzi, L. Č. Popović, M. S. Dimitrijević and D. Stathopoulos <b>THE STRUCTURE OF Si IV REGION IN Be STARS; A STUDY OF Si IV SPECTRAL LINES IN 68 Be STARS</b>	364

<i>P4.2</i> N. Gavrilović-Bon, E. Bon, P. Prugniel and L. Č. Popović	
<b>STELLAR POPULATION IN TYPE 2 ACTIVE GALACTIC NUCLEI</b>	..... 365
<i>P4.3</i> J. Kovačević and L. Č. Popović	
<b>THE PROPERTIES OF THE EMISSION LINES AND THEIR CORRELATIONS IN SPECTRA OF ACTIVE GALACTIC NUCLEI</b>	..... 366
<i>P4.4</i> D. Tankosić, M. M. Abbas	
<b>LABORATORY STUDIES OF CHARGING PROPER- TIES OF DUST GRAINS IN ASTROPHYSI- CAL/PLANETARY ENVIRONMENTS</b>	..... 367

#### Contributed Papers

<i>S4.1</i> G. Jovanović	
<b>GRAVITO-ACOUSTIC WAVES TRANSMISSION</b>	..... 371
<i>S4.2</i> D. Stathopoulos, E. Lyratzi, E. Danezis, A. Antoniou and D. Tzimeas	
<b>A STUDY OF THE C IV BALs IN HiBALQSO SPECTRA</b>	..... 375
<i>S4.2</i> A. Nina and V. M. Čadež	
<b>MODAL FREQUENCIES OF IONOSPHERIC PER- TURBATIONS INDUCED BY SOLAR X-FLARES</b>	..... 379
<i>S4.3</i> A. A. Mihajlov, V. A. Srećković, Lj. M. Ignjatović, M. S. Dimitrijević and A. Metropoulos	
<b>THE NON-SYMMETRIC ION-ATOM ABSORPTION PROCESSES IN THE STELAR ATMOSPHERES</b> □	..... 383
<i>S4.4</i> Lj. Stevanović and D. Milojević	
<b>STARK EFFECT FOR A CONFINED HYDROGEN ATOM WITH DEBYE SCREENING POTENTIAL</b> □	..... 389
<i>S4.5</i> J. Annaloro and A. Bultel	
<b>COLLISIONAL-RADIATIVE MODELS APPLIED TO ENTRY SITUATIONS IN EARTH OR MARS ATMOSPHERE</b>	..... 393
<b>Author Index</b>	..... 399

#### Post Deadline Contributons

<i>PDI-S3.1</i> Frantisek Krcma, Vera Sazavska, Petra Fojtikova, Lucie Radkova, Adam Kujawa, Radek Prikryl, Michal Prochazka, Radka Balastikova, Premysl Mencik, Lucie Blahova, Jakub Horak, Martin Zmrzly, Drahomira Janova	
<b>APPLICATION OF LOW TEMPERATURE PLASMAS FOR THE TREATMENT OF ANCIENT ARCHAEOLOGICAL OBJECTS</b>	..... Pd1

*PD2-S3.2* Nikola Škoro, Saša Gocić, Dragana Marić and  
Zoran Lj. Petrović

**INVESTIGATION OF DC BREAKDOWN IN  
NITROGEN: INFLUENCE OF PRESSURE AND  
ELECTRODE GAP VARIATION**

..... Pd5

# **SECTION 1.**

## **Atomic Collision Processes**

- 1.1 Electron and Photon Interactions with Atomic Particles
- 1.2 Heavy Particle Collisions
- 1.3 Swarms and Transport Phenomena

## **ABSTRACTS OF INVITED LECTURES**



## EXPERIMENTAL STUDIES ON $H_nD_m^+$ COLLISION SYSTEMS $n+m \leq 5$

Dieter Gerlich

*Institute of Physics, University of Technology, 09107 Chemnitz, Germany,  
Charles University, Faculty of Mathematics and Physics 121 16 Prague*

**Abstract:** The hydrogen atom, the diatomic molecules  $H_2^+$ ,  $H_2$ , and the simplest polyatomic molecule  $H_3^+$  play a central role in fundamental atomic and molecular science. In addition, detailed information on low temperature hydrogen and deuterium ion chemistry is of basic importance for tracing chemical and physical processes occurring in the early universe and in dense interstellar clouds. This contribution summarizes a variety of related activities emphasizing on past, present and future experimental work.

As discussed recently [1], the chemistry of  $H_nD_m^+$  systems is complicated by the fact that H and D atoms are fermions and bosons, respectively. Exchange symmetry in such polyatomic molecules or collision systems leads to rather stringent restrictions. A basic example is the ortho to para conversion in  $H^+ + H_2$  collisions (see Honvault *et al.* [2], note the Erratum). State of the art theories and a detailed comparisons between theory and experiment for  $D^+ + H_2$  and  $H^+ + D_2$  have been published recently [3], [4].

Present experimental activities include  $H_3^+$  formation at very low temperatures via radiative and ternary association in  $H^+ + H_2$  collisions [5], electron transfer in  $H^+ + D$  collisions, deuteration in  $H_3^+ + D$ , and the anionic system  $H^- + H$ .

**Acknowledgements:** I thank all my coworkers in Freiburg, Chemnitz and Prague. I am grateful for the hospitality of various groups, especially to S. Schlemmer, J. Roithova, and J. Glosik.

- [1] D. Gerlich, F. Windisch, P. Hlavenka, R. Plašil, J. Glosík, Phil. Trans. R. Soc. Lond. A 364 (2006) 3007
- [2] P. Honvault et al. Phys. Rev. Lett. 107, 023201 (2011), ERRATUM Phys. Rev. Lett. 108, 109903 (2012).
- [3] P.G. Jambrina, J.M. Alvarino, D.Gerlich, M. Hankel, V.J. Herrero, V. Saez-Rabanos, F.J. Aoiz, Phys. Chem. Chem. Phys., 14 (2012) 3346
- [4] T.P. Grozdanov and R. McCarroll, J. Phys. Chem. A, 116 (2012) 4569
- [5] R. Plašil, I. Zymak, P. Jusko, D. Mulin, D. Gerlich, J. Glosík, Phil. Trans. R. Soc. London, accepted

## **TRANSPORT AND COLLISION PHENOMENA INVOLVING ANTIPARTICLES AND ANTIHYDROGEN**

M. Charlton

*Physics Department, College of Science, Swansea University,  
Swansea SA2 8PP, United Kingdom*

**Abstract.** It is now relatively routine to form beams of positrons and antiprotons and to use them to produce trapped samples of both species for a variety of purposes. Positrons can be captured efficiently and in sufficient quantities to form dense, single component plasmas useful for antihydrogen formation, trapping and experimentation. The antihydrogen studies use antiprotons ejected from the Antiproton Decelerator at CERN, which are then manipulated by cloud compression and evaporative cooling to form tailored plasmas.

We will review recent advances that have led to antihydrogen atoms confined in a shallow magnetic minimum neutral atom trap for upwards of 1,000. We will place this in the context of antiparticle transport and collisions, often in the presence of strong electric and magnetic fields, which are integral features of the underlying physics.

The behaviour of positron clouds in the single-particle regime is also important, as devices operating in this regime can, for example, be used to form narrow energy-width beams for a rich variety of collision studies. We will describe how an understanding of positron transport physics is crucial for low energy beam formation, and to elucidate the behaviour of clouds and plasmas in trapping and accumulation devices. Work towards this aim is timely and may lead to an improved understanding of the underlying collision processes and enhanced instrumental capabilities and performance.

## PLASMA-WALL INTERACTIONS IN CESIATED H<sup>-</sup> ION SOURCES

Martin P. Stockli

*Spallation Neutron Source, Oak Ridge National Laboratory,  
Oak Ridge, TN37830, USA*

**Abstract.** The research and development to produce more intense H<sup>-</sup> ion beams is driven by the desire to increase the power of high-power proton accelerators as well as to efficiently heat fusion plasmas with neutral beams. For example the Spallation Neutron Source is currently operating with a 1 MW proton beam to produce intense pulses of moderated neutrons for many different neutron scattering experiments. Significantly increasing the number of neutrons requires the reliable production of H<sup>-</sup> beams with significantly more than 40 mA at a 6% duty factor and a normalized rms emittance not exceeding 0.3  $\pi$  mm-mrad.

The historic breakthrough in producing intense H<sup>-</sup> beams occurred in 1970 when Cesium was introduced into the hydrogen plasma. Its success triggered a large amount of research and development to understand and/or enhance the production of H<sup>-</sup>. In essence, Cesium has a low work function which enhances the capture of an extra electron when an atom leaves a surface. This enhancement seems to favor a fractional monolayer of Cs on certain metal substrates, such as Molybdenum.

As lowering the work function enhances the production of negative ions, it also enhances the emission of electrons, especially from the charged surfaces of negative ion sources and associated negative focusing electrodes. When such emissions grow out of control, the voltages break down and the system becomes inoperable. More reliable are Cesium-free H<sup>-</sup> sources that compromise some of the H<sup>-</sup> yield.

The SNS H<sup>-</sup> source is capable of delivering persistent H<sup>-</sup> beams for up to 6 weeks after releasing an initial dose of a few mg of Cs, which is over three orders of magnitude less than the consumption of other cesiated H<sup>-</sup> sources. The lecture will discuss the evidence that suggests that this is due to a persistent fractional monolayer of Cs, which resists sputtering and thermal emission when properly operated.

## **PHOTOIONIZATION OF ATOMIC AND MOLECULAR POSITIVELY CHARGED IONS**

Jean-Marc Bizau

*Institut des Sciences Moléculaires d'Orsay, CNRS, Bât. 350, Université Paris-Sud, 91405 Orsay cedex, France*

Photoionization (PI) of ionic species is a key process for the modeling of many plasmas, including laser produced plasmas, planetary ionospheres and astrophysical plasmas. The knowledge of PI cross sections is required over extended ionic charge stages and photon energies, both parameters of increasing magnitude with increasing plasma temperature. Until a recent past, few experiments were performed on PI processes, facing the difficulty to combine a high density ionic target with a high flux of X ray radiation. Most of the data on these processes are known mainly from models using more or less sophisticated approximations for the description of electron correlation effects [1-3]. Only with the advent of high photon flux available at synchrotron radiation facilities the experiments have developed. First, merged beams set ups have been used, allowing the determination in absolute values of PI cross sections for ions with charge stages up to 10 [4,5]. One difficulty of this technique consists in an ionic target often composed of a mixture of ions in the ground and metastable states. During the last three years, a new approach is in rapid expansion: the use of ion traps. It has allowed the measurements of PI cross sections on relaxed ions [6], on more highly charged ions [7] and large molecular ions and clusters [8,9]. We will present at the conference recent results we have obtained at SOLEIL, the French synchrotron radiation facility, on the PI of atomic and small molecular positively charged ions, using both a merged beams set up and an ion trap.

### **REFERENCES**

- [1] R. F. Reilmann and S. T. Manson, *ApJS*, 10, 815 (1979).
- [2] D. A. Verner and D. G. Yakovlev, *Astron. Astrophys. Suppl.Ser.* 109, 125 (1995).
- [3] N. R. Badnell *et al*, *MNRAS* 360, 458 (2005).
- [4] J. B. West, *J. Phys. B* 34, R45 (2001).
- [5] H. Kjeldsen, *J. Phys. B* 39, R325 (2006).
- [6] R. Thissen *et al*, *Phys Rev Lett* 100, 223001 (2008).

- [7] M. C. Simon *et al*, J. Phys. B: At. Mol. Opt. Phys. 43, 065003 (2010).
- [8] K. Hirsch *et al*, J. Phys. B: At. Mol. Opt. Phys. 42, 154029 (2009).
- [9] A. R. Milosavljevic *et al*, Phys. Chem. Chem. Phys., 13, 15432 (2011).

## VIBRATIONALLY INELASTIC COLLISIONS OF SLOW ELECTRONS WITH MOLECULES

Roman Čurík<sup>\*</sup>, Petr Čárský<sup>\*</sup>, Michael Allan<sup>†</sup>

<sup>\*</sup>*J. Heyrovský Institute of Physical Chemistry of the ASCR, v.v.i., Dolejškova 3, 18223 Prague*

<sup>†</sup>*Department of Chemistry, University of Fribourg, CH-1700 Fribourg, Switzerland*

Some of lighter hydrocarbons are known as sources of carbon atoms during chemical vapour decomposition reactions. For example, cyclopropane was detected in cooler edges of the fusion plasmas. The interaction of these molecules with free electrons is important for initiating variety of processes.

Recent developments in DMR method [1] now allows to calculate electron-impact vibrational excitation of larger molecular targets aiming in near future for molecules deposited on surfaces. As a side benefit the model also allows fairly accurate computations of vibrational excitation of polyatomic molecules. Our present study concerns cyclopropane molecule for which the most marked feature observed by experiments [2] was assumed to be the excitation of  $\nu_3$  vibration, the C-C ring stretching. Our computational results indicate that the experimental data are a result of 3 overlapping modes, namely the C-C ring stretch  $\nu_3$  an HCH twisting modes  $\nu_{13}$  and  $\nu_4$  as shown in Fig. 1.

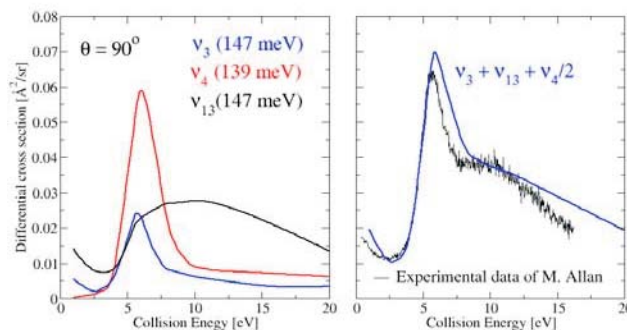


**Figure 1.** Left panel: differential cross section for vibrational excitation of three different modes of cyclopropane as a function of collision energy. Right panel: the sum of all three contributions with assumed experimental half-width of 16 meV.

### References

- [1] P. Čárský, R. Čurík, Š. Varga, *J. Chem. Phys.* **136**, 114105 (2012).  
 [2] M. Allan and L. Andric *J. Chem. Phys.* **105**, 3559 (1996).

## **SINGLE PHOTON DOUBLE K-SHELL IONIZATION OF SMALL MOLECULES**

F. Penent<sup>1</sup>, P. Lablanquie<sup>1</sup>, J. Palaudoux<sup>1</sup>, L. Andric<sup>1</sup>, P. Selles<sup>1</sup>, S. Carniato<sup>1</sup>,  
M. Žitnik<sup>2</sup>, T.P. Grozdanov<sup>3</sup>, E. Shigemasa<sup>4</sup>, K. Soejima<sup>5</sup>, Y. Hikosaka<sup>5</sup>, I. H.  
Suzuki<sup>6</sup>, M. Nakano<sup>6</sup> and K. Ito<sup>6</sup>

*1 LCP-MR, CNRS & Université P. VI, 11 rue P. et M. Curie, 75231 Paris Cedex 05, France*

*2 Jožef Stefan Institute, P. O. Box 3000, SI-1001 Ljubljana*

*3 Institute of Physics, University of Belgrade, Pregrevica 118, 11080 Belgrade, Serbia*

*4 UVSOR Facility, Institute for Molecular Science, Okazaki 444-8585, Japan*

*5 Department of Environmental Science, Niigata University, Niigata 950-2181, Japan*

*6 Photon Factory, Institute of Materials Structure Science, Oho, Tsukuba 305-0801, Japan*

Although the interest of molecular double core hole states (DCHs) for ESCA (Electron Spectroscopy for Chemical Analysis) was pointed out 25 years ago [1], their observation has been possible only very recently, thanks to the development of two different approaches: multi-photon core ionization using XFEL sources [2] or single photon double core ionization using synchrotron sources [3,4]. We have demonstrated that the latter method provides detailed information on the spectroscopy and decay dynamics of DCHs, even if the associated double photoionization cross section is extremely weak. We have observed single-site DCHs, (ss-DCHs:  $K^{-2}$ ) where the two core holes are created on the same atom of the molecule [3], and also two-site DCHs, (ts-DCHs:  $K^{-1}K^{-1}$ ), where the two core holes are on different atoms [4].

The experiments were performed at Photon Factory (Japan) and at SOLEIL (France) using a magnetic bottle time-of-flight spectrometer. We have studied simple molecules:  $N_2$ ,  $O_2$ ,  $CO$ ,  $CO_2$  and  $C_2H_{2n}$  ( $n=1, 2, 3$ ). By detecting in coincidence two photoelectrons with one or two Auger electrons, we have characterized ss-DCHs and ts-DCHs: their binding energies, their respective Auger decay paths and their relative intensity with respect to  $K^{-1}$  single ionization. Single photon double ionization leading to ss-DCHs represents a  $\sim 10^{-3}$  fraction of single K-shell ionization, this figure drops to  $\sim 10^{-5}$  for ts-DCHs formation. A simple collisional knock out model, where an initially ionized K-shell electron hits and ejects a second K-shell electron from the neighboring C atom accounts for this ratio.

These results raise important questions for the theoretical description of the formation, spectroscopy and decay mechanisms of these highly excited species. We will present at the conference our most recent results on photon double K-shell ionization.

**References**

- [1] L. S. Cederbaum et al., J. Chem. Phys. 85, 6513 (1986).
- [2] N. Berrah et al., Proc. Natl. Acad. Sci. U.S.A. **108**, 16912 (2011)
- [3] P. Lablanquie et al., Phys. Rev. Lett. **106**, 063003 (2011).
- [4] P. Lablanquie et al., Phys. Rev. Lett. **107**, 193004 (2011).

## **CITIUS AND LDM@FERMI: VUV LIGHT SOURCES FOR ULTRAFAST SPECTROSCOPY ON ATOMS AND MOLECULES**

Marcello Coreno<sup>1,2</sup>

<sup>1</sup> *CNR-IMIP, Area della Ricerca di Roma, 00016 Monterotondo Scalo (RM), ITALY*

<sup>2</sup> *Sincrotrone Trieste, in Basovizza AREA Science Park, 34149 Trieste, ITALY  
E-mail: marcello.coreno@elettra.trieste.it*

Spectroscopic investigations on the electronic structure of matter profit from continuous advances in laser and synchrotron radiation instrumentation. At the Elettra synchrotron radiation laboratory (Trieste, I) two novel facilities for atomic, molecular and cluster studies with ultrafast VUV photon pulses are currently under commissioning in the framework of the FERMI@Elettra Free Electron Laser (FEL) project: the Low Density Matter beamline at FERMI and CITIUS, a state of the art fs-VUV source, based on laser High Harmonic Generation on rare gases.

The Low Density Matter beamline (LDM) has been recently installed at the FERMI FEL [1]. The current status of activity and results of preparatory experiments will be outlined.

CITIUS, the Interregional Center of Photonic Technologies for Ultrafast Spectroscopy, is an Italo-Slovenian initiative funded within the FP7 Cross Border Cooperation Program to establish a laboratory for ultrafast spectroscopy and femtochemistry experiments at the Ajdovščina campus of Nova Gorica University. The CITIUS VUV light source is based on laser HHG in rare gases and it has been assembled at Elettra, where it is also being characterized [2]. After the commissioning phase it will be moved to Nova Gorica University, where a scientific program in the field of femtochemistry will be carried out in close collaboration with the LDM beam line at FERMI.

### **REFERENCES**

- [1] <http://www.elettra.trieste.it/lightsources/fermi/fermi-beamlines/ldm/ldmhome-page.html>
- [2] <http://www.elettra.trieste.it/lightsources/labs-and-services/citius/citius.html>

## **DIFFERENTIAL CROSS SECTIONS AT 0° AND 180° FOR ELECTRON IMPACT EXCITATION OF H<sub>2</sub> AND CO**

M. M. Ristić<sup>1</sup>, G. B. Poparić<sup>2</sup> and D. S. Belić<sup>2</sup>

<sup>1</sup>*Faculty of Physical Chemistry, University of Belgrade, P.O. Box 137, 11000 Belgrade, Serbia*

<sup>2</sup>*Faculty of Physics, University of Belgrade, P.O. Box 44, 11000 Belgrade, Serbia*

Low energy electron impact excitation of the H<sub>2</sub> and CO molecules has been investigated by use of a crossed beam double trochoidal electron spectrometer in the pulsed mode of operation by the time-of-flight detection of scattered electrons [1], [2]. The forward and backward scattered electrons from the  $^2\Sigma_u^+$  shape resonance in the  $v=0 \rightarrow 1$  vibrational excitation channel of the H<sub>2</sub> molecule have been analyzed. Impact electron energies were 1, 1.5, 2.5 and 5 eV. The same type of experiment has been performed for analyzing electrons in resonant excitation of  $v'=0$  vibrational level of the  $a^3\Pi$  valence state of CO, with impact electron energies of 6.5, 7, 8, 9 and 9.7 eV.

In the both cases, the appropriate normalization procedure has been applied in order to obtain the absolute differential cross section values at 0 and 180°. Comparisons with available experimental measurements [2]-[6] and theoretical predictions [7], [8] have been made.

### **REFERENCES**

- [1] M. Allan, *J. Electron Spectrosc. Relat. Phenom.* 48, 219 (1989).
- [2] G. B. Poparić, S. M. D. Galijaš and D. S. Belić, *Phys. Rev. A* 70, 024701 (2004).
- [3] J. Zobel, U. Mayer, K. Jung and H. Ehrhardt, *J. Phys. B* 29, 813 (1996).
- [4] M. J. Brunger, S. J. Buckman, D. S. Newman and D. T. Alle, *J. Phys. B* 24, 1435 (1991).
- [5] H. Nishimura, A. Danjo and H. Sugahara, *J. Phys. Soc. Jpn.* 54, 1757 (1985).
- [6] F. Linder and H. Schmidt, *Z. Naturforsch.* 26a, 1603 (1971).
- [7] M. A. Morrison, R.W. Crompton, B. C. Saha and Z. Lj. Petrović, *Aust. J. Phys.* 40, 239 (1987).
- [8] T. N. Rescigno, B. K. Elza and B. H. Lengsfeld, *J. Phys. B* 26, L576 (1993).

## **MEASUREMENTS OF DIFFERENTIAL CROSS SECTIONS FOR ELASTIC ELECTRON SCATTERING AND ELECTRONIC EXCITATION OF SILVER AND LEAD ATOMS**

S. D. Tošić

*Laboratory for Atomic Collision Processes, Institute of Physics,  
University of Belgrade, Pregrevica 118, 11080 Belgrade, Serbia*

The results of experimental research on elastic and inelastic medium electron scattering from lead and silver atoms are presented. Generally, electron interaction with metal atom vapours is providing fundamental information on structure and collisional dynamics of atomic system, as well as information on basic interaction between particles in scattering process. The main observable in these processes is differential cross section (DCS). While giving the probability of specific interaction at certain electron energy and scattering angle, the measured DCS data set provide more rigorous test for different theoretical models.

This paper presents absolute differential cross sections (DCSs) for both elastic and inelastic electron scattering by lead and silver atoms in the energy range from 10 to 100 eV. The DCSs were measured as a function of scattering angle. Scattering angles are from  $1^\circ$  to  $150^\circ$  for the excitations of the unresolved  $4d^{10}5p^2P_{1/2, 3/2}$  silver line and  $6p7s^3P_{0,1}$  lead line, while for the elastic scattering they span from  $10^\circ$  to  $150^\circ$ . The measurements utilize crossed beam technique with effusive atomic beam being perpendicularly crossed by electron beam. Monoenergetic electron beam is obtained by means of hemispherical selector and it is focused by cylindrical electrostatic lenses while effusive atomic beam was formed by heating of Knudsen type oven. Absolute values for the resonance states are obtained by normalization of relative differential cross sections to the optical oscillator strengths, while the absolute values for the elastic scattering are obtained from the intensity ratios at particular scattering angles. The experimental results have been compared with the corresponding calculations.

### **Acknowledgements**

The work was supported by the Ministry of Education and Science of Republic of Serbia (Project No. 171020).

## **DISSOCIATIVE ELECTRON ATTACHMENT TO SMALL MODEL MOLECULES**

Dušan Kubala, Olivier May and Michael Allan

*Address: Department of Chemistry, Chemin du musée 9, 1700 Fribourg,  
Switzerland*

Interaction of electrons with molecules gives rise to many interesting physical and chemical processes. One of the most efficient interaction channels for electrons with very low energy ( $<20$  eV) is attachment to molecule, that may lead to dissociation of the molecule (DAE) and formation of new chemical species. Despite the rapid development of computational hardware and improvement of computational techniques, there does not exist reliable theoretical approach to description of DAE and its dynamics. This motivated us to start a series of experimental studies dedicated to basic model molecules (for their simplicity) that could help theorist to shed new light into this problematic. Our molecules of interest were HCN and HCOOH and all their deuterated isotopologues. Both molecules were observed in outer space and DEA to them could play role in chemistry governing synthesis of more complex molecules in the interstellar media and atmosphere of extra-terrestrial bodies [1, 2].

DEA cross sections for production of formate anions and cyanide anions have been measured (Fig. 1) under the resolution of approximately 60 meV by standard trochoidal electron monochromator/quadrupole mass spectrometer instrument and subsequently normalized to absolute values from recently constructed time-of-flight/TEM instrument [3]. The measured spectra were compared to the theoretical prediction of multidimensional model of Rescigno and Oreel [4, 5] and non-local quasi one-dimensional R-matrix model of Gallup *et al.* [6] Some more general patterns have been found comparing the recent spectra with vibrational and DEA spectra of acetylene and several halogen halides, measured by May, Fedor and Allan. [7]

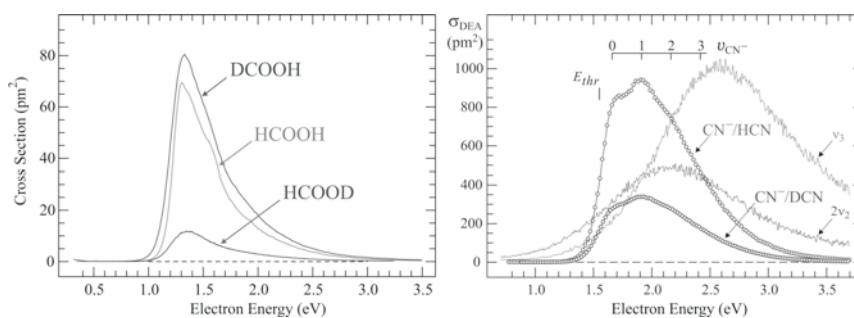


**Figure 1.** Left – cross section for production of formate anions via DEA to the three isotopologues of formic acid; right circles – cross section for production of CN<sup>-</sup> via DEA to HCN and DCN; right solid lines – cross sections for production of HCN in vibrationally excited states. [8]

## REFERENCES

- [1] S. D. Rodgers, S. Charnley, *Mon. Not. R. Astron. Soc.* **320**, L61 (2001).
- [2] S. Gupta, E. Ochiai, P. Ponnampereuma, *Nature (London)* **293**, 725 (1981).
- [3] J. Fedor, O. May, M. Allan, *Phys. Rev. A* **78**, 032701 (2008).
- [4] S. T. Chourou, A. E. Orel, *Phys. Rev. A* **80**, 034701 (2009).
- [5] T. N. Rescigno, C. S. Trevisan, A. E. Orel, *Phys. Rev. Lett.* **96**, 213201 (2006).
- [6] G. A. Gallup, P. D. Burrow, I. I. Fabrikant, *Phys. Rev. A* **79**, 042701 (2009).
- [7] J. Fedor, O. May, M. Allan, *Phys. Rev. A* **78**, 032701 (2008).
- [8] O. May, D. Kubala, M. Allan, *Phys. Rev. A* **82**, 010701(R) (2010).



# **SECTION 1.**

## **Atomic Collision Processes**

- 1.1 Electron and Photon Interactions with Atomic Particles
- 1.2 Heavy Particle Collisions
- 1.3 Swarms and Transport Phenomena

## **CONTRIBUTED PAPERS**



## CHARGE EXCHANGE IN FAST

### $\text{Li}^{3+}$ – He COLLISIONS

I. Mančev and N. Milojević

*Department of Physics, Faculty of Science and Mathematics,  
University of Niš, 18000 Niš, Serbia*

**Abstract.** Total cross sections are computed for single electron capture from the ground state of He by fast  $\text{Li}^{3+}$  ions using the four-body corrected first Born (CB1-4B) approximation. The effect of the dynamic electron correlation is explicitly taken into account through the complete perturbation potential. Detailed comparisons with the available experimental data are carried out, with the purpose of assessing validity of the CB1-4B method for prediction of total cross sections.

#### 1. INTRODUCTION

In recent years much effort has been concentrated on the four-body theories which involve non-relativistic fast ion-atom collisions with two actively participating electrons. Various quantum-mechanical four-body methods have been proposed to study one- and two-electron transitions in scattering of completely stripped projectiles on helium-like atomic systems or in collisions between two hydrogen-like atoms or ions (see for example [1, 2] and references quoted therein).

The four-body boundary corrected first Born approximation (CB1-4B) approximation for single electron capture has been formulated and implemented by Mančev and Milojević [3]. The CB1-4B theory is formulated beyond the usual independent-particle model and obeys the asymptotic convergence criteria [4] for Coulomb potentials. In general, the boundary condition problem means adequate solutions of the asymptotic convergence problem [4] by requiring not only the correct asymptotic behaviors of all the scattering wave functions, but also their proper connections with the corresponding perturbation interactions.

Atomic units will be used throughout unless otherwise stated.

## 2. THEORY

The prior and post forms of the transition amplitude in the CB1-4B approximation can be respectively written by [3]:

$$T_{if}^- = \iiint d\vec{x}_1 d\vec{x}_2 d\vec{R} \varphi_P^*(\vec{s}_1) \varphi_T^*(\vec{x}_2) [V_P(R, s_1) + V_P(R, s_2)] \\ \times \varphi_i(\vec{x}_1, \vec{x}_2) e^{-i\vec{\alpha} \cdot \vec{R} - i\vec{v} \cdot \vec{x}_1} (vR + \vec{v} \cdot \vec{R})^{i\xi},$$

$$T_{if}^+ = \iiint d\vec{x}_1 d\vec{x}_2 d\vec{R} \varphi_P^*(\vec{s}_1) \varphi_T^*(\vec{x}_2) [V_P(R, s_2) + V_T(R, x_1) + V_{\text{corr}}] \\ \times \varphi_i(\vec{x}_1, \vec{x}_2) \exp(-i\vec{\alpha} \cdot \vec{R} - i\vec{v} \cdot \vec{x}_1) (vR + \vec{v} \cdot \vec{R})^{i\xi},$$

where

$$V_P(R, s_i) = Z_P(1/R - 1/s_i), \quad (i = 1, 2),$$

$$V_T(R, x_1) = (Z_T - 1)(1/R - 1/x_1), \quad V_{\text{corr}} = 1/r_{12} - 1/x_1,$$

with  $Z_K$  is the charge of the  $K$ th nucleus  $K = P, T$ , and  $\xi = (Z_P - Z_T + 1)/v$ ,  $v$  is velocity of the projectile. The position vectors of the first and second electrons ( $e_1$  and  $e_2$ ) relative to the nuclear charge of the projectile  $Z_P$  (target  $Z_T$ ) are denoted by  $\vec{s}_1$  and  $\vec{s}_2$  ( $\vec{x}_1$  and  $\vec{x}_2$ ). Further,  $\vec{R}$  is the position vector of  $Z_T$  with respect to  $Z_P$ . The vector of the distance between the two active electrons ( $e_1$  and  $e_2$ ) is labelled by  $\vec{r}_{12} = \vec{x}_1 - \vec{x}_2 = \vec{s}_1 - \vec{s}_2$ . The momentum transfer  $\vec{\alpha}$  is defined by  $\vec{\alpha} = \vec{\eta} - \alpha_z \hat{v}$ ,  $\alpha_z = v/2 - \Delta E/v$ , with  $\Delta E = E_i - E_f$ . The transverse component of the change in the relative linear momentum of a heavy particle is denoted by  $\vec{\eta} = (\eta \cos \phi_\eta, \eta \sin \phi_\eta, 0)$ , ( $\vec{\eta} \cdot \vec{v} = 0$ ).

The function  $\varphi_i(\vec{x}_1, \vec{x}_2)$  denotes the two-electron bound state wave function of the helium atomic system, and in the present article we have used two-parameters Silverman *et al* [6] wave function:

$$\varphi_i(\vec{x}_1, \vec{x}_2) = N[e^{-ax_1 - bx_2} + e^{-ax_2 - bx_1}],$$

where  $a = 2.832$ ,  $b = 1.1885$  and  $N$  is the normalization constant. The functions  $\varphi_P(\vec{s}_1)$  and  $\varphi_T(\vec{x}_2)$  represent bound state wave functions of the hydrogen-like atomic systems  $\text{Li}^{2+}$  and  $\text{He}^+$ , respectively.

In the CB1-4B model, the proper connection between the long-range Coulomb distortion effects and the accompanying perturbation potentials is established according to the well-established principles of scattering theory [4]. Imposing the proper Coulomb boundary conditions in the entrance and exit channels is of crucial importance particularly for ion-atom collisions [2].

### 3. RESULTS AND DISCUSSIONS

The theoretical results for formation of the  $\text{Li}^{2+}$  ion in the  $\text{Li}^{3+} - \text{He}$  collisions at energies 100-5000 keV/amu are plotted in Fig. 1. As can be seen that both prior and post cross sections are very close. Our total cross sections are compared with the experimental data [7, 8, 9, 10] and very good agreement is found especially at higher impact energies. It should be noted that post versions contains the term  $1/r_{12}$ , which explicitly accounts for the dynamical correlations. The contribution from electron-electron interaction during the collision in the  $\text{Li}^{3+} - \text{He}$  scattering has been assessed for the first time by means of four-body continuum distorted wave (CDW-4B) theory [5].

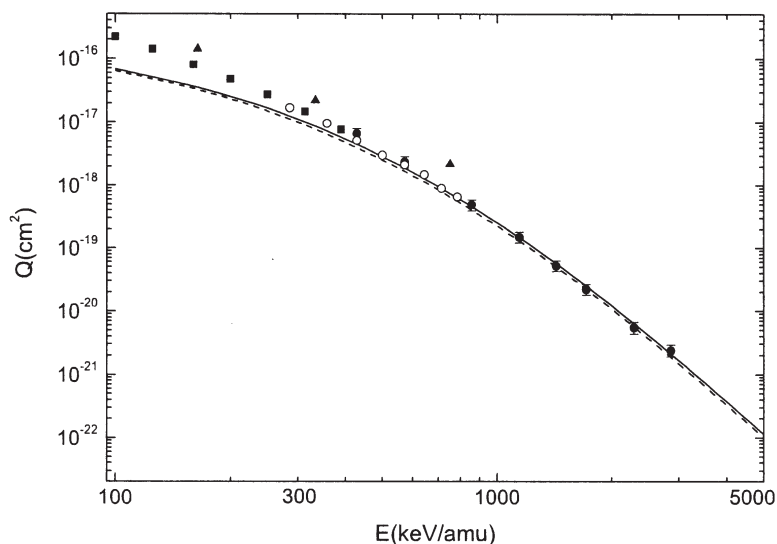


**Figure 1.** The total cross sections (in  $\text{cm}^2$ ) as a function of the laboratory incident energy  $E(\text{keV}/\text{amu})$  for the reaction:  $\text{Li}^{3+} + \text{He} \longrightarrow \text{Li}^{2+} + \text{He}^+$ . The full line represents the post total cross sections of the CB1-4B method (present results), whereas dashed line relates to the prior form of the CB1-4B method (present results). Both curves are obtained with the complete perturbation potential and correspond to the capture in ground state while the contribution from the excited states is accounted by factor 1.202 which additionally multiplies the total cross sections. Experimental data: ■ Shah and Gilbody [8]; ● Woitke *et al* [7]; ○ Sant'Anna *et al* [9]; ▲ Dmitriev *et al* [10].

### Acknowledgements

Authors gratefully acknowledge the financial support from Ministry of Science of the Republic of Serbia through Project No. 171020.

### REFERENCES

- [1] Dž. Belkić, I. Mančev and J. Hanssen, *Rev. Mod. Phys.* **80**, 249 (2008).
- [2] Dž. Belkić, *Quantum Theory of High-Energy Ion-Atom Collisions* (Taylor & Francis, London 2009).
- [3] I. Mančev and N. Milojević, *Phys. Rev. A*, **81**, 022710 (2010).
- [4] Dž. Belkić, *Principles of Quantum Scattering Theory* (Institute of Physics, Bristol 2004).
- [5] I. Mančev, *Phys. Rev. A*, **64** (2001) 012708.
- [6] J. Silverman, O. Platas, and F.A. Matsen, *J. Chem. Phys.* **32**, 1402 (1960).
- [7] O. Voitke, P.A.Závodszky, S.M.Ferguson, J.H. Houck and J.A. Tanis, *Phys. Rev. A*, **57**, 2692 (1998).
- [8] M.B. Shah and H.B. Gilbody, *J. Phys. B: At. Mol. Phys.* **18**, 899 (1985).
- [9] M. M. Sant'Anna, A.C. Santos, L.F. Coelho, G. Jalbert, N.V. de Castro Faria, F. Zappa, P. Focke and Dž. Belkić, *Phys. Rev. A*, **80**, 042707 (2009) .
- [10] I.S. Dmitriev, Ya.A. Teplova, Ya.A. Belkova, N.V. Novikov and Yu.A. Fainberg, *Atomic Data and Nuclear Data Tables*, **96**, 85 (2010) [V.S. Nikolaev, I.S. Dmitriev, L.N. Fateyeva, Ya.A. Teplova, *Zh. Eksp. Teor. Fiz.* **40**, 989 (1961): *JETP* **13**, 695 (1961).

## MODIFIED STATISTICAL MODEL FOR $\text{CH}^+ + \text{H} \rightarrow \text{C}^+ + \text{H}_2$ REACTION

Tasko P. Grozdanov<sup>1</sup>, Ronald McCarroll<sup>2</sup>

<sup>1</sup>*Institute of Physics, University of Belgrade,  
 Pregrevica 118, 11080 Belgrade, Serbia*

<sup>2</sup>*Laboratoire de Chimie Physique-Matière et Rayonnement,  
 (UMR 7614 du CNRS), Université Pierre et Marie Curie,  
 75231-Paris Cedex 05, France*

**Abstract.** We present a modified statistical treatment of the complex-forming reaction  $\text{CH}^+ + \text{H} \rightarrow \text{C}^+ + \text{H}_2$  in order to account for some recent intriguing experimental results. The study of rotationally adiabatic states indicates which rotational states of  $\text{CH}^+$  are likely to lead to linear configurations and therefore become non reactive. By excluding the contribution of these states from the total thermal reaction coefficient a better agreement with experiment is obtained.

### 1. INTRODUCTION

As discussed in a recent experimental paper [1], the reaction



is of considerable interest in astrophysical applications, but also represents a challenge for a theoretical interpretation. Since there exists a deep well in the potential energy surface (PES) of the  $\text{CH}_2^+$ , it would be expected that at low collision energies the reaction proceeds via the formation of a long-lived complex. And, in that case, the application of statistical models should give a reasonable prediction of the reaction rate coefficient. Indeed, one such model, the phase space theory (PST) has been applied [2] and the resulting rate coefficient at low temperatures approaches a constant Langevin value of  $k=1.98 \cdot 10^{-9} \text{ cm}^3 \text{ s}^{-1}$  (see also the full line in Fig.1). However, experiment (see the symbols in Fig.1) predicts a very strong decrease of the rate coefficient in the low temperature regime. Neither quasiclassical trajectory calculations [2, 3] nor quantum mechanical methods [3, 4] using a full PES provide a satisfactory explanation of the experimental results. In the present contribution we explore the possibility of modifying the statistical

model in order to understand and account for the decrease of reactivity at low temperatures.

## 2. THEORETICAL METHODS AND RESULTS

It can be reasonably conjectured that the reduction of the reactivity is linked to the existence of potential barriers in the (near)collinear configurations: C-H-H and H-C-H, which are the consequences of conical intersections [3, 4] and which represent barriers for complex formation. In this work, we have investigated the angular dependence of the rotationally adiabatic states appearing in the adiabatic capture centrifugal sudden approximation (ACCSA) method [5]. These are the eigenfunctions of the rotational Hamiltonian (in atomic units):

$$H_r = B\vec{j}^2 + \frac{|\vec{J} - \vec{j}|^2}{2\mu R^2} - \frac{\alpha}{2R^4} - \frac{2\alpha D \cos \theta}{R^5} - \frac{\alpha D^2 (3 \cos^2 \theta + 1)}{2R^6}, \quad (2)$$

where  $B$  is the rotational constant,  $\vec{j}$  is the rotational angular momentum and  $D$  is the electric dipole moment of the  $\text{CH}^+$  ion,  $\vec{J}$  is the total angular momentum,  $\mu$  is the reduced mass of the reactants,  $\alpha$  is the polarization of the H atom,  $R$  is the distance between the H and C.M. of  $\text{CH}^+$  and  $\theta$  is the angle between the  $\text{CH}^+$  bond and  $R$ . The largest alignment (concentration of location probability towards  $\theta=0$  with decreasing  $R$ ) was found for the adiabatic state labelled with  $(j, \Omega) = (0, 0)$  and to a somewhat lesser degree for the (1,1) and (1,0) states ( $\Omega$  is the modulus of the projection of  $\vec{j}$  and  $\vec{J}$  onto the  $R$ -axis).

We have performed a series of calculations of the thermal rate coefficient for reaction (1), by employing standard statistical theory [6, 7] and using only corresponding  $-\alpha/2R^4$  polarization interactions in both, reactant and product arrangements. The full line in Fig.1 represents results obtained by retaining all the  $(j, \Omega)$  states of  $\text{CH}^+$ . The dotted line was obtained by excluding the contribution of the (0,0) state, which is assumed to be non-reactive due to alignment. However, an additional condition on collision energy  $E_c < 2B$  has been imposed in order to preserve adiabaticity, that is to prevent mixing of the (0,0) state with  $j = 1$  states. The dashed line was obtained by assuming that (0,0) state and (1,1) states are non reactive. The respective additional energy conditions:  $E_c < 6B$  for the (0,0) state and  $E_c < 4B$  for (1,1) states prevent the mixing with  $j = 2$  states, but allow the mixing of (0,0) state and  $j = 1$  states. The dot-dashed line corresponds to the additional assumption that (1,0) state is also non reactive under the same conditions on collision energy.

What can be concluded from results presented in Fig.1? In order to explain the experimental results it seems that the non reactivity of both  $j = 0$  and  $j = 1$  states has to be explained. The problem of alignment

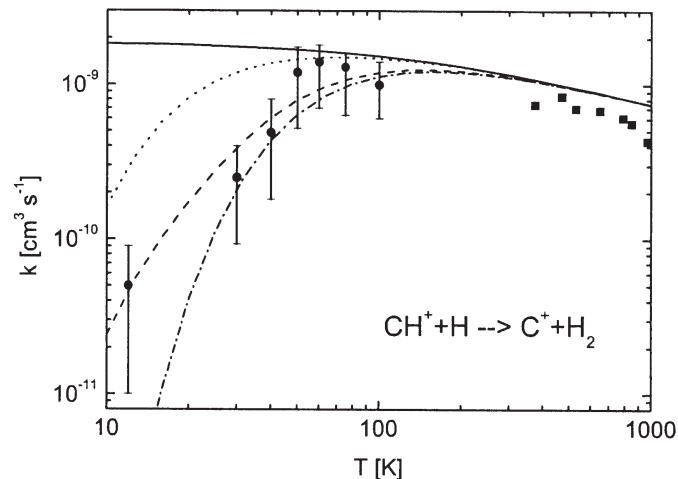


**Figure 1.** Thermal rate coefficient as a function of temperature. Symbols are experimental results: circles [1] and squares [8]. Lines are the results of the standard statistical theory [6, 7] using only corresponding  $-\alpha/2R^4$  polarization interactions in both, reactant and product arrangements: full line includes all  $(j, \Omega)$  states of  $\text{CH}^+$ , dotted line excludes contribution of the  $(0,0)$  state for collision energies  $E_c < 2B$ , dashed line excludes contributions of  $(0,0)$  state for  $E_c < 6B$  and  $(1,1)$  states for  $E_c < 4B$  and dash-dotted line excludes contributions of  $(0,0)$  state for  $E_c < 6B$  and  $(1,1)$  and  $(1,0)$  states for  $E_c < 4B$ .

of these states needs a more sophisticated study as well as account of the detailed form of the PES close to linearity.

We note that we have also been able to compare our results with experiment for rate coefficients corresponding to experimental situations in which the temperature of the  $\text{CH}^+$  ions in the ion trap is different from the temperature of the effusive beam of H atoms [1]. Results will be presented at the conference.

#### Acknowledgements

TPG acknowledges support by Ministry of Education and Science of the Republic of Serbia through the project No. 171020.

## REFERENCES

- [1] R. Plasil, T. Mehner, P. Dohnal, T. Kotrik, J. Glosik and D. Gerlich, *ApJ* 737, 60 (2011).
- [2] Ph. Halvick, T. Stoecklin, P. Larrégaray and L. Bonnet, *Phys. Chem. Chem. Phys.* 9, 582 (2007).
- [3] R. Warmbier and R. Schneider, *Phys. Chem. Chem. Phys.* 13, 10285 (2011).
- [4] T. Stoecklin and Ph. Halvick, *Phys. Chem. Chem. Phys.* 7, 2446 (2005).
- [5] D. C. Clary, *Mol. Phys.* 54, 605 (1985).
- [6] K. Park and J. C. Light, *J. Chem. Phys.* 127, 224101 (2007).
- [7] T. P. Grozdanov and R. McCarroll, *J. Phys. Chem. A* 116, 4569 (2011).
- [8] W. Federer, H. Villinger, F. Howorka, W. Lindinger, P. Tosi, D. Bassi and E. Ferguson, *Phys. Rev. Lett.* 52, 2084 (1984).

## RATE COEFFICIENTS IN CROSSED $E$ AND $B$ FIELDS IN CO

M. Vojnović<sup>1</sup>, M. Popović<sup>1</sup>, M. M. Ristić<sup>2</sup>, M. Vičić<sup>1</sup> and G. B. Poparić<sup>1\*</sup>

<sup>1</sup>*Faculty of Physics, University of Belgrade, P.O. Box 44,  
11000 Belgrade, Serbia*

<sup>2</sup>*Faculty of Physical Chemistry, University of Belgrade, P.O. Box 137,  
11000 Belgrade, Serbia*

\**E-mail: Goran\_Poparic@ff.bg.ac.rs*

**Abstract.** Rate coefficients for electron impact excitation of the CO molecule have been calculated in non-equilibrium conditions, in a presence of electric and magnetic fields. Within the framework of this work, rate coefficients have been determined for the following processes: rotational excitation, vibrational excitation, electronic excitation into various singlet and triplet states and particularly for ionization. The reduced electric field ( $E/N$ ) has been ranged from 0 to 1000 Td, while reduced magnetic field ( $B/N$ ) has been ranged from 0 to 3000 Hx. The mean electron energy has been varied from 0 up to 18 eV. Electron energy distribution functions which were needed for determination of the rate coefficients had been obtained by employing an exact Monte Carlo simulation developed in our laboratory.

### 1. INTRODUCTION

Experimental and theoretical studies of electron transport in the presence of various configurations of dc electric and magnetic fields have numerous practical applications, e.g. in inductively coupled plasma [1-2], magnetically confined gas lasers, plasma processing technology and others [3].

Electron impact excitations of the vibrational levels, excitations of valence and Rydberg states in crossed electric and magnetic fields are investigated. The non-equilibrium rate coefficients have been obtained by sampling the electron energy distribution functions (EEDF) in exact Monte Carlo simulation of electron transport. Differential and integral cross sections for electron impact excitation were measured and estimated in our laboratory. For further calculation of transport data Monte Carlo simulation was used. We have obtained a complete set of rate coefficients for electron impact excitation of the CO gas in  $E \times B$  fields, for wide ranges of reduced electric ( $E/N$ ) and magnetic ( $B/N$ ) fields, where  $N$  is the gas number density.

## 2. MONTE CARLO SIMULATION

The object of simulation is evolution of electron transport through the CO gas under the influence of crossed homogeneous electric and magnetic fields in infinite space. We solved differential equations of electron motion analytically and obtained finite equations, which have been used for precise calculation of electron positions and velocities for each time step ( $\Delta t$ ) in the simulation.

Scattering processes have been included in this modeling by using experimentally measured and estimated data of integral cross sections as a function of energy. The data for vibrational and electronic excitation were mainly measured and estimated in our laboratory. Non-conservative processes are also included, as it was first done by Brennan and Garvie [4]. In the case of ionization, the exact treatment of newborn electron is performed.

The simulation algorithm has been successfully tested on Lucas-Saelee model test gas and compared to the similar Monte Carlo simulation of non-conservative electron swarms in dc  $\mathbf{E} \times \mathbf{B}$ , recently described by Dujko et al. [5].

## 3. RESULTS AND DISCUSSION

Simulations of electron transport in CO gas have been performed in a wide range of E/N and B/N values. Values of B/N were 0, 500, 1000, 2000 and 3000 Hx (1 Hx =  $10^{-27}$  Tm<sup>3</sup>) and for each fixed B/N, E/N were changed in interval from 0 to 1000 Td (1 Td =  $10^{-21}$  Vm<sup>2</sup>), with step value of 20 Td. Mean electron energies in these cases were between 0 and 18 eV. After electrons had reached the steady state, EEDF was sampled in order to calculate the rate coefficients for various processes at given conditions, using the well known relation [6]:

$$K(\bar{E}_{el}) = \sqrt{2/m_e} \int_{\varepsilon_{thres}}^{+\infty} \sigma(\varepsilon) \sqrt{\varepsilon} \cdot f_e(\bar{E}_{el}, \varepsilon) d\varepsilon \quad (1)$$

where  $\bar{E}_{el}$  is the mean electron energy,  $\sigma(\varepsilon)$  is the excitation cross section for considered process,  $\varepsilon_{thres}$  is the threshold energy and  $f_e(\bar{E}_{el}, \varepsilon)$  is the normalized EEDF.

The analysis of results for individual processes showed the following: among  $A^1\Pi$ ,  $C^1\Sigma^+$ ,  $E^1\Pi$ ,  $I^1\Sigma^-$ ,  $D^1\Delta$  and  $B^1\Sigma^+$  singlet states, the greatest contribution to the electron impact excitation of singlet electronic states of CO is one of the  $A^1\Pi$  states, which has the greatest ICS; in case of excitation into triplet electronic states of CO,  $a^3\Pi$  state has the greatest rate coefficient and also only this rate coefficient, among  $b^3\Sigma^+$ ,  $a^3\Pi$ ,  $a^3\Sigma^+$ ,  $d^3\Delta$  and  $e^3\Sigma^-$  states reaches maximum, since it has the lowest threshold and the majority of its ICSs are at relatively low energies (below 10 eV); in both vibrational and rotational excitation processes excitation via  $^2\Pi$  resonance around 3 eV is highly

dominant, and for that reason we obtain pronounced peaks of rate coefficients in this region of energies, which tend toward higher  $E/N$  values as  $B/N$  values increase due to decelerating effect that magnetic field has on electrons; main ionization process is production of  $\text{CO}^+$ , which is followed by  $\text{C}^+$  and  $\text{O}^+$  ions production, while the  $\text{CO}^{2+}$  production is almost negligible process.

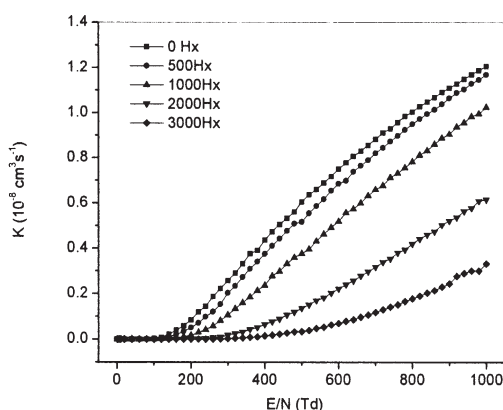


Figure 1. Total rate coefficients for excitation into singlet states for various  $B/N$  values in the conditions of orthogonal electric and magnetic fields

For all of these processes the dependence of the rate coefficients on  $E/N$  indicate the rapid decrease of the rate coefficients with increasing  $B/N$  caused by deceleration of electrons by magnetic field and therefore their incapability to reach thresholds for the given process. This behavior is presented in Fig. 1, where all partial rates are summed for obtaining the total rate coefficient for singlet state electronic excitation of  $\text{CO}$ , which is presented vs.  $E/N$  for various  $B/N$  values.

In figure 2, the comparison is made between total rate coefficients for rotational, vibrational, electronic excitation and ionization at single  $B/N$  value of 1000 Hx. Vibrational and rotational excitations are dominant in the regions of lower  $E/N$ , while rates of electronic excitation (both into singlet and triplet states) and ionization are rising with the electric field and eventually become the dominant excitation channels. This fact is of great importance when energy transfer from electrons to molecules is analyzed, since electronic excitations and ionization have higher energy thresholds than vibrations and rotations.

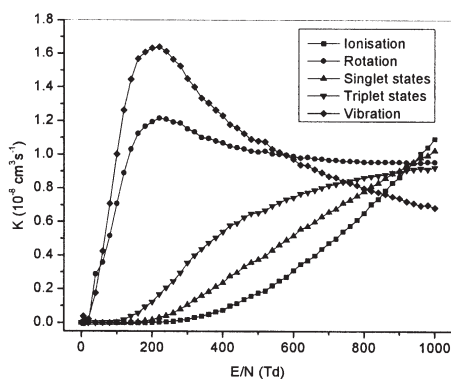


Figure 2. Total rate coefficients for rotational, vibrational, electronic (singlet and triplet states) excitation and ionization at single B/N value of 1000 Hx in the conditions of orthogonal electric and magnetic fields

#### 4. CONCLUSIONS

A complete set of rate coefficients for the electron impact excitation of the CO gas in electric and magnetic fields, for wide ranges of reduced electric and magnetic fields, has been calculated. For performing this calculation, an exact Monte Carlo simulation of electron swarm in  $E \times B$  fields has been developed, which includes treatment of ionization.

#### Acknowledgements

This work was supported in part by the Ministry of Science and Education of the Republic of Serbia by the Project No. 171016.

#### REFERENCES

- [1] M. Tadokoro, H. Hirata, N. Nakano, Z. Lj. Petrović and T. Makabe, *Phys. Rev. E* 57, R43 (1998).
- [2] R. L. Kinder and M. J. Kushner, *J. Appl. Phys.* 90, 3699 (2001).
- [3] J. R. Roth, *Industrial Plasma Engineering*, Vol. 11, IOP, (Bristol and Philadelphia, 1995).
- [4] M. J. Brennan and A. M. Garvie, *Aust. J. Phys.* 43, 765 (1990).
- [5] S. Dujko, R. D. White, Z. Lj. Petrović and R. E. Robson, *Phys. Rev. E* 81, 046403 (2010).
- [6] D. S. Belić, *Chem. Phys.* 130, 141(1989).

# ANALYSIS OF ADIABATIC POTENTIAL CURVES OF HELIUM IN TERMS OF CLASSICAL CONFIGURATIONS

Nenad Simonović

*Institute of Physics, University of Belgrade, P.O. Box 57, 11001 Belgrade, Serbia*

**Abstract.** Classical configurations belonging to reduced phase space of helium atom with fixed hyperradius are examined in order to explain properties of the hyperspherical adiabatic potential curves of the atom.

## 1. INTRODUCTION

Among a variety of theoretical methods used for studying two-electron atomic systems, the so-called hyperspherical approach [1] is one of the most appropriate for describing the single and double excited states of these systems. The electrons radial coordinates  $r_1, r_2$  are here replaced by the hyperradius  $R = (r_1^2 + r_2^2)^{1/2}$  and the hyperangle  $\alpha = \arctan(r_2/r_1)$  ( $0 \leq \alpha \leq \pi/2$ ) which measure the size of the system and the radial correlation of the electrons, respectively. The angular correlation can be described by the mutual angle  $\vartheta = \angle(\mathbf{r}_1, \mathbf{r}_2)$ . The hyperspherical approach is based on the adiabatic (Born-Oppenheimer's type) expansion of two-electron wave function where the adiabatic ("channel") functions are obtained by solving Schrödinger equation at a fixed value of  $R$  (which is here a parameter). For a given symmetry ( $^{2S+1}L^\pi$ ) and a given ionization threshold (determined by the quantum number  $N$  of "inner" electron) the "channel index" can be expressed by the set of approximate quantum numbers  $(K, T)^A$  [2]. Each channel is related to a hyperspherical adiabatic potential curve  $\mathcal{E}(R)$ , determined also from the Schrödinger equation with  $R$  as a parameter.

Beside the quantum mechanical methods a significant contribution in understanding the dynamics of two-electron systems has been done by semiclassical methods. Here we adopt the idea of treating the hyperradius as adiabatic variable and use it in the semiclassical approach. In next sections we study classical configurations belonging to the reduced phase space of helium atom with fixed hyperradius and analyze the hyperspherical adiabatic potential curves in terms of these configurations.

## 2. CLASSICAL DYNAMICS FOR FIXED $R$

The Hamiltonian of a two-electron atom in hyperspherical coordinates, for the total angular momentum  $L = 0$ , at a fixed value of hyperradius  $R$  reads (in atomic units)

$$H_R = \frac{1}{2R^2} \left( P_\alpha^2 + \frac{P_\vartheta^2}{\sin^2 \alpha \cos^2 \alpha} \right) + \frac{C(\alpha, \vartheta)}{R}, \quad (1)$$

$$C(\alpha, \vartheta) = -\frac{Z}{\sin \alpha} - \frac{Z}{\cos \alpha} + \frac{1}{\sqrt{1 - \sin 2\alpha \cos \vartheta}}. \quad (2)$$

Here  $P_\alpha, P_\vartheta$  are the canonical momenta related to  $\alpha$  and  $\vartheta$  coordinates and  $Z$  is the charge of (infinitely heavy) nucleus. In contrast to the full 3D (non-adiabatic) treatment (the full Hamiltonian is  $H = H_R + P_R^2/2$ ) the motion described by the Hamiltonian (1) is always bound.

Due to the scaling properties of Coulomb systems, it is sufficient to calculate the trajectories and all classical quantities for one fixed value of the hyperradius. If  $\epsilon, \tau$  and  $s$  are the values for energy, time and action, respectively, at  $R = 1$ , then the corresponding values for an arbitrary  $R$  are:  $E = \epsilon/R, t = R^{3/2}\tau, S = \sqrt{R}s$ . Then, the scaled potential and the scaled Hamiltonian (with fixed hyperradius) are  $C(\alpha, \vartheta)$  and  $h = RH_R \equiv \epsilon$ , respectively. At  $\alpha = \pi/4, \vartheta = \pi$  the potential  $C$  has the saddle point and takes the value  $\epsilon_{\text{sp}} = C(\pi/4, \pi) = (1-4Z)/\sqrt{2}$  (for  $Z = 2$ :  $\epsilon_{\text{sp}} \approx -4.94975$ ).

A systematic analysis of the reduced phase space at different scaled energies (using the Poincaré sections technique) indicate that five characteristic types of classical configurations exist, which are related to five types of short periodic orbits (POs), see Table 1 and Fig. 1.

Table 1: Properties of the shortest periodic orbits of the two electron system with  $Z = 2$  (helium) at fixed hyperradius.

periodic orbit (PO)	exists for	stability
frozen planet (FP)	$\forall \epsilon$	stable for $\epsilon \in (-6.283, -2.972)$
opposite fr. planet (OFP)	$\epsilon < \epsilon_{\text{sep}}$	stable
asymmetric stretch (AS)	$\epsilon > \epsilon_{\text{sep}}$	stable for $\epsilon \in (\epsilon_{\text{sep}}, -3.487)$
asynchronous (ASC)	$\epsilon > -3.487$	stable for $\epsilon < 0.261$
Langmuir (L)	$\epsilon > \epsilon_{\text{sep}}$	stable for $\epsilon \in (-2.072, -1.969)$

An important class are the collinear configurations where the mutual angle between the electrons is either  $\vartheta = 0$  (the so-called Zee configuration) or  $\vartheta = \pi$  (the eZe configuration) with  $P_\vartheta = 0$  in both cases. For a given scaled energy, each configuration (Zee/eZe) reduces to a single PO. For the Zee configuration this is the FP PO (Fig. 1(a)), whereas for the eZe configuration the corresponding orbit is the OFP PO if  $\epsilon < \epsilon_{\text{sep}}$  and the AS PO if  $\epsilon > \epsilon_{\text{sep}}$  (Fig. 1(b)). For  $\epsilon > -3.487$  the orbit bifurcates to unstable AS (collinear) and stable ASC orbit which is off-collinear (Fig. 1(c,d)).

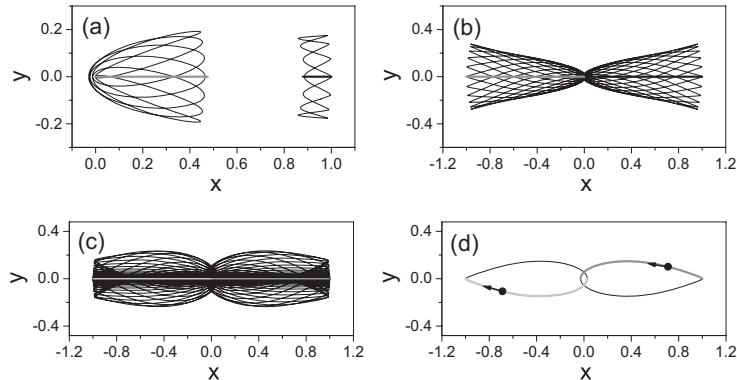


Figure 1: (a) The FP PO and (b) the AS PO (straight lines) at  $R = 1$  and  $\epsilon = -4$  and off-collinear orbits in their vicinities. (c) The unstable AS PO at  $\epsilon = -3.3$  (straight line) and the off-collinear orbit obtained by introducing a very small perpendicular deviation of the former. (d) The ASC PO for the same  $\epsilon$ . The nucleus ( $Z = 2$ ) is located at the origin of coordinate system.

### 3. SEMICLASSICAL POTENTIAL CURVES RELATED TO SHORT POS. DISCUSSION

The first step is numerical evaluation of the scaled action  $s(\epsilon)$  along the chosen type of PO (within the fundamental domain  $\alpha \in (0, \pi/4)$ ) as a function of the scaled energy. Then, the semiclassical potential curves  $\mathcal{E}_N^{(\text{PO})}(R)$  are obtained using scaling relations and the semiclassical quantization condition  $S = 2\pi n + \phi$ , where  $n = N - 1$  is the nodal quantum number along the orbit. The phase shift  $\phi$  depends on the type of PO ( $\phi = 3\pi/2$  for AS and ASC and  $\phi = 2\pi$  for FP and OFP POs). The  $1S^e$  adiabatic energies  $\mathcal{E}_N^{(\text{PO})}(R)$  for  $N = 2, 3$  and 4 of helium ( $Z = 2$ ) which correspond to the AS, OFP, FP and ASC POs are shown in Fig. 2 together with the quantum-mechanically calculated adiabatic energies for the collinear ( $eZe/Zee$ ) models and for the full 3D model.

In a recent quantum-mechanical analysis [3] it has been shown that the adiabatic energies of the 3D atom (thin gray lines in Fig. 2) converging to the same ionization threshold (the curves with the same  $N$  but different  $K$ ) are, for sufficiently large  $R$ , confined in the areas limited from the top and from the bottom by the adiabatic curves for the collinear ( $Zee/eZe$ ) configurations (thick gray lines in Fig. 2). It is noticed, however, that for small  $R$  most of the 3D adiabatic curves cross the lower bordering line ( $eZe$  adiabatic curve) and leave these areas. This behaviour has been explained by the anticrossings between the 3D curves which occur just at the  $eZe$  adiabatic curves (when  $\mathcal{E} > -3.5/R$ ).

The present analysis shows that this class of anticrossings can be

explained by the unstable character of the underlying classical configuration, which is here the AS PO. From the stability data for this orbit (Table 1) the condition for these anticrossings is  $\mathcal{E} > -3.487/R$  (the area above the dotted line in Fig. 2). Besides, it follows that the 3D adiabatic curves at the lowest values of  $R$  (after crossing an eZe adiabatic curve) must be related to the ASC configuration which arises after the AS orbit bifurcates. Fig. 2 shows that just the adiabatic potential curves related to the ASC PO for  $\mathcal{E} > -3.487/R$  become the lower bordering lines for the 3D adiabatic curves.

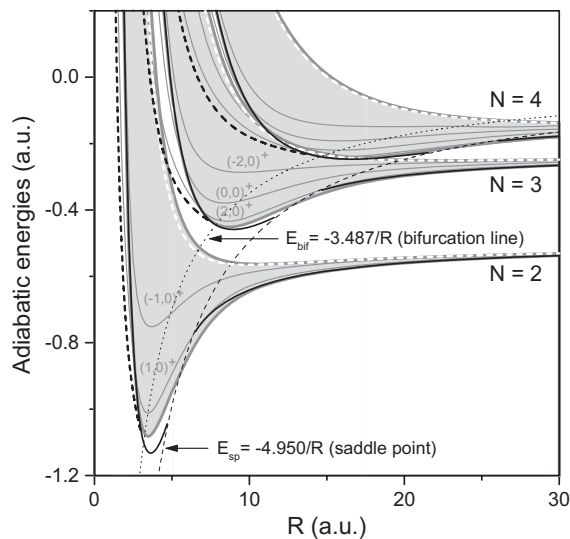


Figure 2: The  $1S^e$  adiabatic energies for  $N = 2, 3, 4$  of helium (quantum-mechanical calculation) for the collinear (eZe/Zee) models (thick gray lines) and for the full 3D model (thin gray lines), as well as semiclassical curves corresponding to the AS/OFP (thick black lines), FP (white dashed lines) and ASC POs (black dashed lines).

### Acknowledgements

This work is supported by Project 171020 of Ministry of Education and Science of Serbia.

### REFERENCES

- [1] J. Macek, J. Phys. B **2**, 831 (1968).
- [2] D. R. Herrick, Adv. Chem. Phys. **52**, 1 (1983); C. D. Lin, Phys. Rep. **257**, 1 (1995).
- [3] N. S. Simonović, J. Phys. B: At. Mol. Opt. Phys. **44**, 105004 (2011).

## MONTE CARLO SIMULATION OF ELECTRON TRANSPORT IN H<sub>2</sub>O VAPOUR

V. Stojanović, J. Sivoš, D. Marić, N. Škoro and Z. Lj. Petrović

*Institute of Physics, University of Belgrade, Pregrevica 118, 11080 Belgrade,  
Serbia*

**Abstract.** In this work we present electron transport coefficients in water vapor for the conditions used in plasma assisted technologies. By using Monte Carlo technique appropriate for steady state Townsend discharges we determined mean energy, drift velocity and effective ionization coefficient for a wide range of reduced electric fields ( $E/N= 100-10000$  Td). We show that agreement with experimental data for drift velocity and effective ionization coefficients exists for moderate  $E/N$  implying that one may properly model the electron multiplication.

### 1. INTRODUCTION

Increasing interest in application of plasmas in medicine, nanotechnologies and environmental remediation [1-5] has drawn attention to studies of discharges in water and with water electrodes [6]. Current studies show that in such systems, discharge is formed in water vapour either from evaporating liquid electrode or in bubbles created by an induced phase transition within the liquid. More generally, all atmospheric discharges contain some degree of water vapour.

It is therefore of immediate interest to determine how discharges are created in water [7–9]. Currently it is thought that discharges can only be formed in water vapor resulting from an induced phase transition. Therefore a starting point must be to have accurate knowledge of the electrical properties of water vapor and in particular its breakdown potential [10,11].

In this paper we study the kinetics of electrons in  $E/N$  using Monte Carlo simulations (MCS) that have been well tested for similar discharges in Ar, H<sub>2</sub> and N<sub>2</sub>. As electrons have a special role in plasmas at high  $E/N$  we focus on electrons leaving out heavy particle collisions which will be dealt with separately. Another motivation is to provide the transport data for the electrons in the mixtures with H<sub>2</sub>O.

## 2. THE MONTE CARLO TECHNIQUE

The MCS code used in our analysis is based on the null collision method, applied to model a steady state Townsend (SST) discharge. The basic code follows the motion of electrons from the cathode and it is possible to get the spatial distribution of the emission and the excitation and ionization coefficients [12]. The second MCS code is used to follow the electrons reflected from the anode surface and the newly created secondary electrons from the cathode. This code is completely independent from the code for simulation of the electrons from the cathode, and it can be included but also excluded from the simulation. Sampling of observable properties specific to idealized SST experiment between two parallel electrode [13] is applied in order to obtain the mean energy, drift velocity and ionization coefficients. The nonintrusive photon flux experiment of Fletcher [14] and Malović *et al.* [15] provides means of directly observing the periodic structures of electron transport properties which can be classified as representation of the non-locality of the EEDF and related electron properties in regions where hydrodynamic approximation is not fulfilled.

In this paper, however, we will present only the data obtained for distances longer than the spatial relaxation length where possible periodic structures vanish.

We used the cross sections data defined in the data base of Phelps [16] initially based on drift velocity measurements of Pack *et al.* [17]. We deduced elastic momentum transfer cross section from the effective momentum transfer cross section and inelastic cross sections recommended in [16] and extrapolated above 80 eV by using data of Hayashi [18]. Latest recommendation by Phelps [16] for cross sections for ionization measured by Stebbings and coworkers [19] is also applied.

## 3. DISCUSSION AND RESULTS

In Figure 1 a) we show SST mean electron energy and in Fig. 1 b) SST drift velocity. Latest measurements of drift velocities (mean arrival time

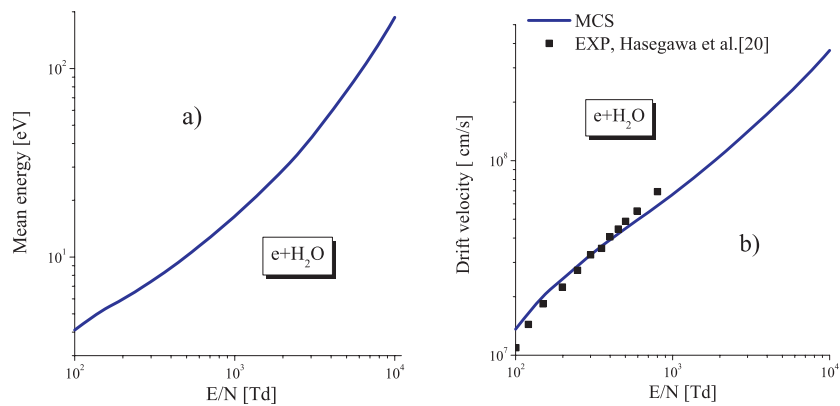


**Figure 1.** SST a) mean energy, b) drift velocity, obtained by MCS as a function of  $E/N$ .

drift velocity measurements [9] of Hasegawa *et al.* [20]) are in good agreement with our MCS results.

Figure 2 shows effective Townsend ionization coefficient in the H<sub>2</sub>O vapour as a function of  $E/N$ . Recent ionization coefficients measurements are presented in works of Hasegawa *et al.* [20] recording arrival time electron spectrum and Škoro *et al.* [21] recording side-on spatial profile that show effective charged particle multiplication and is thus under influence of attachment that reduces the effective ionization. Excellent agreement with experimental data of Hasegawa *et al.* [20] is achieved from 150 Td up to 3000 Td while experimental results of Škoro *et al.* [21] are slightly below following the same trend. Between 100 and 200 Td the  $E/N$  dependence of the data due to Prasad and Craggs [22] is followed. Data of Hasegawa *et al.* [20] indicating a possible strong electron loss towards lower  $E/N$  are not supported by the present cross section set.

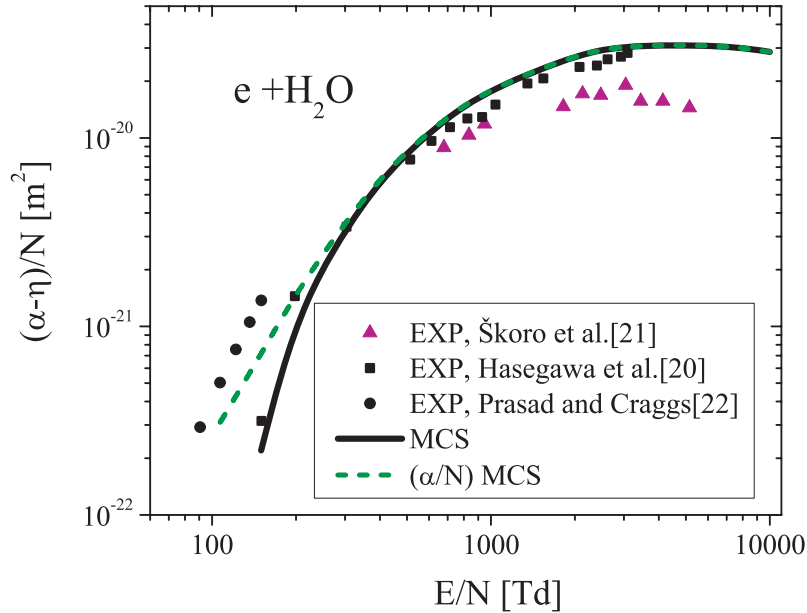


**Figure 2.** Effective ionization coefficient as a function of  $E/N$  in water vapor.

### Acknowledgements

Results obtained in the Laboratory of Gaseous Electronics Institute of Physics University of Belgrade under the auspices of the Ministry of Education and Science, Projects No. ON171037 and III410011.

## REFERENCES

- [1] K. R. Stalder, G. Nersisyan and W. G. Graham, *J. Phys. D: Appl. Phys.* **39** 3457 (2006).
- [2] T. Makabe and Z. Petrović *Plasma Electronics: Applications in Microelectronic Device Fabrication* (Boca Raton, FL: Taylor&Francis, 2006)
- [3] M. Laroussi, *Plasma Process. Polym.* **2**, 391 (2005).
- [4] S. Lazović, N. Puač, M. Miletić, D. Pavlica, M. Jovanović, D. Bugarski, S. Mojsilović, D. Maletić, G. Malović, P. Milenković, and Z. Lj. Petrović, *New J. Phys.* **12**, 083037 (2010).
- [5] K. Kutasi and J. Loureiro, *J. Phys. D* **40**, 5612 (2007).
- [6] P. Bruggeman, D. Schram, M. A. González, R. Rego, M. G. Kong, and C. Leys, *Plasma Sources Sci. Technol.* **18**, 025017 (2009); P. Bruggeman and C. Leys, *J. Phys. D: Appl. Phys.* **42** 053001 (2009).
- [7] G. Ruíz-Vargas, M. Yousfi, and J. de Urquijo, *J. Phys. D* **43**, 455201 (2010).
- [8] Y. Itikawa and N. Mason, *J. Phys. Chem. Ref. Data* **34**, 1 (2005).
- [9] R. E. Robson, R. D. White, and K. F. Ness, *J. Chem. Phys.* **134**, 064319 (2011).
- [10] N. Škoro, D. Marić, G. Malović, W. G. Graham, and Z. Lj. Petrović, *Phys. Rev. E* **84**, 055401(R) (2011).
- [11] M. Radmilović-Radenović, B. Radenović, Ž. Nikitović, Š. Matejčik and M. Klas, *Nucl. Instr. Meth. in Phys. Res. B* **279** pp.103-105 (2012).
- [12] Z. Lj. Petrović, V.D. Stojanović, *J. Vac. Sci. Technol A* **16** (1), 329 (1998).
- [13] J.P. Boeuf and E. Marode, *J. Phys. D: Appl. Phys.* **17** 1133 (1984).
- [14] J. Fletcher, *J. Phys. D: Appl. Phys.* **18** 221 (1985).
- [15] G.N. Malović, J.V. Božin, B.M. Jelenković and Z.Lj. Petrović, *Eur. Phys. J. D* **7** 129 (1999).
- [16] A. V. Phelps, <http://www.jila.edu/collisiondata/> (2002).
- [17] J. L. Pack, R.E. Voshall and A.V. Phelps, *Phys. Rev.* **127** 2084 (1962).
- [18] M. Hayashi, as presented in LXcat database, see S. Pancheshnyi, S. Biagi, M.C. Bordage, G.J.M. Hagelaar, W.L. Morgan, A.V. Phelps, L.C. Pitchford, *Chem. Phys. Chem. Phys.* **398** pp.148-153 (2012).
- [19] H.C. Straub, B.G. Lindsay, K.A. Smith, *J. Chem. Phys.* **108**, 109 (1998).
- [20] H. Hasegawa, H. Date and M. Shimozuma, *J. Phys. D: Appl. Phys.* **40** 2495–2498 (2007).
- [21] N. Škoro, D. Marić, G. Malović, Z.Lj. Petrović, 2nd National Conference on Electronic Atomic and Molecular and Photonic Physics, June 21-25, Belgrade, Serbia (2011).
- [22] A.N. Prasad and J.D. Craggs, *Proc. Phys. Soc.* **76** 223-232 (1960).

## CORE CORRELATION EFFECTS IN THE VALENCE PHOTODETACHMENT OF $\text{Cu}^-$

J. Jose<sup>1,2</sup>, H. R. Varma<sup>1</sup>, P. C. Deshmukh<sup>1,3</sup>, S. T. Manson<sup>4</sup> and V. Radojević<sup>1,5</sup>

<sup>1</sup> School of Basic Sciences, Indian Institute of Technology Mandi, Mandi, India

<sup>2</sup> Department of Chemistry, Texas A&M University, College station, Texas  
77840, U.S.A

<sup>3</sup> Department of Physics, Indian Institute of Technology Madras, Chennai, India

<sup>4</sup> Department of Physics and Astronomy, Georgia State University, Atlanta,  
Georgia 30303, U. S. A

<sup>5</sup> Institute of Physics, University of Belgrade, Pregrevica 118, P.O. Box 68,  
11080 Beograd - Zemun, Serbia

**Abstract.** Photodetachment of  $\text{Cu}^-$  is investigated using the Multi-Configuration Tamm-Dancoff method. Correlations in the initial state have been found to materially affect the photodetachment cross-section significantly.

### 1. INTRODUCTION

Photodetachment studies of anions have attracted wide interest, as these processes are excellent theoretical and experimental test beds to investigate the role of important many-electron correlations. Correlation effects influence photodetachment processes in many ways [1, 2]. The Relativistic-Random-Phase Approximation (RRPA) [3] and the RRPA with relaxation (RRPA-R) [4] are among the major methodologies developed to study many-electron correlation effects in photoionization and photodetachment. A relativistic many-body approximation technique that has grown out of the RRPA is the Multi-Configuration Tamm Dancoff (MCTD) method, developed by Radojević and Johnson (1985) [5]. However, the MCTD approximation has not been extensively applied to many situations since its formulation over a quarter of a century ago. The MCTD method nevertheless has excellent potential, since it includes both the initial state correlations and the final state correlations in a very elegant manner that includes many important non-RPA correlations. The MCTD method thus has the potential of being useful where correlations beyond the RPA are important. The Multi-Configuration Tamm Dancoff (MCTD) method has been applied hitherto only to a few cases, namely to study the photoionization of atomic Be and Mg [5] and to the photodetachment of  $\text{Li}^-$  and  $\text{Na}^-$  [6].

There have been few theoretical and experimental studies on the photodetachment of  $\text{Cu}^-$ . Scheibner and Hazi [7] applied the R-matrix method to investigate photodetachment of  $\text{Cu}^-$ . On the experimental side, Balling *et al.* [8]

and Covington *et al.* [9] have measured the total photodetachment cross-section of  $\text{Cu}^-$  and found an excellent agreement with theoretical results. We employ the MCTD and the RRPA techniques to investigate the core correlation effects on the valence photodetachment of  $\text{Cu}^-$ .

The Multi-Configuration Tamm-Dancoff (MCTD) approximation incorporates the initial state correlation effects by considering a multi-configuration wavefunction to describe the initial state. The final state correlations are addressed in the MCTD in a manner similar to that in the RPA, by including inter-channel coupling. Details of the theory can be found elsewhere [6]. One difference, however, is that in the present work, experimental thresholds are employed. This is because the present calculation does not include any core relaxation and, thus, the theoretical thresholds are rather inaccurate.

## 2. RESULTS AND DISCUSSION

$\text{Cu}^-$  has 30 electrons and it is isoelectronic with neutral Zn in its ground state which has for its  $^1\text{S}_0$  state the configuration  $[\text{Ar}]3\text{d}^{10}4\text{s}^2$ . (Let us recall that  $[\text{Ar}] = 1\text{s}^2 2\text{s}^2 2\text{p}^6 3\text{s}^2 3\text{p}^6$ .)

In order to investigate the core correlation effects, the following two distinct descriptions of initial multiconfigurational state of the negative Cu ion were considered for the present study:

(a) The first initial state includes 3 configurations with states arising from the double electron excitations from the outermost valence shells alone:

$$[\text{Ar}] 3\text{d}_{3/2}^4 3\text{d}_{5/2}^6 (4\text{s}^2 + 4\text{p}_{1/2}^2 + 4\text{p}_{3/2}^2), J = 0.$$

(b) The second initial state includes 7 configurations that in addition to configurations from (a) incorporate the excitations from the 3d core subshells:

$$[\text{Ar}] \{ 3\text{d}_{3/2}^4 3\text{d}_{5/2}^6 (4\text{s}^2 + 4\text{p}_{1/2}^2 + 4\text{p}_{3/2}^2) + (3\text{d}_{3/2}^4 3\text{d}_{5/2}^4 + 3\text{d}_{3/2}^2 3\text{d}_{5/2}^6) 4\text{s}^2 (4\text{p}_{1/2}^2 + 4\text{p}_{3/2}^2) \}, J = 0.$$

The GRASP92 [11] package was used to obtain the relativistic initial state wave functions. As mentioned, due to the discrepancy between experimental and the present MCDF thresholds, we have employed the experimental thresholds for the MCTD calculations.

Initial state wave function (a) includes double electron excitations of 4s valence electrons only, whereas wave function (b) includes double excitations from core 3d subshells as well. Hence a comparison of the MCTD results employing initial state wave functions (a) and (b) enables one to understand the core correlation effects on the photodetachment process. In the present MCTD calculations, all the relativistic dipole channels from the 3d, 4s, and the 4p subshells are coupled to calculate the excited (continuum) state of  $\text{Cu}^-$ , neutral Cu plus a photoelectron.

Figure 1 shows the total photodetachment cross-section of  $\text{Cu}^-$  obtained using the MCTD using the two initial state wave functions (a) and (b). This figure also provides comparison with experimental [8] and the R-matrix [7] results. The length (L) and the velocity (V) forms of the MCTD cross-section are close to each other in both types of calculations. A large peak characterizes the

cross-section profile. The MCTD result with wave function (a) as the initial state has a cross-section of magnitude  $\sim 110$  Mb at the peak, while that with wave function (b) as the initial state has a significantly lower cross-section of magnitude  $\sim 70$  Mb, much closer to the experimental cross-section. The MCTD method is thus found to provide a good account of important core correlation effects in the photodetachment of  $\text{Cu}^-$ . Unfortunately, the experimental data available are only scanty for a more extensive comparison.

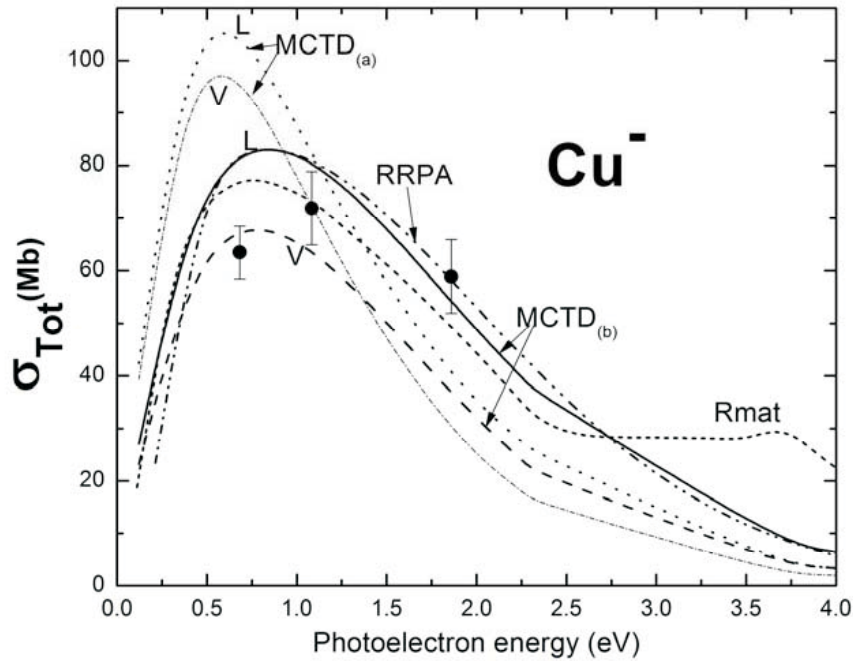


**Figure 1:** Total MCTD length (L) and velocity (V) photodetachment cross-sections of  $\text{Cu}^-$  along with earlier R-matrix (Rmat) [7], present RRPAs and experiment (solid circles) [8]. MCTD(a) and MCTD(b) respectively represent the MCTD calculation making use of configuration (a) and (b).

In Figure 1 the MCTD results are compared also with that from a 13-channel RRPAs calculation in which all the dipole channels from the 4s, 3d, and the 3p subshells are coupled. The MCTD result is in close agreement with the RRPAs which suggests that non-RPAs correlations which MCTD takes into account are only of a minute significance in the energy region considered. This is because the thresholds corresponding to channels from the 4p are considerably above the energy region considered. Hence, correlation effects due to the simultaneous photodetachment channel and the excitation channel from the 4p subshells, which are omitted from the RRPAs description of the process, are not of great importance. Thus, the correlations that result from the common two-electron excitations in RRPAs and the MCTD approximations already provide a

basis for an agreement between the two results when the non-RPA correlations are not important.

There is discrepancy between the R-matrix calculation [7] and MCTD results in the high energy region. The hump in the R-matrix cross section is due to the channels from the 3d subshells, which have thresholds at  $\sim 2.8$  eV. The discrepancy in the 3d threshold between MCDF and R-matrix causes a rather smooth MCTD cross-section in the high energy region. A more accurate description of the 3d threshold energies with the context of the MCTD calculation would likely bring the MCTD into better agreement with the R-matrix result.

From the application of the MCTD to the photodetachment of  $\text{Cu}^-$ , the importance of the core correlation effects in the calculations is thus demonstrated. In a general sense, the present (relativistic) MCTD calculations represents a modification of the RRPA in which the initial state correlations are introduced explicitly via a multi-configuration wavefunction, and the coupling among final (continuum) states includes channels representing two-electron excitations, ionization-plus-excitation.

### Acknowledgments

This work is partially supported by the Department of Science and Technology, Government of India, and by NSF and DOE, Office of Chemical Sciences (USA). V.R. was partially supported by the Ministry of Education and Science of the Republic of Serbia through project no. 171020.

### REFERENCES

- [1] V. K. Ivanov, *Journal of Physics B* **32**, R67 (1999).
- [2] V. K. Ivanov, *Radiation Physics and Chemistry* **70**, 345 (2004).
- [3] W. R. Johnson, and C. D. Lin, *Physical Review A* **20**, 964 (1979).
- [4] V. Radojević, M. Kutzner, and H. P. Kelly *Physical Review A* **40**, 727 (1989).
- [5] V. Radojević, and W. R. Johnson, *Physical Review A* **31**, 2991 (1985).
- [6] J. Jose, G. B. Pradhan, V. Radojević, S. T. Manson and P. C. Deshmukh, *Physical Review A* **83**, 053419 (2011)
- [7] K. F. Scheibner, and A. U. Hazi, *Physical Review A* **8**, 539 (1988).
- [8] P. Balling, C. Brink, T. Andersen, and H. K. Haugen, *Journal of Physics B* **25**, L565 (1992).
- [9] M. Covington, S. S. Duvvuri, E. D. Emmons, R. G. Kraus, W. W. Williams, J. S. Thompson, D. Calabrese, D. L. Carpenter, R. D. Collier, T. J. Kvale, and V. T. Davis, *Physical Review A* **75**, 022711 (2007).
- [10] H. Hotop, R. A. Bennett, and W. C. Lineberger, *Journal of Chemical Physics* **58**, 2373 (1973).
- [11] F. A. Parpia, C. F. Fischer, and I. P. Grant, *Computer Physics Communications* **94**, 249 (1996).

## RATE COEFFICIENTS FOR ELETRON IMPACT IONIZATION IN RF ELECTRIC FIELD IN NITROGEN

M. P. Popović<sup>1</sup>, M. M. Vojnović<sup>1</sup>, M. M. Ristić<sup>2</sup>, M. Vičić<sup>1</sup> and G. B. Poparić<sup>1\*</sup>

<sup>1</sup>*Faculty of Physics, University of Belgrade, P.O. Box 44,  
11000 Belgrade, Serbia*

<sup>2</sup>*Faculty of Physical Chemistry, University of Belgrade, P.O. Box 137,  
11000 Belgrade, Serbia*

*\*E-mail: goran\_poparic@ff.bg.ac.rs*

**Abstract.** We bring the calculus for rate coefficients for the electron impact ionization of the N<sub>2</sub> molecule in non-equilibrium conditions, in the presence of time-dependent electric field. A Monte Carlo simulation technique has been used to determine rate coefficients for relevant ionization processes in N<sub>2</sub> under various frequencies of radio-frequent (Rf) electric field. We obtained the distribution functions of electron energy by using Monte Carlo simulation for the frequency values: 50, 100 and 500 MHz, in reduced electric fields up to 300 Td. This work presents an insight into the characteristics of ionizing process and provides the ionization rate coefficients that can be of use for correct implementation in modeling Rf discharges. A behavior of rate coefficients under the influence of magnitude and frequency of the fields was studied separately revealing some features in time dependence.

### 1. INTRODUCTION

Nitrogen molecule comprises a significant fraction of the Earth's atmosphere and the atmospheres of Titan and Triton. Within these environments, N<sub>2</sub> is subject to significant bombardment both by energetic electrons, as is characteristic of aurorae, and by lower energy photoelectrons produced in the normal atmosphere [1]. As such, it still attracts much interest in various aspects of molecular and environmental physics and chemistry. Electron–nitrogen molecule collision processes play an important role in upper atmosphere as well as in any plasma and discharge technology and applications, such as: diffuse discharge switches [2], plasma etching industry [3], plasma polymerization [4], chemical detectors, etc. In modeling these phenomena, we need to know the cross sections and rate coefficients as functions of energy and their angular distribution for each process involved. Different channels in electron impact excitation of the N<sub>2</sub> molecule have been long and intensively

studied in the past few decades. Laboratory studies have produced a rather complete set of quantitative data for these processes.

Reactive plasmas maintained by radio-frequency (rf) or microwave sources have come to play an important role in the fabrication of microelectronic devices. Modeling of capacitively or inductively coupled plasmas driven by a Rf source has been performed in order to elucidate the discharge structures [5-6]. Under these circumstances, detailed investigation of the ionization rate coefficients is significant and desirable.

The primary aim of this work is to analyze rate coefficients in  $N_2$  and their relation to the cross sections. The non-equilibrium rate coefficients are obtained by sampling the electron energy distribution functions in Monte Carlo simulation of electron transport, with the input data of integral and differential cross sections for electron impact excitation and ionization of  $N_2$  [7-8].

## 2. MONTE CARLO SIMULATION

We have used time-resolved Monte Carlo simulation code for simulating the evolution of electron transport through  $N_2$  gas in the presence of spatially uniform radio-frequent electric fields. Differential equations of electron motion have been solved numerically, by applying the Runge-Kutta method [10], in each step ( $\Delta t$ ) in simulation. Calculations were made for the low-density limit of gas discharge. The non-equilibrium rate coefficients are obtained by sampling the electron energy distribution functions (EEDF) in Monte Carlo simulation.

In this model, we used the cross section data from our recent work [7], and then calculated rate coefficients of  $N_2$  ionization. After relaxation to a quasi-stationary state, the results were averaged over many periods for obtaining better statistics [9]. We obtained compatible results for mean electron energy and rate coefficients.

## 3. RESULTS AND DISCUSSION

We performed simulations of electron swarms in  $N_2$  gas, at  $E_R/N$  (normalized electric field) value up to 300 Td ( $1 \text{ Td} = 10^{-21} \text{ Vm}^2$ ), in absence of magnetic field ( $B/N=0$ ;  $N$  = density of electrons). The external electric field  $E(t)$  is assumed to be uniform in position and to vary with time as follows:

$$\vec{E}(t) = \sqrt{2}E_R \vec{k} \cos(\omega t) \quad (1)$$

where  $E_R$  is effective reduced field strength,  $\omega$  is angular frequency of the rf field and  $k$  is the unit vector in the field direction.

Initial kinetic energy of all  $10^7$  electrons was 5 eV. The density of neutrals was  $3.22 \cdot 10^{22} \text{ m}^{-3}$  which corresponded to the gas pressure of 1 Torr (133.3 Pa). Gas temperature assumed to be 273 K. In each step, after electrons have reached a steady state, EEDF is sampled in order to calculate rate

coefficients for various processes at given conditions, using the well known relation [11]:

$$K(\langle \varepsilon \rangle) = \sqrt{2/m_e} \int_{\varepsilon_{thres}}^{+\infty} \sigma(\varepsilon) \sqrt{\varepsilon} \cdot f_e(\langle \varepsilon \rangle, \varepsilon) d\varepsilon \quad (2)$$

where  $\langle \varepsilon \rangle$  is the mean electron energy,  $\sigma(\varepsilon)$  is the excitation cross section for considered process,  $\varepsilon_{thres}$  is threshold energy and  $f_e(\langle \varepsilon \rangle, \varepsilon)$  is the normalized EEDF. The dependence of the mean energy values on phase in the process indicate a decrease of the mean energy amplitude with increasing frequency caused by the incapability of electrons to follow and adjust to temporal Rf variations of external electric field. This behavior is presented in Fig. 1, that shows the time modulation of the ensemble average of energy,  $\langle \varepsilon(t) \rangle$ , during the electron motion in  $N_2$ , for frequencies 50, 100 and 500 MHz. It has a harmonic of  $2\omega$  as the fundamental wave and smaller than field harmonic. The phase delay increases and the amplitude decreases with increasing field frequency at constant  $E_R/N$ .

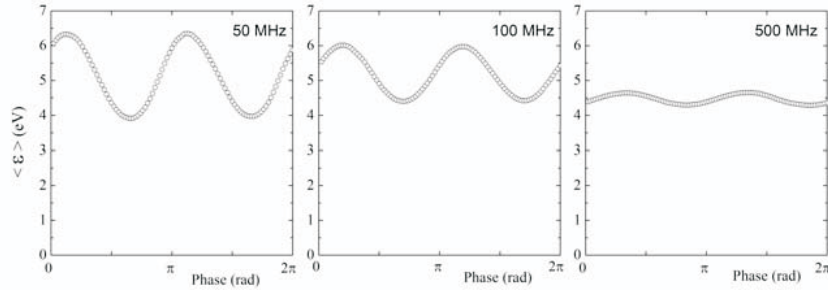


**Figure 1.** Time modulations of mean electron energy  $\langle \varepsilon \rangle$  for  $E_R/N$  value of 200 Td, in nitrogen at 1 Torr, for  $f = 50, 100$  and 500 MHz.

Figure 2 presents the time variation in rate coefficients for ionization process at single  $E_R/N$  value of 200 Td, in three different frequencies of electric field. In this manner we can easily get the insight in electron movement dynamics in  $N_2$ . In both cases, the gradual dissipation of amplitude originates from the relation between the collisional relaxation time of energy and the period of the applied field. The minimum value of  $\langle \varepsilon(t) \rangle$  at first slightly increases with increasing field frequency (Figure 1), because the electrons first lose their ability to relax the energy during the lower field phase.

When the frequency is further increased (up to 500 MHz), the electrons have not enough time to receive enough energy from the external field, and the electron energy maximum starts to decrease [9]. The similar behavior we have for the rate coefficients of ionization of  $N_2$ , but this amplitude decrease is even more rapid in case of increasing frequency values.

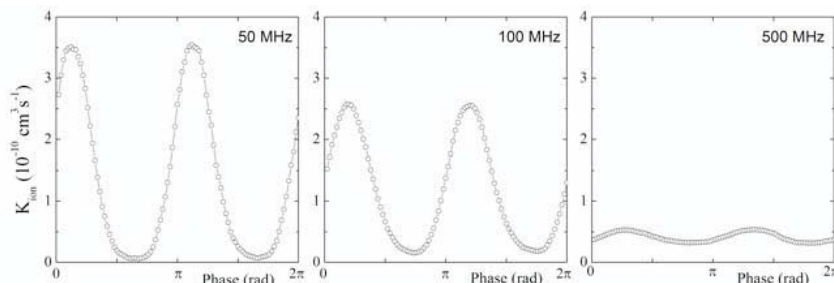


**Figure 2.** Time modulations of ionization rate coefficient  $K_{\text{ion}}$  for  $E_R/N$  value of 200 Td, in nitrogen at 1 Torr for 50, 100 and 500 MHz.

#### 4. CONCLUSIONS

Using a Monte Carlo simulation technique, we calculated rate coefficients for electron impact ionization of the  $N_2$  gas in time dependent reduced electric field, under the conditions of interest for plasma modeling. For performing this calculation, we developed the Monte Carlo simulation of electron swarm in radio-frequent E fields. Data presented here, together with the set of cross sections, are necessary for modeling non-equilibrium plasmas and plasma devices.

#### Acknowledgements

This work was performed under the Project 171016 of the Ministry of Science and Education of the Republic of Serbia.

#### REFERENCES

- [1] P.C. Cosby, J. Chem. Phys. 98, 9544 (1993).
- [2] S.R. Hunter and J.G. Carter, J. Appl. Phys. 58, 3001 (1985).
- [3] W.Z. Collison T.Q. Ni and M.S. Barnes, J. Vac. Sci. Technol. A 16, 100 (1998).
- [4] H. Yasuda and T. Hsu, J. Polym. Sci.: Polym. Chem. Ed. 15, 81 (1977).
- [5] J.P. Boeuf, Ph. Belenger and T. Hbid, Plasma Sources Sci. Technol. 3, 407 (1994).
- [6] K. Maeda, T. Makabe, N. Nakano, S. Bzenic and Z.Lj. Petrovic, Phys Rev E 55, 5901 (1997)
- [7] G.B. Poparić, M. Ristić and D.S. Belić, J. Phys. Chem. A 112, 3816 (2008).
- [8] M. Allan, J. Phys. B. 38, 3655 (2005).
- [9] Z.Lj. Petrović, Z.M. Raspopović, S. Dujko and T. Makabe, Appl. Surf. Sci. 192, 1 (2002).
- [10] R. Morrow, J. Comp. Phys. 43, 1 (1981).
- [11] P. Chantry, Final Technical Report ARPA, Order No 3342 (1978).

## ELECTRON IMPACT STUDY OF AUTOIONIZING STATES IN NEON

J. J. Jureta, A. R. Milosavljević and B. P. Marinković

*Laboratory for atomic collision processes, Institute of Physics, University of Belgrade, Pregrevica 118, 11080 Belgrade, Serbia*

**Abstract.** We present an experimental study on autoionizing states in neon performed by using a crossed electron-atom beams apparatus. The ejected electron energy spectra of neon upon electron excitation are presented for the incident energy range from 40 eV to 1000 eV. The present study brings an extension to previously published results regarding several aspects. Moreover, the measured ejected electron energy spectra in neon were calibrated according to ejected electron spectra in helium, which was introduced into the chamber at the same time in a mixture with neon. We argue that the usual direct method of calibration by using dominant features in neon, could suffer from reduced precision due to an influence of resonance processes.

### 1. INTRODUCTION

Autoionizing states and resonances in neon were studied very extensively in the past by different experimental techniques [1,2]. However, in the case of neon, these states overlap with resonances, therefore their separation and assignment is difficult to perform with a high precision. According to our knowledge, until now there is no an electron-atom experiment in which these features are separated clearly and with high accuracy. In the present contribution, we report a detailed experimental study on autoionizing states in neon by using a high-resolution, standard crossed electron-atom beams collision experiment. We believe that the present results can contribute to better understanding of both autoionization processes in neon upon electron excitation and the interference between autoionizing states and resonant processes.

### 2. EXPERIMENTAL APPARATUS AND PROCEDURE

The apparatus has been already presented at the 2<sup>nd</sup> National Conference on Electronic, Atomic, Molecular and Photonic Physics [3]. The spectrometer OHRHA consists of a high energy electron gun, a high resolution hemispherical analyzer, a hypodermic needle as a source of effusive beam of target gas and a Faraday cup as a collector for the electron beam. The electron

gun was designed by Omicron Vakuumphysik GmbH for electron impact energies from 10 eV to 2.5 keV with a resolution of 0.5 eV and an electron current in the range from 1 to 15  $\mu\text{A}$ ). In these measurements the position of the electron gun is fixed at  $90^\circ$  in reference to the gas beam.

After collisions of incident electrons with the target atoms, the ejected electrons are collected by multi-element zoom lens at the entrance of the analyzer. The hemispherical energy analyzer (EA 125 HR, Omicron) has a mean radius of 125 mm and a variable entrance/exit slits. It is equipped with 7 channeltrons for electron detection and its ultimate projected energy resolution is of the order of 10 meV, depending on the type of experiment (XPS, AUGER and EIS). The residual magnetic field was reduced by using two  $\mu$  metal shields, one inside and the other outside the vacuum chamber. Moreover, both the analyzer and the lenses are shielded separately. The vacuum chamber is homemade and is pumped by three turbo molecular pumps. The background pressure was  $4 \times 10^{-7}$  mbar, while the working pressure with neon was  $3 \times 10^{-6}$  mbar. For a valuable measurement it was necessary to reach stable working conditions, pressure and electron current. Under these conditions the satisfied statistics for one measurement was reached for less than one hour.

The apparatus is not designed for experiments with low-energy electrons; however, we succeeded to perform measurements in this energy region, as well, thanks to the high efficiency of detecting system and appropriate adjustment of parameters. All collected data are stored in PC computer. The program made by OMICRON automatically controlled all parameters in hemispherical analyzer and lenses, which were adjusted before every single measurement.

The estimated energy resolution in ejected electron spectra was between 0.1 and 0.2 eV. The calibration of ejected electron energy scale was done in a mixture of neon and helium at high impact energies (500, 800 eV). The calibration point is taken from ejected electron spectra of helium at 35.55 eV which corresponds to the position of the double excited  $2s2p(^1P)$  state at 60.130 eV [4]. The overall uncertainty is about 0.06 eV. It should be pointed out that an analogue, direct calibration of the neon spectra by using its strong spectral features is not precise enough due to the existence of nearby resonances. The resonant process, which is close in energy to the spectral feature used for calibration, can influence the form of the peak, thus making the position of the feature not well defined.

### 3. RESULTS AND DISCUSSION

Figure 1 shows ejected electron spectra taken at different electron energies. The goal of this presentation is to show main characteristics of the spectrometer, focal properties of the lenses, transmission and resolution in the large electron energy range. Moreover, the presented spectra show the changes in the form of spectral features with changing the incident electron energy ( $E_e$ ).

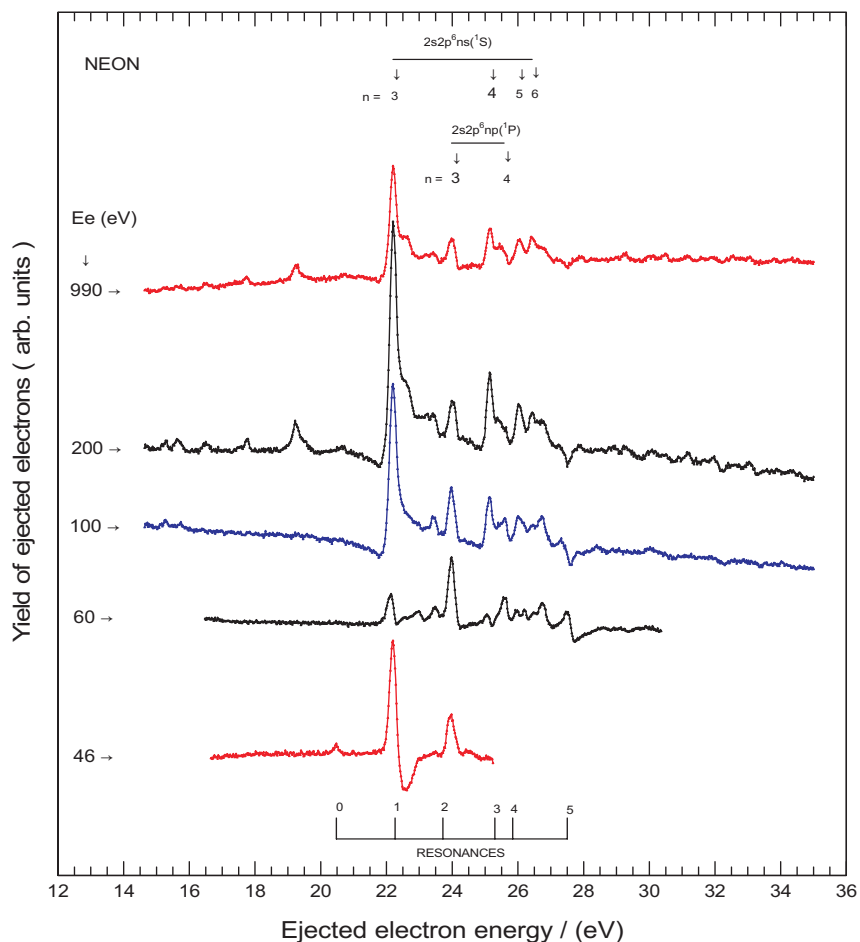


**Figure 1.** Autoionizing states and resonances of Neon recorded as ejected electron spectra at an ejection angle of  $90^\circ$ , in the energy region from 14 to 35 eV in steps of 0.020 eV, with electron incident energies ( $E_e$ ) from 46 to 990 eV (shown on the left hand side of the figure).

The autoionizing states and resonances are shown in the ejected electron energy range between 14 and 35 eV (figure 1), that corresponds to the excited energies between 35.56 and 56.56 eV since the ionization potential of Ne is 21.56 eV. The dominant features in the spectra lie in the energy region between 21 and 29 eV kinetic energy (42.56 to 50.56 eV of excited energies). This energy region has been studied very extensively in the past in electron, photon and ion experiments. Two series of excited states are identified:  $2s2p^6ns(^1S)$  and  $2s2p^6np(^1P)$ , as well as resonances. The first very intense feature  $2s2p^63s(^1S)$  at high impact energies (100 to 990 eV), is a mixture between a resonance and the autoionizing state. Its intensity decreases when the electron energy approaches the threshold of the excited state. At 46 eV of

incident electron energy, about 2.3 eV above the threshold for this state, the resonance is dominant and the peak was shifted to higher ejected energy. The first member of the second series  $2s2p^63p(^1P)$  does not have strong contribution from resonances. Therefore, its intensity does not change significantly with changing the incident electron energy and it can be a referent point for calibration.

Finally, it should be noted that the resonances in neon have been also studied very extensively in the past and the present measurements show only a part of known resonant processes in this energy region (see Buckman and Clark [2] for more details).

#### 4. CONCLUSION

In conclusion, we have presented experimentally obtained ejected electron spectra of neon, upon electron excitation in the incident energy range from 40 eV to 1000 eV. The present study on autoionizing states in neon brings an extension to previously published results with respect to several aspects: the large range of incident electron energy, the high-energy resolution and the large range of kinetic energy of ejected electrons. Moreover, a unique method has been used to perform the energy calibration of the measured spectra, based on the calibration of ejected electron spectra of helium, which was introduced into the chamber at the same time in a mixture with neon. Finally, we argue that the usual direct method of calibration, by using dominant  $2s2p^63s(^1S)$  feature in neon, could suffer from reduced precision due to undefined both position and profile of the feature which is influenced by the nearby resonance.

#### Acknowledgements

This work has been done within the projects MES RS OI 171020 and COST Action MP1002 “Nano-scale insights in ion beam cancer therapy (Nano-IBCT)”.

#### REFERENCES

- [1] Z. P. Zhong, S. L. Wu, R. F. Feng, B. X. Yang, Q. Ji, and K. Z. Xu, Y. Zou, Jia-Ming Li, Phys. Rev. A 55,3388-3393 (1997).
- [2] S. J. Buckman and C. W. Clark, Rev. of Mod. Phys. 66, 539 (1994).
- [3] J. J. Jureta, A. R. Milosavljević and B. P. Marinković, Proc. 5th Conference on Elementary Processes in Atomic Systems (CEPAS2011) and the 2nd National Conference on Electronic, Atomic, Molecular and Photonic Physics (CEAMPP2011), 21st – 25th June 2011, Belgrade, Serbia, Contributed Papers & Abstracts of Invited Lectures, p.126. ISBN: 978-86-82441-32-8
- [4] K. Codling, R. P. Madden, and D. L. Ederer, Phys. Rev. 155, 26 (1967).

## A NEW TESTING OF THE NOETHER'S THEOREM COROLLARY

V.M. Ristić, M.M. Radulović, T.M. Miladinović and J.S. Stefanović

*Faculty of Science, Kragujevac University, R. Domanovića 12,  
34000 Kragujevac, Serbia*

**Abstract.** Recently it was shown that theories treating two interacting objects in a different manner (for instance electromagnetic field of a laser classically, and the interacting atom as a quantum object) have some ambiguities and that they should be named “mixed”. The Noether’s Theorem Corollary about the laws of energy, momentum and angular momentum conservation in mixed theories was proven, showing that aforementioned theories do not support *the law of angular momentum/spin conservation* (not implying that the law of conservation of angular momentum/spin is not valid generally, but that mixed theories give results which might violate this law). In the present work some further difficulties in using mixed theories in the field of radiation physics will be emphasized, which were overcome by introducing fully quantized theory, completely independent of our research, but confirming it regardless.

### 1. INTRODUCTION

The theories that describe a behavior of atoms in strong laser fields treat an atom as quantized object and electromagnetic field classically [1, 2]. We suggest that these theories should be named “mixed”. Although using mixed theories in the beginning of Quantum Theory was considered unpleasant [1], these theories (which combine classical and quantum approach) have shown their vitality not only in the case of strong laser fields but also for super-strong fields. For instance, in radiation physics the calculation of the stopping power was treated (Bethe [3], Sigmund and Haagerup [4]) by using a combination of the classical and quantum approach: a projectile was considered as classical charged particle, the target as a quantum harmonic oscillator. Later, Cabrera-Trujillo [5], leaning on [4], included more thorough (but not completely) quantum mechanical approach. Recently, Stevanović and Nikezić [6] improved his method by treating both the projectile and the target as a set of quantum harmonic oscillators. The results they obtained confirmed predictions of our Corollary, without the authors being even aware of its existence.

## 2. PROVING THE COROLLARY TO NOETHER'S THEOREM

In order to shed some new light on those results here some of our earlier arguments [1] will be repeated regarding the Corollary of Noether's theorem about the behavior of mixed theories when they are dealing with angular momentum/spin.

Following paper [1], the Noether's theorem can be rephrased in the following manner: "To any  $s$ -parametric continuous transformation of field functions and coordinates which keeps variation of action zero, there correspond  $s$ -dynamic invariants (i.e. constant in time combinations of field functions and their derivatives)".

In what follows the Greek indices are denoting 4 space-time coordinates (0,1,2,3), while Latin ones are denoting spatial 3-coordinates (1,2,3). We shall start with following expression [1] for mixed tensor

$$\theta_v^\kappa = -\frac{\partial L}{\partial u_{\alpha;\kappa}}(u_{\alpha;\lambda}X_v^\lambda - \Psi_{\alpha v}) - L(x)X_v^\kappa, \quad (1)$$

If infinitesimal translations  $\delta x^\kappa$  are chosen as parameters of transformation, one obtains

$$X_\lambda^\kappa = \delta_\lambda^\kappa, \quad \Psi_{\alpha\lambda} = 0, \quad (2)$$

which changes the tensor  $\theta_v^\kappa$  in it's fully contravariant form [7]

$$T^{\lambda\kappa} = \frac{\partial L}{\partial u_{\alpha;\kappa}(x)} \frac{\partial u_\alpha}{\partial x^\lambda} - L g^{\lambda\kappa}. \quad (3)$$

In the literature [8] is shown that integrals over three-dimensional configuration space are constant in time. For instance, such an integral for the zero component of tensor  $T^{\lambda\kappa}$  would give a constant-in-time 4-vector

$$P^\lambda = \int T^{\lambda 0} d\vec{x}. \quad (4)$$

This is actually the law of conservation of momentum/energy, which follows from the time/space translation; because time and space are homogenous in the same manner in classical and quantum case, this law is applicable to mixed theories.

For infinitesimal Lorentz rotations:  $\delta x^\kappa \rightarrow \delta L_{\nu\mu}$ , and after some cumbersome calculations [1, 8], the 4-angular momentum tensor is obtained

$$M^{\tau(\rho\sigma)} = x^\sigma T^{\rho\tau} - x^\rho T^{\sigma\tau} - \frac{\partial L}{\partial u_{\nu;\tau}} A_\mu^{\nu(\rho\sigma)} u_\mu(x'). \quad (5)$$

The first two terms represent an orbital angular momentum of the wave field, while the third characterizes its polarization properties, and in the quantized case corresponds to the spin of the particle described by the quantized field.

So, 4-rotations of space-time result in conservation law of 3-angular momentum/spin, but this would not be applicable to mixed theories, as the rotations which are continuous in the classical theory must be quantized in the quantum theory. The type of continuity of parameters is thus changed: in the classical case the continuous function is used, while in the quantum case there is not continuous, but closed angular momentum operator. It can be said that the isotropy of space is broken for mixed theories - **there is no smooth connection between the classical and quantum part of the theory, hence for such theories the conservation of angular momentum and spin is not working.**

In this manner was proven the following [1, 2]

**Noether's Theorem Corollary**

*Physical theories that combine ("mix") quantum and classical approach do **support** the law of energy/momentum conservation, but **do not support** the law of angular momentum/spin conservation.*

This proof, being all-inclusive, is valid for all mixed theories.

Aforementioned result does not imply that the law of conservation of angular momentum and spin is not valid generally, but rather that mixed theories are producing results which might violate this law. This shortcoming of mixed theories is not always evident, as most of these theories do not deal with angular momentum/spin (for instance, the ADK-theory, in tunnel ionization of atoms). So we are here weakening our argument, as it is not needed to rule out the whole mixed theory because it fails to support one special law of conservation. Thus, suggestion to the researchers using mixed theories is to check that part of their results referring to angular momentum/ spin carefully.

### 3. COMPARISON OF THE VARIOUS STOPPING POWERS

In the Fig. 1, taken from [6], are shown the results of Bethe theory ( $S_{\text{Bethe}}$ ), Carera-Trujillo paper ( $S_{\text{C-Trujillo}}$ ) and Stevanović, Nikezić ( $S_{\text{C}}$ ), together with  $S_{\text{SRIM}}$ , based on SRIM's simulation of experimental data.

In the domain of projectile's high energies the stopping power behaves in the same manner in all theories, but at lower energies, there are visible differences in the theories which are mixed to various extents. The best agreement with SRIM simulation results is exhibited by the Stefanović-Nikezić expression for stopping power because their theory is fully quantized (not mixed at all), then Carera-Trujillo approach (slightly mixed - the projectiles are treated classically), and finally the most discrepancy with the SRIM exhibit the Bethe theory, which is mixed the most.

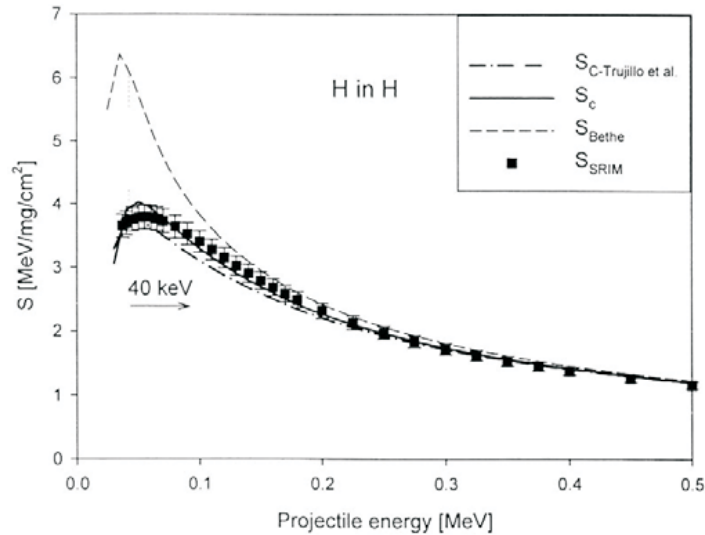


**Figure 1.** Comparing the stopping power calculated in various theories.

#### 4. FINAL REMARKS

The corollary of the Noether's theorem, proven in [1] and briefly presented here, gives us a qualitative criterion for judging the reliability of mixed theories, which are very often used in the field of atomic, molecular and optical physics.

#### Acknowledgements

This work is supported in part by Ministry of Science and Technological Development, Republic of Serbia (Project 171021).

#### REFERENCES

- [1] V.M. Ristić, M.M. Radulović and T.B. Miladinović, *Int. J. of Theor. Phys.* 11, 3602 (2011).
- [2] V.M. Ristić and M.M. Radulović, *Laser Phys. Lett.* 1, 79 (2004).
- [3] H. Bethe, *Ann. Phys.* 5, 325 (1930).
- [4] P. Sigmund and U. Haagerup, *Phys. Rev. A* 34, 892 (1986).
- [5] R. Cabrera-Trujillo, S.A. Cruz, J. Oddershede and J.R. Sabin, *Phys. Rev. A* 55, 2864 (1997).
- [6] N. Stevanović and D. Nikezić, *Eur. Phys. J. D* 42, 397 (2007).
- [7] V.M. Ristić, *Noether's Theorem*, monography (2008).
- [8] N.N. Bogoliubov and D.V. Shirkov, "Introduction to the Theory of Quantized Fields", Interscience, New York (1959).

## PHOTODISSOCIATION OF PURE AND NANOSOLVATED PROTONATED LEUCINE-ENKEPHALIN PEPTIDE

A. R. Milosavljević<sup>1\*</sup>, F. Canon<sup>2</sup>, J. B. Maljković<sup>1</sup>, L. Nahon<sup>3</sup> and A. Giuliani<sup>3,4</sup>

<sup>1</sup> *Laboratory for atomic collision processes, Institute of Physics, University of Belgrade, Pregrevica 118, 11080 Belgrade, Serbia*

<sup>2</sup> *INRA, UMR1324 Centre des Sciences du Goût et de l'Alimentation, F-21000 Dijon, France*

<sup>3</sup> *Synchrotron SOLEIL, L'Orme des Merisiers, Saint Aubin, BP 48, 91192 Gif-sur-Yvette, France*

<sup>4</sup> *UAR 1008 Cepia, Institut National de la Recherche Agronomique (INRA), BP 71627, 44316 Nantes Cedex 3, France*

**Abstract.** We have studied photodissociation of protonated leucine-enkephalin (Leu-Enk) peptide ion, pure or nanosolvated in a cluster with a given number of water molecules and isolated *in vacuo* by means of an ion trap. The methods to isolate hydrated ionic species in the linear trap, with desired number of attached water molecules and enough ion densities are discussed. The results of VUV photo-induced dissociation of selected both  $[\text{Leu-Enk+H}]^+$  and  $[\text{Leu-Enk+4H}_2\text{O+H}]^+$  trapped ions are presented at a photon energy of 8 eV.

### 1. INTRODUCTION

A number of studies on electron, ion and photon interaction with isolated molecules representing building blocks or parts of large biological system such as DNA and proteins have been reported in the last decade, devoted to explore in more detail complex processes associated with the radiation damage of biomaterial on a nanoscale. Particularly, it has been recognized that this research could lead to very important biomedical applications, such as optimizing the type and doze of the radiation in cancer therapy, in order to maximize killing of the cancer cells, while minimizing the damage to surrounding healthy tissue [1]. Most of the results have been reported for relatively small molecules isolated in the gas phase or deposited on surfaces, which allows to study the interaction processes between well defined beam of projectiles (electrons, photons, ions) and a specific molecule, prepared under well defined conditions. However, although this approach leads to the

---

\* e-mail: vraz@ipb.ac.rs

establishing of certain important interaction parameters (e.g. scattering cross sections), the molecules under study are far from the conditions that exist in real biological systems. Therefore, one crucial issue deals with the influence of the environment on both the physical characteristics of complex biomolecules and the processes occurring upon their activation (e.g. the high energy irradiation). In order to overpass the gap between results obtained on isolated biomolecules and their application to real biological systems, the possibility to perform a detailed study on a biomolecule embedded in a cluster with a well defined number of solvent molecules, isolated under well defined, high vacuum conditions, is of great interest.

Recently, Liu et al. [2] have shown that nanosolvated nucleotide anions can be produced directly from the electrospray ionization (ESI) source. They have investigated the fragmentation of singly charged anions of adenosine 5'-monophosphate ( $\text{AMP}^-$ ) induced by collisions with neutral atoms (Ne, Na) at a collision energy of 50 keV. Experiments were performed with isolated  $\text{AMP}^-$  as well as with  $\text{AMP}^-$  anions nanosolvated in a cluster with a given number of water molecules. It was found that the  $\text{AMP}^-$  ion is fully protected when the number of water molecules is larger than about 13. However, according to our knowledge, there is no reported study about photon (or electron) induced dissociation of a nanosolved protein/peptide ion isolated in the gas phase as a function of the size of the cluster (i.e. number of solvent molecules). The likely reason for this is a difficulty to prepare and isolate this kind of species in the gas phase, as well as to couple the target beam/packet to a tunable vacuum ultraviolet (VUV) source of enough intensity to produce a measurable signal.

In the present contribution we report results on synchrotron radiation (SR) VUV photodissociation spectroscopy of electrosprayed leucine-enkephalin (Leu-Enk) peptide either pure or hydrated with a specific number of water molecules. It should be noted that a study on photodissociation of isolated pure protonated leucine-enkephalin (Leu-Enk) peptide, in the VUV range of 8–40 eV, has been reported very recently [3]. Additionally, we discuss the methods to efficiently produce and store in the trap the hydrated systems, either directly from the ESI source or by a controlled introduction of water vapor into the ion trap filled with already isolated precursor ion.

## 2. EXPERIMENTAL APPARATUS AND PROCEDURE

The new experimental system for SR spectroscopy of electrosprayed ions stored in a linear ion trap has been described recently [4,5]. Briefly, the setup is based on a commercial ion trap ("Thermo scientific LTQ XL"), equipped with the an ESI source. The synchrotron beam, from the VUV beamline DESIRS at Synchrotron SOLEIL (France) is introduced into the trap through the back lens of the LTQ XL mass spectrometer. A special frame has been constructed to allow fine-tuning of the position of the spectrometer, i.e. of the trapping region, with respect to the light beam. The vacuum manifold with a turbo pumping stage has been designed to accommodate pressure difference between the beamline ( $10^{-8}$  mbar) and LTQ ( $10^{-5}$  mbar). The experiment is

performed as follows: (1) electrosprayed ions are injected, mass selected and stored in the ion trap; (2) the beam shutter opens, thus starting the irradiation during a well defined period; (3) the mass spectrum is recorded; (4) the monochromator can be then set to the next wavelength and the procedure is repeated.

### 3. RESULTS AND DISCUSSION

Two possibilities for production of nanosolvated protonated biomolecules offering both large number of water molecules and high trapped ions densities were considered: (i) the controlled introduction of water directly into the trap; (ii) direct creation of hydrated biological ions in the ESI source. The first investigated solution was based upon controlled introduction of water vapor through the helium gas feed, by using helium as a carrier. The linear ion trap of the LTQ XL mass spectrometer is filled with helium gas ( $10^{-3}$  mbar), which is introduced through a special feed directly into the trap, in order to achieve better trapping performance. It was investigated if this feed could be used to introduce water directly into the trap by flowing helium through a volume containing water vapour. However, due to a large difference between the pressures of helium and water (and avoiding risk of contamination by heating the water), this solution was not of satisfactory performance.

The second solution was based upon production of hydrated biomolecular ions directly in the ESI source, by tuning an appropriate combination of ESI parameters such as solvent type and concentration of the sample solution, transfer tube temperature, voltages and sheath gas flow rate. This means that have worked under non-standard conditions of the commercial spectrometer, which normally performs in a way such as to reduce as much as possible water and other solvent adducts. Although it was indeed difficult to reduce all contamination in the spectra, the obtained results appear to be very promising for producing hydrated biomolecules. By adjusting the ESI parameters, we were able to isolate in the trap hydrated protonated ions of small peptides and nucleotides with up to 20 water molecules, which was confirmed by monitoring the water losses upon collision induced dissociation in the MS<sup>2</sup> mode. Nevertheless, the density of ions in the trap to perform photon spectroscopy with reasonable signal/noise ratio was high enough only for the clusters with up to about 5 water molecules. Still, it should be noted that these are very first results and we expect further improvements of the method in the future.

As an exemple, we show in Figure 1 the photon induced dissociation of protonated Leu-Enk and a cluster of Leu-Enk with 4 water molecules, at the incident photon energy of 8 eV, after subtraction of a background and recorded under the same experimental conditions. Figure 1a shows the fragmentation pattern for the case of pure protonated molecule. This pattern corresponds well to the theoretical peaks table, as well as to recently published results by Bari et al. [3]. However, the fragmentation is significantly different in the case of

hydrated protonated precursor (Figure 1b). First, the intensive fragmentation is reduced, showing a “shielding” effect of a water solvation shell, and the dominant channel corresponds to the loss of one water molecule. Additionally, it is very interesting to note several clearly resolved peaks which correspond to the fragments of the pure peptide molecule, but still complexed with 4 water molecules.

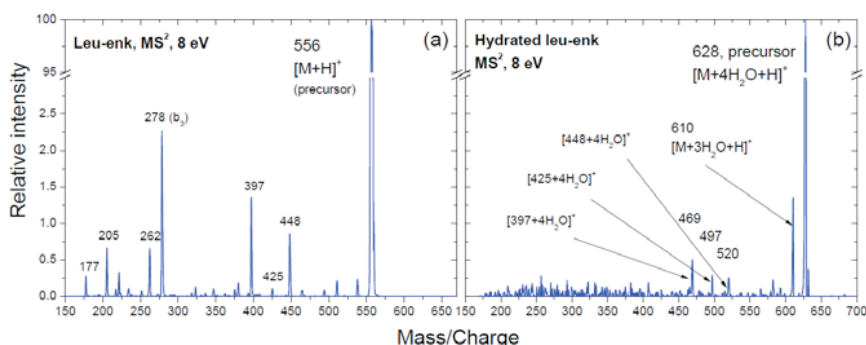


**Figure 1.** Tandem mass spectra of (a) protonated leucine-enkephalin (Leu-Enk, denoted by M) and (b) protonated hydrated Leu-Enk ( $M+4H_2O$ ) ions upon activation by 8 eV photons.

## Acknowledgements

This work was supported by the Agence Nationale de la Recherche Scientifique (Project #BLAN08-1\_348053) as well as by the Ministry of Education and Science of Republic of Serbia (Project No. 171020), the COST Action MP1002 “Nano-scale insights in ion beam cancer therapy (Nano-IBCT)” and the “Pavle Savić” project of bilateral scientific collaboration between Serbia and France “Photon and electron spectroscopy of pure and nano-solvated biomolecules isolated in gas phase” (680-00-132/2012-09/06). We are grateful to the general SOLEIL staff for running the overall facility, and support under project #20110694.

## REFERENCES

- [1] COST Action MP1002, Nanoscale insights into Ion Beam Cancer Therapy (Nano-IBCT); [<http://fias.uni-frankfurt.de/nanoibct/overview/>].
- [2] Liu et al., Phys. Rev. Lett. 97, 133401 (2006).
- [3] S. Bari et al., J. Chem. Phys. 134, 024314 (2011).
- [4] A. R. Milosavljević, C. Nicolas, J. Lemaire, C. Dehon, R. Thissen, J.-M. Bizau, M. Réfrégiers, L. Nahon, and A. Giuliani, Phys. Chem. Chem. Phys. 13, 15432 (2011).
- [5] A. R. Milosavljević, C. Nicolas, J.-F. Gil, F. Canon, M. Réfrégiers, L. Nahon, and A. Giuliani, J. Synchrotron Rad. 19, 174 (2012).

## **SECTION 2.**

### **Particle and Laser Beam Interactions with Solids**

- 2.1 Atomic Collisions in Solids
- 2.2 Sputtering and Deposition
- 2.3 Laser and Plasma Interaction with Surfaces

### **ABSTRACTS OF INVITED LECTURES**



## **PRELIMINARY RESULTS FROM RECENT EXPERIMENTS AND FUTURE ROADMAP TO SHOCK IGNITION FOR INERTIAL CONFINEMENT FUSION**

Dimitri Batani

*Univ. Bordeaux, CEA, CNRS, CELIA (Centre Lasers Intenses et Applications),  
UMR5107, F-33400 Talence, France  
Responsible of the WP 10 (Fusion Experiments) of the HiPER Project*

In 2007 Betti et al. [1] proposed a novel approach to ICF. It consists of igniting the target by a very strong converging shock ( $P \approx$  several hundreds of Mbar), produced by intense laser spikes ( $1 \cdot 10^{16}$  W/cm<sup>2</sup>), which must hit the target at the end of the compression phase. The scheme represents a very attractive solution for the HiPER project since it maintains the advantages of direct drive, of separating the ignition and compression phases, and it is substantially compatible with present day laser technology (used to build NIF and LMJ). A proof of principle of shock ignition could be realized on LMJ within the next decade.

In the talk, I will present:

i) the results of preliminary experiments conducted at PALS in order to study shock generation and laser-plasma interaction in an intensity regime which is relevant for shock ignition, and ii) the status of the discussion within HiPER on the shock ignition roadmap, including the plan for future experiments on European laser facilities (PALS, LULI, Orion, LIL, etc) and for finally approaching SI demonstration on LMJ.

Experiments at PALS were done using two beams, with time duration 300 ps. The first beam, at intensity  $I=1.2 \cdot 10^{13}$  W/cm<sup>2</sup>, was used to create a  $\approx 1$  mm preformed plasma, and the second, at  $I=1 \cdot 10^{16}$  W/cm<sup>2</sup>, to create the final strong shock. Several diagnostics were employed to characterize both the preformed plasma (Phase 1), and the shock formation and laser-plasma interaction (Phase 2). In Phase 1, they included X-ray deflectometry and Optical interferometry for the plasma density profile, and X-ray spectroscopy to get plasma temperature.

In Phase 2 Energy Encoded pin-hole camera to measure plasma extension, characterize its emission but also to give evidence of the presence of hot electrons; shock chronometry to measure the ability to produce a strong shock and the effect of the extended plasma corona on the laser-shock coupling; X-ray (K-a) imaging again for hot electrons, Optical spectroscopy and

calorimetry to get the amount of backreflected light from parametric instabilities (SRS, SBS, TDP).

**Acknowledgements**

Thanks to L.Antonelli, S.Atzeni, J.Badziak, M.Decroisette, L.Gizzi, E.Krousky, X.Ribeyre M.Richetta, G.Schurtz,

[1] *Shock ignition of thermonuclear fuel with high areal density* Betti R, et al. Phys. Rev. Lett., 98, 155001 (2007)

## **THE ORIGIN OF THE PLASMA GROWN NANOSTRUCTURES AT THE SOLID-SOLID INTERFACE**

Uroš Cvelbar

*Jozef Stefan Institute, Jamova cesta 39, SI-1000 Ljubljana, Slovenia*

**Abstract.** The research on the growth of various nanostructure materials was significant in recent years, especially on application of plasmas as a tool for fabrication. Nanowires are predominantly synthesized using catalyst clusters in either the vapour phase, in a supercritical fluid phase, or by using an oxide-assisted growth technique without catalyst clusters. Another prominent method employed is bulk nucleation and growth of nanowires with plasma assisted growing from the melts of low-melting point material and also directly from the solid phase from bulk material. The subject of particular interest is application of low temperature reactive plasmas, also called chemically active plasmas, for direct plasma surface nanofabrication processes. These plasmas are mostly generated in high frequency discharges like microwave or radiofrequency discharges, where suitable radicals for nanofabrication can be generated. In presented cases, we used rf oxygen plasma glow discharge of weakly ionized highly dissociated plasma for nanostructuring various bulk metals. On the surface of metals, metal oxide nanowires / nanocones / nanobelts / nanodots can be grown during exposure to oxygen radicals directly on solid-solid interface. As simulations and experimental results showed, the ionized gas environment is decisive in sustaining the growth of tall and sharp nanotips or nanowires. It is, however, not yet known, how the surface properties of a material change with the growth of nanostructures and the presence of other radicals. This becomes very important when we deal with reactive plasma process, where nanostructures like nanowires grow spontaneously from solid state material, so no building material is supplied from the gas phase. The growth of metal oxide nanostructures from bulk phase can be explained by of synergetic interaction of low energy ions and high flux of neutral oxygen atoms entering to the surface and changing its structural properties. After initial solid phase transformation of metal to metal oxide where nuclei are formed on the surface and the surface is in unstable stage. This stage of growth can be seen in some nanowires like neck region without proper crystal lattice orientation, and is responsible for later growth and shape of nanowires. It seems that the surface charge and its distribution create this unstable environment in which the nanowires can be erected and grown vertically instead of growing into thin film.

## PROPERTIES OF PLASMAS PRODUCED BY LASER ABLATION WITH SINGLE AND DOUBLE PULSES

J. Hermann, L. Mercadier, S. Noël, E. Axente, S. Beldjilali, M. Cirisan,  
E. Mothe, W.L. Yip

*LP3, CNRS - Aix-Marseille University, Luminy, Marseille, France*

**Abstract.** Pulsed laser ablation has attracted a strongly increasing interest over the past two decades. The advances in the understanding of laser-material interactions as well as the technological progress in compact and reliable laser systems made laser ablation promising for many applications such as thin film deposition, nanostructuring of materials, surface treatment, nanoparticle generation and material analysis. Due to the high power density of focused laser radiation, pulsed laser ablation leads to the formation of a plasma characterized by large initial values of temperature and density. The plume undergoes fast expansion during which the temperature and density rapidly decrease.

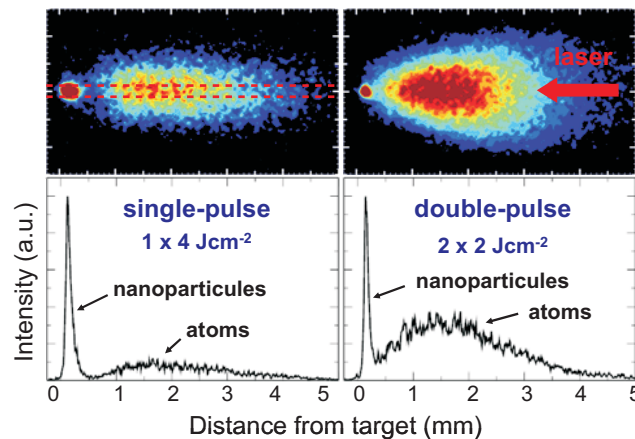


**Figure 1.** Plasma images and derived intensity distribution for short pulse laser ablation of titanium. The double pulse increases the plume atomization.

Recent investigations demonstrated that the irradiation with so-called “double-pulses” may improve the properties of the laser-induced plasmas in the view of different applications. In the present paper, we discuss the physical mechanisms responsible for the plume changes that occur when an additional delayed laser pulse is applied.

## **GUIDING OF SLOW HIGHLY CHARGED IONS THROUGH TAPERED GLASS CAPILLARIES**

Tokihiro Ikeda

*Atomic Physics Laboratory, RIKEN, 2-1 Hirosawa, Wako, Saitama 351-0198  
Japan*

**Abstract.** We have developed a method to produce microbeams of keV energy highly charged ions (HCIs) with tapered glass capillary optics. Slow (keV energy) HCIs have high ability to modify surfaces and cause efficient sputtering without damaging the substrate very much. Once a microbeam is available, these functions specific to slow HCIs can be used to realize, e.g., micro-patterning of modifications and element-sensitive micro-imaging. However, microbeam of slow HCIs is not yet practically available because HCI beams are sometimes so weak for using a collimator or slit. In addition, when magnetic and/or electrostatic lenses are combined, good emittance is required. We have proposed the capillary guiding of slow HCI beams through tapered insulator capillaries which is based on a self-organized charge up on the capillary inner wall. We obtained the following findings using 8 keV Ar<sup>8+</sup> beam through a tapered glass capillary whose outlet diameter was 24  $\mu\text{m}\phi$  [1]; (1) the transmission started a few seconds after the initial beam entered the capillary inlet, (2) the initial charge state and the kinetic energy were kept, and (3) the extracted beam followed the capillary axis even when the capillary was tilted by up to 5°. Furthermore, the taper can provide the advantages; (A) it can enhance the density of the extracted beam, and (B) the size of the extracted beam is the same size of the outlet. And relatively low cost to introduce the capillaries for microbeams is also an attractive point. In this lecture, the transmission feature of slow HCI beams including bent Teflon tubes [2] will be reported. And microbeams of MeV ions produced by the tapered glass capillaries with end windows [3] for the irradiations of human cancer cells and Escherichia coli bacteria, and micro-patterned coating on polymer surfaces, will be introduced.

### **REFERENCES**

- [1] T. Ikeda, Y. Kanai, T. M. Kojima, Y. Iwai, T. Kambara, Y. Yamazaki, M. Hoshino, T. Nebiki, and T. Narusawa, *Appl. Phys. Lett.* 89, 163502 (2006).
- [2] T. M. Kojima, T. Ikeda, Y. Kanai, Y. Yamazaki, and V. A. Esaulov, *J. Phys. D: Appl. Phys.* 44, 355201 (2011).
- [3] <http://www.riken.jp/ap/nanobeam/index-en.html>

## COMPREHENSIVE PLASMA DIAGNOSTICS FOR AN ECR ETCHER

Vladimir Milosavljević

*Faculty of Physics, University of Belgrade, Serbia*

*School of Physical Science & NCPST, Dublin City University, Dublin, Ireland*

**Abstract.** Semiconductor processes using non-equilibrium plasmas are indispensable for the manufacture of ultra large scale integration, solar cells, liquid crystal devices, etc. In the last two decades, electrical and optical emission spectroscopies have been successfully used for measurements and control of plasma products in technological relevant plasma chambers. This work presents a Phase Resolved Optical Emission Spectroscopy (PROES) in conjunction with Retarding Field Energy Analyzer (RFEA), for one of the typical industrial chambers as the Electron Cyclotron Resonance (ECR) plasma etcher. The PROES study a light modulation by the RF bias of ECR and the RFEA measures an ion energy distribution function. The experiment is conducted in pure argon discharge and with SiO<sub>2</sub> wafer. The ECR etcher has a 2.45 GHz microwave generator with a maximum power up to 2kW, magnetic field of 90 mT and 2MHz RF bias with maximum power of 250 W. The PROES is done by the ICCD camera which can be operated with a repetition rate of 2 MHz synchronously (triggered) with the RF bias. The integration gate is locked to a fixed phase position within the RF cycle (500 ns) and gives exactly 128 intervals over the  $2\pi$  RF cycle.

The measurement of atomic oxygen spectral lines intensity from 777 triplet, in the respect of RF bias, is presented. At the beginning of a discharge (pure argon plasma) there is no oxygen in gas phase, but there is oxygen in the solid state, i.e. in SiO<sub>2</sub> lattice. Thus, measurement of ion-flux is essential for quantification of oxygen in the discharge. The frequency of the microwave generator is too high (too fast) for triggering of the ICCD camera, and therefore the PROES is done in the respect of RF bias. This can be justified by the fact a production of oxygen is mostly due to RF voltage oscillation across the wafer and argon ion bombarding of the its surface (SiO<sub>2</sub> wafer). We use a floating RFEA design for RF driven bias. The RFEA is designed to sit on the wafer surface and signal cabling is taken out through a reactor turbo vacuum pumps tunnel. The strong correlation between the ion-flux, ellipsometry and the PROES data has recorded.

This work was a part of the projects supported by the Ministry of Education and Science of the Republic of Serbia (grant No. OI171006) and SFI Precision project of Republic of Ireland.

## **ON PLASMON PROPERTIES OF NANOMETRIC SYSTEMS EXPOSED TO ION BOMBARDMENT**

J.L. Gervasoni<sup>#</sup>

*Centro Atómico Bariloche, Comisión Nacional de Energía Atómica, Avenida Bustillo 9500, 8400 S.C. de Bariloche, Río Negro, Argentina.*

<sup>#</sup> Also member of Scientific and Technological National Council (CONICET), Argentina

The discovery of graphene monolayers and the relevance of their potential applications have stimulated the interest in describing its electronic properties, and in particular those that distinguish it from graphite. Electron energy loss experiments provide a way to study electronic structure of solids and are especially useful for characterizing surfaces and nanostructures [1]. In addition, the low energy-loss part of a spectrum, dominated by collective (plasmon) excitations, is very sensitive to the geometry of the sample.

In this talk, we give a brief description of the excitation of plasmons due to the incidence of a charged particle on a graphene monolayer, applying a quantization procedure to the two-fluids hydrodynamic model developed by Mowbray et al. [2] for planar surface.

We calculate the dispersion relation of characteristic plasmon modes and the average number of plasmons excited for various trajectories of the incident particle corresponding to different experimental situations [3]. With this, we are able to obtain the energy loss probability for a particle passing through or reflecting from a graphene layer and compare it with experimental spectra.

This approach enables us to study the effects of multiple plasmon excitations by ion beams, similar to the EELS studies of thin metallic films on solid surfaces. Such a study can help elucidate which plasmon modes are most effectively excited depending on the incident ion trajectory.

The present calculation allows us to obtain several quantities in terms of the average number of excited plasmons, such as the stopping power, energy loss spectra and total energy loss.

We study these quantities as functions of various relevant parameters with physical meaning: the velocity of the incident ion, the distance to the surface, the inclination of the trajectory with respect to the tube's axis, etc.

The obtained results can be directly compared with experimental energy loss data and may help to understand the role of electronic channels in energy deposition in carbon nanostructures during ion irradiation.

## REFERENCES

- [1] T Eberlein, U. Bangert, R.R. Nair, R. Jones, M. Gass, A. L. Bleloch, K. S. Novoselov, A. [1] T Eberlein, U. Bangert, R.R. Nair, R. Jones, M. Gass, A. L. Bleloch, K. S. Novoselov, A. Geim, P. Briddon, Phys. Rev. B 77, 233406 (2008); Y. Liu, R. F. Willis, K. V. Emtsev, Th. Seyller, Phys. Rev. B 78 201403(R) (2008).
- [2] D.J. Mowbray, Z.L. Miskovic, F.O Goodman and Y-N Wang, Phys.Rev. B 70, 195418 (2004).
- [3] D. J. Mowbray, S Segui, J. L. Gervasoni, Z. L. Miskovic and N. R. Arista, Physical Review B 82, 035405 (2010), and references therein.

## THE NON-RESONANT NEUTRALIZATION DYNAMICS OF THE MULTIPLY CHARGED RYDBERG IONS ESCAPING SOLID SURFACES

S. M. D. Galijaš, N. N. Nedeljković, M. D. Majkić and M. A. Mirković

*University of Belgrade, Faculty of Physics, P. O. Box 368, Belgrade, Serbia*

**Abstract.** The theoretical study of the neutralization dynamics is essential for describing a variety of complex ion-surface processes. We investigate the intermediate and final population of the Rydberg states ( $n_A \gg 1, l_A = 0 - 3, m_A$ ) of multiply charged ions escaping solid surfaces by using the two-state vector model (TVM). All our calculations have been carried out for intermediate velocities ( $v \approx 1$  a.u.) of the considered ions. Within the framework of the proposed time-symmetrized quantum model, the state of a single active electron is described by two wave functions  $\Psi_1$  and  $\Psi_2$ . The electron capture is a non-resonant and characterized by the selective population of the ionic Rydberg states. The final population probabilities are obtained in relatively simple analytical form, which enable us to elucidate the role of the ionic core polarization and to analyze the  $n_A$ ,  $l_A$  and  $v$  probability distributions. We consider the ions SVI, CIVII and ArVIII with core charges  $Z = 6, 7$  and  $8$ , respectively, and the ions KrVIII and XeVIII with  $Z = 8$ . Moreover, we apply the model on two different surfaces in order to emphasize the influence of the solid work functions.

A discussion also concerns the appearance of resonances (pronounced maxima at  $n_A = n_{\text{res}}$ ) in the probability distributions for the population of the Rydberg states. The resonances are explained by means of an electron tunneling in the very vicinity of the ion-surface potential barrier top. To include this specific feature of electron transitions, the appropriate etalon equation method is used in the calculation of the function  $\Psi_1$ . The effect of the ionic core polarization is associated with the function  $\Psi_2$ . The population probabilities for  $n_A \approx n_{\text{res}}$  are complementary to those obtained for  $n_A < n_{\text{res}}$ , and in sufficiently good agreement with available beam-foil experimental data. The pronounced resonance in the final population distributions are recognized only in the case of ArVIII ion and for the lower values of the solid work function (argon anomaly).

## INTERMEDIATE STAGES OF THE NEUTRALIZATION OF MULTIPLY CHARGED IONS INTERACTING WITH SOLID SURFACES

M. D. Majkić, N. N. Nedeljković and S. M. D. Galijaš

*University of Belgrade, Faculty of Physics, P. O. Box 368, Belgrade, Serbia*

**Abstract.** We consider the electron capture (neutralization) into Rydberg states of multiply charged ions interacting with solid surface in the normal (escaping) and in the grazing incidence geometry. The time-symmetrized two-state vector model is used to investigate the intermediate stages of the population dynamics. For the fixed initial and final states of the active electron, the two wave functions which evolve simultaneously in two opposite directions of time (by two scenarios), are used to describe the transitional electron state.

We analyze the population of the Rydberg states of multiply charged ions SVI, CIVII, ArVIII, KrVIII and XeVIII, escaping solid surfaces in the normal direction, at low perpendicular velocity  $v_{\perp} \ll 1$  a.u. Also, in order to get a possible experimental verification of the two-state vector model, we consider the intermediate stages of the Rydberg state-population dynamics in the scattering geometry. We examine the multiply charged ions, considering the  $\text{Ar}^{Z+}$ ,  $\text{Kr}^{Z+}$  and  $\text{Xe}^{Z+}$  ions with core charges  $Z \in [5, 35]$  (in a.u.) colliding with conducting solid surface at velocity  $v$  with parallel component  $v_{\parallel} < v_F$ , where  $v_F$  is the Fermi velocity of the solid, and with low perpendicular component ( $v_{\perp} \ll 1$  a.u.). In both considered geometry, the main idea is to obtain the information about the position and the magnitude of the population process for the fixed initial and final states of the active electron.

The results are compared with the classical overbarrier predictions and the measured kinetic energy gain due to the image acceleration of the ions. Relevance of the obtained results for the multielectron population is briefly discussed. It is demonstrated that the parallel ionic velocity influences the position and the magnitude of the population process.

## **COMPOSITION AND STRUCTURE MODIFICATION OF A WTi/Si SYSTEM BY NANOSECOND AND PICOSECOND LASER PULSES**

Suzana Petrović

*Institute of nuclear science Vinča, Universtity of Belgrade, P.O.B. 522, 11001  
Belgrade, Serbia*

A study of morphological and composition changes of the WTi/Si system induced by nanosecond and picosecond laser pulses is presented. Laser-induced damage of solid materials, particularly on the surface, depends on the material characteristics (surface state, fabrication, etc), laser parameters (pulse duration, wavelength, number of accumulated pulses, etc) and conditions of irradiation (vacuum, gas atmosphere, the gas pressure, etc). In the case of laser pulses longer than a few tenths of a picosecond, the laser-induced processes can be considered as thermally activated. The material on the surface is melted and resolidified in almost all cases. Thermal effects are more expressed for the nanosecond laser pulses used. The advantage of applying shorter laser pulses for material modification is better localization of surface changes and negligible collateral thermal damage. WTi alloy as a refractory material possesses very good physico-chemical properties, such as thermochemical stability, high melting temperature, etc.

A 190 nm thick WTi film was deposited on a silicon substrate of n-type (100). The pulsed laser systems used were: nanosecond TEA CO<sub>2</sub> laser (emission, 10.6  $\mu$ m; pulse FWHM; pulse duration 120 ns) and picosecond Nd:YAG laser (emission, 532 nm; pulse FWHM; pulse duration 10 ps). The laser-induced morphological and composition modifications showed a dependence on pulse duration. The following morphological changes were observed: (i) ablation/exfoliation of the WTi thin film, (ii) appearance of hydrodynamic features such as resolidified material, and (iii) formation of nano-sized grains and globules. Overall morphological modifications were more pronounced after the picosecond laser

action. The surface composition analysis showed a quite different distribution of sample components depending on the pulse duration. Formation of the silicon dioxide ( $\text{SiO}_2$ ) was recorded only in the case of irradiation of the WTi/Si system by picosecond laser pulses (duration 40 ps). During experiments the used fluences had similar values, of about  $20 \text{ J cm}^{-2}$  in case of the TEA CO<sub>2</sub> laser and approximately of  $16 \text{ J cm}^{-2}$  for the Nd:YAG laser.

## **LOW DIMENSIONAL TI-OXIDE BASED STRUCTURE: FROM SrTiO<sub>3</sub> TO TiO<sub>2</sub>**

Milan Radović<sup>1,2,3</sup>

<sup>1</sup> *VINCA Institute of Nuclear Sciences Atomic Physics Laboratory,  
University of Belgrade, Serbia*

<sup>2</sup> *Institut de la Matière Complexe, EPF Lausanne, CH-1015, Lausanne,  
Switzerland*

<sup>3</sup> *Swiss Light Source, Paul Scherrer Institut WSLA 206 CH-5232 Villigen,  
Switzerland*

Transition metal oxides (TMO) form altogether a very wide class of materials, which has attracted since decades the attention of scientists for showing highly diversified and unusual electronic properties.

**Strontium titanate** (SrTiO<sub>3</sub>) belongs to the class of particularly important TMO materials with the general formula ABO<sub>3</sub>. This material is a common used a substrate material for electronic oxide thin film devices. This, widespread, application of SrTiO<sub>3</sub> (STO) requires the optimization of the processes that can reproducibly produce a high quality terminated surface. While TiO<sub>2</sub> terminated surface can be routinely obtain by the chemical etching and the post-annealing processes, SrO termination is very difficult to achieve. Here, the development of obtaining high quality SrO termination by resorting of STO heteroepitaxial growth on the A-site terminated (110) NdGaO<sub>3</sub> substrate will be presented [1].

**Titanium dioxide (TiO<sub>2</sub>)**, another representative of TMO materials, occurs in several forms such as rutile, anatase and brookite. Anatase is a TiO<sub>2</sub> polymorph which is less stable than rutile (it is a low-temperature phase), but more efficient for several applications such as catalysis or dye-sensitized solar cells. Anatase powder is commercially available but in form of thin solid film is more appropriate for **photocatalytic** applications. Therefore, improving techniques of the anatase TiO<sub>2</sub> thin film deposition is of great importance and some of new progress will be discussed [2].

### **REFERENCES**

- [1] Milan Radović, Nathascia Lampis, Paolo Perna, Zoran Ristic, Marco Salluzzo, Fabio Miletto Granozio, Christian Schlepütz, Applied Physics Letters 94, 022901 (2009).
- [2] M. Radović, M. Salluzzo, Z. Ristic, R. Di Capua, N. Lampis, R. Vaglio and F. Miletto Granozio, The Journal of Chemical Physics 034705 (2011).

## ELECTRON EMISSION FROM A METAL NANO-TIP BY ULTRASHORT LASER PULSES

G. Wachter<sup>1</sup>, C. Lemell<sup>1</sup> and J. Burgdörfer<sup>1</sup>

<sup>1</sup>*Institute for Theoretical Physics, Vienna University of Technology, Wiedner Hauptstraße 8-10, A-1040 Vienna, Austria, EU*

**Abstract.** The interaction of few-cycle laser pulses with nanoscale metal tips provides a unique testing ground for strong-field physics in a confined solid state environment. We theoretically investigate the spectrum of emitted electrons, which is directly related to the quantum dynamics at the surface.

The light field near the nano tip is described by solving Maxwell's equations by the finite differences time domain method (FDTD) (Fig. 1a). Strongly enhanced fields near the apex of tips of subwavelength size trigger coherent electron emission from a nanoscale emission area. The time-dependent electric field at the tip surface enters a quantum simulation of surface electron dynamics based on time-dependent density functional theory (TDDFT). The energy spectrum of emitted electrons calculated from the time-dependent electron density is in good agreement to experiment (fig.1b). An intuitive wavepacket model is used to interpret the electron spectra, allowing for example the extraction of the locally enhanced electric field at the tip apex.

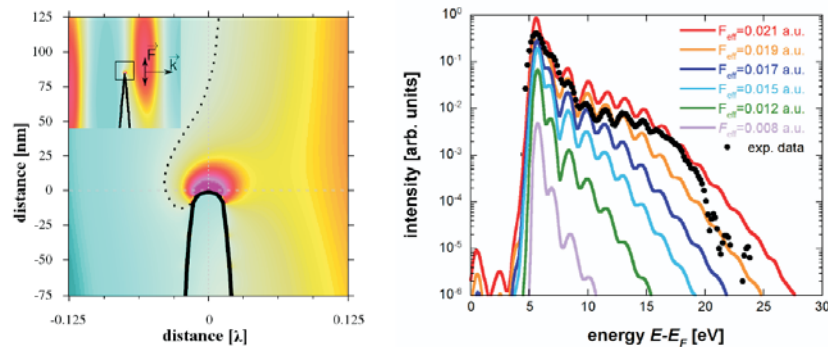


**Figure 1.** (a) A near-infrared laser pulse polarized along the axis of the tip impinges upon a tungsten tip. Near the tip, the electric field is phase-shifted and distorted. (b) The kinetic energy spectrum of emitted electrons calculated by time-dependent density functional theory (TDDFT).

## **DISSOCIATIVE ELECTRON ATTACHMENT MEASUREMENTS AND TDDFT CALCULATIONS OF THE EXCITATION ENERGIES IN Pt(PF<sub>3</sub>)<sub>4</sub>: SYNERGY BETWEEN THE EXPERIMENT AND THEORY**

Matija Zlatar<sup>1</sup>, Olivier May<sup>2</sup>, Maja Gruden-Pavlović<sup>3</sup> and Michael Allan<sup>2</sup>

<sup>1</sup>*Center for Chemistry, Institute for Chemistry, Technology and Metallurgy,  
University of Belgrade, Belgrade, Serbia*

<sup>2</sup>*Department of Chemistry, University of Fribourg, Fribourg, Switzerland*

<sup>3</sup>*Faculty of Chemistry, University of Belgrade, Belgrade, Serbia*

**Abstract.** Pt(PF<sub>3</sub>)<sub>4</sub>, is a tetrahedral d<sup>10</sup> complex, used as a platinum precursor for the deposition of a carbon-free platinum nano-sized wires in the method of focused electron beam induced processing (FEBIP). In an attempt to understand the mechanism of the deposition process several electron driven processes were studied: i) elastic scattering, which changes the direction of electron propagation and spreads the electron beam; ii), vibrational excitation, which cools the electron and heats the sample; iii) electronic excitation, which leads to a decomposition of the excited precursor into neutral fragments; iv) dissociative electron attachment, which leads directly to the decomposition of the precursor molecules. Electronic structure of the complex was analyzed with the aid of Density Functional Theory (DFT), using fragment molecular orbital approach and energy decomposition analysis. Relativistic effects were included via zeroth-order regular approximation self-consistently in the ground state calculations, in two ways: scalar-relativistic, which takes into account velocity of the electrons near the nuclei, and two-component approximation that takes into account spin-orbit coupling. Excitation energies were calculated with the time dependent DFT (TDDFT) formalism in a non-relativistic, scalar-relativistic and spin-orbit coupling manner with SAOP (the statistical average of orbital potentials) potential. Taking into account relativistic effects, is found to be crucial for a good agreement with the experimental findings. In summary, various experimental investigations of the electron driven processes in Pt(PF<sub>3</sub>)<sub>4</sub> combined with electronic structure calculations, are indispensable for deeper understanding of the mechanism of the deposition process, which may indeed help to improve the quality of the FEBIP generated material and to possible design of the new ones.



## **SECTION 2.**

### **Particle and Laser Beam Interactions with Solids**

- 2.1 Atomic Collisions in Solids
- 2.2 Sputtering and Deposition
- 2.3 Laser and Plasma Interaction with Surfaces

### **CONTRIBUTED PAPERS**



## ENERGY AND ANGULAR DISTRIBUTION OF ELECTRONS TRANSMITTED THROUGH A SINGLE GLASS MICROCAPILLARY

A. R. Milosavljević<sup>1\*</sup>, R. J. Berezky<sup>2</sup>, M. Kovačević<sup>3</sup>, K. Tőkési<sup>2</sup> and  
B. P. Marinković<sup>1</sup>

<sup>1</sup> *Laboratory for atomic collision processes, Institute of Physics, University of  
Belgrade, Pregrevica 118, 11080 Belgrade, Serbia*

<sup>2</sup> *Institute of Nuclear Research of the Hungarian Academy of Sciences  
(ATOMKI), H-4001 Debrecen, P. O. Box 51, Hungary*

<sup>3</sup> *School of Electrical Engineering, University of Belgrade, Bulevar kralja  
Aleksandra 73, 11120 Belgrade, Serbia*

**Abstract.** We present an experimental study on transmission of low-energy electrons at the incident energy of 200 eV through a single glass microscopic capillary (inner diameter: 0.15 mm, length: 12.4 mm). The energy and angular distributions of electrons passing through the cylindrical shaped capillary were measured for different tilt angles of the capillary in reference to the incident electron beam direction. The angular distributions suggest possible existence of guiding effect. However, the measured energy spectra show that electrons also suffer inelastic processes inside the capillary,

### 1. INTRODUCTION

The transmission of electrons through insulating (micro) nanocapillaries with high aspect ratio has been attracting large interest in recent years. This research is motivated both by potential application of low-energy electron manipulation at (micro) nanometer scale in highly developing biotechnology and possibility to investigate fundamental processes of electron-surface interactions. The investigation of the transmission of electrons through highly insulating nanocapillaries has been triggered by an intensive research on guiding of highly charged ions (HCI) by insulating capillaries. The first pioneering experiment on guiding of HCI by insulating PET nanocapillaries were reported by Stolterfoht and coauthors in 2002 [1], followed by a large amount of papers presenting both experimental and theoretical results, as well as interesting applications of this effect (see e.g. [2]).

---

\* e-mail: vraz@ipb.ac.rs

The first results on electron guiding by array of insulating nanocapillaries made in  $\text{Al}_2\text{O}_3$  and PET were reported in 2007 by Milosavljević et al. [3] and Das et al. [4], respectively. In recent years, a number of experimental and theoretical results on electron guiding have been reported for different types of insulating micro and nanocapillaries [5]. Furthermore, the processes of electron transmission through insulating capillaries appeared to be more complex than in the case of HCl guiding, where the guiding is dominantly due to the Coulomb deflection. In the case of electrons the close electron-surface interaction and secondary electron emission, as well as Coulomb deflection, must be taken into account [6]. Actually, different reported results suggest that some of these processes can be more or less pronounced, which might also depend for example on the type of insulating capillaries, the incident electron current, and energy.

In the present contribution we present preliminary results on transmission of low-energy electrons of 200 eV through a single glass capillary of high aspect ratio. We investigate both angular distribution of electrons transmitted with the incident energy and energy distribution of electron escaping the capillary.

## 2. EXPERIMENTAL

### 2.1 Preparation of microcapillaries

The glass capillary sample was prepared at the ATOMKI laboratory in Debrecen, Hungary. The high aspect ratio single glass capillary was obtained by heating a straight glass tube made of Borosilicate glass and stretching it by applying constant force at the two ends. The final capillary sample with a desired diameter was cut by a diamond cutter and polished in order to obtain smooth surface. Previous measurements in the ATOMKI laboratory for similar samples have shown a smoothness of about 3 nm, and x-ray photoelectron spectroscopy (XPS) shows the cleanliness.

The front side of the capillary tube and its holder was coated with a layer of graphite to prevent excess charges upon electron bombardment of the capillary holder. The sample was fixed into an aluminium disk holder and a UHV compatible glue was used to fix the tubes. In the present case, the glass capillary has the inner diameter of  $d=0.15$  mm and the length of  $l=12.4$  mm, therefore, the aspect ratio ( $l/d$ ) is 82.6.

### 2.2 Experimental setup

The measurements of transmission of electrons through the single glass microcapillary were performed in the Laboratory for atomic collision processes at the Institute of Physics Belgrade, Serbia. The modified crossed-beams experimental setup has been essentially described previously [3,6]. Briefly, the setup includes an electron gun and a double cylindrical mirror energy analyzer. This system allows measurements of transmitted current at incident electron energies from about 100 eV to 350 eV, variation of both tilt and observation angles and an energy analysis of transmitted electrons. The electron gun

produces a well collimated electron beam, with a diameter and an angular divergence estimated to be approximately 1 mm and  $1^\circ$  at 200 eV of the incident energy, and with an energy spread of about 0.5 eV. The used incident electron beam current sent to the entrance of the microcapillary was typically about 10 nA but further measurements are needed for an estimation of the electron flux entering the capillary. The base pressure in the experimental chamber was about  $5 \times 10^{-7}$  mbar.

The glass capillary sample fixed on its holder was mounted on a target holder made of Al, allowing a change of the orientation of the capillary axis with respect to the electron beam direction (see Figure 1). The transmitted electrons, after being selected by energy are detected by a single-channel electron multiplier working in a single-counting mode. The energy spectra of outgoing electrons were measured in the constant pass-energy mode of the energy analyzer by adjusting the retarding potential of the entrance electrode, with the overall resolution of about 1.0-1.5 eV (full width at half-maximum – FWHM).

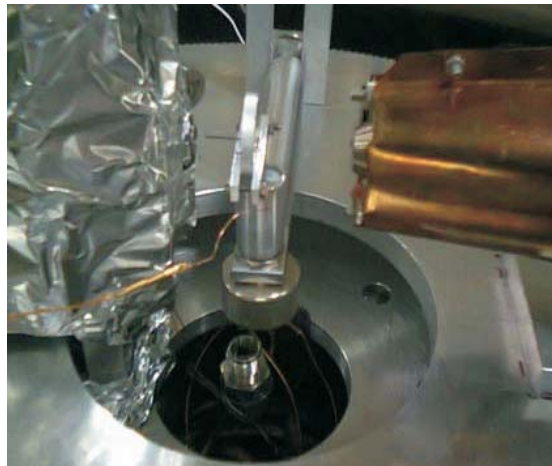


**Figure 1.** Photo of the experimental setup. The capillary sample, mounted on a rotatable holder, is shown in the middle of figure; the entrance of the energy analyzer is on the left and electron gun on the right side.

### 3. RESULTS

Figure 1 shows the results of our preliminary measurements. Figure 1a shows the angular distributions of electrons transmitted through the single glass capillary at the incident energy of 200 eV, at three different tilt angles of the incident electron beam with respect to the capillary direction. The measurements were performed by fixing the angle between the capillary and the incident beam (measured by a resistor) and then by recording the signal intensity (count rates) of transmitted electron current as a function of the observation angle – the angle between the capillary direction and the axis of the

entrance electron lens of the analyzer. The zero tilt angle has been approximately defined in the present case according to the maximum transmitted signal. The results show transmission of electrons even at large tilt angles, where direct transmission should be geometrically prevented, thus suggesting an existence of the guiding effect.

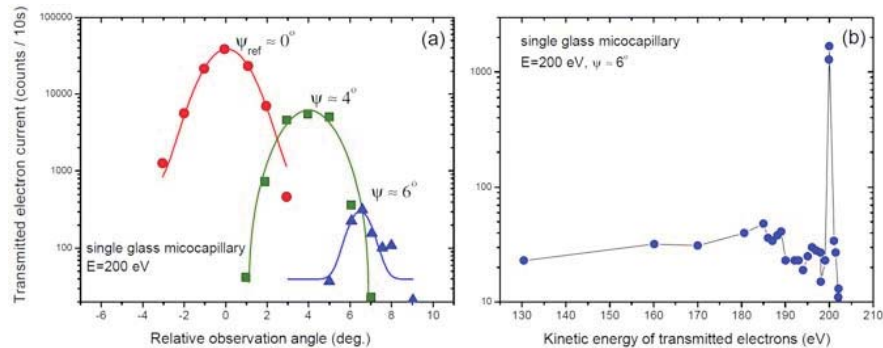


**Figure 2.** (a) Angular distribution of electrons transmitted through the capillary at the incident energy, for different tilt angles ( $\psi$ ). (b) Kinetic energy distribution of electrons escaping the capillary at the tilt angle of  $6^\circ$ .

Figure 2b. shows the measured kinetic energy distribution of electrons escaping the capillaries at large tilt angle. Except the dominant peak at about 200 eV corresponding to elastic transmission, there is a significant fraction of electrons that suffer inelastic collisions.

## Acknowledgements

The work was supported by the Ministry of Education and Science of Republic of Serbia (Project No. 171020) and by the Hungarian Scientific Research Fund OTKA No. NN 103279.

## REFERENCES

- [1] N. Stolterfoht et al., Phys. Rev. Lett. **88** (2002) 133201.
- [2] T. Ikeda et al. Appl. Phys. Lett. **89** (2006) 163502.
- [3] A. Milosavljević et al., Phys Rev A **75**, 030901(R) (2007).
- [4] Das et al., Phys Rev A **76**, 042716 (2007).
- [5] B. S. Dassanayake, et al., Phys. Rev. A **83**, 012707 (2011).
- [6] Milosavljevic et al., Nucl. Instr. Meth. B 279, 190 (2012).

## **SURFACE MODIFICATION OF HIGH DENSITY POLYETHYLENE BY GOLD ION IMPLANTATION**

M. Nenadović<sup>1</sup>, J. Potočnik<sup>1</sup>, S. Štrbac<sup>2</sup> and Z. Rakočević<sup>1</sup>

<sup>1</sup> INS Vinca, Laboratory of Atomic Physics, University of Belgrade, Mike  
Alasa 12-14, 11001, Belgrade, Serbia

<sup>2</sup> ICTM-Institute of Electrochemistry, University of Belgrade, Njegoseva 12,  
11000 Belgrade, Serbia

**Abstract.** High density polyethylene (HDPE) has been modified by Au<sup>+</sup> ions implantation with the energy of 200 keV. The doses of implanted gold ions were:  $1 \times 10^{15}$ ,  $5 \times 10^{15}$  and  $1 \times 10^{16}$  ions/cm<sup>2</sup>. Surface topography was observed by atomic force microscopy (AFM), while surface composition changes were detected by phase imaging AFM. Phase analysis of AFM images has shown that both physical and chemical changes occurred on the surface of HDPE and that those changes depended on the implantation dose. Physical changes are confirmed by the analysis of mean square roughness and power spectral density (PSD) slopes as functions of the implantation dose.

### **1. INTRODUCTION**

Polymeric solid materials have been applied to many fields ranging from everyday life to low- and high-technology engineering due to their many unique advantages such as light weight, mold ability, ability to form complicate shapes, corrosion resistance, versatile electronic properties, and low manufacturing cost [1]. It has been proven that ion implantation technology is very attractive for modifying the surface properties of metals and semiconductors as well as polymers [2]. The structural changes caused by high energy ions give improvements in hardness, wet ability, surface chemical activity, cross-linking and other properties [3].

## 2. EXPERIMENTAL PROCEDURE

Commercial 2 mm thick table of high density polyethylene ( $0.945 \text{ g/cm}^3$ ) was mechanically polished with 4000 grade polishing paper, cleaned in ultra-sonic bath in ethanol solution and rinsed with  $18.2 \text{ M}\Omega$  deionised water. Initial HDPE samples were implanted by  $\text{Au}^+$  ions with 200 keV in the ion implanter chamber. The working pressure in the chamber was  $1 \times 10^{-6} \text{ Pa}$ . The source of gold ions was a gold wire with very a high purity. Multimode quadrex SPM with Nanoscope IIIe controller (Veeco Instruments, Inc.), operated under ambient conditions was used in this work using probe holder with a commercial Veeco FESP probe with a cantilever length of  $225 \mu\text{m}$ .

## 3. RESULTS AND DISCUSSION

AFM images of the untreated HDPE (not shown) consist of relatively smooth grainy structure with grain boundaries not clearly defined in a corresponding phase image. Figure 1 shows surface topography (left column) and phase AFM images (right column) of the HDPE samples implanted by  $\text{Au}^+$  ions with the doses of  $1 \times 10^{15} \text{ ions/cm}^2$  (a,b),  $5 \times 10^{15} \text{ ions/cm}^2$  (c,d) and  $1 \times 10^{16} \text{ ions/cm}^2$  (e,f). Z range for all topography images is 100 nm, while for phase images is  $100^\circ$ .

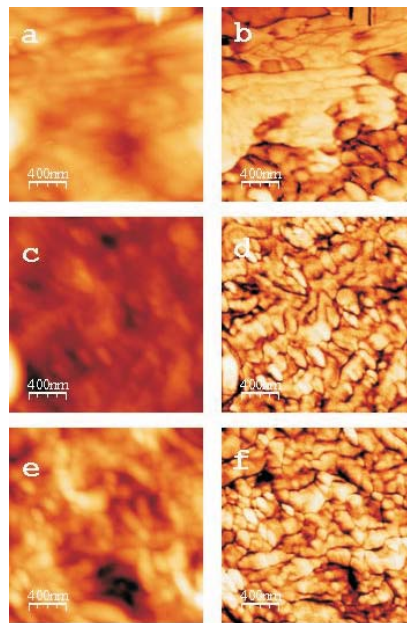


**Figure 1.** Surface topography and phase AFM images  $2 \mu\text{m} \times 2 \mu\text{m}$  of the HDPE implanted by Au ions

The sample implanted by gold with the dose of  $1 \times 10^{15}$  ions/cm<sup>2</sup> shows the presence of larger grains and great increase in surface roughness. Increasing the implantation dose to  $5 \times 10^{15}$  ions/cm<sup>2</sup>, leads to the disappearance of large polymer grains and to the formation of smaller and more densely packed, narrow shaped agglomerates. For the highest implantation dose of  $1 \times 10^{16}$  ions/cm<sup>2</sup>, there is no significant change compared to the previous case, except that the grains are more compact.

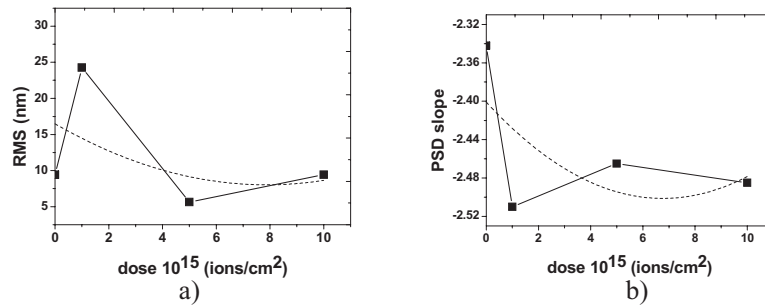


**Figure 2.** a) The dependence of the average surface roughness of Au/HDPE samples on the implantation dose; b) The dependence of the PSD slope on the implantation dose.

The maximum surface roughness of 24.3 nm is achieved for the lowest implantation dose of  $1 \times 10^{15}$  ions/cm<sup>2</sup>. Increasing the dose up to  $5 \times 10^{15}$  ions/cm<sup>2</sup>, the roughness is highly reduced to 5.6 nm, while with a further increase to  $1 \times 10^{16}$  ions/cm<sup>2</sup> the roughness again increases insignificantly to 9.4 nm. According to the RMS roughness measurements, calculations of the two-dimensional power spectral density (2-D PSD) were performed from AFM topography images. Slope of PSD function tells us about the dominant processes in the subsurface area of the HDPE sample due to the implantation of gold ions. For the lowest implantation dose of Au ions, a great change of the PSD slope is observed compared to the untreated HDPE. It can be concluded that the RMS and PSD gives the opposite trend in defining the parameters of the surface.

Phase diagrams of the changes that occurred on the surface of HDPE after the implantation of Au ions are presented in Fig.3. The peak position of the untreated HDPE is at the value of 35.12°. For the implantation dose of  $1 \times 10^{15}$  ions/cm<sup>2</sup>, the phase peak shifts slightly to the value of 33.98°. This confirms very small change in the surface viscosity but the relative peak intensity is reduced. Increasing the implantation dose up to  $5 \times 10^{15}$  ions/cm<sup>2</sup>, there is a further shift of the phase peak to the value of 9.62°. Significant changes in surface viscosity can be explained by a greater degree of re-arranging and better cross-linking [4]. For the highest implantation dose large changes in surface viscosity are not observed.

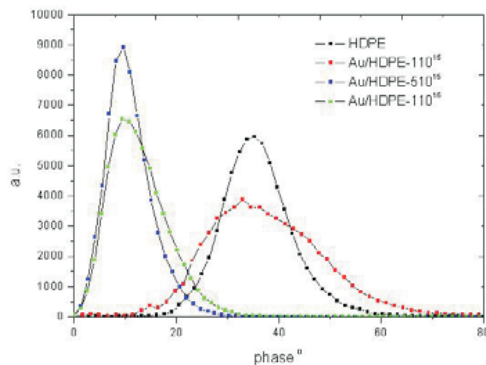


**Figure 3.** Surface phase composition of the HDPE implanted with  $\text{Au}^+$  ions [4]

The high dose of gold ions breaks covalent bonds and releases a large number of free electrons. A number of unpaired electrons and free radicals are the basis for the complex reactions that occur in the polymer after implantation.

#### 4. CONCLUSIONS

High density polyethylene has been modified by  $\text{Au}^+$  ion implantation with the energy of 200 keV, with the doses of 1, 5 and  $10 \times 10^{15}$  ions/cm<sup>2</sup>. As a consequence of gold ion implantation, significant structural and morphological changes on the surface of HDPE are observed. AFM microscopy was confirmed that as a result of ion implantation both physical and chemical changes occur. Analysis of RMS and PSD parameters confirmed different reaction mechanisms as a function of implantation dose.

#### Acknowledgement

This work was financially supported by the Ministry of Education and Science of the Republic of Serbia; project no. III45005.

#### REFERENCES

- [1] J.M. Charrier, *Polymeric Materials and Processing: Plastics, Elastomers and Composites*, Hanser Publishers, Munich, New York, 1991.
- [2] V.N. Popok, *Rev.Adv.Mater. Sci.* 30, 1-26 (2012).
- [3] W.Yuguang, Z. Tonghe, L.Andong, Z.Gu, *Surf. Coat. Technol.*157, 262-266 (2002).
- [4] M.Nenadović, J.Potočnik, M.Ristić, S.Štrbac and Z.Rakočević, *Surf. Coat. Technol.* 206, 4242-4248 (2012).

## ENERGY LOSS OF CHARGED PARTICLES MOVING OVER MULTILAYER GRAPHENE

Ivan Radović<sup>1</sup>, Duško Borka<sup>1</sup> and Zoran L. Mišković<sup>2</sup>

<sup>1</sup>*VINČA Institute of Nuclear Sciences, University of Belgrade, P.O. Box 522,  
11001 Belgrade, Serbia*

<sup>2</sup>*Department of Applied Mathematics, University of Waterloo, Waterloo,  
Ontario, Canada N2L 3G1*

**Abstract.** We study dynamic polarization of freestanding multilayer graphene induced by an external charged particle moving at an arbitrary angle of incidence. We evaluate the probability density for energy loss of fast electrons traversing graphene and compare it with available experiments.

### 1. INTRODUCTION

Graphene is a flat monolayer of carbon atoms tightly packed into a two-dimensional (2D) honeycomb lattice [1]. It is a basic building block for graphitic materials of all other dimensionalities: highly oriented pyrolytic graphite (a stack of graphene layers), carbon nanotubes (rolled-up cylinders of graphene) and fullerene molecules (consisting of wrapped graphene by the introduction of pentagons on the hexagonal lattice) [2]. Interactions of moving charged particles with various carbon nanostructures have been investigated in recent years, e.g., in the electron energy loss spectroscopy (EELS) of carbon nanotubes [3], isolated layers of freestanding graphene [4] and single-layer graphene (SLG) lying on a strongly polar substrate, such as SiC [5].

In order to better understand particle interactions with layered graphitic nanostructures and motivated by these developments, we derive the expressions for the total energy loss and the probability density for losing the energy.

Note that we use Gaussian electrostatic units, set  $\hbar = 1$  and denote the charge of a proton by  $e > 0$ .

### 2. BASIC THEORY

We use a Cartesian coordinate system  $\{\vec{R}, z\}$  with  $\vec{R} = \{x, y\}$  and assume that graphene layers occupy planes  $z_n = (n-1)d$ , where  $n = 1, 2, \dots, N$  and  $d \approx 3.35 \text{ \AA}$  is the interlayer spacing. Following Ref. [6],

one can express the induced potential in the system  $\Phi_{ind}(\vec{R}, z, t)$  by using the Fourier transform with respect to coordinates in the  $xy$  plane,  $\vec{R} \rightarrow \vec{k}$ , and time,  $t \rightarrow \omega$ , as:

$$\Phi_{ind}(\vec{k}, z, \omega) = \sum_{n=1}^N \frac{2\pi}{k} \sigma_n(\vec{k}, \omega) e^{-k|z-z_n|} \quad (1)$$

where  $\sigma_n(\vec{k}, \omega)$  is the Fourier transform of the induced charge density (per unit area) on the  $n$ th layer, which may be written in a self-consistent field approximation as:

$$\sigma_n(\vec{k}, \omega) = -e^2 \chi(\vec{k}, \omega) [\Phi_{ext}(\vec{k}, z_n, \omega) + \Phi_{ind}(\vec{k}, z_n, \omega)] \quad (2)$$

with  $\chi(\vec{k}, \omega)$  being the polarizability function of the SLG and  $\Phi_{ext}(\vec{R}, z, t)$  being the external potential. From the charge density of the incident electron,  $\rho_{ext}(\vec{R}, z, t) = Ze\delta(\vec{R} - \vec{v}_{\parallel}t)\delta(z - v_{\perp}t)$ , where  $Z = -1$  and  $\vec{v}_{\parallel}$  and  $v_{\perp}$  are the components of the particle velocity parallel and perpendicular to the graphene planes, respectively, one obtains:

$$\Phi_{ext}(\vec{k}, z, \omega) = \frac{4\pi Z e v_{\perp}}{(\omega - \vec{k} \cdot \vec{v}_{\parallel})^2 + (k v_{\perp})^2} e^{\frac{i(\omega - \vec{k} \cdot \vec{v}_{\parallel})z}{v_{\perp}}} \quad (3)$$

On inserting Eq. (3) into Eq. (2) and combining with Eq. (1), one may obtain a self-consistent expression for the induced potential. Then, the total energy lost by the incident electron may be evaluated from [7]:

$$E_{loss} = -\int \rho_{ext}(\vec{R}, z, t) \frac{\partial \Phi_{ind}(\vec{R}, z, t)}{\partial t} d^2 \vec{R} dz dt \quad (4)$$

Using the symmetry properties of the function  $\chi(\vec{k}, \omega)$  at zero temperature, one may express Eq. (4) as:

$$E_{loss} = \int_0^{\infty} \omega P_N(\omega) d\omega \quad (5)$$

### 3. RESULTS

We evaluate the probability density  $P_N(\omega)$  for losing the energy  $\omega$  that appears in Eq. (5) and compare it with the experimental EEL spectra of

freestanding multilayer graphene for  $N=1$  and  $2$ , corresponding to a SLG and a bilayer graphene (BLG), which were taken under the normal electron incidence (hence  $\vec{v}_{\parallel} = \vec{0}$ ) at energy 100 keV [4].

To do so, we adopt from Ref. [7] a planar version of the 2D, two-fluid hydrodynamic model for graphene's  $\sigma$  and  $\pi$  electrons that gives  $\chi = \chi_{\sigma} + \chi_{\pi}$  for SLG, where:

$$\chi_{\nu}(k, \omega) = \frac{\frac{n_{\nu}^0 k^2}{m_{\nu}^*}}{s_{\nu}^2 k^2 + \omega_{\nu r}^2 - \omega(\omega + i\gamma_{\nu})} \quad (6)$$

with  $n_{\nu}^0$ ,  $m_{\nu}^*$ ,  $s_{\nu}$ ,  $\omega_{\nu r}$  and  $\gamma_{\nu}$  being the equilibrium surface number density of electrons, effective electron mass, acoustic speed, restoring frequency and the damping rate in the  $\nu$ th fluid (where  $\nu = \sigma, \pi$ ), respectively.

Taking  $m_{\nu}^*$  to be the free electron mass and using the unperturbed surface electron densities of SLG,  $n_{\sigma}^0 \approx 115 \text{ nm}^{-2}$  and  $n_{\pi}^0 \approx 38 \text{ nm}^{-2}$ , we treat the remaining parameters in Eq. (6) as adjustable. The best fit to the experimental EEL spectra is found for  $\omega_{\sigma r} = 13.06 \text{ eV}$ ,  $\omega_{\pi r} = 4.08 \text{ eV}$ ,  $\gamma_{\sigma} = 2.72 \text{ eV}$  and  $\gamma_{\pi} = 2.45 \text{ eV}$ .

The results for  $P_N(\omega)$  were calculated with  $N=1, 2$  and  $3$  for three values of the incident electron energy and presented in Fig. 1. The most important trends seen in Fig.1 are that when the incident electron energy  $E$  decreases and the number of carbon layers  $N$  increases both the  $\pi$  and  $\sigma + \pi$  plasmon peak positions move to higher energies  $\omega$  and the peak heights increases.

The density  $P_N(\omega)$  is also compared in Fig. 1(b) with the experimental curves from Fig. 1(e) of Ref. [4], corresponding to a SLG and a BLG. One notes that the experimental curves are well reproduced for energies  $\omega \geq 3 \text{ eV}$ , both in magnitude and in the shape of spectra. The complete vanishing of the experimental spectra at energies below  $3 \text{ eV}$  may be a consequence of the method used in their subtraction of the zero-loss peak.

We have also evaluated the total energy losses from Eq. (5) and found that, for  $N=1, 2$  and  $3$ ,  $E_{loss} = 5.55, 10.5$  and  $15.3 \text{ eV}$  for  $E = 1 \text{ keV}$ ,  $E_{loss} = 0.89, 1.72$  and  $2.51 \text{ eV}$  for  $E = 10 \text{ keV}$ , and  $E_{loss} = 0.14, 0.28$  and  $0.42 \text{ eV}$  for  $E = 100 \text{ keV}$ , showing that the total energy loss approximately scales with  $N$ .

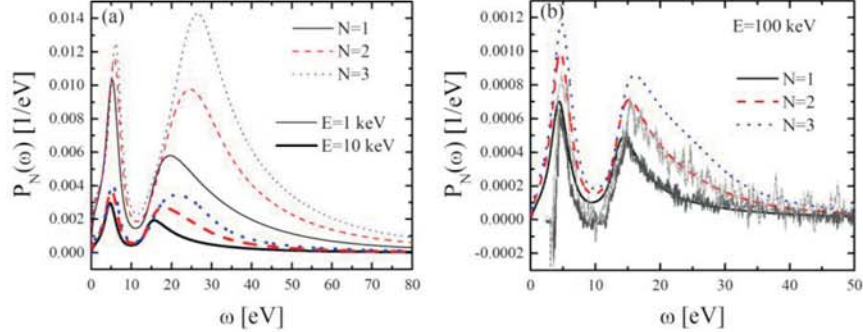


**Figure 1.** Probability density  $P_N(\omega)$  (in  $1/\text{eV}$ ) versus energy loss  $\omega$  (in eV), calculated for  $N = 1$  (solid lines),  $N = 2$  (dashed lines) and  $N = 3$  (dotted lines) graphene layers, at three energies of incident electrons: (a)  $E = 1$  keV (thin lines) and  $E = 10$  keV (thick lines), and (b)  $E = 100$  keV along with the corresponding experimental EEL spectra from Ref. [4] for  $N = 1$  and  $N = 2$  [noisy (gray) curves].

### Acknowledgements

This work is supported by the Ministry of Education and Science of the Republic of Serbia (Project No. 45005). Z.L.M. also acknowledges support from the Natural Sciences and Engineering Research Council of Canada.

### REFERENCES

- [1] A. K. Geim and K. S. Novoselov, *Nature Mater.* 6, 183 (2007).
- [2] A. H. Castro Neto, F. Guinea, N. M. R. Peres, K. S. Novoselov and A. K. Geim, *Rev. Mod. Phys.* 81, 109 (2009).
- [3] C. Kramberger, R. Hambach, C. Giorgetti, M. H. Rummeli, M. Knupfer, J. Fink, B. Buchner, L. Reining, E. Einarsson, S. Maruyama, F. Sottile, K. Hannewald, V. Olevano, A. G. Marinopoulos and T. Pichler, *Phys. Rev. Lett.* 100, 196803 (2008).
- [4] T. Eberlein, U. Bangert, R. R. Nair, R. Jones, M. Gass, A. L. Bleloch, K. S. Novoselov, A. K. Geim and P. R. Briddon, *Phys. Rev. B* 77, 233406 (2008).
- [5] Y. Liu, R. F. Willis, K. V. Emtsev and Th. Seyller, *Phys. Rev. B* 78, 201403(R) (2008).
- [6] V. Borka Jovanovic, I. Radovic, D. Borka and Z. L. Miskovic, *Phys. Rev. B* 84, 155416 (2011).
- [7] D. J. Mowbray, S. Segui, J. Gervasoni, Z. L. Miskovic and N. R. Arista, *Phys. Rev. B* 82, 035405 (2010).

# POPULATION PROBABILITIES OF MULTIPLY CHARGED IONS INTERACTING WITH SOLID SURFACE: PARALLEL VELOCITY EFFECT

N. N. Nedeljković, M. D. Majkić, S. M. D. Galijaš and M. A. Mirković

*University of Belgrade, Faculty of Physics, P. O. Box 368, Belgrade, Serbia*  
*University College of Civil Engineering and Geodesy, Belgrade, Serbia*

**Abstract.** The time-symmetrized, two-state vector model is used to investigate the intermediate stages of the population dynamics of the Rydberg states of multiply charged ions interacting with solid surface in the grazing incidence geometry. The effect of parallel projectile velocity (in respect to the surface) is considered as kinematic effect. The population probabilities, with inclusion of the reionization, are obtained in the analytic form. The ion  $\text{Ar}^{12+}$  interacting with Al-surface is considered as an example. It is demonstrated that the parallel ionic velocity influences the position and the magnitude of the population process.

## 1. INTRODUCTION

In order to elucidate the intermediate stages of the electron exchange dynamics in the ion-surface system, we developed the two-state vector model (TVM); the model has been introduced in [1] in which the proton neutralization was considered and has been developed ever since in our group. In our recent works we have analyzed the population of the Rydberg states of multiply charged ions escaping solid surfaces in the normal direction, at low velocity [2] and for  $v \approx 1$  a.u. [3]. However, the scattering geometry that provides interesting new phenomena and insight into ion-surface interactions [4] has not yet been considered by the model.

In the present article, we examine the multiply charged ions  $\text{Ar}^{12+}$  in the scattering geometry under the grazing incidence within the framework of the TVM. The primal idea is to obtain the information about the position and the magnitude of the population process for the fixed initial and final states of the active electron. We recall that the TVM is developed to resolve that kind of problems; for this, the transitional electron state is described simultaneously by two state vectors  $|\Psi_1(t)\rangle$  and  $|\Psi_2(t)\rangle$  evolving in two opposite directions of time. The first state vector evolves from the initial state (electron in the solid) "preselected" at the initial time  $t = t_{\text{in}}$  towards

the future, while the second state vector evolves from the fixed final state (electron bound to the ion), "postselected" at the final time  $t = t_{\text{fin}}$ .

## 2. TVM FOR THE INCIDENCE GEOMETRY

In order to adapt the TVM to the grazing incidence geometry, the population process is considered in the coordinate system  $S$  moving with velocity  $v_{\parallel}$  along the surface. We use the simple fact that the state  $|\Psi_1(t)\rangle$  in the  $S$  and the state  $|\Psi_1^{(0)}(t)\rangle$  in the system  $S^{(0)}$  in rest (for  $v_{\parallel} = 0$ ) are connected kinematically. That is, it is sufficient to take into account the shifting  $\vec{k} \rightarrow \vec{k}' = \vec{k} + \vec{Q}$  of the metal electrons momenta by constant momentum  $\vec{Q} = -\vec{v}_{\parallel}$ , using an angle averaging  $\langle f \rangle_{\Omega_{\vec{k}'}}$  of the velocity modified Fermi-Dirac distribution [5]. The state  $|\Psi_2(t)\rangle$  in the  $S$  and the state  $|\Psi_2^A(t)\rangle$  in the rest frame  $S_A$  of the moving ion (which moves at velocity  $\vec{v}_{\perp}$  in respect to  $S$ ) differ by the Galilei phase factor  $\exp(i\hat{G}_{\perp})$ . At the intermediate time  $t$ , the states  $|\Psi_1^{(0)}(t)\rangle$  and  $|\Psi_2^A(t)\rangle$  can be expressed via the parabolic eigenstate  $|\mu_M(R)\rangle$  of the in-Hamiltonian  $\hat{H}_1(R)$  of the first scenario and the spherical eigenstate  $|\nu_A(R)\rangle$  of the out-Hamiltonian  $\hat{H}_2(R)$  of the second scenario, respectively [2].

Using the standard TVM procedure we calculate the intermediate transition probability density  $T_{\mu'_M, \nu_A}(t)$  for shifted initial quantum numbers  $\mu'_M$ , intermediate transition probability

$$T_{\nu_A}(t) = \sum_{\mu'_M} \langle f \rangle_{\Omega_{\vec{k}'}} T_{\mu'_M, \nu_A}(t) \quad (1)$$

and the population probability  $P_{\nu_A}(t) = 1 - \exp[-T_{\nu_A}(t)]$ . The basic physical quantity in the calculation of  $T_{\nu_A}(t)$  is the mixed flux through the moving Firsov plane  $S_F$ , which separates the solid and the ionic subsystems. Applying the mixed flux concept it is possible to solve the problem by using the asymptotic forms of the wave functions  $\Psi_1(\vec{r}, t)$  and  $\Psi_2(\vec{r}, t)$  within the framework of quasi-stationary approximation.

## 3. RESULTS

In Figure 1 we present the population probability  $P_{\nu_A}(t)$ , considering the ion ArXII. For all considered velocities  $v_{\parallel}$  we get the peak-shaped probability, with maximum  $P_{\nu_A}^{\text{max}}$  at  $R = R_{\text{max}}$ ; the increasing character of the population probability with decreasing  $R$  in the initial stages of the process can be attributed to the pure electron capture. With further decrease of  $R$ , i.e. for  $R < R_{\text{max}}$ , population probability decreases, which means that the reionization channel partially suppresses the neutralization. The ion-surface distance  $R_{\text{max}}$  determines the final time  $t = t_{\text{fin}}$  for the particular neutralization process.

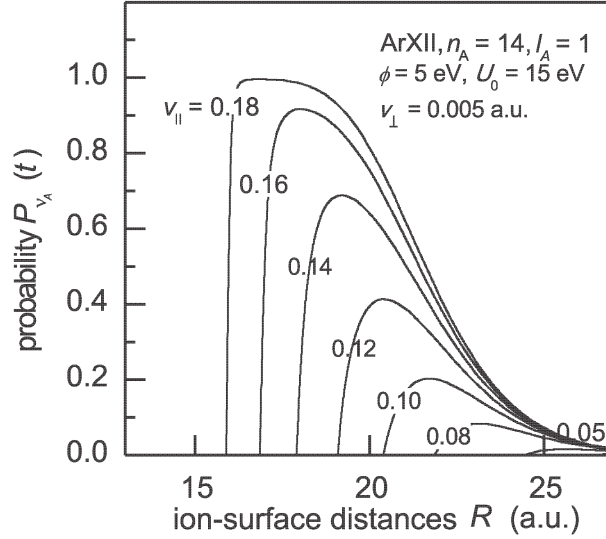


**Figure 1.** The TVM population probability  $P_{\nu_A}(t)$  of the Rydberg state  $n_A = 14$ ,  $l_A = 1$  and  $m_A = 0$  of the ArXII ion approaching the conducting solid surface (work function  $\phi = 5$  eV, depth of the potential well  $U_0 = 15$  eV), for some characteristic parallel velocities  $v_{||}$  (expressed in a.u.) and for perpendicular velocity component  $v_{\perp} = 0.005$  a.u.

The position  $R_c^N > R_{\max}$  (neutralization distance) of maximum of the positive mode of the population rate  $\Gamma_{\nu_A} = dP_{\nu_A}/dt$  determines the localization of the process. In Figure 2 we present the neutralization distances via projectile velocities  $v_{||}$  for the ArXII ion and for  $n_A = 10 - 18$ . From Figure 2 we see that the population of the higher Rydberg levels are at larger ion-surface distances  $R = R_c^N$ . This conclusion (that can be recognized at each projectile velocity) has to be considered simultaneously with the corresponding population probabilities. That is, the states  $|\nu_A\rangle = |n_A, l_A, m_A\rangle$  with larger  $n_A$  are populated with lower probabilities  $P_{\nu_A}$ .

The TVM population dynamics considered in the present article depends on the projectile velocity. The most pronounced is the parallel velocity effect. With increase of  $v_{||}$  we have the shift of the population distributions toward smaller ion-surface distances  $R$  (decrease of  $R_c^N$ ) and an increase of  $P_{\nu_A}^{\max}$ , see Figures 2 and 1, respectively.

The observed parallel velocity effect could be important when the full multielectron process of the neutralization of multiply charged ions is considered within the framework of the TVM.

**Acknowledgment** This work was supported in part by the Ministry of Education and Science, Republic of Serbia (Project 171016).

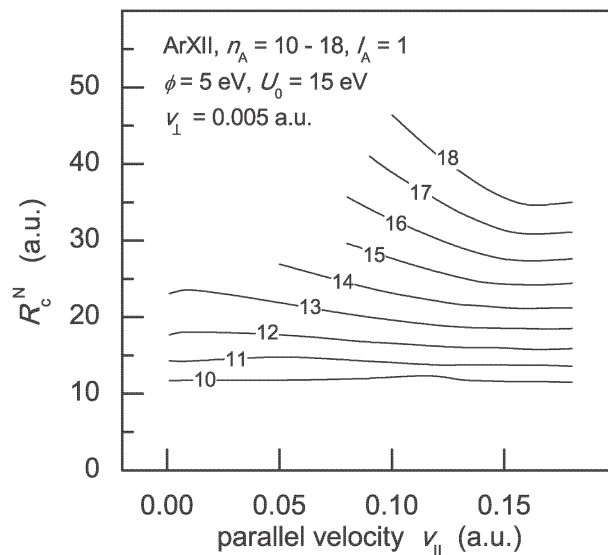


**Figure 2.** Neutralization distances  $R_c^N$  for the ArXII ion via parallel ionic velocity  $v_{||}$ , for the Rydberg states  $n_A = 10 - 18$ ,  $l_A = 1$  and  $m_A = 0$ .

## REFERENCES

- [1] N. N. Nedeljković, Lj. D. Nedeljković, R. K. Janev and Z. L. Mišković, Nucl. Instrum. Methods Phys. Res. B 58, 519 (1991).
- [2] N. N. Nedeljković and M. D. Majkić, Phys. Rev. A 76, 042902 (2007).
- [3] S. M. D. Galijaš, N. N. Nedeljković and M. D. Majkić, Surf. Sci. 605, 723 (2011).
- [4] H. Winter, Phys. Rep. 367, 387 (2002).
- [5] R. Zimny, Z. L. Mišković, N. N. Nedeljković and Lj. D. Nedeljković, Surf. Sci. 255, 135 (1991).

## POPULATION OF THE RYDBERG STATES OF THE ArVIII, KrVIII AND XeVIII IONS AT SOLID SURFACE FOR GRAZING INCIDENCE

S. M. D. Galijaš, N. N. Nedeljković, M. D. Majkić and I. P. Prlina

*University of Belgrade, Faculty of Physics, P. O. Box 368, Belgrade, Serbia*

**Abstract.** We consider the ArVIII, KrVIII and XeVIII ions interacting with solid surface in the grazing incidence geometry. We analyze the effect of the polarization of ionic core and the parallel velocity effect on the intermediate stages of the population process. Within the framework of the two-state vector model, it is demonstrated that the increase of the ionic polarization induces an increase of the population probability maxima and the population process is shifted to the smaller ion-surface distances. With increase of the projectile velocity, the population maxima increase and the region of the most effective population process becomes closer to the surface.

### 1. INTRODUCTION

Recently, we have analyzed the population of the Rydberg states of multiply charged ions ArVIII, KrVIII, and XeVIII, escaping solid surfaces in the normal direction, at low velocity [1] and for  $v \approx 1$  a.u. [2]. For description of the process we developed the appropriate two-state vector model (TVM). The similar analysis can be performed for the scattering geometry, by taking into account the effective modification ( $\vec{k} \rightarrow \vec{k}'$ ) of the angle averaged Fermi-Dirac distribution  $\langle f \rangle_{\Omega_{\vec{k}}}$  of the electron momenta  $\vec{k}$  in the solid due to the ionic motion component parallel to the surface with velocity  $v = v_{||}$  [3,4].

In the present article, we examine the multiply charged ions ArVIII, KrVIII and XeVIII in the scattering geometry under the grazing incidence within the framework of the TVM. The aim of the present analysis is to elucidate the role of the ionic core polarization on the intermediate stages of the population process in the considered geometry; namely, by taking into account the ionic core polarization, the ions with the same core charges will have different population histories. Within the framework of the TVM the process is defined under the teleological conditions, i.e., the state of a single active electron is described by two state vectors  $|\Psi_1(t)\rangle$  and  $|\Psi_2(t)\rangle$

evolving from the initial time toward the future and from the final time toward the past, respectively [1,2,4].

## 2. POPULATION DYNAMICS IN THE TVM

We consider the TVM electron exchange probabilities under the grazing geometrical conditions and for fixed initial and final electronic states. These states are determined by the parabolic quantum numbers  $\mu_M = (\gamma_M, n_{1M}, m_M)$  and the spherical quantum numbers  $\nu_A = (\gamma_A, n_{1A}, m_A)$ , where  $\gamma_M$  and  $\gamma_A(R)$  are the corresponding continuous and discrete energy parameters, respectively, of the electron in the solid and bounded to the ion at ion-surface distance  $R$ .

We calculate the intermediate transition probability density  $T_{\mu'_M, \nu_A}(t)$  for kinematically shifted initial quantum numbers  $\mu'_M$ , the velocity dependent intermediate transition probability

$$T_{\nu_A} = T_{\nu_A}^{(0)} \langle f \rangle_{\Omega_{\vec{k}'}} f_{\gamma}(\gamma'_M) \frac{v_{\perp} [\gamma'_M + \gamma_A(R)]^2}{\gamma'_M \tilde{\beta}} \left( 1 + \frac{2\tilde{\alpha}}{\tilde{\beta}} \frac{1}{R} \right) R^{2\tilde{\alpha}} e^{-2\tilde{\beta}R}, \quad (1)$$

where  $\gamma'_M = \gamma_A(R)$ , and the corresponding population probability  $P_{\nu_A}$  [4]. In (1) we have  $\tilde{\alpha} = Z/\tilde{\gamma}_A - 1/2 + 1/4\gamma_M'$  and  $\tilde{\beta} = \gamma'_M + (\tilde{\gamma}_A - \gamma'_M)g$ , where  $g = 1/2$  and  $\tilde{\gamma}_A$  is the ionic energy parameter for the polarized core. The quantity  $T_{\nu_A}^{(0)}$  is independent of  $\gamma'_M$  and  $R$ , and

$$f_{\gamma}(\gamma'_M) = 2^{\frac{1}{\gamma'_M}} \gamma'_M \frac{1}{\gamma'_M} + 1 (2e)^{\frac{1}{2\gamma'_M}} (3/4)^{\frac{2Zv_{\perp}^2}{\gamma'_M(\gamma'_M + v_{\perp}^2)}}. \quad (2)$$

Polarization of the electron-cloud of the ionic core has been effectively taken into account by means of the Simons-Bloch potential [5].

## 3. RESULTS

The intermediate transition probability  $T_{\nu_A}(t)$  given by (1), as well as the population probability  $P_{\nu_A}(t)$ , are peak-shaped, with maximum  $P_{\nu_A}^{\max}$  at  $R = R_{\max}$ . The neutralization distances  $R_c^N > R_{\max}$  (positions of maxima of the positive mode of the population rates  $\Gamma_{\nu_A} = dP_{\nu_A}/dt$ ) can be considered as ion-surface distances at which the process is mainly localized.

In Figure 1 we present the population maxima  $P_{\nu_A}^{\max}$  via parallel ionic velocity  $v_{\parallel}$ , for the ions ArVIII, KrVIII and XeVIII. An interesting rule can be recognized from the figure: population maxima for  $n_A$ ,  $n_A + 1$  and  $n_A + 2$  of the ions ArVIII, KrVIII and XeVIII behave similarly. For a given  $n_A$ , with increase of the core polarization (ArVIII  $\rightarrow$  KrVIII  $\rightarrow$  XeVIII) population maxima increase; the quantities  $P_{\nu_A}^{\max}$  for a given ion increase with increasing of the parallel projectile velocity  $v_{\parallel}$ .

In Figure 2 we present the neutralization distances via parallel ionic velocity for the population of the Rydberg states  $n_A = 8 - 16$  of the ions

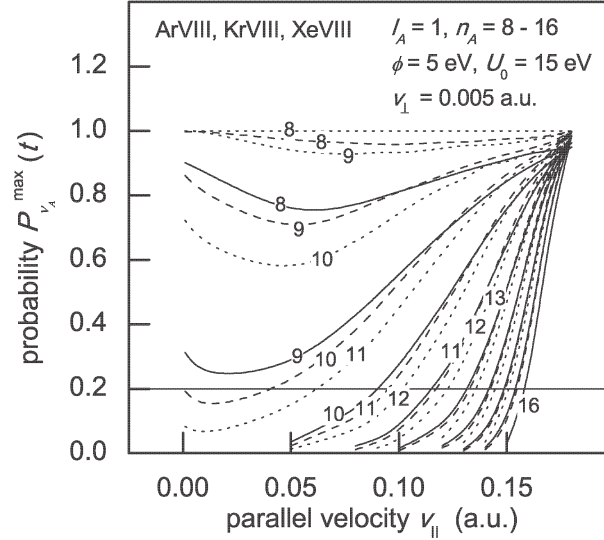


**Figure 1.** The population maxima  $P_{\nu_A}^{\max}$  via parallel ionic velocity  $v_{\parallel}$ , for the ions ArVIII, KrVIII and XeVIII, full, dashed and dotted curves, respectively.

ArVIII, KrVIII and XeVIII. With increase of the polarization of the ionic core and the increase of parallel ionic velocity we see a decrease of the neutralization distances  $R_c^N$  for population of the Rydberg state with a given  $n_A$ .

In Figure 2 we also present (by open circles) the minimal velocities necessary for population of the considered Rydberg state. For the parallel velocities smaller than this value the corresponding population probability is less than 0.2, see also Figure 1. Some of the Rydberg levels could be populated at each velocity; the neutralization distances for these states are independent of the projectile velocities. Polarization effect induces an increase of the probability maxima so that the minimal velocities decrease: for example, the Rydberg state  $n_A = 10$  of the XeVIII can be populated at all velocities, the the population of the same Rydberg state of the ion KrVIII is possible only for  $v_{\parallel} > 0.04$  a.u., and for ArVIII only for  $v_{\parallel} > 0.09$  a.u.

The recognized influence of the core polarization (by which the ions  $\text{Ar}^{Z+}$ ,  $\text{Kr}^{Z+}$  and  $\text{Xe}^{Z+}$  of the same  $Z$  are distinguished) on the position and magnitude of the population process, together with the parallel velocity effects on these intermediate characteristics of the process, introduces interesting new elements in the understanding of some ion-surface interactions phenomena. At present, these effects can be tested only indirectly, by comparing the measured kinetic energy gain due to the image acceleration of the ions with the corresponding quantity calculated using the TVM

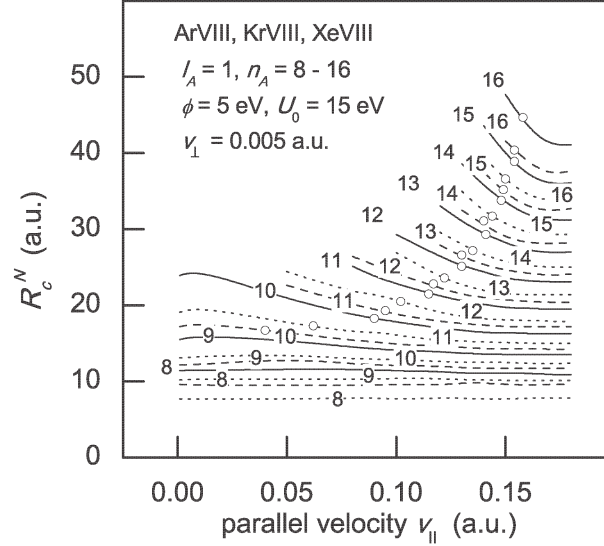


**Figure 2.** The neutralization distances  $R_c^N$  via parallel ionic velocity  $v_{||}$ , for the ions ArVIII, KrVIII and XeVIII, full, dashed and dotted curves, respectively.

results.

**Acknowledgment** This work was supported in part by the Ministry of Education and Science, Republic of Serbia (Project 171016).

## REFERENCES

- [1] N. N. Nedeljković and M. D. Majkić, Phys. Rev. A 76, 042902 (2007).
- [2] S. M. D. Galijaš, N. N. Nedeljković and M. D. Majkić, Surf. Sci. 605, 723 (2011).
- [3] R. Zimny, Z. L. Mišković, N. N. Nedeljković and Lj. D. Nedeljković, Surf. Sci. 255, 135 (1991).
- [4] N. N. Nedeljković, M. D. Majkić, S. M. D. Galijaš and M. A. Mirković, this conference (2012).
- [5] G. Simons and A. N. Bloch, Phys. Rev. B 7, 2754 (1973).

## TVM v.s. KINETIC ENERGY GAIN FOR MULTIPLY CHARGED IONS INTERACTING WITH SOLID SURFACES

M. D. Majkić<sup>1</sup>, N. N. Nedeljković<sup>1</sup>, R. J. Dojčilović<sup>1</sup> and M. B. Obradović<sup>2</sup>

<sup>1</sup>*University of Belgrade, Faculty of Physics, P. O. Box 368, Belgrade, Serbia*

<sup>2</sup>*University of Belgrade, Vinča Institute of Nuclear Sciences, P.O. Box 522, Belgrade, Serbia*

**Abstract.** We compare the measured projectile kinetic energy gain  $\Delta E^{(Z)}$  with the corresponding quantity obtained on the base of the first neutralization distances calculated within the framework of the two-state vector model. To calculate the energy gain of the ionic projectile  $Z+$  we use the "staircase" model, considering the multielectron capture process as cascade neutralization  $Z \rightarrow Z - 1 \rightarrow \dots 1 \rightarrow 0$ , together with quantum results used to estimate the principal quantum number  $n_c$  of the Rydberg state that is populated in the particular cascade and the corresponding ion-surface distance. It is demonstrated that the obtained energy gains depend on the parallel ionic velocity. The agreement of the theoretical curves with available experimental data in the large  $Z$  case can be addressed to the parallel velocity effect.

### 1. INTRODUCTION

In our recent studies it is demonstrated that the two-state vector model (TVM) can be used to elucidate the intermediate stages of the electron exchange dynamics in the ion surface system [1,2]. The corresponding experimental evidence is only indirect (kinetic energy gain experiments [3]) and exists only in the scattering geometry. In order to establish the link of our theoretical model with experiments, we adapted the TVM to the grazing incidence geometry [4].

In the present article, we perform the TVM analysis of the intermediate stages of the Rydberg level population of the multiply charged ions  $\text{Xe}^{Z+}$ , where  $Z \in [5, 35]$ , under the grazing incidence on a conducting solid surface. We recall that the basic TVM assumption is that the single electron state is described simultaneously by two state vectors  $|\Psi_1(t)\rangle$  and  $|\Psi_2(t)\rangle$ . In the considered ion-surface problem, the first state vector evolves from the initial state (electron in the solid) towards the future, while the second state vector evolves from the fixed final state (electron bound to the ion) towards the past.

The main outputs of the model (population probabilities  $P_{\nu_A}(t)$  and neutralization distances  $R_c^N$  [4]) at each step of the multielectron cascade give the sufficient information for the calculation of the kinetic energy gain  $\Delta E^{(Z)}$  of the ion due to the image acceleration.

## 2. TVM AND KINETIC ENERGY GAIN

An indirect experimental insight into the intermediate stages of the population dynamics can be deduced from the measured projectile kinetic energy gain  $\Delta E^{(Z)}$ . That is, it is possible to compare the measured quantity  $\Delta E^{(Z)}$  with the corresponding quantity obtained on the base of the first neutralization distances calculated within the framework of the TVM. In the present article we analyze the experimental output for  $\text{Xe}^{Z+}$  ions [5,6]. In the experiments the final angular shift for incidence of the cited multiply charged ions (in respect to the neutral projectile) has been measured under the grazing incidence conditions, from which it was straightforward to obtain the quantity  $\Delta E^{(Z)}$ .

Considering the multielectron capture process as cascade neutralization  $Z \rightarrow Z-1 \rightarrow \dots \rightarrow 1 \rightarrow 0$ , we assume that the charge  $Q$  of the projectile is instantaneously reduced to the charge  $Q-1$  when the neutralization distance  $R_c^{N,Q}$  for the population of the Rydberg state  $n_A = n_c(Q)$  is reached. The image-force interaction of the projectile with the surface is changing accordingly: in each interval  $R \in [R_c^{N,Q}, R_c^{N,(Q-1)}]$  the intensity of the image force is given by  $F = (Q-1)^2/4R^2$ . For a complete neutralization sequence this results in the image energy gain

$$\Delta E^{(Z)} = \sum_{Q=1}^Z \frac{2Q-1}{4R_c^{N,Q}}. \quad (1)$$

To calculate the TVM quantity  $\Delta E^{(Z)}$ , we need two information: what is the Rydberg state that is populated at each step of the process and at which ion-surface distances the process takes place. Within the quantum TVM the answers are nontrivial and depend on the values of  $P_{\nu_A}^{\max}$  of the probability maxima, the widths of the population probability distributions and the position of the population rates, for a given  $Q$  and for the neighboring  $Q$  values.

In Figure 1 we illustrated the mechanism of the cascade neutralization according to the TVM for the ion  $\text{XeX}$ . For the considered ionic velocity ( $v_{||} = 0.1$  a.u.) the Rydberg level  $n_c = 14$  is populated firstly at ion surface distance  $R_c^N = 22.9$  a.u.; at this distance the ionic charge is changed from  $Z = 10$  to  $Z = 9$ . After that, the population of the Rydberg states of the  $\text{XeIX}$  begins; the Rydberg state  $n_c = 13$  of this ion is populated at ion-surface distance  $R_c^N = 21.6$  a.u. In the considered case, the condition  $R_c^{N,Z} - R_c^{N,Z-1} < \Delta/2$ , where  $\Delta$  is the width of the population distribution.

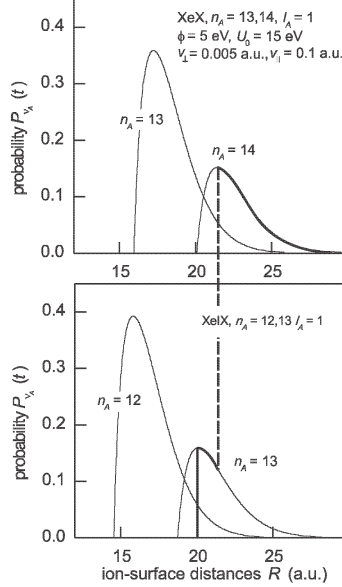


**Figure 1.** Cascade neutralization  $Z = 10 \rightarrow Z = 9$  in the case of XeX ion impinging a solid surface at parallel velocity  $v_{\parallel} = 0.1$  a.u. and perpendicular velocity  $v_{\perp} = 0.005$  a.u.

At larger velocities, the former condition is not satisfied for some Rydberg states, which in that case become unstable (and can be destroyed via resonant ionization). For that reason, the  $n_c$  values considered as a function of the projectile parallel velocity exhibit a saturation, for  $v_{\parallel}$  greater than some characteristic value for a given  $Z$ .

### 3. COMPARISON WITH EXPERIMENTS

In Figure 2 we present the kinetic energy gain  $\Delta E^{(Z)}$  calculated according to (1) via core charge  $Z$  for the ions  $\text{Xe}^{Z+}$ , where  $Z \in [5, 35]$ ; we use the recursive relation  $\Delta E^{(Z)} = \Delta E^{(Z-1)} + (2Z - 1)/4R_c^{N,Z}$ , taking for  $\Delta E^{(4)}$  the experimental data. Perpendicular ionic velocity is given by  $v_{\perp} = v \sin \Phi$ , where the angle of incidence  $\Phi = 1.5^\circ$ , and  $v_{\parallel} \in [0.003 \text{ a.u.}, 0.18 \text{ a.u.}]$ . For the surface parameters in (a) we use the values  $\phi = 5$  eV and  $U_0 = 15$  eV; the work function  $\phi = 4.3$  eV in (b) is taken in accordance with experimental conditions. By dashed curves in figures (a) and (b) we present the corresponding COB expression  $\Delta E^{(Z)}$  [7]. The curves presented in Figure 2(a) can be considered as branching of the velocity independent COB-curve.

The obtained agreement of the TVM curves with available experimental data in the large  $Z$  case can be addressed to the parallel velocity

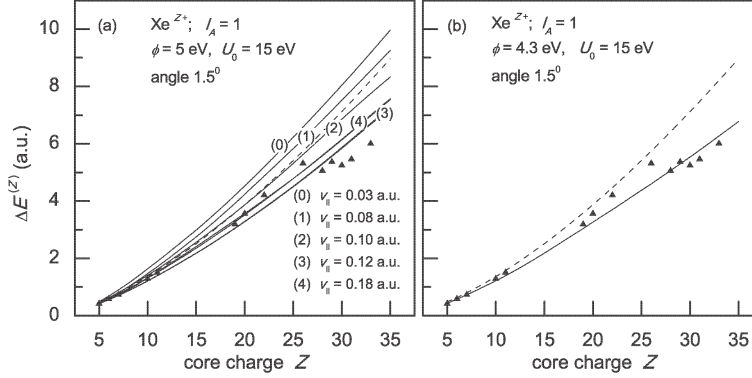


**Figure 2.** Kinetic energy gain  $\Delta E^{(Z)}$  via ionic core charge  $Z$  of the ions  $\text{Xe}^{Z+}$  according to (1) for (a) some characteristic parallel velocities  $v_{||}$  whose values are exposed in the figure and (b) under the experimental conditions. Solid triangles represent the experimental data taken from [6]. All curves are for  $v_{\perp} = v \sin 1.5^\circ$  and for (a)  $\phi = 5$  eV and (b)  $\phi = 4.3$  eV, and for  $U_0 = 15$  eV. Dashed curves are the COB quantity  $\Delta E^{(Z)} \approx \phi Z^{3/2}/3\sqrt{2}$  [7].

effect. The change of the solid work function induces the scaling of the  $\Delta E^{(Z)}$ . We note that for the surface parameters in Figure 2(b), i.e., for  $\phi = 4.3$  eV and  $U_0 = 15$  eV, our results are in better agreement with experiments.

**Acknowledgment** This work was supported in part by the Ministry of Education and Science, Republic of Serbia (Project 171016).

## REFERENCES

- [1] N. N. Nedeljković and M. D. Majkić, Phys. Rev. A 76, 042902 (2007).
- [2] S. M. D. Galijaš, N. N. Nedeljković and M. D. Majkić, Surf. Sci. 605, 723 (2011).
- [3] H. Winter, Phys. Rep. 367, 387 (2002).
- [4] N. N. Nedeljković, M. D. Majkić, S. M. D. Galijaš and M. A. Mirković, this conference (2012)
- [5] H. Winter, Europhys. Lett. 18, 207 (1992).
- [6] H. Winter, C. Auth, R. Schuch and E. Beebe, Phys. Rev. Lett. 71, 1939 (1993).
- [7] C. Lemell, H. P. Winter, F. Aumayer, J. Burgdörfer and F. Meyer, Phys. Rev. 53, 880 (1996).

## ANALYSIS OF SIGNAL BROADENING IN CHARGE TRANSFER PROCESSES BETWEEN RYDBERG ATOMS AND METAL SURFACE

J. Pajović<sup>1,2</sup>, R. J. Dojčilović<sup>1,2</sup>, D. K. Božanić<sup>2</sup>, F. G. Kilibarda<sup>1</sup> and N. N. Nedeljković<sup>1</sup>

<sup>1</sup> *University of Belgrade, Faculty of Physics, P.O. Box 368, Belgrade, Serbia*

<sup>2</sup> *University of Belgrade, Vinča Institute of Nuclear Sciences, P.O. Box 522, Belgrade, Serbia*

**Abstract.** The problem of broadening of the ion signal in charge transfer processes between hydrogen Rydberg atoms and metal surfaces reported recently by So et al. (Phys. Rev. A, 107, 093201 (2011)) was investigated within the framework of etalon equation method (EEM). The results reveal that the possible reason for the shallow rise of the number of ions collected with the increase in applied electric field is in broad distribution of the initial velocities of Rydberg atoms within the incoming beam.

### 1. INTRODUCTION

Rydberg atoms in which one electron is in highly excited state (e.g. principal quantum number  $n \gg 1$ ) are sensitive probes of atom-surface interactions. Namely, due to their large physical size ( $\approx n^2$  a.u.) and weak binding of the excited electron, the presence of the metallic surface results in formation of the hybridized Stark-like  $(n, n_1, m)$  states even at large ion-surface distances [1]. These states readily decay, preferentially via tunneling of the excited electron into a vacant level in the surface, leading to charge transfer process between the incoming atoms and the surface. Recent theoretical studies based on the wave package propagation method by So et al. [2] and the etalon equation method by Nedeljković and Nedeljković [3] suggested that such ionization process is well localized in the atom-surface distance range of approximately 50 a.u. The landmark experimental investigations of the charge transfer process by Dunning and co-workers [4], performed by collecting the surface ionized xenon Rydberg atoms using a weak electric field, have opened a question of the localization of the ionization process. Wethekam et al. [5] attributed the delocalization of the ionization process to the presence of local electric fields that arise due to the surface inhomogeneities.

Nedeljković and Božanić [6], more recently, presented a detailed analysis of the ionization process in the experiment based on the quantum decay model and etalon equation method (EEM). According to the model,

the projectile motion and the decay of the electron cloud should be treated simultaneously that results both in the preservation of the localization of ionization process and good agreement with the experimental observations. This theoretical study indicated that the velocity distribution of the atoms within the impinging beam contributes to the delocalization of the experimental signal.

Charge transfer of Rydberg hydrogen atoms at a metal surface were investigated recently [2]. In their experimental setups the authors have achieved control over the orientation of the electronic wave function and, consequently, the dependence of the distances at which the charge transfer process occurs (e.g. ionization distances  $R_c^I$ ) on the excited electron's Stark states and principal quantum numbers  $n$  ranging from 20 to 36. It was demonstrated that the ionization of the most redshifted states ( $n_1 = 0, m = 0$ ) occurs at  $R_c^I = 2.5 - 4.3 n^2$  a.u., while the most blueshifted states ( $n_1 = n - 1, m = 0$ ) ionize at  $R_c^I = 1.6 - 2.1 n^2$  a.u. The semiempirical model based on classic over barrier method, with mentioned delocalization considered, was employed to describe the slow rise of the ion signal, the essential output of cited experiments.

In this article we employ the decay model and the etalon equation method [3,6] that, unlike other theoretical models, inherently parameterizes states of Rydberg atoms in the presence of metal surface in parabolic quantum numbers  $\mu$ , to elucidate the novel experimental finding by So et al. [2].

## 2. FORMULATION OF THE PROBLEM

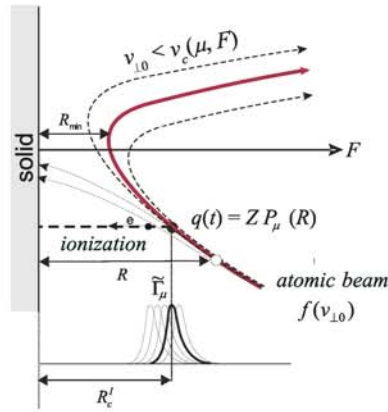


**Figure 1.** Decay model of ionization dynamics of the beam of atomic particles, with initial perpendicular velocity distribution  $f(v_0)$ .

We consider the ionization of a beam of slow hydrogen Rydberg atoms by a solid surface in a presence of a weak external electric field  $F$ .

The described model of beam ionization, corresponding to the experimental situation, is presented schematically in Figure 1. Each trajectory stands for the representative member of the subensemble of Rydberg atoms/ions with a given initial perpendicular velocity  $v_0$ . Only the projectiles with  $v_0 < v_c(\mu, F)$ , after the ionization (mainly localized at ionization distance  $R_c^1(\mu, v_0, F)$ ), will be collected by the external electric field  $F$  and detected experimentally. The trajectories of these projectiles are characterized by the minimal ion-surface distance  $R_{\min}$ .

### 3. RESULTS

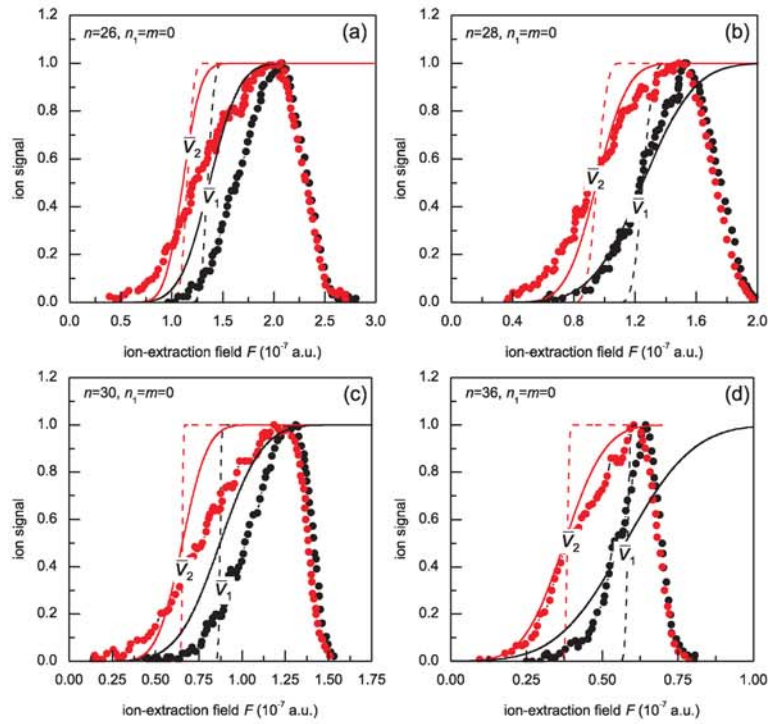


**Figure 2.** Averaged ionization probabilities  $\Sigma_\mu(F)$  for (a) H ( $n = 26$ ), (b) H ( $n = 28$ ), (c) H ( $n = 30$ ) and (d) H ( $n = 36$ ) for atomic projectiles with  $v_0 = \bar{v}_1 = 1.8 \times 10^{-4}$  a.u. and  $\Delta = 0.9 \times 10^{-4}$  a.u. (solid line);  $v_0 = \bar{v}_1$  and  $\Delta = 0.18 \times 10^{-4}$  a.u. (dashed line);  $v_0 = \bar{v}_2 = 3.0 \times 10^{-4}$  a.u. and  $\Delta = 1.5 \times 10^{-4}$  a.u. (solid line) and  $v_0 = \bar{v}_2$  and  $\Delta = 0.3 \times 10^{-4}$  a.u. (dashed line). Available experimental data (black and gray circles) for  $v_0 = \bar{v}_1$  and  $v_0 = \bar{v}_2$ , respectively, are taken from [2].

According to the model, the complex eigenenergies  $E_\mu(R) = \text{Re}E_\mu(R) - i\Gamma_\mu(R)/2$  of the system Hamiltonian (corresponding to the decaying Ryd-

berg state  $\Psi_\mu$  of the active electron) can be obtained using the EEM without explicit calculation of the wavefunctions. Details of solving the complex energy eigenvalue problem are given explicitly in Reference [3]. The ionization rates  $\Gamma_\mu(R)$  are further used to calculate ionization probabilities  $P_\mu(R; v_0, F)$  and total rates  $\tilde{\Gamma}_\mu(R)$  that describe the intermediate stages of ionization and determine the most probable distance at which the charge transfer process occurs ( $R_c^I$ ). The experimental procedure [2] produces a normalized number of ionized atoms as a function of the applied field, or ion signal. These results can be compared with the probability  $\Sigma_\mu(F)$ , that is described as the average of probability  $P_\mu(R; v_0, F)$  over the distribution of initial velocities of atoms in a beam  $f(v_0)$ . In the case of Gaussian distribution of initial velocities, the averaged probability  $\Sigma$  is

$$\Sigma_\mu(F) = \frac{1}{2} \left[ 1 + \text{Erf} \left( \frac{v_c(\mu, F) - \bar{v}}{\Delta} \right) \right] \quad (1)$$

where  $\bar{v}$  stands for mean initial velocity and  $\Delta$  is the width of the distribution. The field dependence of critical velocity  $v_c(\mu, F)$  is characteristic of each state  $\mu$  and is explicitly given in reference [6].

In Figures 2(a), 2(b), 2(c) and 2(d) we present the averaged probabilities  $\Sigma_\mu(F)$  for  $n = 26, 28, 30$  and  $36$ , and  $n_1 = m = 0$ , for the experimental values of mean initial velocity  $\bar{v}$  and arbitrary values for  $\Delta$ . The averaged probabilities are compared to the available experimental data.

**Acknowledgment** This work was supported in part by the Ministry of Education and Science, Republic of Serbia (Project 171016).

## REFERENCES

- [1] P. Nordlander, Phys. Rev. B, 53, 4125 (1996).
- [2] E. So, M. Dethlefsen, M. Ford and T. P. Softley, Phys. Rev. A, 107, 093201 (2011).
- [3] N. N. Nedeljković and Lj. D. Nedeljković, Phys. Rev. A, 72, 032901 (2005).
- [4] Y. Pu, D. D. Neufeld and F. B. Dunning, Phys. Rev. A, 81, 042904 (2010).
- [5] S. Wethekam, H. R. Dunham, J. C. Lancaster and F. B. Dunning, Phys. Rev. A, 73, 032903 (2006).
- [6] N. N. Nedeljković and D. K. Božanić, Phys. Rev. A, 81, 032902 (2010).

## SPATIAL DISTRIBUTIONS OF BODIES IN HENON-HEILES INTERACTION POTENTIAL

Vesna Borka Jovanović and Duško Borka

*Atomic Physics Laboratory (040), Vinča Institute of Nuclear Sciences,  
University of Belgrade, P.O. Box 522, 11001 Belgrade, Serbia*

**Abstract.** In this work we investigate the regular and chaotic motion of bodies of unit mass in Hénon-Heiles type of potential. In reality, potential along the Si <111> crystal is well described by the Hénon-Heiles potential and potential near galactic plane is well described by the same form of potential. We also investigate the regular and chaotic part of their spatial distributions. We determine regular and chaotic areas in impact parameter plane of Hénon-Heiles potential using Poincaré maps. We present our results as a function of dwell time ( $t$ ), which is varied from 0.25 to 100 T. The obtained results show the periodicity of the regular part of spatial distributions with the period of 0.5 T, and chaotic parts of the spatial distributions show no periodicity.

### 1. INTRODUCTION

Chaotic systems are analysed more than two hundred years. More about deterministic chaos see e.g. in [1, 2]. Hénon and Heiles studied stellar trajectories through a galaxy [3] and introduced 2-dimensional Hénon-Heiles potential. Also the classical Hénon-Heiles Hamiltonian was introduced in the study of galactic dynamics to describe the motion of stars around a galactic center [4]. For details about regular and chaotic motion of charged particles channeling in crystals see e.g. [5].

### 2. THEORY

This paper study the regular and chaotic motion of bodies of unit mass in Hénon-Heiles type of potential. We have chosen this potential because it is simple and universal. It describes potential between stars and galaxy [3] and also ion-atom potential in hyperchanneling of ions along the Si <111> crystal [5]. In the present paper, we approach the problem by numerical computation. In order to have more general form (because this problem is universal, applicable on motion of body in small nanocrystal or huge galaxy) we neglect

channeling or astronomical origins of problem and we solve it more generally for body of unit mass.

We consider a body moving along the Hénon-Heiles potential. The particles are chosen to start at some points  $(x_i, y_i)$  with zero transversal initial velocities:  $(v_x)_i = (v_y)_i = 0$ , so that their transversal energies are given by the initial potential energy:  $E_i = V(x_i, y_i)$ . Moving along longitudinal direction is uniform, i.e.  $(v_z)_i = v_z$  is constant. For the model potential, the Hénon-Heiles type of potential is used [3]:  $V = 0.5(x^2 + y^2) + (x^2y - y^3)/3$ .

The transverse components of the body position,  $x$  and  $y$  as a function of dwell time  $t$ , are determined via the numerical solution of the body's equations of motion in the transverse plane. The spatial distributions of bodies is generated using the computer simulation [6]. The impact parameters of bodies are chosen from 2 dimensional uniform distribution within the triangular region. The initial number of bodies is around 326 000.

### 3. RESULTS AND DISCUSSION

Using Poincaré cross section [1, 7], we formed a maps in 2-dimensions. For each of the 326 000 lattice points  $(x_i, y_i)$  we followed its Poincaré map and the trajectory. According to these maps and trajectories, for every lattice points it is determined in the impact parameter plane whether it is regular or chaotic [7]. Results are presented in Fig. 1(left). In Fig. 1(right), the relative ratio of regular and all (regular and irregular) trajectories is presented, normalized to one in the function of energy  $E$ . It can be noticed there is "shoulder" for energy around  $E = 0.123 - 0.132$ .

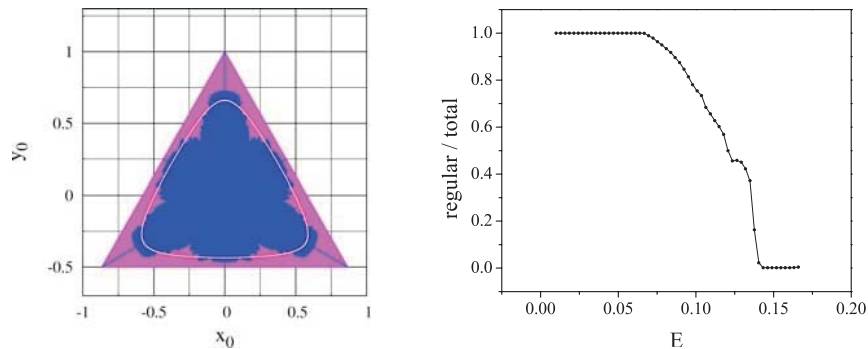


**Figure 1.** (left) Triangular channel of Hénon-Heiles potential. The two different areas show regularity (inner area) and irregularity (outer area) of the trajectories for certain initial coordinates  $(x_0, y_0)$ . The contour line for potential  $V = 0.128$  is added to Hénon-Heiles regular-chaotic triangle. (right) Relative ratio of regular and all (regular and irregular) trajectories, normalized to one, depending of energy  $E$ .

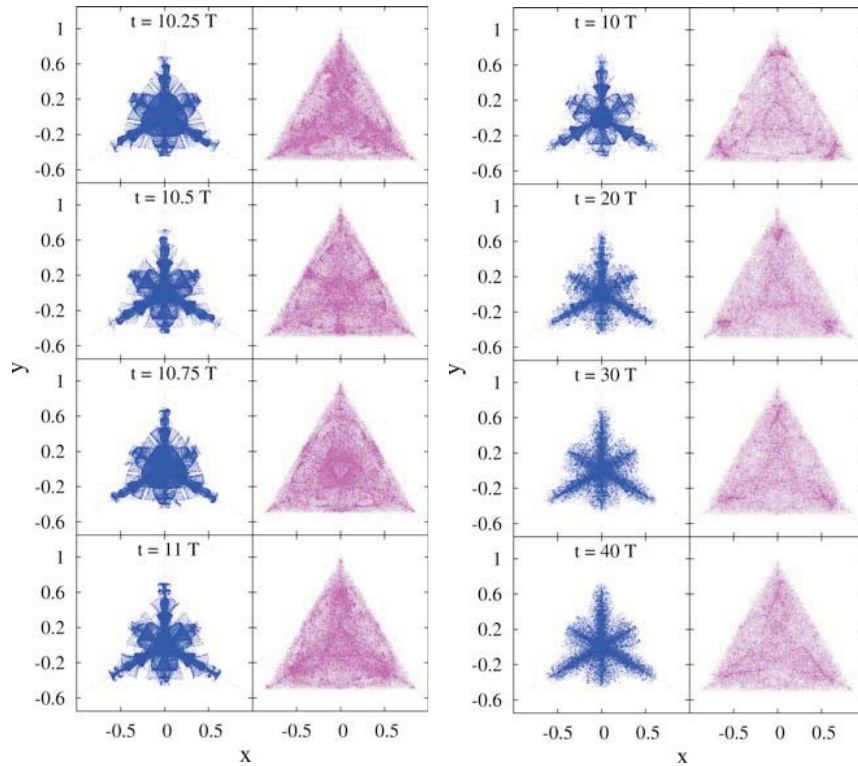


**Figure 2.** (*left panel*) The spatial distributions of the bodies for variable  $t$  equal to (a) 10.25, 10.50, 10.75 and 11 T, respectively. (*right panel*) The spatial distributions of the bodies for variable  $t$  equal to 10, 20, 30 and 40 T, respectively.

When we compare this shoulder with boundary between the regular and chaotic area in Fig. 1(left), it is obvious that shoulder is result of a diffuse shape of regular - chaotic boundary.

Fig. 2(left panel) shows the spatial distributions of the bodies for variable  $t$  equal to 10.25, 10.50, 10.75 and 11 T, respectively. All our results are presented as a function of body dwell time  $t$  within the triangular channel of Hénon-Heiles potential. This variable for periodic orbit can be also given in units of T, where T is a period of transversal oscillation of unit mass body close to the axis of triangular channel. For the non-periodic orbit we present corresponding results for the same value of variable  $t$  (the same value of time interval) as in the periodic case. In Fig. 2(left column of left panel), we can see the periodicity of the spatial distribution with the period of 0.5 T. The shapes of spatial distributions for  $t = 10.25$  and 10.75 T are qualitatively similar, and the shapes of spatial distributions for  $t = 10.5$  and 11 T are qualitatively similar too. The values of  $t = 10.25, 10.75, 11.25$  T ... correspond to the beginnings of

periodic cycles of the spatial distribution [8]. One can also observe in all four cases that the spatial distributions have six symmetrical "arm" structures around the center of the position plane. They consist of two curved triangular structures. It should be noted that the spatial distributions presented here have the  $C_{3V}$  symmetry which is the consequence of the  $C_{3V}$  symmetry of the Hénon-Heiles type of potential. Comparing the chaotic parts of spatial distributions in Fig. 2(right column of left panel), it is clear that they are showing no periodicity. Spatial distributions become more equilibrated and are smeared out covering whole triangular region. Fig. 2(right panel) shows the spatial distributions of the bodies for variable  $t$  equal to 10, 20, 30 and 40 T, respectively. We can see that regular parts of spatial distributions are characterized by the symmetrical coaxial maxima around the center of the position plane. As the variable  $t$  increases the number of coaxial maxima increases and the average distance between them decreases. It is interesting to note that the same tendency is observed for the angular distributions of 1 GeV protons channelled through the long (11, 9) single-wall carbon nanotubes [9]. Comparing the chaotic parts of spatial distributions in Fig. 2(right column of right panel) we can conclude that these distributions become more equilibrated and are smeared out covering whole triangular region.

## Acknowledgements

This work is supported by the Ministry of Education and Science of the Republic of Serbia (Project No. 45005).

## REFERENCES

- [1] P. Cvitanović, R. Artuso, R. Mainieri, G. Tanner and G. Vattay, *Chaos: Classical and Quantum*(Niels Bohr Institute, Copenhagen, 2009), <http://www.chaosbook.org>.
- [2] H.G. Schuster and W. Just, *Deterministic Chaos* (WILEY-VCH Verlag GmbH & Co. KgaA, 2005).
- [3] M. Hénon and C. Heiles, *Astron. J.* 69, 73 (1964).
- [4] R. Barrio, F. Blesa and S. Serrano, *Europhys. Lett.* 82, 10003 (2008).
- [5] A.I. Akhiezer, V.I. Truten and N.F. Shulga, *Phys. Rep.* 203, 289. (1991).
- [6] D. Borka, D. J. Mowbray, Z. L. Mišković, S. Petrović, and N. Nešković, *New J. Phys.*12, 043021 (2010).
- [7] V. Borka Jovanović, S. Petrović, D. Borka and N. Nešković, *Publ. Astron. Obs. Belgrade* 89, 93 (2010).
- [8] H. F. Krause, J. H. Barrett, S. Datz, P. F. Dittner, N. L. Jones, J. Gomez del Campo and C. R. Vane, *Phys. Rev. A* 49, 283 (1994).
- [9] S. Petrović, I. Telečki, D. Borka and N. Nešković, *Phys. Lett. A* 372, 6003 (2008).

## EFFECTS OF VANADIUM IONS IRRADIATION ON THE MICROSTRUCTURE OF CrN LAYERS

M. Novaković<sup>1</sup>, A. Traverse<sup>2</sup>, M. Popović<sup>1</sup>, K.P. Lieb<sup>3</sup>, K. Zhang<sup>3</sup> and N. Bibić<sup>1</sup>

<sup>1</sup> VINČA Institute of Nuclear Sciences, University of Belgrade, 11001 Belgrade, Serbia

<sup>2</sup> Laboratoire de Chimie Physique, UMR 8000, CNRS, Université Paris-Sud, 15 rue Georges Clemenceau, 91405 Orsay-Cedex, France

<sup>3</sup> II. Physikalisches Institut, Georg-August-Universität Göttingen, Friedrich-Hund-Platz 1, 37077 Göttingen, Germany

**Abstract.** We report on modifications of 280 nm thin polycrystalline CrN layers caused by 80-keV vanadium ion implantation. The CrN layers were deposited at 150°C by d.c. reactive sputtering on Si(100) wafers and then implanted at room temperature with 80-keV V<sup>+</sup> ions to the fluences of  $1 \times 10^{17}$  and  $2 \times 10^{17}$  ions/cm<sup>2</sup>. Structural characterization of the layers was performed with Rutherford backscattering spectroscopy (RBS), cross-sectional transmission electron microscopy (XTEM), and X-ray diffraction (XRD). It was found that strong influence of chemical effects leads to the formation of the Cr<sub>0.9375</sub>V<sub>0.0625</sub>N phase in a V-rich region of CrN films.

### 1. INTRODUCTION

Transition metal nitrides such as chromium nitride (CrN) have an extreme hardness, low friction, high corrosion resistance and excellent mechanical and high-temperature stability [1,2]. Due to these favorable tribological characteristics, they have become important materials for protective and abrasion-resistant coatings.

The present work complements and extends previous microstructural analyses of Ar-ion irradiated polycrystalline CrN films [3] into the following direction: by using vanadium as another ion species, we have tried to distinguish between purely defect-related effects induced by ion implantation, and chemical effects due to the presence of vanadium as the second transition metal. *A priori*, one expects the formation of either V or Cr precipitation in the form of clusters, or the compound VN, or a solid solution of the type Cr<sub>1-x</sub>V<sub>x</sub>N [4]. According to work by Traverse, Borowski and collaborators [5], the heat of formation of the initial nitride and other possible phases has to be considered when predicting the new final phase(s). Since the heat of formation of VN is more negative than the one of CrN, VN should be formed providing the correct

stoichiometry and sufficient mobility are given. Yet  $\text{Cr}_{1-x}\text{V}_x\text{N}$  seems to be stable, too, and its occurrence cannot be excluded.

## 2. EXPERIMENTAL DETAILS

Chromium nitride thin films were deposited to a thickness of 280 nm by d.c. reactive sputtering from a Cr target of 99.9% purity, using Ar for sputtering and  $\text{N}_2$  as reactive gas. The base pressure in the chamber was around  $1 \times 10^{-6}$  mbar, the argon and nitrogen partial pressures during deposition were  $1 \times 10^{-3}$  mbar and  $5 \times 10^{-4}$  mbar, respectively. The substrates used were (100) Si wafers.

The samples were implanted at room temperature with 80-keV  $\text{V}^+$  ions to the fluences of  $1 \times 10^{17}$  and  $2 \times 10^{17}$  ions/cm<sup>2</sup>. The chosen ion energy guaranteed that the average projected range,  $R_p = 35$  nm, estimated with the SRIM2003 code [6], was well separated from the CrN/Si interface in order to avoid any ion beam mixing and interface reactions.

Structural and compositional characterizations were performed with Rutherford backscattering spectroscopy (RBS), X-ray diffraction (XRD) and (high-resolution) transmission electron microscopy (XTEM, HRTEM). RBS measurements were performed with 1.2 MeV  $\alpha$ -particles provided by the SAFIR facility [7]. The backscattering spectra were taken at normal beam incidence and were analyzed with the RBX [8] and WiNDF codes [9]. Cross-sectional TEM was done with a JEOL 100CX electron microscope and HRTEM measurements of some selected samples were performed by means of a Philips CM200-FEG microscope. All the samples were analyzed by XRD with a BRUKER D8 Advance diffractometer by using the  $\text{CuK}_\alpha$  radiation.

## 3. RESULTS

Figure 1.a shows the concentration profile for the nominal fluence of  $2 \times 10^{17}$  V/cm<sup>2</sup>. Firstly, we note a decrease of the metallic component near the surface, which could be a consequence of either preferential metal sputtering or surface oxidation during implantation. At larger depths, changes in stoichiometry were observed for the ion-implanted sample. The fits were performed assuming the presence of Cr atoms only and the number and profiles of V-atoms were deduced from the supplementary metal atoms. For the nominal fluence of  $2 \times 10^{17}$  V/cm<sup>2</sup>, this resulted in a value of  $2.3 \times 10^{17}$  V/cm<sup>2</sup>. The V profile peaked at a depth of  $R_p = 38$  nm with a full width at half maximum (FWHM) of 26 nm. SRIM2003 code provided a projected range of  $R_p = 35$  nm and the implantation width of  $\Delta R_p = 24$  nm. The V content in the implantation profile is about 20 at.%.

XRD spectra of the as deposited and implanted films are shown in Figure 1.b. The as deposited film exhibits the (111) and (200) reflexes of the cubic CrN phase. The calculated lattice constant of 0.4153 nm is in the range of the values found in polycrystalline CrN films,  $a_0 = 0.4133 - 0.4185$  nm [10].

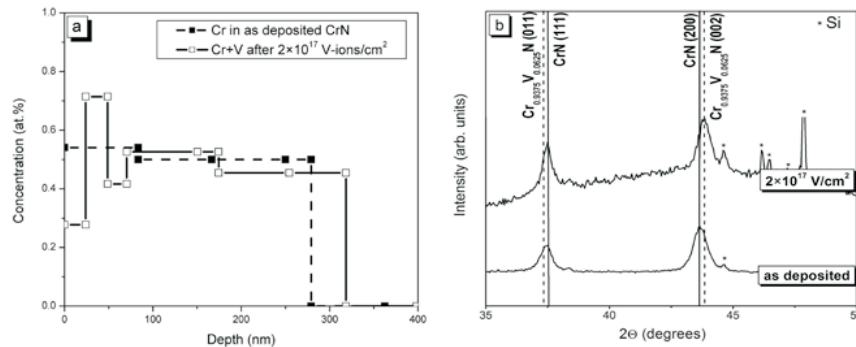


**Figure 1.** CrN/Si bilayer before and after irradiation to  $2 \times 10^{17}$  V/cm<sup>2</sup>: (a) RBS depth profiles of Cr and Cr+V; (b) XRD spectra.

Small shifts are visible for the implanted films, but the deduced lattice constants are still in the same range. A wide signal is observed superimposed on the background around  $2\theta = 42^\circ$  which might be an indication of an amorphized (oxidized) surface layer. The (200) diffraction peak for the implanted sample shows a small shift (from  $2\theta = 43.72^\circ$  to  $43.84^\circ$ ). This may be a consequence of (i) an accumulation of irradiation defects leading to lattice compression; (ii) the formation of Cr<sub>1-x</sub>V<sub>x</sub>N ternary phases or a solid solution; or (iii) a partial oxidation of CrN. Indeed, the position of the (200) peak would match that of the cubic compound Cr<sub>1-x</sub>V<sub>x</sub>N ( $x = 0.0625$ ).

XRD provides information averaged over the whole film thickness. To discriminate the depth-dependent structural evolution the CrN films were also studied by XTEM and HRTEM. Figure 2 shows the cross-sectional bright-field

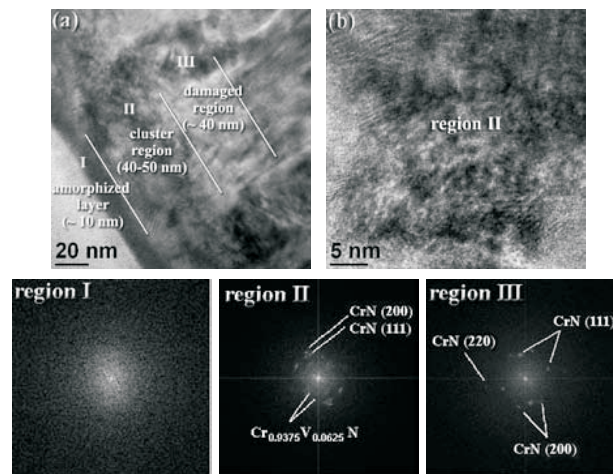


**Figure 2.** XTEM analysis of the CrN/Si sample implanted with  $2 \times 10^{17}$  V-ions/cm<sup>2</sup>: (a) bright field image; (b) high-resolution image. Fourier transforms from different regions are presented in the lower part of the figure.

image (a) and high-resolution image (b) of the sample implanted with  $2 \times 10^{17}$  V-ions/cm<sup>2</sup>. Fourier transforms taken from different regions of the sample are presented in the lower parts of the figure. One observes various microstructural inhomogeneities in the CrN layer. The top 10-nm layer is amorphous, as proven by the Fourier transform of region I. The subsequent region II corresponds to the vanadium-enriched zone and contains a high concentration of agglomerated defects. The high-resolution image displayed in Figure 2.b and its Fourier transform indicate the presence of CrN plus additional spots. These additional spots correspond to Cr<sub>0.9375</sub>V<sub>0.0625</sub>N phase. Beyond this layer, the damage region III merges into the non-implanted CrN matrix.

#### 4. CONCLUSIONS

We have studied the effects of V<sup>+</sup>-ion irradiation on the microstructure of CrN films. At a fluence of  $2 \times 10^{17}$  ions/cm<sup>2</sup>, a V-rich zone near the projected range of some 35 nm was generated, centered in a 50-80 nm wide damaged region and leaving an about 200 nm thick non affected CrN layer. In a V-rich zone the presence of Cr<sub>0.9375</sub>V<sub>0.0625</sub>N phase was observed.

#### Acknowledgements

This work was supported by the Ministry of Sciences and Environmental Protection of the Republic of Serbia (Project No. III 45005), by Deutsche Forschungsgemeinschaft, and by the French-Serbian CNRS-MSTD bilateral collaboration (No. 23119).

#### REFERENCES

- [1] B. Bushan and B.K. Gupta, *Handbook of Tribology*, p. 454, (McGraw-Hill, New York, 1991).
- [2] Y.Y. Chang and D.Y. Wang, *Surf. Coat. Technol.* 188-189, 478 (2004).
- [3] M. Novaković, M. Popović and N. Bibić, *Nucl. Instr. Meth. B* 268, 2883 (2010).
- [4] H.K. Danielsen and J. Hald, *Computer Coupling of Phase Diagrams and Thermochemistry* 31, 505 (2007).
- [5] D. Zanghi, A. Traverse, S. Gautrot and O. Kaïtasov, *J. Mater. Res.* 16, 512 (2001).
- [6] J.F. Ziegler, J.P. Biersack and U. Littmark, *The Stopping and Range of Ions in Solids*, (Pergamon Press, New York, 1985); code SRIM2003: <http://www.srim.org>.
- [7] SAFIR at [www.insp.jussieu.fr/safir/](http://www.insp.jussieu.fr/safir/).
- [8] E. Kotai, *Nucl. Instr. Meth. B* 85, 588 (1994).
- [9] N.P. Barradas, C. Jeynes and R.P. Webb, *Appl. Phys. Lett.* 71, 291 (1997).
- [10] K.W. Wang, T.N. Lin and D.Y. Wang, *Thin Solid Films* 516, 1012 (2008).

## MICROSTRUCTURAL CHANGES OF TiN FILMS INDUCED BY 200 keV ARGON IONS

M. Popović, M. Novaković, M. Šiljegović and N. Bibić

*VINČA Institute of Nuclear Sciences, University of Belgrade, 11001 Belgrade,  
Serbia*

**Abstract.** This paper reports on a study of microstructural changes in TiN/Si bilayers due to 200 keV Ar<sup>+</sup> ions irradiation at room temperature. The 240 nm TiN/Si bilayers were prepared by d.c. reactive sputtering on crystalline Si(100) substrates. After deposition the TiN/Si bilayers were irradiated to the fluences of 5–20×10<sup>15</sup> ions/cm<sup>2</sup>. The structural changes induced by ion irradiation were analysed by Rutherford Backscattering Spectroscopy (RBS), X-ray diffraction analyses (XRD) and Transmission Electron Microscopy (TEM). The irradiations caused the microstructural changes in TiN layers, but no amorphization even at the highest argon fluence of 2×10<sup>16</sup> ions/cm<sup>2</sup>. It is also observed that the mean crystallite size decreases with the increasing ion fluence.

### 1. INTRODUCTION

Thin films of TiN have been studied extensively due to their excellent mechanical properties, such as high hardness, high corrosion and wear resistance. The interest in this system is generally motivated by the fact that the combination of properties such as high melting point, low electrical resistivity, good chemical stability and high reflectivity in the infrared region is suitable for wide range of applications [1-3].

Modification of the ceramic coatings and layered structures by ion irradiation is a powerful tool to tailor the structural, optical, electrical, magnetic etc., properties of a wide class of materials. Moreover, the precise control of irradiation parameters along with selection of suitable materials offer advantages in structuring materials on a nanometer scale, nowadays one of the most relevant technological challenge [4,5]. Heavy-ion irradiation of thin coatings may change their microstructural properties and specifically the grain size. This study grew out based on these considerations.

The aim of the experiments described in this paper is to discuss in more detail the changes of the microstructure of TiN/Si bilayer after irradiation with 200 keV Ar<sup>+</sup> ions. By combining ion irradiation and analysing techniques the conditions to tailor of the mean grain size of the TiN coatings were investigated.

## 2. EXPERIMENTAL DETAILS

TiN thin films were deposited by d.c. reactive sputtering from a Ti target of 99.9% purity in a Balzers Sputtron II system, using sputtering (Ar) and reactive ( $N_2$ ) gases. The substrates used were (100) Si wafers. The TiN films were deposited at the substrate temperature of  $150^\circ\text{C}$  to a thickness of 240 nm.

After deposition the samples were irradiated with 200 keV  $\text{Ar}^+$  ions. The implanted fluences were  $5\text{--}20 \times 10^{15}$  ions/ $\text{cm}^2$ . Ion irradiations were performed at room temperature and the beam current was maintained at  $\sim 1 \mu\text{A}/\text{cm}^2$  in order to avoid heating effects during irradiations. Irradiation energy was chosen in such a way that the projected range of ions and energy deposition density were in TiN side of the TiN/Si bilayers, according to simulation done with the SRIM 2003 code [6].

The RBS analyses were performed with a 900 keV  $\text{He}^{++}$  ion beam provided by the IONAS facility in Göttingen, with two Si surface detectors positioned at a  $165^\circ$  backscattering angle. Backscattering spectra were taken at normal incidence and the changes in the concentration profiles of Ti, Si, N and Ar were analysed with the WiNDF [7]. Further structural characterization of as deposited and irradiated samples was performed with cross-sectional transmission electron microscopy (XTEM) and x-ray diffraction analyses (XRD). Cross-sectional TEM was done on a JEOL 100CX microscope, and we also used micro-diffraction (MD) technique to study the crystalline structure. HRTEM measurements of some selected samples were also performed by means of a Philips CM200 FEG microscope operated at 200 keV. All the samples were analysed by X-ray diffraction with a BRUKER D8 Advance diffractometer by using the  $\text{CuK}_\alpha$  radiation.

## 3. RESULTS

The elemental composition of the TiN/Si bilayers was extracted from RBS experimental spectra using WiNDF code. Generally, it was found that the

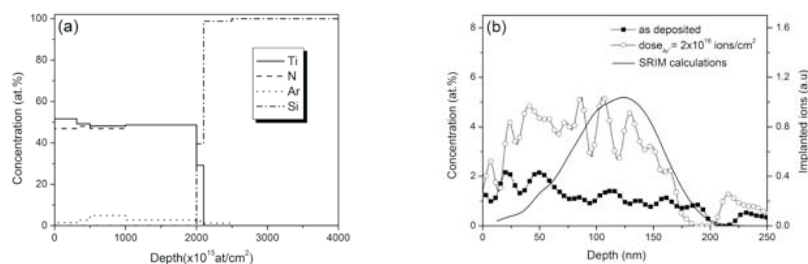


**Figure 1.** RBS analyses of TiN/Si bilayers: (a) extracted concentration profiles of Ti, N, Si and Ar for TiN sample irradiated to  $2 \times 10^{16}$  Ar/ $\text{cm}^2$  and (b) Ar depth profiles of as deposited sample and sample irradiated to  $2 \times 10^{16}$  Ar/ $\text{cm}^2$

as deposited TiN thin coatings, as well as irradiated were pure TiN. Figure 1a shows the experimental data fitted by introducing Ti, N, Ar, and Si in the Data furnace structure files for the sample irradiated to  $2 \times 10^{16}$  Ar/cm<sup>2</sup>. An approximate ratio of Ti:N=1:1 thus indicating the formation of TiN phase. Argon concentration profiles are presented in Figure 1b. This figure demonstrates an almost homogenous Ar concentration profile for as deposited sample with an average concentration of 2at.%. Additionally, analysis reveals that the additional 3at % of the Ar was incorporated after irradiation of the sample to  $2 \times 10^{16}$  ions/cm<sup>2</sup>. The results of SRIM simulation for the same experimental parameters are included as a solid line demonstrating good agreement with experimental data.

Figure 2(a and b) shows the cross-sectional bright filed images of the as deposited sample (a) and the sample irradiated to  $5 \times 10^{15}$  Ar/cm<sup>2</sup>(b). HRTEM image taken from the sample irradiated to  $2 \times 10^{16}$  Ar/cm<sup>2</sup> is also presented on the same figures. The TEM analysis confirms, as show in Figure 2a, that the as deposited layer consists of polycrystalline TiN phase. This is concluded from crystallographic data obtained from electron diffraction. The TiN layer exhibits a growth of dense columnar structure, with column diameters in the range from 20 to 30 nm. For the irradiated sample, XTEM shows (2b) a pronounced change of the layer microstructure and substantial amount of disorder, the columnar structure seems to be destroyed inside of  $\sim 110$  nm at the surface of the TiN layer. This is in agreement with the MD analyses (inset in Figure 2b), which show the ring-like diffraction patterns indicating very fine grain structure corresponding to the typical reflections seen for the as deposited layer. This analysis may be taken as a first hint that Ar ions irradiation induces the formation of the smaller crystallites.

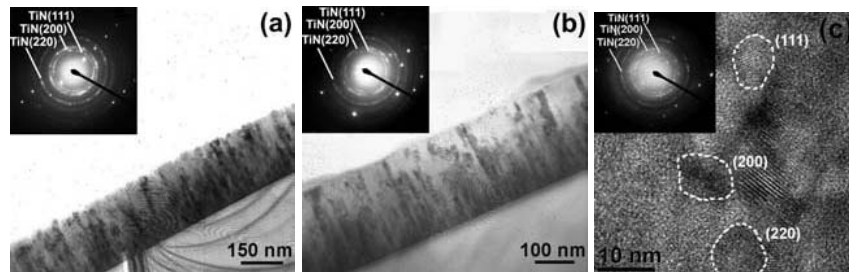


**Figure 2.** XTEM analysis and corresponding MD patterns of TiN/Si bilayers: (a) as deposited sample, (b) sample irradiated to  $5 \times 10^{15}$  Ar/cm<sup>2</sup> and (c) sample irradiated to  $2 \times 10^{16}$  Ar/cm<sup>2</sup>

Indeed, the HRTEM image (Figure 2c) shows that the TiN layer has a structure with the nanocrystalline nature of the grains. The image suggests the grain size of  $\sim 8$  nm with nearly spherical morphology. The formation of the smaller crystallites may reflect the particles size optimization for the stable structure induced by Ar ions irradiation. Generally, ion irradiation induces an energy transfer which provides conditions for the interaction of the surfaces and boundaries of the nanocrystals with an internal free energy of the system that

has a local minimum with respect to the size (volume) of the nanocrystal. In addition, the MD patterns taken from the labeled grains confirms that the layer is a pure TiN.

The decrease in crystallite size can be understood by analyzing the XRD data. The crystallite size was estimated using Scherrer equation [8]. The mean crystallite size was found to be 16 nm for as deposited sample and ~8 nm for the sample irradiated to  $2 \times 10^{16}$  ions/cm<sup>2</sup>. This results demonstrates excellent agreement with the HRTEM analyses. Correspondingly, the Ar ions irradiation creates defects and causes the loss of the columnar structure of the TiN layers, leading to the formation of the smaller crystallite.

#### 4. CONCLUSIONS

Summarizing the above observations leads to the conclusions that ion irradiation induces the formation of small crystallites, the size of which decreased with the increase in the fluence. The HRTEM and XRD analyses revealed the crystallites size of ~8 nm after irradiation to the highest ion fluence. Generally, the microstructure of the TiN layers sensitively depends on Ar ions irradiation, which causes the loss of the typical columnar structure.

#### Acknowledgements

This work was supported by the Ministry of Sciences and Environmental Protection of the Republic of Serbia (Project No. III 45005). The authors are grateful to Deutsche Forschungsgemeinschaft for supporting the visits of M.P. and M.N. in Göttingen.

#### REFERENCES

- [1] D.M. Sanders, *J. Vac. Sci. Technol. A* 7 , 2339 (1998).
- [2] J.E. Sundgren, *Thin Solid Films* 128, 21 (1985).
- [3] J. Musil, *Surf. Coat. Technol.* 125, 322 (2000).
- [4] Y.P. Sharkeev, S.J. Bull, A.J. Perry, M.L. Klingenberg, S.V. Fortuna, M. Michler, R.R. Manory, I.A. Shulepov, *Surf. Coat. Technol.* 200 , 5915 (2006).
- [5] H. Wang, R. Araujo, J.G. Swadener, Y.Q. Wang, X. Zhang, E.G. Fu, T. Cagin, *Nucl. Instrum. Methods B* 261, 1162 (2007).
- [6] J.F. Ziegler, J.P. Biersack, U. Littmark, *The Stopping and Range of Ions in Solids* (Pergamon Press, N. Y., 1985); code SRIM2003: <http://www.srim.org>.
- [7] N.P. Barradas, C. Jaynes, R.P. Webb, *Appl. Phys. Lett.* 71 , 291 (1997).
- [8] B.D. Cullity, *Elements of X-ray diffraction*, (Addison-Wesley, Wokingham, 1967).

## **SECTION 3.**

### **Low Temperature Plasmas**

- 3.1 Plasma Spectroscopy and other Diagnostic Methods
- 3.2 Gas Discharges
- 3.3 Plasma Applications and Devices

### **ABSTRACTS OF INVITED LECTURES**



## **MODELING OF PLASMA AND PLASMA-SURFACE INTERACTIONS FOR ENVIRONMENTAL, MEDICAL AND NANO APPLICATIONS**

Annemie Bogaerts, Maksudbek Yusupov, Wouter Van Gaens, Robby Aerts, Ming Mao, Wesley Somers and Erik Neyts

*Research group PLASMANT, University of Antwerp, Dept. of Chemistry, Universiteitsplein 1, B-2610 Wilrijk-Antwerp, Belgium*

Plasmas are gaining increasing interest for medical, environmental and nano applications. In order to improve these application fields, a good insight in the underlying processes is required. We try to obtain this by computer modeling. In this talk, some examples will be given, both with respect to modeling the plasma chemistry and the plasma-surface interactions.

For plasma medicine applications, we have developed a comprehensive plasma chemistry model describing a He or Ar plasma jet expanding into ambient air. The formation of reactive oxygen and nitrogen species, as well as water clusters, will be described, for a range of different air humidities, and N<sub>2</sub> and O<sub>2</sub> admixtures to the discharge gas. Results of a 0D model as well as a 2D plasma model will be presented. Moreover, the interaction mechanisms of reactive oxygen species with bacterial cell walls, more specifically with peptidoglycan, which is the outer protective barrier in bacteria, will be explained, as revealed by atomic-scale molecular dynamics (MD) simulations.

For environmental applications, the plasma chemistry taking place in a DBD, in CO<sub>2</sub>/CH<sub>4</sub> gas mixtures, as obtained by a 0D model, will be presented, with the aim of converting these greenhouse gases into value-added chemicals. Special attention will be given to the underlying reaction mechanisms, and the conversion of the greenhouse gases, the yields and selectivities of the reaction products, and the energy efficiency of the process. Moreover, some first results of the interaction of hydrocarbon species at a Ni catalyst surface, as obtained from MD simulations, will be presented, with the aim of obtaining a better insight in the (possibly) synergistic effects of plasma catalysis.

Finally, for nano applications, plasma chemistry simulations will be illustrated for various hydrocarbon-based gas mixtures typically used for carbon nanotube (CNT) growth, to elucidate which are the important growth species. Moreover, MD simulations will be presented, showing how a single-walled CNT with a definable chirality, can be grown, and how plasma effects, such as the electric field as well as ion bombardment, can affect the growth process.

**EXTREMELY FAR FROM EQUILIBRIUM:  
THE MULTISCALE DYNAMICS OF STREAMER**

U. Ebert

*Eindhoven University of Technology, Netherlands*

## **MODEL BASED DESIGN OF LOW TEMPERATURE PLASMA REACTORS**

Mark J. Kushner

*University of Michigan  
Department of Electrical and Computer Science  
Ann Arbor, MI 48109-2122 USA  
mjkush@umich.edu*

**Abstract.** Modeling of low temperature plasmas has long held the promise of speeding the rate of technology development through computer based virtual prototyping of new systems. Although this goal has not been universally achieved, there has been impressive progress. For example, plasma reactors for microelectronics fabrication are regularly optimized, if not designed, using computer modeling. Thermal plasma sources, such as torches for plasma spray deposition, are also regularly optimized and designed using 3-dimensional computer models. In talk, the basic requirements and computational infrastructure required for robust, model based design of non-equilibrium plasma reactors will be discussed. An overview of computational techniques and databases now used for such modeling will be provided, followed by examples of model based design of low and atmospheric pressure plasmas for materials processing and biological applications. Requirements for advancing the field and truly meeting the potential of virtual prototyping of plasma reactors will be discussed.

**ANTITUMORAL EFFECT OF NON THERMAL  
PLASMAS ALONE OR IN COMBINATION  
WITH CHEMOTHERAPY**

J-M. Pouvesle

*GREMI University of Rleans, France*

## **THE COMPLEX DIAGNOSTICS OF BARRIER DISCHARGES - AN EXPERIMENTAL CHALLENGE**

Hans-Erich Wagner

*University of Belgrade Faculty of Physics, 11001 Belgrade, P.O.Box 368,  
Serbia*

Non-thermal plasmas at atmospheric pressure are effective sources of radicals and excited species. Therefore, they have found many technical applications in the large field of plasma chemistry, lighting and recently also in life-science. In this group the barrier discharges (BDs) have a key position with long tradition. It is well-known that BDs can be operated in various discharge modes, namely the filamentary and diffuse one. In the latter it has to be distinguished between a Townsend-like and glow-like mode. The appearance of different operation modes depends on the feeding gas mixture and flow rate, gas pressure, operation frequency and the shape of applied voltage, dielectric electrode material and the reactor geometry (e.g. gap spacing). For large aspect ratios (lateral extension to gap distance) an increased tendency of pattern formation is observed. Many investigations in the past have contributed to the better understanding of the complex processes. But, despite the great progress in this field in the last decade, the diagnostics of these phenomena is still a challenge.

In the talk a review on the advanced diagnostics of BDs is given, discussing important milestones in this field together with recent own experimental results. Filamentary BDs consist of a great number of microdischarges (MDs) with sub-millimeter size and nanosecond duration. Their spatio-temporally and spectrally resolved development in the volume succeeded by the technique of cross-correlation emission spectroscopy (CCS). An extremely high sensitivity of the CCS combined with the temporal resolution in a sub-nanosecond range is the main advantage, as compared to other methods of emission spectroscopy. Investigations in  $N_2$ - $O_2$  mixtures allowed the quantitative estimation of the electric field and relative electron density in single MDs. The knowledge of the basic plasma parameters enabled a deeper understanding of the process of the electrical breakdown, including discharge physics and chemistry. The investigations were extended to diffuse BDs in  $N_2$ , noble gases and their mixtures. In particular, the transition between the filamentary and diffuse modes has been studied in detail. Recently, a discharge cell configuration has been developed which combines the CCS with the temporally resolved detection of surface charges on the dielectric surfaces. This succeeded by the application of the electro-optic Pockels effect in combination with a CCD camera. Surface

charges play an important role for the re-ignition of the discharge (memory effect). Furthermore, the new set-up enabled the quantitative determination of metastable  $N_2(A)$  molecules by the laser induced fluorescence spectroscopy. In this way, it was possible to correlate relevant surface and volume processes under identical and well-defined experimental conditions. The presented results are an extensive source for the comparison with kinetic models.

- [1] H.-E. Wagner, K.V. Kozlov, R. Brandenburg, Cross-correlation emission spectroscopy applied to non-equilibrium plasma diagnostics, vol. 1, p. 271, in: *Low Temperature Plasmas - Fundamentals, Technologies and Techniques*, Editors: R. Hippler, H. Kersten, M. Schmidt, K.H. Schoenbach, 2<sup>nd</sup> edition, 2008 WILEY-VCH Verlag GmbH & Co. KGaA, Weinheim.
- [2] M. Bogaczyk, S. Nemschokmichal, A. Zagoskin, G. B. Sretenovic, J. Meichsner, and H. E. Wagner, Spatio-temporally Resolved Investigation of Surface Charges,  $N_2(A)$  Metastables and Discharge Development in Barrier Discharges, *J. Adv. Oxid. Technol.* 15 (2012) 310.

## **EXPERIMENTAL TRANSITION PROBABILITY MEASUREMENTS IN PULSED LAMPS: CRITICAL POINTS**

J. A. Aparicio<sup>1</sup>, M. T. Belmonte<sup>1</sup>, R. J. Peláez<sup>2</sup>, S. Djurović<sup>3</sup> and S. Mar<sup>1</sup>

<sup>1</sup> Departamento de Física Teórica Atómica y Óptica, Universidad de Valladolid, P. Prado de la Magdalena s/n, 47071 Valladolid, Spain

<sup>2</sup> Laser processing Group, Instituto de Óptica, CSIC, C/ Serrano 121, 28006 Madrid, Spain

<sup>3</sup> Faculty of Sciences, Department of Physics, Trg Dositeja Obradovića 4, 21000 Novi Sad, Serbia.

The importance of transition probabilities are out of doubt. In many scientific, industrial or astrophysical fields, transition probabilities are used to determine plasma temperature and, from this, element abundances and other physical parameters of interest can also be obtained. Pulsed lamps may be very promising sources of high quality/low uncertainty transition probability data. Among its intrinsic advantages, it is remarkable the possibility of making measurements at very different plasma conditions. However, several critical points should be very carefully considered when designing and using these light sources with this scientific purpose.

The calculation of the geometry involved in the process emission-detection of the radiation coming from a spectral line makes commonly the determination of its absolute transition probability an unfeasible task. In this case, only relative transition probabilities are available. However, when only one relative scale is tried and lines coming from different upper levels are involved, the characterization of the equilibrium state in the plasma becomes a new significant problem. In this case, the existence of excitation equilibrium along the measured plasma volume should be carefully guaranteed. The Boltzmann-plot technique is a useful tool to check the exponential population of the excited states of the radiation emitters.

The experimental difficulties are not negligible either. If the uncertainty associated to the determined transition probability value is tried to be low, it is necessary a high homogeneity in the emitting plasma volume whose radiation is detected. This requires, among others, the absence of cold layers which may emit the same spectral radiation at very different intensity than that emitted in the hottest regions. Furthermore, although the homogeneity might be checked in a reliable way, this is not enough. Self-absorption may become a serious problem whose control is of vital importance. When the quantification of this effect is possible and is not too severe, different experimental and numerical procedures exist in the literature which may help us to reconstruct the original emitted profile and to make possible the comparison of line intensities.

From the experimental point of view, other cautions should also be considered and its effects quantitatively evaluated. Among them, we could remark the need of a precise calibration of the spectrometric system and the possible influence of electrode sputtering on spectral transmittance of lamp windows.

## **PHYSICO-CHEMISTRY OF PLANETARY ATMOSPHERIC ENTRY PLASMAS**

Arnaud BULTEL, Julien ANNALORO and Vincent MOREL

*UMR CNRS 6614 CORIA, University of Rouen  
Site universitaire du Madrillet BP12 – 76801 Saint-Etienne du Rouvray -  
FRANCE*

During the atmospheric entry of a spacecraft, the hypersonic flow is converted into a high enthalpy flow through a shockwave: the temperature reached during this phase induces the dissociation of the molecules and the ionization of the gas [1]. The gas is therefore converted into plasma. The related complex chemistry involves a lot of radicals and ionized species. In the case of an Earth's atmospheric entry, the species produced are  $N_2$ ,  $O_2$ , Ar, NO, N, O,  $N_2^+$ ,  $O_2^+$ ,  $Ar^+$ ,  $NO^+$ ,  $N^+$ ,  $O^+$ , and  $e^-$ , whereas they are  $CO_2$ ,  $N_2$ , Ar,  $O_2$ , NO, CO, CN,  $C_2$ , C, N, O,  $N_2^+$ ,  $Ar^+$ ,  $O_2^+$ ,  $NO^+$ ,  $CO^+$ ,  $CN^+$ ,  $C_2^+$ ,  $C^+$ ,  $N^+$ ,  $O^+$ , and  $e^-$  in the case of a Martian atmospheric entry. The behavior of these mixtures is complex and is now far from being completely understood. In addition, the characteristic hydrodynamic times scales are short, which prevents a complete relaxation of the flow: this flow is therefore in thermal and chemical non-equilibrium [2]. In this context, the chemistry of the flow plays a key role, for example in the radiative flux transferred to the spacecraft and in the recombination processes taking place on the fuselage. To avoid any damaging of the vehicle, a thermal protection system is used. Its sizing and its characteristics depend on the chemistry of the flow: this chemistry has therefore to be well understood.

Understanding this complex chemistry is one of the main objectives of the works developed in our laboratory. We elaborate tools able to give us detailed information on the behavior of the mixture in thermodynamic non equilibrium in different situations. These tools are all based on the specific treatment of the balance equation of each species on excited states considered as independent. Collisional and radiative elementary processes are taken into account in the source term of the related balance equation. The state-to-state collisional-radiative (CR) model thus developed can be implemented to:

- study the relaxation of the mixture starting from a non-equilibrium situation in constant pressure and temperatures conditions,
- simulate the subsonic flow behind a strong shockwave using crossing conditions of the Rankine-Hugoniot type related to flight situations or able to be observed in shock tubes,

- reproduce the flow conditions in a diverging nozzle such as those used to produce supersonic jets.

In this invited topical lecture, the elaboration of these CR models will be illustrated and the results will be analyzed. In particular, the attention will be focused on the vibrational distribution of molecules and on the atomic excited states in pure nitrogen, behind a strong shockwave during Earth's reentry and in a typical nozzle flow.

[1] Ya.B Zel'dovich, Yu P. Raizer *Physics of shock waves and high-temperature hydrodynamic phenomena* (Dover Publications, N. Y., 2002)

[2] Lin S.C. (1961) *Planetary and Space Science* **6** 94

## **THE PLASMA BASED FORMATION AND FUNCTIONALIZATION OF NANOPARTICLES AND NANOCOMPOSITE MATERIALS**

E. Kovacevic<sup>1</sup>, J. Berndt<sup>1</sup>, H. Acid<sup>1</sup>, Th. Maho<sup>1</sup>, L. Boufendi<sup>1</sup>

<sup>1</sup>*GREMI, University of Orleans, France*

Low temperature plasmas are nowadays frequently used in many technological processes. Their distinctive non-equilibrium character (low gas temperature and high electron temperature) offer unique possibilities of the production and treatment of different materials. In particular thermally unstable materials can be either functionalized, activated, etched or synthesized by these kinds of plasmas.

This contribution is focused on the polymerization and functionalization of carbonaceous nanoparticles, thin films and nanocomposites.

The structure and properties of plasma polymerized materials, as for example the degree of crosslinking or the hydrogen content, strongly depend on: a) the intensity and energy of the species bombarding the growing material b) the surface temperature and c) the species contributing to the growth of the materials. The formation of nanoparticles induces strong changes of the plasma parameters and thus of the above mentioned factors. These changes reflect consequently on the material characteristics of the nanoparticles growing in the plasma.

One example concerns nanoparticles formed in acetylene containing plasmas exhibiting a core-shell structure. Nanoparticles under 10nm radius shows strongly graphite-like character, The bonding situation changes with the increasing size of the nanoparticles, showing the formation of a sp<sup>2</sup> poor mantle around the graphite-like core. These results can be explained in terms of the nucleation and growth process of nanoparticles, i.e. due to: a) size-dependent heating of the nanoparticles and b) differences in the gas phase species involved in the early growth stage vs those involved in the surface growth of the larger particles. This phenomenon is especially interesting for applications, e.g. for the production of nanocomposites with variable characteristics.

Besides the variation of the material characteristics of the deposit by the choice of the nanoparticle size, it is also possible to vary the surface properties by plasma functionalization. In this contribution we will report on surface functionalization of such deposits by low temperature plasmas and by photon irradiation.

## **CATHODE SHEATH AND HYDROGEN BALMER LINES MODELING IN A MICRO-HOLLOW GAS DISCHARGE**

Djordje Spasojevic

*University of Belgrade Faculty of Physics, 11001 Belgrade, P.O.Box 368,  
Serbia*

**Abstract.** We present a model of the cathode sheath (CS) processes responsible for the broadening of the hydrogen Balmer beta line recorded from a micro-hollow gas discharge (MHGD) and used for simultaneous diagnostics of plasma and CS parameters. The MHGD was generated in a microhole (diameter 100  $\mu\text{m}$  at narrow side and 130  $\mu\text{m}$  at wider side) of a gold-alumina-gold sandwich in the pressure ranges: (100–900) mbar in argon with traces of hydrogen, and (100–400) mbar in pure hydrogen. The electron number density is determined from the plasma broadened line width of the central part of Balmer beta profile, while the average value of electric field strength in the CS and the CS thickness are determined from the extended line wings induced by the dc Stark effect.

## INVESTIGATION OF ENERGETIC HYDROGEN ATOMS IN GLOW DISCHARGES

N. Cvetanović<sup>1</sup>

<sup>1</sup> *Faculty of Transport and Traffic Engineering, University of Belgrade,  
Vojvode Stepe 305, 11000 Belgrade*

**Abstract.** Hydrogen Balmer lines that are excessively Doppler broadened have been detected in various types of discharges during the last two decades (see Ref. [1] and references therein). This phenomenon is also found in plasma fusion experiments. Namely, widely broadened profiles have shown the presence of hydrogen atoms with high kinetic energies, up to several hundreds of electronvolts. According to the collision (CM) or field acceleration (FAM) model [2, 3] hydrogen ions ( $H^+$ ,  $H_2^+$ ,  $H_3^+$ ) are accelerated by electric field in the sheath regions of the discharge where they undergo charge exchange reactions thereby generating energetic H atoms. Also, ions are backscattered from the cathode as fast hydrogen atoms after undergoing neutralization and fragmentation. Recently, alternative explanations have emerged. In order to investigate the population of fast H atoms and verify the CM we have performed a series of experiments with different types of glow discharges. Balmer alpha emission spectroscopy was used for abnormal glow discharge operating in DC and pulse mode in two directions of observation, hollow cathode discharge and glow mode of dielectric barrier discharge. End-on profiles were used to obtain the energy distributions of exited energetic atoms. Using previously adopted method for line profile decomposition [3] axial evolution of side-on profiles was analyzed. Influence of cathode with low atom reflection and influence of discharge conditions on energetic H atoms was investigated [4]. Temporal evolution of exited fast atoms' population was investigated in a pulse glow discharge. Preliminary non-self-consistent simulation was developed for fast hydrogen atoms, and its results are compared with the experiment.

### REFERENCES

- [1] A.V. Phelps, Plasma Sources Sci. Technol. 20 043001 (2011)
- [2] Z. Lj. Petrović, B. M. Jelenković and A. V. Phelps, Phys. Rev. Letters 68 325 (1992)
- [3] N. Cvetanović, M.M. Kuraica, N. Konjević, J. Appl. Phys. 97 033302(2005)
- [4] N. Cvetanović, B.M. Obradović and M. M. Kuraica, J. Appl. Phys. 109 013311 (2011) and J. Appl. Phys. 110 073306 (2011)

## **DIAGNOSTICS AND BIOMEDICAL APPLICATIONS OF RADIOFREQUENCY PLASMAS**

Saša Lazović<sup>1</sup>

<sup>1</sup>*Institute of Physics, University of Belgrade, Pregrevica 118, 11080 Belgrade,  
Serbia*

**Abstract.** Radiofrequency plasmas at low and atmospheric pressure exhibit complementary features when it comes to biomedical applications. Non equilibrium plasma of large volume can easily be generated and maintained at low pressures. Samples can be successfully treated achieving high uniformity. A large scale cylindrical asymmetric RF is used to treat textile and improve antibacterial properties with addition of nanoparticles like that of silver. Langmuir and catalytic probe are used to determine the optimal treatment parameters by recording the ion and atomic oxygen spatial profiles. Although it is harder to generate non thermal plasma at atmospheric pressure, it is necessary to do so for the in-vivo applications and treatment of samples that cannot undergo vacuum. Plasma needle and micro atmospheric pressure plasma jet ( $\mu$ APPJ) were diagnosed using mass spectrometry. The difference in geometry and therefore configuration of electric fields has provided that ion and neutral spectra were recorded for the plasma needle and only neutral spectra for the  $\mu$ APPJ. Electrical characterization of all plasma sources is performed using derivative probes. Both at low and atmospheric pressure, balance of charged and neutral species play an important role in determining the nature of the plasma treatment. The selectivity of the plasma was investigated using the plasma needle on biological model consisting of two types of bacteria (*Escherichia coli* and *Staphylococcus aureus*) and human peripheral blood mesenchymal stem cells (hPB-MSC). It was shown that by proper choice of plasma parameters, sterilization of bacteria can be achieved without causing the damage to the surrounding tissue (modeled by hPB-MSC). The research is a milestone on a route towards the in-vivo application of the plasma needle for treatment of paradontopathy.

## **STUDIES OF MULTIPHOTON PROCESSES IN NOBLE GAS ATOMS**

Andrej Mihelič<sup>1</sup>

<sup>1</sup>*Jožef Stefan Institute, Jamova cesta 39, Ljubljana, Slovenia*

Due to their availability in monatomic form and their closed-shell electronic structure, noble gas atoms are often considered suitable atomic systems for studying nonlinear optical processes, such as multiphoton ionisation and excitation, above-threshold ionisation, high-order harmonic generation, or dynamic Stark shift. The processes which involve absorption or emission of several photons require intense light sources and, as is the case with two-colour excitations, exact synchronisation and spatial alignment of the photon beams. I will present recent theoretical and experimental results of two-colour synchrotron (pump) plus IR laser (probe) experiments with noble gas atom targets, where either (i) angular distributions of photoelectrons ejected from the synchrotron-polarised atoms are measured or (ii) metastable atom yields reached by radiative decay cascades are measured. These experiments provide evidence on the interaction coupling strengths and electron correlation in noble gas atoms, and are in agreement with our calculations.

## **SPECTROSCOPIC STUDY OF HYDROGEN BALMER LINE SHAPES IN A HOLLOW CATHODE GLOW DISCHARGE IN NH<sub>3</sub> AND Ar/NH<sub>3</sub>, Ar/CH<sub>4</sub> AND Ar/C<sub>2</sub>H<sub>2</sub> MIXTURES**

N. M. Šišović

*University of Belgrade, Faculty of Physics, Belgrade, P.O. Box 368, Serbia*

**Abstract.** The considerable interest has been shown for the shape of Balmer lines emitted from a low-pressure discharges operating with hydrogen isotopes or with inert gas–hydrogen mixtures, see [1] for comprehensive literature review. The interest is triggered primarily by large excessive Doppler broadening (EDB) of hydrogen Balmer lines detected first time in a hollow cathode glow discharge (HCGD) run with hydrogen and hydrogen–inert gas mixtures.

Different broadening mechanisms are used to explain Balmer line components in hydrogen low-pressure gas discharge. The overall line shape was named Anomalously Doppler Broadened (ADB) profile. The narrow part of the line profile represents convolution of several profiles emitted by thermalized excited hydrogen atoms and H\* generated by dissociative excitation in electron impact collisions with H<sub>2</sub>. The broader middle part of the line profile is, in most cases, related to the dissociative ionization of H<sub>2</sub> via several reactions with the respect to the Franck–Condon (FC) principle. The presence of large excessive Doppler broadening (EDB) determined from the broadest part of multi-component ADB profile, explains so-called plasma-sheath “Collision Model”.

The aim of this work is to study atomic hydrogen line shapes in a hollow cathode glow discharge in ammonia and argon–ammonia, argon–methane and argon–acetylene gas mixtures. The intention is to test applicability of earlier results of electron beam dissociation of NH<sub>3</sub> [2], CH<sub>4</sub> and C<sub>2</sub>H<sub>2</sub> [3] for analysis of narrow and medium width Gaussians of Balmer line profile in HCGD. Although the processes of dissociative excitation and ionization were of major interest, the EDB of hydrogen Balmer lines in all working gases was also observed and studied.

### **REFERENCES**

- [1] G.Lj. Majstorović , N.M. Šišović , N. Konjević , Phys. Plasmas 14 043504 (2007).
- [2] J. Kurawaki and T. Ogawa, Chem. Phys. 86, 295 (1984).
- [3] T. Ogawa, J. Kurawaki, M. Higo, Chem. Phys. 61, 181 (1981).

## **BREAKDOWN AND DISCHARGE REGIMES IN STANDARD AND MICROMETER SIZE DC DISCHARGES**

Nikola Škoro

*Institute of Physics, University of Belgrade, P. O. Box 68, 11080 Belgrade,  
Serbia*

**Abstract.** Low temperature non-equilibrium discharges draw attention both from the side of basic-level investigations and from application motivated research. Advances in fundamental research lead to emergence of new applications but the vice versa approach is also present in many cases. In either way, due to the complexness of the discharges, full understanding of discharge processes is necessary for making efficient and reliable applications.

On one side, our investigations were directed towards low-pressure dc breakdown and discharge regimes in standard (cm) size chamber with plane parallel electrodes. This research is continuation of previously well-established experimental method, now applied for the gases of interest for applications: fluorocarbons and water vapour. Breakdown properties for these gases were investigated in a wide interval of  $pd$  (pressure x electrode gap) parameter. From recorded discharge emission profiles we were able to point out the most important processes governing the breakdown and low-current regimes and to extract the data of ionization coefficient and secondary electron yield. Apart from measurements of current-voltage characteristics in all gases, time resolved recordings provided information about particle kinetics during formation of different discharge regimes.

Another direction of investigation was aiming to explore properties of micro-discharges: the discharges with electrode gaps of several hundreds of  $\mu\text{m}$  that operate at pressures up to atmospheric. Diagnostics of these discharges is quite limited due to their very small size. Thus, it is important to find out how much of the existing knowledge about low-pressure discharges can be applied to their micro counterparts. Scaling laws can give that answer providing that they are valid for small gaps. Hence, results of breakdown and current-voltage characteristics obtained from parallel plate micro discharge chamber are interpreted in the sense of investigation of validity of scaling laws. Special attention was given to precise determination of scaling parameters from obtained experimental results. Moreover, measurements were performed also with complex geometry electrodes. In this case, analysis of results is more complicated due to the effects induced by electrode geometry, but these electrode configurations are more suitable for applications.

## **SECTION 3.**

### **Low Temperature Plasmas**

- 3.1 Plasma Spectroscopy and other Diagnostic Methods
- 3.2 Gas Discharges
- 3.3 Plasma Applications and Devices

### **CONTRIBUTED PAPERS**



## CALCULATION OF RADIATION TRANSFER IN SF<sub>6</sub> ARC PLASMAS USING THE P1- APPROXIMATION

M. Bartlova, V. Aubrecht, N. Bogatyreva

<sup>1</sup>Addresses: Faculty of Electrical Engineering and Communication, Brno  
University of Technology, Technicka 10, 616 00 Brno, Czech Republic

**Abstract.** The objective of this paper consists of approximate calculations of radiative heat transfer in SF<sub>6</sub> arc plasmas at the plasma temperatures in the range of 1000 – 35 000 K and pressures from 0.5 to 5 MPa. As a mathematical tool for the radiation field prediction, the P1-approximation was used. To simplify the calculations, the frequency dependence of absorption coefficients has been handled by means of Planck and Rosseland averaging methods. Calculations have been performed for cylindrical plasma of various radii (0.01 – 10) cm with given temperature profile. Contribution to the net emission of different spectral regions is discussed.

### 1. INTRODUCTION

The electric (switching) arc is responsible for proper disconnecting of a circuit in high power circuit breakers. In the mid and high voltage region, SF<sub>6</sub> self-blast circuit breakers are widely used. Radiative heat transfer influences very much the physical processes occurring in the arc plasmas. Detailed information about the local arc structure can only be given by mathematical models

Several approximate methods of accounting for radiative transfer in the arc plasma have been developed (method of net emission coefficient [1-3], method of partial characteristics [4, 5], etc.). In this paper, attention has been given to the P1-approximation [6], which consists of expanding radiative intensity in spherical harmonics and including only the first order terms. Under this assumption the equation of radiative transfer leads to one simple elliptic equation for the density of radiation  $U_\nu$

$$\operatorname{div} \left[ -\frac{c}{3\kappa_\nu} \operatorname{grad} U_\nu \right] + \kappa_\nu c U_\nu = 4\pi B_\nu \kappa_\nu \quad (1)$$

where  $\kappa_\nu$  are the spectral absorption coefficients,  $c$  is the speed of light, and  $B_\nu$  is the Planck equilibrium radiation. The reason for using the P1-approximation is the computational efficiency. Solving equation (1) we can find the spectral radiation flux

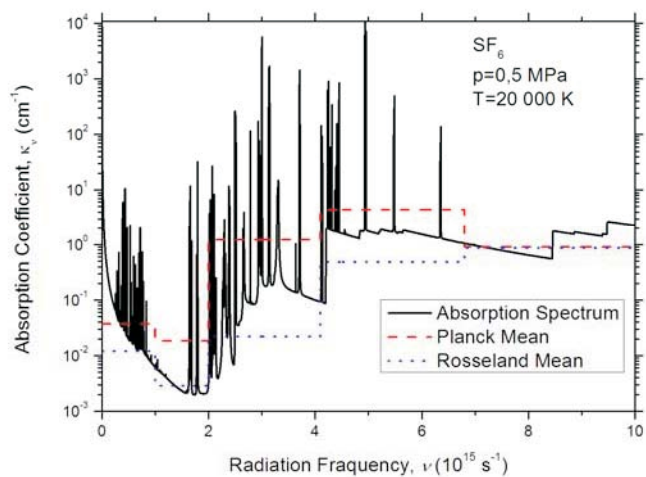


**Figure 1.** The real absorption spectrum compared with Planck and Rosseland means for  $T = 20\,000\text{ K}$  and  $p = 0.5\text{ MPa}$ .

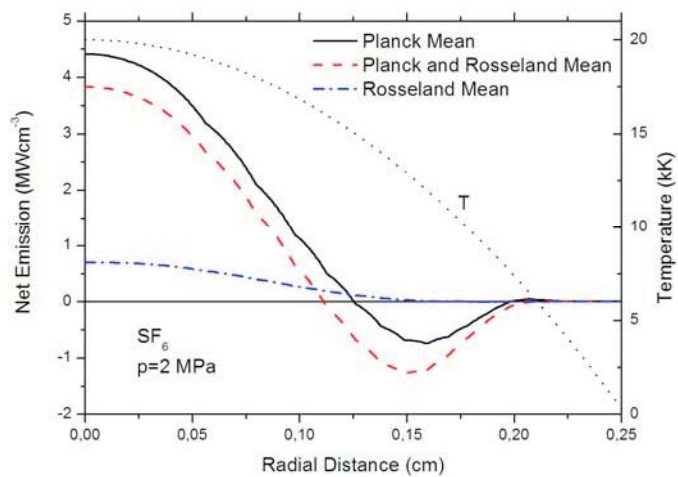


**Figure 2.** Net emission in P1-approximation for various spectral averaging.

$$\vec{F}_\nu = -\frac{c}{3\kappa_\nu} \text{grad}U_\nu, \quad (2)$$

and the spectral divergence of radiation flux – the net emission from an infinitesimal gas volume. Integrating over frequency the total radiation flux and total net emission are obtained.

## 2. MEAN ABSORPTION COEFFICIENTS

One of the methods for simplifying the calculation is the multigroup approximation [7]. The frequency spectrum is cutted in several groups in which the absorption coefficient is supposed to be constant with certain average value. The mean values of absorption coefficients are generally taken as either Rosseland ( $\kappa_R$ ) or Planck ( $\kappa_P$ ) means:

$$\kappa_R^{-1} = \int_{\nu_k}^{\nu_{k+1}} \kappa_\nu^{-1} \frac{dB_\nu}{dT} d\nu \bigg/ \int_{\nu_k}^{\nu_{k+1}} \frac{dB_\nu}{dT} d\nu; \quad \kappa_P = \int_{\nu_k}^{\nu_{k+1}} \kappa_\nu B_\nu d\nu \bigg/ \int_{\nu_k}^{\nu_{k+1}} B_\nu d\nu \quad (3)$$

## 3. RESULTS

We have calculated radiation characteristics of SF<sub>6</sub> cylindrical plasma for pressures from 0.5 to 5 MPa. In calculation of absorption spectrum, contribution of SF<sub>6</sub> molecules, S, F neutral atoms, and S<sup>+</sup>, S<sup>+2</sup>, S<sup>+3</sup>, F<sup>+</sup>, F<sup>+2</sup> ions were taken into account. The frequency interval (10<sup>12</sup> – 10<sup>16</sup>) s<sup>-1</sup> was splitted in five groups with following cutting frequencies (in units 10<sup>15</sup> s<sup>-1</sup>):

$$\nu_k = \{0.001, 1, 2, 4.1, 6.8, 10\}$$

Planck and Rosseland means were calculated for temperatures (1000 – 30 000) K. Planck and Rosseland means for temperature 20 000 K and pressure 0.5 MPa are shown in Fig. 1. It can be seen that Rosseland means neglect the contribution from the absorption peaks; on the other hand, Planck means overestimate the absorption.

P1-approximation was used for calculation of radiation characteristics using Planck means, Rosseland means, and also their combination. Parabolic temperature profile was assumed. Fig. 2 shows results of the net emission for different averaging methods for plasma cylinder at the pressure of 2 MPa and with the radius of 0.25 cm. Rosseland averaging gives very low values of emission of radiation in hot parts of the plasma, and also neglects the absorption of radiation in cold edge of the plasma cylinder (the negative values of the net emission). The contribution of individual frequency groups to the total net emission is presented in Fig. 3. The plasma pressure is of 0.5 MPa and radius of 0.25 cm. It can be clearly noted the domination role of the UV radiation in interval 75 – 150 nm, i.e. 2x10<sup>15</sup> – 4.1x10<sup>15</sup> s<sup>-1</sup>.

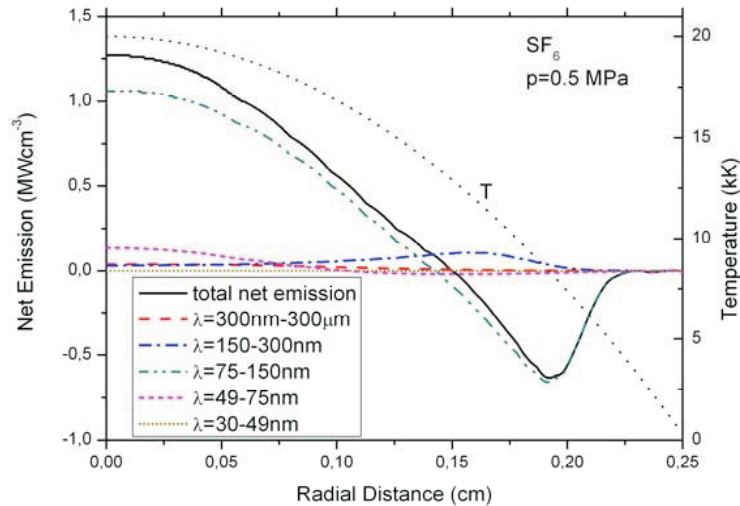


**Figure 3.** Contribution of individual frequency groups to the total net emission.

#### 4. CONCLUSION

Comparison of the net emission in  $\text{SF}_6$  plasma predicted using P1-approximation and various averaging methods have been performed. Rosseland means underestimate both emission and absorption of radiation. We have also performed analysis of radiation in various spectral regions. The dominant role of UV radiation in interval 75 – 150 nm has been shown.

#### Acknowledgements

This work has been supported by Czech Science Foundation under project No. GD102/09/H074 and by European Regional Development Fund under projects Nos. CZ.1.05/2.1.00/01.0014 and CZ.1.07/2.3.00/09.0214.

#### REFERENCES

- [1] J. J. Lowke, JQSRT 14, 111 (1974).
- [2] A. Gleizes et al, J. Phys. D: Appl. Phys. 24, 1300 (1991).
- [3] V. Aubrecht, M. Bartlova, Plasma Chem Plasma Process 29, 131 (2009).
- [4] V. Aubrecht, J. Lowke, J. Phys. D: Appl. Phys. 27, 2066 (1994).
- [5] G. Raynal, A. Gleizes, Plasma Sources Sci. Technol. 4, 152 (1995).
- [6] H. Nordborg, A. A. Iordanidis, J. Phys. D: Appl. Phys. 41, 135205 (2008)
- [7] C. G. Pomraning, *The Equation of radiation Hydrodynamics*, p. 399, (New York: Dover Publications, 1973).

## TRANSITION PROBABILITIES MEASUREMENTS OF SEVERAL XE II LINES

M. T. Belmonte<sup>1</sup>, J. A. Aparicio<sup>1</sup>, R. J. Peláez<sup>2</sup>, S. Djurović<sup>3</sup> and S. Mar<sup>1</sup>

<sup>1</sup> *Departamento de Física Teórica Atómica y Óptica, Universidad de Valladolid,  
P. Prado de la Magdalena s/n, 47071 Valladolid, Spain*

<sup>2</sup> *Laser processing Group, Instituto de Óptica, CSIC, C/ Serrano 121, 28006  
Madrid, Spain*

<sup>3</sup> *Faculty of Sciences, Department of Physics, Trg Dositeja Obradovića 4, 21000  
Novi Sad, Serbia.*

**Abstract.** Several spectral lines of Xe II have been measured in this work, which has permitted to get a set of new values for the transition probability of this element. Spectral lines were emitted by a pulsed plasma whose temperature goes between 15000 and 24000 K.

### 1. INTRODUCTION

Knowledge of atomic parameters, for example transition probabilities, have a great importance not only in the theoretical sphere, but also in the diagnostics of every source emitting radiation, such as conventional lamps, lasers, industrial plasmas, fusion science or Astrophysics.

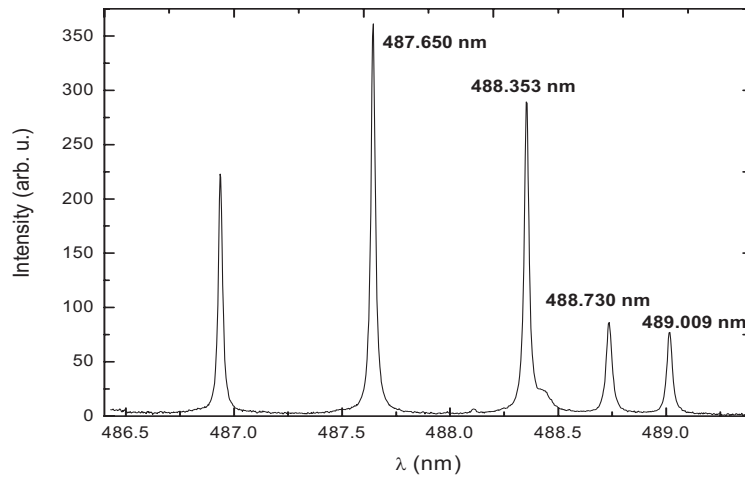
Nowadays, plasma diagnostics in fusion apparatus, such as the ITER project, is the most important application of transition probabilities. In a very hot plasma, as it happens in thermonuclear fusion research, impurities of heavy ions radiate a huge quantity of energy, cooling the plasma. Accurate transition probabilities data are necessary to analyse and model these problems related to the loss of energy. In Astrophysics, determination of the abundance of various elements in stars is the main application of transition probabilities, being these data especially useful in the interpretation of spectral emission lines for ionized species.

However, these necessities are not covered by the available data. In this work, a number of XeII spectral lines between 200-600 nm have been measured, getting new transition probabilities of this element. The method used is based on the measurement of relative intensities of spectral lines emitted by a pulsed discharge lamp, where a plasma of Xenon is generated. The plasma temperature is determined by using the Boltzmann-plot technique. The absolute values of the new transition probabilities are obtained from 7 XeII spectral lines whose  $A_{ki}$  are well established in the literature. Table 1 shows, for the 7 reference lines, the  $A_{ki}$  value taken as reference, the mean value calculated in this work and its standard deviation  $\sigma$ .

**Table 1.** Transitions used as a reference. Calculated transition probabilities are denoted with  $A_{ki}$ [TW].

$\lambda$ (nm)	$g_k$	$E_k$ (eV)	$A_{ki}$ Ref.	Ref.	$A_{ki}$ [TW] ( $s^{-1} 10^{-8}$ )	$\sigma$ ( $s^{-1} 10^{-8}$ )
458.548	8	16.80	0.62	[1]	0.67	0.09
459.205	6	17.78	0.88	[1]	0.80	0.08
460.300	4	14.48	0.82	[2]	0.67	0.07
487.650	8	16.12	0.63	[2]	0.64	0.07
488.353	4	15.08	0.67	[1]	0.67	0.07
488.730	4	15.28	0.27	[1]	0.30	0.03
489.009	6	15.07	0.09	[1]	0.09	0.01

The experimental arrangement and the experimental data treatment are explained in detail in previous work [1, 3-5]. The mixture of helium (59.46%) and xenon (40.54%) at a pressure of 180 Pa continuously flowed through the discharge lamp. Under these conditions, plasma emission lasted for about 200  $\mu$ s. Thousands of spectra have been recorded and processed, several of them for every line during the life of the plasma. The recorded spectra were fitted to sums of symmetrical Lorentzian functions which represent spectral profiles. An example of a part of XeII spectrum and its fit is shown in Fig.1. Wavelengths were taken from reference [6]

**Figure 1.** Example of a part of XeII experimental spectrum and its fit.

The Fig.2 shows a Boltzmann-plot obtained with the set of 7 XeII reference lines for two different moments in the life of the plasma.

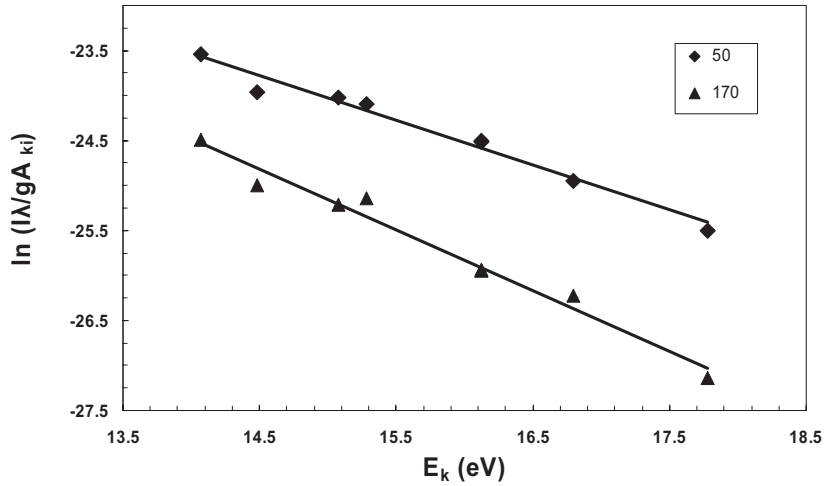


Figure 2. Boltzmann-plot obtained for 50 and 170  $\mu\text{s}$

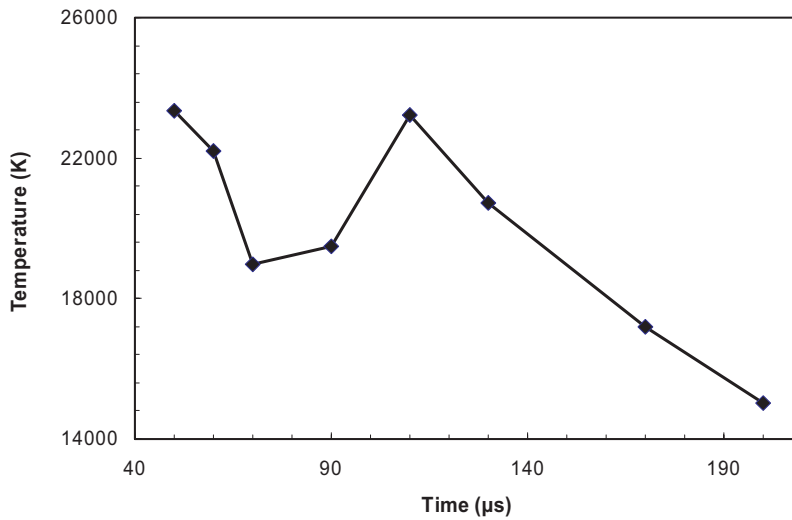
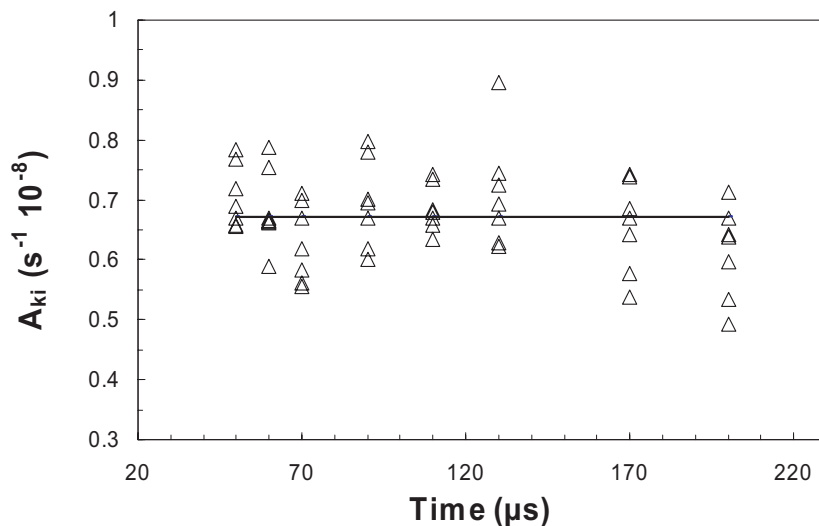


Figure 3. Temporal evolution of the electron temperature.

Once the plasma temperature is known, a mean value of  $A_{ki}$  can be calculated. Fig.4 shows  $A_{ki}$  values for 488.353 nm XeII line through the different moments of measurement. The main value is also represented with the horizontal line. The uncertainty in the  $A_{ki}$  of every line depends on many different factors (intensity of the line, quality of processing, uncertainty in the calculation of temperature, standard deviations...). However, an estimation of the uncertainties can be made, normally being under 20% in this type of measurement.



**Fig. 4.** Example of XeII 488.353 nm line transition probabilities calculated with all the reference lines

Full results will be presented at the conference and will be published shortly.

### Acknowledgements

Authors thank S. González for his work in the experimental device. S. Djurovic thanks to the Ministry of Science of the Republic of Serbia for the support (Project 171014).

### REFERENCES

- [1] M. A. Gigosos, S. Mar, C. Pérez and I. de la Rosa, Phys. Rev. E 49, 1575 (1994)
- [2] J. R. Fuhr and W. L. Wiese, CRC Handbook of Chemistry and Physics, NIST atomic transition probability tables, 79th Edition, 10-88-10-146. CRC Press, Boca Raton, FL (1998)
- [3] J.A Aparicio, M. A. Gigosos and S. Mar, J. Phys. B, 30, 3141 (1997)
- [4] J. A. del Val, S. Mar, M. A. Gigosos, M. I. de la Rosa, C. Pérez and V. R. González, Jpn J. Appl. Phys. 37, 4177 (1998)
- [5] S. Djurović, R. J. Peláez, M. Ćirisan, J. A. Aparicio and S. Mar, J. Phys. B 39, 2901 (2006)
- [6] NIST Atomic spectra database, <http://physics.nist.gov/asd>

# EFFECTS OF THE SECONDARY ELECTRON EMISSION INDUCED BY ARGON IONS AND FAST NEUTRALS

Aleksandar Bojarov<sup>1</sup>, Marija Radmilović-Radjenović<sup>1</sup> and Zoran Lj. Petrović<sup>1</sup>

<sup>1</sup>*Institute of Physics, 11080 Belgrade, Serbia*

**Abstract.** Secondary electron emission from electrode surfaces is examined, regarding a capacitively coupled plasma reactor (CCP) with external circuit. The presented results are obtained using an implicit "Particle in cell" (PIC) 1D code, with Monte Carlo treatment of collisions. The secondary electron emission coefficient on the electrodes is modeled by expressions proposed by Phelps and Petrović for argon (Ar) neutrals and ions, obtained from a large set of experimental data, concerning the energy of impacting ions and fast atoms and surface type atomically "clean" or "dirty".

## 1. INTRODUCTION

The implicit field solver supports a complete model of an external passive circuit on both of the electrodes[1-4]. The reactor is symmetrical, powered by two sources. One source is used to sustain the discharge (13.56MHz at 300 V peak to peak) and the other source (2.712 MHz at 1000 V peak to peak) is connected on the opposite electrode and has a bias of -400 V. This source configuration, often named dual-frequency discharge, is used as a way to independently control the energy distribution and flux of impacting ions[5]. The electrode separation is 2.54cm with electrode diameter of 10.16cm. The secondary electron emission depends on the characteristics of the surface material and on the energy of the impacting particles, in plasma modeling the coefficient  $\gamma$  is often taken as a constant, thus producing disagreements between experiment and theory [6,7]. In this paper the  $\gamma$  coefficient is modeled by formulas that depend on the ion energy  $\epsilon_i$  and neutral energy  $\epsilon_n$ . These analytic formulas have been suggested by Phelps and Petrović[8]:

$$\gamma_{i,\text{clean}} = 0.07 + 10^{-5} \frac{(\epsilon_i - 500)^{1.2}}{1 + (\epsilon_i/70000)^{0.7}}, \quad (1)$$

$$\gamma_{i,\text{dirty}} = \frac{0.002\epsilon_i}{1 + (\epsilon_i/30)^{1.5}} + 1.05 \cdot 10^{-4} \frac{(\epsilon_i - 80.0)^{1.2}}{(1 + (\epsilon_i/8000))^{1.5}}, \quad (2)$$

$$\gamma_{n,\text{clean}} = 10^{-5} \frac{(\epsilon_n - 500)^{1.2}}{1 + (\epsilon_n/70000)^{0.7}}, \quad (3)$$

$$\gamma_{n,\text{dirty}} = 7 \cdot 10^{-5} \frac{(\epsilon_n - 32)^{1.2}}{1 + (\epsilon_n/2800)^{1.5}} + 10^{-4} \frac{(\epsilon_n - 90)^{1.2}}{1 + (E/8000)^{1.5}}. \quad (4)$$

According to the above relations, there are two surface conditions: treated (atomically clean) surface and untreated (atomically dirty) surface. Second terms in equations (1), (2) and (4) are zero below 500 eV, 80 eV and 90 eV respectively, also  $\gamma_{n,\text{clean}}$  and  $\gamma_{n,\text{dirty}}$  are zero below 500 eV and 32 eV respectively. We denote fast argon atoms as argon neutrals to make a distinction from the background argon atoms, as we only observe fast atoms above energy of 32 eV. We have used cross sections for Ar-Ar collisions from [9]. Neutrals are allowed to escape the discharge if the lateral distance is greater than the electrode radius. We have made simulations for parallel plate Ar dual frequency discharge at 50 mTorr. We have used analytical formulas for secondary emission under conditions where secondaries are important.

## 2. DENSITY OF PARTICLES

Production of fast neutrals is by collisions with particles with similar masses as the gas particles. Considering that the ions drift through the sheath, from the bulk plasma to the electrodes, they gain kinetic energy that is transferred to the background gas. The discharge has an electrode that is biased by -400 V with a large sheath and voltage drop, where a larger production of neutrals is expected, Figure 1.

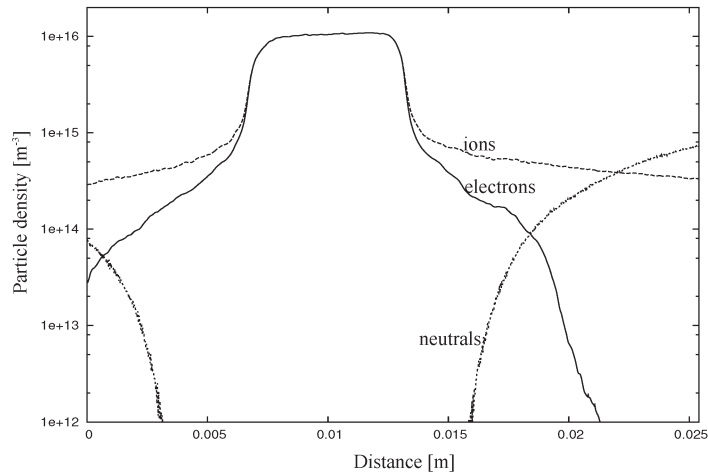


**Figure 1.** Ion, electron and fast neutrals densities in the discharge between powered ( $z=0$  m) and biased ( $z=0.0254$  m) electrode

### 3. ENERGY DISTRIBUTIONS ON ELECTRODES

For a dirty surface condition, the ion and neutrals energy distribution on the electrodes is presented in Figure 2. The powered electrode shows lower production of neutrals, which is also the reason for the peak at 80 eV, which corresponds to ions that traverse the sheath without collision. From the bulk to the biased electrode ions transfer momentum to background gas at such a rate that at the electrode there are more fast neutrals than ions. Traversing the sheath to the biased electrode, ions collide multiple times with neutrals and due to more effective momentum transfer it results in greater production of fast neutrals.

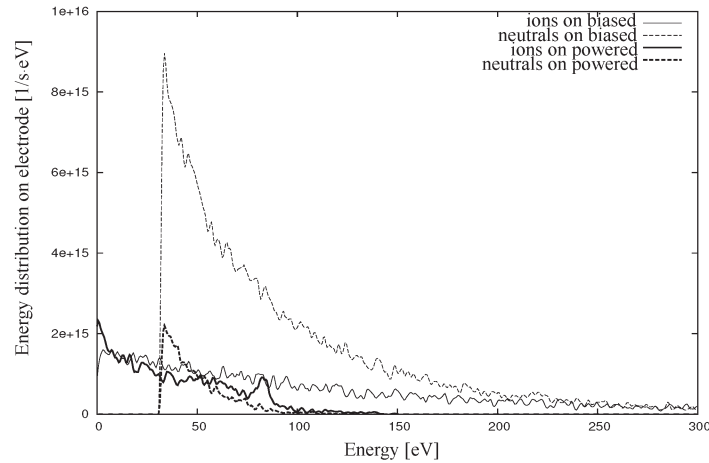


**Figure 2.** Ion and neutrals energy distribution on the biased and powered electrode, presented as a number of particles hitting the electrode normalized in time and energy.

### 4. SECONDARY ELECTRON EMISSION

We have chosen regime where the discharge is strongly affected by the secondary emission[10]. Secondary emission of electrons from electrodes can be a governing process for sustaining the discharge. In this section we chose four different situations often encountered in simulations. In Figure 3 it is shown that for constant secondary emission (0.07 or 0) the discharge cannot be sustained. On the other hand, for the same external voltage, secondary emission for dirty and clean electrodes balances itself leading to sustainable discharge.

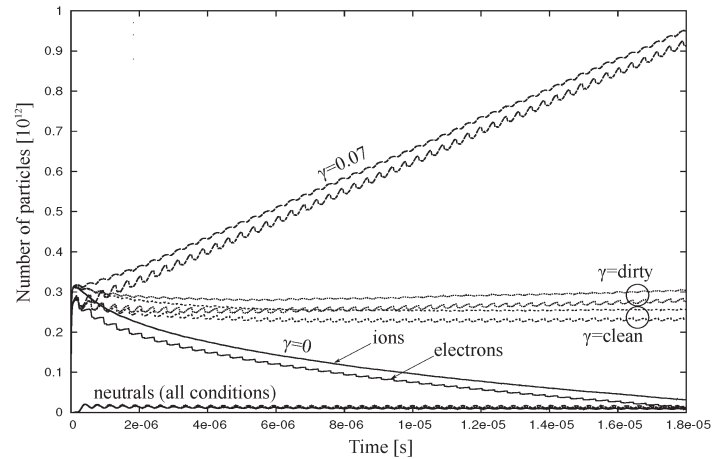


**Figure 3.** Number of particles in the discharge for four different types of secondary emission.

## REFERENCES

- [1] J. P. Verboncoeur, *Plasma Phys. Control. Fusion* A231, 47 (2005).
- [2] C. K. Birdsall and A. B. Langdon, *Plasma Physics via Computer Simulation* (New York: McGraw-Hill, 1985).
- [3] V. Vahedi and G. DiPeso, *J. Comput. Phys.* 131, 149-63 (1997).
- [4] H. Wang et al., *Plasma Sources Sci. Technol.* 19, 045023 (2010).
- [5] T. Makabe and Z. Lj. Petrovic, *Plasma Electronics: Applications in Microelectronic Device Fabrication* (New York: Taylor and Francis, 2006).
- [6] M. Soji and M. Sato, *J. Phys. D: Appl. Phys.* 32, 1640 (1999).
- [7] H. B. Smith et al., *Phys. Plasmas*. 10, 875 (2003).
- [8] A. V. Phelps and Z. Lj. Petrovic, *Plasma Sources Sci. Technol* 8, R21 (1999).
- [9] A. V. Phelps, <http://jila.colorado.edu/~avp> (2001).
- [10] M. Radmilovic-Radjenovic and Z. Lj. Petrovic, *Europ. J. Phys. D* 54, 445 (2009).

## STUDY OF THE OPTICAL THICKNESS OF LASER-INDUCED PLASMA FOR IMPROVED CALIBRATION-FREE LIBS ANALYSIS

M. Cirisan<sup>1</sup>, M. Cvejic<sup>2</sup>, J. Hermann<sup>1</sup>, S. Jovicevic<sup>2</sup> and N. Konjevic<sup>3</sup>

<sup>1</sup> *LP3, CNRS – Université Aix-Marseille, Marseille, France*

<sup>2</sup> *Institute of Physics, University of Belgrade, Belgrade, Serbia*

<sup>3</sup> *Faculty of Physics, University of Belgrade, Belgrade, Serbia*

**Abstract.** In order to improve the precision of calibration-free laser-induced breakdown spectroscopy measurements, the existing database of Stark parameters needs to be significantly expanded. In this work, we have evaluated the optical thickness of laser-induced plasma for several Al II lines to be used for laser plasma diagnostics.

### 1. INTRODUCTION

Laser-induced breakdown spectroscopy (LIBS) is an emerging technique for elemental analysis of materials. It is a promising “tool” for applications in many areas, such as quality control in industrial production, material recycling, environmental survey, interplanetary exploration etc. Even though the LIBS ability of performing precise analysis has been demonstrated for a significant number of materials, quantitative measurements are still difficult in many cases. The low precision is mainly due to the difficulty of calibrating LIBS measurements.

In order to overcome this difficulty, calibration-free LIBS procedures have been developed. We have proposed a method for quantitative LIBS analysis based on comparing the measured intensities of atomic spectral lines to the spectral radiance of plasma, that is generally supposed to be in local thermodynamic equilibrium [1]. The absorption coefficient  $\alpha(\lambda)$ , used for the calculation of plasma spectral radiance, takes into account the dominant spectral line broadening mechanisms. In order to achieve high precision of calibration-free LIBS measurements, a large database of Stark parameters needs to be available. The amount of Stark parameters data existing in the literature is very limited and they are often imprecise.

By employing optical emission spectroscopy to laser induced plasma one may measure Stark parameters of the spectral lines of any element present in

the irradiated sample. Still, laser-induced plasma is in most cases very dense, and for a number of spectral lines the plasma is optically thick. Self-absorption may lead to distortion of the spectral line profile, thus producing an apparently large line halfwidth and introducing a large error in the measured value of the Stark halfwidth coefficient [2]. This is why analyzed spectral line needs to be checked on self-absorption, before proceeding to intensity and Stark halfwidth measurement.

In this work, we have employed the method of duplicating the optical path through the plasma with a spherical mirror [2] in order to check the optical thickness of laser-induced plasma for several spectral lines and find the optimal conditions for Stark parameters measurements.

## 2. EXPERIMENT

A schematic representation of the experimental set-up is given in figure 1. Laser ablation of an Al alloy (92.5% Al, 7% SiO<sub>2</sub>, 0.45% Mg) was performed using an Nd:YAG laser (266 nm wavelength, 5 ns pulse duration, 10 Hz frequency, 10 J/cm<sup>2</sup> fluency) in Ar at a pressure of 50 mbar.

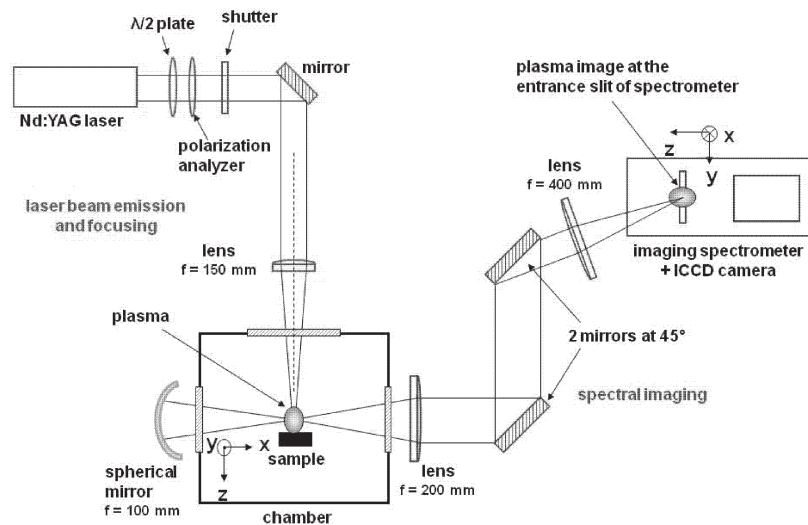


Figure 1. Experimental set-up.

The plasma plume was imaged to the entrance slit of the imaging spectrometer, coupled to an ICCD camera (Fig. 1). Spectroscopic observations of the plasma plume were performed perpendicularly to the laser beam axis, by selecting a plasma layer of  $50 \mu\text{m}$  thickness at  $0.4$  mm distance from the sample surface. A spherical mirror was mounted along the observation axis at 2 focal distances behind the plasma in order to project the image of the plasma plume on itself.

### 3. RESULTS AND CONCLUSIONS

In this study, optical thickness of several Al II lines has been studied. Spectra of the analyzed Al lines have been recorded with and without the spherical mirror. An example is given in Fig. 2. Plasma transmission coefficient has been calculated using the expression:

$$T = R^{-1} \left( \frac{B_{\lambda}^M}{B_{\lambda}} - 1 \right) = \exp(-\tau) \quad (1)$$

where  $B_{\lambda}^M$  and  $B_{\lambda}$  represent plasma spectral radiances recorded with and without the mirror, respectively; while  $R$  is a factor that takes into account mirror reflectivity, losses on chamber windows and geometrical effects.  $R$  factor was determined from the corresponding continuum radiation recorded with and without the mirror.  $\tau$  is the optical thickness.

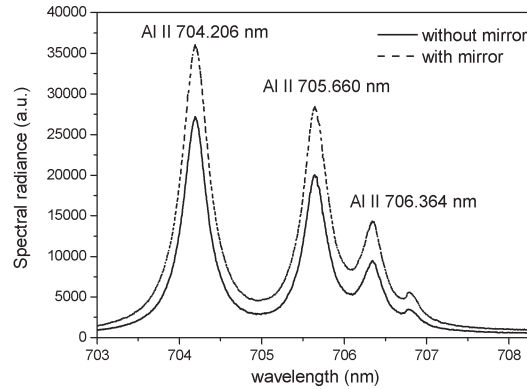


**Figure 2.** Spectra of three Al II lines recorded with and without the mirror.

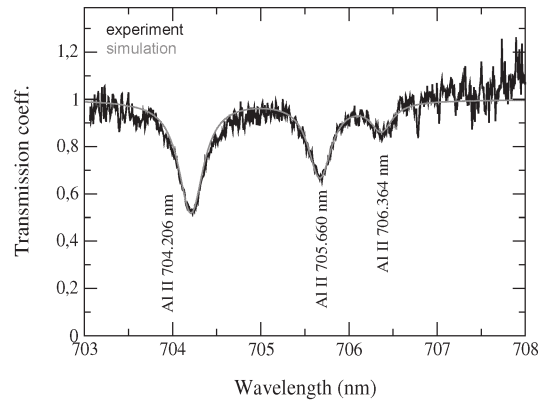


**Figure 3.** Transmission coefficient: experimental and simulated spectra.

Applying calibration-free LIBS procedure to the obtained transmission coefficient spectrum of Al II lines (Fig. 3) enabled us to estimate the plasma

parameters ( $N_e = 3.5 \cdot 10^{17} \text{ cm}^{-3}$ ,  $T = 1.8 \cdot 10^4 \text{ K}$ ) and calculate the plasma optical thickness for the observed lines.

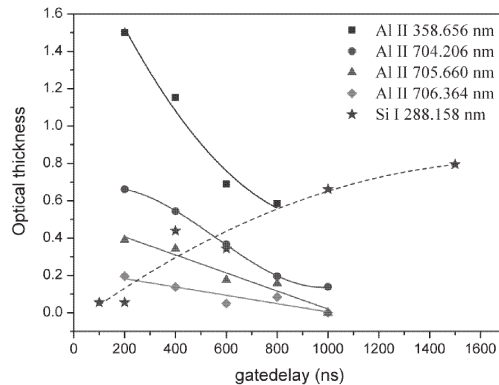


**Figure 4.** Temporal evolution of the optical thickness.

The temporal evolution of the self-absorption effect in laser-induced plasma was studied by measuring the optical thickness for several Al II lines and one Si I line at different gatedelays of the plasma life (Fig. 4). In case of ionic spectral lines, optical thickness decreases with time, indicating a reduction of the self-absorption effect. On the other hand, self-absorption of Si I line becomes more pronounced with time. Temperature of laser-induced plasma decreases with time, leading to a depopulation of higher energy levels and ions recombination, thus decreasing the number of ions and increasing the number of atoms present in the plasma. Due to this, self-absorption of ionic lines decreases, while the self-absorption of neutral spectral lines increases with time.

In conclusion, optimal conditions for Stark parameters measurements in laser-induced plasmas are different for neutral and ionic spectral lines. An early gatedelay is favourable for neutral lines, since there is no or very low self-absorption, and lines are strongly broadened. On the other hand, ionic lines are strongly self-absorbed at early gatedelays, while at later gatedelays the lines become very narrow due to electron density decrease. So, in order to find optimal conditions for Stark parameters measurements of ionic lines one should use a sample containing a low percentage of the analyzed element, in order to reduce the self-absorption effect, and then choose an early gatedelay.

### Acknowledgements

This work is partly supported by Serbian Ministry of Education and Science under the project NO 171014.

### REFERENCES

- [1] J. Hermann, Patent WO 2010/052380 (A1).
- [2] N. Konjevic, Phys. Rep. 316, 339 (1999).

## PROCEDURE FOR PROCESSING SPECTRAL IMAGES AND SELFABSORPTION CORRECTION

M. Cvejić, M. Gavrilović and S. Jovićević

*Institute of Physics, University of Belgrade, P.O. Box 68, 11080, Belgrade, Serbia*

**Abstract.** Here we present a program developed in Matlab® for processing spectral images taken with ICCD camera mounted on the exit plane of a spectrometer. The images represent time and space resolved spectral lines originating from the laser induced plasma. Main steps of this procedure include image cropping along its dimensions, intensity correction, symmetrisation, smoothing, self absorption correction and Abel inversion of image. These steps will be described using Li I 460.3 nm spectral line. The procedure described here, in general, can be applied to any spectral line image from different cylindrical plasma sources when checking and correction for self absorption is needed.

### 1. INTRODUCTION

Laser induced breakdown spectroscopy (LIBS) has attracted a lot of attention in recent years due to its unique properties, see e.g. ref. 1. Determination of plasma parameters, in first place electron temperature,  $T_e$ , and electron density,  $N_e$ , is important for application of LIBS. To determine correctly plasma parameters, one should consider optical thickness of laser induced plasma (LIP) and determine whether spectral lines of interest are self absorbed. This is essential for both, the analytical applications and for diagnostic purposes. Experimental setup based on duplicating optical path length of plasma emission by placing a spherical mirror behind plasma in order to check self absorption (SA) and to perform correction is described in [2]. When self absorption is low enough, the line profile can be corrected according to formula (31) in Ref. 2.

The LIBS experimental setup for time and space resolved spectral measurements and SA correction was installed in our laboratory. In our experiment we used focusing lens and flat mirror instead spherical mirror, in order to estimate SA. To process experimental data efficiently, Matlab program was developed in our laboratory. The novelty of this program is related to SA correction on experimental data.

## 2. PROCEDURE

Matlab is chosen for processing experimental data, for several main reasons: *i.* the inherent property of all numerical data are in the matrix form; *ii.* large collection of specialized functions that are applicable to matrix form of numerical data is available; *iii.* the surrounding for developing customizable windows as graphical interfaces.

Spectral recordings (experimental data) are images (matrices) from ICCD camera (1024 x 256 pixels) placed on the exit slit of the spectrometer. The first column in matrix (image) represents wavelengths, the first row lateral positions, and other fields of the matrix are intensities. The program in Matlab along with graphical user interface (GUI), is shown on fig. 1, and will be described in next paragraphs. GUI consists of several sections, which are visually separated.

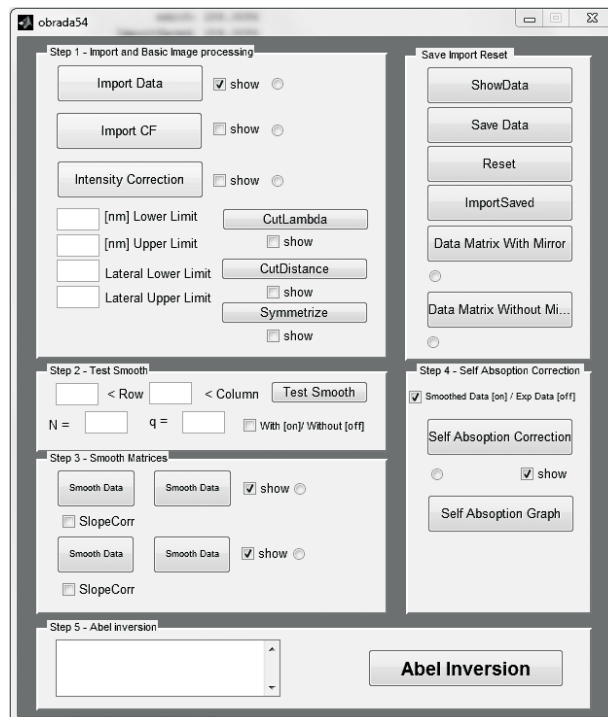


**Figure 1.** Appearance of the main window

In the first section, called “Basic Image Processing”, experimental data matrix are imported along with correction factor. After intensity correction, image should be cropped. That is done by specifying cropping limits (along lambda axis and also along lateral axis –see fig 2a.). Next step in this section is

symmetrisation (this step is optional). Symmetrisation is important for applying Abel inversion. Image matrix after symmetrisation is shown in fig. 2b.

The section, entitled “Save Import Reset” deals with common functions such as saving processed data, importing processed data and resetting the program.

In the next section, called “Step 2 – Test smooth”, user can define filter for smoothing matrix data. The smoothing is important as a noise removal tool and as a step for preparation of image matrices for self absorption correction. Smoothing filter is based on “Savitzky – Golay filter”, see ref. 3. By inputting number of column and row of image matrix, and by specifying filter parameters, with the press of “Test Smooth” button, new windows will show to the user: the line profile at given column number along with its smoothed profile and also the lateral profile for required row number along with its smoothed profile.

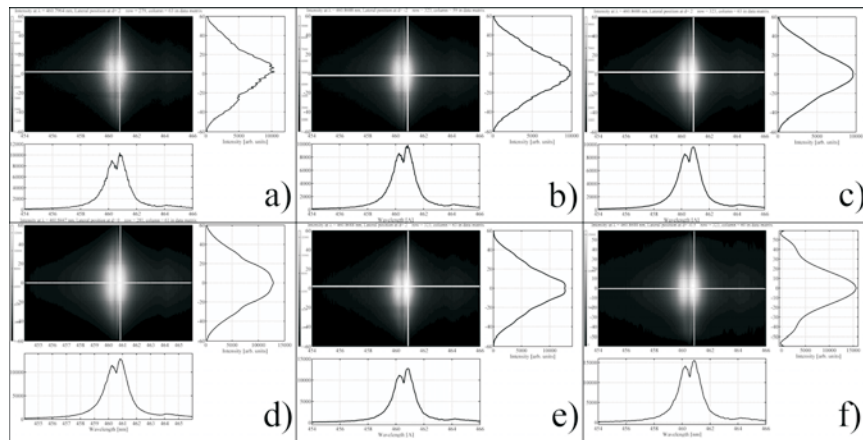


**Figure 2.** a) Data recorded without back mirror after crop, b) Data recorded without back mirror after symmetrisation, c) data recorded without back mirror after smoothing, d) data matrix recorded with back mirror after crop, symmetrisation and smoothing, e) data matrix after SA correction (see figure 3.) f) data matrix after Abel inversion.

In section, “Step 3 – Smooth Matrices”, see Fig. 1, matrices (recorded without back mirror and with a back mirror) are smoothed with defined filter first along lateral and then optionally along wavelength direction. If check boxes are on, smoothed matrices will be shown in new windows – see fig. 3c, d.

The most important section is called “Self-Absorption Correction”. Theoretical background is given in ref. 2 and 4. Input parameters for this procedure are ratios of continuum recorded without and with back mirror and ratios of recorded line profiles without and with back mirror. Novelty in this procedure is that it calculates ratios for every lateral position individually, and then determines the correction factor at each lateral position (in this case for every matrix column separately). Example of self absorption correction for a

line profile starting from the center of plasma (center of matrix) is given in fig. 3a. The lateral profiles at line maximum (460.3 nm) for matrices recorded without and with back mirror, and the profile of SA corrected matrix are shown in Fig. 3b.

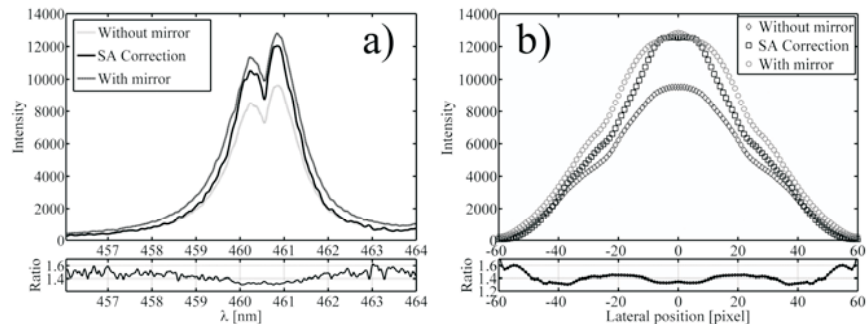


**Figure 3.** a) Line profiles of Li I 460.3 nm spectral line from plasma center (center of data matrix) recorded without back mirror, with back mirror, and SA corrected profile; b) Lateral profiles of the same line at the maximum intensity ( $\lambda = 460.3$  nm) with the lateral profile corrected for SA.

The procedure of Abel inversion, as a last section, is performed by using Jacobi polynomials (see ref. 5). In this section, one of the processed matrices in the list box can be selected, and then by pressing the “Abel inversion” button a new window appears. The input parameters for the Abel inversion procedure can be chosen in this window and at the end Abel inverted matrix is shown (see fig. 2f).

In conclusion, the presented procedure is applicable to all experimental data in the matrix form obtained from various kinds of side-on experiments with cylindrical plasmas, where spectra line recordings have to be corrected for SA.

### Acknowledgements

The authors acknowledge discussions with N.Konjevic. This work is supported by Ministry of Education and science under the project NO 171014 .

### REFERENCES

- [1] D. W. Hanh, N. Omenetto, *Appl. Spectroscopy*, 64, 12, 336A (2010)
- [2] N. Konjević, *Phys. Rep.* 316, 339 (1999).
- [3] <http://www.mathworks.com/products/>
- [4] H-Y. Moon, K. K. Herrera, N. Omenetto, B. W. Smith, J.D. Winefordner, *Spectchimica Acta Part B*, 64, 702 (2009).
- [5] S. Djurović, *Journal of Research in Physics*, 28, 2, 153 (1999)

## GENERALIZED LIGHTNING TCS MODEL WITH CURRENT REFLECTIONS

Cvetic J.<sup>1</sup>, Djuric R.<sup>1</sup>, Ponjavic M.<sup>1</sup>, Sumarac D.<sup>1</sup>, Trifkovic Z.<sup>2</sup>

<sup>1</sup>*Faculty of Electrical Engineering Belgrade, Belgrade, Serbia*

<sup>2</sup>*Faculty of Mechanical Engineering, Belgrade, Serbia*

**Abstract.** The generalized travelling current source model (GTCS) is extended to take into account the current reflections occurring at ground and at the upper end of the lightning channel. The ground reflection and the top reflection factors are overtaken from the extended TCS model. The current sources are placed along the activated length of the lightning channel and represented by the channel discharge function introduced earlier in the GTCS model. The multiple reflections originate current waves moving up and down on the lightning channel. The total current is composed by the source current according to the original GTCS model and the reflected currents. The current along the channel can be represented as two sums of the integrals of the current sources along the channel.

### 1. INTRODUCTION

During the return stroke process, the current flows through the lightning channel lowering the leader charge to earth. The lightning return stroke models which belong to “engineering” – models commonly assume the lightning channel as transmission line, where the current reflections are ignored at the terminations. In reality, the channel-base is terminated by the ground impedance and current reflections occur at the transition from the channel in air to ground. Current reflections are also expected at the upper end of the lightning channel acting like the open end of a transmission line. Objective of the paper is to extend the GTCS model in order to take into account these current reflections.

### 2. THE GTCS MODEL WITH CURRENT REFLECTIONS

The case of the GTCS return stroke model [1, 2] is analyzed. The classical TCS model [3] can be derived as a special case of the GTCS model [1]. The GTCS model with the current reflections occurring at the ground and at the upper end of the lightning channel during the return stroke is shown in Figure 1. The ground reflection coefficient is defined as

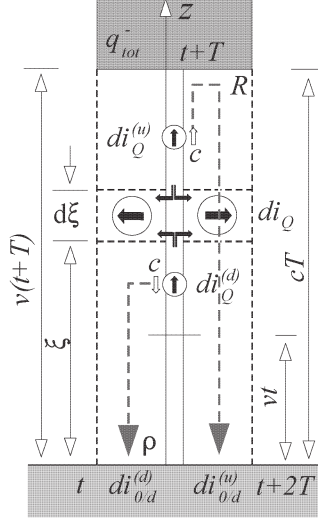


**Figure 1.** The current reflections from the ground and from the upper end of the channel according to the GTCS model

and from the upper end of the channel according to the GTCS model

$$\rho = i_{0/u} / i_{0/d}, \quad (1)$$

where  $i_{0/u}$  is the upward (reflected) and  $i_{0/d}$  is the downward moving current wave at the channel-base having the current reference directions along the  $z$ -axis. The channel top current reflection coefficient is [3]

$$R = -A, \quad A = (c - v)/(c + v), \quad (2)$$

where  $v$  is the return stroke velocity and  $c$  is the speed of the light. Since  $v \leq c$  from Eq.(2) one obtains

$$-1 < R < 0. \quad (3)$$

The values of the ground reflection coefficient is determined by the soil characteristics and it spans the interval  $[-1, 1]$ . For a good grounding system the ground reflections are taken into account with  $\rho > 0$ . In that case both current waves in Eq.(1) have the same direction. The total current at the ground level can be represented as the sum of the downward moving current wave and the upward moving current wave reflected from the ground, that is:

$$i_0 = i_{0/d} + i_{0/u} = (1 + 1/\rho) i_{0/u} = (1 + \rho) i_{0/d}. \quad (4)$$

The current at the ground level can be determined either by knowing downward current or the upward current at the ground level. The GTCS model assumes that the current sources  $di_Q$  are homogeneously distributed over the activated part of the channel. In Figure 1, an infinitesimal current source at some height is depicted. According to the GTCS, the current of the source is given by:

$$di_Q(u) = q_{tot}^-(\xi) \frac{\partial}{\partial u} f(u) d\xi, \quad (5)$$

where  $u = t - z/v$  is the generalized time,  $f(u)$  is the channel discharge function [1, 2], and  $q_{tot}^-$  is the negative leader line charge density deposited along the channel corona sheath prior to the return stroke. Note that  $di_Q > 0$  since the discharge of the negative charged channel is considered. The current pulse generated by the current source splits into two components. The downward moving current source component is

$$di_Q^{(d)} = p di_Q, \quad (6)$$

where  $p \in [0, 1]$  is the current source split factor, Figure 1. It is directed upwards since  $p > 0$  i.e.  $di_Q^{(d)} > 0$ . The upward moving current source component is

$$di_Q^{(u)} = -(1-p) di_Q. \quad (7)$$

If  $p = 1$ , there is no upward moving current component i.e. one obtains the classical TCS model. The first current component  $i_{0/d}^{(d)}$  originates from the downward portion of the injected current pulse  $di_Q^{(d)}$  including all reflections from the ground and later from the upper end of the channel, Figure 1. The second component  $i_{0/d}^{(u)}$  is generated by the upward portion of injected current pulse  $di_Q^{(u)}$  including all reflections from the upper end of the channel and later from the ground. The total downward current at the channel-base is

$$i_{0/d} = i_{0/d}^{(d)} + i_{0/d}^{(u)}. \quad (8)$$

According to (4) the total channel-base current will be

$$i_0 = (1+p)(i_{0/d}^{(d)} + i_{0/d}^{(u)}). \quad (9)$$

### 3. THE TOTAL CURRENT ALONG THE CHANNEL

According to [3] the downward current pulse  $i_{0/d}^{(d)}$  at the channel base generated by the current source component  $di_Q^{(d)}$  is

$$i_{0/d}^{(d)}(t) = p \sum_{\nu=0}^{N \rightarrow \infty} (R\rho)^\nu \int_0^{v^* A^\nu t} q_{tot}^-(\xi) \frac{\partial}{\partial u} f(u) d\xi, \quad u = A^\nu t - \xi / v^*, \quad (10)$$

where the current generator pulse is defined by the initial line charge density (corona charge)  $q_{tot}^-$  along the channel and the channel discharge function  $f(u)$  where  $u \geq 0$  represents the generalized time [2, 3].

$$di_Q(u) = q_{tot}^-(\xi) \frac{\partial}{\partial u} f(u) d\xi, \quad u = t' - \xi / v = t / A - \xi / v^*, \quad u \geq 0. \quad (11)$$

In a similar way it can be shown that the downward current pulse  $i_{0/d}^{(u)}$  at the channel base generated by the current source component  $di_Q^{(u)}$  is

$$i_{0/d}^{(u)}(t) = -(1-p) \sum_{\nu=0}^{N \rightarrow \infty} R^{\nu+1} \rho^\nu \int_0^{v^* A^\nu t} q_{tot}^-(\xi) \frac{\partial}{\partial u} f(u) d\xi, \quad u = A(A^\nu t - \xi / v^*). \quad (12)$$

The total current at the channel-base can be calculated using Eqs.(9), (10) and (12). The current at some altitude in the channel consists of the upward

and the downward moving components,  $i_u(z, t)$  and  $i_d(z, t)$ , respectively. Since  $i_u(z, t) = i_{0,u}(t - z/c)$  and  $i_d(z, t) = i_{0,d}(t + z/c)$ . Using (4) it follows

$$i(z, t) = [\rho i_0(t - z/c) + i_0(t + z/c)] / (1 + \rho), \quad (13)$$

where the channel-base current  $i_0$  is given by Eq.(9).

#### 4. CONCLUSION

The GTCS-model suggests that the lightning current is injected by a current source located along the increasing lightning channel. From there the current wave propagates up to the channel top and down to earth with the speed of light. Based on these assumptions, the GTCS-model is extended to take into account the current reflections at the channel top and the ground. The ground impedance is considered by a ground reflection factor  $\rho$  having a constant value. When the downward moving current wave arrives at ground, it is reflected and then this reflected current wave move up on the return stroke channel. When this upward moving current arrives at the top of the lightning channel, it is totally reflected. Otherwise, the current would be stored as charge in the lightning channel, which seems to be unrealistic. Due to this turn-on process, the top reflection factor  $R$  depends on the return stroke velocity  $v$ . The top reflection factor  $R$  just describes the property of a current wave arriving at the moving open end of a transmission line. Therefore, it is not restricted to the assumptions of the GTCS model and it is possible to use it in different "engineering" models.

#### Acknowledgements

The Ministry of Education and Science of the Republic of Serbia supported this work under contracts ON171007 and TR37019.

#### REFERENCES

- [1] J. Cvetic and B. Stanic, "An improved return stroke model with specified channel-base current and charge distribution along lightning channel", in Proc. Int. Conf. on Electromagnetics in Advanced Applications, Turin, Italy, 1995, 00.109-112.
- [2] J.Cvetic and P.Osmokrovic, "Dynamics of Lightning Discharge During Return Stroke", IEEE Transaction on Plasma Science, Vol.37, Issue 1, 2009.
- [3] F.Heidler, "Review and Extension of the TCS – Model to Consider the Current Reflections at Ground and at the Upper End of the Lightning Channel," Journal of Lightning Res., vol.1, 2007.

## MODIFIED LIGHTNING TRAVELING CURRENT SOURCE RETURN STROKE MODEL

Cvetic J.<sup>1</sup>, Djuric R.<sup>1</sup>, Ponjavic M.<sup>1</sup>, Sumarac D.<sup>1</sup>, Trifkovic Z.<sup>2</sup>

<sup>1</sup>*Faculty of Electrical Engineering Belgrade, Belgrade, Serbia*

<sup>2</sup>*Faculty of Mechanical Engineering, Belgrade, Serbia*

**Abstract.** The classical lightning travelling current source (TCS) return stroke model without current reflections is considered. The TCS model is modified to take into account the current component caused by the transferred line charge density along the channel core below the return stroke wave-front. For the TCS model without current reflections this modification has yielded the final results similar to those of the Bruce-Golde model (BG). In the modified TCS model the distribution of the channel current is uniform i.e. there is no line charge along the core below the return stroke wave-front. Nevertheless, the physical picture of the discharge differs significantly from that of the BG model. For the TCS model with the current reflections from the ground and from the upper end of the lightning channel the modification is more complex. In this case the transferred line charge density along the channel core can be calculated from the equation of continuity.

### 1. THE MODIFICATION OF THE TCS MODEL

Side view of the lightning channel containing channel core and the corona sheath during the return stroke stage is depicted in Fig.1. Transferred line charge density component  $q'_{tr} = \partial q_{tr} / \partial z$  for the TCS model is [1]

$$q'_{tr} = -i_{0TCS}(t + z/c) / c, \quad t \geq 0, \quad z \leq vt. \quad (1)$$

The deposited line charge density component  $Q'_{de} = dQ_{de} / dz$  above the return stroke wave-front for the TCS model is given in [3]

$$Q'_{de} = i_{0TCS}(z/v^*) / v^*, \quad z \leq vt. \quad (2)$$

where  $i_{0TCS}(t)$  is the channel base current in the TCS model. The channel-base current can be expressed by the deposited charge density component if one substitutes  $z = v^* t$  in Eq.(2). It follows

$$i_{0TCS}(t) = v^* Q'_{de}(v^* t). \quad (3)$$

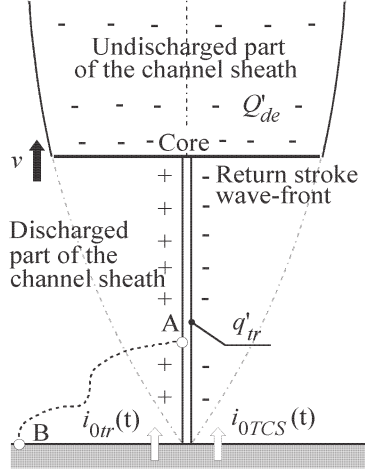


**Figure 1.** Side view of the channel containing the core and the corona sheath during the return stroke stage.

component  $i_{0ir}(t)$  should be generated. This component carries positive charge neutralizing the negative line charge  $q'_{ir}$  adding to the existing channel-base current. Moreover, due to the vicinity of the negative charge in the corona sheath above the return stroke wave-front and the finite conductivity of the channel core, an excess of positive charges along the core should be expected. However, for the purpose of this paper their presence is neglected although there is clear experimental proof of their existence [2].

First, we calculated the total negative transferred charge along the channel (seen from the channel base). It is placed along the entire activated part of the channel i.e. up to the height  $vt$  i.e.

$$q_{ir}|_{z=0} = -\int_0^{vt} i_{0TCs}(t+z/c)/c dz, \quad t \geq 0, \quad z \leq vt. \quad (5)$$

where  $i_{0TCs}$  is the channel-base current in the TCS model. According to the aforesaid assumption, the transition channel-base current component carrying the positive charge will be

$$i_{0ir} = \left. \frac{dq_{ir}}{dt} \right|_{z=0} = \frac{1}{c} \int_0^{vt} (di_{0TCs}(\xi)/dt) dz + (v/c) i_{0TCs}[t(1+v/c)], \quad (6)$$

where  $\xi = t + z/c$ ,  $t \geq z/v$ . Since

$$di_{0TCs}(\xi)/dt = (di_{0TCs}(\xi)/dz)c, \quad (7)$$

The current at some altitude in the TCS model [3] is given by

$$i_{TCS}(z,t) = i_{0TCs}(t+z/c), \quad z \leq vt. \quad (4)$$

If one neglects the rotational electric field component generated by the axial time-variable current then the line charge density  $q'_{ir}$  below the return stroke wave-front (Eq.(1)) generates the negative electric field in the vicinity of the channel. This field is not observed in the measurements [2]. Besides, due to the perfectly conducting channel core and the absence of the rotational electric field, the voltage drop between point A and point B at the ground surface should be zero, Fig.1. It follows that the total radial electrostatic field component near the core should be zero i.e. the additional channel-base current

the transition channel-base current component  $i_{0tr}$  reduces to

$$i_{0tr}(t) = \int_0^{vt} di_{0TCS}(t+z/c) + (v/c)i_{0TCS}(kt) = k i_{0TCS}(kt) - i_{0TCS}(t). \quad (8)$$

where  $k = 1 + v/c$ . The total channel-base current according to the MTCS model is the sum of the additional current component Eq.(8) and the current component  $i_{0TCS}(t)$  in the classical TCS model

$$i_{0MTCS}(t) = i_{0tr} + i_{0TCS} = k i_{0TCS}(kt). \quad (9)$$

If  $v \ll c$  Eq.(9) reduces to the current expression in the classical TCS model. If  $v \leq c$  the differences are more pronounced, the peak of the current multiplies by factor greater than one and it comes earlier. Using Eq.(3) one obtains

$$Q'_{de}(z) = i_{0MTCS}(z/v)/v. \quad (10)$$

The deposited charge component Eq.(10) is similar as in the BG model [4].

## 2. CURRENT DISTRIBUTION ALONG THE CHANNEL ACCORDING TO THE MTCS MODEL

Similar as it is shown in Eq.(5) the negative line charge  $q_{tr}|_z$  above altitude  $z$  is

$$q_{tr}|_z = - \int_z^{vt} [i_{0TCS}(t+z/c)]/c dz, \quad t \geq 0, \quad z \leq vt. \quad (11)$$

The additional channel current  $i_{ztr}$  carrying positive charge neutralizes the negative line charge above altitude  $z$

$$i_{ztr} = \frac{d|q_{tr}|_z}{dt} = \frac{1}{c} \int_z^{vt} \frac{di_{0TCS}(\xi)}{dt} dz + \frac{v}{c} i_{0TCS}[t(1+v/c)]. \quad (12)$$

Using Eq.(7) from Eq.(12) it follows

$$i_{ztr}(z,t) = \int_z^{vt} di_{0TCS}(t+z/c) + \frac{v}{c} i_{0TCS}(kt) = k i_{0TCS}(kt) - i_{0TCS}(t+z/c). \quad (13)$$

The total channel current at some altitude according to the MTCS model is the sum of the additional current component Eq.(13) and the current component  $i_{TCS}(z,t)$  in the classical TCS model, Eq.(4)

$$i_{MTCS}(z,t) = i_{ztr} + i_{TCS} = k i_{0TCS}(kt). \quad (14)$$

Comparing Eq.(14) and Eq.(9) one obtains

$$i_{MTCs}(z,t) = i_{0MTCs}(t) = k i_{0TCS}(kt) . \quad (15)$$

According to the MTCs model the current distribution along the channel is uniform. It follows that no charge is present along the activated part of the channel for  $z \leq vt$  .

$$i_{MTCs}(z,t) = i_{0MTCs}(t) = k i_{0TCS}(kt) . \quad (16)$$

### 3. CONCLUSION

The transferred line charge density is analysed in the TCS model without current reflections. The total (negative) transferred line charge along the channel as a function of time is calculated. The TCS model is modified to take into account the current component caused by the transferred line charge density along the channel core below the return stroke wave-front. For the TCS model without current reflections this modification has yielded the final result similar to that of the Bruce-Golde model. In the modified TCS model the distribution of the channel current is uniform i.e. there is no line charge along the core below the return stroke wave-front. Nevertheless, the physical picture of the discharge differs significantly from that of the BG model.

### Acknowledgements

The Ministry of Education and Science of the Republic of Serbia supported this work under contracts ON171007 and TR37019.

### REFERENCES

- [1] R.Thottappillil, V.A.Rakov and M.A.Uman,"Distribution of charge along the lightning channel: Relation to remote electric and magnetic fields and to return-stroke models," J. Geoph.Res., vol.102, D6, 1997.
- [2] J.Schoene, M.A.Uman, V.A.Rakov, K.J.Rambo, J.Jerauld and G.H.Schnitzer, "Test of the TL model and the TCS model with triggered lightning return strokes at very close range" J. Geoph. Res. vol. 108, D23, 2003.
- [3] F.Heidler, "Review and Extension of the TCS – Model to Consider the Current Reflections at Ground and at the Upper End of the Lightning Channel," Journal of Lightning Res., vol.1, 2007.
- [4] C.E.R.Bruce and R.H.Golde, "The Lightning Discharge" The Journal of Inst. of El. Eng. 88, No.6, pp . 487-505, 1941.
- [5] J.Cvetic and P.Osmokrovic, "Dynamics of Lightning Discharge During Return Stroke", IEEE Transaction on Plasma Science, Vol.37, Issue 1, 2009.

## INCIDENT SHOCK FRONT VELOCITY MEASUREMENTS IN A T-TUBE

S. Djurović, Z. Mijatović, Z. Nađ, L. Gavanski and R. Kobilarov

*Faculty of Sciences, trg Dositeja Obradovića 4, 21000 Novi Sad, Serbia*

**Abstract.** The incident shock front velocity in a T-tube filled with hydrogen, helium and argon has been measured. The velocity dependence of mass of atom of used gas is analyzed. The discharge energy has been the same for all the cases.

### 1. INTRODUCTION

The electromagnetically driven T-tube has been widely used as one of plasma sources for spectroscopic investigation of atomic processes in plasma. The parameters of the gas behind the shock front as flow velocity, gas pressure and temperature strongly depends on shock front velocity. By changing the shock velocity one can change parameters of the plasma produced in a T-tube. Because the shock front velocity depends on the input discharge energy (voltage across the discharge electrodes and capacity of discharge capacitors) and type of the gas and its pressure it is possible to produce the moving plasma with requested parameters by changing these parameters. It is clear that the velocity of the shock front appears as a quantity of primary importance in shock tubes.

Here we give the results of incident shock front velocity measurement in a T-tube filled with hydrogen, helium and argon.

### 2. EXPERIMENT

The plasma source used in this experiment is a small electromagnetically driven T-tube made of glass with an inner diameter of 27 mm. The T-tube was energized by a capacitor bank consisting of four 1  $\mu$ F fast capacitors charged to 20 kV. The filling pressure of 300 Pa was the same for all used gases, hydrogen, helium and argon.

The basic experimental setup is shown in Figure 1. The method of velocity measurements is modified and improved method used earlier [1, 2]. The two narrow tubules, on the mutual distance of  $\Delta x = 9$  mm, are placed close to the horizontal part of the T-tube. The tubules were coupled with the photomultiplier via optical fibers. The passage of the luminous front image of a shock wave in front of the tubules changes the photomultiplier signal. The signal from the photomultiplier was led to the digital oscilloscope.

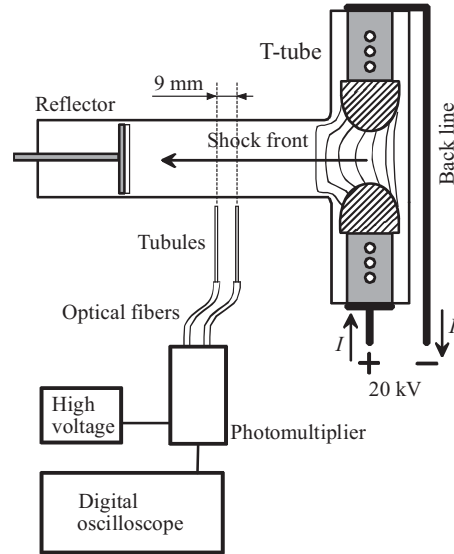


**Figure 1.** Experimental setup.  $I$  is discharge current.

The obtained oscillogram is shown in Figure 2. The time interval  $\Delta t = t_2 - t_1$  between two maxima  $t_1$  and  $t_2$  is the time during which the incident shock front pass the distance  $\Delta x$  between the tubules. In this way the shock front velocity on the observed point along the T-tube axis can be obtained as  $v_1 = \Delta x / \Delta t$ .

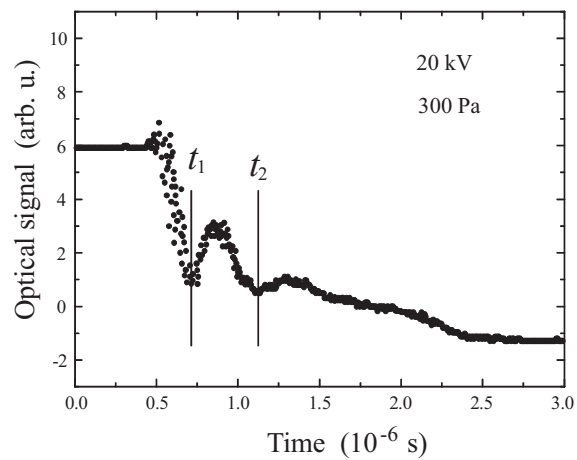


**Figure 2.** Signal from oscilloscope.

## 2. RESULTS AND DISCUSSION $\approx$

The time interval  $\Delta t$  was measured at two different positions along the T-tube axis, 40 mm and 110 mm from the discharge electrodes. The obtained results of incident shock front velocity measurements through different gases, hydrogen, helium, and argon are given in Figure 3.

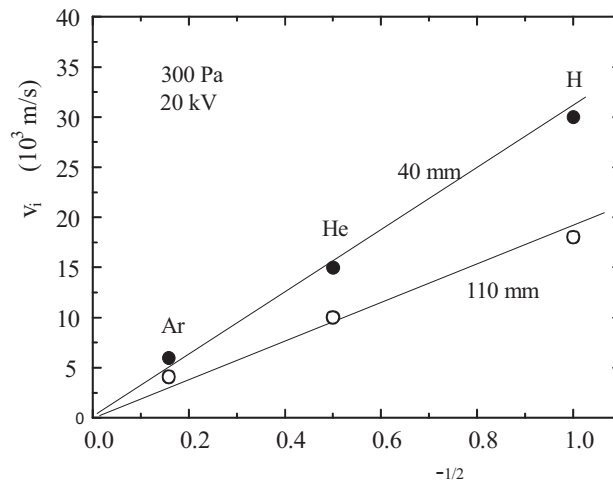


**Figure 3.** Incident shock front velocity versus  $1/(\text{square root of atomic mass})$ .

The electromagnetic force which initiates the shock front depends of intensity of discharge current i.e. of discharge energy. The discharge energy is equal in all three cases and the shock front velocity will depend on the applied gas in the T-tube and its pressure. Pressure also was constant during experiment. The kinetic energy,  $E = mv_i^2/2$ , of the gas particle in the shock wave depends of mass of the particle and is proportional to the input energy. Since input energy also is constant we analyzed relation  $v_i \approx m^{-1/2}$  (Figure 3). The linear dependence of  $v_i$  on  $m^{-1/2}$  confirms our assumption about the relation of input energy and the atomic mass of filling gas. The values of the shock front velocity measured at 110 mm position are lower than ones at 40 mm position and indicate the attenuation of the shock front at larger distances from the discharge electrodes.

### Acknowledgements

This work was supported by the Ministry of Sciences, Republic of Serbia, under Project 171014.

## REFERENCES

1. S. Djurović and M. Pavlov, *Rev. Res. Fac. Sci. Novi Sad* 10, 263 (1980).
2. S. Djurović, Z. Mijatović, M. Pavlov, R. Kobilarov and B. T. Vujičić, *J. Appl. Spectrosc.* 64, 578 (1997)

## LIGHT INTENSITY OSCILLATIONS IN WALL STABILIZED ARC DURING HIGH CURRENT PULSES

S. Djurović, Z. Mijatović, R. Kobilarov and I. Savić

*Faculty of Sciences, trg Dositeja Obradovića 4, 21000 Novi Sad, Serbia*

**Abstract.** In this paper some optical characteristics of plasma from wall stabilized arc in pulsed regime are presented. Through the arc which working under atmospheric pressure high current pulses were applied. The current pulses disturb the plasma and make some plasma oscillations.

### 1. INTRODUCTION

Wall-stabilized arc working at atmospheric pressure, are used very often in spectroscopy for various experiments and measurements [1]. We usually used the stabilized arc as plasma source for measurement of Stark parameters of spectral lines emitted from neutral argon atoms [2, 3] and for testing of the new introduced deconvolution procedure of plasma broadened non-hydrogenic neutral atom lines [4, 5]. The wall-stabilized arc also can be used as optical source in analytical chemistry [6, 7]. The arc usually operates in the dc regime with current typically of few tens of amperes. Under this condition only spectral lines emitted by neutral atoms can be observed. With applied current of 100 A, or higher, it is possible to investigate the spectral lines emitted by ionized atoms [8 – 11].

The high arc current in this experiment was realized by using high current pulses from ac network [12]. In this work we used maximal current of 270 A. Increasing the arc current causes an increase of plasma temperature, electron density and plasma emissivity. Typical electron densities and temperatures of plasma from our wall-stabilized arc operated with 30 A are up to  $3 \times 10^{22} \text{ m}^{-3}$  and 10000 K [2, 3]. Using the pulses of 240 A superimposed on current of 30 A in the dc regime, electron densities reached up to  $1.6 \times 10^{23} \text{ m}^{-3}$  while electron temperatures reached up to 14100 K [12].

In this paper we present the optical characteristics of the plasma during high current pulsed plasma in wall-stabilized arc at atmospheric pressure. The plasma light oscillations were observed and analyzed in end on and side on direction.

## 2. EXPERIMENT

A wall stabilized electric arc was used as a plasma source [12]. The arc operates in the pure argon at the atmospheric pressure and a mixture of argon and 2% of hydrogen is introduced in the central part of the arc. The hydrogen is necessary for recording the Balmer  $H_{\beta}$  line, which is used for electron density determination. Wall stabilized arc in DC regime is supplied from current stabilized electrical source with the current stability of 0.3 %. Maximum current which can be reached is 30 A. To obtain the higher current through arc we applied high current pulses (HCP) superimposed to the DC current. This was done by using civil AC network of 220 V in combination with appropriate electronic circuit [12]. In combination with appropriate resistor it provides current pulses lasting 8 ms, with the peak current of 180 A and 240 A. In this case the total currents were 210 A and 270 A. Block scheme of the electric circuit is presented in Figure 1. DC source is connected to the arc via diode,

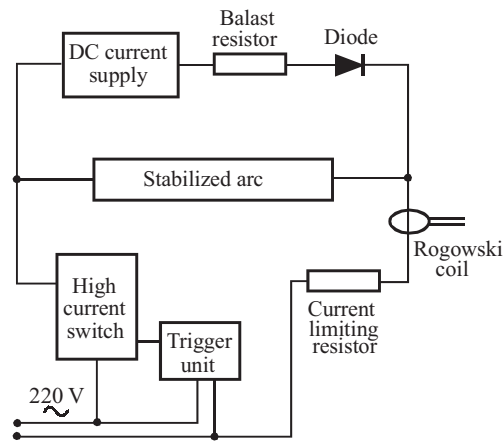


**Figure 1.** Block scheme of the electric circuit.

which protects DC power supply from high current pulses. We usually used every 16<sup>th</sup> of 50 Hz cycle to produce high current pulse. So, repetition rate of the high current pulses is 3.12 Hz. This repetition rate is low enough not to affect temperature of the arc walls which were water cooled in usual manner. The pulsed current was measured by means of Rogowski coil, and monitored by digital oscilloscope.

Spectroscopic observations are made along the arc axis (end on) through a cathode hole and perpendicularly to the arc axis (side on). Scheme of the optical and control system is presented in Figure 2 [12].

Plasma electron density was determined from halfwidth of the Balmer  $H_{\beta}$  spectral line. The obtained values were  $1.3 \times 10^{23} \text{ m}^{-3}$  for current of 210 A and  $1.6 \times 10^{23} \text{ m}^{-3}$ . The corresponding electron temperatures which determined

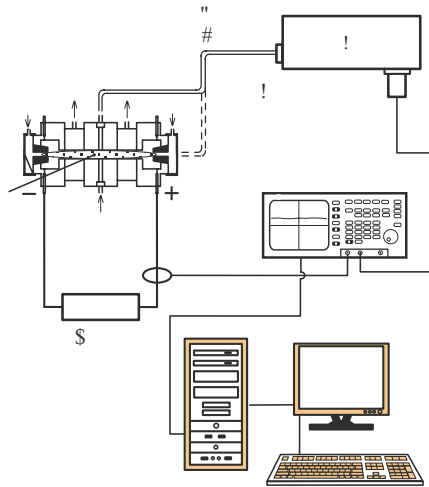


**Figure 2.** Schematic diagram of the spectroscopic observation

from electron density and plasma composition data [13], were 13500 K and 14100 K respectively.

## 2. OPTICAL MEASUREMENTS

During the current pulses one can expect some oscillatory behavior of the plasma. The oscillations in the current are almost negligible while oscillations in emitted light and some mechanical oscillations of plasma column were observed. The current pulse and plasma light oscillations, observed end on and side on, are shown in Figure 3. The observation was made at continuum wavelength position of 535 nm by two optical fibers (see Figure 2).

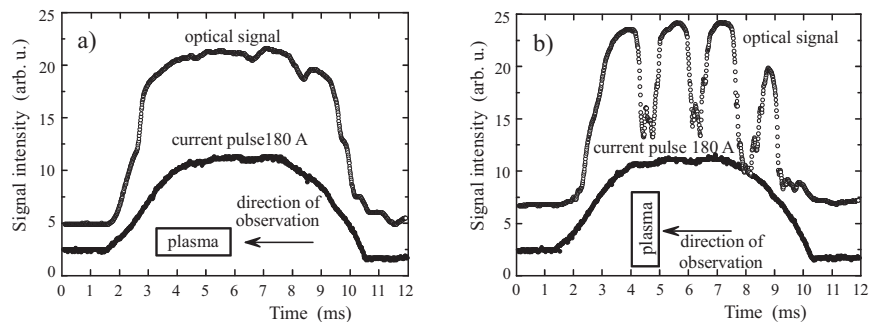


**Figure 3.** Plasma light oscillations observed (a) end on and (b) side on. Pulsed current of 180A (total current 210 A) was applied.

The oscillations of the light observed along the arc axis are very small. If plasma light was observed perpendicular to plasma column, the considerable light oscillations occur. The same situation is in case when higher current pulse was applied. In case of side on direction, plasma was observed through small tube, 2 mm in diameter, used for gases exhaust. Through this tube plasma can expand due to sudden shock resulting from a sharp increase of the current. Plasma could not expand in the end on direction since the ends of the arc are closed. The difference in plasma space limitations can explain the observed difference in light emission oscillations. On the other hand the expansion of the plasma in longitudinal direction could be very small in comparison with plasma column length.

### Acknowledgements

This work was supported by the Ministry of Sciences, Republic of Serbia, under Project 171014.

### REFERENCES

1. H. R. Griem, *Plasma Spectroscopy*, p 156, (New York: McGraw-Hill, 1964).
2. S. Djurović, Z. Mijatović, R. Kobilarov and N. Konjević, *J. Quant. Spectrosc. Radiat Transfer* 57, 695 (1997).
3. S. Djurović, D. Nikolić, Z. Mijatović, R. Kobilarov and N. Konjević, *Plasma Sources Sci. Technol.* 11, 95 (2002).
4. D. Nikolić, Z. Mijatović, S. Djurović, R. Kobilarov and N. Konjević, *J. Quant. Spectrosc. Radiat Transfer* 70, 67 (2001).
5. D. Nikolić, S. Djurović, Z. Mijatović, R. Kobilarov, B. Vujičić and M. Ćirišan, *J. Quant. Spectrosc. Radiat Transfer* 86, 285 (2004).
6. M. A. Eid, H. R. Moustafa, E. A. Al Ashkar and S. S. Ali, *Spectrochim. Acta B* 61, 450 (2006).
7. N. H. Bings, A. Bogaerts and J. A. C. Broekaert, *Anal. Chem.* 80, 4317 (2008).
8. D. E. Kelleher, *J. Quant. Spectrosc. Radiat. Transfer* 25, 191 (1981).
9. J. P. Knauer and M. Kock, *J. Quant. Spectrosc. Radiat. Transfer* 56, 563 (1996).
10. K. Dzierzega and K. Musiol, *J. Quant. Spectrosc. Radiat. Transfer* 52, 747 (1994).
11. S. Pellerin, K. Musiol and J. Chapelle, *J. Quant. Spectrosc. Radiat. Transfer* 57, 377 (1997).
12. S. Djurović, Z. Mijatović, R. Kobilarov and I. Savić, *Plasma Sources Sci. Technol.* 21, 025007 (2012).
13. C. H. Popenoe and J. B. Shumaker Jr, *J. Res. Natl Bur. Stand.* 69A, 495 (1965).

## CHARACTERIZATION OF LASER-INDUCED PLASMA BY OPTICAL EMISSION SPECTROSCOPY

M. Gavrilović<sup>1</sup>, M. Cvejić<sup>1</sup>, S. Jovičević<sup>1</sup> and N. Konjević<sup>2</sup>

<sup>1</sup>*Institute of Physics, University of Belgrade, P.O. Box 68, 11080, Belgrade, Serbia*

<sup>2</sup>*Faculty of Physics, University of Belgrade, P.O. Box 368, 11000, Belgrade, Serbia*

**Abstract.** The results of radial distribution measurements of excitation temperature,  $T_e$ , and electron number density,  $N_e$ , in laser induced plasma are presented. All spectral recordings were checked for the presence of self-absorption and then Abel inverted. The electron density is measured from the width of Al II and Mg II lines. The excitation temperature is determined from relative intensities of Al II lines using Boltzmann plot technique. Radial distributions of plasma parameters measurements are presented for the distance of  $\sim 1.5$  mm from the target surface,  $1\mu\text{s}$  after laser pulse. LIBS plasma is generated with Nd:YAG laser beam focused in air at atmospheric pressure on the target containing  $\text{Al}_2\text{O}_3$  900 mg :  $\text{Li}_2\text{CO}_3$  400 mg :  $\text{MgCO}_3$  100 mg. Measured values of  $T_e$  were in range 8380 – 10040K and  $N_e$   $1.72 - 2.74 \cdot 10^{23}\text{m}^{-3}$ .

### 1. INTRODUCTION

Laser induced breakdown spectroscopy (LIBS) is a very popular analytical method for rapid in-situ analysis of solid, liquid or gaseous samples in different surroundings transparent for the laser radiation [1,2]. From an analytical point of view it is necessary to understand the complex nature of the laser-sample interaction processes, which depend upon both laser characteristics and sample properties. The plasma-ablated particle interaction which is space and time dependent is important also. All these processes influence spectral line intensity, which is basis for both, analytical application and plasma diagnostics. Thus, one can conclude that LIBS is very complex system, which requires knowledge of several plasma parameters simultaneously for reliable analytical application.

In this report we present results of radial distribution measurements of excitation temperature and electron density in laser induced plasma of solid sample in air at atmospheric pressure.

## 2. EXPERIMENT

The experimental setup is shown in fig 1. For plasma generation Nd:YAG laser was used. The laser pulse energy was 50 mJ and pulse duration 15 ns FWHM at the wavelength of 1064 nm (Molelectron MY34). The laser beam was perpendicularly directed towards target surface and focused by means of a 100 mm focal length lens (L1).

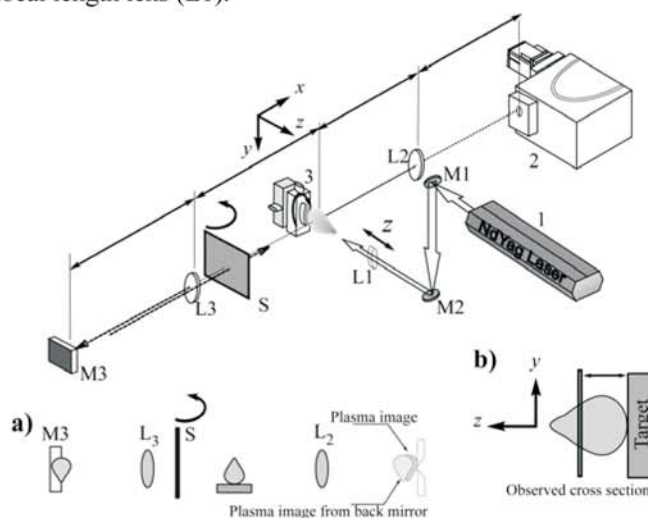


**Figure 1.** Experimental setup for LIBS

The target was placed in the holder, which can be rotated and translated along the  $x$  and  $z$  axes. The impact spot diameter at the sample surface was  $200\ \mu\text{m}$ . The image of plasma plume was projected with 1:1 magnification onto the entrance slit ( $10\ \mu\text{m}$  width and  $2.5\ \text{mm}$  height) of the spectrometer (Shamrock sr-303i, Czerny-Turner type, focal length  $303\ \text{mm}$ , with three gratings  $600$ ,  $1200$ , and  $2400$  grooves/mm), using a lens (L2) of  $170\ \text{mm}$  focal length;  $50\ \text{mm}$  diameter quartz lens (L3) with a focal length of  $100\ \text{mm}$ , flat mirror and shutter (S) were placed behind the plasma to verify the absence or presence of self-absorption (see fig 1a). The flat mirror was placed at a distance equal two double focal length of the lens (L3) in respect to the plasma plume. The lens and flat mirror were placed in such a way that the image of the plasma projected onto the entrance slit of spectrometer coincided with the primary plasma image. The shutter inserted between the sample stage and the flat mirror allowed to obtain spectra with and without back mirror.

The plasma radiation was recorded with the ICCD detector (Andor Technology, DH720-18F-63,  $1024 \times 256$ ,  $26\ \mu\text{m}$ ,  $5\text{ns}$ ,  $18\text{mm}$ , GIII, P43, DDG), which was placed on the exit plane of the spectrometer. The ICCD was operated by a pulse generator (DG-535, Stanford Research Systems), allowing the choice of gate width and delay time for time resolved acquisition. The gate width and the delay time between the laser pulse and the beginning of the acquisition can

be adjusted to maximize the signal-to-background and the signal-to-noise ratio. The data acquisition was controlled with the iStar software (Andor Technology).

All measurements were performed in air at atmospheric pressure. The laser pulse energy was 50 mJ and target ( $\text{Al}_2\text{O}_3$  900 mg :  $\text{Li}_2\text{CO}_3$  400 mg :  $\text{MgCO}_3$  100 mg) was rotated or translated after 8 laser shots. The plasma was observed perpendicular to the laser beam and parallel to the target at a distance of  $\sim 1.5$  mm from the target surface, (see fig1b). Time resolved observation of plasma was performed with the gate width of 200 ns, for all recordings. The delay time was changed from 0.5  $\mu\text{s}$  after laser pulse to 7  $\mu\text{s}$ , in steps of 500 ns. All spectral recordings were obtained with the ICCD camera operated in the imaging mode.

### 3. RESULTS AND DISCUSSION

All experimental data were processed with program developed in our laboratory using Matlab®. Main steps of the procedure include intensity correction, self absorption correction and Abel inversion of image.

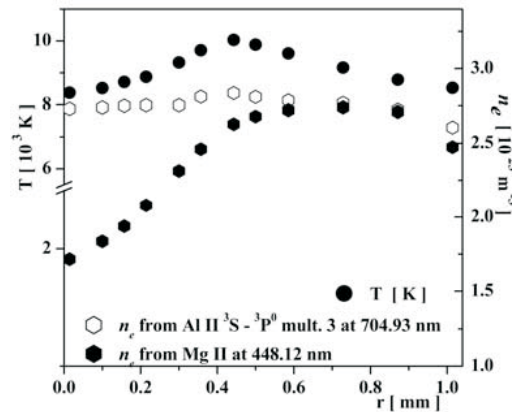


**Figure 2.** Radial distribution of  $T_e$  and  $N_e$  at delay time  $1\mu\text{s}$  and 1.5 mm from the surface of the target.

The self absorption test showed that all studied ionic lines of Al II and Mg II may be corrected for self absorption at the delay time of 1  $\mu\text{s}$ , and this procedure is applied before these lines are used for temperature measurements. The radial distributions of temperature and electron density are shown in Fig.2. The excitation temperatures were obtained from the Boltzmann plots at each radial position of ionic lines of Al II.358.6, 466.2 and 704.93 nm. The electron density is determined from the profiles of Al II triplet line (704.93 nm) and Mg II singlet line (448.12 nm) by comparing the experimental profiles with theoretical ones, generated from equations 10. and 11. from [3] and using data for Stark parameters from [4]. The overall profiles generated this way are shown in figure 3. together with experimental ones. The results for  $T_e$  and  $N_e$  are given in table 1.

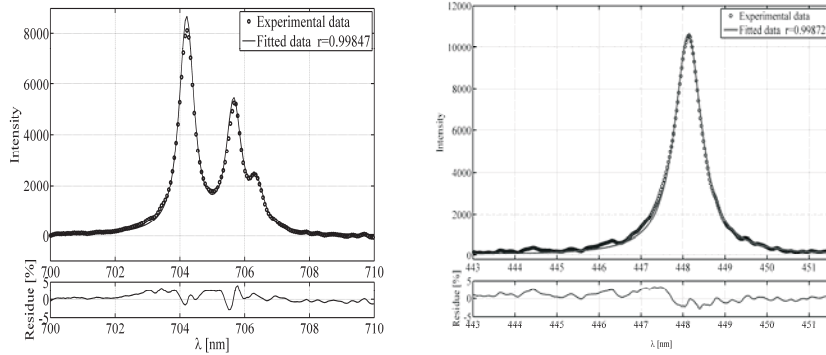


**Figure 3.** Experimental profiles fitted with computed ones

**Table 1.** Values of excitation temperature and electron density

r (mm)	T (K)	$n_e$ ( $10^{23} \text{ m}^{-3}$ ) Al II $^3\text{S} - ^3\text{P}^0$ mult. 3 at 704.93 (nm)	$n_e$ ( $10^{23} \text{ m}^{-3}$ ) Mg II 448.1 nm
0.014	8370	2.73	1.71
0.100	8520	2.74	1.84
0.214	8870	2.75	2.08
0.300	9320	2.75	2.31
0.443	10030	2.83	2.63
0.500	9880	2.81	2.68
0.728	9160	2.77	2.74
1.014	8530	2.60	2.47

## Acknowledgements

This work is supported by Ministry of Education and Science of the Republic of Serbia, project no 171014

## REFERENCES

- [1] L. J. Radziemski, Spectrochim. Acta B, 57, 1109-1113, (2002)
- [2] D. W. Hanh, N. Omenetto, Appl. Spectroscopy, 66, 4, 347 (2012)
- [3] N. Konjević, Phys. Rep. 316, 339 (1999).
- [4] H.R. Griem: Spectral line broadening by plasmas (Academic press, New York and London 1974)

## SPECTROSCOPIC CHARACTERISATION OF MICRO APGD IN HELIUM

M. Gavrilović<sup>1</sup>, S. Jovičević<sup>1</sup> and N. Konjević<sup>2</sup>

<sup>1</sup>*Institute of Physics, University of Belgrade, P.O. Box 68, 11080, Belgrade, Serbia*

<sup>2</sup>*Faculty of Physics, University of Belgrade, P.O. Box 368, 11000, Belgrade, Serbia*

**Abstract.** Laboratory made direct-current micro glow discharge in helium at atmospheric pressure has been studied. The discharge was operated in the current range (20 – 50) mA with the voltage of about 0.6 kV and gas flow rate of 100 ml/min. Negative current-voltage characteristics of this low-current high voltage discharge source suggests that the discharge operates as an atmospheric pressure glow discharge. Spectroscopic measurements were performed end-on and side-on in respect to the axis of discharge. The rotational temperature of 980K was evaluated from the shape of OH bands while electron number density in the range  $(0.16 - 5.0) \cdot 10^{15} \text{ cm}^{-3}$  was determined from the profiles of the  $H_{\beta}$  and He I lines.

### 1. INTRODUCTION

For a long time different types of glow discharges (GD) were used as radiation source in atomic analytical spectroscopy. With various types of glow discharges operated under different conditions, samples of different aggregate states were analyzed. Reduced pressure GDs have the advantage of high excitation and ionization efficiency while atmospheric pressure GDs have significantly lower operational cost and they are simple to construct and use [1]. High pressure microplasma discharges have received considerable attention in recent years. Having higher gas temperature APGDs are also suitable for the analysis of gases and liquids [2] while reduced pressure GDs are mostly used for analysis of solids.

In this report we present the results of spectroscopic characterization of micro APGD source in helium for analytical application.

### 2. EXPERIMENT

The experimental setup is presented in Fig 1. The micro APGD is constructed following the design described in ref. [1]. The discharge is formed

between two steel electrodes, with 10 mm electrode gap. The cathode is stainless steel tube with inner and outer diameter of 1 and 1.7 mm, respectively.

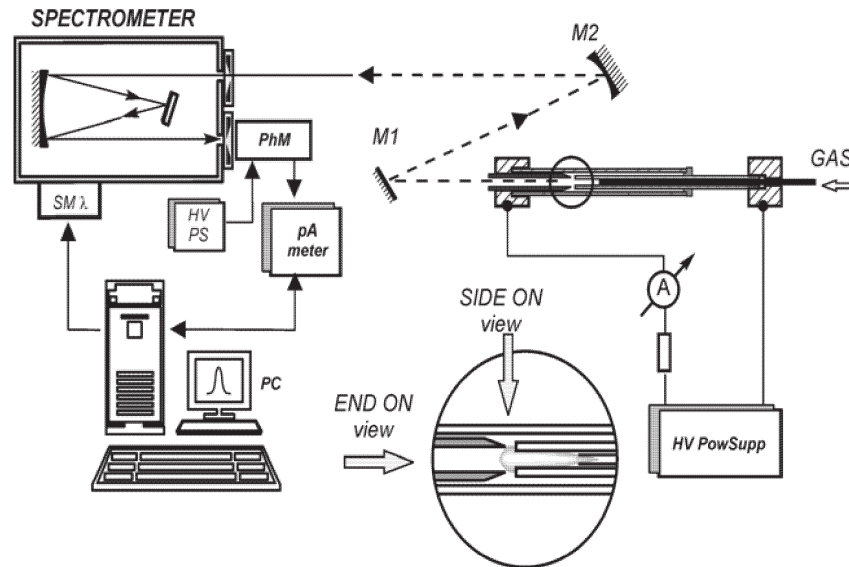


**Figure 1.** Experimental setup for OES study of micro APGD

The anode is steel ring with 3.5 inner diameter. The anode is conically shaped to enable easier ignition of discharge. The cathode and the discharge gap are enclosed in a quartz tube with 2 mm inner diameter. High purity He (99.999%) was introduced in the discharge through the cathode with gas flow rate of 100 ml/min.

A 1:1 image of the plasma source is projected by the system of mirrors on the entrance slit (20  $\mu\text{m}$  width and 1 mm height) of 0.5-m Ebert type scanning spectrometer having reciprocal dispersion of 1.6 nm/mm. For spectral intensity measurements photomultiplier mounted on the exit slit of spectrometer was used. Spectroscopic side-on and end-on measurements in respect to discharge axis were performed. The discharge was mounted on PC-controlled X-Y table so it was possible to scan plasma longitudinally between cathode and anode.

### 3. RESULTS AND DISCUSSION

The current-voltage characteristics of micro APGD was recorded, see fig 2. The shape of current-voltage characteristics suggests that our APGD in helium is an atmospheric glow discharge, see e.g. [3] and [4] and references therein.

The emission spectrum of He APGD microdischarge is given in fig 3.

The rotational temperature was measured from the shape of OH bands by comparing experimental data with computed synthetic spectrum [5]. Using the assumption that the rotational temperature is equal to the gas temperature,  $T_g$ , we determined  $T_g \approx 980$  K.

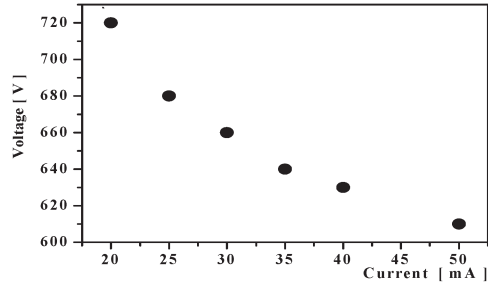


**Figure 2.** Current-voltage characteristic of micro APGD in helium

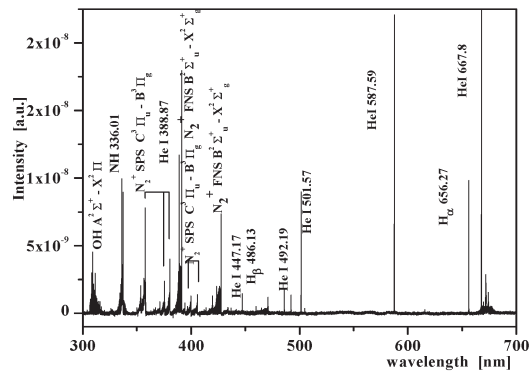


**Figure 3.** Emission spectrum of He APGD at 0.6 kV, 28 mA, 100 ml/min He

For determination of  $N_e$ , Stark width of the H $\beta$  line was used by employing the procedure for low  $N_e$  diagnostics with this line described in [6]. The electron number density was also determined by fitting asymmetrical profile of the 501.6 nm line and from the wavelength separation  $s$  between allowed and forbidden line components of 449.2 nm He I line [7], and the results are given in table 1. It can be seen that values of  $N_e$  from the H $\beta$  and from He I lines differ considerably. What is more intriguing  $N_e$  results from various He I lines differ also. That discrepancy, most likely, is caused by different physical conditions in various regions of discharge gap, see Fig.4. Helium lines are primarily excited in the cathode fall region where DC Stark effect influences line shape, while the

$H_{\beta}$  is emitted from the plasma region. This tentative explanation can't explain large differences of Ne obtained from various He I lines.

**Table 1.** Electron number density calculated from the  $H_{\beta}$  and He I lines

$\lambda$ [nm]	Ne [ $\text{cm}^{-3}$ ]	
	End-on	Side-on
$H_{\beta}$ 486.1	$1.63 \cdot 10^{14}$	$2 \cdot 10^{14}$
He I 501.6	$4.6 \cdot 10^{15}$	$2.3 \cdot 10^{15}$
He I 492.2	$3.69 \cdot 10^{14}$	/

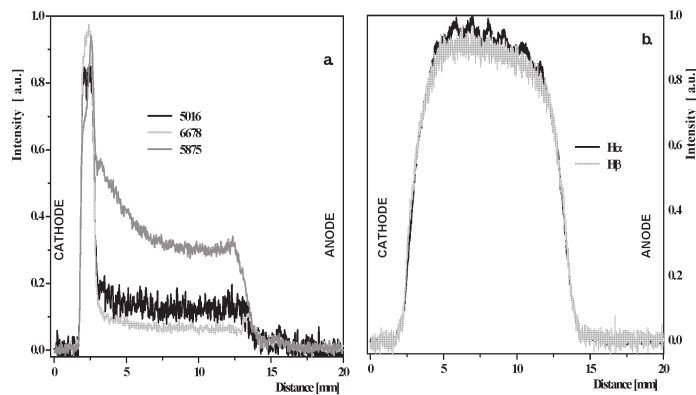


**Figure 4.** Intensity distribution along discharge axis of He I lines (a) and  $H_{\beta}$  line(b)

### Acknowledgement

This work is supported by Ministry of Education and Science of the Republic of Serbia, project no 171014

### REFERENCES

- [1] B. Gielniak et al., Spectrochim. Acta B,66, 21–27, (2011)
- [2] S. Baude et al, J. Anal. At. Spectrom.,15, 1516-1525, (2000)
- [3] V. I. Arkhipenko et al, J. Appl. Spectrosc., 67, 910-918, (2000)
- [4] F. J. Andrade et al, J. Anal. At. Spectrom., 21, 1175–1184, (2006)
- [5] Ch. de Izarra, J. Phys. D: Appl. Phys., 33 ,1697–1704, (2000)
- [6] M. Ivković et al, Spectrochim. Acta B, 59, 591–605, (2004)
- [7] N. Lara et al., Astron. Astrophys., accepted, (2012)

## THE STARK BROADENING OF THE HE I 492.1 NM LINE WITH FORBIDDEN COMPONENTS IN DENSE COOL PLASMA

M. Ivković<sup>1</sup>, M. Á. González<sup>2</sup>, N. Lara<sup>3</sup>, M. A. Gigosos<sup>3</sup> and N. Konjević<sup>4</sup>

<sup>1</sup>*Institute of Physics, University of Belgrade, P.O. Box 68, 11080 Belgrade, Serbia*

<sup>2</sup>*Depart. de Fisica Aplicada, Universidad de Valladolid, 47071 Valladolid, Spain*

<sup>3</sup>*Departamento de Optica, Universidad de Valladolid. 47071, Valladolid, Spain*

<sup>4</sup>*Faculty of Physics, University of Belgrade, P.O. Box 368, 11001 Belgrade, Serbia*

**Abstract.** We present the results of an experimental study of the He I 492.1 nm line with forbidden components emitted by low-electron temperature high electron number density plasma. The laser interferometry at 632.8 nm and shape of the He I 447.1 nm line were used to measure electron number density in the range  $(1 - 7) \times 10^{23} \text{ m}^{-3}$ , while electron temperatures are in the range from 25 000 K to 35000 K. The experimental profiles are compared with the results of theoretical calculations obtained using computer simulation method. The agreement of experimental with computer simulation results is within 10% what is well within theoretical and experimental uncertainty.

### 1. INTRODUCTION

The study of the helium lines with forbidden components attracted attention some time ago because they appear in spectra of B-type stars, see e.g. Lecrone [1]. The very complex overall shapes of these spectrally overlapping lines are very sensitive to charged particle density. The forbidden component appear in the vicinity of several visible He I lines as a consequence of mixing upper energy level of allowed transition with close perturbing energy level (or levels) in plasma microfield. Therefore, the comparison of the overall experimental profile of these lines with results of theoretical calculations may be used as a sensitive test of Stark broadening theories. Also, they can be very useful in diagnostics of astrophysical and laboratory plasma containing helium, used either as matrix gas or as an additive to matrix gas.

Recently, the results of computer simulation technique for evaluation of overall shape of He I line with forbidden components at 447.1 nm has been reported [2] and compared with a number of experiments [2, 3]. Due to the fact that this line is usually covered with many other spectral lines, another He I line with forbidden components at 492.2 nm has been studied also recently [4]. Here,

we shall focus our attention on 492.2 nm line in plasmas with medium and high electron densities  $N_e$  in the range  $(0.5 - 7) * 10^{23} \text{ m}^{-3}$ .

## 2. COMPUTER SIMULATIONS

Computer simulations permit to obtain the electric field that alters the emitter evolution giving rise to Stark broadening. For this, the movement of the particles in the plasma is reproduced numerically and the temporal evolution of the electric microfield undergone by the emitter is calculated. The temporal sequence of this microfield is carried to the differential equations that give the emitter evolution and the emitter dipole moment autocorrelation function is obtained [5]. Finally, the line shape is obtained as the Fourier transform of an average of the calculated autocorrelation functions. For more details on computer simulation technique see Gigoso et al [6].

## 3. EXPERIMENT AND PLASMA DIAGNOSTICS

The plasma source and experimental setup were already described in [3] and therefore, only minimum details are given here for completeness. Linear pulsed discharge with the tungsten electrodes (placed inside quartz tube, inner diameter 8 mm) was used. Each electrode has 0.6 mm diameter openings to enable interferometry and spectroscopy measurements along the axis of plasma column. In this discharge the electron densities up to  $10^{24} \text{ m}^{-3}$  were obtained in continuous flow of helium. Typical current shape is displayed in Figure 1a. For line profiles recording a 1:1 image of the plasma source is projected onto the entrance slit of a 1 m monochromator (with a photomultiplier mounted on exit slit) equipped with a stepping motor for grating rotation. The eight (or 16) PMT signals for each wavelength step were recorded and averaged by digital storage oscilloscope. From recorded data, spectral line shapes of the He I 492.2 nm, together with overlapping He I 501.6 nm lines at different times of plasma decay are presented in Figure 1b.

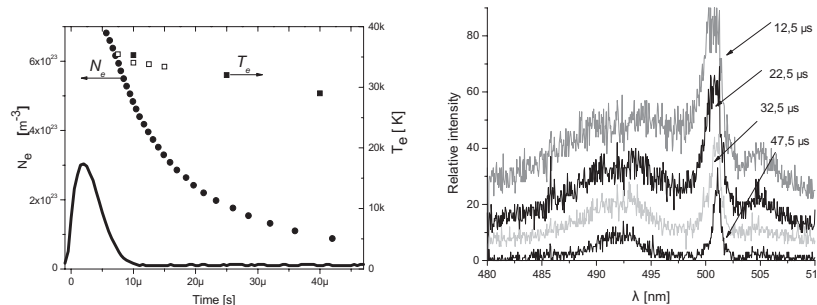


**Figure 1.** a) Current pulse, temperature and electron density decay. b) The overall shape of the recorded He I lines at different times of plasma decay. Initial pressure in discharge tube: 100 mb He.

The electron density was determined with single wavelength Michelson interferometer at 633 nm and from the shapes of He I at 447.1 nm line recorded under same plasma conditions [3].

The electron excitation temperature,  $T_e$  was determined in two ways: from line to underlying continuum ratio of He I 388.8, 667.8, 706.5 and 728.1 nm lines in conjunction with theoretical ratios; see Fig. 13-5 in [7] and from the Boltzmann plot of O II impurity lines. The decay of electron density and electron temperature during plasma afterglow is presented in Figure 1a.

#### 4. RESULTS

The results of numerical simulation for the profile of He I 492.2 nm line and forbidden component in He plasma at  $T_e = 20\,000$  K for different values of  $N_e$  are shown in Figure 2.

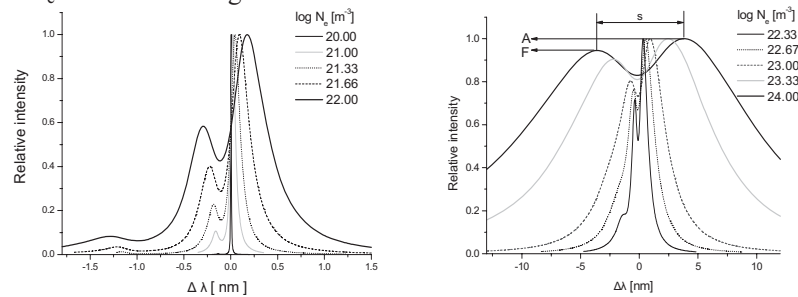


**Figure 2.** Overall shape of the He I 492 nm line at  $T_e = 20\,000$  K and different electron densities.

As shown in Figure 2, the complex shape of this line besides allowed component  $4d - 2p$  has two forbidden components  $4p - 2p$  and  $4f - 2p$ . Also, at higher electron densities this line becomes overlapped with He I line at 501.6 nm, see Figure 1b. Thus, for determination of 492.2 nm line shape at high  $N_e$  one has to take in account the contribution of the neighboring 501.6 nm line.

The  $N_e$  values obtained from the 492.2 nm line and from the shape of the 447.1 nm line recorded under same plasma conditions differs only few percents what indicate the consistency between theoretical data for 447.1 and for the 492.2 and 501.6 nm lines [2, 4]. The agreement between experimental and computer simulation profile shapes is very good i.e. within the fluctuation of photomultiplier signal caused by plasma shot-to-shot reproducibility.

From the peak separation -  $s$  of 492.2 nm line and from the ratio of intensities between main forbidden ( $4f - 2p$ ) and allowed component -  $F/A$ , see Fig.2b are determined and compared with other experimental and recent simulation result [4]. As can be seen from the Figure 3, the agreement between our experimental and simulation results are within 10% what is well within theoretical and experimental uncertainty of  $s$  and  $F/A$  parameter dependences on  $N_e$ .

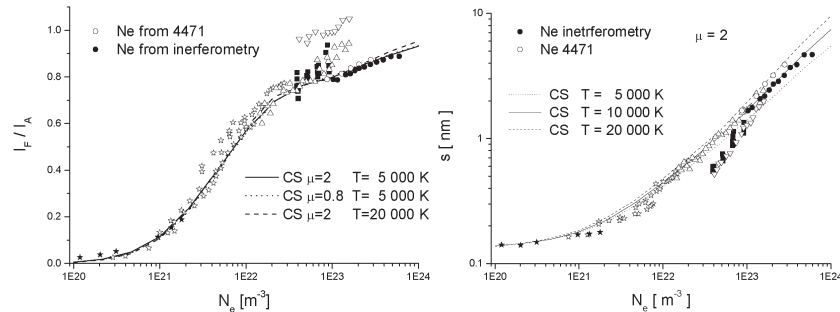


**Figure 3.** Comparison of  $F/A$  and  $s$  values obtained by experiments: ● and ○ - This work, ▽ - [8], ■ - [9], ★ - [10], △ - [11], ☆ - [12], and computer simulation [4].

The discrepancies between our results and trends of experimental results reported in [8] can be attributed to possibly plasma inhomogeneity and non applying Abel inversion to the spectra of the laser induced plasma. The discrepancies for  $F/A = f(N_e)$  with results from [11] appears only at higher  $N_e$  and the most possible cause is self-absorption, while differences of  $s = f(N_e)$  with results presented in [9] can be attributed to the use of complex system for line shape recordings.

### Acknowledgements

This work has been partially financed by Spanish Ministerio de Educación y Ciencia through grant ENE2007-63386/FTN, ENE2010-19542/FTN, and by the Junta de Castilla y León through grant VA007A09 and by the Ministry of Education and Science of the Republic of Serbia under Project 171014.

### REFERENCES

- [1] Lecrone S, 1971, *Astron. Astrophys.* **11**, 387.
- [2] Gigosos M.A. & González M.A., 2009, *A. & A.* **503**, 293.
- [3] Ivković M, Gonzalez M.A., Jovičević S., Gigosos M.A. & N. Konjević, 2010, *Spectrochim. Acta B*, **65**, 234.
- [4] N. Lara, González M.A. & Gigosos M.A., 2012 *A. & A.* Accepted.
- [5] Gigosos M, González M.Á. & N. Konjević N, 2006, *E. Phys. J. D* **40**, 57.
- [6] Gigosos, M González M.Á. & Cardeñoso V, 2003, 2003, *Spectrochim. Acta B*, **58**, 1489.
- [7] Griem H.R, 1964, *Plasma Spectroscopy*, McGraw-Hill, New York.
- [8] Baravian, G., Bretagne, J., Godart, J. & Sultan G 1975, *Z. Physik B* **20**, 255.
- [9] Nelson, R. H. & Barnard, A. J. 1971, *J. Q. S. R. T* **11**, 161.
- [10] Adler, G. & Piel, A. 1991, *J. Q. S. R. T* **45**, 11.
- [11] Perez, C., de la Rosa, I., Aparicio, J. A., Mar, S. & Gigosos, M. A. 1996, *Jpn. J. Appl. Phys.* **35**, 4073.
- [12] Diatta, C. S., Czernichowski, A. & Chapelle, J, 1976, *Physica* **84C**, 425.

## EMISSION SPECTROSCOPY OF PLASMA DURING ELECTROLYTIC OXIDATION (PEO) OF Mg- AND Al-ALLOY

J. Jovović, S. Stojadinović, N.M. Šišović, N. Konjević

*University of Belgrade, Faculty of Physics, Belgrade, P.O. Box 368, Serbia*

**Abstract.** We used emission spectroscopy to characterize Plasma during Electrolytic Oxidation (PEO) of magnesium- and aluminium-alloy. The focus is on the plasma process, related to the ejection of evaporated anode material through micro-discharge channel. The electron excitation temperature of 4100 K is determined from relative intensities of Mg I lines using Boltzmann plot technique. Electron density  $N_e$  in the range  $(0.9-1.6)\times 10^{17} \text{ cm}^{-3}$  is detected using Stark broadening and shift of aluminium and magnesium singly charged ion lines. Lower densities  $N_e < 4 \times 10^{16} \text{ cm}^{-3}$  are determined from the width of the same ion lines, most likely observed at the late time of plasma decay.

### 1. INTRODUCTION

Plasma electrolytic oxidation (PEO) is high-voltage anodizing process of deposition of thick highly crystalline oxide films on the surface of lightweight metals such as aluminium, titanium, zirconium, etc. This process is followed by formation of micro-discharges on the metal surface accompanied by gas evolution [1]. It is known that three types of microdischarge occurs during PEO process: (i) discharge in relatively small holes near the surface of oxide layer, (ii) discharge in the micropores at the surface of oxide layer and (iii) discharge through narrow breakdown channel in oxide layer [2]. The third process is the process with largest  $N_e$ , and in the case of aluminium anode, it was related to metal evaporation from anode [3]. In order to assess in more detail third process of plasma ejection from micro-channel we employed Boltzmann plot (BP) technique and Stark broadening theory to evaluate electron temperature and electron number density, respectively. In this study, Mg-Al alloys were used as anode material.

### 2. EXPERIMENTAL

The PEO process was carried out in an electrolytic cell previously described in [4]. In the experiment, Mg-alloy (Al 2.5 %-3.5 %) and Al-alloy (2.6 %-3.4% Mg.) were used as anode in two separate experiments. In both cases, water

solution of 4 g/L  $\text{Na}_2\text{SiO}_3 \cdot 5\text{H}_2\text{O}$  + 4 g/L KOH ( $\text{pH} \approx 12.8$ ) was used as electrolyte. Current density was  $100\text{mA}/\text{cm}^2$  and voltage between electrodes 350-450 V. The recordings of Al II  $4s^3S - 4p^3P^0$  multiplet 3 at 704.93 nm and Mg II  $3d^2D - 4f^2F^0$  multiplet 4 at 448.12 nm were performed with 2 m Ebert type spectrometer (inverse linear dispersion 0.74 nm/mm in the first diffraction order). The Mg I lines used for Boltzmann plot were recorded with 0.67 m Czerny-Turner spectrometer (inverse linear dispersion of 0.83 nm/mm). Both spectrometers were equipped with thermoelectrically cooled CCD (2048 x 506 pixels,  $-10^\circ\text{C}$ ). A standard coiled-coil tungsten halogen lamp was used for a wavelength sensitivity calibration of the spectrometer-detector system.

### 3. RESULTS AND DISCUSSION

The spectra of seven neutral magnesium lines (Mg I 516.73 nm, Mg I 517.27 nm, Mg I 518.36 nm, Mg I 382.94 nm, Mg I 383.23 nm, Mg I 383.83 nm and Mg I 552.84 nm) recorded during PEO with Al-alloy were utilized for evaluation of electron excitation temperature  $T_{\text{exc}}$  in microdischarge through oxide layer. For this purpose, the BP technique was used, see Figure 1. Atomic data for Mg I lines are taken from [5]. In this type of microdischarge, we assume a thermal equilibrium conditions, i.e.  $T_e = T_{\text{exc}}$ .

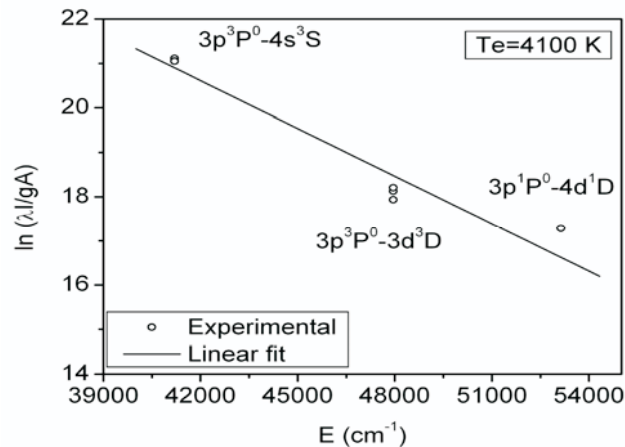


**Figure 1.** Boltzmann plot of seven Mg I lines recorded during PEO with Al-alloy anode.

In Figure 2a, the Al II  $4s^3S-4p^3P$  multiplet 3 at 704.93 nm, recorded during PEO with Al-alloy is presented. It was proven, using relative line intensities of Al II lines, that the multiplet is not self-absorbed, see e.g. [6,7]. Thus, the strongest line 704.2 nm is selected for the evaluation of electron number density. The profile of each line of the Al II multiplet in Fig. 2a is asymmetric, which is not expected for ion lines see e.g. [8]. Since the spectrometer was excluded by comparison with other line profiles, fitting of

experimental profile with two profiles was the only reasonable solution, see Figure 2b. The fit with two Lorentzian profiles having different width and shift fits much better experimental profile than single Lorentzian fit, see Fig. 3 in [3]. The line shift is measured in respect to Ne I 705.92 nm line. It is important to note that line asymmetry of the Al II 704.2 nm line was hardly visibly in Ref [3] due to different experimental conditions and different anode material.

The measurement of electron number density during PEO of Mg-alloy was performed by analyzing the shape of  $3d^2D - 4f^2F^0$  multiplet 4 with an average wavelength 448.12 nm, see profiles recording in Figure 3. The presented line shape consists of two close line profiles at 448.11 nm and 448.13 nm. The influence of small difference in wavelength of 0.02 nm to the line width measurement is well within the precision of this experiment. As for Al II line in Figure 2b, the fitting of experimental profile with two mutually shifted profiles was performed, see Figure 3.

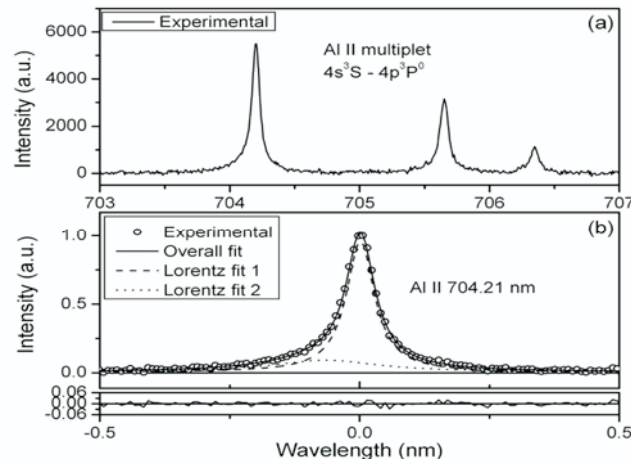


**Figure 2.** a) The experimental profile of Al II  $4s^3S - 4p^3P^0$  multiplet 3 at 704.93 nm; b) The experimental profile of Al II 704.21 nm line fitted with two mutually shifted Lorentzians. The multiplet was recorded during PEO with Al - alloy anode. The instrumental profile full-half-width 0.028 nm.

In order to obtain electron number density the experimental line widths and shifts of Al II 704.2 nm and Mg II 448.12 nm are corrected first for the contribution of Van der Waals broadening. Then,  $N_e$  is estimated from the comparison with Stark broadening parameters evaluated using formulas given in [7] for  $T_e=4100$  K, see Figure 1. The broadest Lorentzian profile gives  $N_e \sim 1.2 \times 10^{17} \text{ cm}^{-3}$  while  $N_e \sim 2.8 \times 10^{16} \text{ cm}^{-3}$  is obtained from the narrow Lorentzian profile of Al II 704.2 nm line shape. From the shift of the broadest Lorentzian one can obtain the value of electron density  $\sim 0.9 \times 10^{17} \text{ cm}^{-3}$ . From the narrow Lorentzian profile of Mg II 448.12 nm line,  $N_e \sim 2.2 \times 10^{16} \text{ cm}^{-3}$  is derived while  $N_e \sim 1.6 \times 10^{17} \text{ cm}^{-3}$  is derived from the broadest Lorentzian of Mg II line.

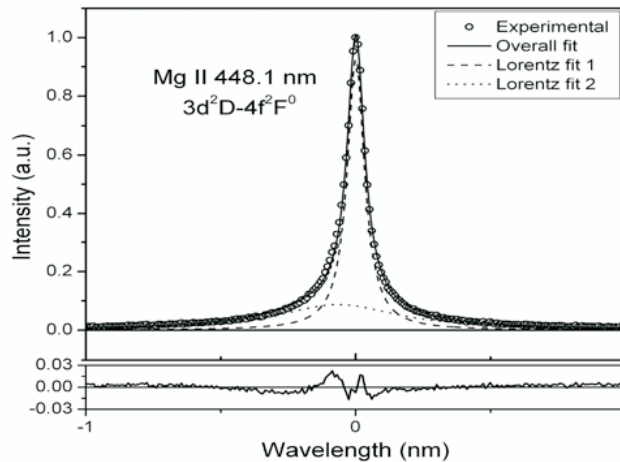


**Figure 3.** The experimental profile of Mg II  $3d^2D - 4f^2F^0$  multiplet 4 at 448.12 nm fitted with two mutually shifted Lorentzians and residue plot. The multiplet was recorded during PEO with Mg - alloy anode. The instrumental profile full-half-width 0.028 nm.

### Acknowledgement

This work is supported by the Ministry of Education and Science of the Republic of Serbia under Projects Nos. 171014 and 171035.

### REFERENCES

- [1] A.L. Yerokhin, X. Nie, A. Leyland, A. Matthews, S.J. Dowey, Surf. Coat. Technol. 122, 73 (1999).
- [2] R.O. Hussein, X. Nie, D.O. Northwood, A. Yerokhin, A. Matthews, J. Phys. D: Appl. 43, 105203 (2010).
- [3] J. Jovović, S. Stojadinović, N.M. Šišović, N. Konjević, Surf. Coat. Technol. 206, 24 (2011).
- [4] S. Stojadinovic, I. Belca, M. Tadic, B. Kasalica, Z. Nedic, Lj. Zekovic, J. Electroanal. Chem. 125, 619 (2008).
- [5] [http://physics.nist.gov/PhysRefData/ASD/lines\\_form.html](http://physics.nist.gov/PhysRefData/ASD/lines_form.html).
- [6] N. Konjević, Phys. Reports 316, 339 (1999).
- [7] N. Konjević, M. Ivković, S. Jovičević, Spectrochim. Acta Part B 65, 593 (2010).
- [8] H.R. Griem, Spectral Line Broadening by Plasmas, Academic Press, New York, 1974.

## SPECTROSCOPIC AND 2D MODELING STUDY OF THE INFLUENCE OF SMALL HYDROGEN ADDITION IN NONUNIFORM NITROGEN MICROWAVE DISCHARGE

J. Jovović<sup>1</sup>, I.L. Epstein<sup>2</sup>, N. Konjević<sup>1</sup>, Yu.A. Lebedev<sup>2</sup>, N.M. Šišović<sup>1</sup>,  
A.V. Tatarinov<sup>2</sup>

<sup>1</sup>*University of Belgrade, Faculty of Physics, Belgrade, P.O. Box 368, Serbia*

<sup>2</sup>*Topchiev Institute of Petrochemical Synthesis RAS, Moscow, Leninsky  
Prospect 29, Russia*

**Abstract.** The results of spectroscopic and 2D modeling study on the influence of small hydrogen addition in nitrogen non-uniform plasma of electrode microwave discharge are presented. The axial intensity distributions of  $N_2$  337.0 nm ( $2^+$  system) and  $N_2^+$  391.4 nm ( $1^-$  system) molecular bands are determined for different hydrogen admixtures. By means of 2D modeling, spatial distributions of nitrogen molecules in  $C^3\Pi_u$  state and spatial distributions of  $N_2^+$  and  $N_4^+$  ions are determined in pure nitrogen and nitrogen-hydrogen mixtures.

### 1. INTRODUCTION

Several studies of the influence of gas addition on plasma parameters in homogeneous self-sustained discharges were carried out, see Refs. [1-4]. The mechanism of an influence of small gas addition can be more complex in non-uniform discharges like e.g. in microwave electrode discharges. As a result of inhomogeneity, the effect of gas additive in different regions of discharge can be different. One example is the influence of small amount of Ar (1-5 %) to the properties of strongly non-uniform Electrode Microwave Discharge (EMD) in nitrogen [5]. In this case, the change of plasma ion composition suggests the relation between plasma kinetics and discharge topology, which is not observed in the homogeneous discharges.

Here, we report the results of detailed spatially resolved spectroscopy study of the influence of small hydrogen addition to nitrogen EMD supported with results of 2D modeling. This study is an extension of the previous spectroscopic and 1D modeling investigation, presented in [6].

### 2. EXPERIMENTAL

Experiments were performed with EMD source which is described in detail in Ref. [7]. The only difference now is design of cylindrical copper antenna tip, which has now conical truncated tip instead of a tungsten rod with sharp conical ending, see Fig. 1.

The experiments were carried out in pure nitrogen (99.999 %) and nitrogen-hydrogen mixtures ( $N_2+1\% H_2$ ,  $N_2+5\% H_2$  vol.) at 1 Torr gas pressure and 60 sccm gas flow rate. The incident microwave power was  $\approx 125$  W. Spectroscopic measurements were performed with 2 m Ebert type spectrometer (inverse linear dispersion 0.74 nm/mm in the first diffraction order with 651 grooves/mm grating blazed at 500 nm). The discharge image was projected on the entrance slit of spectrometer with unity magnification by means of an achromatic lens (focal length 250 mm). Thermoelectrically cooled CCD (2048 x 506 pixels, pixel size 12 x 12  $\mu\text{m}$ ;  $-10^\circ\text{C}$ ) was used as a radiation detector. The axial distribution measurements were realized by moving lens along the vertical direction (coordinate  $d$ ), in equidistant steps of 0.5 mm. A standard coiled-coil tungsten halogen lamp was used for a wavelength sensitivity calibration of the spectrometer-detector system.

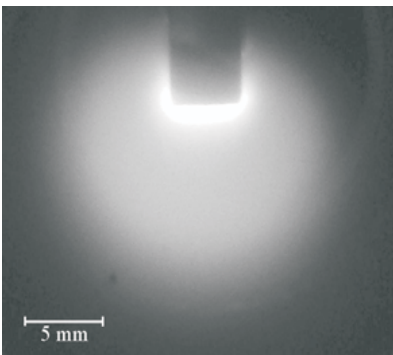


**Figure 1.** (a) The image of non-uniform microwave nitrogen discharge at 1 Torr. The incident microwave power is approximately 125 W.

### 3. RESULTS AND DISCUSSION

A self-consistent 2D model [8], incorporated in commercially available package COMSOL 3.5a [9], is used to determine spatial distributions of nitrogen molecules in  $C^3\Pi_u$  state and spatial distributions of  $N_2^+$  and  $N_4^+$  ions in pure nitrogen and in nitrogen-hydrogen mixtures.

In the simulation, the discharge pressure is set to 1 Torr, the percentage of the hydrogen additive was 1% and 5%, the gas temperature 300 K and the microwave absorbed power 30 W. The geometry and dimensions of the discharge chamber in simulations coincide with those of EMD source used in experiment.

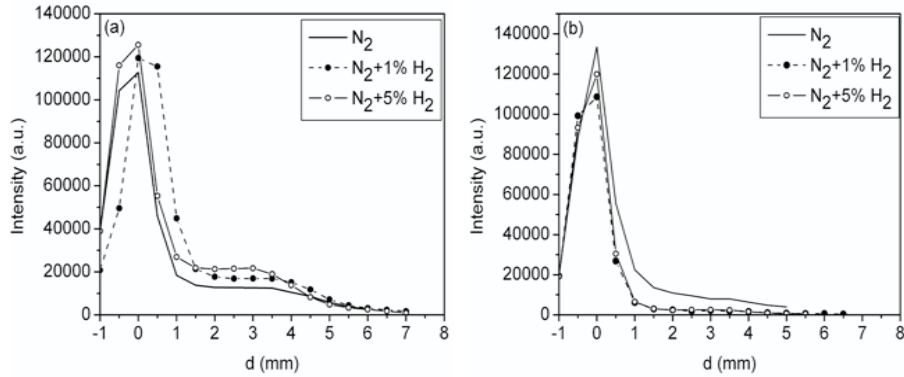


**Figure 2.** Axial intensity distributions of (a)  $2^+$  band of nitrogen and (b)  $1^-$  band of nitrogen ion at incident power 125 W in pure nitrogen,  $N_2+1\% H_2$ ,  $N_2+5\% H_2$ .

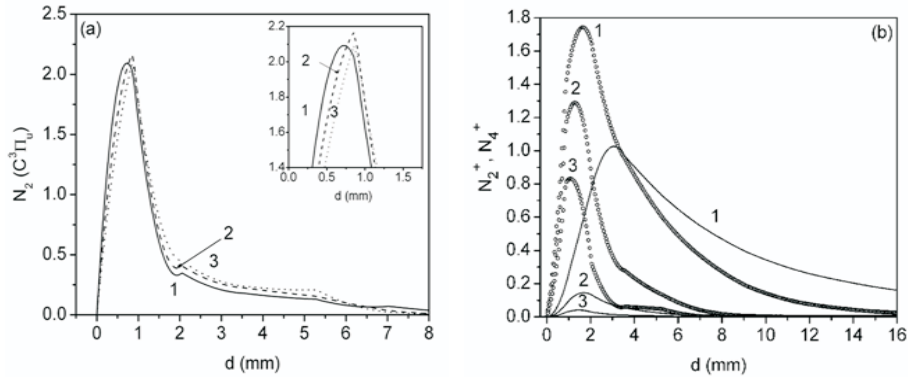


**Figure 3.** Axial profiles of concentrations of (a)  $N_2(C^3\Pi_u)$  molecules and (b)  $N_2^+$  (dotted) and  $N_4^+$  (solids) ions in (1) pure nitrogen, (2)  $N_2+1\%H_2$  and (3)  $N_2+5\%H_2$ . Concentrations are normalized to the critical plasma electron density  $n_c$  ( $n_c \approx 7 \times 10^{10} \text{ cm}^{-3}$ )

The change of axial distributions of  $2^+$  and  $1^-$  system of nitrogen bands with hydrogen content is presented in Figure 2. One can see a non-monotonous change of  $2^+$  band intensity in the near electrode region and increase of  $2^+$  band intensity in the periphery of the discharge (spherical part) with addition of hydrogen. Moreover, the addition of hydrogen strongly decreases the intensity of  $1^-$  nitrogen ion emission in both, near electrode and spherical part of the discharge, see Fig 2b. The dimension of EMD is also decreasing function of hydrogen concentration.

Axial distributions of the concentration of nitrogen molecules in  $C^3\Pi_u$  state, responsible for  $2^+$  bands emission, as well as concentration of  $N_2^+$  and  $N_4^+$  ions, obtained by 2D modeling, are presented in Figure 3. The changes in concentration of  $N_2(C^3\Pi_u)$  molecules in near electrode region are similar to the experiment and show non-monotonous dependence on hydrogen concentration (compare with Fig.2a).

The increase of  $N_2$  ( $C^3\Pi_u$ ) concentration in the spherical part of the discharge with addition of hydrogen is also detected. The concentration of  $N_2^+$  ion significantly decreases, which is more pronounced in the spherical part of EMD (compare Fig. 3b and Fig. 2b). Maxima of  $N_2^+$  and  $N_4^+$  concentrations move towards the electrode along the discharge axis with addition of hydrogen. In  $N_2+5\%$   $H_2$  gas mixture, concentration of  $N_4^+$  is very small.

The  $N_2^+$  and  $N_4^+$  are principal ions in near electrode and spherical part of nitrogen EMD, respectively [8]. The results of spectroscopic and theoretical study presented in this paper shows reduction in the concentration of  $N_2^+$  and  $N_4^+$  which indicate the fast conversion reactions of nitrogen ions to  $N_2H^+$  ion [6].

### Acknowledgement

This work is supported by the Ministry of Education and Science of the Republic of Serbia under Project No. 171014 and Russian Foundation for Basic Research under grant #11-02-00075.

### REFERENCES

- [1] V.E Fortov. (ed), *Encyclopedia of Low Temperature Plasma*, Introductory vol 3, chapter 8, (Nauka, Moscow, 2000).
- [2] C. Gomes-Aleixandre, O. Sanches, A. Castro, J.M. Albella, *J Appl Phys* 74, 3752 (1993).
- [3] L. Bardos, H. Barankova, Yu.A. Lebedev, T. Nyberg, S. Berg, *Diamond Relat. Mater.* 6, 224 (1997).
- [4] J. Asmussen, Y. Gu, J. Lu, *Proceedings of 8<sup>th</sup> International Workshop "Strong Microwaves and Terahertz Waves: Sources and Applications"*, Vol 5, p. 5, Nizhny Novgorod, Russia (2011).
- [5] Yu. Lebedev, T. Mavlyudov, I. Epstein, A. Tatarinov, A. Chvyreva, *Plasma Sources Sci Technol* 21, 015015 (2012).
- [6] Yu.A. Lebedev, T.B. Mavlyudov, V.A. Shakhatov, I.L. Epstein, *High Temp* 48, 315 (2010).
- [7] J. Jovović, N.M. Šisović, N. Konjević, *Vacuum* 85, 187 (2010).
- [8] Yu.A. Lebedev, A.V. Tatarinov, I.L. Epstein, *Plasma Sources Sci Technol* 16, 726 (2007).
- [9] [http:// www.comsol.com/](http://www.comsol.com/)

## CHARACTERISTICS OF TOLUENE DEGRADATION BY WATER FALLING FILM DBD REACTOR

Vesna V. Kovačević<sup>1</sup>, Ronny Brandenburg<sup>2</sup>, Bratislav M. Obradović<sup>1</sup>, Goran B. Sretenović<sup>1</sup> and Milorad M. Kuraica<sup>1</sup>

<sup>1</sup>*University of Belgrade, Faculty of Physics, Studentski trg 12-16, 11000  
Belgrade, Serbia*

<sup>2</sup>*Leibniz Institute for Plasma Science and Technology (INP Greifswald), Felix-  
Hausdorff-Str. 2, 17489 Greifswald, Germany  
E-mail: vesna@ff.bg.ac.rs*

**Abstract.** Toluene degradation by water falling film dielectric barrier discharge (DBD) at atmospheric pressure was studied. This DBD reactor can generate non-thermal plasma with and without water falling film at one of the electrodes. The reactor enables the combined performance of non-thermal oxidation and scrubbing of soluble by-products which is beneficial for industrial applications.

### 1. INTRODUCTION

Non-thermal plasma (NTP) technologies using electrical discharges at atmospheric pressure has been widely investigated as an alternative for conventional methods of pollution control. The most distinctive characteristic of NTP as a chemical process is its ability to induce various chemical reactions via radicals and/or ions at atmospheric pressure and room temperature, while conventional methods based on thermal incineration require the heating of the entire gas stream [1-3]. In industrial processes NTP is usually combined with catalyst, adsorbents or scrubbing. The simultaneous use of gas discharge and scrubbing (hybrid process) for the removal of hydrocarbons has already been described in [3]. The NTP can convert nonsoluble compounds into soluble, which can be scrubbed. Recently, a novel water falling film dielectric barrier discharge (DBD) has been developed and investigated for water purification [4]. It is featured by a very compact design, while the enclosed gas gap enables the treatment of gases, too. This contribution presents application of this reactor for removal of volatile organic compounds (VOCs). The motivation is to demonstrate the synergetic effect of simultaneous NTP-treatment and scrubbing for the degradation of toluene as a typical water-insoluble VOC.

## 2. EXPERIMENTAL SET-UP

A schematic overview of experimental set-up is given in Fig. 1. The reactor consists of two electrodes and a dielectric barrier, placed concentrically. The dielectric is a quartz tube with the inner diameter of 26 mm, length of 500 mm. The inner electrode is made of stainless steel with an external diameter of 20 mm and a length of 500 mm. An outer electrode made of aluminum foil (length 400 mm) is wrapped around the quartz tube. When the discharge source works as water falling film reactor, water flows up through the vertical hollow cylindrical electrode and flows down making a thin film over the electrode. Water flows from the reservoir through the discharge by means of a peristaltic pump, with a flow rate of 100 mL/ min.

The low frequency ac power supply used in this study consists of a high voltage transformer and a frequency inverter. For this reactor configuration optimal operating conditions are found to be at frequency of 300 Hz. The DBD is generated within  $\sim 3$  mm gap by applying voltage of up to 20 kV. The inner electrode is grounded via capacitor of 470 nF and the outer electrode is connected to power supply. Electrical parameters were measured using a digital oscilloscope Tektronix DPO 4104 (1 GHz bandwidth, 5 GSamples/s) and a high voltage probe Tektronix P6015A. Lissajous figures were used for the determination of energy dissipated into the plasma in one period of the applied voltage. Gas containing toluene ( $C_6H_5CH_3$ ) was prepared by mixing synthetic air (80% nitrogen, 20% oxygen) and toluene from test gas cylinder (50 ppm of toluene in nitrogen, Air Liquide). IR analysis of gas composition was performed with FTIR spectrometer Bruker Alpha (Bruker Optik GmbH, Germany). Also, Gasmeter CR-2000 (Ansyco, Germany) FTIR spectrometer was used for online quantitative gas analysis. For continuous monitoring of the concentration of total hydrocarbons in the plasma treated gas, flame ionizing detector FID TESTA 2010T (TESTA GmbH, Germany) was used. Conversion of toluene was determined by FID analyzer using measured initial concentration of total hydrocarbon (TOC) at the exit of the reactor and concentration of total hydrocarbon as a function of specific energy density (SED; derived from the discharge power and gas flow).

## 3. RESULTS AND DISCUSSION

Conversion efficiency of toluene with respect to the SED and presence of water film in the reactor is presented in Fig. 2 for two initial concentrations (20 ppm and 40 ppm). In plasma treated air without toluene  $HNO_3$ ,  $N_2O$  and  $O_3$  were formed (not shown). Toluene degradation products are presented in Fig. 3.  $CO_2$ , CO and formic acid ( $HCOOH$ ) in very small concentrations were identified as the major products of toluene degradation.

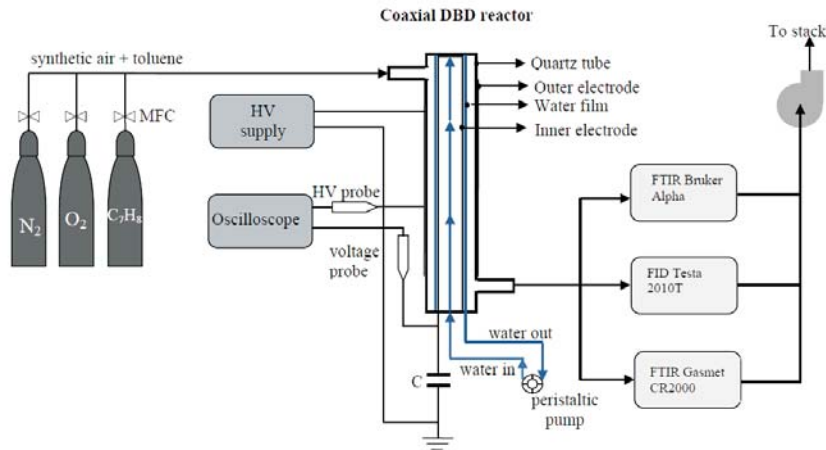


**Figure 1.** Schematic overview of experimental setup.

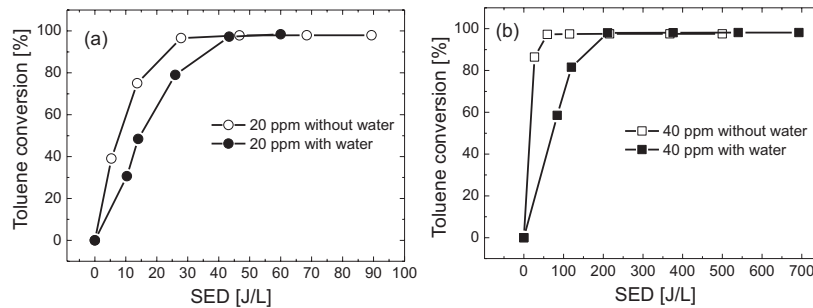


**Figure 2.** Toluene conversion for initial concentration of: a) 20ppm and b) 40ppm.

Examples of FTIR spectra obtained in air-toluene mixtures for initial toluene concentration of 20 ppm are presented in Fig. 4. About 97 % of initial toluene (20 ppm) can be decomposed with an SED of 28 J/L. The energy consumption for the degradation of toluene significantly increases with increasing initial concentration. The absence of formic acid and nitric acid absorption bands (Fig 4b) in the FTIR spectra of gas treated in discharge with water flow inside the reactor indicated the scrubbing of soluble by-products from the gas phase. This significantly improves the pollution control processes where plasma converts non-soluble pollutants into soluble ones.

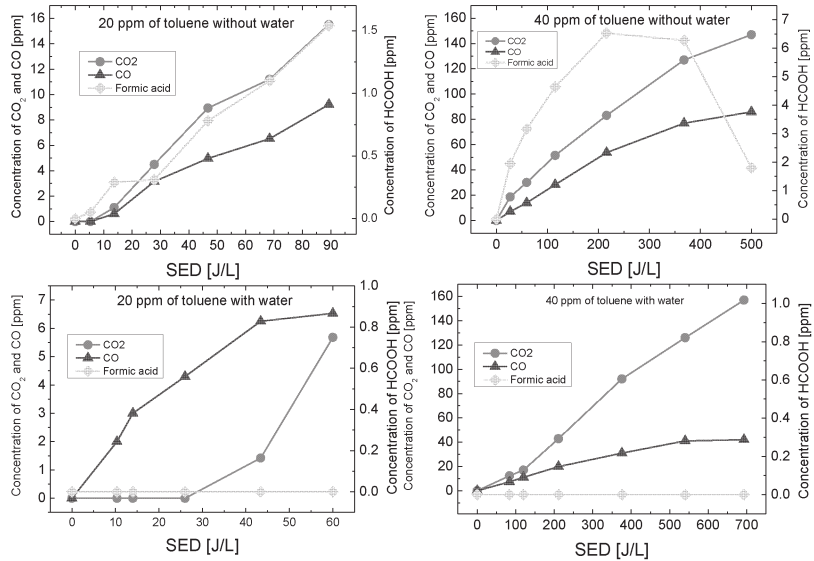


**Figure 3.** CO<sub>2</sub>, CO and HCOOH concentrations as a function of specific energy density presented for different initial concentrations of toluene.

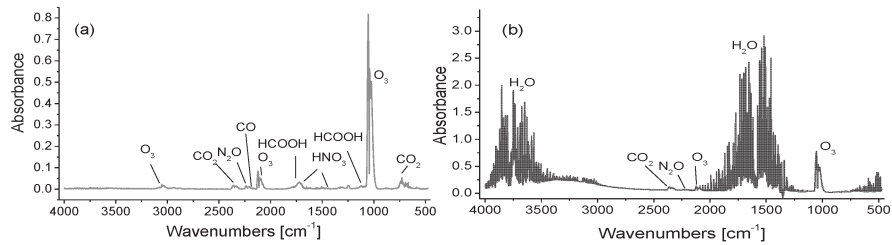


**Figure 4.** FTIR spectra of air containing toluene after plasma treatment: (a) without water and (b) with water at 10 kV.

### Acknowledgements

This study is supported by the Ministry of Education and Science of the Republic of Serbia (projects No. 171034 and No. 33022) as well as the project “PlasTEP” (part-financed by the EU).

### REFERENCES

- [1] Kim H. H., *Plasma Process. Polym.*, 1, (2004), pp. 91–110.
- [2] Penetrante B. M., Brusasco R. M., Merritt B. T. and Vogtlin G. T., *Pure Appl. Chem.*, (1999), 71, pp. 1829-35.
- [3] Fridman A., Chirokov A. and Gutsol A., *J. Phys. D: Appl. Phys.* 38, (2005), R1- R24
- [4] Kuraica M. M., Obradović B. M., Manojlović D., Ostojić D. R. and Purić J., *Vacuum* 73, (2004), pp. 705-708.

## MEASUREMENT OF $N_2(X, v=19)$ METASTABLES DURING THE NITROGEN POST-DISCHARGE BY MERCURY VAPOR TITRATION

Frantisek Krcma, Vera Mazankova, Ivana Teslikova

*Brno University of Technology, Faculty of Chemistry, Purkynova 118, 612 00  
Brno, Czech Republic*

**Abstract.** The pure nitrogen DC discharge in flowing regime was used for the presented measurements. The experiments were carried out at the constant applied energy. The total gas pressure was varied in range of 500–3000 Pa at nitrogen flow in the range of 120–680 sccm that ensured the constant flow velocity for all gas pressures. Mercury vapor was introduced into the system by the titration tube at different post-discharge times. The mercury line at 254 nm was excited by the resonance energy transfer reaction during collisions of mercury atoms with nitrogen ground state metastables excited to vibrational level 19. Thus this technique allows an indirect qualitative study of highly excited nitrogen ground state metastables that are not determinable by any other contemporary diagnostics.

### 1. INTRODUCTION

The post-discharge phenomena in nitrogen and various nitrogen based mixtures have been studied extensively for more than 50 years but still there are many open questions [1, 2]. It is well known that all kinetics is strongly dependent on the metastables [3] that can carry very high excitation energy up to 7 eV [4]. The electronically excited metastables like  $N_2(A^3\Sigma_u^+)$  or  $N_2(a^1\Pi_g, a'^1\Sigma_u^-)$  can be detected directly by weak spectral emission or by laser absorption techniques. Unfortunately, the main energy during the post-discharge period is kept in vibrationally excited ground state metastables that have extremely long lifetime and nowadays there is no suitable diagnostic technique allowing their direct or non-direct determination. Recently, we found a collisionally induced resonance energy transfer reaction between nitrogen  $N_2(X^1\Sigma_g^-, v=19)$  molecules and mercury atoms [5]. Our contemporary knowledge allows qualitative observations of these highly excited molecules by a mercury vapor titration during the post-discharge. The presented results clearly demonstrate the qualitative changes in  $N_2(X^1\Sigma_g^-, v=19)$  concentration during the pure nitrogen post-discharge at selected pressures.

## 2. EXPERIMENTAL

The DC flowing post-discharge was used for the experimental study. A simplified schematic drawing of the experimental setup is given in Fig. 1. The active discharge was produced in a Quartz discharge tube with a 120 mm electrode distance and the constant discharge power of 130 W. The total gas pressure was varied in the range of 500–3000 Pa. Hollow molybdenum electrodes were placed in the side arms of the main discharge tube. Nitrogen was of 99.9999% purity and it was further cleaned by an Oxiclear trap. The reactor system was pumped continuously by a rotary oil pump. The gas flows were controlled by Bronkhorst mass flow controllers. The flow of nitrogen was varied in the range of 120–680 sccm that ensured the constant flow velocity for all gas pressures. Mercury vapor was introduced into the system by a titration tube at different post-discharge times. The titration capillary (i.d. 0.5 mm at the end) was made of Pyrex and it was immersed upstream from the discharge into the post-discharge tube at its axis. The mercury vapor was introduced into the system by an auxiliary pure nitrogen flow with the fixed flow rate of 7.5 sccm.

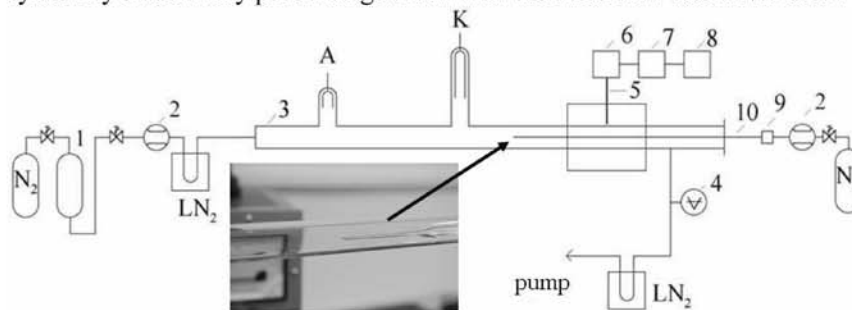
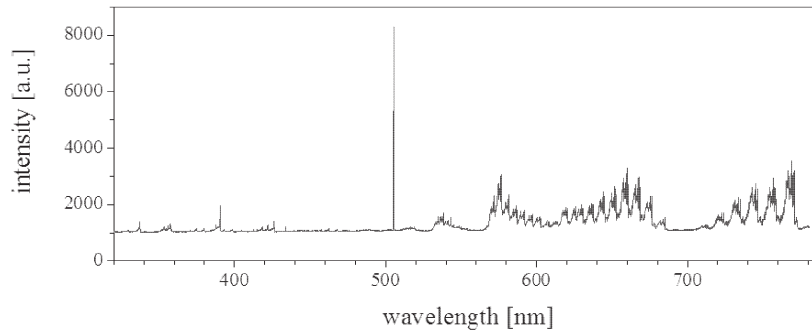


**Figure 1.** Scheme of the experimental set up. 1 – catalyzer Oxiclear; 2 – mass flow controller; 3 – Quartz discharge tube; 4 – capacitance gauge; 5 – Quartz optical fiber; 6 – monochromator Jobin Yvon Triax 550; 7 – CCD; 8 – PC, 9 – vessel with mercury; 10 – movable Pyrex titration capillary. Inserted picture: Detail of the titration capillary end.

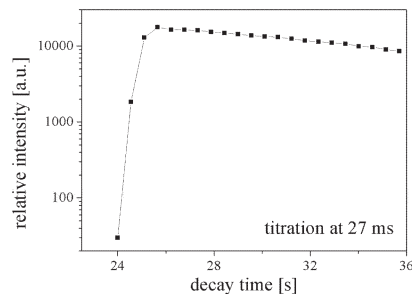
## 3. RESULTS

Figure 2 shows an example of the optical emission spectrum during the post-discharge. The mercury line at 508 nm (spectrum of the second order) is well visible besides nitrogen first and second positive and first negative spectral bands. The maximum mercury line emission is observed before the titration point (see Fig. 3) because mercury is introduced into the post-discharge backward to the main gas flow and the gas velocity in the main stream and titration one are nearly the same. The increase of the mercury intensity is very rapid and thus we can suppose that the energy transfer reaction exciting the mercury is very fast however its value is not known up to now. The mercury intensity slowly and more or less exponentially (figure is semilogarithmic)

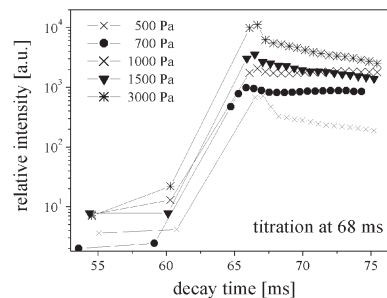
decreases after its maximal value (at position of about 2 ms before the titration point). This reflects further excitation of the  $N_2(X^1\Sigma_g^-, v = 19)$  molecules by up pumping processes.



**Figure 2.** Example of nitrogen post-discharge spectrum at the decay time of 36 ms with mercury line at 254 nm observed in the second order spectrum (i.e. at 508 nm). Mercury was introduced at decay time of 27 ms.



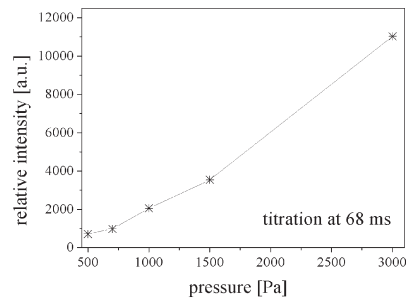
**Figure 3.** Emission response on the mercury addition (1 kPa).



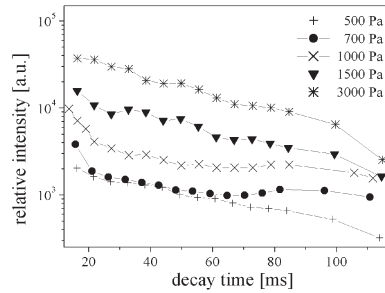
**Figure 4.** Emission response on the mercury addition at later decay time for selected gas pressures.

Figure 4 demonstrates an emission response on the mercury titration at the later decay times. It can be pointed that the shape of the response is nearly independent on the total gas pressure and the mercury line intensity reaches its maximal value at the same time position. Thus we can suppose that the maximal mercury line intensity fully corresponds to its precursor concentration.

Figure 5 demonstrates that maximal mercury line intensity is directly proportional to the total gas pressure at given experimental conditions (mainly at the fixed applied power). Finally, Fig. 6 shows the complete set of the results obtained during this experimental work. It clearly shows the more or less exponential decrease of the mercury maximal intensity during the post-discharge at all experimental conditions. The time at x-axis means the time of the mercury titration position. The observed differences from the exponential dependence at some pressures will be a subject of the further research.



**Figure 5.** Pressure dependence of the maximal mercury line intensity at the selected decay time.



**Figure 6.** Mercury line maximal intensities during the post-discharge for selected gas pressures.

#### 4. CONCLUSION

The presented work showed the first results of a highly excited nitrogen ground state metastables presence during the pure nitrogen post-discharge obtained by the newly developed mercury vapor titration method. The results showed that concentration of the  $N_2(X^1\Sigma_g^-, v = 19)$  state is nearly directly proportional to the total gas pressure at the fixed applied power. Concentration of these metastables is exponentially decreasing during the post-discharge period as we have expected.

#### Acknowledgements

This work was supported by the Czech Science Foundation, projects No. 202/08/1106 and No. 104/09/H080.

#### REFERENCES

- [1] A. Kurnosov, A. Napartovich, S. Shnyrev, M. Cacciatore, *J. Phys. Chem. A* 111, 7057 (2007)
- [2] V. Guerra, P. A. Sa, J. Loureiro, *J. Phys. D, Appl. Phys.* 34, 1745 (2001)
- [3] J. Loureiro, V. Guerra, P. A. Sa, C. D. Pintassilgo, M. L. da Silva, *Plasma Source Sci. & Technol.* 20, 024007, 2011
- [4] F. R. Gilmore, R. R. Laher, P. J. Espy, *J. Phys. Chem. Ref. Data* 21 1005 (1992)
- [5] V. Kanicky, V. Otruba, A. Hrdlicka, P. Krasensky, F. Krcma, *J. Atom. Anal. Spectrom.* 22, 754 (2007)

## LOW-TEMPERATURE AIR PLASMA PRE-SOWING SEEDS TREATMENT AGAINST PHYTOPATHOGENIC FUNGI AND BACTERIA

Irina Filatova<sup>1</sup>, Viktor Azharonok<sup>1</sup>, Svetlana Goncharik<sup>1</sup>, Galina Gadzhieva<sup>2</sup>  
and Alexander Zhukovsky<sup>2</sup>

<sup>1</sup> *Institute of Physics NAS of Belarus, Nezavisimosti Ave. 68, 220072 Minsk, Belarus, E-mail: filatova@imaph.bas-net.by*

<sup>2</sup> *Institute of Plant Protection NAS of Belarus, Mira Street 2, Priluki BY-223011, Minsk District, Minsk Oblast, Belarus  
E-mail: zhukow\_a@mail.ru*

**Abstract.** An effectiveness of low pressure RF air plasma seeds pretreatment against some plant diseases caused by pathogenic fungi and bacteria has been studied. It is shown that the treatment provided fungicidal and bactericidal effects, contribute to seeds germination enhancement and the early stages of seedling development.

### 1. INTRODUCTION

Low-temperature non-equilibrium plasma is an efficient tool for thermolabile materials treatment. This method is considered functionally, energetically and ecologically as the most acceptable for surface functionalization and decontamination of biomaterials [1]. Last years it has been successfully applied in agriculture for pre-sowing seed treatment. It has been shown that plasma pre-treatment of seeds stimulate their germination and sprouting process, lead to suppression of fungal and bacterial pathogens that cause various plant diseases [1–4]. At the same time the nature of plasma interactions with biological substances still remains unclear. It is obvious, that plasma treatment influences upon morphological and sowing characteristics of seeds in different ways [5] due to the complexity of plasma producing fluxes of various neutral or ionized active species as well as energetic photons interacting with treated samples. Seeds are an extremely complex system too, and vitally important biological processes may be affected by plasma in a number of different ways.

In this paper, we have studied of the efficacy of low-pressure capacitively coupled RF plasma treatments of seeds of some important agricultural crops against plant diseases caused by pathogenic fungi and bacteria. An influence of treatments on seed germination was also investigated.

## 2. EXPERIMENTAL

Seeds of spring wheat, blue lupine (*Lupinus angustifolius*) (sort “Pershatsvet”) and maize (“Nemo 216 CB” gybride) were chosen for investigations. Tested species were treated with 5.28 MHz air plasma at a pressure 40 Pa. The discharge was operated between two plane-parallel water-cooled copper electrodes with the diameter of 120 mm placed in a stainless steel vacuum chamber with the inner volume of 53.2 m<sup>3</sup> [1]. A distance between electrodes was varied between 20 and 40 mm according to the number and size of the treated seeds. A supplied full specific RF power could be changed in a range 0.1 – 0.7 W/cm<sup>3</sup> in dependence on treatment conditions. A Petri dish with seeds to be treated by the plasma was put on the grounded electrode before the vacuum chamber pumping. The exposure duration was 2.5, 5 and 10 min.

To study an influence of vacuum on seeds germinating characteristics, a part of tested seeds were kept in vacuum chamber at the operation pressure of 40 Pa for at least 15 min.

Under the experimental conditions the gas temperature did not increase beyond 310°C. Optical emission spectra (OES) were obtained with a Compact Wide-Range Spectrometer S100 “SOLAR LS” in the optical range from 190 to 1100 nm with average spectral resolution of 1 nm to identify the species present in plasma during the treatment.

The effectiveness of pre-sowing plasma seed treatments was examined by means of evaluation of the laboratory germination ability, seed vitality, biometric characteristics (mean root and plant length) as well as a level of fungal infection on sprouting seeds for treated and untreated (control) samples. Seeds were grown on a moist filter paper in sterile Petri dishes in a thermostat at 20° C (for wheat and lupine) and 25° C (for maize) under a light-dark regime. The seed germination and the seed infection were estimated after 7 and 10 days incubation for wheat and lupine/maize correspondingly.

## 3. RESULTS AND DISCUSSION

It has been found that plasma pretreatments of seeds positively influenced their germination and biometric characteristics of sprouts (Fig. 1). The plasma treatment of seeds with low germination ability (spring wheat, maize) stimulated their germination and the early stages of seedling development, while it did not affect negatively the germination of seeds with high germination ability (lupine). The seed pre-treatments for 2.5 and 5 min were the most effective for seeds germination enhancement for all species. The seedling of spring wheat was 2.1 cm higher for treated seeds than that in the control (Fig. 1b). The same result was observed for maize seeds as a result of plasma treatment during 2.5 min. Large seedlings have higher survival and growth rates than small seedlings that will provide the good conditions for plant growth at the later stages of ontogenesis.

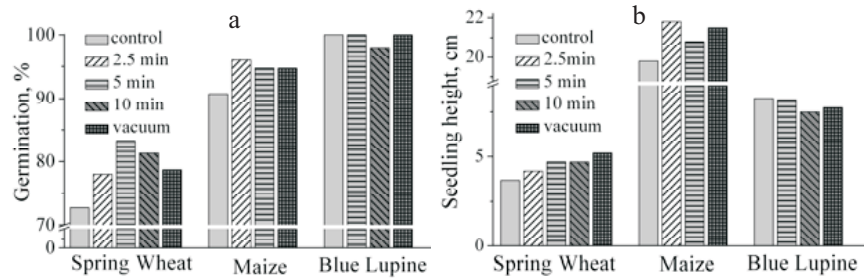


**Figure 1.** Germination (a) and seedling height (b) of spring wheat, maize and blue lupine as a result of plasma and vacuum seed pre-treatments.

The control seeds of spring wheat were infected mainly with *Fusarium spp.* and *Alternaria spp.*, seeds of maize – with *Fusarium spp.* and *Penicillium spp.*, blue lupine seeds – with pathogenic fungi *Colletotrichum gloeosporioides* and *Kabatiella caulivora*, saprophytic fungi (*Alternaria spp.*, *Cladosporium spp.*, *Mucor spp.*, *Penicillium spp.*) and bacteria (Fig. 2).

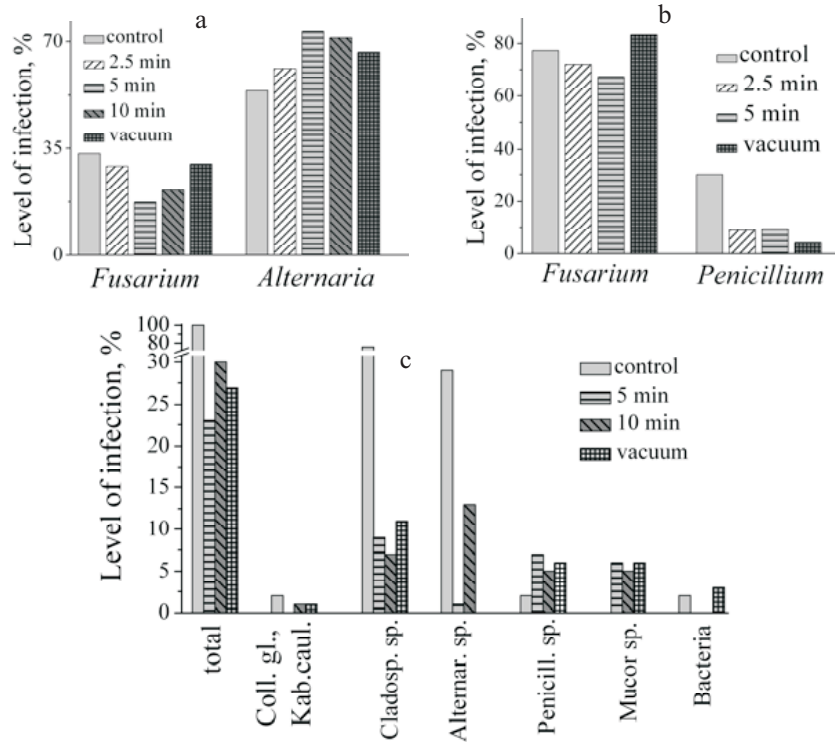


**Figure 2.** Seeds infection level of spring wheat (a), maize (b) and blue lupine (c) with pathogenic fungi and bacteria as a result of plasma seed pretreatments.

The wheat seeds exposure to plasma for 10 min resulted in decrease of *Fusarium* by 17 %. The maize seeds treatment suppressed by 12% and 20% *Fusarium* and *Penicillium* correspondingly (Fig. 2a, b). A significant decrease (by 77%) was observed in the total infection level of blue lupine seeds after the treatment for 5 min (Fig. 2c). At the same time no fungicidal effect on the spring wheat seeds was observed against *Alternaria* (Fig. 2a). We have even observed a stimulative effect on *Alternaria* growth after the treatment. This fact needs additional further investigations for verification.

The inactivation is attributed to the reactive oxygen species and radicals generated in plasma due to the oxygen contained molecules dissociation that was revealed from the OES investigations of the discharge plasma [1, 6].

#### 4. CONCLUSIONS

This study shows that the low temperature air plasma pre-treatment of seeds of some important agricultural crops is an effective tool against a number of pathogenic fungi and bacteria that cause severe plant diseases. The treatment improves germination percentage, shoot and root growth for seeds with low germination ability (spring wheat and maize). The most effective fungicidal and bactericidal effects achieved for the seeds with high germination ability. It was observed drastic reduction of the total infection level of blue lupine seeds that decreased from 100% in the control up to 23% for the plasma treated seeds during 5 min. Further studies are necessary for the other crops or groups of crops with different germination ability to explain the observed inability of the plasma treatment to suppress growth of *Alternaria spp.* on the tested spring wheat seeds.

#### Acknowledgements

This work is partly supported by the Belarusian Republican Foundation for Fundamental Research under the grant No Ф11СРБ-015.

#### REFERENCES

- [1] Z. Machala et al. (eds.), *Plasma for Bio-Decontamination, Medicine and Food Security*, p. 469, (NATO Science for Peace and Security Series A: Chemistry and Biology, Springer, Berlin, 2012).
- [2] A. Dubinov, E. Lazarenko, and V. Selemir, *IEEE Trans. Plasma Sci.* 20, 180 (2000).
- [3] M. Selcuk, L. Oksuz, and P. Basaran, *Bioresource Technology*, 99, 5104 (2008).
- [4] S. Živković et al., *Seed Science and Technology*, 32, No. 3, 693 (2004).
- [5] B. Será et al., *IEEE Transactions on Plasma Science*, 38 2963 (2010).
- [6] V. Azaronok et al., *Rom. Journ. Phys.*, 56, Supplement, 62 (2011).

## ELECTRICAL AND SPECTRAL CHARACTERISTICS OF DBD PLASMA JET

Ivan B. Krstić, Goran B. Sretenović, Vesna V. Kovačević, Bratislav M. Obradović, and Milorad M. Kuraica

*University of Belgrade, Faculty of Physics, P.O. Box 44, 11000 Belgrade,  
Serbia*

*E-mail: ivan@ff.bg.ac.rs*

**Abstract.** Electrical and spectroscopic investigations of the low frequency DBD plasma jet in helium have been performed. Different discharge characteristics for the positive and the negative half cycle of the voltage signal are examined. During the positive half cycle the discharge works in the bullet/streamer mode, while in the negative half cycle it works more like a glow-like dielectric barrier discharge.

### 1. INTRODUCTION

Atmospheric-pressure plasma jet may exist in three distinct operating modes: the chaotic mode, the bullet mode and the continuous mode [1]. This study will be focused on the atmospheric-pressure plasma jet operating in the bullet mode. Dawson's photon-ionization theory gives a possible explanation of propagation mechanism of plasma bullet [1]. It claims that the streamer head consists of numerous positive ions which emit photons able to create photoelectrons at a small distance in front of the head. The high electric field between photoelectrons and positive streamer head causes rapid electron acceleration, thus producing an avalanche. Provided that the avalanche produces a sufficient number of electrons, the streamer head is neutralized completely resulting in the creation of a new positive region a small distance ahead of the original streamer head. The most recent modeling of bullet propagation in atmospheric pressure helium plasma jets predicts that plasma bullet has streamer characteristics, such as velocity and electric field [2, 3]. Those predictions are confirmed experimentally by electric field measurements based on the Stark polarization spectroscopy of He I 492 nm line [4, 5]. Streamer/bullet properties of the plasma jet are observed in the positive voltage half cycle, while in the negative half cycle jet operates more as a glow-like atmospheric pressure discharge. It is found that the electric field is high along the whole plasma jet for the positive current pulse, with values up to 30 kV/cm. On the other hand for the negative current peak splitting of the He I 492 nm line is not recorded which

suggests different discharge operation mode. Based on the measurement results of spatial distributions of characteristic excited species, excitation mechanisms and behavior of main species in the jet are discussed. Role of the metastables and Penning ionization is highlighted, too. It is found that these results agree with Dawson's photon ionization theory.

## 2. RESULTS AND DISCUSSION

Experimental set-up and measurements procedures can be found in our other publications [4, 5]. Fig. 1(a) presents recorded current and voltage signals of the plasma jet operating in the bullet mode. It is obvious that each half cycle is characterized by one strong current peak, typical for some types of the dielectric barrier discharges. Magnitude of the current is significantly higher in the positive half cycle than in the negative one which implies two different operational regimes of the plasma jet in the each cycle.

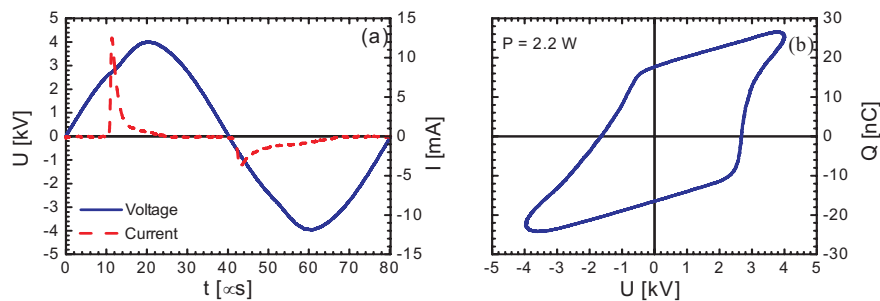


**Figure 1.** (a) Current and voltage signals of the plasma jet operating in the bullet mode. (b) Lissajous figure (Q-U plot) showing dissipated power.

Charge versus voltage (Q-U) plot, i.e. Lissajous figures is presented in the Fig. 2(b). Lissajous figure is asymmetrical due to the asymmetric arrangement of the discharge. Low discharge power of about 2 W is characteristic for the bullet mode and in agreement with measurements presented in other studies [1]. Cross-sections of the line with x-axis on the Q-U graph show breakdown voltages for both negative and positive cycle. As can be seen from the Fig. 2(b) breakdown occurs at 2.8 kV for the positive half cycle, which is much more than for the negative half cycle when 1.6 kV is required. This is due to accumulation of negative charge i.e. electrons on the inner walls of the glass tube in the positive half cycle. This fact decreases required breakdown voltage in the negative half cycle. That is not the case for the grounded copper electrode.

An overview spectrum in the UV-visible-near IR range (200 – 900 nm) is presented in Fig. 2. This fully qualitative method can give information

about presence of some reactive species desirable or necessary for some discharge applications, particularly plasma medicine. As can be seen from the presented spectrum NO- $\gamma$  system, nitrogen second positive system – N<sub>2</sub> (C-B), OH (A-X), nitrogen first negative system - N<sub>2</sub><sup>+</sup> (B-X) and some O I, H I and He I lines could be detected. Atomic oxygen, hydroxyl radical and NO are some of the most important reactive species in plasma medicine applications. Presence of atomic oxygen directly points out the presence of the ozone, and vice-versa which is also important factor for such applications. Relatively high intensity of the N<sub>2</sub><sup>+</sup> (B-X) comes from the resonant reaction channel between metastables of helium and nitrogen in the ground state, which produce very effective excited ions N<sub>2</sub><sup>+</sup> (B<sub>2</sub> $\Sigma_u^+$ )<sub>v'</sub>. This Penning process is followed by the emission of the first negative system. The second positive system of nitrogen is mainly produced by direct electron excitation. Emission of He I 706 nm line (3s<sup>3</sup>S state, threshold energy of 22.7 eV) which is an indicator of energetic electrons is also observed [1]. Due to the significant amount of water vapor in open air abundant emission of OH (A-X) is detected. The formation of OH (A) comes through a direct dissociative electron excitation of water or dissociative recombination of H<sub>2</sub>O<sup>+</sup> or H<sub>3</sub>O<sup>+</sup>. If the ground state OH (X) density is sufficiently large, direct electronic excitation to OH (A) can play substantial role, too.

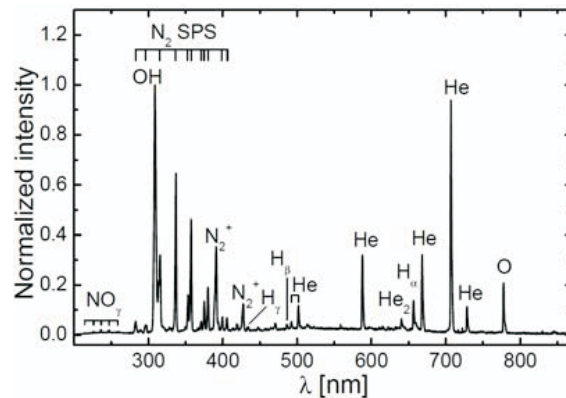


**Figure 2.** Optical emission spectrum of the low frequency DBD plasma jet.

The spatially resolved intensity distributions of the 1 cm DBD plasma jet are presented in Fig. 3. This figure shows the normalized intensities of some lines and bands for positive and negative current peaks. The intensity distributions of the He I 706 nm line, O I 777 nm line, H $\beta$  486 nm line, OH band in the range of 306-309 nm, and nitrogen second positive system (SPS) and first negative system (FNS) at 337 nm and 391 nm respectively. Depending on the excitation mechanism of radiative states, two groups of lines/bands can be distinguished: direct excitation by energetic electrons and indirect excitation involving metastables. First group (He 706 nm and N<sub>2</sub> SPS 337 nm) correspond

to the high electric field and electron density and its appearance follows the current pulse. The second group (O I 777 nm, H $\beta$  486 nm, OH 306-309 nm and N $_2^+$  391 nm) is usually delayed in respect to the current pulse due to the necessary preceding dissociation or ionization of existing species and participation of metastables in these processes. From the Fig. 3(a) enormous difference between intensities for the positive and the negative current peaks suggests significant existence of energetic electrons only for the positive current peak, while for the negative current peak, the intensity of the line is non-negligible only near the grounded electrode – instantaneous anode. This evidence supports earlier claim that plasma bullets tend to form in the positive half-cycle which is confirmed by measurements presented in Ref. 4.

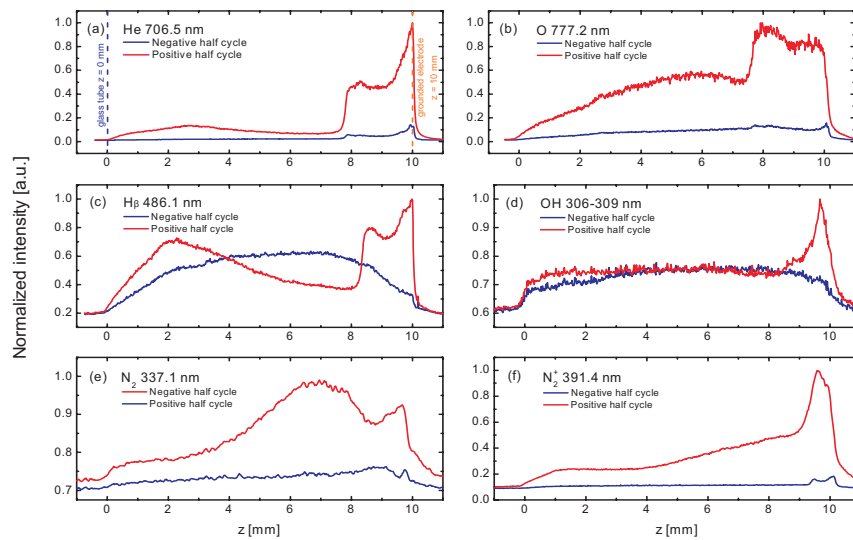


**Figure 3.** Spatially resolved intensity distributions of various emissions for the positive and the negative current peaks of the jet.

### Acknowledgements

This work is supported by the Ministry of Education and Science of the Republic of Serbia through the Project No. 171034 and the Project No. 33022.

### REFERENCES

- [1] J. L. Walsh et al., J. Phys. D: Appl. Phys. 43, 075201 (2010).
- [2] G. V. Naidis, J. Phys. D: Appl. Phys. 43, 402001 (2010).
- [3] G. V. Naidis, J. Phys. D: Appl. Phys. 44, 215203, (2011).
- [4] G. B. Sretenović et al., Appl. Phys. Lett. 99, 161502 (2011).
- [5] G. B. Sretenović et al., IEEE Trans. Plasma Sci. (2012) *submitted*.

## SPECTROSCOPIC TEMPERATURE MEASUREMENTS IN DEUTERIUM HOLLOW CATHODE GLOW DISCHARGE

Gordana Lj Majstorović<sup>1</sup> and Nikola M Šišović<sup>2</sup>

<sup>1</sup>*University of Defence, Military Academy, 11105 Belgrade, Pavla Jurišića –  
Šturma 33, Serbia*

*e-mail: gordana.majstorovic@va.mod.gov.rs*

<sup>2</sup>*University of Belgrade, Faculty of Physics,  
11001 Belgrade, P.O. Box 368, Serbia*

**Abstract.** The results of the radial distribution of rotational temperature  $T_{rot}$  of deuterium molecules in a hollow cathode (HC) glow discharge is reported. The optical emission spectroscopy measurements are carried out using titanium hollow cathode discharge operated in pure deuterium. The rotational temperature of excited electronic states of  $D_2$  was determined from relative line intensities of the Q [ $v'=v''=2$ ] branch of the Fulcher- $\alpha$  diagonal band.

### 1. INTRODUCTION

The hollow cathode glow discharges (HCGD) have been extensively used for study of fundamental discharge processes [1], as well as for plasma assisted technologies [2]. For both, fundamental and applied research, the knowledge of discharge parameter like the translational gas temperature  $T_t$  of molecules and radicals is of a particular importance since it determines the rate of chemical reactions.

Recently, the rotational, vibrational and translational temperatures of hydrogen molecules in the hollow cathode glow discharge (HCGD) have been determined using relative line intensities within Fulcher- $\alpha$  bands [3]. The rotational temperature of excited electron energy levels is determined from the Boltzmann plot of rotational line intensities, belonging to Fulcher- $\alpha$  diagonal band ( $d^3\Pi_u \rightarrow a^3\Sigma_g^+$ ) electronic transition; P, Q and R branches ( $v'=v''=0$ ). The rovibronic temperature of hydrogen molecule ground state was assessed from results of rotational line intensities.

The aim of this paper is to investigate the results of spectroscopic measurements of rotational temperature in deuterium HCGD from  $d^3\Pi_u, v' \rightarrow a^3\Sigma_g^+, v''$  transition. The experiment is carried out in deuterium discharge using titanium HC. The radial distribution of rotational temperature within hollow cathode diameter are determined as well.

## 2. EXPERIMENTAL

The HCGD source with two symmetrically positioned kovar anodes and titanium (Ti) cathode operated in deuterium is used. The HC tube was 100 mm long with 6 mm internal diameter and 1 mm wall thickness. The discharge source is described in details elsewhere [3,4]. Here, only few important information related to the optical setup for spectra recordings will be described. The radial distribution spectra recordings were performed with unity magnification in equidistant steps perpendicular to the discharge axis, with an estimated spatial resolution of 0.40 mm. For radial intensity measurements the discharge was run between HC and rear anode, located at 20 mm from the cathode. The results of test measurements using front or rear anode did not show a difference within experimental uncertainty. The light from the discharge was focused with an achromat lens (focal length 75.8 mm) onto the entrance slit of a Carl Zeiss PGS-2 spectrometer (2 m focal length with 651 g/mm reflection grating; the reciprocal dispersion of 0.74 nm/mm in first diffraction order). All spectral measurements were performed with an instrumental profile very close to Gaussian form with measured full half-width of 0.018 nm. Signals from CCD detector (29.1mm length, 3648 channels) are A/D converted, collected and processed by PC.

## 3. RESULTS AND DISCUSSION

In the previous study we used Q-branch ( $\nu'=\nu''=0$ ) of the Fulcher- $\alpha$  diagonal bands as the most reliable for hydrogen temperature estimation in HCGD [3]. Now, we investigate the possibility of using Q-branch ( $\nu'=\nu''=2$ ) of the  $d^3\Pi_u, \nu', N' \rightarrow a^3\Sigma_g^+, \nu'', N''$  deuterium molecular system for temperature measurement. From the example of recorded spectra in Fig. 1 it is evident that R, Q and P branch lines of the ( $\nu'=\nu''=2$ ) electronic transition are well resolved and have high intensities in the 610-630 nm wavelength region (wavelength data are taken from [5]).

First, the applicability of Hönl-London (HL) factors within  $d^3\Pi_u^+, 2 \rightarrow a^3\Sigma_g^+, 2$  transition, is investigated by means of procedure described in [6]. Since the transition probabilities are unknown for the rotationally resolved rovibrational transitions, HL factors will be used as line strengths. In such case, the so-called rotational branching ratio must be determined experimentally from line intensity ratios correlated with relative line strengths  $S_R/S_P$ . The ratios of measured line intensities within pair of lines (in R and P-branch) starting from the same rotational levels (see e.g. Grotrian diagram for Fulcher- $\alpha$  band transition,  $\nu'=\nu''=0$  in Fig. 2(a) of [3]) has been used as good indicator for applicability of HL factors for temperature measurements within  $d^3\Pi_u, 2 \rightarrow a^3\Sigma_g^+, 2$  transition.

The ratio values predicted by the HL formulae for Fulcher- $\alpha$  band ( $\Delta\nu=2, \nu'=2$ ) are plotted in Fig. 2(a) as a function of rotational quantum

number. The comparison of data shows that experimental ratio of line intensities for R and P branch is close to prediction of HL formula.

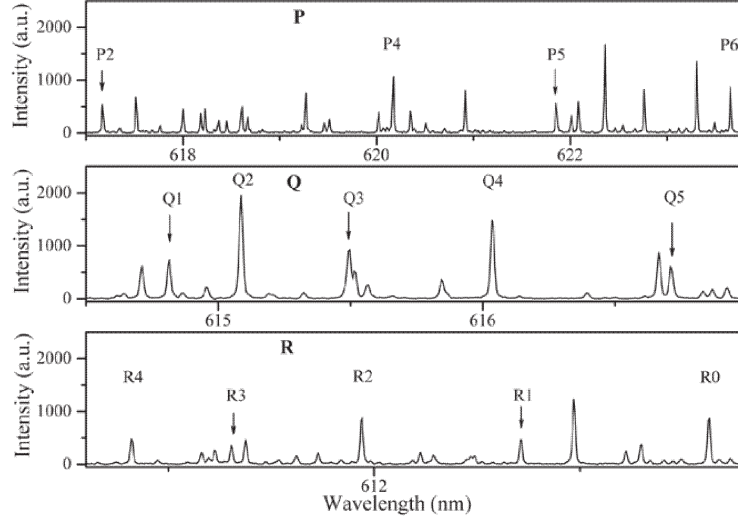


**FIGURE 1:** Emission spectra of rotational lines for  $d^3\Pi_u^\pm \rightarrow a^3\Sigma_g^+$  system; R, Q, P branches with  $\nu'=\nu''=2$ . Experimental conditions: titanium HC discharge in  $D_2$  at  $p=2.5$  mbar;  $I=90$  mA;  $U=490$ V

The rotational temperature is derived from the population of Q branch of  $D_2$  Fulcher- $\alpha$  band,  $\nu'=\nu''=2$  using HL factors and data from [5]. The values of the rotational temperature at different radial position, see part (b) of Fig. 3 show that temperature change along HC diameter, as well as radial intensity distribution of the deuterium Fulcher- $\alpha$  system with the maximum at HC axis.

In the framework of the model discussed in [7] the logarithm of the scaled rovibrational population density should be a linear function of the rotational energy in ground  $X^1\Sigma_g^+$ ,  $\nu = 0$  vibronic state:

$$\ln N_{n'\nu'N'}^* \equiv \ln \frac{N_{n'\nu'N'}}{g_{a.s.}(2N'+1)\tau_{n'\nu'N'}} = -\frac{hc E_{X0N}}{k T_0(n', \nu')} + const.$$

where is:  $N_{n'\nu'N'}^*$  - scaled rovibronic population density,  $\tau_{n'\nu'N'}$  - radiative lifetime of  $n', \nu', N'$  level and  $E_{X0N}$  - rovibronic term value of ground vibronic state. Further, according to [7], the rotational temperature of the ground vibronic state,  $T_0(n', \nu')$  can be considered as a valid estimation of the ground state rovibronic temperature i.e.  $H_2$  translational temperature  $T_{tr}$ .

Thus, values of the rotational temperature derived from the Q branch population of  $D_2$  Fulcher- $\alpha$  band ( $\nu'=\nu''=2$ ) were used in conjunction with previous relation to determine  $T_0$  of the ground vibronic state  $X^1\Sigma_g^+(\nu=0)$ . Under present experimental conditions the temperature  $T_0$  for the ground vibronic state

of deuterium molecule is two times larger than the rotational temperature of excited state  $d^3\Pi_u$ .

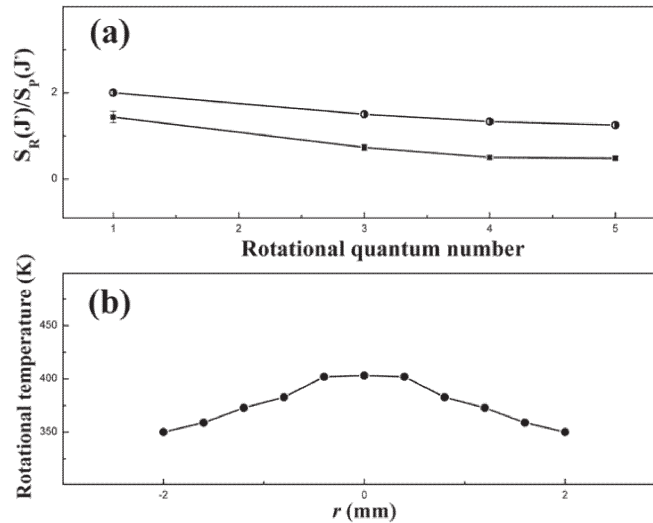


**FIGURE 2:** (a) The comparison of measured branching ratios with the ratios of Hönl-London (HL) factors for ( $\nu'=\nu''=2$ ) transition of the Fulcher- $\alpha$  band; and (b) Radial distribution of the rotational temperature measured from Q-branch ( $\nu'=\nu''=2$ ) of the Fulcher- $\alpha$  band; Discharge conditions: titanium HC discharge in  $D_2$  at  $p=2.5$  mbar;  $I=90$  mA;  $U=491$  V.

## Acknowledgements

This work is supported by the Ministry of Education and Science of the Republic of Serbia under Project No. 171014

## REFERENCES

- [1] P. J. Slevin and W.W. Harrison 1975 *Applied Spectroscopy Reviews* 10(2), 201 (2005)
- [2] C. F. Da Silva, T. Ishikawa, S. Santos, Jr. C. Alves and A. E. Martinelli *International Journal of Hydrogen Energy*, 31, 49 (2006)
- [3] N. M. Šišović, G. Lj. Majstorović and N. Konjević, *Plasma Sources Sci Technol.* 16, 750 (2007)
- [4] N. M. Šišović, G. Lj. Majstorović and N. Konjević, *Eur Phys J D* 32, 347 (2005)
- [5] R. S. Freund, J. A. Schiavone and H.M. Crosswhite *J. Chem.Phys.Ref. Data* 14, 235 (1985)
- [6] M. Osiac, B. P. Lavrov, Röpcke *JQSRT* 74, 471 (2002)
- [7] S. Astashkevich, M. Käning, E. Käning, N. V. Kokina, B. P. Lavrov, A. J. Ohl. Röpcke *JQSRT*, 56, 72 (1996)

## QUASISTATIONARY PLASMA FLOW AND EXTERNAL MAGNETIC FIELD ACTION ON THE SILICON SURFACE

Mihailo M Martinović, Ivan P Dojčinović and Jagoš Purić

*University of Belgrade, Faculty of Physics, P.O.Box 44, 11001 Belgrade, Serbia*

**Abstract.** Modification of silicon single crystal surface by the quasistationary plasma flow in the presence of external magnetic field is studied. Quasistationary plasma flow is generated by magnetoplasma compressor operating in residual mode in hydrogen as working gas ( $1 \text{ MJ/m}^2$  in 0.1 ms). During single pulse surface treatment wave-like periodic structures are obtained on the silicon samples. As a result of local overheat and surface boiling, phenomena of strong ablation appear on the surface if magnetic field is present.

### 1. INTRODUCTION

The main objective of plasma surface interaction investigation is simulation of the expected edge localized modes (ELMs) and disruption loads in ITER and other fusion devices [1]. Intense thermal loads in fusion devices which occur during ELMs will result in macroscopic erosion associated with the formation of cracks, droplets, melting, evaporation or sublimation. Compression plasma flow (CPF) action with silicon solid surface was studied here, and submicron cylindrical periodic structures were obtained [2-3]. Magnetic field influence on surface modification, as well as the material removing from surface in these conditions is represented in the form of vapour and liquid droplets caused by surface local overheat. Here is studied only a part of effects of plasma flow in presence of strong external magnetic field. Special attention was devoted to the influence of magnetic field on phenomena of ablation. It was found that intensities of these processes strongly depend on the magnetic field presence. Namely, the ablation is one of the most presented processes in the plasma flow interaction with materials if the applied magnetic field is perpendicular to the surface. It was also found that compression plasma flow parameters are strongly affected by the external magnetic field.

### 2. EXPERIMENTAL SETUP

A plasma source used in this experiment is a quasistationary plasma accelerator (plasma gun) of magnetoplasma compressor (MPC) type. MPC represents a

magnetoplasma analogue of Laval nozzle that was described in details elsewhere [4].

The plasma acceleration by the Ampere force in MPC interelectrode gap is accompanied by formation of a supersonic CPF at the outlet of the discharge device [4]. In the MPC inter electrode region the plasma is accelerated due to the Ampere force. The experimental setup is schematically shown in Figure 1.

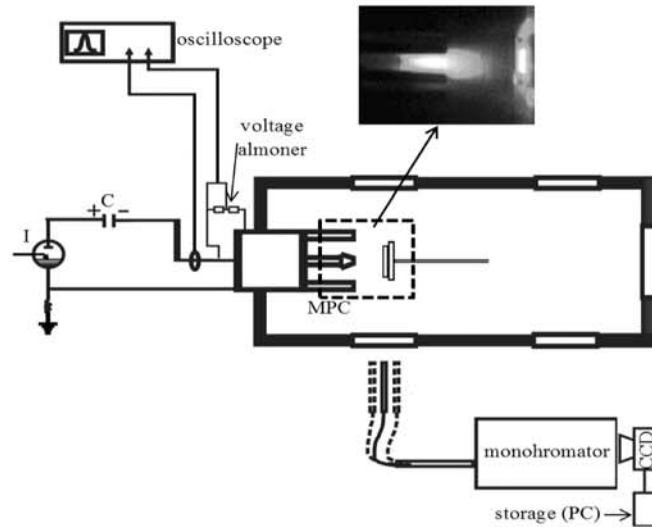


**Figure 1.** Schema of experimental setup

Using hydrogen as working gas at 1 kPa pressures and 800  $\mu\text{F}$ , 4 kV capacitor bank, the obtained current maximum was up to 100 kA and time duration up to 120  $\mu\text{s}$ . For the interaction studies of the CPF with silicon surfaces, commercial one-side polished n-type silicon wafer (100 orientation) 1 mm thick and 10 mm in diameter were used. The sample is mounted on the cylindrical brass holder of the same diameter, and placed in front of the MPC cathode at the distance of 5 cm. Two different variations of experiment were used: (i) without external magnetic field and (ii) with magnetic field oriented perpendicular to the target surface. Silicon samples are exposed to a single plasma pulse.

The optical emission spectroscopy measurements are performed by side-on observations. This enables to follow plasma flow and silicon spectral lines dynamics during whole discharge.

### 3. RESULTS AND DISCUSSION

After a single CPF treatment of silicon sample cylindrical wave-like structures have been noticed. As example of the structures obtained without presence of external magnetic field, SEM micrographs of treated Si (100) surfaces are given in Figure 2.

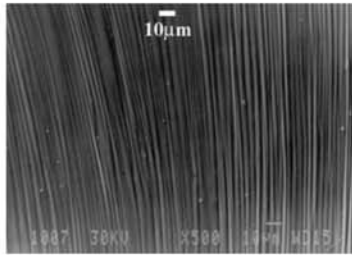


**Figure 2.** SEM photograph of silicon sample surface treated by CPF single pulse without external magnetic field

It is worth emphasizing that these highly oriented periodic structures are obtained by single plasma pulse treatment of the silicon sample surface. They are frozen capillary surface waves quenched at a particular moment during a process of melt resolidification [4].

Small craters that resemble to traces of eruptions were noticed on sample surface after being treated simultaneously by CPF and perpendicular magnetic field. SEM photo of these structures is shown on figure 3. These craters have been measured using AFM and found to be 2-3 mm in diameter. The bubble structures on target surface were observed frozen either before or after popping.



**Figure 3.** SEM photo of section of Si (100) sample treated by MPC in presence of normally orientated 480 mT magnetic field

The formation of observed surface features may be explained by energetic action of CPF on the surface (absorbed energy 10 -15 J per pulse, flow power density  $10^5$  W/cm<sup>2</sup> [4]). A typical thickness of shock-compressed plasma layer is about 1 cm [2]. Energetic action of CPF causes the fast heating and melting of the surface layer and the presence of high dynamic pressure of CPF of the order of several atmospheres. Interaction of CPF with silicon sample surface causes the evaporation of a thin surface layer and formation of a shock-compressed plasma layer (plasma plume) [5]. Formation of this cloud of dense target plasma results in shielding of a processed surface from a direct action of a CPF when perpendicularly orientated magnetic field is present. Energy transfer from plasma flow to the plasma layer induces temperature growth of both, plasma layer and surface (figure 4). Such high temperature in plasma surface layer indicates local overheat and ablation of the surface, which produces bubbling (boiling) effects where surface liquid relaxes explosively.

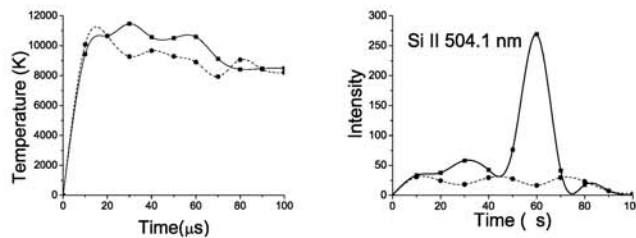


**Figure 4.** Plasma temperature (K) and spectral line intensity (arbitrary units) dependence of time results for no magnetic field presence (circles) and normally orientated magnetic field presence conditions (squares)

#### 4. CONCLUSION

From the surface structures studied here it is possible to conclude that they are similar to those originating from macroscopic erosion processes observed from the first wall and divertor surface in fusion devices. Quasistationarity of MPC plasma source is its main characteristic that makes it suitable for simulation of ELMs and their studies in future fusion devices, including ITER. Periodical wave-like patterns are observed on silicon single crystal surface treated by CPF. When perpendicularly orientated magnetic field is present in sample environment and sample itself different structures occur, such as small craters, because different phenomena take part in creating them.

#### Acknowledgements

This work is supported by the Ministry of Education and Science of the Republic of Serbia within the project 171034.

#### REFERENCES

- [1] G. Federici, P. Andrew, P. Barabaschi, J. Brooks, R. Doerner and A. Geiser, *J Nucl. Mater.* 11, 313 (2003)
- [2] J. Purić, I. P. Dojčinović, V. M. Astashynski, M. M. Kuraica, *Vacuum* 73, 561 (2004)
- [3] V. V. Uglov, V. M. Anishchik, V. V. Astashynski, V. M. Astashynski, S. I. Ananin, V. V. Askerko, E. A. Kostyukevich, A. M. Kuz'mitski, N. T. Kvasov and A. L. Danilyuk *Surf. Coat. Technol.* **158-159** 273 (2002)
- [4] J. Purić, I. P. Dojčinović, V. M. Astashynski, M. M. Kuraica and B. M. Obradović, *Plasma Sources Sci. Technol.* 13, 74 (2004)
- [5] I. P. Dojčinović, M. M. Kuraica and B. M. Obradović, and J. Purić, *Appl. Phys. Lett.* 89, 071501 (2006)

## IMPORTANCE OF MULTIPHOTON IONIZATION DURING THE CREATION OF ALUMINUM PLASMA PRODUCED BY LASER WITH MODERATE FLUENCE

*Vincent Morel(\*), Arnaud Bultel, Gilles Godard*

*UMR CNRS 6614 CORIA, Université de Rouen,  
76801 Saint-Etienne du Rouvray, France*

**Abstract.** Several phenomena are concomitant in laser-induced plasmas. Modelling the creation phase of this kind of plasma requires understanding these phenomena and their interactions. A 0D model (named CoRaM-Al) is elaborated in the purpose of providing a complete non equilibrium description of the ablation of an aluminium target. Solid heating and vaporisation of the sample, vapour excitation and ionisation processes, among others, are taken into account. The plasma is assumed to store energy in more than one hundred levels of Al, Al<sup>+</sup>, Al<sup>2+</sup>, Al<sup>3+</sup> and free electrons interacting through seven types of elementary processes. In this paper, we propose to analyse the relative role of the multiphoton ionisation and the other processes.

### 1. INTRODUCTION

Laser Induced Breakdown Spectroscopy (LIBS) is more and more used as diagnostic method in spite of awkward drawbacks. The identification of the composition of a material is an essential task and different methods can be used. Among them, LIBS is currently developed since it provides this determination in situ after few microseconds only. This method consists to light a target with a nanosecond laser pulse, therefore to create plasma and to study its radiative signature. The composition is finally derived from the comparison between the measured emission spectra and the databanks previously elaborated in laboratory from known samples. The distant objective of our work is to avoid resorting to these databanks.

The treatment of LIBS signals is classically based on the hypothesis of Local Thermodynamic Equilibrium (LTE) [1]. The conditions required to obtain plasma in LTE cannot be systematically verified. Since the interaction between the laser pulse and the sample leads to a strong initial non equilibrium, the relaxation of non-LTE plasmas can be observed. As a result, the treatment of LIBS signals assuming LTE can provide bad information in this context.

## 2. PHYSICAL MODEL

In this work, a 0D model is developed in the purpose of providing a complete description of the ablation of an aluminum alloy target. This model, called CoRaM-Al, takes into account simultaneously the laser light absorption, the sample heating, melting and vaporization, the excitation and the ionization of the species. Owing to the characteristic time scales of these phenomena, the excited states behave in a different way: as a result, a large set of excited states (107 levels of Al, Al<sup>+</sup>, Al<sup>2+</sup> and Al<sup>3+</sup>) is considered.

The main objective of the present work is to study the relaxation of the plasma produced in typical (nanosecond) laser conditions on aluminum sample from the start of the laser-sample interaction until few microseconds in the purpose of qualifying the departure from equilibrium. In order to avoid shockwave production and propagation, the sample is assumed in vacuum.

According to the laser fluence, the literature reports either classical phase transition or strong ejection of matter by droplets resulting from hydrodynamic instabilities. This latter regime is called explosion phase. The transition from the first regime to the explosion phase is observed at a threshold of  $F_0 = 8.5 \text{ J cm}^{-2}$  [2]. The present model is available to situations where the laser fluence  $F$  is under  $F_0$ . This leads also to moderate sample heating: the vaporization of the metallic pool can be therefore treated in a classical way, the temperature being less than the critical temperature  $T_c = 6700 \text{ K}$  [3].

Our model assumes a laser pulse having a Gaussian profile with a full width at half maximum of  $\tau = 4 \text{ ns}$  and a characteristic energy of  $E = 65 \text{ mJ}$ . The laser light is focused on a surface of  $d = 1 \text{ mm}$  in diameter on an aluminum target. The laser pulse is assumed completely absorbed by the sample. In order to determine the temperature profile into the target, the balanced equation for the conservation of energy is treated and the evaporation is supposed starting when the aluminum is in liquid phase ( $T_m = 933 \text{ K}$ ). Besides, the strong ejection of matter due to the vaporization relaxes inside a Knudsen layer located between the target edge and the plasma: this layer is accounted for.

The translation mode of all species is assumed in Maxwellian equilibrium, but the plasma is in non-thermal equilibrium. The plasma is described by a 2 Temperature model: electron temperature  $T_e$  and heavy temperature  $T_A$ . Each excited state behaves freely through 7 collisional radiative processes and their backward processes (Multi-photon ionization, Inverse Bremsstrahlung, electron excitation, electron ionization, elastic collisions, spontaneous emission and thermal Bremsstrahlung)

These processes induce an evolution in time of the energy of the electrons and of the heavy species (atoms and ions) respectively driven by equations (1) and (2)

$$\frac{\partial e_e}{\partial t} = P_e - \text{div}(\vec{\varphi}_e) \quad (1)$$

$$\frac{\partial e_A}{\partial t} = P_A - \text{div}(\vec{\varphi}_A) \quad (2)$$

where  $e$  is the energy of particles by unit volume,  $P$  the production term and  $\vec{\varphi}$  the energy flux density. The subscripts  $e$  and  $A$  refer respectively to the electrons and to

the heavy species. The energy flux density results from the ejection of matter from the target. Furthermore, the plasma is assumed to be uniform, such that  $\text{div}(\overline{\varphi_{e,A}})$  is equal to  $-\varphi_{e,A}/Z$  where  $Z$  is the plasma thickness. This latter parameter is assumed driven by the arithmetic mean speed resulting from the temperature  $T_A$  of the heavy species.

### 3. RESULTS

CoRaM-Al can compute the creation of the plasma considering various conditions. In this paper figure 1 illustrates the results obtained by the present model concerning the population densities and temperatures when the sample temperature evolves like the laser flux density. These results illustrate the importance of the heating of electrons by multi-photon ionization and the rapid reaching of high population densities during the laser pulse. During the conference we will present results considering a more important laser flux density and so a surface target temperature approaching the critical temperature of aluminum.

In the same conditions of laser flux density, figure 2 illustrates the influence of each process on the temperatures evolution. The scale of the Y axis corresponds to decimal logarithm of the parameter. For example, the  $n^{\text{th}}$  value means that the process induces an increase of the temperature of  $10^n \text{ K s}^{-1}$  for the positive values and a decrease for the negative values of  $n$ .

Furthermore, this figure illustrates the weak influence of the Inverse Bremsstrahlung process on the evolution of electron temperature. Besides, this figure puts forward that electronic de-excitation and ionic recombination induced by electron impact are predominant during the recombination phase.

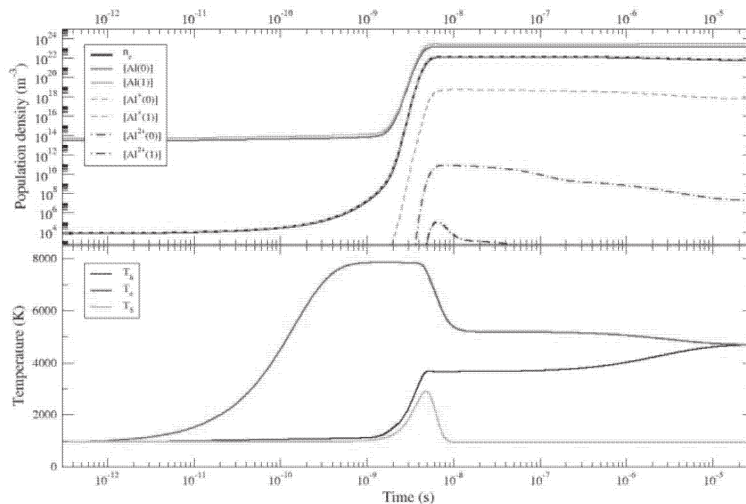


**Fig. 1.** Population density (up) and temperatures (down) of plasma components calculated by the CoRaM-Al model.

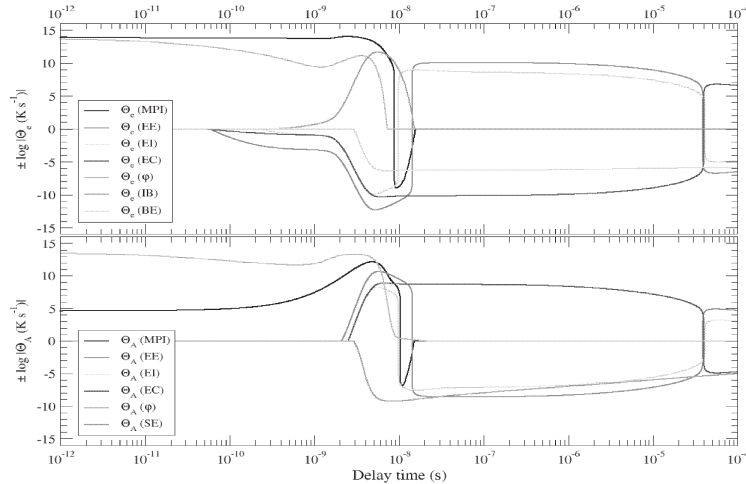


**Fig.2.** Influence of elementary processes on electron temperature (up) and heavy temperature (down) evolutions.

#### 4. CONCLUSION

The collisional radiative model CoRaM-Al is elaborated in the purpose of describing the creation and the recombination of aluminum laser-induced plasma below the limit above which the explosion phase of the sample is observed. CoRaM-Al provides the temporal evolution of the plasma temperatures and densities in various conditions. Besides, using Boltzmann plots, the evolution in time of the excitation temperatures can be plot and thus the determination of the excitation equilibrium time is possible. Therefore, the model enables the determination of the characteristic time required to reach thermal equilibrium and excitation equilibrium, in other words the local thermodynamic equilibrium. However, the LTE characteristic time depends on many parameters as the pulse energy, the time duration, the fluence value, the surface target temperature but also on the time evolution of the energy flux density. During the conference, we will present the temporal evolution of densities, temperature resulting from various values of these parameters in different situations. Finally, the main parameters inducing strong non-equilibrium will be identified and the characteristic time to reach LTE in each condition will be determined.

#### References

- [1] D. Bulajic, M. Corsi, G. Cristoforetti, S. Legnaioli, V. Palleschi, A. Salvetti, E. Tognoni, *Spectrochim. Acta B* 57 (2002) 339–353
- [2] J.M. Fishburn, M.J. Withford, D.W. Coutts, J.A. Piper, *Appl. Surf. Sci.* 252 (2006) 5182-5188
- [3] V. Morel, A. Bultel, B.G. Chéron, *Int. J. Thermophys.* 30 (2009) 1853-1863

## MONTE CARLO SIMULATIONS IN Ar/H<sub>2</sub> MIXTURES

Željka Nikitović, Vladimir Stojanović and Zoran Lj. Petrović

*Institute of Physics, University of Belgrade, Pregrevica 118, 11080 Belgrade, Serbia*

**Abstract.** In this work we present electron transport coefficients in Ar/H<sub>2</sub> mixtures for the conditions used in plasma assisted technologies for semiconductor production i.e. in moderate and very high  $E/N$ . We used numerical solution of Boltzmann equation analysis obtained by program ELENDF and Monte Carlo technique. We show that a good agreement with experimental data exists for low and moderate  $E/N$  and that based on the tests for pure H<sub>2</sub> and Ar we can model properly the high  $E/N$  development. Results are in abundances of H<sub>2</sub> from 1% to 15%, which are necessary in kinetic models for this mixture.

### 1. INTRODUCTION

Argon is a typical buffer gas in a number of technologies. It allows control of electron temperature (mean energy may be quite high and one may support the selected processes with high threshold. Mixtures with hydrogen in rf plasmas may be useful for ashing of photoresists in microelectronic processing but may be used in a broader range of procedures.

In this paper we study the kinetics of electrons in  $E/N$  by using Monte Carlo simulations that have been well tested for similar discharges in [Ar, H<sub>2</sub> and N<sub>2</sub>]. As electrons have a special role in plasmas and in high  $E/N$  discharges we focus on them leaving out heavy particle collisions which will be dealt with separately. Another motivation is to provide the transport data for the electrons in the mixtures of Ar and H<sub>2</sub> for modeling of such plasmas and also to point out the need to employ a more detailed kinetic modeling in sheath regions. These results can be used as the basis for modeling of anomalously broadened Doppler profiles which are particularly pronounced in Ar-H<sub>2</sub> mixture [1], fast neutral plasma etchers for organic dielectrics and the whole range of plasma ashing/cleaning devices.

## 2. THE MONTE CARLO TECHNIQUE

The MC code used in our analysis is based on the null collisions method, applied to model stationary Townsend discharge and it consists of four codes. The first follows the motion of electrons from the cathode the other one follows the motion of ions created in collisions of electrons and atoms of the gas the third follows the motion of electrons created by the ions. By analyzing all three parts it is possible to get the space distribution of the emission and the excitation coefficients [2]. The fourth MC code is used to follow the electrons reflected from the surface and the secondary electrons created at the surface. This code is completely independent from the code for simulation of the electrons from the cathode, and it can be included but also excluded from the simulation. In this paper we have used data for the steel and graphite electrodes [3].

For a limited range of calculations in this paper we have used a two term computer code ELENDF [4] to solve Boltzmann's equation. This is in fact the finite difference method which allows for such a formulation of the Boltzmann equation in which many processes as well as the time evolution of the distribution function can be included. The code has limitations due to inherent approximations, but they are well known and have been studied [5, 6]. The two term code has been used to extend calculations to low  $E/N$  where two term theory is valid and also to give indication of the failure of the two term theory as it is used often without testing it in plasma modeling. For non-equilibrium (non-local) conditions this code is not applicable.

We use the argon cross sections from our calculations for Argon electron (and ion) swarms [5]. For hydrogen we use the data defined in the data base of Phelps [7]. Both sets are based on accurate low energy cross sections that were tested against the best swarm data at low  $E/N$  and have been tested against the emission profiles at high  $E/N$  and energy distribution functions. Thus there is no reason to question application of such set for the mixture of two gases covering similar energies.

## 3. DISCUSSION AND RESULTS

First we will show the results for moderate  $E/N$  typical for mean energies in standard discharges where experimental swarm data are available. In Figure 1 we show electron energy distribution function (EEDF) for the mixture of Ar and a small yet variable percentage of  $H_2$ . For example for the reduced electric field  $E/N = 10$  Td the effect of hydrogen addition from 1% to 15% is reduction of electrons in 10 eV energy group by two orders of magnitude. The shape of the EEDF changes considerably and the highest energy electrons are depleted as hydrogen is added.

Figure 2 shows electron drift velocity in the mixture Ar/ $H_2$  as a function of  $E/N$ . Even a smallest addition of  $H_2$  completely changes the shape of the drift velocity and induces effect of negative differential conductivity

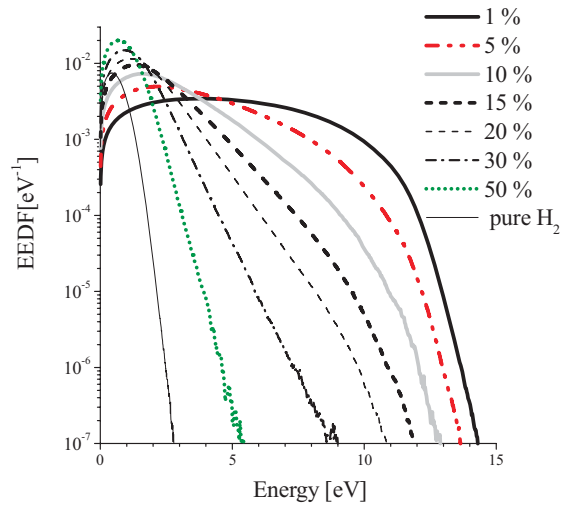


**Figure 1.** EEDF obtained by MCS for a broad range of the Ar/H<sub>2</sub> mixtures where the parameter is taken as a percentage composition of hydrogen in the mixture.

(NDC). The range of NDC is however reduced by a further increase of hydrogen concentration and is eventually lost beyond 15% of added hydrogen.

In drift velocity plots we have also used the ELENDIF to calculate drift velocity at lower energies where Monte Carlo simulation becomes inefficient (for higher H<sub>2</sub> abundances lower energies extend to higher  $E/N$ ). Agreement with experimental results of Engelhardt and Phelps [8] (EXP) confirms that a well-chosen set of sections is used to describe the behavior of electrons in Ar/H<sub>2</sub> mixtures.

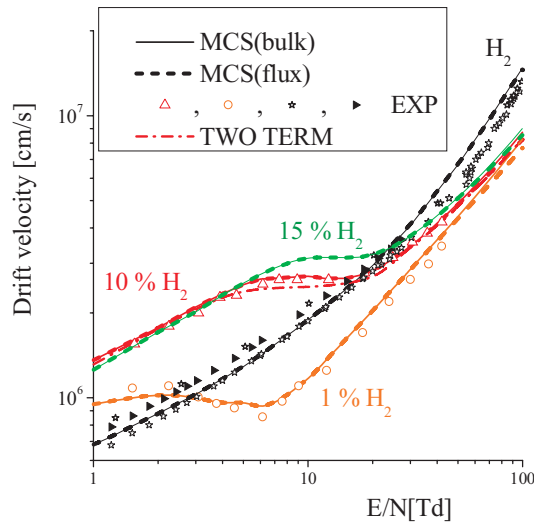


**Figure 2.** Electron drift velocity for the mixture of Ar and H<sub>2</sub>. EXP values for pure H<sub>2</sub> are from Dutton [9].

## Acknowledgements

Results obtained in the Laboratory of Gaseous Electronics Institute of Physics University of Belgrade under the auspices of the Ministry of Education and Science, Projects No. 171037 and 410011.

## REFERENCES

- [1] M. Miyauchi, Y. Miyoshi, Z. Lj. Petrović and T. Makabe, *Solid-State Electronics* 51, 1418 (2007).
- [2] S. Veprek, Ch. Eckmann and J. Th. Elmer, *Plasma Chemistry and Plasma Processing* 8 (4), 445 (1988).
- [3] R. A. Ditzio, G. Liu, S. J. Fonash, B. C. Hsieh, D. W. Greve, *Applied Physics Letters* 56, 1140 (1990).
- [4] C-F. Yeh, T-J. Chen, J. T. Gudmundsson and M. A. Liebermann, *IEEE Electron Device Letters* 20, 223 (1999).
- [5] Z. Lj. Petrović and V. D. Stojanović, *J. Vac. Sci. Technol A* 16 (1), 329 (1998).
- [6] S. Samukawa, *Appl. Surf. Sci.* 253, Issue 16, 6681 (2007).
- [7] Z. Lj. Petrović and A. V. Phelps, *Phys. Rev. E* 80, 066401 (2009).
- [8] A. G. Engelhardt and A.V. Phelps, *Phys. Rev.* 133, A375-A380 (1962).
- [9] J. Dutton, *J. Phys. Chem. Ref. Data* 4, 577 (1975).

# DETECTING LEAD USING LASER INDUCED BREAKDOWN SPECTROSCOPY

Dragutin Šević, Maja Rabasović and Bratislav Marinković

*Institute of Physics, University of Belgrade, Serbia*  
e-mail: sevic@ipb.ac.rs

**Abstract.** Lead is ubiquitous in the environment, brought in by human activity. Namely, lead has many useful properties, in particular, ease of production, ease of melting and joining, malleability, and good corrosion resistance. However, it is well known that lead exposure has negative health effects. In this paper preliminary results regarding testing of our LIBS (laser induced breakdown spectroscopy) experimental set-up for detecting lead are presented.

## 1. INTRODUCTION

Lead has many useful properties, in particular, ease of production, ease of melting and joining, malleability, and good corrosion resistance, so, the lead is ubiquitous in the environment, brought in by human activity. However, it is well known that lead exposure has negative health effects [1].

Many reports, [2-4] and references therein, show that leaded petrol has caused more exposure to lead pollution in human beings than any other single source. Therefore, many countries have outlawed or strictly regulated the use of leaded petrol. In some countries, including ours, the leaded petrol was used until recently. However, it is believed by automotive experts that fuel tanks of obsolete cars (which need lead to lubricate the engine valve seats) still have accumulated lead to last for a few years.

The lead atom was intensively studied in our laboratory using electron spectrometry [5-7].

Our experimental set-up for LIBS and results regarding optical spectroscopy of indium atom are presented in [8-10].

## 2. RESULTS

A small piece of lead was cut from lead plate. The lead plates are used as counter weights for cone elevator in our experimental apparatus

“ESMA”. Streak image of lead LIBS signal and its one dimensional profile are shown in figures 1. and 2. respectively.

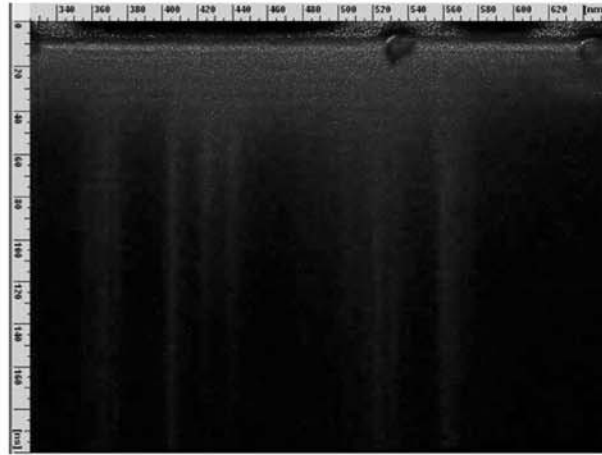


Figure 1. Streak image of lead LIBS signal.

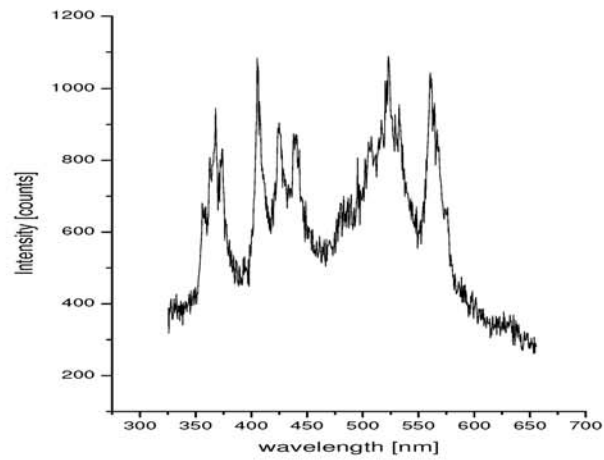


Figure 2. One dimensional profile of lead LIBS signal from Fig. 1.

Identified lead lines [11] are given in Table 1. It is interesting to note that other lines, visible on figures 1. and 2. are not from zinc or copper, as expected. They belong to iron [11]. Namely, it is not uncommon to improve the mechanical properties of lead weights by iron.

**Table 1.** The most intense spectral lines of Lead in the emission spectrum of laser generated plasma.

$\lambda$ (nm)	Atom, ion	Transition	$E_{high}-E_{low}$ (eV)
560.885	Pb (II)	$6s^27p(^2P_{3/2}^0) - 6s^27s(^2S_{1/2})$	2.21
520.144	Pb (I)	$6p8s(^1P_1^0) - 6p^2(^1S_0)$	2.387
438.646	Pb (II)	$5s^25f(^2F_{5/2}^0) - 6s^26d(^2D_{3/2})$	2.827
424.492	Pb (II)	$5s^25f(^2F_{7/2}^0) - 6s^26d(^2D_{5/2})$	2.92
405.78	Pb (I)	$6p7s(^3P_1^0) - 6p^2(^3P_2)$	3.056
373.993	Pb (I)	$6p7s(^3P_2^0) - 6p^2(^1D_2)$	3.315
368.346	Pb (I)	$6p7s(^3P_0^0) - 6p^2(^3P_1)$	3.366
363.957	Pb (I)	$6p7s(^3P_1^0) - 6p^2(^3P_1)$	3.407
357.273	Pb (I)	$6p7s(^1P_1^0) - 6p^2(^1D_2)$	3.471

### 3.CONCLUSION

Preliminary results regarding testing of our LIBS experimental set-up for detecting lead are presented in this paper.

#### Acknowledgements

This work has been supported by the MES of the Republic of Serbia under project grant No. 171020.

#### REFERENCES

- [1] Iain Thornton, Radu Rautiu, Susan Brush, *LEAD the facts*, Ian Allan Printing Ltd, (2001) <http://www.ila-lead.org/>.
- [2] Danish working group, *Lead contamination*, The ministry of environment: Denmark (1977) <http://www2.mst.dk/Udgiv/publications/1977/87-503-2292-3/pdf/87-503-2292-3.pdf>
- [3] Anselimo O. Makokha, Leonard R. Mghweno, Happy S. Magoha, Amina Nakajugo and John M. Wekesa, *African Journal of Environmental Science and Technology* 2, 349 (2008).
- [4] Awofolu O R, *J. Appl. Sci. Environ. Mgt.* Vol. 8 (1) 23 (2004).

- [5] S. Milisavljevic, M. S. Rabasovic, D. Sevic, V. Pejcev, D. M. Filipovic, Lalita Sharma, Rajesh Srivastava, A. D. Stauffer and B. P. Marinkovic, *Phys. Rev. A* 75, 052713 (2007).
- [6] S. Milisavljevic, M. S. Rabasovic, D. Sevic, V. Pejcev, D. M. Filipovic, Lalita Sharma, Rajesh Srivastava, A. D. Stauffer and B. P. Marinkovic, *Phys. Rev. A* 76, 022714 (2007).
- [7] S. D. Tosic, M. S. Rabasovic, D. Sevic, V. Pejcev, D. M. Filipovic, Lalita Sharma, A. N. Tripathi, Rajesh Srivastava, A. D. Stauffer and B. P. Marinkovic, *Phys. Rev. A* 77, 012725 (2008).
- [8] Maja Rabasovic, Dragutin Sevic, Mira Terzic and Bratislav Marinkovic, Proc. 25th Summer School and International Symposium on Physics of Ionized Gases SPIG, 30th Aug 4th Sept. 2010, Donji Milanovac, Serbia, Book of Contributed Papers and Abstracts of Invited Lectures, Topical Invited Lectures and Progress Reports, editors: L. C. Popovic and M. M. Kuraica, ISBN 978-86-80019-37-6, Publ. Astron. Obs. Belgrade No. 89, July 2010, ISSN: 0373-3742 pp. 229 232.
- [9] M.S. Rabasovic, D. Sevic, V. Pejcev, B.P. Marinkovic *Nucl.Instrum. Meth. B. Volume 279*, 58, (2012).
- [10] Dragutin Sevic, Maja Rabasovic, and Bratislav P. Marinkovic, *IEEE Trans. Plasma Sci.* 39(11) 2782-2783 (2011).
- [11] Yu Ralchenko, A.E. Kramida, J Reader and NIST ASD Team (2010), NIST Atomic 253 Spectra Database (version 4.0.1), [Online]. Available: <http://physics.nist.gov/254/asd> [2011, May 30] National Institute of Standards and Technology, 255 Gaithersburg, MD.

## CHARACTERIZATION OF HYDROGEN BASED RF PLASMAS SUITABLE FOR REMOVAL OF CARBON LAYERS

Nikola Škoro<sup>1,2</sup> and Evangelos Gogolides<sup>1</sup>

<sup>1</sup>*Institute of Microelectronics, NCSR Demokritos, Aghia Paraskevi, Attiki  
15310, Greece*

<sup>2</sup>*Institute of Physics, University of Belgrade, P. O. Box 68, 11080 Belgrade,  
Serbia*

**Abstract.** Characterization of RF H<sub>2</sub>/Ar plasma was performed with the parameters similar to those used in laser induced plasma for an in-situ removal of carbon contaminants from EUV optics. Plasma emission spectra were recorded in a wide interval of wavelengths. The most important processes in the plasma were identified. Using optical methods of actinometry and the technique with different Balmer lines, the dissociation degree of hydrogen was calculated. The results were compared with the estimation of the dissociation extent from pressure rise measurements.

### 1. INTRODUCTION

In the course of time, to improve attainable resolution, optical lithography processes have been shifted towards shorter illumination wavelengths to fabricate microelectronics devices with smaller transistors. Taking into account that conventional lithography (248nm or 193nm) is reaching its boundaries, new technologies are being developed to sustain Moore's Law. One of the solutions is extreme UV (EUV) lithography, which uses a wavelength of 13.5 nm. However, the lifetime of projection optics in EUV is threatened by two effects: carbon deposition and oxidation [1]. Therefore, to develop a viable application of the EUV lithography, cleaning methodologies for contamination removal, preferably in-situ procedures, have to be established.

Until now, methods of removal of carbon layers using hydrogen have been studied in RF plasmas [1-3] and by generation of atomic hydrogen for an in-situ contamination removal technique [4]. It was proven that hydrogen atoms play an important role in successful removal of carbon from the surface [2]. In order to study the process of carbon contamination removal from EUV optics we performed measurements in RF plasmas with gas mixtures and pressures similar to those present in EUV-induced plasmas in lithography tools.

The first step in the investigation was optical characterization of H<sub>2</sub>/Ar plasma and determination of the extent of hydrogen dissociation.

## 2. EXPERIMENTAL SETUP

Low pressure RF plasma at 13.56 MHz was produced in a helicon-type plasma reactor (Micromachining Etching Tool, MET, Adixen -Alcatel). The reactor chamber consists of two parts: the upper part is plasma generation region with a quartz tube surrounded by one-turn coil-antenna below which is a diffusion region with a sample holder. The power was applied to the antenna while aluminum sample holder was grounded and cooled with He-backside pressure. For the plasma characterization a blank sample holder was used. Plasma emission from the diffusion region was transferred by an optical fiber to the Spectra-Pro 500 spectrometer from Acton Research Corporation equipped with a CCD camera. The plasma was ignited in a mixture of hydrogen with 5% of Ar at a pressure of 1 Pa and flow-rate of 50 sccm.

## 3. RESULTS AND DISCUSSION

### 3.1 Optical emission spectra

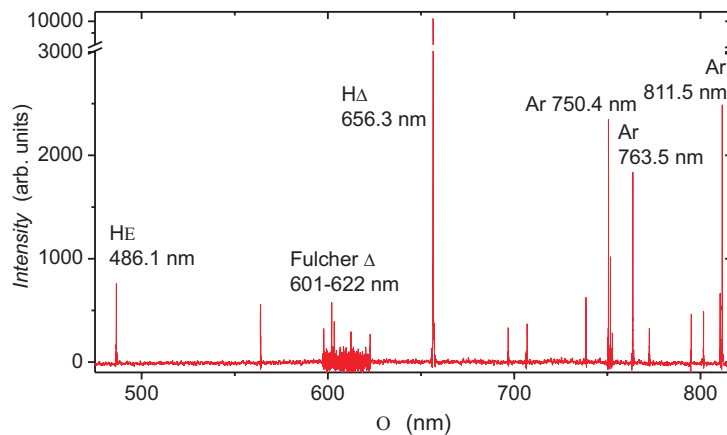


**Figure 1.** Spectra of H<sub>2</sub>/Ar plasma at 1 Pa. Line intensities are relatively scaled.

Spectrum recorded from plasma ignited in hydrogen/argon gas mixture is shown in Fig.1 for a wide interval of wavelengths. Line intensities are scaled relatively and important lines are designated. Apart from atomic lines in H and Ar, Fulcher  $\alpha$  bands (electronic transitions in H<sub>2</sub> molecule) were also recorded.

### 3.2 Determination of hydrogen dissociation degree

The degree of dissociation of molecular hydrogen is very important parameter in hydrogen and hydrogen-containing low-temperature plasmas when comes to understanding of the surface processes. One simple technique for

determining the dissociation degree in the plasma is optical actinometry [5]. In addition, for hydrogen discharges, another optically based method that uses relative intensities of different Balmer lines can be employed [6].

For the case of hydrogen plasma with Ar as actinometer gas, important kinetic processes in the plasma taken into account for actinometer and „Balmer lines” technique calculations are given in Table 1. Since the discharge pressure is below 100 Pa, the quenching can be neglected [7].

**Table 1.** Processes in H<sub>2</sub>/Ar low-pressure plasma. The reference data is given in the right column.

		Process	Ref.
1	Atom excitation	$H(n=1) + e \rightarrow H(n=3,4) + e$	[8]
2	Dissociative excitation	$H_2 + e \rightarrow H(n=3,4) + H(n=1) + e$	[8]
3	Radiative de-excitation	$H(n=3,4) \rightarrow H(n=2) + h\nu (H\alpha, H\beta)$	[9]
4	Direct excitation	$Ar(3p) + e \rightarrow Ar(4p) + e$	[10]
5	Radiative de-excitation	$Ar(4p) \rightarrow Ar(4s) + h\nu (Ar750nm)$	[9]

Besides optical methods, the degree of hydrogen dissociation in plasma is estimated from the pressure rise after discharge ignition which can be attributed to the creation of new species in plasma. Providing constant gas flow in the chamber, the relative increase in total gas pressure after breakdown should be proportional to the dissociation degree.

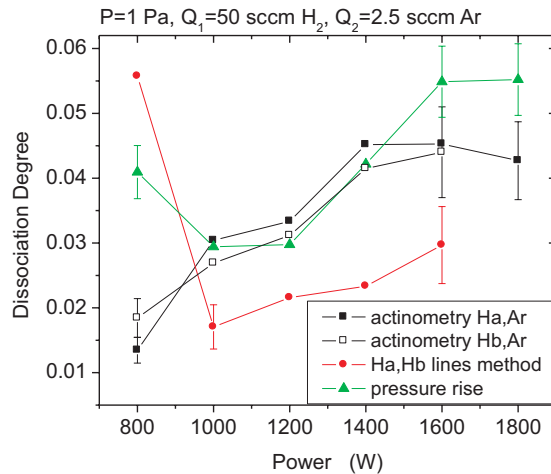


**Figure 2.** The dependence of the hydrogen dissociation degree on RF power determined from actinometry, „Balmer lines” technique and pressure rise.

In Fig.2 dissociation degrees calculated using three different methods are shown. Results obtained using Ar actinometry (squares) and pressure rise

(triangles) agree well within experimental errors. Balmer lines formula (circles), using ratio of hydrogen atomic lines, give somewhat lower values. This discrepancy may originate from rate coefficients since this technique is very sensitive on the shape of the rate coefficient function. All methods predict similar increment in the dissociation extent with power.

#### 4. CONCLUSIONS

Helicon-type RF plasma reactor can be used for a simulation of plasma conditions similar to the laser induced plasmas for an in-situ cleaning of EUV optics from carbon contaminations. As a first step in the research, optical characterization of H<sub>2</sub>/Ar plasma has been performed by spectra recoding in a wide wavelength interval. Using different lines of the spectra, calculation of the dissociation degree was conducted by employing different optically-based methods and pressure rise. Reasonable agreement of the results have been found for all plasma powers investigated.

#### Acknowledgements

This work is supported by Surface Physics for Advanced Manufacturing - S.P.A.M, project of FP7 Marie Curie Research and Initial Training Network .

#### REFERENCES

- [1] S. Bajt, H. N. Chapman, N. Nguyen, J. Alameda, J.C. Robinson, M. Malinowski, E. Gullikson, A. Aquila, C. Tarri o and S. Grantham, Proceedings of the SPIE 5037, 236 (2003).
- [2] S. Graham, C. Steinhaus, M. Clift and L. Klebanoff, J. Vac. Sci. Technol. B 20, 2393 (2002).
- [3] I. Nishiyama, H. Oizumi, K. Motai, A. Izumi, T. Ueno, H. Akiyama and A. Namiki, J. Vac. Sci. Technol. B 23, 3129 (2005).
- [4] S. Graham, C. Steinhaus, M. Clift, L. Klebanoff and S. Bajt, Proceedings of the SPIE 5037, 460 (2003).
- [5] A. Gicquel, M. Chenevier, Kh. Hassouni, A. Tserepi and M. J. Dubus, Appl. Phys.83, 7504 (1998).
- [6] V. Schulz-von der Gathen and H. F. Doebele, Plasma Chem. Plasma Process. 16, 461 (1996).
- [7] M. J. Wouters, J. Khachan, I. S. Falconer and B. W. James, J. Phys. B: At. Mol. Opt. Phys. 32, 2869 (1999).
- [8] B. P. Lavrov B P and A. V. Pipa, Opt. Spectrosc. 92, 647 (2002).
- [9] <http://www.nist.gov/pml/data/asd.cfm> (NIST)
- [10] M. Hayashi, "National Institute For Fusion Science", Report No. NIFS-DATA -72 (2003).

## SPECTROSCOPIC MEASUREMENTS OF ELECTRIC FIELD IN LOW FREQUENCY DBD PLASMA JET

Goran B. Sretenović, Ivan B. Krstić, Vesna V. Kovačević, Bratislav M. Obradović, and Milorad M. Kuraica

*University of Belgrade, Faculty of Physics, P.O. Box 44, 11000 Belgrade,  
Serbia*

*E-mail: sretenovic@ff.bg.ac.rs*

**Abstract.** Atmospheric-pressure helium plasma jet has been studied by optical emission spectroscopy. Streamer/bullet properties of the plasma jet are observed in the positive voltage half cycle, while in the negative half cycle jet operates more as a glow-like atmospheric pressure discharge. Electric field strength distribution is measured using Stark polarization spectroscopy of He I 492.19nm line. Obtained radial distribution of the axial electric field of the bullet exhibits a ring-shaped structure. It was shown that under observed experimental conditions, electric field in the bullet reaches the value of almost 30 kV/cm, while in the negative half cycle electric field strength has values below 4kV/cm.

### 1. INTRODUCTION

Non-thermal plasma jets are widely used for polymeric surface modification, bacterial and bio-molecule inactivation, wound healing and nanostructure inactivation [1]. Atmospheric plasma jets can be generated in several different ways such as: dc jets, kilohertz, pulsed and sinusoidal jets, radiofrequency (RF) jets and microwave excited jets. Different jet configurations and feedings bring different plasma characteristics. It has been shown that atmospheric-pressure plasma jet may exist in three distinct operating modes: the chaotic mode, the bullet mode and the continuous mode [1]. Dawson's photonization theory gives a possible explanation of propagation mechanism of plasma bullet [1]. The most recent modeling of bullet propagation in atmospheric-pressure helium plasma jets predicts that plasma bullet has streamer characteristics, such as velocity and electric field [4, 5]. Axial and radial distribution measurements of time integrated electric field of plasma bullet, based on Stark spectroscopy, confirmed these theoretical predictions [6]. High electric field with the pulsating nature, like the one in the streamer head finds biomedical applications such as tumor treatment.

## 2. EXPERIMENTAL SET-UP

Discharge device considered in this study is dielectric barrier discharge plasma jet. It consists of a glass tube 2 cm in length (2 mm inner diameter, 3 mm outer diameter) with a 1 cm wide copper electrode wrapped tightly around it at the distance of 1 cm from the tube nozzle. A second grounded copper electrode is placed 1 cm downstream from the nozzle. The helium flow (99.996%) through the tube was 5 l/min. Helium flowed into the ambient air. A laboratory-built power supply operated at 12 kHz, able to provide high voltage sinusoid signal with variable amplitude up to 20 kV, was connected to the wrapped electrode. The applied voltage was measured using P6015A Tektronix high-voltage probe and a Rogowsky coil placed between the grounded electrode, and the grounding point was used for current measurements as presented in Figure 1. A Tektronix TDS 2024B digital storage oscilloscope (200MHz, 2 GS/s) was employed to record voltage and current signals.

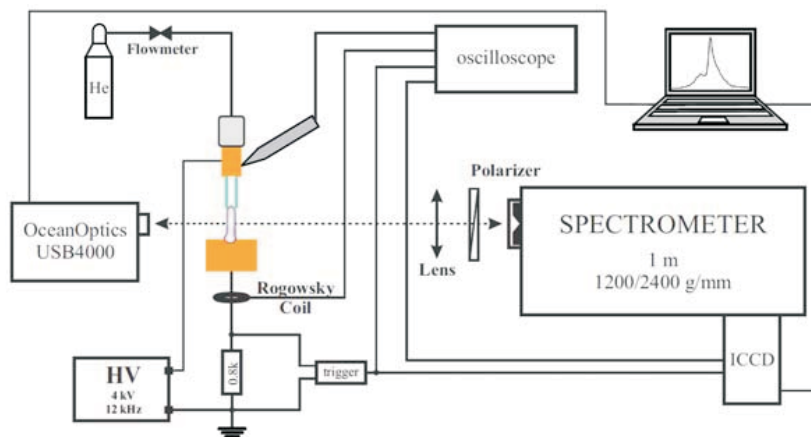


**Figure 1.** Experimental set-up.

For a space resolved emission measurements, projection optics was used to project the whole plasma jet onto the entrance slit of a 1m spectrometer (SOLAR TII, model MSDD 1000) with 1200 g/mm diffraction grating. Radiation from the jet was detected using an ICCD (PI-MAX2, Princeton Instruments) with 1024×1024 pixels, size of the pixel 13  $\mu\text{m}$ . ICCD was triggered using time delayed pulse signal from the non-inductive 800  $\Omega$  resistor inserted between grounded electrode and the grounding point as shown in Figure 1. Each recorded image is made of 50 accumulations, each of 50 000 gates per exposure. The gate was triggered at the beginning of the current peak with duration of 5  $\mu\text{s}$ . Resolution of spectral apparatus was 10.8 pm/pixel. With an entrance slit of 30  $\mu\text{m}$  full width at the half of maximum (FWHM) of corresponding instrumental profile was 0.035 nm.

### 3. RESULTS AND DISCUSSION

Optical emission spectroscopy technique based on the application of the polarization-dependent Stark splitting and shifting of He I 492 nm line, and its forbidden counterpart is used for electric field measurements. Following the methods demonstrated in [5, 6], axial electric field in the space between the glass tube and the grounded electrode is determined. Examples of typical  $\pi$ -polarized spectra of He I 492 nm line recorded for the positive and negative current peak are shown in Figure 2. According to [5], with the polarizer mounted with its axis parallel to the external field three components are detected: allowed line, its forbidden counterpart and a field-free component (ff) originating from the area where the electric field is negligible. Spectral lines are fitted with pseudo-Voigt profiles in order to estimate peak-to-peak distance between the forbidden and allowed counterparts according to which the electric field is determined. For the positive current peak of the plasma jet the ff component is Van der Waals broadened while the forbidden and allowed lines are broadened predominantly due to the overlapping of shifted spectral lines emitted by atoms placed at various positions in the streamer head electric field. The measured electric field distribution along the discharge axis actually represents time integrated electric field in the head of the streamer propagating along the axis.

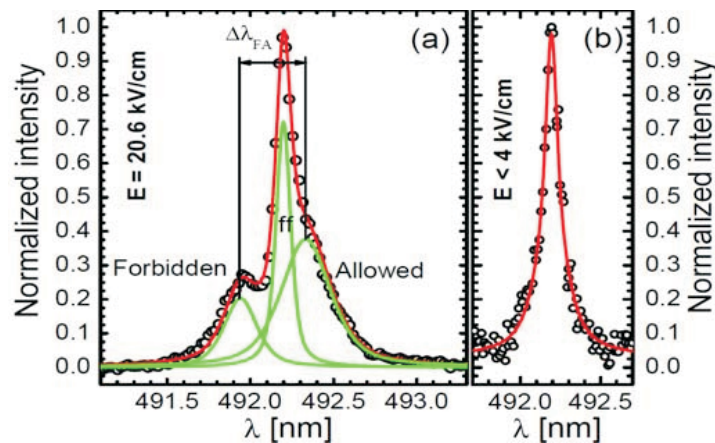


**Figure 3.** Typical  $\pi$ -polarized spectra of He I 492.19 nm line recorded from the plasma jet for (a) positive and (b) negative current pulse.

Concerning the negative current peak, measurements were performed also - see Figure 3(b). As shown at Figure 3(b) substantial splitting of the line is not observed, which implies low electric field strength along the jet for the negative current peak. Method used for electric field determination is suitable for electric field strength down to 3-4 kV/cm, depending on the signal to noise ratio of the

recorded line. According to this, electric field strength of the jet, for the negative current peak for given experimental conditions, is lower than 4 kV/cm, which is in agreement with modeling results presented in [7]. In order to estimate radial distribution of axial electric field of the plasma bullet at different positions in the plasma jet, lateral profiles of the plasma jet for the positive current pulse are recorded and the Abel inversion procedure was applied. Then, fitting of line profiles resulted in the electric field strength distribution data.

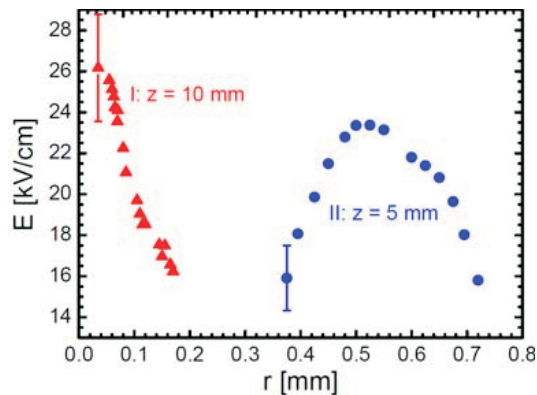


**Figure 4.** Radial distribution of the axial electric field in the plasma jet operating in the bullet mode at two characteristic axial positions.

Radial distribution of axial electric field has the ring shaped structure at the middle of plasma jet ( $z = 5$  mm), see Figure 4. Near the grounded electrode the electric field reaches maximal value of 26 kV/cm at the axis ( $z = 5$  mm), while in the middle of the jet maximum is off-axis with values up to 23 kV/cm. These experimentally obtained results also confirm modeling outcomes, and calculations presented in [2, 3].

### Acknowledgements

This work is supported by the Ministry of Education and Science of the Republic of Serbia through the Project No. 171034 and the Project No. 33022.

### REFERENCES

- [1] J. L. Walsh et al., J. Phys. D: Appl. Phys. 43, 075201 (2010).
- [2] G. V. Naidis, J. Phys. D: Appl. Phys. 43, 402001 (2010).
- [3] G. V. Naidis, J. Phys. D: Appl. Phys. 44, 215203, (2011).
- [4] G. B. Sretenović et al., Appl. Phys. Lett. 99, 161502 (2011).
- [5] M. M. Kuraica and N. Konjević, Appl. Phys. Lett. 70, 1521 (1997).
- [6] B. M. Obradović et al., Appl. Phys. Lett. 92, 191501 (2008).
- [7] G. V. Naidis, Appl. Phys. Lett. 98, 141501 (2011).

## ON MAGNETO-INDUCED PROPERTIES OF HOLLOW CATHODE DISCHARGE

D. Zhechev and V. Steflekova

*Institute of Solid State Physics, 72 Tsarigradsko Chaussee Blvd., Bulgarian  
Academy of Sciences, 1784 Sofia, Bulgaria*

**Abstract.** Galvanic, kinetic and spectral magneto-induced manifestations are studied in a hollow cathode discharge. Magnetic field applied reduces the voltage across the discharge and influences the maximum energy of the accelerated particles. Redistribution of the current processes takes place and the spectral lines of the sputtered atoms increase their intensity.

### 1. INTRODUCTION

The magnetic action on a gas discharge manifests itself by various optical and galvanic phenomena under the region [ $\approx 10^{-1} \div 10^3$ ] G. Both magnetic disordering of aligned/self-aligned atoms and depolarization of their spontaneous emission take place in a weak magnetic field  $B \in [\approx 10^{-1} \div \approx 10]$  G [1]; simultaneously a magneto-galvanic reaction was observed [2, 3]. Level crossing arises also at magnetic field  $B > 10$  G [1]. Magnetic increasing of the opto-galvanic reaction is reported in [4].

An external  $B$ - field applied is one of the tools enhancing the analytical ability the traces of elements/molecules to be identified in various objects including artifacts of archeological importance. A modification of the glow discharge, i.e. hollow cathode discharge (HCD) is of particular spectral-analytical importance. Really, all elements may be atomized and excited in a conventional HCD. It is based on two characteristic properties, i.e. intensive sputtering of the cathode surface/probe inserted and specific electron energy distribution function (EEDF) containing also fast electrons up to  $(2 \div 4) \times 10^2$  eV. [5,6]. Earlier the magnetic field effect on intensity of some spectral lines, continuous background and molecular bands excited in a HCD of helium or argon buffer gases was studied [7]. The observed increase of the spectral intensities is among the most important consequences due to  $B$ - field applied.

Here HCD in helium buffer gas is used for diagnostic of the operating conditions at magnetic field applied. The magnetic influence on some lines of atomized metals in HCD is studied in neon buffer gas.

## 2. EXPERIMENT

Figure 1 illustrates the experimental scheme. The discharge in Al-, Fe- and Cu-cup-like hollow cathodes, 40 mm long and 16 mm in diameter is studied. Helium at a pressure of  $10^{-1}$  Torr and neon ( $3 \cdot 10^{-1}$  Torr) are used as buffer gases. The operating parameters (voltage across the HCD, discharge current, intensity of the spectral line emitted and its radial profile) are investigated vs. magnetic field  $B \in [0 \div 8 \cdot 10^2]$  G (Helmholz's coils) applied to the discharge. Monochromator MDR2 is used combined with a rotating glass parallel plane plate for measuring the spectral line radial profile. Photomultiplier type 106 and Lock-in nanovoltmeter type 232B are used in the lock-in spectral line measuring. In order to improve the optical resolution of the radial HCD light profile the lens  $L$  (focal distance  $f_0 = 50$  cm) is focused on the middle  $\ell/2$  of the cathode-cylinder of length  $\ell$ . Then a plasma cone of height  $\ell/2$  and base  $x$  determines the optical system resolution  $x$  according to the relation  $d/x = 2f_0/\ell$ , where  $d = 0.5$  mm is the monochromator slit. It turns out  $x \in [0.7 - 1.5]$  mm for cathodes of  $\ell \in [10 \div 40]$  mm.

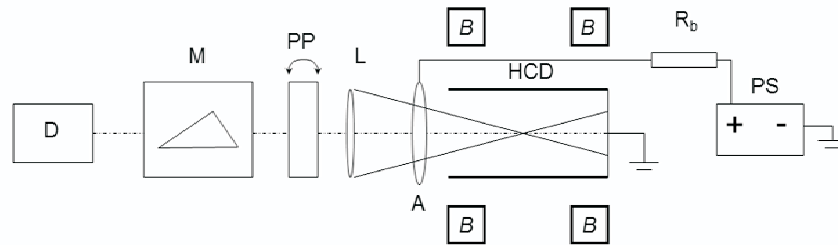


**Figure 1.** HCD-hollow cathode tube, A-anode, B-Helmholz's coils, PS-power supply, R<sub>b</sub>-ballast resistor, L-lens, PP-parallel plane plate, M-monochromator, MDR2, D-nanovoltmeter

The studied buffer's lines He I 388.9 nm, He I 396.5 nm, He II 468.6 nm, He I 471.3 nm, He I 501.6 nm and He I 504.7 nm are selected as diagnostic ones. They are of both different excitation potentials and typical singlet/triplet ones. They later distinguish strongly in their optical functions of excitation  $f(e)$  [8]. This difference is important since the specific electron energy distribution function (EEDF) contains also fast electrons and the lines are sensitive vs. different parts of EEDF. The magnetic influence is studied also on the spectral lines of atoms of the cathode material Cu I 521.18 nm, Cu I 578.2 nm, Fe I 516.7 nm and Fe I 523.2 nm or inserted one. The geometry where magnetic field  $B$  is co-axial with the geometric axes of the cathode-cylinder (Fig.1) respectively with optical one turned out to be the most suitable among the rest possible geometries.

### 3. RESULTS AND DISCUSSIONS

1. Voltage  $U_c$  across HCD is observed to decrease in B- field substantially (Fig.2). The reduction  $\Delta U_c \sim B^{-1}$  reaches more than 40 V. Taking into account the importance of this voltage as accelerating the charged particles the observed reduction should influence their kinetics. Some He- triplet ( $tr$ ) and -singlet ( $s$ ) lines are used as optical probe. Their intensity  $I_{s/tr}$  is studied vs. intensity of B- field applied (Fig.3). The triplets HeI 471.3 nm ( $f^{\max}(e)$  at 27 eV) and HeI 388.9 nm ( $f^{\max}(e)$  at 28 eV) increase their intensity as  $I_{tr} \sim B$ . On the contrary, the singlet's HeI 396.5 nm ( $f^{\max}(e)$  at (100-120) eV), HeI 501.6 nm ( $f^{\max}(e)$  at (100-110) eV) and ion line HeII 468.6 nm ( $f^{\max}(e)$  at (170-190) eV) (all data in [8]) decrease in intensity  $I_s \sim B^{-1}$ .

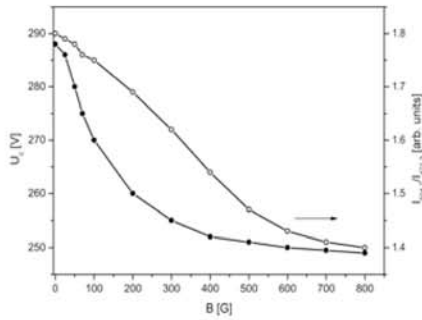


**Figure 2.** Dependence of both voltage  $U_c$  across the HCD and intensity relation of two He lines  $I_{504.7}/I_{471.3}$  on the magnetic field applied B.

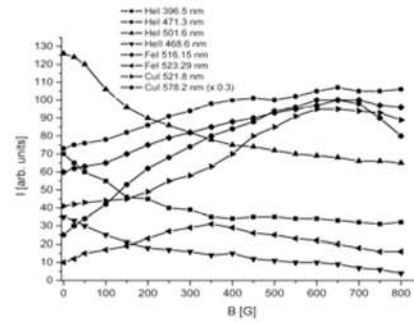


**Figure 3.** Intensity  $I$  of some spectral lines vs. magnetic field applied B.

Doubtless, the magnetic reduction of the voltage  $\Delta U_c$  cuts the highest energy of the electrons in the dark space and the balance of the processes displaces to that of lower energy ones. Thus, the B- field applied influences the intensity of triplet/singlet lines in contrary way. Then the diagnostic sensitivity  $I=I(B)$  may be enhanced by using  $I_{tr}/I_s = \varphi(B)$  ratio.

For  $i \rightarrow k$  line  $I_{ik} = A_{ik} h \nu_{ik} n_0 n_e \int_{e_i}^{U_c} F(e) f_i(e) de$ , where  $n_0$  and  $n_e$  are the density of carriers and electrons,  $e_i$  the excitation energy,  $F(e)$  is EEDF and intensities ratio  $I_{tr}/I_s = f(B)$  is strongly sensitive vs. B- field. It characterizes the magneto-induced tendency in processes of excitation:

$$I_{tr}/I_s \propto \left\{ \int_{e_{tr}}^{e_{U_c}} F(e) f_{tr}(e) de \right\} \left\{ \int_{e_s}^{e_{U_c}} F(e) f_s(e) de \right\}^{-1}$$

In the case of  $F(e)$  Maxwellian (positive column) the ratio  $I_{tr}/I_s = f(B)$  may be calculated at different electron temperature  $T_e$ . This procedure is invalid for HCD since its  $F(e)$  is not Maxwellian. Here the magnetic action is estimated qualitatively only. HeI 504.7nm is used together with HeI 471.3 nm. Fig. 2 illustrates the ratio  $I_{tr}/I_s$  vs  $B$ . Since  $f(e)$  does not depend on  $B$ , Fig.2 suggests that  $B$ - field reduces the fast electrons number in EEDF  $F(e)$  and increases those of lower energy.

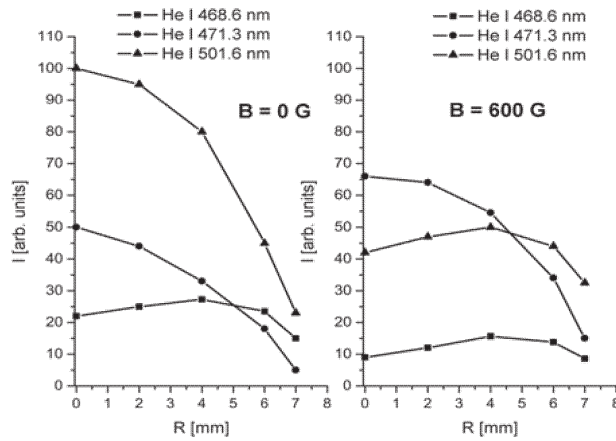


**Figure 4.** Radial profile of the spectral line intensity  $I$  at magnetic field applied  $B = 0$  G at  $B = 600$ .G.

This quantitative interpretation is in agreement with the probe measurements of EEDF in [9], Figure 4 illustrates the space redistribution of the intensity due to magnetic field. The radial profiles suggest that decreasing  $I \sim B^{-1}$  of the singlet HeI 501.6 nm (Fig. 3) occurs due to its reduction along the axes ( $R = 0$ ). Decreasing of the ion line HeII 468.6 nm in  $B$ - field takes place because of its reduction over the entire radius  $R$ . This line keeps its characteristic radial profile  $I(R)$  of  $I(R)^{max}$  near cathode dark space (CDS) at  $R = 7$  mm.

2. Magnetic increasing of the intensity of sputtered atom's line is observed (Fig.3). These lines are closer in intensity to those of He- triplets. The lines studied characterize the atoms of Cu and Fe. They are known as elements of difficult atomization. In this case the magnetic field acts on both sputtering and excitation of the cathode material. The ion of carrier gas sputters the cathode surface at velocity  $V_i$  depending on the electric field intensity near the surface, for example  $eU_c/d = mV_i^2 [n_0\sigma_n(V_i)]/4$ , where  $d$  is the CDS length,  $m$

the ion mass,  $\sigma_n(V_i)$  the cross-section of the resonant charge exchange between carriers  $atom + ion \rightleftharpoons ion + atom$ . The latter is the process of the greatest cross-section vs carrier ion in the CDS [10]. The equation suggests directly the relation  $V_i \sim U_c$ . On the other hand  $\sigma_n \sim V_i$  under the typical  $V_i$ -values according to [10]. Taking in mind  $-\Delta U_c(B)$  (Fig. 2) one may state that quantitatively the magneto-intensified excitation of sputtered atoms dominates their magneto-decreased sputtering.

#### 4. CONCLUSIONS

The magnetic field reduces both the voltage  $U_c$  across HCD and the highest energy of the electrons in the dark space. The balance of the processes displaces to that of lower energy ones. The intensity of triplet/singlet He lines changes in contrary way. Magnetic field increases the spectral lines of sputtered atoms in intensity although lower sputtering ability of ion-buffer.

#### Acknowledgements

National scholarships “For the women in science” – Scholarships awarded by L’Oreal Bulgaria for women scientists in Bulgaria with the support of the UNESCO National Commission of the Republic of Bulgaria and the Sofia State University “St. Kliment Ohridski”) supported this study.

#### REFERENCES

- [1] E. B. Alexandrov, G. I. Hvostenko and M. P. Chajka, *Interference of Atomic State* (Springer Series on Atoms and Plasmas, Vol. 7, Springer Berlin, Heidelberg, New York, 1993).
- [2] G. Todorov, P. Karavassilev and D. Zhechev, *Physica Scripta* 57, 634 (1998).
- [3] D. Zhechev, Doctoral Theses (2001).
- [4] R. Dyulgerova, D. Zhechev, I. Jaskowska and L. Lukaszewsky, Proc. 20<sup>th</sup> EGAS Conf. Graz, 370 (1988).
- [5] S. Caroli, *Improved Hollow Cathode Lamps for Atomic Spectroscopy*, (London, New York: Ellis Harwood Limited – Publishers, 1985).
- [6] R. K. Marcus, *Glow Discharge Spectroscopies*, p. 9 (Plenum Press, New York and London, 1993).
- [7] N. K. Rudnevsky and D. E. Maksimov, in: *Improved Hollow Cathode Lamps for Atomic Spectroscopy*, S. Caroli Ed., (Harwood Limited Publ. p.148, 1985).
- [8] I. P. Zapisochnij, P. V. Fel'zan, *Ukr. Fiz. J.* 10 , 11 (1965).
- [9] V. P. Hofmaister, Doctoral Theses (SP University, S. Peterburg, 1968).
- [10] S. Smirnov, PhD Thesis, p. 21 (Moskva: Kourchatov Inst. 1966).



## STARK BROADENING REGULARITIES WITHIN NEUTRAL SODIUM SPECTRAL LINES

D. Jevtić, I. P. Dojčinović, I. Tapalaga and J. Purić

*University of Belgrade, Faculty of Physics, P. O. Box 44, 11000 Belgrade,  
Serbia*

**Abstract.** Stark widths dependences on the upper level ionization potential within different spectral series of the neutral sodium have been studied and discussed. It was found that differences among the studied series decrease with temperature increasing. After establishing these dependences predictions were made for Stark widths of neutral sodium spectral lines not measured or calculated until now.

### 1. INTRODUCTION

The purpose of this paper is to analyse functional dependence of Stark broadening (FWHM) on upper level ionization potential. More specifically, Stark broadening dependence within each spectral series is analysed. A simple model that depends only on upper level ionization potential and type of transition could provide Stark broadening data for transitions that have not yet been calculated due to the lack of parameters needed in more complicated models.

Stark broadening data used for this analysis was taken from [1-3]. Most of this data is available online [4]. Only four spectral lines of Na I are found in literature in works of Purić et al. [5], Djeniže et al. [6] and Mioković & Veža [7] and are used for a comparison with theoretical results. Data for ionization potential of Na I spectral lines are taken from NIST database [8]. A total of 25 spectral lines of Na I have been collected and analysed. Within these data the following series have been investigated: 3s-np (2), 3p-ns (2), 3p-nd (2), 3d-np (2). Next to the series notation there is a number in parentheses (2) indicating doublet spectral lines.

### 2. THEORETICAL BACKGROUND

Purić et al. [9] evaluated Stark width as the function of the upper level ionisation potential and the rest core charge of the emitter. The dependences were found to be of the form:

$$\omega[\text{rad} \cdot \text{s}^{-1}] = a \cdot (\chi[\text{eV}])^{-b} \quad (1)$$

where  $\omega$  is the line width (in angular frequency units),  $\chi$  is the corresponding upper level ionization potential (in eV). Coefficients  $a$  and  $b$  are dependent of the chosen temperature and electron density, but independent of the ionization potential for particular transition.

The available Stark broadening data is given for different conditions and cannot be used equally or compared without normalisation to equal conditions of environment. Electron density in plasma has to be considered as Stark width is proportional to electron density. Consequently, Stark broadening data has to be normalised to the same electron density and in this paper all data was normalized to  $N_e=10^{16} \text{ cm}^{-3}$ .

Temperature of plasma also influences Stark broadening and it was commonly expected to be expressed as weak function of temperature. For instance  $w \sim T^{1/2}$  was used for the case of ion spectral lines. However, the whole spectrum of different temperature dependences has to be used in this case instead in order to match the data more precisely. Similar dependences has to be used, also, in the case of neutrals as

$$f(T) = A + B \cdot T^{-C} \quad (2)$$

It was shown that this dependence is appropriate for every spectral line. Coefficients  $A$ ,  $B$  and  $C$  are independent of temperature and different for each spectral line.

### 3. RESULTS AND DISCUSSION

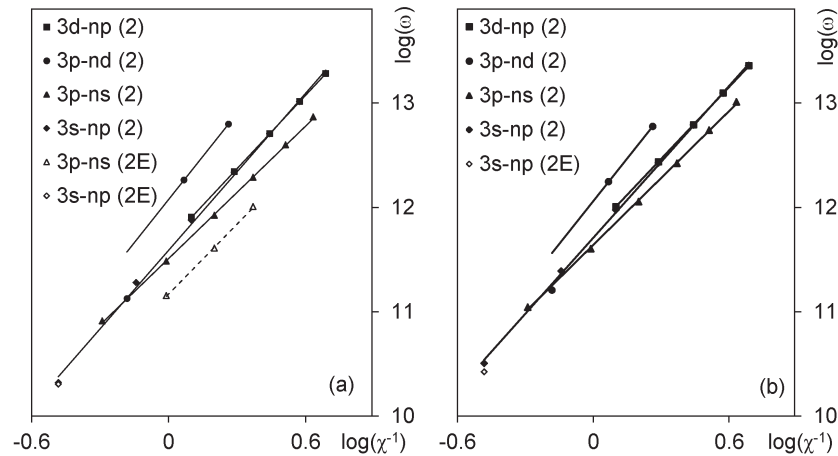


**Figure 1.** The total Stark widths (in rad·s<sup>-1</sup>) versus inverse upper level ionization potential (in eV) presented in log-log scale at temperature 10 000 K (a) and 50 000 K (b). The corresponding experimental values (Mioković & Veža 2001; Purić et al. 1976; Djeniže et al. 1992) are included.

Stark widths dependences versus inverse value of the upper level ionization potential for investigated spectral series of neutral sodium with principal quantum number of lower level equal to  $n=3$  are presented in Figure 1(a) at temperature of 10 000 K and in Figure 1(b) at temperature 50 000 K. Charts are given at two temperatures to show the temperature influence on Stark broadening and the effect of series merging at higher temperature. Having found these temperature dependences one can find the corresponding dependences of the Stark widths on the upper level ionization potential for any spectral line within spectral series studied here for every temperature. It is interesting to notice that dispersion of Stark widths data is decreasing with temperature increasing. The similar behaviour was noticed in preceding papers [10-13].

When the studied spectral series were treated separately the majority of the corresponding coefficient of determination  $R^2$  were better than 0.99. If 3p-3d transition is excluded from trend analysis, obtained  $R^2$  values for electron contribution are much better. For example  $R^2=0.9930$  instead of  $R^2=0.9681$  for temperature of 10 000 K.

**Table 1.** The calculated values for the electron and proton impact contribution to the Stark widths (FWHM)  $w$  (nm) of Na I spectral lines; at  $T_e = 10\,000\text{ K}$  and  $T_e = 50\,000\text{ K}$  normalized to an electron density of  $N_e = 10^{22}\text{ m}^{-3}$  are given.

Ion	$\lambda$ (Å)	Transition	Terms	w (nm)	
				T=10 000K	T=50 000K
Na I	90930.30	3d-4p	$^2D-^2P_0$	0.781	10.358
Na I	4277.97	3p-10d	$^2P_0-^2D$	1.184	9.775
Na I	4243.27	3p-11d	$^2P_0-^2D$	1.940	15.822
Na I	4217.25	3p-12d	$^2P_0-^2D$	3.055	24.627
Na I	4345.95	3p-10s	$^2P_0-2S$	0.103	1.438
Na I	4292.21	3p-11s	$^2P_0-2S$	0.160	2.250
Na I	4253.71	3p-12s	$^2P_0-2S$	0.240	3.384
Na I	4225.15	3p-13s	$^2P_0-2S$	0.347	4.920
Na I	2476.29	3s-11p	$^2S-^2P_0$	0.162	1.756
Na I	2465.13	3s-12p	$^2S-^2P_0$	2.596	2.740

Comparing experimental values of total line width with theoretical ones we found an agreement for 3s-3p transition on both investigated temperatures, distinction was within 10% on 10 000 K temperature and 20% on 50 000 K. For the only series for which Stark parameters were measured so far, 3p-ns on 10 000 K, agreement was found to be within 50%.

Using the described theory 10 spectral lines missing so far from 4 spectral series studied here are given in Table 1. Based on the above described analysis it is possible to predict Stark widths at any temperature but the results in this paper are given only for  $T = 10\,000\text{ K}$  and  $T = 50\,000\text{ K}$ .

#### 4. CONCLUSION

This work successfully proves the existence of the functional Stark widths dependences on the upper level ionization potential for the lines originating from the same series. These dependences were obtained and found to be of the form given by Equation (1). In order to achieve better linear fitting for 3p-nd series, transition 3p-3d has to be neglected for further analysis.

It was confirmed that temperature dependences agree with Equation (2). The Stark widths linear dependences on electron density was confirmed and used for data normalisation at  $N_e=10^{16}\text{cm}^{-3}$ . Like in the case of He I, Be I, Mg I and Ca I, high temperatures tend to eliminate differences in Stark broadening for all other parameters except for upper level ionization potential.

#### Acknowledgements

This work is financially supported by the Ministry of Education and Science of the Republic of Serbia within the project 171034.

#### REFERENCES

- [1] Dimitrijević M. S., Sahal-Brechot S., 1985, JQSRT, 34, 149
- [2] Dimitrijević M. S., Sahal-Brechot S., 1990, JQSRT, 44, 421
- [3] Dimitrijević M. S., Sahal-Brechot S., 1990, Bull. Obs. Astron. Belgrade, 142, 59
- [4] Sahal-Bréchet, S., Dimitrijević, M.S., Moreau N., 2012. Stark-B database, [online]. Available: <http://stark-b.obspm.fr> [Feb 13, 2012]. Observatory of Paris, LERMA and Astronomical Observatory of Belgrade
- [5] Purić J., Labat J., Djeniže S., Ćirković Lj., Lakićević I., 1976, Phys. Lett. A, 56, 83
- [6] Djeniže S., Srećković A., Labat J. and Platiša M., 1992, Phys. Scr., 45, 320
- [7] Mioković Ž., Veža D., 2001, Fizika, 10, 129
- [8] Ralchenko Yu., Kramida A. E., Reader J., and NIST ASD Team (2012). NIST Atomic Spectra Database (ver. 4.1.0), [Online]. Available: <http://physics.nist.gov/asd> [2012, January 17]. National Institute of Standards and Technology, Gaithersburg, MD
- [9] Purić J., Miller M. H., Lesage A., 1993, ApJ, 416, 825
- [10] Tapalaga I., Dojčinović I. P., Purić J., 2011, Mon. Not. R. Astron. Soc., 415, 503
- [11] Tapalaga I., Dojčinović I. P., Milosavljević M. K., Purić J., 2012, Publ. Astron. Soc. Aust., 29, 20
- [12] Dojčinović I. P., Tapalaga I., Purić J., 2011, Publ. Astron. Soc. Aust., 28, 281
- [13] Dojčinović I. P., Tapalaga I., Purić J., 2012, Mon. Not. R. Astron. Soc., 419, 904

## STARK BROADENING WITHIN 3s-np AND 3d-np SPECTRAL LINES OF NEUTRAL LITHIUM

I. P. Dojčinović<sup>1</sup>, I. Tapalaga<sup>1</sup>, M. Šćepanović<sup>2</sup> and J. Purić<sup>1</sup>

<sup>1</sup>*University of Belgrade, Faculty of Physics, P. O. Box 44, 11000 Belgrade, Serbia*

<sup>2</sup>*Faculty of Sciences and Mathematics, University of Montenegro, P.O. Box 211, 81 000 Podgorica, Montenegro*

**Abstract.** Stark widths dependences on the upper level ionization potential have been studied and discussed for 3s-np and 3d-np spectral series of neutral lithium. It was found that differences among the studied series decrease with temperature increasing. After establishing these dependences, found relations were used for prediction of Stark widths for the missed lines, thus avoiding much more complicated calculation procedures.

### 1. INTRODUCTION

The aim of this paper is to analyse functional dependence of Stark widths of spectral lines (FWHM) on the upper level ionization potential ( $\chi$ ) of the corresponding transition within spectral series of Li I. Using proposed simple model one can provide Stark broadening data for transitions that have not yet been calculated due to the lack of parameters needed in more complicated models.

Stark broadening data used for this analysis was taken from [1-3]. Most of this data is available on-line [4]. Data for ionization potential of Li I spectral lines were taken from NIST database [5]. A total of 9 spectral lines of Li I have been collected and analysed. Within these data the following series have been investigated: 3d-np(2), 3s-np(2). Next to the series notation there is a number in parentheses (2) indicating doublet spectral lines.

### 2. THEORETICAL BACKGROUND

Purić et al. [6] evaluated Stark width as the function of the upper level ionisation potential and the rest core charge of the emitter. The dependences were found to be of the form:

$$\omega[\text{rad} \cdot \text{s}^{-1}] = a \cdot (\chi[\text{eV}])^{-b} \quad (1)$$

where  $\omega$  is the line width (in angular frequency units),  $\chi$  is the corresponding upper level ionization potential (in eV). Coefficients  $a$  and  $b$  are dependent of the chosen temperature and electron density, but independent of the ionization potential for particular transition.

Stark broadening is dependent both on characteristics of emitters and on environmental conditions. This paper investigates only the dependence on emitter characteristics while the environmental conditions remain the same for all transitions. For this reason only data given at same electron density  $N_e = 10^{13} \text{cm}^{-3}$  was used in this paper.

Temperature of plasma also influences Stark broadening. It was commonly expected for Stark width broadening to be a weak function of temperature. For ion spectral lines dependence was found to be of the form  $\omega \sim T^{1/2}$ . Temperature dependence in the case of neutrals has to be of the form:

$$f(T) = A + B \cdot T^{-C} \quad (2)$$

### 3. RESULTS AND DISCUSSION

Stark widths dependences versus inverse value of the upper level ionization potential for investigated spectral series of neutral are presented in Figure 1(a) at temperature of 10 000 K and in Figure 1(b) at temperature 50 000 K. Charts are given at two temperatures to show the temperature influence on Stark broadening is small and that the series merge at higher temperature. Having found these temperature dependences one can find the corresponding dependences of the Stark widths on the upper level ionization potential for any spectral line within spectral series studied here for every temperature.

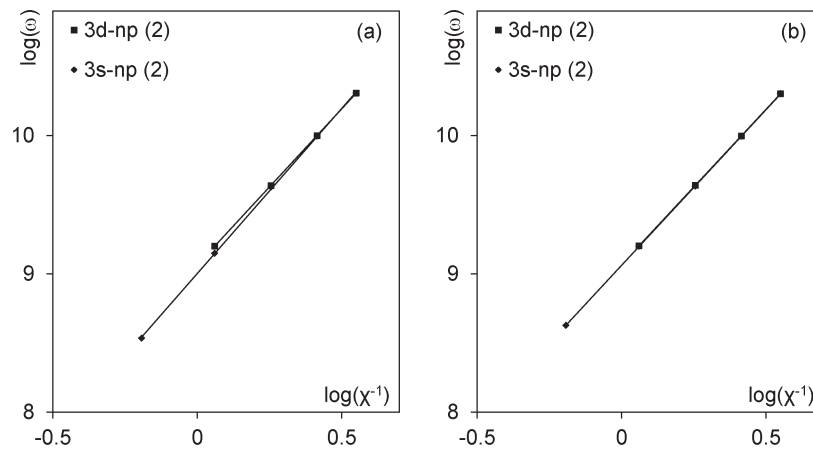


**Figure 1.** The total Stark widths (in  $\text{rad}\cdot\text{s}^{-1}$ ) versus inverse upper level ionization potential (in eV) presented in log-log scale at temperature 10 000 K (a) and 50 000 K (b).

The dominant influence of  $\chi$  on  $\omega$  is evidenced by the small difference in Stark broadening of two different series. Although we have investigated two different series, Stark broadening of these series is very similar due to the fact that they have the same  $\chi$ . It is interesting to notice that dispersion of Stark widths data is decreasing with temperature increasing. The similar behaviour was noticed in preceding papers [7-10]

As shown in Table 2 the dependence of Stark widths is not always linear on electron concentration. Broadening of spectral transitions from 3s-np and 3d-np series is linear with electron density. This dependence is mostly linear but Debye shielding and dense plasma can alter this behaviour. Due to this, only Stark broadening data for  $N_e = 10^{13} \text{ cm}^{-3}$  was used.

**Table 1.** The calculated values for the electron and proton impact contribution to the Stark widths (FWHM)  $\omega(\text{\AA})$  of Li I spectral lines; at  $T_e=10\ 000\ \text{K}$  and  $T_e=50\ 000\ \text{K}$  normalized to an electron density of  $N_e = 10^{19} \text{ m}^{-3}$  are given.

Ion	$\lambda$ (Å)	Transition	Terms	$\omega$ (Å)	
				T=10 000K	T=50 000K
Li I	9550	3d-8p	$^2\text{D}-^2\text{P}_0$	0.179	0.177
Li I	9227	3d-9p	$^2\text{D}-^2\text{P}_0$	0.285	0.281
Li I	9010	3d-10p	$^2\text{D}-^2\text{P}_0$	0.438	0.430
Li I	6873	3s-8p	$^2\text{S}-^2\text{P}_0$	0.093	0.086
Li I	6704	3s-9p	$^2\text{S}-^2\text{P}_0$	0.156	0.139
Li I	6589	3s-10p	$^2\text{S}-^2\text{P}_0$	0.249	0.215

In addition to trend analysis, the obtained Stark width dependences on the upper level ionization potential can be used for prediction of Stark widths data for the lines of interest in astrophysics as well as in atomic physic, not investigated until now. Stark widths data for 6 predicted lines missing so far from 2 spectral series studied here are predicted and given in Table 1.

**Table 2.** Stark width dependence on electron concentration ( $w=f(N_e)$ ) for 2p-6d transition at  $T = 10000\text{K}$ .

$N_e$ ( $\text{cm}^{-3}$ )	$10^{13}$	$10^{14}$	$10^{15}$	$10^{16}$	$10^{17}$
$\omega(\text{\AA})$	$2.45 \cdot 10^{-3}$	$2.42 \cdot 10^{-2}$	$2.21 \cdot 10^{-1}$	$1.81 \cdot 10^0$	$1.28 \cdot 10^1$

#### 4. CONCLUSION

This work successfully proves the existence of the functional Stark widths dependences on the upper level ionization potential for the lines originating from the same series. These dependences were obtained and found to be of the form given by equation 1. It was confirmed that temperature dependence agree with equation 2 and found a deflection from linear dependence on electron

density as shown in Table 2. Electron and proton impact contribution to Stark broadening have the same type of behaviour, but the proton contribution is significantly smaller. These results can also be used to evaluate the results of Stark broadening data that is already measured or calculated, although the main intention of authors is to obtain new data that is of interest in astrophysical calculations. High values for coefficients of determination suggest a good match between data and proposed models, thus enabling to predict widths of higher transitions with great confidence. Finally, the effect of series data merging with temperature increasing was found. These two series merge to common Stark widths dependences on the upper level ionization potential because of the same upper level and the fact that Stark broadening is dependent on upper level parameters.

### Acknowledgements

This work is financially supported by the Ministry of Education and Science of the Republic of Serbia within the project 171034.

### REFERENCES

- [1] Dimitrijević M. S., Feautrier N., Sahal-Brechot S., 1981, *J. Phys. B*, 14, 2559
- [2] Dimitrijević M. S., Sahal-Brechot S., 1991, *J. Quant. Spectrosc. Radiative Transfer*, 46, 41
- [3] Dimitrijević M. S., Sahal-Brechot S., 1991, *Bull. Astron. Belgrade*, 143, 29
- [4] Sahal-Bréchot, S., Dimitrijević, M.S., Moreau N., 2012. Stark-B database, [online]. Available: <http://stark-b.obspm.fr> [Feb 13, 2012]. Observatory of Paris, LERMA and Astronomical Observatory of Belgrade
- [5] Ralchenko Yu., Kramida A. E., Reader J., and NIST ASD Team (2012). NIST Atomic Spectra Database (ver. 4.1.0), [Online]. Available: <http://physics.nist.gov/asd> [2012, January 17]. National Institute of Standards and Technology, Gaithersburg, MD
- [6] Purić J., Miller M. H., Lesage A., 1993, *ApJ*, 416, 825
- [7] Tapalaga I., Dojčinović I. P., Purić J., 2011, *Mon. Not. R. Astron. Soc.*, 415, 503
- [8] Tapalaga I., Dojčinović I. P., Milosavljević M. K., Purić J., 2012, *Publ. Astron. Soc. Aust.*, 29, 20
- [9] Dojčinović I. P., Tapalaga I., Purić J., 2011, *Publ. Astron. Soc. Aust.*, 28, 281
- [10] Dojčinović I. P., Tapalaga I., Purić J., 2012, *Mon. Not. R. Astron. Soc.*, 419, 904

## TRANSIENT REGIMES OF DC GLOW DISCHARGE IN ARGON AT LOW PRESSURE: EXPERIMENT AND MODELLING

V. Lj. Marković<sup>1\*</sup>, S. N. Stamenković<sup>1</sup>, S. R. Gocić<sup>1</sup>, A. P. Jovanović<sup>1</sup>  
and M. N. Stankov<sup>1</sup>

<sup>1</sup> *Department of Physics, Faculty of Natural Sciences and Mathematics,  
University of Niš, Višegradska 33, P.O. Box 224, 18000 Niš, Serbia*  
*\*e-mail: vidosav@pmf.ni.ac.rs*

**Abstract.** The transient regimes including relaxation kinetics in argon afterglow and establishment of glow discharge in argon at low pressure are studied. The formative time delay  $t_f$  as a function of relative overvoltage  $\Delta U/U_s$  ( $U_s$  is the static breakdown voltage) is determined by the breakdown time delay  $t_d$  measurements at different interelectrode distances  $d$ . Experimental data are modelled on the basis of an analytical model with spatio-temporal avalanche development, taking into account the electron ionization coefficient  $\tilde{\alpha}$  decreased due to radial diffusion loss of electrons. Also, the relaxation kinetics in argon afterglow is studied and the diffusion coefficient of argon ions is determined.

### 1. INTRODUCTION

Argon is a constituent of the atmosphere and has many applications in different areas of science and technology: for surface sputtering and plasma processing [1], lamps and lighting [2], gas filled switches [3], particle and radiation detectors [4], lasers, plasma display panels, etc. On the other side, the breakdown time delay is relevant to some other applications, such as spark counters, ECR ion sources and micro-discharges.

Electrical breakdown in argon at low pressure was studied by the breakdown time delay measurements, applying rectangular (step) [5] and linearly rising (ramp) pulses [6]. Relaxation kinetics in argon afterglow at low pressure was studied by measuring a memory curve  $t_d(\tau)$  from very short relaxation times  $\tau$  in afterglow up to the saturation level determined by cosmic rays and natural radioactivity. Memory effect in argon was explained by charged particle decay to about 100 ms and from that time to the saturation level by the surface recombination of nitrogen atoms present as impurities [5]. These conclusions were confirmed by measurements of dynamic breakdown voltages [6].

Electrical breakdown in argon at low pressure was studied by ICCD imaging of the repetitive, pulsed regime in parabolic electrode geometry [7]. Also, ICCD recordings of space-time development in argon with current and voltage measurements were performed in [8]. Discharge regimes include low current Townsend discharge, oscillations and constrictions of discharge, as well as a high current diffuse glow discharge. The space time resolved structures of the discharge show formation of different regimes of low pressure argon discharge [8].

This paper is continuation of the earlier studies [5,6], and the formative time delay of argon discharge at low pressure is now measured as a function of relative overvoltage and under different interelectrode distances. The formative time is determined as described in [9], and modelled on the basis of an approximate analytical model with Townsend spatio-temporal avalanche development [10].

## 2. EXPERIMENTAL DETAILS

The measurements were carried out on a gas tube made of borosilicate glass with volume of  $V \approx 60 \text{ cm}^3$  and the plane-parallel cylindrical copper cathode with radius  $R = 11 \text{ mm}$  and variable interelectrode distances  $d = 10, 15, 20 \text{ mm}$ . The tube was filled with research purity argon at the pressure of  $2 \text{ mbar}$  (Matheson Co. with a nitrogen impurity below  $1 \text{ ppm}$ ). The static breakdown voltages were  $U_s = 218, 240, 262 \text{ V}$ , respectively. The time delay measurements were carried out at glow current  $I_g = 130 \mu\text{A}$ , glow time  $t_g = 1 \text{ s}$ , afterglow period  $\tau = 43 \text{ ms}$  and at different relative overvoltages  $\Delta U / U_s$ . More details about the experimental procedure can be found in [9,10].

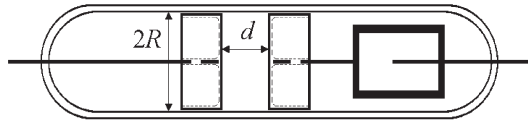


**Figure 1.** Gas tube with plane-parallel electrode system and variable gap  $d$ .

## 3. RESULTS AND DISCUSSION

The formative time delays were determined as described in [9], giving the approximately same values for the formative time delay. Its voltage dependence is fitted on the basis of approximate analytical model with spatio-temporal avalanche development [10], giving the formative time delay in the form:

$$t_f = \frac{\tilde{q} t_i}{\tilde{q} - 1} \ln \frac{1 + (\tilde{q} - 1)(i / i_0)}{\tilde{q}} \quad (1)$$

where  $i_0$  is the initial electron current,  $\tilde{q} = \tilde{\gamma} \frac{\alpha}{\tilde{\alpha}} [\exp(\tilde{\alpha} d) - 1]$  multiplication factor of electron avalanche with radial diffusion loss of electrons,  $t_i = d / w_i$  ion drift time from anode to cathode and  $w_i$  ion drift velocity of  $Ar^+$  ions. The electron ionization coefficient decreased due to radial diffusion loss of electrons is expressed by [11]:

$$\tilde{\alpha} = \alpha - (D_e / w_e)(2.4 / R)^2 \quad (2)$$

where  $D_e$  is the transverse electron diffusion coefficient,  $w_e = \mu_e E$  is the electron drift velocity and  $\mu_e$  electron mobility. Electron ionization coefficient  $\alpha / N(E/N)$  is taken from [12], where reduced electric field is expressed in Townsends ( $1Td = 10^{-17} Vcm^2$ ). Also, data for the drift velocity  $w_i$  of  $Ar^+$  are taken from [12], while

$$D_e / \mu_e = 4.24 + 0.005(E/N) \quad [V] \quad (3)$$

is our fit based on experimental data from [13] in the interval  $260 - 870Td$ .

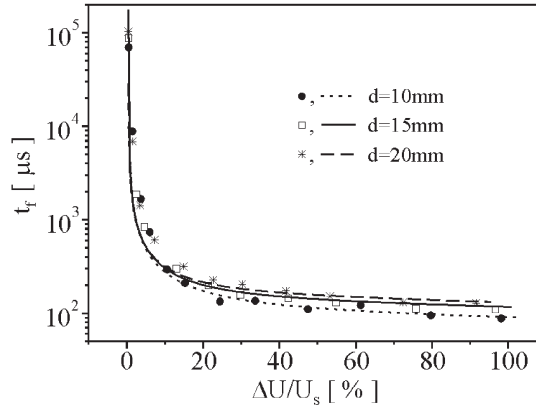


**Figure 2.** Formative time delays (●, □, \*) and the corresponding line fits.

The best fit of experimental data for the formative time delays as a function of relative overvoltages is shown in Fig. 2 by lines and is obtained for the following values of fitting parameters  $i/i_0 = 3 \times 10^5$ ,  $1 \times 10^4$ ,  $1 \times 10^3$  and  $\tilde{\gamma} = \tilde{\gamma}_s = 0.0072$ ,  $0.0077$ ,  $0.0092$ , respectively. The values for the secondary electron yields  $\tilde{\gamma}_s$  are calculated from breakdown condition with radial diffusion loss of electrons (finite R) [11]  $\tilde{\alpha}d = \ln(1 + \tilde{\alpha} / \alpha \tilde{\gamma})$ , which reduces to one-dimensional Townsend breakdown condition  $\alpha d = \ln(1 + 1/\gamma)$ , when  $\tilde{\alpha} \rightarrow \alpha$ ,  $\tilde{\gamma} \rightarrow \gamma$  and radial diffusion loss of electrons can be neglected (infinite R).

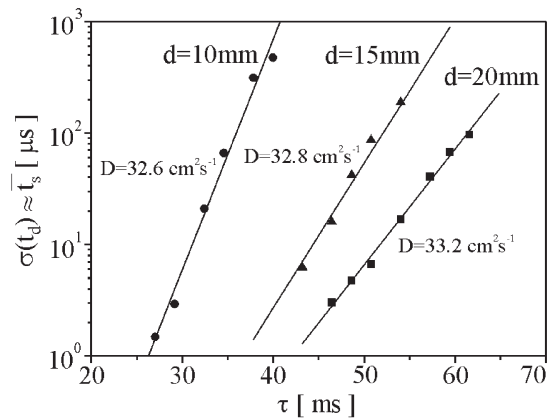


**Figure 3.** Diffusion coefficients  $D$  of molecular argon ions in afterglow.

### Acknowledgements

The authors are grateful to Ministry of Education and Science of Serbia for the support (project 171025).

### REFERENCES

- [1] M. A. Lieberman and A. J. Lichtenberg, *Principles of Plasma Discharges and Material Processing*, (Wiley, New York, 1994).
- [2] G. Zissis and S. Kitsinelis, *J. Phys. D: Appl. Phys.* **42**, 173001 (2009).
- [3] J. Chang, H. Wang, Q. Zhang and A. Qiu, *Plasma Sci. Technol.* **13**, 719 (2011).
- [4] A. Devismes, Ch. Finck, et al, *Nucl. Instrum. Methods A* **482**, 179 (2002).
- [5] V. Lj. Marković, S. R. Gocić, S. N. Stamenković and Z. Lj. Petrović, *Phys. Plasmas* **12**, 073502 (2005).
- [6] V. Lj. Marković, S. N. Stamenković, S. R. Gocić and Z. Lj. Petrović, *Contrib. Plasma Phys.* **45**, 476 (2005).
- [7] E. Wagenaars, N. W. B. Perriens, W. J. M. Brok, M. D. Bowden, E. M. Van Veldhuizen et al, *J. Phys. D: Appl. Phys.* **39**, 3831 (2006).
- [8] D. Marić, G. Malović and Z.Lj. Petrović, *Plasma Sources Sci. Technol.* **18**, 034009 (2009).
- [9] V. Lj. Marković, Z. Lj. Petrović and M. M. Pejović, *Plasma Sources Sci. Technol.* **6**, 240 (1997).
- [10] V. Lj. Marković, S. N. Stamenković, S. R. Gocić and S. M. Djurić, *Eur. Phys. J. Appl. Phys.* **38**, 73 (2007).
- [11] V. I. Kolobov and A. Fiala, *Phys. Rev. E* **50**, 3018 (1994).
- [12] A. V. Phelps and Z. Petrović, *Plasma Sources Sci. Technol.* **8**, R21 (1999).
- [13] C. S. Lakshminarasimha and J. Lucas, *J. Phys. D: Appl. Phys.* **10**, 313 (1977).

## STOCHASTICS OF ELECTRICAL BREAKDOWNS IN SYNTHETIC AIR

Aleksandar P. Jovanović, Vidosav Lj. Marković, Marjan N. Stankov and  
Suzana N. Stamenković<sup>1</sup>

<sup>1</sup> *Department of Physics, Faculty of Sciences and Mathematics, University of  
Niš, Višegradska 33, P.O. Box 224, 18000 Niš, Serbia*

**Abstract.** In this paper the stochastics of electrical breakdowns in synthetic air at low pressures are studied. Statistical analyses of measured electrical breakdown time delays are carried out and experimental data are fitted by Gaussian, Gauss-exponential and exponential distributions. For the sake of comparison the electrical breakdown time delay data are also described by two-parameter Weibull distribution.

### 1. INTRODUCTION

The new distributions of the statistical time delay of electrical breakdown in nitrogen were reported in paper [1]. The Gaussian, Gauss-exponential and exponential distributions of statistical time delay have been obtained on the basis of measurements on a gas tube with a plane-parallel electrode system made of copper. The distributions of the statistical time delay were theoretically founded on binomial distribution for the occurrence of initiating electrons in interelectrode space and described by using simple analytical and numerical models. It was shown that the shapes of statistical time delay distributions depend on the electron yield in the interelectrode space originating from residual states and that distribution changes from exponential and Gauss-exponential to Gaussian due to the influence of residual ionization [1]. The same results were confirmed in neon. It was shown that the formative ( $t_f$ ) and statistical time ( $t_s$ ) delays are dependent variables for  $t_s < t_f$  and their correlations were estimated. The linear correlation coefficient is  $\rho \approx 1$  at high electron yields (rates of electron production) and  $\rho \approx 0$  at low electron yields [2].

In this paper the electrical breakdown time delays in synthetic air at low pressure with steel electrodes are studied. Experimental data are fitted by analytical expression of Gaussian, Gauss-exponential and exponential distributions. Also, the electrical breakdown time delays are presented on the Weibull plot for the sake of comparison.

## 2. EXPERIMENTAL DETAILS

The measurements are conducted on a gas tube filled with synthetic air at the pressure of  $3 \text{ mbar}$ . The tube is made of molybdenum glass. The electrodes are made of steel with diameter  $D = 6 \text{ mm}$ , with mildly rounded edges and with a variable interelectrode distance. Synthetic air used in the experiment is a mixture of (21–23) % vol. oxygen with less than  $3.5 \text{ ppm}$  of impurities and remaining percentage of nitrogen with less than  $5 \text{ ppm}$  of impurities. Gas tube was pumped down to the pressure of  $10^{-5} \text{ mbar}$ , degassed at  $650 \text{ K}$  and then filled with synthetic air to the pressure of  $3 \text{ mbar}$ .

The measurements were conducted in 5 series, with 100 data acquired in single series at different preionization levels (relaxation times  $\tau$ ). Static breakdown voltage was  $U_s = 360 \text{ V}$ . Time delay measurements were conducted on 25% overvoltage, at glow current  $I_g = 300 \mu\text{A}$ , glow time  $t_g = 1 \text{ s}$  and with interelectrode distance  $d = 6 \text{ mm}$ . During the time delay measurements, the tube was protected from external light. More details about experimental procedure can be found in [1, 2].

## 3. RESULTS AND DISCUSSION

Obtained experimental distributions of statistical time delay are presented in this paper. With the decrease of preionization level (increasing of relaxation time), the shape of distributions changes from Gaussian for  $\tau = 1 \text{ ms}$ , Gauss-exponential for  $\tau = 2 \text{ ms}$  to exponential distribution for  $\tau = 5 \text{ ms}$ . This distributions are fitted by analytical expression of Gauss, Gauss-exponential and exponential distribution.

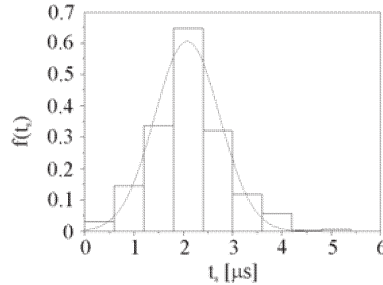


**Figure 1.** Gaussian density distribution of statistical time delay at  $\tau = 1 \text{ ms}$

The analytical expression of Gaussian density distribution used for fitting the statistical time delay at relaxation time  $\tau = 1\text{ ms}$  (Fig 1) is:

$$f_G(t_s) = \frac{1}{\sqrt{2\pi}\sigma_g} \exp\left(-\frac{(t_s - \bar{t}_{sg})^2}{2\sigma_g^2}\right) \quad (1)$$

with fitting parameters  $\bar{t}_{sg} = 2.08\ \mu\text{s}$  and  $\sigma_g = 0.66\ \mu\text{s}$ .

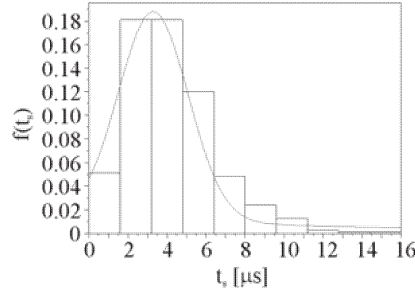


**Figure 2.** Gauss-exponential density distribution of the statistical time delay at  $\tau = 2\text{ ms}$

The analytical expression of Gauss-exponential density distribution used for fitting the statistical time delay at relaxation time  $\tau = 2\text{ ms}$  (Fig. 2) is:

$$f_{GE}(t_s) = a_g / (\sqrt{2\pi}\sigma_g) \exp\left(-\frac{(t_s - \bar{t}_{sg})^2}{2\sigma_g^2}\right) + a_e / \bar{t}_{se} \exp\left(-\frac{t_{se}}{t_s}\right) \quad (2)$$

and fitting parameters are  $\bar{t}_{sg} = 3.3\ \mu\text{s}$ ,  $\sigma_g = 1.785\ \mu\text{s}$ ,  $\bar{t}_{se} = 14.5\ \mu\text{s}$ ,  $a_g = 0.789$  and  $a_e = 0.211$ .

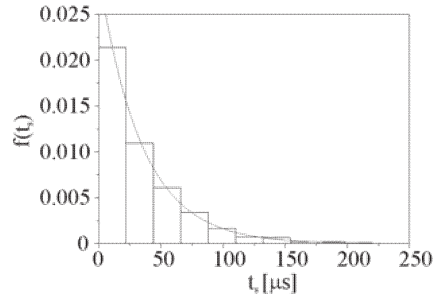


**Figure 3.** Exponential density distribution of statistical time delay at  $\tau = 5\text{ ms}$

The analytical expression of exponential density distribution used for fitting the statistical time delay at relaxation time  $\tau = 5\text{ ms}$  (Fig. 3) is:

$$f(t_s) = 1/\bar{t}_s \exp(-t_s/\bar{t}_s) \quad (3)$$

with fitting parameter  $\bar{t}_s = 34.6 \mu s$ .

Weibull distribution is widely applied for describing time delay of electrical breakdown. The two-parameter Weibull distribution, given by Equation (4), is now applied to the time delay data:

$$f(t_s) = (\kappa/\eta)t_s^{\kappa-1} \exp(-t_s^\kappa/\eta) \quad (4)$$

where  $\kappa$  is the shape parameter and  $\eta$  is the scale parameter of the distribution. In order to test the applicability of the Weibull distribution to the experimental data, time delay measurements are presented in the Weibull plot (figure 4). If the experimental data follow the Weibull distribution, linear dependence is expected on a Weibull plot. As can be seen in Fig. 4, this distribution can approximately describe experimental data, but distribution parameters do not have a physical meaning, as previously shown in the case of neon [3].

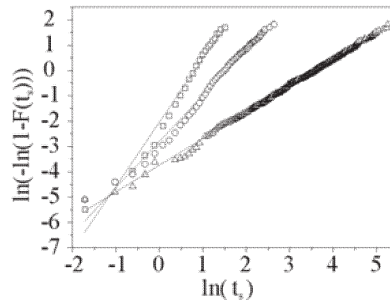


**Figure 4.** Weibull plot of statistical time delays of electrical breakdown for  $\tau = 1 ms$  (squares),  $\tau = 2 ms$  (circles) and  $\tau = 5 ms$  (triangles)

### Acknowledgements

The authors are grateful to the Ministry of Education and Science of the Republic of Serbia for partial support (project 171025).

### REFERENCES

- [1] V. Lj. Marković, S. R. Gocić, S. N. Stamenković, J. Phys. D. 39, 3317 (2006).
- [2] V. Lj. Marković, S. R. Gocić, S. N. Stamenković, J. Phys. D. 42, 015207 (2009).
- [3] S. N. Stamenković, S. R. Gocić, V. Lj. Marković, A. P. Jovanović, J. Appl. Phys. 110, 103304 (2011).

## STARK PARAMETERS REGULARITIES WITHIN TRANSITION ARRAYS OF MULTIPLY CHARGED IONS

Mara Šćepanović<sup>1</sup>, Ivan P. Dojčinović<sup>2</sup>, Irinel Tapalaga<sup>2</sup>, Mijat K.  
Milosavljević<sup>3</sup> and Jagoš Purić<sup>2</sup>

<sup>1</sup> *Faculty of Natural Sciences and Mathematics, University of Montenegro, P.  
O. Box 211, 20000 Podgorica, Montenegro;  
e-mail address: mara.scepanovic@gmail.com*

<sup>2</sup> *Faculty of Physics, University of Belgrade, P. O. Box 44, 11000 Belgrade,  
Serbia*

<sup>3</sup> *University of Priština, Faculty of Technical Sciences, K. Miloša 20, 28220 K.  
Mitrovica, Serbia*

**Abstract:** Stark parameters published data are used to demonstrate the existence of various regularities within similar spectra of different elements and their ionization stages. The emphasis is on the Stark parameter dependence on the upper level ionization potential and on the rest core charge of the emitter for the lines from transition arrays of multiply charged ions. The found relations connecting Stark widths and shift parameters with upper level ionization potential, rest core charge and electron temperature were used for Stark broadening data prediction, thus avoiding much more complicated procedures.

### 1. INTRODUCTION

The aim of this paper is to analyze functional dependence of Stark parameters of spectral lines (FWHM) on the upper level ionization potential of the corresponding transition within 3p-4s and 3p-5s spectral arrays of the following ions: Be II, Li II, Al III, Si III, S IV, N V, O V, O VI, S VI, FVI and FVII, taken from [1-8]. This work is in continuation with recently published papers devoted to the checking of Stark widths dependences on the upper level ionization potential within spectral arrays of the ions of different ionization stages [9] and references therein; and within spectral series of neutral helium, magnesium, beryllium and calcium. See reference [10-13]. The emphasis is on the Stark parameter dependence on the upper level ionization potential and on the rest core charge of the emitter for the lines from transition arrays of multiply charged ions.

## 2. THEORY

Theoretically derived functional relations for line width and shift, successfully fitted to a number of spectral lines as shown in a series of articles [14-16], are of the form:

$$\omega, d = N_e f_{1,2}(T) a_{1,2} Z_c^{c_{1,2}} \chi^{-b_{1,2}} \quad (1)$$

where  $\omega$  and  $d$  are the line width and shift,  $f_{1,2}(T)$  is function of electron temperature for the Stark width and shift, respectively,  $\chi$  is the corresponding upper state ionization potential,  $a_{1,2}$  and  $b_{1,2}$  are coefficients independent on the electron density and ionization potential for particular transition, and  $Z_c$  is the rest core charge of the emitter, as seen by the electron undergoing transition.

However, Stark parameters dependence on the electron temperature is different from line to line for all spectra. Therefore, the correction to the temperature dependence has to be done with great care for all data used, in particular case of the verification of certain type of mentioned dependencies and regularities. For instance, instead of the commonly adopted temperature dependence of  $T^{-1/2}$  for widths of ion lines, one has to use, from line to line [14,16], the whole spectrum of functions of the form:

$$f(T) = A + BT^{-C} \quad (2)$$

One can determine empirically, from experiment or more sophisticated calculations, averaged empirical values for  $A = aN_e f(T)$  and  $b$ . A general form of that dependence in the case of the particular transition array is

$$W^*, D^* = \omega, d / z^c = a \chi^{-b} \quad (3)$$

where  $W^*$ ,  $D^*$  is the line width/shift in angular frequency units;  $\chi$  is the corresponding upper level ionization potential expressed in eV;  $z$  is the rest core charge of the emitter as seen by the electron undergoing the transition. The coefficients  $a$ ,  $b$  and  $c$  are independent of the ionization potential (for particular electron temperature and density) for a given transition. Even more, it has been found that coefficient  $c$  is constant approximately equal 5.20 in majority of the cases. The Stark parameter dependence on the electron density is well established, and in the case of nonhydrogenic emitters is linear.

## 3. RESULTS AND DISCUSSION

A comprehensive set of Stark broadening data of the investigated ions has been used here to demonstrate the existence of Stark width data regularities within a group of spectral lines originating from 3p-4s and 3p-5s transition arrays. The procedure for Stark broadening data predictions were described elsewhere [14-16].

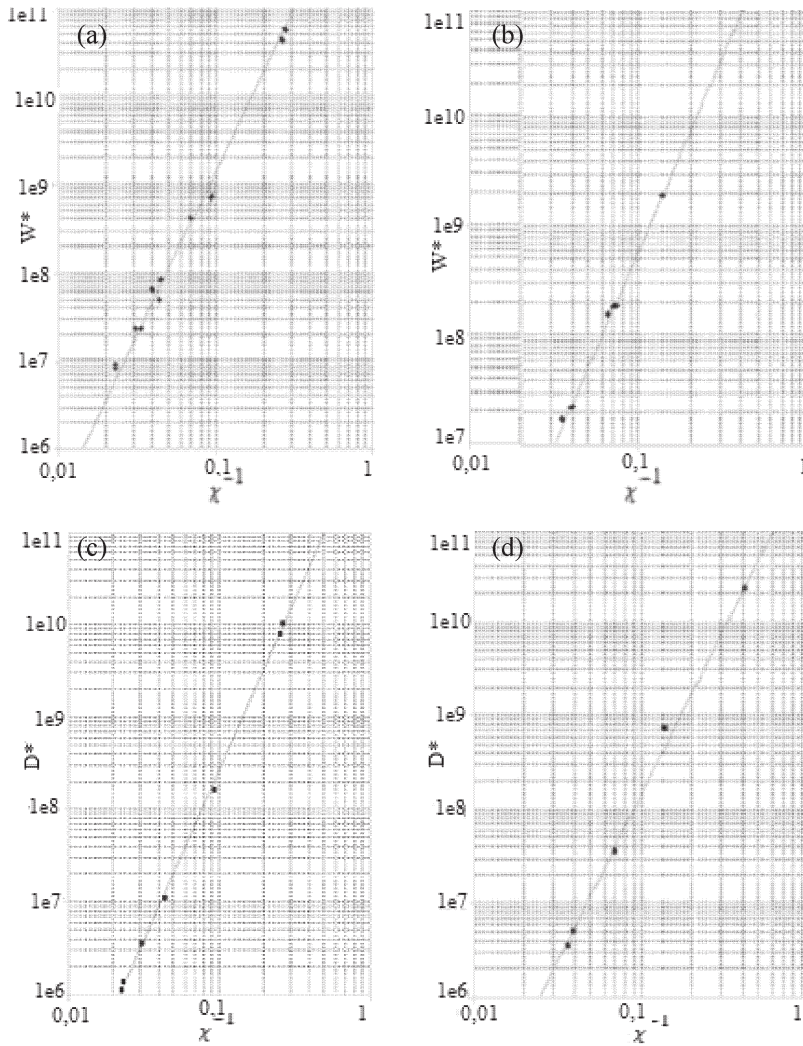


**Figure 1.** Reduced Stark widths  $W^*$ (rad·s<sup>-1</sup>) (a and b) and reduced Stark shift (c and d) vs. inverse value of the upper level ionization potential  $\chi$  (eV) for 3p-4s (a and c) and 3p-5s (b and d) transition arrays, respectively; square for calculated width and line for trend.

It has been verified [14-16] that the Esq. (3) is appropriate for all investigated transitions in all groups of the ions, above mentioned, at different temperatures and electron densities. Namely, for Stark width, it was found that the best fit can be obtained if  $f(T)$  is taken as given by Eq. (2) instead of  $T^{1/2}$ . Due to the lack of Stark shift data at different temperatures the best fit of the form  $f(T)=T^{1/2}$  was used.

In this paper we used the theoretical results to find the systematic trends for reduced Stark widths  $W^*$  and Stark shift  $D^*$  on the inverse value of

upper level ionization potential  $\chi$  within similar spectra of the multiply charged ion and we are presented in Figure 1.

In table 1. we presented appropriate coefficients  $a$  and  $b$ .

**Table 1.** Values of coefficients  $a_{W^*}$ ,  $b_{W^*}$  (from eq.3 for Stark width) and  $a_{D^*}$  and  $b_{D^*}$  (from eq.3 for Stark shift)

<i>transition</i>	$a_{W^*}$	$b_{W^*}$	$a_{D^*}$	$b_{D^*}$
3p-4s	$7,72 \times 10^{12}$	3,75	$1,47 \times 10^{12}$	3,82
3p-5s	$2,33 \times 10^{12}$	3,58	$5,48 \times 10^{11}$	3,58

The corresponding correlation's factor for all the charts was almost equal to unity. Therefore, they can be used to estimate the needed Stark widths and shifts for the spectral lines not investigated so far.

All data correspond to an electron density  $N_e = 10^{23} \text{ m}^{-3}$  and for different temperatures being normalized using equation (2) at  $T = 10^5 \text{ K}$ .

This work successfully proves the existence of the regularities for 3p-ns ( $n=4,5$ ) transition arrays.

## REFERENCES

- [1] M.S. Dimitrijević and S. Sahal-Brechot, *J.Q.S.R.T* Vol 48, 397, (1992),
- [2] M.S. Dimitrijević and S. Sahal-Brechot, *Phzsica Scripta* Vol 54, 50, (1996),
- [3] M.S. Dimitrijević and S. Sahal-Brechot, *A&A.Supp. Ser.* 76, 53 (1988),
- [4] M.S. Dimitrijević and S. Sahal-Brechot, *A&A.Supp. Ser.* 99, 585 (1993),
- [5] M.S. Dimitrijević and S. Sahal-Brechot, *A&A.Supp. Ser.* 95, 109 (1992),
- [6] M.S. Dimitrijević and S. Sahal-Brechot, *A&A.Supp. Ser.* 93, 359 (1992),
- [7] M.S. Dimitrijević and S. Sahal-Brechot, *A&A.Supp. Ser.* 100, 81 (1993),
- [8] M.S. Dimitrijević and S. Sahal-Brechot, *A&A.Supp. Ser.* 101, 587 (1993),
- [9] H. Elabidi and S. Sahal-Brechot, *Eur. Phys. J. D* 61, 285–290 (2011).
- [10] Tapalaga I., Dojčinović I. P., Purić J., *Mon. Not. R. Astron. Soc.*, 415, 503, (2011),
- [11] Tapalaga I., Dojčinović I. P., Milosavljević M. K., Purić J., *Publ. Astron. Soc. Aust.*, 29, 20, (2012),
- [12] Dojčinović I. P., Tapalaga I., Purić J., 2011, *Publ. Astron. Soc. Aust.*, 28, 281, (2011),
- [13] Dojčinović I. P., Tapalaga I., Purić J., *Mon. Not. R. Astron. Soc.*, 419, 904, (2012),
- [14] J. Purić and M. Šćepanović: *ApJ*, 521, 490 (1999).
- [15] M. Šćepanović and J. Purić:, *J.Q.S.R.T*, 78, 197 (2003).
- [16] J. Purić, I.P. Dojčinović, M. Nikolić, M. Šćepanović, B.M. Obradović and M.M. Kuraica: *ApJ*, 680, 803 (2008).

## ELECTRON TRANSPORT COEFFICIENTS IN GASES FOR RESISTIVE PLATE CHAMBERS

D. Bošnjaković, S. Dujko and Z.Lj. Petrović

*Institute of Physics, University of Belgrade,  
Pregrevica 118, 11080 Belgrade, Serbia*

**Abstract.** Electron transport coefficients for electron swarms in isobutane,  $C_2H_2F_4$  and their mixtures are calculated using a Monte Carlo simulation technique and a multi term solution of non-conservative Boltzmann equation. Values of drift velocity and rate coefficients are reported here. Results can be used as input parameters for simulation-aided design and optimization of Resistive Plate Chambers.

### 1. INTRODUCTION

Introduced in 1980s, Resistive Plate Chambers (RPCs) [1,2] quickly became a widely used gaseous particle detector in high energy physics experiments mainly because of their simple construction, good rate capability, and timing resolution. They can also have a benefit of high position resolution which makes them a good alternative to scintillator and solid state detectors used in medical imaging applications [3].

Since their introduction, several gas mixtures have been proposed and tested with the goal of achieving optimum performance characteristics such as efficiency and timing. Isobutane ( $iC_4H_{10}$ ) and Freon 134a ( $C_2H_2F_4$ ) are the most frequently used gases in RPCs. They have good quenching and streamer suppression properties. The mixture of  $C_2H_2F_4$  and isobutane, with a small addition of  $SF_6$ , is usually used in RPCs at the CMS, LHCb and ALICE experiments.

During last 15 years, several numerical simulations of RPC's operation have been performed [4-7]. They have been meant to give an insight into the underlying physical phenomena (by comparison with experimental measurements) and to be used as a tool for detector design and optimization. Electron swarm properties including the drift velocity, diffusion tensor, and ionization and attachment coefficients were input parameters in these simulations.

In this work, as a first step in our ongoing investigation on RPCs we present electron transport coefficients in isobutane,  $C_2H_2F_4$  and in their mixtures as a function of reduced electric field strength  $E/N$ . Results are obtained using a

Monte Carlo simulation technique and multi term Boltzmann equation analysis. Our results are compared with experimental data when possible and with those obtained by the MAGBOLTZ simulation program [8].

## 2. METHODS

In this work we apply Monte Carlo simulation technique and multi term solution of non-conservative Boltzmann equation. Computer codes behind of these methods are verified for a number of benchmarks [9,10]. In the present Monte Carlo code we follow a large number of electrons (typically  $10^4$ - $10^6$ ) over small time steps. The electron swarm is assumed to develop in an infinite gas under uniform fields. All calculations are performed for zero gas temperature. It is assumed that all electron scattering is isotropic. After relaxation to a steady-state, all transport properties are averaged over the time in order to obtain better statistics. The reader is referred to a recent review [10] for a detailed discussion of the multi term Boltzmann equation solution technique.

For comparison, electron transport coefficients are calculated by the MAGBOLTZ [8], a Monte Carlo simulation tool which is well known in gaseous particle detector community. MAGBOLTZ uses its own cross section database which is imbedded in the code. For calculations made by our codes, we have employed MAGBOLTZ's set of cross sections for isobutane as no other cross section sets for isobutane exist [11]. For  $C_2H_2F_4$ , however, we have used a cross section set recently developed by our group [12].

## 3. RESULTS AND DISCUSSION

In this work we consider the electric field strength range: 1-1000 Td ( $1 \text{ Td} = 10^{21} \text{ Vm}^2$ ). Typical RPC operating field strengths are between 200 and 500 Td. The gas number density is  $3.54 \times 10^{22} \text{ m}^{-3}$  which corresponds to the pressure of 1 Torr at 273 K. Here, we present only those results which could be directly compared to experimental data obtained in a narrow  $E/N$  range, usually using RPC-like configuration for measurement.

Figure 1 (left) shows our Monte Carlo results for the ionization coefficient in isobutane. Our results are compared with the MAGBOLTZ calculations and experimental data. We see that our results mostly agree with those from MAGBOLTZ except for higher and/or lower electric fields. Experimental data from Nakhostin *et al.* [13] for higher electric fields fit quite well with our calculations while those from Lima *et al.* [14] for lower electric fields are closer to MAGBOLTZ's predictions.

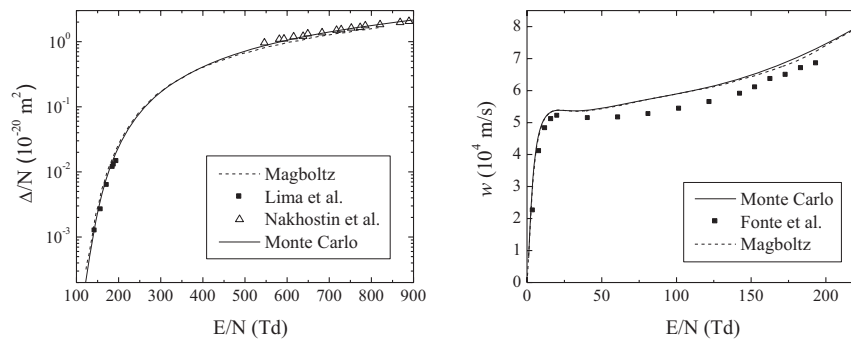


**Figure 1.** Variations of the first Townsend ionization coefficient ( left) and drift velocity (right) with  $E/N$  in isobutane.

In Figure 1 (right) we show the variation of the drift velocity with  $E/N$  in isobutane. Our results are compared with those obtained by the MAGBOLTZ and with the experimental data taken from Fonte *et al.* [11]. For  $E/N$  between 1 and 225 Td, calculations performed by our Monte Carlo code show no differences between the flux and bulk drift velocity components. Our results agree quite well with those obtained from MAGBOLTZ, except between 150 and 200 Td. On the other hand, the experimental data for higher field strengths do not fit well to numerical calculations. Reported systematic errors in this range are about 10% which questions the quality of the experimental technique.

In Figure 2 we display the drift velocity in  $C_2H_2F_4$ -isobutane mixture (90-10%) as a function of  $E/N$ . Calculations are performed by a multi term theory for solving Boltzmann's equation and compared with those obtained by the MAGBOLTZ and with measurements by Colucci *et al.* [15]. It is evident that our results strongly disagree with those from MAGBOLTZ. This can be

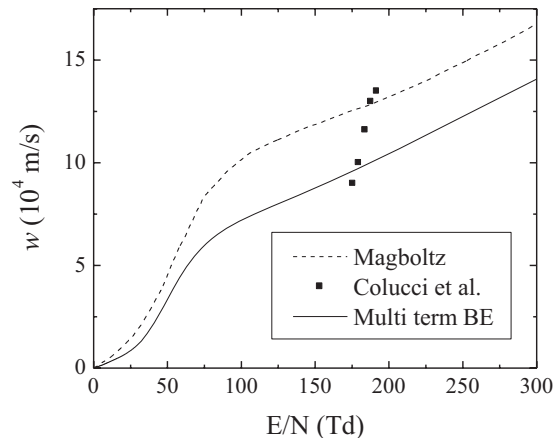


**Figure 2.** Variation of the drift velocity with  $E/N$  in  $C_2H_2F_4$ -isobutane gas mixture (90-10%).

attributed to different cross sections used for  $C_2H_2F_4$ . We see that the measurements do not fit well to either our or MAGBOLTZ results.

From this work we see that discrepancies between the measured swarm parameters and those calculated using the independently assessed cross section sets may be due to several causes: (1) uncertainties in the cross sections; (2) uncertainties in the measured swarm parameters; and (3) due to the effects of collisions between electrons and excited molecules. Much remains to be done in order to improve the existing sets of cross sections for gases of interest for RPCs.

### Acknowledgements

This work is supported by MPN, Serbia, under the contract number OI171037.

### REFERENCES

- [1] R. Santonico, R. Cardarelli, Nucl. Instr. and Meth. 187, 377 (1981).
- [2] R. Santonico, R. Cardarelli, A.D. Biagio, A. Lucci, Nucl. Instr. and Meth. A 263, 20 (1988).
- [3] A. Blanco, N. Carolino, C.M.B.A. Correia, R. Ferreira Marques, P. Fonte, D. González-Díaz, A. Lindote, M.I. Lopes, M.P. Macedo, A. Policarpo, Nucl. Instr. and Meth. A 533, 139 (2004).
- [4] M. Abbrescia, et al., Nucl. Phys. B 78, 459 (1999).
- [5] W. Riegler, C. Lippmann, R. Veenhof, Nucl. Instr. and Meth. A 500, 144 (2003).
- [6] S.H. Ahn, et al., Nucl. Instr. and Meth. A 533, 32 (2004).
- [7] L.K. Khorashad, et al., Nucl. Instr. and Meth. A 628, 470 (2011).
- [8] S. Biagi, Nucl. Instr. and Meth. A 421, 234 (1999).
- [9] Z.M. Raspopović, S. Sakadžić, S. Bzenić and Z.Lj. Petrović, IEEE Trans. Plasma Sci. 27, 1241 (1999).
- [10] S. Dujko, R.D. White, Z.Lj. Petrović and R.E. Robson, Phys. Rev. E 81 046403 (2010).
- [11] P. Fonte, A. Mangiarotti, S. Botelho, J.A.C. Goncalves, M. Ridenti, C.C. Bueno, Nucl. Instr. and Meth. A 613, 40 (2010).
- [12] O. Šašić, et al., (2012), unpublished.
- [13] M. Nakhostin, M. Baba, T. Ohtsuki, T. Oishi, T. Itoga, Nucl. Instr. and Meth. A 572, 999 (2007).
- [14] I.B. Lima, et al., Nucl. Instr. and Meth. A 670, 55 (2012).
- [15] A. Colucci, et al., Nucl. Instr. and Meth. A 425, 84 (1999).

## OPTOGALVANIC SIGNALS FROM IRON POSITIVE IONS IN HOLLOW CATHODE DISCHARGE

V. Mihailov<sup>1</sup>, R. Djulgerova<sup>1</sup>, J. Koperski<sup>2</sup>, Z. Lju. Petrovic<sup>3</sup>,

<sup>1</sup>*Institute of Solid State Physics, BAS, 1784 Sofia, Bulgaria*

<sup>2</sup>*Institute of Physics, Jagellonian University, 30-059, Krakow, Poland*

<sup>3</sup>*Institute of Physics, 11080 Zemun, Belgrade, Serbia*

**Abstract.** Dynamic optogalvanic signals from Fe positive ions in Kr/Fe hollow cathode discharge are experimentally registered. Peculiarities in amplitude and time shapes dependences on discharge current and their correlation with the voltage-current characteristic of the lamp are shown. The resonant signals from Kr atoms and non-resonant signals are also presented.

### 1. INTRODUCTION

The optogalvanic signal arises whenever the discharge is illuminated by laser light whose frequency is resonant with some spectral transition of atoms molecules or ions present in the plasma. The absorbed (typically laser) light, perturbs the effective ionization balance or mobility of the particles in the plasma. This signal is detected as an impedance variation in the electric discharge. In this way, being directly operated by electrical signals rather than the optical ones, the optogalvanic spectroscopy turns out to be simpler in comparison with several other spectroscopic techniques [1]. The dynamic optogalvanic signal (DOGS), representing plasma reaction after a short (ns) laser pulse absorption, is significantly more informative than the stationary signal because the former is characterized not only by its amplitude and sign but also by its time dependency shape and peculiarities. The optogalvanic technique has been widely used for frequency stabilization, wavelength calibration, atomic and molecular spectroscopy [2], isotopic analysis [3], plasma diagnosis [4], and the Penning ionization effect [5].

The hollow cathode discharge proves to be very favorable plasma source in plasma spectroscopy due to the wide spread utilization of the commercial hollow cathode lamps. One of the most attractive features of the hollow cathode discharge is its ability to atomize the substance on the cathode walls predominantly through a sputtering by the working gas ions. By this way the hollow cathode lamps are perfect optogalvanic detectors due to their rich and stable spectra, which include the emitted spectral lines of both working gas and

sputtering atoms of the cathode materials. Most of the investigations deal with optogalvanic effect from atomic and molecular transitions. There are only few data for optogalvanic signals from positive ions and most authors do not discuss the optogalvanic effect origin. Any data about dynamic optogalvanic signals from ions of a sputtered material it is not found in literature.

## 2. EXPERIMENTAL RESULTS

In this work a DOGSs from Kr atoms, Fe ions and non-resonant signals are registered as a function of discharge current in Fe/Kr hollow cathode discharge.

The Iron/ Krypton fill hollow cathode lamp made by Photron Pty. Ltd. (model. P826K) was used in experiment. The hollow cathode lamps are illuminated by a pulse (5ns width,, 10Hz frequency, 3mJ energy) dye laser (Sopra LCRI pumped by Nd:YAG laser). The incident laser beam passes on the cathode axes and illuminates both the hollow cathode plasma and the cathode bottom. The optogalvanic signals are measured using a two-channel digital real-time oscilloscope (Le Croy 9361) and processed by a computer.

Three types DOGS are registered as a function of discharge current:

- from Kr atoms, corresponding to 439.9nm optical transition,
- Non-resonant optogalvanic signals, recorded at laser wavelengths far enough from the Kr and Fe optical transitions.
- from Fe positive ions, corresponding to 220.8nm optical transition.

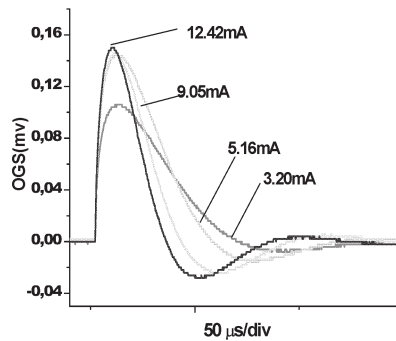


**Figure 1.** DOGS from Kr atoms, corresponding to 439.9 nm optical transition

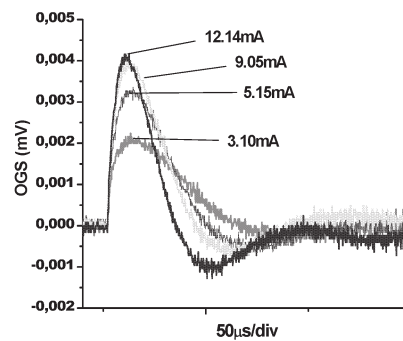


**Figure 2.** Non resonant optogalvanic signals as a function of discharge current

It is seen in Fig. 1 and Fig. 2 that the amplitudes for both type of DOGS increase at growing values of  $i$ , but their widths decrease. Saturation at 5mA for optogalvanic signals from Kr atoms and at 9mA for non resonant signals is observed in these uniform dependencies. The time-resolved non-resonant background signals exhibited the same shape and time behaviour as the

resonant ones, however, with a one order lower magnitude. The formation of the resonant optogalvanic signal is due to the increased population of the upper levels as a result of laser illumination, which can be much easily ionized than the origin levels. By this way first positive part of the signal is formatted. The next part of the DOGS reveals the relaxation behaviour of the disturbed atomic level and electrical plasma properties. The reason for arising of non-resonant signals is consider being direct photoionization from the highest levels since the atoms lying on them are very easily ionised even by absorption of excited laser light with small energy [6]. Contribution of the photoeffect from the cathode bottom material is also possible for non-resonant DOGSs formation [7].

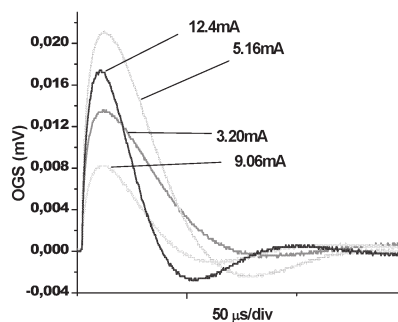


**Figure 3.** DOGS from  $\text{Fe}^+$  ions, corresponding to  $\text{Fe II } 220.8\text{nm}$  optical transition

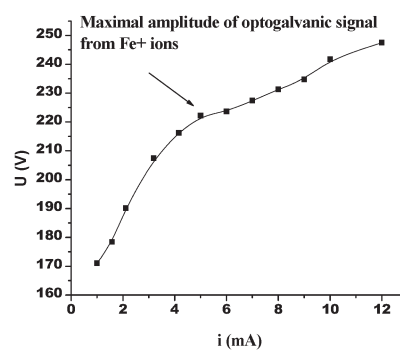


**Figure 4.** V-I characteristic of Kr/Fe hollow cathode discharge

Different dependences of  $\text{Fe II}$  optogalvanic signal (Fig. 3) compared to signals from Kr atoms are observed. First increasing the discharge current from 3mA to 5mA causes the DOGS amplitude to increase. Further increasing of the current dramatically decreases the amplitude following the amplitude increasing again. The V-I dependence (Fig. 4) of a discharge shows two different regions: one with a steep slope at low current and the other one, with a smaller slope at higher current. It was found that the average amount of excitation per electron emitted by the cathode was maximal value at the V(I) points corresponding to the transition region, which suggests the optimal discharge conditions for the occurrence of the hollow cathode effect [8]. In this area an optogalvanic signal from  $\text{Fe}^+$  ions change the tendency from increase to reduction. Correlation of DOGS amplitude behavior and V-I dependence of a hollow cathode discharge demonstrate high sensitivity of such kind of signals to electrical characteristics of the discharge. Possible explanation for optogalvanic formation is a change in electron-ion recombination rate in negative glow and charge-exchange rate in dark space. Change in ion-electron emission from cathode walls is also possible [9]. Non resonant component in the signal can not

be excluded because of high energy of the illuminating photons. For quantitative explanation a measurement of radial distribution of the amplitude and shape of the signal together with numerical modeling is necessarily.

### 3. CONCLUSION

In the present work we are offering for the first time dynamic optogalvanic signals arising from positive ions of sputtered material. They are compared with experimental results for optogalvanic signals from atoms, and non-resonant signals registered in Kr/Fe hollow cathode lamp. Difference in its shape and amplitude dependency together with V-I characteristic of the discharge is shown. Due to the markedly different dependences of  $\text{Fe}^+$  signal compared to neutral Kr and non-resonant optogalvanic signal it was possible to effectively separate ionic from neutral optogalvanic spectra. This proved to be a powerful advantage in studying the fundamental aspects of the sputtering, such as the spatial distribution of the sputtered particles, their transport and interaction with the other plasma species.

### Acknowledgements

Support for this work by joint projects between the Institute of Solid State Physics - BAS (Sofia, Bulgaria), the Institute of Physics of Jagellonian University (Krakow, Poland) and the Institute of Physics (Belgrade, Serbia) is gratefully acknowledged. The work was done as part of the project "Laser diagnostics in archaeology", DO02-274/2008, financed by the Bulgarian National Science Fund.

### REFERENCES

- [1] B. Barbieri, N. Beverini, and A. Sasso, *Rev. Mod. Phys.* 62, 603 (1990)
- [2] A. Sasso, M. I. Schisano, G. M. Tino, and M. Inguscio, *J. Chem. Phys.* 93, 7774 (1990)
- [3] P. Pianarosa, Y. Demers, and J. M. Gagne, *J. Opt. Soc. Am. B Opt. Phys.* 1, 704 (1984)
- [4] A. Ben-Amar, G. Erez, S. Fastig, and R. Shuker, *Appl. Opt.* 23, 4529 (1984)
- [5] J. H. Lee, Hyuck Cho, E. C. Jung, and J. M. Lee, *J. Korean Phys. Soc.* 38, 99 (2001)
- [6] Djulgerova R.; Mihailov V. *Specr. Lett.* 27, 1271 (1994)
- [7] Djulgerova R.; Mihailov V. *Appl. Phys. B* 56, 301 (1993)
- [8] N. Bagger, A. Bogaerts and R. Gijbels, *Spectrochim. Acta Part B* 57, 311 (2002)
- [9] Djulgerova R.; Mihailov V. *Europhys. Lett.* 36, 571, (1996)

## VOLT-AMPERE CHARACTERISTICS OF LOW-PRESSURE DC DISCHARGES IN WATER VAPOR

Jelena Sivoš, Nikola Škoro, Dragana Marić,  
Gordana Malović and Zoran Lj. Petrović

*Institute of Physics, University of Belgrade,  
Pregrevica 118, 11000 Belgrade, Serbia  
e-mail: [sivosj@ipb.ac.rs](mailto:sivosj@ipb.ac.rs)*

**Abstract.** In this paper we present the Volt-Ampere ( $V$ - $I$ ) characteristics of a DC discharge in water vapor at 0.6 Torr (at the minimum of the Paschen curve) and corresponding emission profiles. Measurements were performed for different electrode gaps (from 0.5 to 3.1 cm).  $V$ - $I$  characteristics are compared by using standard scaling parameter  $j/p^2$  ( $j$  - current density;  $p$  - pressure). Some of the issues in proper determination of parameter are discussed. For the gap  $d = 0.5$  cm, a case of coexistence of two discharge channels is presented.

### 1. INTRODUCTION

Today, many investigations are focused on discharges in liquids (water or some electrolyte), discharges in heterogeneous water-air bubble systems [1] and to atmospheric discharges which operate in ambient air. Many possible applications for treatment of materials, biomedical applications of plasmas [2] and mercury-free sources of lighting [3] are reason for such interest. These discharges operate either in a gas mixture that contains a significant percentage of water vapor or inside vapor bubbles in liquids. It is thus important to know fundamental processes and parameters for pure water vapor discharge ignited in simple geometry. Our goal is to investigate non-equilibrium parallel-plate DC discharge in water vapor with different parameters and obtain a reference set of data (ionization coefficients, secondary electron yield, breakdown voltages) that can be used in modeling of gaseous dielectrics, breakdown, gas discharges and collisional plasmas.

Measurements of breakdown voltages and spatial profiles of DC discharges in water vapor were presented in our earlier paper [4]. Here we present measurements of  $V$ - $I$  characteristics, which are necessary for a complete analysis of secondary electron production in addition to breakdown data [5].

## 2. EXPERIMENTAL SET-UP

Discharge chamber consists of two parallel-plate electrodes 5.4 cm in diameter, placed inside a tightly fitting quartz tube. Electrodes separation is adjustable. The cathode is made of copper and the anode is a transparent with a conductive film of platinum deposited on a quartz window. Chamber construction allows us recording of axial and radial profiles of emission. Profiles are recorded by sensitive ICCD camera (Andor IStar DH720-18U-03). Details of the measurement technique are described in [4].

Water vapor, obtained from bi-distilled de-ionized water, is introduced into the discharge chamber from a container through a pressure regulative valve at a slow flow rate. When initial period of boiling is completed, the water in the container become devoid of dissolved oxygen and volatile constituents. In order to saturate the chamber walls, water vapor is maintained at a moderate pressure in the chamber for periods of 1-2 h [4].

## 3. RESULTS AND DISCUSSION

In figure 1 we show discharge voltage as a function of the reduced current density ( $j/p^2$ ), for electrode gaps from 0.5 cm to 3.1 cm, at  $pd = 0.6$  Torr $\cdot$ cm (at the minimum of the Paschen curve [4]). Voltage is presented as the difference between discharge voltage and breakdown voltage ( $\Delta V = V - V_b$ ), as the breakdown voltage may vary from day to day measurements. At low currents (Townsend regime), the agreement between  $V$ - $I$  characteristics at different gaps is good. In normal and abnormal glow discharge, voltages are higher at larger gaps. This is consistent with increased diffusion losses and edge effects at larger gap/diameter ratios and lower pressures [6].

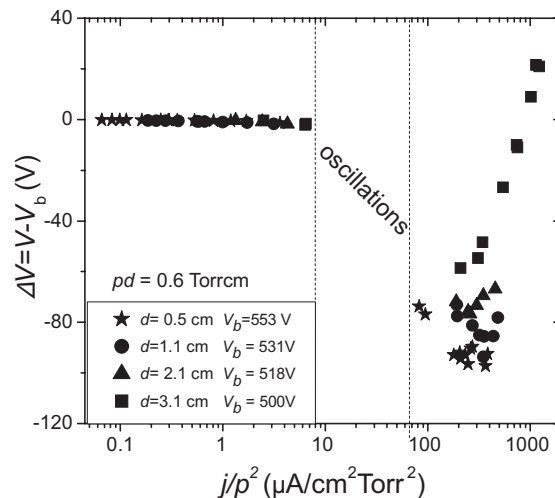


**Figure 1.**  $V$ - $I$  characteristics at  $pd=0.6$  Torr $\cdot$ cm for four electrode gaps. Voltage is shown as a difference between discharge ( $V$ ) and breakdown ( $V_b$ ) voltage.

One has to be aware of some important issues in determination of the scaling parameter  $j/p^2$ . First, when calculating current density from discharge current it is essential to use effective discharge diameter instead of the electrode diameter [7]. We usually determine effective discharge diameter from end-on images of the discharge, recorded by ICCD camera through the transparent anode. However, in measurements presented here, at lower pressures we were not able to record radial (end-on) profiles due to low emission intensities under those conditions and due to limited transparency of the anode. Therefore, we extracted radial profiles of emission from side-on recordings by separating the intensity along the radius of the discharge chamber at the position of the peak of emission. Since in cylindrical geometry, each pixel of the image corresponds to a different volume, depending on the distance from the chamber axis, it was necessary to perform Abel inversion.

Another issue that can be important in determination of  $j/p^2$  parameter comes from the fact that, even at the same  $pd$ , discharge tends to be more constricted at higher pressures [8]. Constriction is rarely formed at the center of the discharge volume [9]; at certain conditions it can move across the surface [10]; we have even observed the coexistence of double constricted discharge channels. In such cases, estimation of the effective diameter of the discharge is very difficult. There are many possible causes for this kind of complex behavior – if electrodes are not ideally parallel, or if the cathode surface is not homogeneous, if there are high local fields due to roughness of the surface or around the edges etc. The constricted discharge channel will always adjust its position to reach optimal, the most efficient, discharge conditions.

Fig. 2 shows double channels of the discharge that were observed in Townsend and normal glow regime. Axial profiles of emission (at  $d=0.5$  cm) along the channels and corresponding 2D images of discharge are presented. The emission intensity of the secondary channel is lower, but similarity of the profiles proves that channels operate in the same regime. In order to make comparison of profiles, maximum intensities of secondary channels are normalized to the maximum intensity of corresponding main channels. It is interesting to note that profiles for different currents are normalized by the same factor, which means that relative intensities in dual channels are preserved in different regimes of the discharge. The coexistence of two channels in the discharge could be related to a small diffusion length at higher pressures and large electrode diameter (compared to the gap), where constrictions can operate independently [8,9].

In the case presented here, effective discharge diameter can be estimated as a sum of diameters of the two channels. However, it is difficult to claim that such estimation is realistic, as distribution of the electric field along the channels may not be the same.

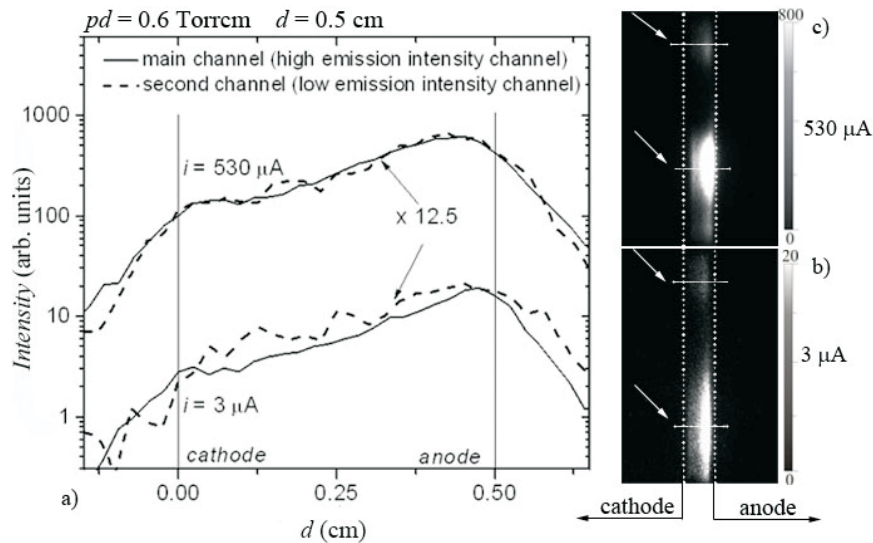


**Figure 2.** Profiles of emission along the constricted channels (a), indicated by solid white lines at corresponding 2D images (b, c) in Townsend regime of the discharge ( $3 \mu\text{A}$ ) and in normal glow ( $530 \mu\text{A}$ ).

### Acknowledgements

This work is supported by the MESRS project ON 171037 and III 41011.

### REFERENCES

- [1] P. Bruggeman, C. Leys, *J. Phys. D: Appl. Phys.*, 42, 053001 (2009).
- [2] K. R. Stalder, G. Nersisyan, W. G. Graham, *J. Phys. D: Appl. Phys.* 39, 3457 (2006).
- [3] E. Artamonova, T. Ar tamonova, A. Beliaeva, *et al.*, *J. Phys. D: Appl. Phys.*, 41, 155206 (2008).
- [4] N. Škoro, D. Marić, G. Malović, W. G. Graham and Z. Lj. Petrović, *Phys. Rev. E*, 84, 055401(R) (2011).
- [5] A. V. Phelps and Z. Lj. Petrović, *Plasma Sources Sci. Technol.*, 8, R21 (1999).
- [6] D. Marić, P. Hartmann, G. Malović, Z. Donko, and Z. L. Petrović, *J. Phys. D: Appl. Phys.*, 36 (21), 2639 (2003).
- [7] N. Škoro, D. Marić, and Z. Lj. Petrović, *IEEE Trans. on Plasma Sci.*, 36 (4), 994 (2008).
- [8] Z. Lj. Petrović, N. Škoro, D. Marić, C. M. O. Mahony, P. D. Maguire, M. Radmilović-Radjenović and G. Malović, *J. Phys. D: Appl. Phys.* 41, 194002 (2008)
- [9] D. Marić, G. Malović, and Z. Lj. Petrović, *Plasma Sources Sci. Technol.*, 18, 034009 (2009).
- [10] Z. Lj. Petrovic and A. V. Phelps, *Phys. Rev. E*, 56(5), 5920 (1997)

## ELECTRONIC DENSITIES OF ATOMS IN A LASER FIELD

Svetlana Vučić

*Institute of Physics, University of Belgrade, P.O.Box 57, 11001 Belgrade, Serbia*

**Abstract.** The hydrogen and argon atoms exposed to a linearly polarized laser fields are studied by using the non-perturbative non-Hermitian Floquet theory. The electronic densities of quasi-energy ground states versus electron coordinate are analyzed. We conclude that the decay of an atom in a low intensity non-resonant laser field occurs from the very tail of the ground state. For a higher intensity, the ionization proceeds by the mechanism of interchange of the character of the ground state with a radiatively coupled excited state(s). The process of electron emission is governed by the excited-bound-state-part of the resonance wave function. With the increase of intensity the electron is ionized at smaller distances from the nucleus.

### 1. THEORY

Let us consider an atom in a laser field which we treat as a classical monochromatic wave of constant intensity, spatially homogeneous and linearly polarized, with vector potential given by

$$\mathbf{A}(t) = \text{Re} \mathbf{A}_0 e^{-i\omega t}. \quad (1)$$

A free electron oscillates in the field with a displacement about its equilibrium position equal to  $\vec{\alpha}(t) = -(e/mc\omega)\mathbf{A}(t)$ , and the cycle-averaged kinetic energy of a free electron that has zero drift velocity is the ponderomotive energy  $U_p = F^2/(4\omega^2)$ .

The dressed states of the atom are described by solutions of the Schrödinger equation of the form [1]

$$\Psi(t) = e^{-iEt/\hbar} \sum_N e^{-iN\omega t} \mathcal{F}_N. \quad (2)$$

The index  $N$  characterizes the net number of real or virtual photons absorbed by the atom. In the velocity gauge, the (time-independent) harmonic components  $\mathcal{F}_N$  satisfy the following system of coupled equations

$$(E + N\hbar\omega - H_{\text{at}})\mathcal{F}_N = V_+\mathcal{F}_{N-1} + V_-\mathcal{F}_{N+1}, \quad (3)$$

where  $H_{\text{at}}$  is the Hamiltonian of the field-free atom, and the interaction of the atom with the external field is given by (the atomic units will be used throughout)

$$V(t) = -\mathbf{A}(t) \cdot \mathbf{p}. \quad (4)$$

In Floquet Eqs. (3),  $V(t)$  is separated into two parts,  $V(t) = V_+e^{-i\omega t} + V_-e^{i\omega t}$ , corresponding to the absorption or the emission of a single photon. Note that the term in  $A^2$  is omitted from  $V(t)$ ; in the dipole approximation, this term does not depend on position and can be removed by a simple gauge transformation.

The solutions describing dressed bound states decaying by multi-photon ionization are obtained in the position space by imposing the Siegert boundary conditions on the harmonic components. We solve the Floquet equations (3), by expanding the harmonic components on a discrete basis of spherical harmonics and of complex Sturmian functions. The complex parameter  $\kappa$  of the Sturmian basis is chosen in the first quadrant in the complex  $k$  plane. This choice provides an analytic continuation of the matrix eigenvalue equation (3), beyond the real energy axis onto the second sheet of the complex energy plane. The resonance energy is obtained as one of the complex eigenvalues of the analytically continued matrix eigenvalue equation. The complex quasienergy of an atomic level  $i$  is given by,  $E_i = E_o + \Delta_i - i\Gamma_i/2$ , where  $E_o$  is the field-free energy,  $\Delta_i$  is a.c. Stark shift of the level which tends to zero when the field tends to zero, while  $\Gamma_i$  is the induced energy width.  $\Gamma_i$  is the total ionization rate from level  $i$ . The system of equations is solved numerically by inverse iteration method, or by Arnoldi iterations which permits to find a number of closely-spaced energy levels [2].

The temporal dependence of electronic density of quasi-energy initial state versus electron coordinate is given by

$$\begin{aligned} |\Psi(r, \theta, t)|^2 = e^{2\text{Im}Et} \times \\ \{ \text{Re} [ \sum_{Nnl} \frac{S_{nl}^\kappa(r)}{r} Y_{l0}(\Omega) c_{nl}^N \cos(N\omega t) ]^2 + \\ \text{Re} [ \sum_{Nnl} \frac{S_{nl}^\kappa(r)}{r} Y_{l0}(\Omega) c_{nl}^N \sin(N\omega t) ]^2 \}. \end{aligned} \quad (5)$$

We have calculated the electronic density along the direction parallel to the field polarization. The variation of this quantity during an optical cycle for a flat part of a long laser pulse of various intensity has been investigated.

## 2. Electronic Density

We show in figure 1 the electronic density in the forward direction for H atom embedded in a laser field of 121.5 nm wavelength and the intensity of  $10^9$  W/cm<sup>2</sup>, which matches the ground state H(1s) into one-photon

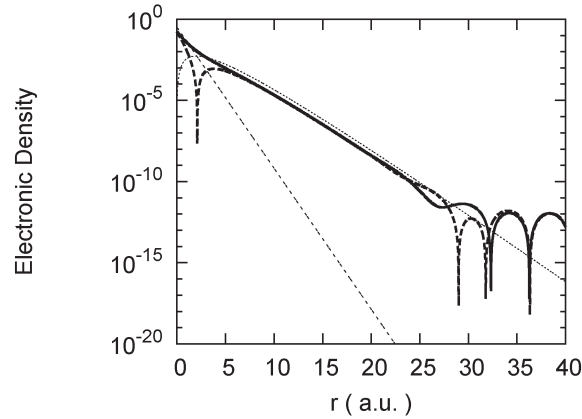


Figure 1: The electronic density in the forward direction  $|\Psi(r, \theta = 0, t)|^2$  for H atom embedded in a laser field of 121.5 nm wavelength and for intensity of  $10^9$  W/cm<sup>2</sup>, which matches the ground H(1s) state into one-photon resonance with H(2p) state. —, full curve: the density at the beginning of an optical cycle; - - -, broken curve: the density at a half of an optical cycle; - - -, short-dashed curve: density of the field-free H(1s) state; ... , dotted curve: density of the field-free H(2p) state.

resonance with the H(2p) state. At the beginning of an optical period, the laser-assisted density for small radius  $r \leq 1$  a.u., is almost the same as for the unperturbed 1s state, for larger radius it acquires the character of the unperturbed 2p state, and for  $r \geq 25$  a.u., the density shows regular oscillatory behavior corresponding to the free electron wave function. This shows that the electron is ionized from the tail of the H(2p) state. For a half of an optical cycle, there is a broad minimum in electronic density at around  $r = 2$  a.u., (where the 1s and 2p<sub>0</sub> wave functions have the same values in the forward direction) which is a consequence of destructive interference in the Floquet wave function.

As an example of the ground state probability density in strong laser fields, we show in figure 2 the electronic density  $|\Psi(r, \theta = 0, t = 0)|^2$ , for a resonant intermediate intensity  $I_1 = 6.32 \times 10^{13}$  W/cm<sup>2</sup>, which corresponds to the most pronounced peak between the 11-th and 12-th ionization thresholds, and for the intensity  $I_2 = 9.97 \times 10^{13}$  W/cm<sup>2</sup>, with no distinguished resonant enhancement. The electronic density for the intensity  $I_1$  is the same as for the field-free ground state up to a value of radius  $r \leq 6$  a.u., where it begins to take on the character of a dressed not very excited state (the dominant character is of the 6f non-perturbed state) due to the multiphoton coupling between the states. For  $r \geq 80$  a.u., the electronic density shows regular oscillatory behavior. Qualitative behavior of the electronic density for the intensity  $I_2$  is similar, but the ground state interchanges the

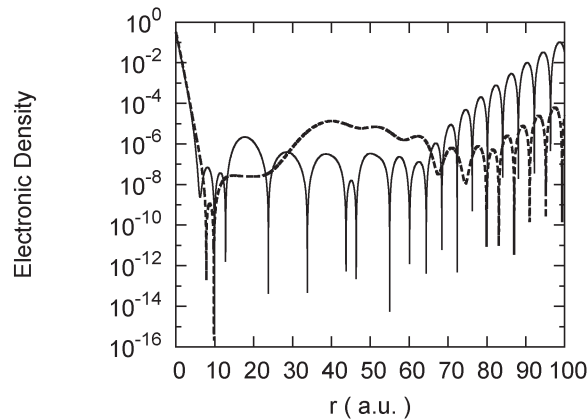


Figure 2: The Floquet probability density for the electron ejected in the forward direction at the beginning of an optical cycle. The wavelength of the field is 800nm and the intensity  $I_1 = 6.32 \times 10^{13} \text{ W/cm}^2$  ( -- , broken curve ), or  $I_2 = 9.97 \times 10^{13} \text{ W/cm}^2$  ( -, full curve ).

character with an excited state at somewhat smaller radius than in previous case, and the electron is also ionized at smaller distances from the nucleus. At large field intensity the bound-excited state part of the Floquet wave function has a character of high-order polynomial with slow exponential decay. It is likely that some minima in the wave function are due to interference effects. At a high intensity, the electronic density varies appreciably during an optical cycle. Note that the lifetimes of resonant excited states are of the order of magnitude of an optical cycle.

## Acknowledgement

The author thanks Dr. Tasko Grozdanov for useful suggestions. The work was supported by the Ministry of Education and Science of the Republic of Serbia under project 171020.

## REFERENCES

- [1] R. M. Potvliege and R. Shakeshaft, *Adv. At. Mol. Opt. Phys. Suppl.* 1, 373 (1992).
- [2] R. M. Potvliege, *Comput. Phys. Commun.* 114, 42 (1998).
- [3] Y. K. Ho, *Phys. Rep.* 99, 1-68 (1983).

## ON THE POPULATION PROCESSES IN THE In III

Authors: M. Burger, M. Skočić, Z. Nikolić, S. Bukvić and S. Djenize

*Address: University of Belgrade, Faculty of Physics, POB 368, Belgrade, Serbia*

**Abstract.** In pulsed argon and helium discharges, radiation from number of In III spectral lines, ranged between 200 nm and 650 nm, is measured. For some In III lines, in the helium plasma, intense after-radiation is observed. This phenomenon is attributed to the helium metastable atoms.

### 1. INTRODUCTION

The unusual chemical and physical properties make indium (In) interesting in many fields of the industry, technology and research [1-3]. Indium has two isotopes ( $^{113}\text{In}$  4.3% and  $^{115}\text{In}$  95.7% in natural indium) with isospins of a 9/2. The shape of natural indium spectral lines is defined, due to the hyperfine structure effect, by both isotopes in amount that strongly depends on plasma parameters and particular quantum transition. While energy diagrams of the neutral and singly ionized indium are well known, the knowledge of the In III energy levels is far to be complete. Within the identified In III transitions [4, 5], the  $5d\ ^2D_{3/2} - 4f\ ^2F_{5/2}$  with wavelength of 298.280 nm is particularly intense. To the knowledge of the authors, transition probability of this transition is still not known. The aim of this work is to advance understanding of the processes, which provide significant population of  $4f\ ^2F_{5/2}$ , the upper level of the 298.280 nm spectral line.

### 2. EXPERIMENT

A linear low-pressure pulsed arc [6, 7] was used as an optically thin plasma source. The pulsed discharge (see Figure 1) was produced in a Pyrex discharge tube with quartz windows at its ends. More detailed description is reported in [8]. The schematic of the experimental setup is presented in Figure 2. As working gases helium and argon were used at 400 and 133 Pa flowing pressures, respectively. The discharges were created by using a capacitor of 14  $\mu\text{F}$  charged up to 45 J of stored energy. Elements of the electrical circuit are chosen to provide a sub-critical damping, i.e. the discharge current displays only two half-periods.

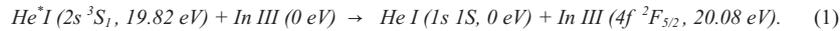
### 3. RESULTS AND DISCUSSION

We have monitored intensity of the 298.280 nm In III line during the decaying helium and argon plasmas. Temporal evolutions of the intensities, normalized to the maximum line intensity, are presented in Figure 3.

There is evident difference between two curves. In the argon plasma only one maximum exists. It is realized at the moment when our plasma abides in the state with maximum of the electron density ( $N_e$ ). In the case of helium plasma two maxima are present. The first one behaves in a way similar with the single maximum in the argon plasma, but the second one is realized later, at about 26<sup>th</sup>  $\mu$ s after the beginning of the discharge, when the electron density is about 3 times smaller than in its maximum.

The first intensity maximum in the helium plasma and a single maximum of the same spectral line in the argon plasma are caused by the same processes. Collisions of free electrons with the ground state of the In III is the leading population process of the parent (upper) state of the 298.280 nm In III transition. However, in the helium plasma, beside electrons, the helium triplet metastables ( $\text{He}^*I$ , with 19.82 eV excitation energy) also significantly contribute to the population of the considered upper level.

It seems that extra population of the  $4f\ ^2F_{5/2}$ , the parent level of the considered spectral line with 20.08 eV excitation energy [5], can be attributed to the helium metastables ( $2s\ ^3S_1$ ) due to process



This process is responsible for the intense after-radiation of the In III 298.280 nm line in the helium plasma. The energy deficiency of 0.28 eV is compensated by intense thermal motion of particles with average energy of  $\sim 3\text{eV}$  (35000K) [9].

### 5. CONCLUSION

We have found that our plasma source provides intense In III spectral lines in the argon and helium discharges. Beside collisions with electrons, we propose that helium metastables play an important role in the In III  $4f\ ^2F_{5/2}$  energy level population. Therefore, the high intensity of the 298.280 nm In III spectral line at plasma conditions with low electron density is most likely provided by the above mentioned process.

## 6. FIGURES



**Figure 1.** The glass discharge tube, with cylindrical indium plates, used in the experiment.

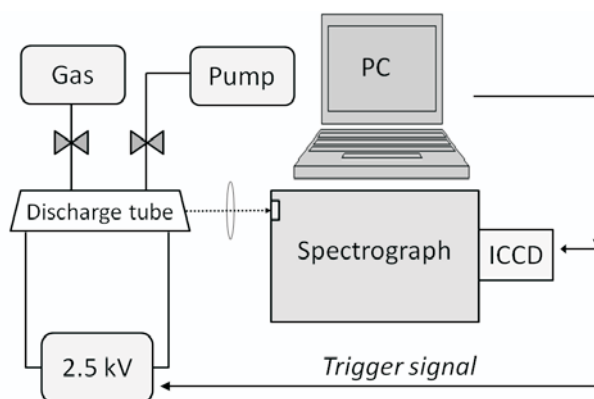


**Figure 2.** The schematic of the experimental setup.

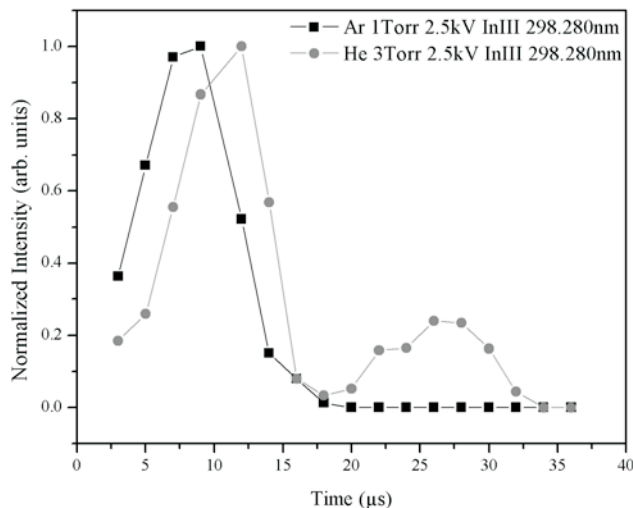


**Figure 3.** Temporal evolutions of the 298.280 nm In III line intensities, normalized to the maximal value obtained at 2.5kV discharge voltage and 400 Pa flowing pressure in the helium and 133 Pa in the argon plasma.

### Acknowledgements

This work is part of the “Determination of atomic parameters on the basis of spectral line profiles” (ON171008) project supported by Ministry of Education and Science of the Republic of Serbia.

### REFERENCES

- [1] Lin Fu-cheng, Applied Physics A: Materials Science & Processing, Vol 24, 299, (1981).
- [2] Robert Ruyves, Volodymyr Kelman, Yuriy Zhmenyak, Yuriy Shpenik, Radiation Physics and Chemistry, Vol 68, 269 (2003).
- [3] A. K. Shuaibov, A. I. Dashchenko, I. V. Shevera, Technical Physics Letters, Vol 26, (2000).
- [4] NIST, Atomic Spectra Database, <http://www.physics.nist.gov> (2012).
- [5] K.S. Bhatia, J. Phys. B: Atom. Molec. Phys. Vol 11, 14 (1978).
- [6] S. Djeniže, A. Srećković, S. Bukvić, Spectrochim. Acta B, Vol 61, 588 (2006).
- [7] S. Djeniže, A. Srećković, S. Bukvić, The European Physical Journal D, Vol 62, 185 (2011).
- [8] M. Skočić, M. Burger, S. Bukvić and S. Djeniže, STARK BROADENING IN THE In III SPECTRUM, In this Proceedings.
- [9] M. Skočić, M. Burger, S. Bukvić and S. Djeniže, Journal of Phys D. Submitted paper

## STARK BROADENING IN THE In III SPECTRUM

Authors: M. Skočić, M. Burger, S. Bukvić and S. Djeniže

Address: University of Belgrade, Faculty of Physics, POB 368, Belgrade, Serbia

**Abstract.** Stark widths of three doubly ionized indium (In III) spectral lines (298.280 nm, 403.232 nm and 524.877 nm) have been obtained in the pulsed helium discharge. The linear low-pressure arc, with two tiny indium cylinders, has been used as a plasma source. The plasma  $N_e = (1.36 \pm 0.18) \times 10^{23} \text{ m}^{-3}$  and  $T_e = 35\,000 \text{ K} \pm 5\,000 \text{ K}$  were obtained by using standard diagnostic techniques. Our results were compared with existing theoretical and experimental data. Presented Stark widths are smaller than calculated ones. Previously measured Stark widths were obtained at 13 000 K electron temperature, therefore, direct comparison between two sets of experimental data is not straightforward.

### 1. INTRODUCTION

The energy spectrum of the doubly ionized indium (In III) is poorly known [1, 2] in spite of increasing interest in indium in many technological applications. The identified In III transitions are presented in [1]. NIST [2] presents only 31 In III wavelengths ranged between 200 nm and 650 nm without corresponded quantum transitions. Besides, the Stark widths ( $W$ ) of the In III lines are investigated in only two works (Djeniže et al [3], and Simić et al [4]). The measured experimental  $W$  values [3] are much smaller than ones calculated in [4]. In this work we present  $W$  values for three prominent In III spectral lines measured in experiment very similar to the one described in [3].

### 2. EXPERIMENT

A linear low-pressure pulsed arc [3, 5] was used as an optically thin plasma source. A pulsed discharge was produced in a Pyrex discharge tube (with quartz windows at its ends). As a working gas we employed helium at 400 Pa pressure in flowing regime. The tube had a 5 mm inner diameter, and the plasma length was 14 cm. Indium atoms were sputtered from the indium cylindrical plates (15  $\mu\text{m}$  thickness) located at the ends of the homogeneous axial part of the discharge tube. The pure indium (99.9%) plates were produced by the cold-rolling method.

The discharge was created by using a capacitor of 14  $\mu\text{F}$  charged up to 45 J of stored energy. The electrical circuit is adjusted to provide sub-critical damping, i.e. the discharge current shows only two half-periods.

The spectroscopic observations were made end-on along the axis of the discharge tube. A McPherson model 209 spectrograph (with a 1.33 m focal length) equipped with a holographic grating containing 2400 grooves/mm was used. This spectrograph had a reciprocal linear dispersion of 0.28 nm/mm in the first order. An Andor DH740-18F-03 iStar intensified CCD camera was employed as a detection system. The system was calibrated by using a set of pen-light sources (Ne, Ar and Hg) produced by the LOT-Oriel. Instrumental FWHM of 8.6 pm was found as a result of the instrumental (spectrograph + ICCD camera) broadening at about 280 nm.

Plasma parameters were obtained by using well known spectroscopic methods. So, the electron density ( $N_e$ ) was obtained from the measured He II  $P_\alpha$  (468.6 nm) spectral line width [6]. The electron temperature ( $T_e$ ) was obtained by using a Boltzmann-plot method applied to 15 O III spectral lines, present as impurities due to erosion of the glass walls. The Stark FWHM values were measured at the 5<sup>th</sup>  $\mu$ s after the beginning of the discharge. At that moment the plasma parameters were:  $N_e = (1.36 \pm 0.18) \times 10^{23} \text{ m}^{-3}$  and  $T_e = 35\,000 \text{ K} \pm 5\,000 \text{ K}$ . Having in mind that indium atoms are essentially impurities, we assume absence of the self-absorption for investigated In III spectral lines originating from high lying upper energy levels.

As an example, the profile of the 298.280 nm In III spectral line is presented in Figure 1, recorded 5<sup>th</sup>  $\mu$ s after the beginning of the discharge.

### 3. LINE DECONVOLUTION PROCEDURE

Profiles of the measured In III spectral lines are of the Voigt type mainly due to the convolution of the Lorentzian Stark and Gaussian profile caused by Doppler broadening, and additionally due to instrumental profile of our experimental setup (spectrograph + ICCD), which is found to be of the Voigt type. Standard deconvolution procedure Davies & Vaughan [7], based on the least-squares method, is applied in order to evaluate spectral line parameters. Spectrum baseline is estimated independently by the procedure proposed by Bukvić and Spasojević [8] and Bukvić et al [9]. The measured profile of the 298.280 nm In III line is presented in Figure 1.

### 4. RESULTS AND DISCUSSION

Our measured  $W_m$  values are listed in Table 1, together with existing experimental ( $W_{Dj}$ , [3]) and theoretical data ( $W_{th}$ , [4]). One can see that our  $W_m$  values are smaller than ones in [4], calculated only for electrons as perturbers. Previous experimental  $W_{Dj}$  values were obtained at 13 000 K electron temperature and therefore, direct comparison between two sets of experimental data is impossible.

## 5. FIGURES

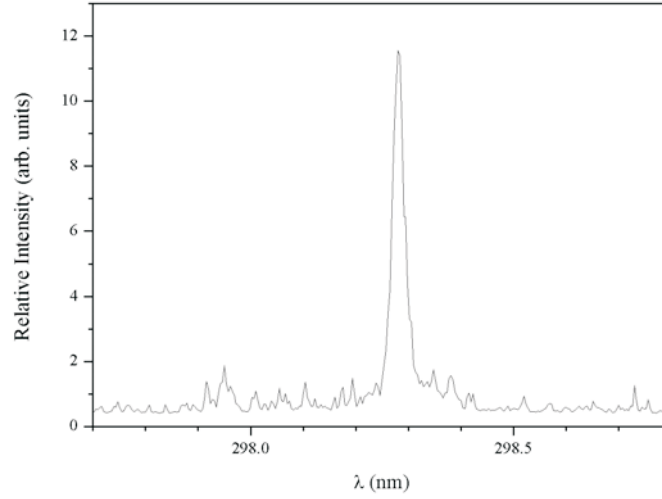


**Figure 1.** The recorded profile of the 298.280 nm In III spectral line at 400 Pa flowing pressure and 45 J bank energy.

## 6. TABLES

**Table 1.** Our Stark FWHM ( $W_m$ ) at various electron temperatures ( $T_e$ ) and  $N_e = 1.00 \times 10^{23} \text{ m}^{-3}$  with other experimental ( $W_{Dj}$ , [3]) and theoretical data ( $W_{th}$ , [4]).

Transition	$\lambda$ (nm)	$T_e$ ( $10^4$ K)	$W_m$ (pm)	$W_{Dj}$ (pm)	$W_{th}$ (pm)
$5d \ ^2D_{3/2} - 4f \ ^2F_{5/2}$	298.280	3.5	$9.3 \pm 2.3$		21.9
		1.3		16.2	
$6p \ ^2P^0_{3/2} - 6d \ ^2D_{5/2}$	403.232	3.5	$21.9 \pm 5.5$		
		1.3		34.8	
$6s \ ^2S_{1/2} - 6p \ ^2P^0_{3/2}$	524.877	3.5	$28.5 \pm 7.1$		78.5
		1.3		48.4	

### Acknowledgements

This work is part of the “ Determination of atomic parameters on the basis of spectral line profiles” (ON171008) project supported by Ministry of Education and Science of the Republic of Serbia.

### REFERENCES

- [1] K.S. Bhatia, J. Phys. B: Atom. Molec. Phys. Vol 11, 14 (1978).
- [2] NIST, Atomic Spectra Database , <http://www.physics.nist.gov> (2012).
- [3] S. Djeniže, A. Srećković, S. Bukvić, Spectrochim. Acta B, Vol 61, 588 (2006).
- [4] Z. Simić, M. Dimitrijević, A. Kovačević, S. Sahal-Bréchet, Baltic Astronomy, Vol 20, 613, 213 (2011).
- [5] M. Gavrilov, M. Skočić, M. Burger, S. Bukvić, S. Djeniže, New astronomy, Vol 17, 624 (2012).
- [6] H.R. Griem, “Plasma Spectroscopy”, (McGraw Hill, New York, 1964).
- [7] J.T. Davies, J.M. Vaughan, ApJ, Vol 137, 1302 (1963).
- [8] S. Bukvić , Dj. Spasojević, Spectrochim. Acta B, Vol 60, 1308 (2005).
- [9] S. Bukvić , Dj. Spasojević, V. Žigman, A&A, Vol 477, 967 (2008).

## SPECTROSCOPIC CHARACTERISATION OF ATMOSPHERIC PRESSURE GLOW DISCHARGE

M. Cvejić<sup>1</sup>, S. Jovičević<sup>1</sup> and N. Konjević<sup>2</sup>

<sup>1</sup>*Institute of Physics, University of Belgrade, P.O. Box 68, 11080, Belgrade, Serbia*

<sup>2</sup>*Faculty of Physics, University of Belgrade, P.O. Box 368, 11001, Belgrade, Serbia*

**Abstract.** Spectroscopic investigation of dc atmospheric pressure glow discharge (APGD) in helium with traces of hydrogen is presented. The discharge was operated with 8 mm electrode gap using 1 A dc current and voltage of 270 V. From the spatial intensity distribution recorded at the Balmer H<sub>β</sub> wavelength it is shown that APGD is non uniform. Our measurements showed the absence of the He spectral lines in the positive column of APGD. The spectral recordings of the H<sub>β</sub> in cathode zone of APGD suggest the presence of strong electric field. The rotational temperature of 960 K in the negative glow region is measured from Q branch of molecular hydrogen Fulcher - Δ band system d <sup>3</sup>Π<sub>u</sub><sup>+</sup> - a <sup>3</sup>Σ<sub>g</sub><sup>+</sup>(0,0).

### 1. INTRODUCTION

Various kinds of atmospheric pressure glow discharges (APGDs) have been studied [1, 2, 3] in past two decades. The interest was focused to micro discharges, dielectric barrier discharges in variety of configurations and in the current range of several μA to several A. The operation of these discharges at atmospheric pressure without requirement of vacuum pumps and unique properties make this discharges very attractive for applications. In this study we present results of spectroscopic investigation of APGD source made in our laboratory following the design described in [1].

### 2. EXPERIMENT SETUP

A schematic of experimental setup used for the generation of APGD is shown in figure 1a. The cathode was made of copper with water cooling what ensured efficient cooling of the cathode surface. The cathode surface is a circle with 30 mm diameter. The anode, made of tungsten, is placed in anode holder which is also water cooled. Tip of anode rod (dia. 6 mm) is sharpened to facilitate ignition of discharge. The electrode gap was set to 8 mm. The vacuum chamber was a hollow cylinder (inner dia. 10 cm), with windows on top and

bottom, and a gas inlet and outlet. Before the discharge ignition the vacuum chamber was evacuated to the base pressure of  $10^{-3}$  mbar and then filled with gas mixture to atmospheric pressure. The experiment was carried out with helium – hydrogen mixture ( $\text{He} + 3\% \text{H}_2$  by volume), with continuous gas flow rate of 0.2 L/min at standard ambient temperature and pressure. To operate the discharge in dc mode, a voltage source is used (0-500 V, 0 - 5A). Parallel to filling the chamber with gas, dc voltage was turned on, and the discharge was ignited. When the pressure reached the value of 1 bar, dc current was set to 1 A and the voltage of 270 V.

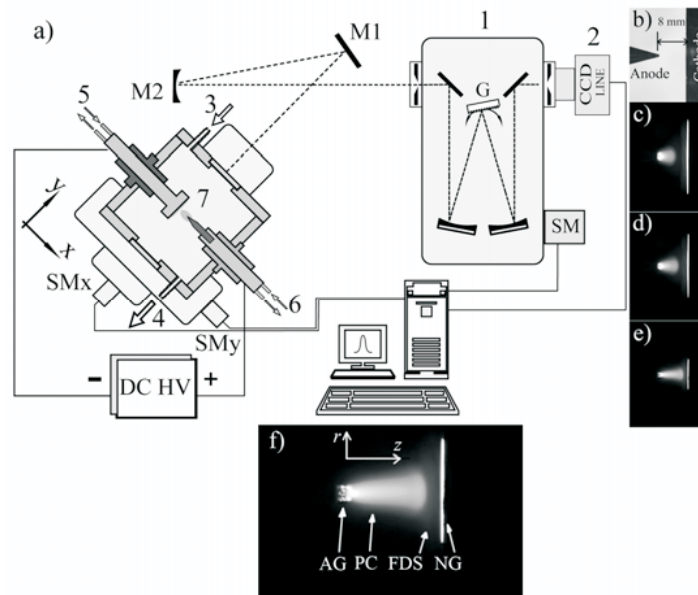


**Figure 1.** a) The experimental setup: 1 – monochromator, 2 – CCD or PMT, 3 – gas inlet, 4 – gas outlet, 5 – water cooling of cathode, 6 – water cooling of anode, 7 – vacuum chamber with windows, M1 – flat mirror, M2 – spherical mirror  $f = 1$  m, SMx – step motor that translates stage along x axis, SMy – step motor that translates stage along y axis, SM – step motor that drives optical grating G, DC HV – high voltage dc source. The images of a) electrodes configuration without plasma, c) plasma at  $\sim 400$  mbar, d) plasma at  $\sim 700$  mbar, e) plasma at  $\sim 1000$  mbar, taken side on, with dslr camera; f) The regions of dc APGD: AG – anode glow, PC – positive column, FDS – Faraday dark space, NG – negative glow.

The light from the discharge was focused with unity magnification by flat mirror M1 and spherical mirror M2 (focal length 1 m) onto the entrance slit of Czerny-Turner type monochromator (1 m focal length with 1800g/mm reflection grating). The width of entrance and exit slit was  $15 \mu\text{m}$ . The spectral line recordings were performed with an instrumental profile very close to

Gaussian with measured FWHM of 0.021 nm. For spectral line recordings of APGD positive column, CCD line detector (3648 px,  $8 \times 200 \mu\text{m}$ ) was placed parallel to the exit slit. The spectra of APGD cathode zone were recorded with a photomultiplier tube.

The APGD chamber is mounted on a PC-controlled X-Y table. By translating the table along  $y$  direction, fine focusing of plasma image onto the entrance slit was achieved, while by translating along  $x$  direction, scanning of the discharge along axial axis was performed. The wavelength scanning is achieved by a rotating monochromator grating with stepping motor, controlled by the same PC.

### 3. RESULTS AND DISCUSSION

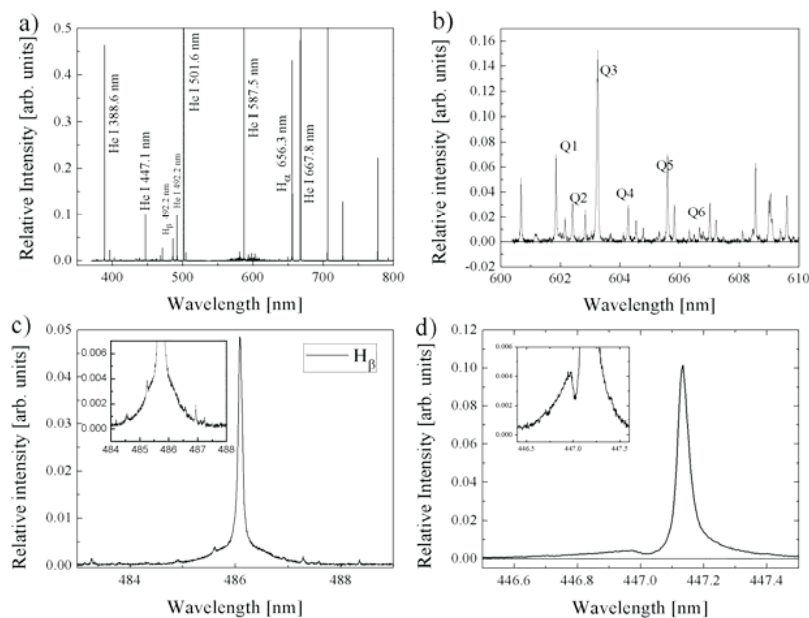


**Figure 2.** a) APGD emission spectra; b) Fulcher -  $\alpha$  band system, c) profile of the H $\beta$  line and in the inset magnified view of extended line wings; d) the profile of He I 447.1 nm line and in the inset magnified view of forbidden component is given. Presented spectra in this figure are recorded from the APGD cathode zone.

The results of spectra recording at the distance of 1.5 mm from cathode surface are presented in figure 2. The emission spectrum is shown at fig 2a, (380 – 810 nm). He I lines appear together with hydrogen Balmer lines. The spectrum of  $d^3\Pi_u^\pm - a^3\Sigma_g^+(0,0)$  Fulcher molecular band is presented in fig 2b. From relative line intensities and by using the Boltzman plot technique [4], the rotational temperature of 960 K is determined. Because of high purity helium and evacuation of chamber before discharge ignition no rotational and

vibrational spectra of OH and N<sub>2</sub> bands were observed in all zones of APGD. Broadened wings of the H<sub>β</sub> (figure 2c.) and forbidden component of He I 447.1 nm spectral line, indicate a presence of strong electric field in this region of APGD, see ref. 1 and 3.

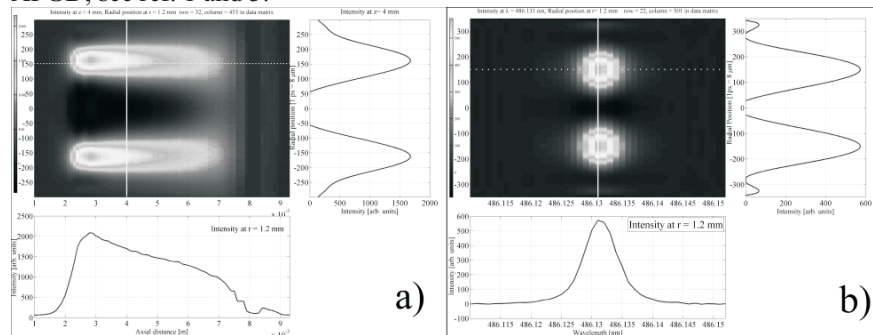


**Figure 3.** a) Spatial intensity distribution of APGD at  $\lambda = 486.13$  nm, the graph below image shows axial distribution at  $r = 1.2$  mm from the axis of discharge; the graph to the right of image shows radial distribution at  $z = 4$  mm. b) Radial distribution of H<sub>β</sub> line at  $z = 4$  mm from the tip of anode.

Figure 3a. shows spatial intensity distribution of the H<sub>β</sub> line. The figure was obtained in following way. The monochromator grating was set to maximum intensity of the H<sub>β</sub> line at  $\sim 486.13$  nm. The CCD line detector was placed parallel to the exit slit. By translating the table with chamber along  $x$  direction, using 0.1 mm steps, lateral intensity distribution was recorded at each position. Then all recordings were merged together. Resulting image was then processed with program developed in our lab. Figure 3. shows that hydrogen is exited in the outer regions of discharge. Our recordings showed absence of helium lines in positive column of discharge.

In order to explain the observed phenomena related to the distribution of hydrogen lines and lack of helium lines, further investigation are in progress.

## Acknowledgements

This work is supported by Ministry of Education and Science of the Republic of Serbia, project no 171014.

## REFERENCES

- [1] V.I. Arkhipenko et al., Self-sustained dc atmospheric pressure normal glow discharge in helium: from microamps to amps, *Plasma Sources Sci. Technol.*, 18, 045013 (17pp), (2009)
- [2] D. Staack et al., *Plasma Sources Sci. Technol.*, 14, 700-711, (2005)
- [3] M. Cvejić et al., *Journal of Applied Physics*, 110, 033305 (10pp), (2011)
- [4] B. P. Lavrov i D. K. Omorbaev, *Opt. Spek.*, 45, 1074, (1978)

## THE OPTICAL EMISSION SPECTROSCOPY EXPERIMENT OF OPEN AIR PLASMAS

S.Mijović, M. Vučeljić and M. Šćepanović,

*University of Montenegro, Faculty of Natural Sciences and Mathematics ,  
G. Washington, Podgorica, Montenegro  
e-mail mara.scepanovic@gmail.com*

**Abstract.** A plasma spectroscopy experiment is described and its performances are given. Ways of excitation different regimes of free-burning plasma at atmospheric pressure is analyzed in detail. The fixed-grating spectrograph *PGS-2* Carl Zeiss Jena is actually a variation on the very first spectrometer design, where photo-plate was replaced with a detector array of *PIXIS*-Roper Scientific camera. Abilities of the system are analyzed and its limitations are determined.

### 1. INTRODUCTION

Typical and widespread examples of dense low-temperature equilibrium plasmas, sustained by electric field, are arcs at atmospheric pressure, including those in open air [1]. It should be mentioned, however, that in the arc fringes, and especially fast moving arcs (gliding arcs), non-equilibrium plasma conditions can also be found and can be utilized for technical applications [2]. Plasmas generated and maintained at atmospheric pressure experience a renaissance in the 1980s, mostly driven by application such as high power lasers, opening switches, novel plasma processing and sputtering, absorber and reflector of electromagnetic radiation, remediation of gaseous pollutants, medical sterilization and biological decontamination and excimer lamps and other non-coherent light sources [3].

### 2. EXPERIMENTAL SET-UP

The scheme of the experimental set-up for optical emission spectroscopy (OES) measurements in a UV-visible range  $200\text{-}560\text{nm}$ , is shown in (Fig. 1), comprises a 2m spectrograph (with a possibility to extend to double light path), and a  $1024\times 256$  pixel CCD camera (*PIXIS 256*). The side on light from plasma (1) is directed through the system of lens (2) at the entrance slit of the *PGS-2* spectrograph with the grating (6) of  $651\text{lines/mm}$  and the blaze wavelength at  $300\text{nm}$ . The deflection mirror (4) sends the light beam to the

lower part of the concave mirror (5) and after reflection of the grating to the upper part of the mirror (5), finally re-directs the light to the CCD array of the camera.

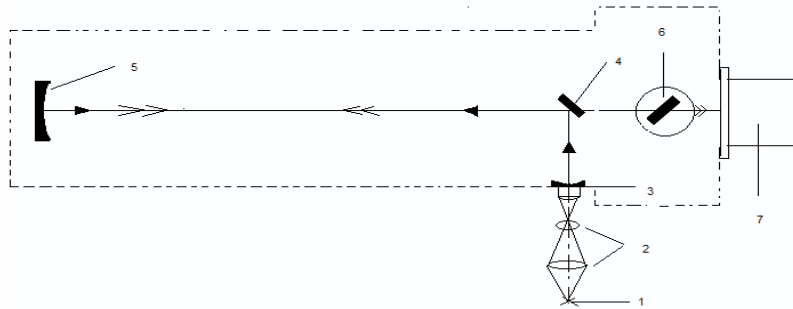


**Fig 1.** Experimental set-up for OES of plasmas

## 2.1 PIXIS camera

PIXIS is a fully integrated camera system. The camera contains all of the electronics necessary to read out and control the CCD device. It houses precision analog-to-digital converters, positioned close to the CCD for lowest noise and has USB 2.0 electronics to interface with the host computer. Significant reduction of dark current is achieved through thermoelectric cooling of the CCD array. The camera operates by using *WinSpec/32*, Princeton Instrument's 32-bit Windows software package, designed specifically for spectroscopy. With the pixel size of  $0.026\text{mm}$  and dispersion of  $0.74\text{nm/mm}$  in the first order of diffraction gives spatially resolution of  $0.02\text{nm}$ , and for using higher orders of diffraction and doubled light paths this resolution is much higher.

## 2.2 Plasma generator

The commercial Universal arc-pulse generator UBI-2, Carl Zeiss Jena can produce different types of electrical discharges (Fig.2). The input transformer (1), with the secondary coils voltage of  $350\text{V}$ , gives AC or DC (through the rectifier (2)) voltages at the air gap (13), where are different discharges generated. To get a low voltage discharges a high frequency voltage of about  $20\text{kV}$  is needed, which in any half-period of alternate current generates a high frequency pulse. It is done when the pulse-transformer (9) gives an ignition voltage to spark gap (10) by discharging its capacitor. The ignition voltage directs through Tesla's transformer (11) to the main circuit. By help of the pulse generator (8), a rhythm in interruptible regimes of discharges and phase angle of the ignition are tuned. Six regimes of creating plasmas are possible: interruptible AC arc with six steps from 100 to 1.6 GHz; interruptible DC arc;

low voltage DC arc (smoothed); low voltage spark discharge with changeable polarities and HF spark discharge.

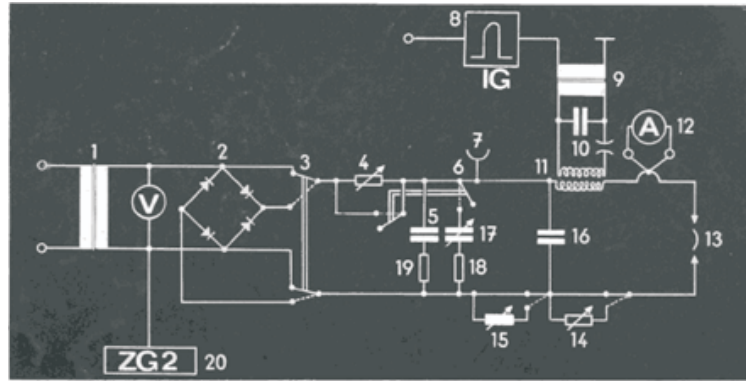


**Fig.2** The scheme of the universal plasma generator UBI-2

Powerful capacitors (17), shunted in a step way with (13), ignite low-voltage sparks with the same spectral characteristics as the spark gap of the high voltage generator.

### 3. THE RECORDED SPECTRA AND RESULTS

The internal structures of the chamber, where are the open air plasmas generated, and the picture of the DC arc with electrodes of spectroscopic pure graphite, the cloud of zinc vapor and discharge current  $I_d = 9A$  are shown in Fig. 3.

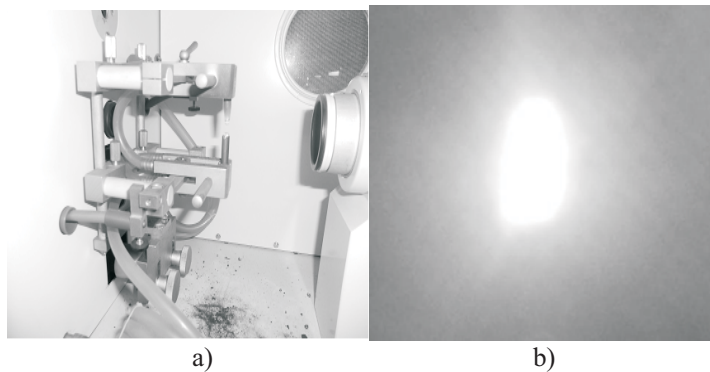


**Fig. 3** The internal structures of the chamber with water-cooled electrodes a) and arc in open air b)

The DC and DC interruptible arcs are created vertically, between two electrodes whose gaps were in the range of 2-8mm. The discharge current is changed from 2 to 10A. In one position of the grating, approximately 20nm of a specter can be taken. Spatial and temporal mapping of the specters are taken. The CCD's exposure time can be regulated and in this experiment it was typically 100ms.

As an example of the image specter and its graph, is shown in Fig 4. with the discharge current of 10A, in the interruptible regime..

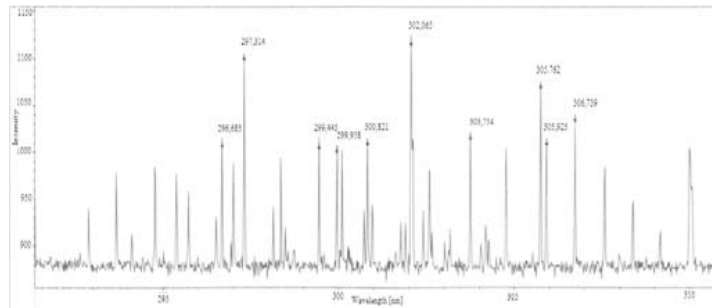


**Fig.5** The graph of the iron specter

#### 4. CONCLUSION

An OES experiment is a power-full tool for characterization the free burning plasmas at the atmospheric pressure. The experimental set-up, designed mainly for spectro-chemical analysis, is used to extract many physical features of the plasma at atmospheric pressure.

#### Acknowledgements

This work is supported by Ministry of Sciences of Montenegro under the grant No 01- 382.

#### REFERENCES

- [1] Y. P. Raizer, *Gas Discharge Physics*, p. 399, (Springer Verlag, Berlin 1997).
- [2] A. Fridman, S. Nester, L. A. Kennedy, A. Saveliev and O. Mutaf-Yardimci, *Progr. Energy Combust. Sci.* 25, 211-231 (1999).
- [3] K. H Becker, U. Kogelschatz, K. H. Schoenbach, R. J. Barker, *Non-equilibrium Air Plasmas at Atmospheric Pressure, p.XIV*, ( IOP Publishing Ltd. 2005).

## SPECTROSCOPIC TEMPERATURE MEASUREMENTS IN A FREE-BURNING ZINC- VAPOR ELECTRIC ARC

M. Šćepanović, M. Vučeljić and S. Mijović,

*University of Montenegro, Faculty of Natural Sciences and Mathematics, G.  
Washington, Podgorica, Montenegro  
e-mail mara.scepanovic@gmail.com*

**Abstract.** A spectroscopy study was conducted to determine plasma temperature and its variation with respect to spatial mapping and plasma operating conditions. Low voltage DC arc (smoothed) and interruptible DC arc were used for excitation of free-burning zinc-vapor plasmas at atmospheric pressure. The fixed-grating spectrograph *PGS-2* Carl Zeiss Jena is actually a variation on the very first spectrometer design where photo-plate was replaced with a detector array of *PIXIS-Roper* Scientific camera. Abilities of the system are analyzed and plasma temperatures with graphite electrodes and zinc vapors were determined by using *Zn I* spectral lines ratios.

### 1. INTRODUCTION

Electric arcs at atmospheric pressure are typical examples of dense low-temperature equilibrium plasmas, sustained by electric field, including those in open air [1]. In an electric arc electrode material enters electrode gap by evaporating under the action of the current. Having a lower ionization potential, as compared to atoms of the ambient gas, the metal atoms have substantial effect on the processes of heat, mass, and electron transfer in the plasma [2]. A detailed and complete knowledge of plasma temperature field and its dependence on the plasma operating parameters such as discharge current, regime of arcs excitation etc., are needed.

### 2. EXPERIMENTAL SET-UP

The scheme of the experimental set-up for optical emission spectroscopy (OES) measurements in a UV-visible range *200-560nm*, described in detail [3], comprises a 2m spectrograph (with a possibility to extend double light path), and a *1024x256* pixel CCD camera (*PIXIS 256*). The side on light from plasma is directed through the system of lens at the entrance slit of the

PGS-2 spectrograph with the grating of  $651\text{lines/mm}$ , and finally re-directs the light to the CCD array of the camera.

PIXIS is a fully integrated camera system. The camera contains all of the electronics necessary to read out and control the CCD device. It houses precision analog-to-digital converters, positioned close to the CCD for lowest noise and has USB 2.0 electronics to interface with the host computer. The camera operates by using *WinSpec/32*, Princeton Instrument's 32-bit Windows software package, designed specifically for spectroscopy. With the pixel size of  $0.026\text{mm}$  and dispersion of  $0.74\text{nm/mm}$  in the first order of diffraction gives spatially resolution of  $0.02\text{nm}$ , and for using higher orders of diffraction and doubled light paths this resolution is much higher.

### 3. THE ARC TEMPERAURE DETERMINATION

One of the most common method for electron temperature determination is by using relative intensities of atomic and ionic spectral lines in emission spectra (the Ornstein method) [4], which requires the plasma to be in local thermodynamic equilibrium (LTE), or at least partial LTE for the excited levels of these spectral lines [5]. Properly corrected emission intensities (optically thin) can be used to determine the temperatures based on the Boltzmann distribution given by

$$n_i = n_0 \frac{g_i}{Z} \exp(-E_i/kT) \quad (1)$$

where  $n_i$  is population of the  $i$ th excitation state,  $g_i$  is the known statistical weight of the excited state,  $Z$  is the partition function,  $E_i$  is the excitation energy,  $k$  is the Boltzmann constant and  $T$  is the absolute temperature.

Here, zinc lines  $\text{ZnI } 307.21\text{nm}$ ;  $\text{ZnI } 307.59\text{nm}$  and  $\text{ZnI } 328.23\text{nm}$  are used with relatively high excitation potentials-  $E_1-8.08\text{eV}$ ;  $E_2-4.01\text{eV}$  and  $E_3-7.73\text{eV}$  respectively [6]. The working formulas for the temperature determination are [7]

$$T = \frac{20510}{2.58 - \log \frac{I_{307.21}}{I_{307.59}}} \quad (2)$$

$$T = \frac{18850}{3.26 - \log \frac{I_{328.23}}{I_{307.59}}}, \quad (3)$$

where  $I$ , are intensities of the chosen lines.

The DC and DC interruptible arcs are created vertically, between two spectroscopic pure graphite electrodes, where the cathode has a crater and where metallic zinc is putted to evaporate due high temperature of the discharge, or a brass cathode is used. The gaps between electrodes are in the range of 2-8mm. The discharge current is changed from 2 to 10A. In one position of the grating, approximately 20nm of a specter can be taken. Spatial and temporal mapping of the specters are taken. The CCD's exposure time can be regulated and in this experiment it was typically 100ms.

The temperatures are mainly determined by using Eq. 2, and Eq. 3, provides control measurements. The disagreement in the plasma temperature determination was about 400°C. The lines Zn I 307.21nm; Zn I 307.59nm are very suitable because they are very closed each other and even relative calibration of the system is not needed. Moreover, these two lines are very well choice for the range of expected temperatures. Otherwise, lines, from different ionization states of the same element, are needed to be chosen.

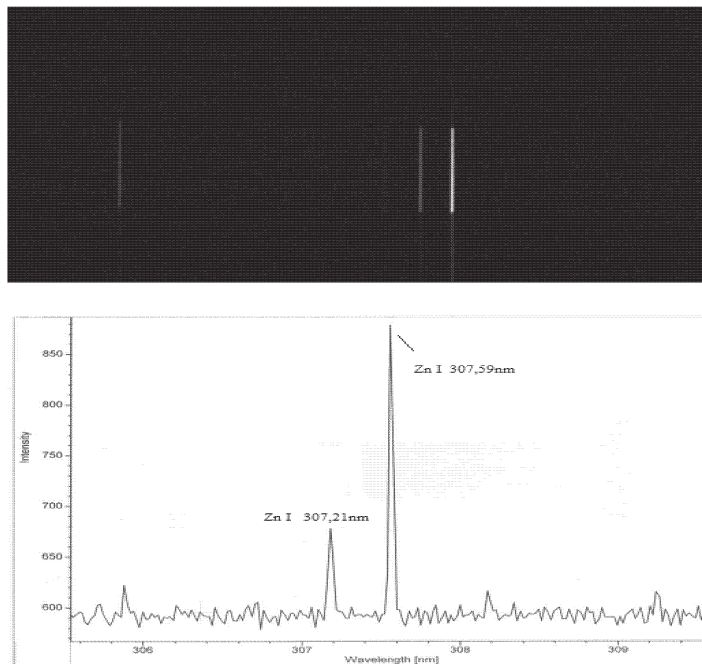


**Fig.5** The image of the zinc specter and its graph

As an example of the image specter and its graph, is shown in Fig 1., with the discharge current of 10A, in the interruptible DC regime. The determined temperature in the given case was about 6400°C. Mostly, the calculated temperatures were in the range of 6400-7100°C, and the maximum temperature was estimated near the cathode, about 9000°C. Radial

measurements are also performed by shifting the both electrodes simultaneously and taking the average intensities from different locations. The ratio of the intensities of the measured lines continually decreased if we measured from center to periphery of discharge, as we expected to be.

#### 4. CONCLUSION

An OES experiment is a power-full tool for characterization the free burning plasmas at the atmospheric pressure. Experimental results on the plasma temperature field in zinc vapor are described and discussed. The experiment involved imaging plasma radiation along a radial cord onto spectrometer, which resolved it into its spectral features. Boltzmann distribution of the excited  $Zn I$  species was the basis for temperature determination.

#### Acknowledgements

This work is supported by Ministry of Sciences of Montenegro under the grant No 01-382.

#### REFERENCES

- [1] Y. P. Raizer, *Gas Discharge Physics*, p. 399, (Springer Verlag, Berlin 1997).
- [2] I.L. Babich, A. N. Veklich, V. A. Zhovtyanskii and A. I. Cheredarchuk, *J. of Engineer. Phys. and Thermophys.*, vol. 71., No1, 127-134 (1998).
- [3] S. Mijovic, M. Vuceljic, M. Scepanovic, *The Optical Emission Spectroscopy Experiment of Open Air Plasma* (sent to SPIG 2012)
- [4] W. Lotche-Holtgreven, *Plasma Diagnostics*, p.186, (Nord. Holl. Pub. C., Amsterdam 1968).
- [5] T. Fujimoto, *Plasma Spectroscopy*, p.24, (Clarendon Press, Oxford 2004).
- [6] A. N. Zajdelj, B. K. Prokofjev, S. M. Rajskij, *Tabljici spektralnih linij*, p. 530 (Gosudarstvenoe Izdateljstvo tehniko-teoreticheskij literature, Moskva 1952). (in Russian).
- [7] A. K. Rusanov, *Osnovi kolichestvenogo spektraljnogo analiza rud i mineralov*, p.35, (Nedra, Moskva, 1971). (in Russian)

## INFLUENCE OF SURFACE CHARGES ON DC GLOW DISCHARGE IN NEON WITH Au-Ni CATHODE SPOTS

S. N. Stamenković<sup>1</sup>, V. Lj. Marković<sup>1</sup>, S. R. Gocić<sup>1</sup>, A. P. Jovanović<sup>1</sup>,  
M. N. Stankov<sup>1</sup> and N. D. Nikolić<sup>2</sup>

<sup>1</sup>*Department of Physics, Faculty of Sciences and Mathematics, University of Niš,  
Višegradska 33, 18000 Niš, Serbia*

<sup>2</sup>*Department of Chemistry, Faculty of Sciences and Mathematics, University of  
Niš, Višegradska 33, 18000 Niš, Serbia*

**Abstract.** The influence of surface charges on DC glow discharge in neon with *Au-Ni* cathode spots was studied by measuring the static breakdown voltage  $U_s$  as a function of pressure times distance  $pd$  (Paschen curves). Also, it was found that glow current changes (decreases with time) during the discharge. The measurements carried out on the gas tube with a hard galvanic gold layer on the cathode were compared to the ones on the gas tube with a vacuum deposited gold layer.

### 1. INTRODUCTION

It is well known that intermediate nickel film is used as a diffusion barrier between gold and copper. However, grain boundaries of *Au* serve as quick diffusion channel for diffusion of *Ni* to the surface [1]. Moreover, nickel atoms that diffused from the substrate to the outer surface of the gold could be oxidized [2-4]. Also, nickel diffusing through the gold layer causes an increase in the number of defects i.e. leads to the formation of an inter-metallic *Au-Ni* layer. These effects are manifested by the occurrence of dielectric islands on the gold surface i.e. surface regions (spots) with reduced conductivity that can retain the charges. The influence of surface charges on DC gas-discharge systems with high-ohmic electrode was studied in [5], where semi-insulating *GaAs* wafer was used as the cathode. It was found that the surface charges reduce the discharge current, due to their deposition on the surface of the high-ohmic electrode. Also, the surface charges affect the breakdown probability [6] and require the introduction of the multi-component non-stationary exponential distribution of the breakdown voltages [7].

The influence of surface charges on DC glow discharge in neon is studied by comparing the measurements of  $U_s(pd)$  dependence carried out on the gas tube with the galvanic gold layer on the cathode with the measurements

performed on the gas tube with a vacuum deposited gold layer. In addition, the decreasing of the glow current with time is observed in the case of galvanic gold layer. Also, SEM image and EDS spectrum of the galvanic gold layer, as an evidence of the presence of the regions with reduced conductivity, are presented.

## 2. EXPERIMENTAL DETAILS

The measurements were performed on a gas tube made of borosilicate glass with a  $0.5\mu\text{m}$  hard galvanic layer of gold and  $7\mu\text{m}$  sub-layer of nickel on the oxygen-free high conductivity (OFHC) copper cathode [6]. The electrodes were cylindrical with the diameter  $D = 6\text{ mm}$ , while the inter-electrode distance  $d$  was varied in order to obtain  $U_s(pd)$  dependence. The tube was evacuated down to  $10^{-7}\text{ mbar}$  with baking at  $600\text{ K}$  for  $24\text{ h}$  and then filled with research purity neon at  $p = 13.3\text{ mbar}$ . The measurements with galvanic gold layer were compared with those carried out on the tube with the OFHC copper cathode, gold plated by vacuum deposition ( $100\text{ nm}$  thick layer).

## 3. RESULTS AND DISCUSSION

The Paschen curve measured on the gas tube with a galvanic gold layer on the cathode is presented in Fig. 1 ( $\blacktriangle$ ). Moreover,  $U_s(pd)$  dependence obtained on the gas tube with a vacuum deposited gold layer ( $\square$ ) is also shown in Fig. 1, for the sake of comparison. It is obvious that static breakdown voltages for galvanic gold layer are less than the ones for the vacuum deposited gold layer. Also, it is observed that the glow current  $I_g$  for galvanic gold layer decreases with time as it is shown in Fig. 2. This behavior of galvanic layer may be explained by residual surface charges trapped on the cathode spots i.e. on the defects in the  $\text{Au-Ni}$  layer due to diffusion of nickel atoms [8] and on the oxidized nickel inclusions [4].

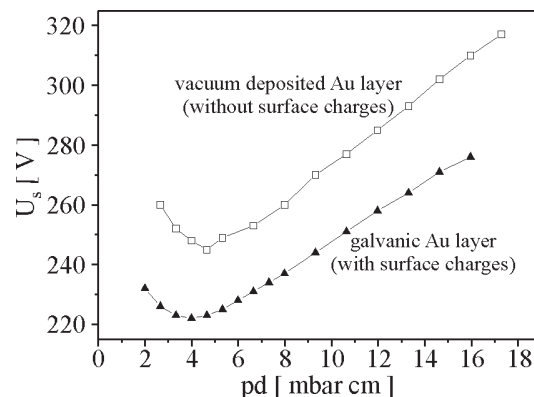


**Figure 1.** The static breakdown voltages as a function of  $pd$  (Paschen curves).

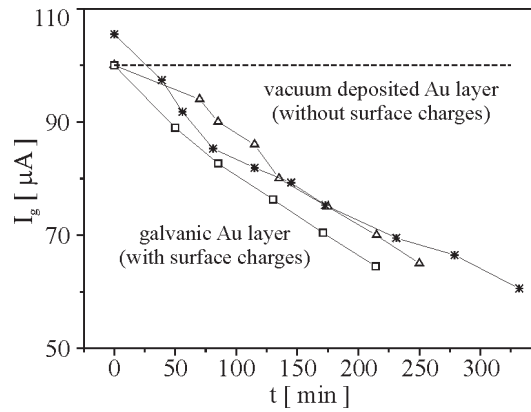


**Figure 2.** The glow currents  $I_g$  as a function of time.

As already stated, nickel is used as a diffusion barrier between gold and copper layers. However, nickel atoms diffuse to the outer gold surface where can be oxidized [4] and thus form regions with reduced conductivity which retaining surface charges (estimated diffusion coefficient of nickel  $D \sim 10^{-15} \text{ cm}^2 / \text{s}$  [2]). Moreover, diffusion of nickel atoms through the gold layer increases the number of defects in the galvanic layer and leads to considerable loss in conductivity, too [8]. Indeed, the regions with sub-micrometer dimensions on the galvanic layer of gold (black dots, spots) with reduced conductivity are confirmed by scanning electron microscopy (SEM) image (Fig. 3) and energy dispersive X-ray (EDS) spectrum (Fig. 4).

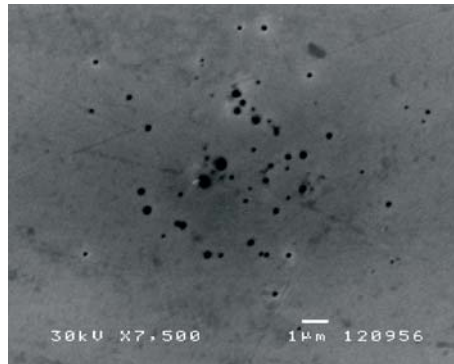


**Figure 3.** The scanning electron microscopy image of  $Au-Ni$  cathode spots.

We estimated the accumulated surface charges that could reduce the glow current [5]. Taking into account the data for conductivity  $\sigma = (10^{-2} - 10^{-6}) \Omega^{-1} \text{ cm}^{-1}$  available in the literature we obtained the density of the surface charges retaining on the cathode spots  $q \sim (10^{-15} - 10^{-10}) \text{ C} / \text{cm}^2$ . Thus, the charges accumulated on the cathode surface spots reduce the

breakdown voltages during the establishment of the discharge (Fig. 1), and decrease the glow current (Fig. 2). These effects are not observed in the case of vacuum deposited gold layer. Reduction of the discharge current was noticed in paper [5] where the mixed DC system with high-ohmic electrode was used. It was found that the charges store on the surface and affect discharge properties. Therefore, it can be concluded that inter-metallic *Au-Ni* cathode shows similar behaviour as a high-ohmic semi-insulating electrode.

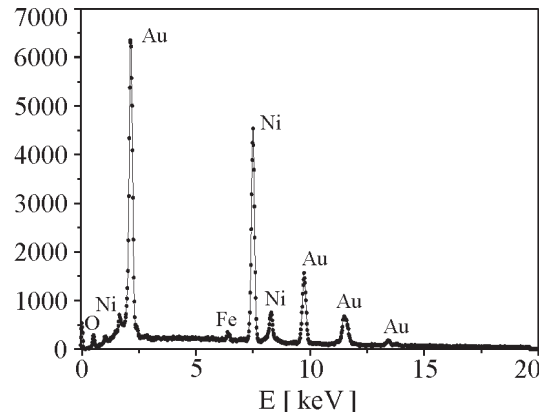


**Figure 2.** The energy dispersive X-ray (EDS) spectrum of *Au-Ni* cathode spots.

### Acknowledgements

The authors are grateful to Ministry of Education and Science of the Republic of Serbia for partial support (project 171025). We are grateful to M. Miljković for his help in preparing SEM and EDS images.

### REFERENCES

- [1] L.-C. Chen, F.-R. Chen, J.-J. Kai, L. Chang, J.-K. Ho, C.-S. Jong, C. C. Chiu, C.-N. Huang, C.-Y. Chen, and K.-K. Shin, *J. Appl. Phys.* 86, 3826 (1999).
- [2] H. G. Tompkins and M. R. Pinnel, *J. Appl. Phys.* 48, 3144 (1977).
- [3] T. E. Brady and C. T. Hovland, *J. Vac. Sci. Technol.* 18, 339 (1981).
- [4] J. R. Rairden, C. A. Neugebauer, and R. A. Sigsbee, *Metallurg. and Mater. Trans. B* 2, 719 (1971).
- [5] E. L. Gurevich, A. W. Liehr, Sh. Amiranashvili and H. G. Purwins, *Phys. Rev. E* 69 036211 1 (2004).
- [6] V. Lj. Marković, S. R. Gocić and S. N. Stamenković, *Appl. Phys Lett.* 96, 061501 1 (2010).
- [7] S. N. Stamenković, S. R. Gocić, V. Lj. Marković and A. P. Jovanović, *J. Appl. Phys.* 110, 103304 (2011).
- [8] A. M. Abdul-Lettif, N. N. Rammo and M. N. Makadsi, *Surf. Interface Anal.* 32, 117 (2001).

## CATALYTIC PROBE MEASUREMENTS OF ATOMIC OXYGEN CONCENTRATION IN LARGE VOLUME OXYGEN CCP

Kosta Spasić<sup>1</sup>, Saša Lazović<sup>1</sup>, Nevena Puač<sup>1</sup>, Zoran Lj Petrović<sup>1</sup>, Gordana Malović<sup>1</sup>, Miran Mozetič<sup>2</sup> and Uroš Cvelbar<sup>2</sup>

<sup>1</sup>*Institute of Physics, University of Belgrade, Pregrevica 118,  
11080 Belgrade, Serbia*

<sup>2</sup>*Jožef Stefan Institute, Jamova 39, 1000 Ljubljana, Slovenia  
e-mail: kostasp@ipb.ac.rs*

**Abstract.** Large scale chamber with asymmetric electrodes has been developed for low pressure treatment of seeds textile and wool. Since neutrals in plasma have very active role, it is of great importance to analyze their behavior in discharges. For this paper we have used catalytic probe in order to determine concentrations and spatial profiles of atomic oxygen. This diagnostic tool has been chosen due to its low cost, simplicity and possibility of real-time use, which makes it suitable for industrial purposes.

### 1. INTRODUCTION

Catalytic probe is simple, yet effective tool for measuring concentration of neutral species. They are usually constructed as thermocouple and the hot end is the probe tip, where catalytic activity is taking place. Probe tip can be made of nickel [1], iron [2], copper [3], silver [4] and, gold [5]. This technique has been used for measurement of concentrations of atomic oxygen [1], nitrogen [6] and hydrogen [5], most frequently in RF plasmas, ICP [1] as well as CCP [7] and almost exclusively in low pressure. Some applications have also been reported in microwave discharges [6]. Recent research has proved that this kind of equipment can be used for continuous data acquisition [1].

In comparison with other methods for measuring concentration of neutral species catalytic probe comes at low price and it is simple to use. Direct interpretation of results is one of the biggest advantages of this method. Problem is that recombination coefficient cannot be determined with precision higher than 30% [1], so the probe itself cannot have accuracy above this mark. Even though probes are usually made to have small dimensions, their presence in discharge is still affecting plasma. When interpreting results, one should take care about the fact that probe cannot make difference whether species were excited or not when they arrived on its surface.

In our laboratory we have large scale discharge chamber in which we can have conditions similar to plasmas that are used for industrial purposes. Asymmetric geometry allows samples to be exposed to different intensity of treatment simply by adjusting their position. So far it has been used for treatment of wool [8], textile [9] and seeds [10].

Beside charged particles, neutral species have also very important role in plasma treatment. Presence of atomic oxygen in discharge can have influence on activation of surfaces of textile and seeds. Therefore, in order to have adequate treatment, it is of great importance to properly determine spatial profiles of atomic oxygen concentration inside the chamber. For this paper we have used nickel catalytic probe to measure concentration of atomic in CCP RF discharge at pressure of 450 mTorr.

## 2. EXPERIMENTAL SET-UP

Experimental set-up is shown on Figure 1. Our discharge chamber has cylindrical geometry. It is 2.5 m long and 1.17 m wide with walls, which are used as grounded electrode, made of stainless steel. Powered electrode is made of aluminum and it is placed axially, it is 1.5 m long and has diameter of 3 cm.

Our catalytic probe is placed side-on, perpendicular to powered electrode. Tip of it is disc made of nickel whose diameter is 1.5 mm and it is 0.04 mm thick. Since our probe is placed inside glass tube we have used Wilson seal to allow ease of movement and to secure that vacuum is maintained. Measurements were performed with real-time recording multimeter.

To create and sustain our plasma we have used 13.56 MHz power supply and matching network. Vacuum is achieved by mechanical pump, while needle valve was used to control flow of working gas.

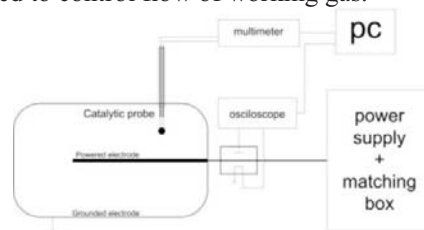


**Figure 1.** Experimental set-up.

## 3. RESULTS AND DISCUSSION

Typical measurements with catalytic probe require plasma to be turned off whenever data acquisition is needed. Speed of probe tip cooling when discharge is turned off provides information about power that is transferred to it when plasma is turned on. Since recombination is main cause of probe tip temperature increase, heating power can be used to derive atomic oxygen

concentration [11]. It has been discovered that, for same gas and same plasma parameters, temperature time derivative of probe tip depends on maximum temperature [2]. When that dependency is known, atomic oxygen concentration can be determined in real-time while plasma is on without interruption.

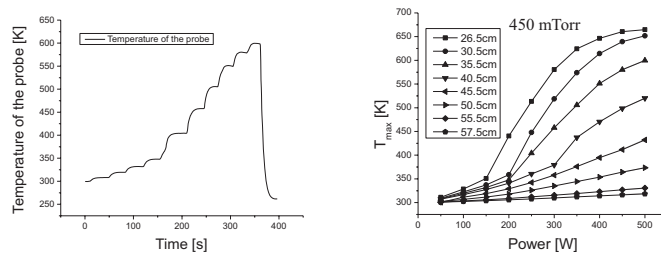


**Figure 2.** Standard measured curve (left), and maximum temperatures for whole set of measurements (right).

On Figure 2, on the left hand side, we have presented one of typical measured curves. We can see that after applying certain power, temperature is starting to rise and after few seconds it reaches saturation or maximum temperature,  $T_{max}$ . On the right hand side of the picture, set of maximum temperatures for different conditions is presented.

Spatial profiles of atomic oxygen concentration in large scale CCP device at 450 mTorr are shown in Figure 3. The closest distance to the powered electrode where measurements were taken was chosen according to technical capabilities and it was 26.5 cm. The most distant point was at chamber wall. Applied RF power was between 50 W and 500 W with increasing step of 50 W.

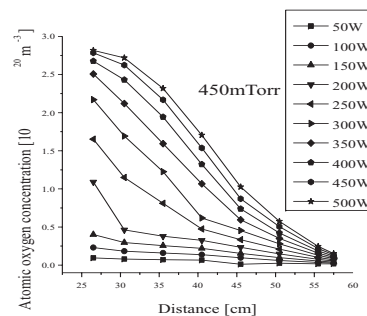


**Figure 3.** Spatial profiles of atomic oxygen concentration for different applied RF power at 450mTorr.

In the vicinity of the powered electrode the highest concentrations of  $2.75 \cdot 10^{20} \text{ m}^{-3}$  were recorded. As probe was moved closer to the chamber wall concentrations were decreasing, and at the lowest point they were more than one order of magnitude lower. This big difference can be, in part, explained by very different size of electrodes. The biggest drop is between 35 cm and 45 cm.

For fixed position of the probe, rising of applied RF power resulted in rise of concentration of atomic oxygen

#### 4. CONCLUSION

Catalytic probe was used to diagnose large volume CCP discharge at 13.56 MHz in oxygen at 450 mTorr for powers between 50 and 500 W. The highest concentrations are measured near the powered electrode, while at the chamber wall we measured concentrations that were order of magnitude lower. Higher applied power also produced higher concentrations. Since in all plasma treatments oxygen atoms play crucial role it is important to know concentrations of O atoms in order to be able to optimize the treatments. Also, knowledge of atom concentrations for different distances and different applied powers gives us opportunity to finely tune the treatments for variety of samples by just adjusting the distance from the powered electrode. It is shown that for the smaller distances from the powered electrode similar concentration of O atoms can be obtained as for greater distances, but much higher powers and this can significantly reduce the cost of treatments since same effects can be obtained for smaller power consumption

#### Acknowledgements

This research has been supported by the Ministry of Education and Science of Serbia under the contract numbers III41011 and ON171037

#### REFERENCES

- [1] I Šorli and R Ročak, J. Vac. Sci. Technol. A 18 2, 0734-2101 (2000)
- [2] M Mozetic, A. Vesel, U. Cvelbar and A. Ricard, Plasma Chem Plasma Process 26:103 (2006)
- [3] M Mozetic and U Cvelbar, Plasma Sources Sci. Technol. 18 034002 (2009)
- [4] M R. Carruth and A F Whitaker, Rev. Sci. Instrum., 61 (4) (1990),
- [5] M. Mozetic et al, Journal of Nuclear Materials 363, 1457 (2007)
- [6] F Gaboriau, U Cvelbar, M Mozetic, A Erradi and B Ruffet, J. Phys. D: Appl. Phys. 42 055204 (2009),
- [7] T. Vrlinic et al., Vacuum 83 792 (2009)
- [8] M Radetic, D Radojevic, V Ilic , D Jovic, D Povrenovic, N Puač, Z Lj. Petrovic and P Jovancic , Trends in Applied Sciences Research, 1 564 (2006)
- [9] M Radetić, P Jovančić, N Puač, Z Lj Petrović, Z Šaponjić, Textile Research Journal 79 558 (2009)
- [10] N. Puač, Z.Lj. Petrović, S. Tivković, Z. Giba, D. Grubišić and A.R. Đorđević, Plasma Processes and Polymers, 203 (2005),
- [11] A Drenik, U Cvelbar, K Ostrikov and M Mozetic, J. Phys. D: Appl. Phys. 41 11520 (2008)

## AXIAL PROFILES OF PLASMA BULLET WITH DIFFERENT ELECTRODE GAPS

Nenad Selaković<sup>1</sup>, Dejan Maletić<sup>1</sup>, Nevena Puač<sup>1</sup>, Saša Lazović<sup>1</sup>,  
Gordana Malović<sup>1</sup>, Antonije Đordjević<sup>2</sup> and Zoran Lj. Petrović<sup>1</sup>

<sup>1</sup>Institute of Physics, University of Belgrade, Pregrevica 118, 11080 Belgrade, Serbia

<sup>2</sup>School of Electrical Engineering, University of Belgrade, Bulevar kralja Aleksandra 73, 11000 Belgrade, Serbia

**Abstract.** We used fast ICCD imaging in order to record time evolution of plasma bullet formation. Plasma jet was made of Pyrex glass tube with two transparent electrodes made of polyester (PET) foil whose position can be easily adjusted. The excitation voltage was approximately 10 kVpp at frequency of 80 kHz. The power transmitted to the plasma in all measurements was 4 W. The working gas was helium with constant flow rate of 4 slm. In this paper we shall show the total axial light emission profiles of plasma jet bullets obtained for three different electrode gaps, of 10, 15 and 20 mm.

### 1. INTRODUCTION

One of the main reasons for the development of new low temperature plasma sources which are working at atmospheric pressure is their simple, non-expensive design with great potential for possible applications. These plasma sources are used for treatment of polymers, cells, tissues, etc. [1-3]. One of the newest scientific fields developed from this high-end research is plasma medicine [4]. Achieving high temperatures of electrons, much higher than the temperatures of ions and ambient gas, is crucial for sustaining stable non-equilibrium plasmas. In order to reduce the breakdown voltage in these discharges, noble gases are used, usually helium or argon [5]. For powering plasma jets, various types of signals at high frequencies are used [6], as well as different geometries [7, 8]. By choosing different materials for the electrodes, different electrode gaps and sizes, one can significantly change the behavior of plasma jets and control if the plasma jet will form bullets or not. The optimal geometry parameters can be found in order to maximize the distance that plasma bullets can reach. In this paper we present axial profiles for several gaps between the powered and the grounded electrode.

## 2. EXPERIMENTAL SETUP

The atmospheric pressure plasma jet used in these experiments is shown in Fig. 1. Its body was made of a Pyrex glass tube (O. D. of 6 mm and I. D. of 4 mm) with two transparent thin conductive PET foil electrodes (width of 15 mm) wrapped around the glass tube. The copper foil was used to connect electrodes to an external electrical circuit. The electrode closer to the edge of the glass tube was the powered one, and the other electrode was grounded (see Fig. 1). A resistor of 100 k $\Omega$  between the grounded electrode and the ground was connected for current measurements. During all measurements, the helium flow rate was 4 slm. As the power supply, a signal generator was used, and it was connected to a home-made amplifier. The excitation signal was sinusoidal and the working frequency was 80 kHz. Since the maximum value of the voltage at the output of the amplifier is around 1 kV, it was necessary to make a high-voltage transformer to increase the signal from the amplifier up to 10 kV peak-to-peak. The calculated power transmitted to plasma in all measurements was 4 W. The gap between electrodes was 10, 15 and 20 mm. The distance between the powered electrode and the edge of the glass tube was kept constant at 7 mm for all measurements.

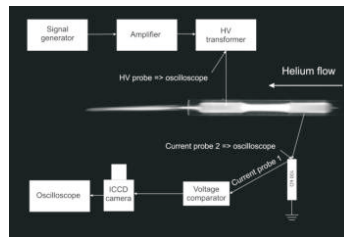


**Figure 1.** Experimental setup

## 3. RESULTS AND DISCUSSION

Signals of current and voltage, with trigger positions, are presented in Fig. 2 (left). The voltage signal has pure sine waveform, while the current signal is a somewhat deformed. Three triggering positions of ICCD imaging were selected to present behavior of plasma at different time positions of the whole cycle. The first trigger position is close to the minimum, the second one is near the zero and the third is right after the maximum of the voltage signal. Axial (along the glass tube axis) profiles of plasma emission were calculated from the obtained ICCD images (see Fig. 2 (right)-3). The presented profiles are calculated as a sum of the emission intensity coming from plasma along the axis of the glass tube diameter. In Fig. 2 (right)-3, the right edge of the grounded electrode is chosen to be the reference (zero) position, the positions of the powered and the grounded electrode are marked by vertical solid lines and the edge of the glass tube by a vertical dashed line. The direction of helium flow is from the grounded toward the powered electrode (as shown in Fig. 2 (right)-3).

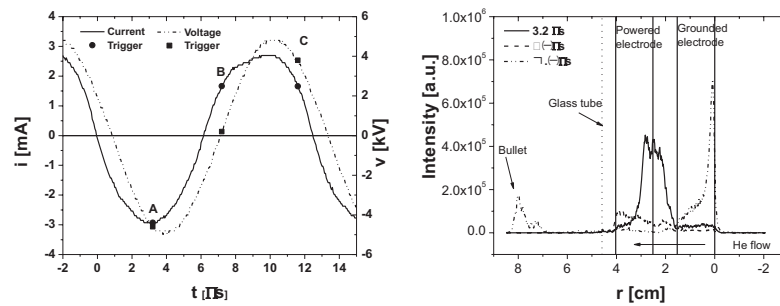


**Figure 2.** Current and voltage signals with trigger positions for 15 mm electrode gap (left); Axial light emission profiles for 10 mm electrode gap for three different trigger delays ( $3.2 \mu\text{s}$ ,  $7.2 \mu\text{s}$  and  $11.6 \mu\text{s}$ ), 4 slm flow of helium and power of 4 W

Axial profiles of light emission for the gap of 10 mm between electrodes are shown in Fig. 2 (right). For the minimum of the voltage and current signal, the maximum emission intensity coming from the discharge is on the right edge of the powered electrode (Fig. 2 (right), black solid curve). At the same time, the emission intensity in other areas is several orders of magnitude smaller. With increase of the voltage and current signals, plasma is moving towards the left edge of the powered electrode and the emission intensity decreases.

For the delay of  $7.2 \mu\text{s}$  (Fig. 2 (right), black dashed curve) the intensity is very small with the maximum near the left edge of the powered electrode. A plasma bullet is formed at the maximum values of current and voltage signals and it reaches the maximum distance of 3.5 cm from the edge of the glass tube for the delay time  $11.6 \mu\text{s}$ . Also, there is another well-defined maximum at the right edge of the grounded electrode.

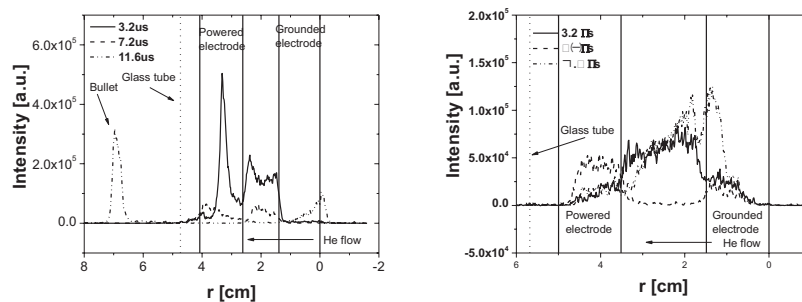


**Figure 3.** Axial light emission profiles for 15 mm (left) and 20 mm (right) electrode gap for three different trigger delays ( $3.2 \mu\text{s}$ ,  $7.2 \mu\text{s}$  and  $11.6 \mu\text{s}$ ), 4 slm flow of helium and power of 4 W

Axial profiles for the gap of 15 mm are presented in Fig. 3 (left). A well-defined peak of light emission can be seen in the powered electrode, as

well as significant emission between electrodes (for the delay of 3.2  $\mu\text{s}$ , solid black curve). For the delay of 7.2  $\mu\text{s}$ , the intensity significantly drops in and between the electrodes (dashed black curve). For the delay of 11.6  $\mu\text{s}$ , there are two distinct peaks: one inside the grounded electrode and the second one outside the tube approximately at 2.2 cm from the edge of the glass tube. For the 15 mm gap, the bullet is better defined than in the case of other electrode gaps used in this paper.

For the largest electrode gap in Fig. 3 (right), the emission intensity is much smaller than in other two cases. For the delays of 3.2  $\mu\text{s}$  and 7.2  $\mu\text{s}$ , there are no well-defined peaks. For the delay of 11.6  $\mu\text{s}$ , there is no light emission outside the glass tube. This electrode gap is not suitable for treatment of surfaces because plasma does not leave the glass tube.

#### 4. CONCLUSION

Using ICCD imaging it has been shown that the light emission is highly dependent of the electrode geometry. In this study it has been shown that if it is needed to obtain a well-defined plasma bullet, the most suitable configuration is a gap of 15 mm between the electrodes. In other two configurations, the plasma bullet is distorted or it does not leave the glass tube at all. One of the directions for future research could be to record emission profiles by using filters for different wavelengths.

#### Acknowledgements

This research has been supported by the Ministry of Education and Science, Serbia, under projects ON171037 and III41011.

#### REFERENCES

- [1] F. Iza, G. J. Kim, S. M. Lee, J. K. Lee, J. L. Walsh, Y. T. Zhang, M. G. Kong, *Plasma Process. Polym.* 5, 322–344 (2008).
- [2] A. Shashurin, M. Keidar, S. Bronnikov, R. A. Jurjus, M. A. Stepp, *Appl. Phys. Letters* 93, 181501 (2008).
- [3] S. J. Kim, T. H. Chung, S. H. Bae, S. H. Leem, *Appl. Phys. Letters* 97, 023702 (2010).
- [4] A. V. Nastuta, I. Topala, C. Grigoras, V. Pohoata, G. Popa, *J. Phys. D: Appl. Phys.* 44,105204(2011).
- [5] H. S. Park, S. J. Kim, H. M. Joh, T. H. Chung, S. H. Bae, S. H. Leem, *Phys. Plasmas* 17, 033502 (2010).
- [6] Q. Xiong, X. P. Lu, K. Ostrikov, Y. Xian, C. Zou, Z. Xiong, Y. Pan, *Phys. Plasmas* 17, 043506 (2010).
- [7] E. Karakas, M. Koklu, M. Laroussi, *J. Phys. D: Appl. Phys.* 43,155202 (2010).
- [8] N. Jiang, A. Ji, Z. Cao, *J. Appl. Phys.* 108, 033302 (2010).

## STARK WIDTHS OF SEVERAL Ar II SPECTRAL LINES EMITTED FROM PULSED ARC PLASMAS

T. Gajo, I. Savić, R. Kobilarov and Z. Mijatović

*Department of Physics, Faculty of Sciences, University of Novi Sad,  
Trg Dositeja Obradovića 4, 21000 Novi Sad, Serbia*

**Abstract.** Results presented in this paper are part of a wider study of Stark widths of Ar II spectral lines in the visible spectrum. A pulsed wall stabilized arc was used as a plasma source with an electron density of about  $2 \cdot 10^{23} \text{ m}^{-3}$  and a temperature of about 15000 K. The attained peak value of the pulsed current was 240A. Stark widths of Ar II 461.0 and 480.6 nm were compared with theoretical results and with the results of various experiments as well. A considerable disagreement between experimental results was found.

### 1. INTRODUCTION

A number of plasma chambers, sources and reactors use some of the noble gases as a working gas due to its chemical inertion. For plasma diagnostics (plasma electron density and temperatures measurements) various methods can be applied. One of them is the method based on Stark broadening of the spectral lines in plasmas. For that purpose reliable theoretical and experimental data of Stark widths and shifts of the spectral lines must be used. Because of a simple application of this method to hydrogen and helium lines, a certain amount of hydrogen or helium is often introduced into the gas mixture. Sometimes, though, this is not possible for a number of different reasons. In that case, pure noble gases are used. Due to the low ionization potential of 15.8 eV, important for plasma creation, the argon is one of the most frequently used gases.

In the case of plasmas of high electron density (more than  $10^{23} \text{ m}^{-3}$ ) and temperatures (15000 K or more) spectral lines of neutral argon are not suitable for plasma diagnostic purposes due to their weak intensity or even their disappearance. In such case the spectral lines of ionized argon can be used. The problem with the argon lines generally is the great disagreement (up to 100 %) between experimental data obtained from various experiments. A complete set of data was obtained for 13 Ar II spectral lines from which the results for 461.0 and 480.6 nm Ar II spectral lines recorded from the pulsed electrical arc with plasma electron density of about  $2 \cdot 10^{23} \text{ m}^{-3}$ , and temperature of about 15000 K is presented.

## 2. EXPERIMENTAL AND DATA PROCESSING

The plasma source used in this experiment was the wall stabilized electric arc working in DC regime but fed by high current pulses with the frequency of 1 Hz. The operating DC current was 30 A, while the peak pulse currents were 180 A and 240 A. The arc operated under atmospheric pressure with the mixture of argon (96 %) and hydrogen (4 %). The detailed description of the pulsed working mode can be found in [1]. The optical observation was made end-on. The middle part of the arc column was focused, by means of a concave mirror, onto the entrance slit of 1-m monochromator equipped with a 1200 g/mm diffraction grating. The intensified CCD camera (Stanford Quick 4 Edig ) was placed at the exit focal plane of the monochromator. In this arrangement the spectral interval covered by the CCD chip was about 12 nm. For the instrumental width measurements a series of different hollow cathode lamps (Cu, Ar, ...) was used. The instrumental width of the system was found to be 0.052 nm. Since observation was done end-on, self-absorption of all recorded spectral lines was checked by means of the back mirror method [2]. In most cases self-absorption was found to be negligible, but in some cases it was up to 10 %, when the corresponding correction was applied [2]. Spectral line recordings were made at the peak of the pulsed current. Every line profile is obtained as the average of 100 recordings. As an example, the recorded spectral line profile of Ar II 461.0 nm is presented in Figure 2.

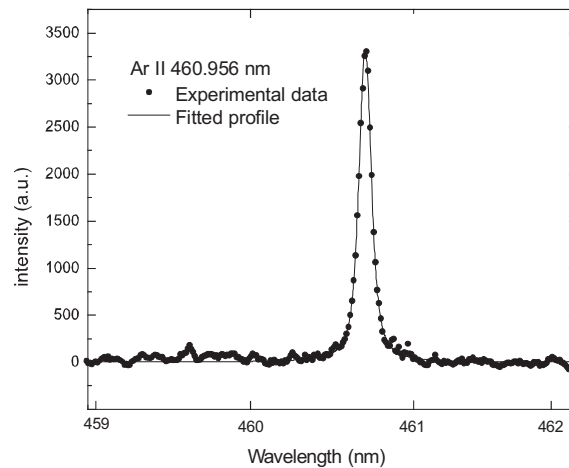


**Figure 1.** Experimental profile of Ar II 461.0 nm spectral line.

Plasma electron density  $N_e$  was determined from the Stark width of the hydrogen  $H_\beta$  spectral line in conjunction with [3], while plasma temperature  $T$  was determined from a Boltzmann plot of 13 Ar II spectral lines [4] as well as from plasma composition data [5]. Measured quantities for lower current pulses were  $N_e = 1.27 \cdot 10^{23} \text{ cm}^{-3}$  and  $T = 13400 \text{ K}$ , and for higher  $N_e = 1.60 \cdot 10^{23} \text{ cm}^{-3}$  and  $T = 14200 \text{ K}$ .

The contribution of Doppler width, for the measured plasma temperatures, was found to be negligible for all measured spectral lines. Commercial software as well as software developed during this work was applied for the deconvolution of the Gaussian and the Lorentzian part of the recorded Ar II spectral line profiles. Both methods gave practically the same results. After that, the obtained Lorentzian widths were corrected to the van der Waals and resonant broadening.

### 3. RESULTS

Obtained Stark widths are compared to the values calculated using the semiempirical formula [6] and the values based on Griem results [7]. Experimental results from other authors ([8-10] and references therein) are also taken into account. For that purpose, theoretical values are scaled to the plasma electron densities and temperatures which correspond to the experimental values, cited by the authors.

The results of comparisons between different experiments are presented in Fig. 2 (a) and (b). Experimental results are normalized to the theory [6]. The full lines represent the average values obtained for the available experimental data ([8-10] and references therein). The standard deviation of the average, taking into account all results, is about 20 % for all of the investigated lines. This is the reason why we chose this corridor to present in Fig 2.

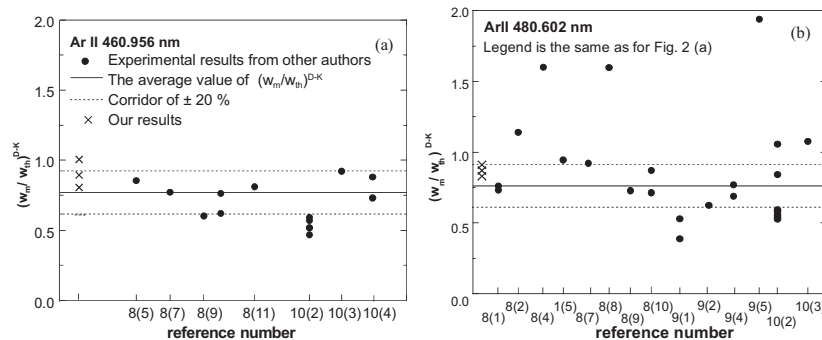


**Figure 2.** Comparison of experimental results obtained from different experiments. Reference numbers are related to the reference in this work. Numbers in parenthesis are reference numbers in cited papers.

Figure 2 shows that experimental results converge to some values, in these cases to 0.9. This fact implies that, for the plasma diagnostics purposes, new and valuable experimental data are necessary, utilizing new measurement techniques and plasma sources.

#### 4. CONCLUSIONS

Here we reported results of Stark width measurements of two Ar II spectral lines, 461.0 and 480.6 nm, which are a part of a wider study of 13 Ar II spectral lines. Obtained results were compared with other experimental results. These comparisons showed considerable disagreement between the experiments, but newer results converge to the same value. This fact suggests that more measurements should be done applying more accurate and reliable experimental techniques in connection with appropriate data processing.

#### Acknowledgements

This work is partially supported by the Ministry of Education and Science under the project No. 171014.

#### REFERENCES

- [1] S. Djurović, Z. Mijatović, R. Kobilarov, I. Savić, *Plasma Sources Sci. Technol.* **21**, 1, (2012).
- [2] S. Djurović, R. Kobilarov, B. Vujičić, *Bull. Astron. Belgrade* **153**, 41-56, (1996).
- [3] C. R. Vidal, J. Cooper and E. W. Smith, *J. Suppl. Ser. No. 214*, **25**, 37 (1973).
- [4] W. Lochte-Holtgreven, *Plasma Diagnostics*, (North-Holland, Amsterdam, 1968.)
- [5] C. H. Popenoe, J. B. Shumaker, Jr., *J. of Research of NBS, Phys. And Chem.*, **69A**, 495, (1965).
- [6] M. S. Dimitrijević and N. Konjević, *JQSRT* **24**, 451 (1980).
- [7] H. R. Griem, *Spectral Line Broadening by Plasmas*, (Academic, New York, 1974).
- [8] N. Konjević and W. L. Wiese, *J. Phys. Chem. Ref. Data* **5**, 259 (1976).
- [9] N. Konjević, M. S. Dimitrijević, W. L. Wiese, *J. Phys. Chem. Ref. Data* **13**, 649 (1984).
- [10] N. Konjević, W. L. Wiese, *J. Phys. Chem. Ref. Data* **19**, 1307 (1990).

## ICCD SPECTROMETER – CHARACTERIZATION OF INSTRUMENTAL LINE PROFILES AND SATURATION LEVEL DETERMINATION

I. Savić, L. Gavanski, S. Djurović, Z. Mijatović and R. Kobilarov

*University of Novi Sad, Faculty of Sciences, Department of Physics, Trg  
Dositeja Obradovića 4, 21000 Novi Sad, Serbia*

**Abstract.** In this paper the use of modified Gauss function for characterization of instrumental profiles and system saturation level determination is described.

### 1. INTRODUCTION

Atomic and ionic transitions in the visible region are routinely used as indicators of plasma temperature and density [1]. Therefore, precise measurements of plasma radiation in the optical region are of great importance.

At present day, manufacturing technologies of dispersion and optical elements and detectors are significantly improved with the aim of enhancing the resolution, the sensitivity and the signal-to-noise ratio. Even having such high quality spectroscopic elements, it is a challenge to set up a spectroscopic instrument that can efficiently detect dispersed radiation. Common tasks, problems and main results of coupling the ICCD camera to the spectrometer have been recently shown in [2].

### 2. EXPERIMENTAL

The instrument is schematically shown in Fig. 1. (for details see [2] ) The monochromator is a McPherson 1.00 m scanning monochromator (model 2061 B) equipped with a grating of 1200 G/mm and a computer controlled scanning system. As a detector an ICCD camera is used (4 Quik E dig Stanford Computers Optics).

For all instrument characterizations presented in this paper, the isolated spectral line Pb I  $\lambda = 405.7807$  nm is used. This line is emitted from a hollow cathode lamp placed in front of entrance slit. In order to obtain the instrumental profile FWHM (full width at half maximum) dependence on the position on CCD channels, the given spectral line is positioned on different places on the CCD chip by setting different grating positions and recorded.

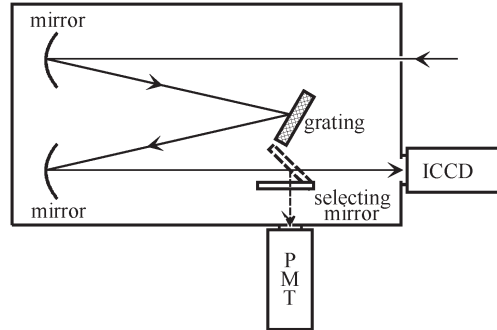


**Figure 1.** The instrument. A light beam is passing through the entrance slit. The dispersed light can be focused either on the ICCD or by use of a selecting mirror on the exit slit where a photomultiplier (PMT) is used as a detector.

The linearity response level determination is performed by recording the spectral line at one given position of the grating but on two different ways:

- by keeping the exposure time constant and changing the MCP (micro channel plate) gain voltage in steps
- by using a typical constant MCP gain voltage and changing the exposure time.

All recorded images are readout over all channels as summed counts between the 500th and the 600th row and divided by 100 in order to have an one row averaged value in this row interval. Spectral profiles obtained on this way are fitted to the modified Gauss function [3]:

$$I_{\lambda} = I_0 \exp \left[ - \ln 2 \left( 4 \frac{(\lambda - \lambda_0)^2}{w^2} \right)^s \right] \quad (1)$$

where  $I_0$  is the amplitude,  $\lambda_0$  is the line center,  $w$  is the FWHM and  $s$  determines the line shape. This function gives "rectangular" line shapes for  $s > 1$ , "sharp" line shapes for  $s < 1$  and the "original" Gaussian" for  $s = 1$ .

### 3. RESULTS AND DISCUSSIONS

In order to get the instrumental profile FWHM dependence on the position on CCD channels, the spectral line is positioned on different places of the CCD chip by setting different grating positions. Experimental profiles are fitted to function given by equation (1) using  $s$  as a free parameter and as  $s = 1$ . Fitting results for FWHM for these two cases are shown in Fig. 2. a). Fitting results for parameter  $s$  as a free parameter are shown in Fig. 2. b)

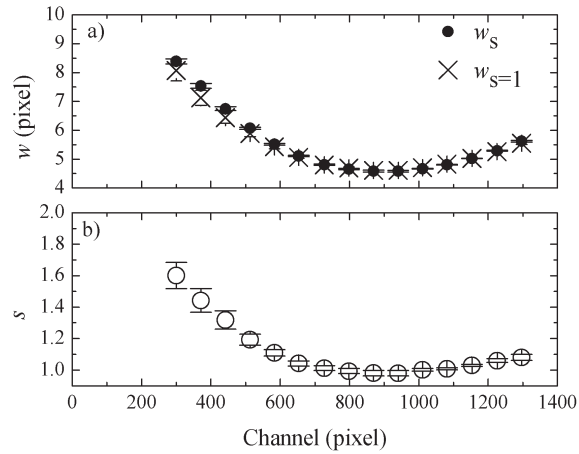


**Figure 2.** a) FWHM of Pb I spectral line  $\lambda = 405.7807$  nm across channels (• - using  $s$  as a free fitting parameter,  $\times$  - using  $s = 1$ ). b) The free fitting parameter  $s$  across channels.

In order to determine the linearity response level at a constant exposure time, the spectral line is positioned on the CCD chip position which corresponds to the approximately minimal FWHM. Exposure time  $t_{\text{exp}}$  is kept constant ( $t_{\text{exp}} = 700 \mu\text{s}$ ) whereas MCP gain voltage ( $U_{\text{MCP}}$ ) is changed. Fitting results are shown in Figure 3.

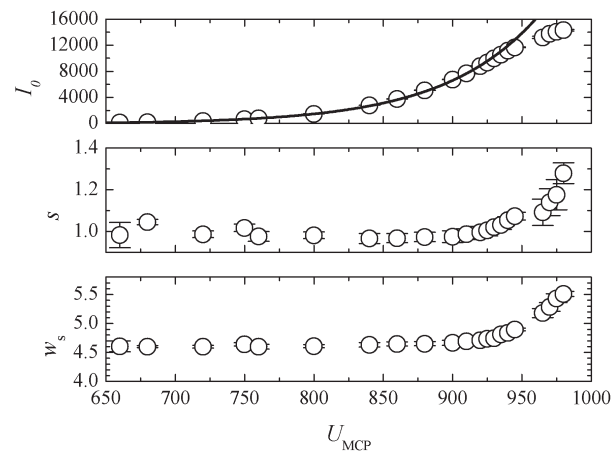


**Figure 3.** Fitting results for  $I_0$ ,  $s$  and  $w_s$  as functions of  $U_{\text{MCP}}$  at  $t_{\text{exp}} = 700 \mu\text{s}$  (○ - experimental points, — - exponential growth function).

In order to determine the linearity response level at a constant MCP gain voltage, the spectral line is positioned on the CCD chip as for the test

described above. The exposure time  $t_{\text{exp}}$  is changed while gain voltage is kept at 750 V. Fitting results are shown in Figure 4.

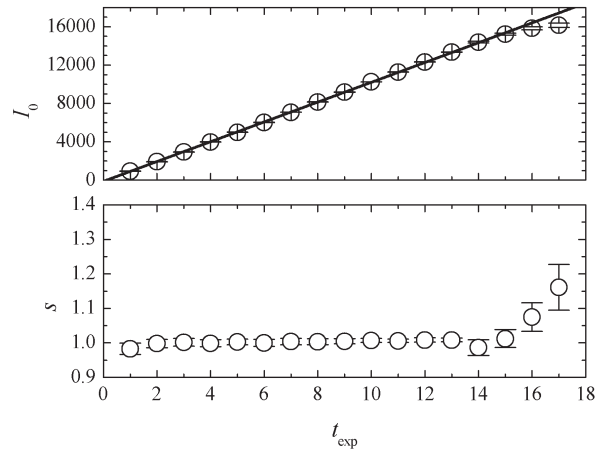


**Figure 4.** Fitting results for  $I_0$ , and  $s$  as functions of  $t_{\text{exp}}$  at  $U_{\text{MCP}} = 750$  V (○ - experimental points, — - linear function).

From Fig. 2, it can be seen that within the interval between the 500th and the 1360th channel, differences between “original” and “rectangular” Gaussians are small and therefore this channel interval can be used for measuring very narrow spectral lines. FWHMs of “Rectangular” Gaussians are slightly greater in comparison to those of “original” Gaussians. Figures 2, 3 and 4 lead to the conclusion that the increase of the parameter  $s$  can be used as an indicator of false system imaging or of detector saturation. The safe limit of 10000 counts per pixel is obtained.

### Acknowledgements

This work is supported by Ministry of Education and Science of Republic of Serbia under the Project 171014.

### REFERENCES

- [1] H. R. Griem, *Spectral Line Broadening by Plasmas*, (Academic Press, New York, 1974).
- [2] I. Savić, L. Gavanski, S. Djurović, Z. Mijatović and R. Kobilarov, *Journal of Research in Physics*, **35**, 55 (2011).
- [3] R. E. Bell, L. E. Dudek, B. Grek, D. W. Johnson and R. W. Palladino, *Rev. Sci. Instrum.*, **70**, 821 (1999).

## DC ATMOSPHERIC PRESSURE GLOW DISCHARGE COLD PLASMA FOR BACTERIA INACTIVATION

A. A. Kirillov<sup>1</sup>, Y. A. Safronau<sup>1</sup>, L. V. Simonchik<sup>1</sup>, N. V. Dudchik<sup>2</sup> and  
O. E. Nezhvinskaya<sup>2</sup>

<sup>1</sup> *Stepanov Institute of Physics NAS of Belarus, Nezalezhnasci Ave. 68,  
220072 Minsk, Belarus, e-mail: y.safronau@ifanbel.bas-net.by*

<sup>2</sup> *Republican Scientific-Practical Center of Hygiene, Akademichnaya St. 8,  
220072 Minsk, Belarus*

**Abstract.** The study of microbial inactivation using created sources of cold nonequilibrium plasma: atmospheric pressure glow discharges (APGD) with plasma cathode and normal APGD plasma jet was performed. The parameters of the non-equilibrium discharge plasma at inactivation effect were determined. D-time of inactivation is on the order of several minutes for vegetative bacteria *S. aureus* and *E. Coli* and decreases with discharge current increase.

### 1. INTRODUCTION

Atmospheric pressure nonequilibrium plasmas were shown to be very promising for biomedical applications, which include decontamination and modification of surfaces as well as a number of therapeutic applications of plasma [1–4]. One of the unique properties of non-equilibrium plasma is high reactivity at low gas temperatures. This feature opens up new possibilities of using non-equilibrium plasma for processing of heat-sensitive materials including biological tissue. The large area of non-equilibrium plasma applications in medicine aimed at reducing the number of viable cells of microorganisms on medical products, sophisticated high-technology medical equipment, or on the wound surface. The potential use in biomedical applications has driven the development of a variety of reliable plasma sources: surface and volume dielectric barrier discharges [5], atmospheric pressure plasma jets [6], etc. In this paper bacteria inactivation using atmospheric pressure glow discharges (APGD) with plasma cathode in the three-electrode system [7] and normal APGD plasma jet in different plasma-forming gases is considered. The discharges are stationary that makes easier the identification of linkages between inactivation characteristics and plasma parameters, which is important for elucidating the mechanisms of plasma inactivation.

## 2. RESULTS

The three-electrode system [7] makes possible to obtain stable discharges with relatively long scale (up to ten cm) and/or large volume positive columns ( $>20 \text{ cm}^3$ ) in inert and molecular gases and their mixtures at atmospheric pressure which can be potentially used in the field of plasma medicine and biotechnologies. In this paper a helium large-volume diffuse non-self-sustained APGD at a current 1 mA and 5 mA at 3 cm interelectrode gap is used for surface decontamination from bacteria. The plasma cathode is normal helium APGD initiated at a current of 300 mA in a gap of 0.5 mm between the tungsten weekly rounded cathode and 1 mm copper with 2 mm central hole. Working gas (helium) at a flow of  $\sim 1 \text{ slm}$  was fed through the plasma cathode.

Microorganisms were deposited on stainless steel 2x2 cm samples with average surface density of about  $10^6 \text{ cm}^{-2}$ . After preparation a procedure of sample exposure to plasma was performed. The samples for plasma treatment were placed on the anode (bottom electrode) for an exposure time. Figure 1a shows an image of sample exposure in which the sample is covered with plasma. For quantitative determination of inactivation effect a direct cell counting method was used.

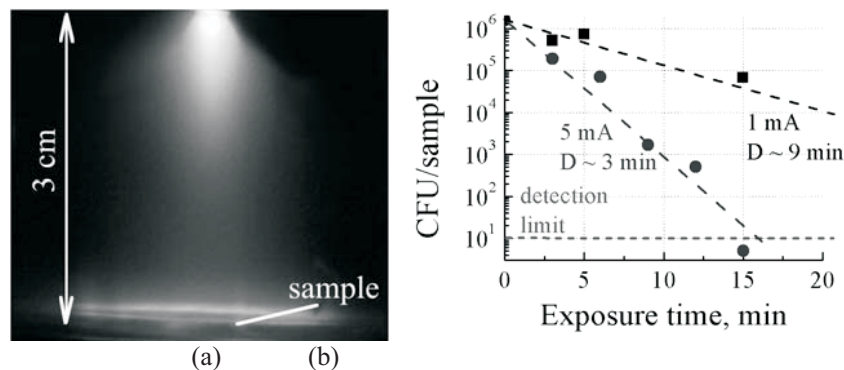


**Figure 1.** Image of sample exposure in 5 mA helium APGD (a) and inactivation curves for vegetative bacterial cells *Staphylococcus aureus* ATCC 6538 at 1 mA and 5 mA (b).

Close to the sample surface an anode region of less than 1 mm thick with significant voltage drop develops. The reduced electric field strength reaches about 20 Td which might correspond to the mean electron energy of 7 eV. Electron density close to the sample was estimated as about  $2 \cdot 10^{10} \text{ cm}^{-3}$ . The gas temperature does not exceed 50 °C and, hence, the thermal effect of the plasma can not have a significant effect on the inactivation of microorganisms. It is shown that in the discharge an ultraviolet radiation also has no considerable effect on bacteria. The spectrum of ultraviolet radiation revealed the presence of chemically active species of NO and OH, resulting from plasma-chemical reactions with the participation of impurities in the plasma-forming gas (the total concentration of  $\text{H}_2$ ,  $\text{N}_2$ ,  $\text{O}_2$ , Ar,  $\text{CO}_2$ , CO, Ne,  $\text{H}_2\text{O}$  in the used helium is up to

0.02%). Apparently, the effect of chemically active species of NO and OH is the main mechanism leading to the death of the bacteria. It is established that the plasma treatment in a low-current APGD the number of viable microorganisms decreases exponentially with time. Figure 1b shows the inactivation curves for vegetative bacterial cells *Staphylococcus aureus* ATCC 6538 at 1 mA and 5 mA. The characteristic D-times of inactivation are in the order of a few minutes for both Gram-positive *Staphylococcus aureus*, and for Gram-negative *Escherichia coli*, despite the significant difference in the structure of the bacterial cell wall. Moreover, with increasing discharge current from 1 mA to 5 mA observed a threefold increase in the rate of inactivation. Significantly less efficiency of non-self-sustained APGD cold helium plasma is for bacterial spores: 20 minutes treatment reduces the number of viable spores of *Bacillus subtilis* slightly more than 1 order of magnitude.

In many cases for applications such as plasma medicine the generation of cold plasma in open space is needed rather than in confined gaps. Thus, there is no limitation on the size of the object to be treated. Their tool-like, small size, and light-weight plasma generation unit allows fast and almost arbitrary three-dimensional movement.

Plasma cathode previously used for three-electrode system was modified to be in plasma jet mode. In order to obtain a normal APGD plasma jet a gas flow through the plasma cathode was increased to  $\sim 5$  slm, the diameter of the hole was decreased to 1.5 mm and a quartz tube with a small inner diameter was fastened to a hole in the anode. The APGD plasma jets were obtained for different plasma-forming gases and their mixtures such as  $N_2$ , air,  $He/O_2$ ,  $Ar/O_2$ , etc. The plasma generated in the APGD gap propagates into surrounding air to distances of about several centimeters from the edge of the tube. An image of the APGD plasma jet at plasma treatment of 90 mm Petri dish with *S. aureus* on the agar surface is presented in Figure 2a.

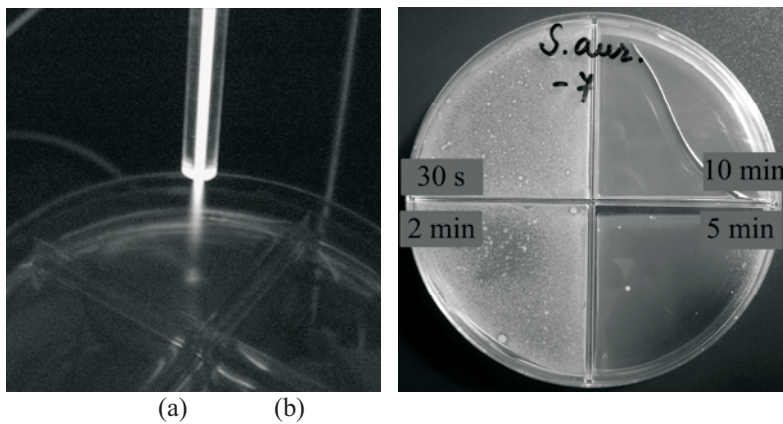


**Figure 2.** Image of Petri dish exposure by APGD plasma jet (a) and the results of air APGD plasma jet treatment of *S. aureus* on agar after incubation at different treatment times (b).

Bactericidal activity of the APGD plasma jet was investigated at different discharge parameters and plasma-forming gases. Therefore, 100  $\mu$ l suspension of an overnight-grown *Staphylococcus aureus* ATCC 6538 with initial concentration of  $10^7$  CFU/ml have been plated onto agar surface containing undifferentiated dense nutrient medium and distributed over the surface with a spatula. After preparation, a central part of each of 4 sectors of a 90 mm Petri Dish has been treated by the APGD plasma jet for different exposure times, respectively. The temperature at the treatment point was monitored using a thermocouple. After plasma treatment, the agar plates have been cultivated for at least 18 h at 37 °C.

The results of air APGD plasma jet treatment (current 100 mA; gas flow 5 slm) of *S. aureus* at different exposure times from 30 s to 10 min are shown in Figure 2b. As it can be seen the number of colonies grew after incubation decreases with exposure time. There is a visible inactivation area at the centre of the sector corresponding to 2 min exposure. At 5 min exposure the only a few bacteria survived at corner of the sector and after 10 min of plasma treatment the complete bacteria inactivation occurs. The inactivation effect of nitrogen APGD plasma jet was observed to be smaller in comparison to air which can be attributed to the smaller concentration of the active species. It should be noted that despite the small diameter of the tube, inactivation is observed in the whole sector.

### Acknowledgements

This work is partly supported by BRFFI under the grant F11SRB-002.

### REFERENCES

- [1] G. Fridman et al., Plasma Process. Polym. 5, 503 (2008).
- [2] M. Laroussi. IEEE Trans. Plasma Sci. 37, 714 (2009).
- [3] M.G. Kong et al., New Journal of Physics 11, 115012 (2009).
- [4] K.-D. Weltmann et al., Pure Appl. Chem. 82, 1223 (2010).
- [5] U. Kogelschatz, J. Phys.: Conf. Ser. 257, 012015 (2010).
- [6] X. Lu, M. Laroussi and V. Puech, Plasma Sources Sci. Technol. 21, 034005 (2012).
- [7] V. I. Arkhipenko et al., IEEE Trans. Plasma Sci. 37, 740 (2009).

## THEORETICAL PREDICTIONS OF THE MICROWAVE BREAKDOWN FIELD

M. Savić, M. Radmilović-Radjenović, B. Radjenović

*Institute of Physics, University of Belgrade, Bregjevica 118, 11080 Belgrade,  
Serbia*

**Abstract.** This paper contains the results of theoretical studies of the breakdown characteristics in argon, xenon and krypton discharges at microwave frequencies. Results of theoretical predictions based on the phenomenological method and the breakdown criteria derived from the diffusion-controlled model are compared and analyzed.

### 1. INTRODUCTION

Microwave discharges show relative simplicity as compared to the DC or low-frequency discharges since electrode phenomena need not play a role in high-frequency discharges [1]-[3]. On the other hand, microwave breakdown in RF equipment is a serious problem in many different applications [4,5]. The basic physics involved in the microwave-induced breakdown process is well known: a rapid growth in time of the free electron density in the device, when the ionization rate caused by microwave accelerated free electrons hitting neutral gas particles or device walls exceeds the rate of electron losses [6]. The concomitantly increasing plasma density eventually changes the transmission properties in the device and significantly interferes with normal operation characteristics. The consequences range from increased noise levels and link budget degradation in RF communication systems to catastrophic damage in high power microwave systems like accelerators and systems for microwave hitting of fusion plasmas. The primary aim of this study is to obtain a better understanding of the physical phenomena involved in microwave breakdown processes and to be able to predict accurately the breakdown voltage.

### 1. BREAKDOWN MECHANISM

As long as the electrons and ions have sufficient time to transit the electrode gap within an ac cycle, the gas breakdown mechanism in low frequency alternating electric fields is essentially the same as for DC fields, i.e. it is controlled by secondary electron emission due to ion impact. At sufficiently high frequencies, however, ions are not capable to respond to the ac field and

electrons are "trapped" in an oscillatory motion within the inter-electrode gap. When this occurs, the electron loss is dominated by diffusion and a significant reduction of the breakdown voltage is observed as compared to the DC case.

### 1.1 Fluid approach

In microwave electric fields, gas breakdown can be regarded as an avalanche-like increase in time of the free electron density caused by collision ionization of the neutral gas molecules by free electrons that are being accelerated to high energies by microwave field. The evolution of the electron density  $n$  is described by the continuity equation [7]:

$$\frac{\partial n}{\partial t} = \nabla \cdot (D_e \nabla n) + \nu n, \quad (1)$$

where  $D_e$  is the electron diffusion coefficient and  $\nu$  is the net production rate of electrons per electron represented as the difference between the electron-impact ionization rate of the gas molecules denoted by  $\nu_i$  and the attachment frequency of the free electrons on neutral molecules per electron denoted by  $\nu_a$ .

According to a fluid approach based on the diffusion-controlled model, the microwave breakdown for a non-attaching gas ( $\nu_a = 0$ ) can be determined as a balance between the ionization rate and the loss rate of electrons by diffusion and described by the relation:

$$\nu_i = D_e / \Lambda^2 \quad (2)$$

with  $\Lambda$  the diffusion length which depends on the geometry of the discharge vessel, i.e. radius  $R$  and height  $L$  and is given by:

$$\frac{1}{\Lambda^2} = \left(\frac{2.4}{R}\right)^2 + \left(\frac{\pi}{L}\right)^2 \quad (3)$$

The equation (2) represents the breakdown criteria for a non-attaching gas and indicates that the breakdown field rises both in the high and low-pressure regimes. Using the relationship  $\nu_i = \alpha \mu E$ , where  $\mu$  is the electron mobility, the criteria (2) can be rewritten in the form:

$$\frac{\varepsilon}{\Lambda^2} = \frac{\alpha E_r}{\sqrt{1 + \left(\frac{\omega}{\nu_c}\right)^2}} \quad (4)$$

where  $\varepsilon = D_e / \mu$  is the characteristic energy and, in this study, is assumed to be independent of the electric field strength. In the presence of an ac electric field  $\sqrt{2}E_r \cos \omega t$  in a weakly ionized gas, a dominant collision processes are electron-neutral collisions. In order to encompass the frequency effect in total, it is convenient to use the effective field strength defined by:

$$E_{eff} = \frac{v_c}{\sqrt{v_c^2 + \omega^2}} E_r \quad (5)$$

In accordance with the equation (5),  $E_{eff}$  becomes  $E_{DC}$  at  $\omega = 0$  and  $v_c E_r / \omega$  at  $\omega \rightarrow \infty$ . Substituting expression for the first Townsend's coefficient  $\alpha = A_k p \exp[-B_k (p/E_{DC})^{1/2}]$  and replacing  $E_{DC}$  by  $E_{eff}$  given by equation (5), we can obtain expression for the electric field  $E_r$  as a function of the pressure  $p$ :

$$E_r = \frac{\epsilon \sqrt{v_c^2 + \omega^2} \exp \left[ B_k \left( p \sqrt{v_c^2 + \omega^2} / v_c E_r \right)^{1/2} \right]}{v_c \Lambda^2 A_k p} \quad (6)$$

### 1.1 Phenomenological approach

According to the Kihara's theory, the equation governing microwave breakdown can be written in the form [8]:

$$\frac{B_0 p}{E} \left[ 1 + \left( \frac{C_1 L / \lambda}{A_1 p L} \right)^2 \right]^{1/2} = 2 \ln(A_1 p L) \quad (7)$$

The previous equation has been derived supposing that a microwave field is imposed on a low pressure gas between two parallel plates which are separated at the distance  $L$ . The breakdown field  $E$  is expressed in terms of the product  $pL$  and  $L/\lambda$  the ratio of the gap length  $L$  to the vacuum wavelength of the applied field  $\lambda$  expressed in cm. Values of molecular constants  $A_1$ ,  $B_0$  and  $C_1$  are given in [8]. Possible secondary emission of electrons from the electrodes has not been taken into account in the Kihara's theory.

## 2. RESULTS

Figure 1 shows the electrical field strength as a function of the gas pressure at the gap spacing of 500  $\mu\text{m}$  in: a) argon, b) xenon and c) krypton microwave discharges at 2.45 GHz.

For all gases, there are similar trends between different theoretical predictions, although disagreement between them increases with increasing the pressure. Results based on the phenomenological approach are systematically higher for all gases.

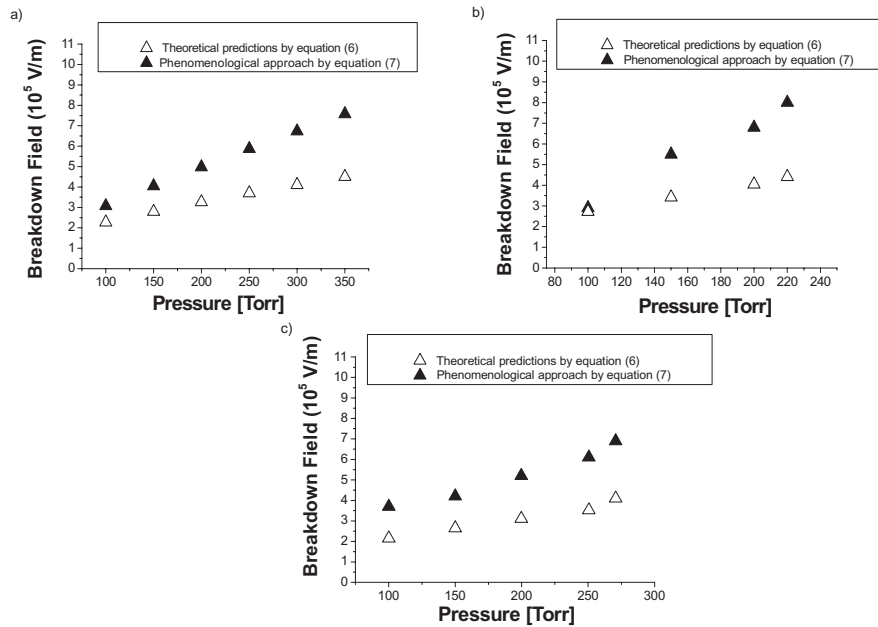


**Figure 1.** Breakdown field as a function of the gas pressure: a) argon, b) xenon and c) krypton, at the gap spacing of 500 $\mu$ m and the microwave frequency of 2.45 GHz.

### Acknowledgements

The present work has been supported by Ministry of Education and Science, Republic of Serbia project O171037project.

### REFERENCES

- [1] M.J. Druyvestayn and F.M. Penning, *Rev. Mod. Phys.* 12 (1940), 87-174.
- [2] D.Q. Posin, The Microwave Spark, *Phys. Rev.* 73 (1948), 496-509.
- [3] S. Krasik, D. Alpert and A.O. McCoubreyn, *Phys. Review* 76 (1949), 722-730.
- [4] F.C. Fehsenfeld, K.M. Evenson and H.P. Broida, *Rev. Sci. Instruments* 36 (1965), 294-298.
- [5] W. L. Hsu, D. M. Tung, E. A. Fuchs, K. F. McCarty, A. Joshi and R. Nimmagadda, 55 (1989), 2739-2741.
- [6] M.A. Harlin and S.C. Brown, *Phys. Review* 74 (1948)291.
- [7] M. Sato, *Bull. Yamagata Univers.* 25 (1999) 119-125.
- [8] T. Kihara, *Rev. Modern Physics* 24 (1952) 45-61.

## MONTE CARLO SIMULATIONS OF RF BREAKDOWN

M. Savić, M. Radmilović-Radjenović, D. Marić, M. Šuvakov, Z.Lj. Petrović

*Institute of Physics, University of Belgrade, Bregjevica 118, 11080 Belgrade,  
Serbia*

**Abstract.** This paper presents first results in development of complete Monte Carlo (MC) collision code for radio-frequency (rf) breakdown. Our goal is to explain fundamentals of rf breakdown. MC code includes electrons only. Obtained simulation results clearly show a region, occurring at low pressure, where multiple values of the breakdown voltage exist at a given pressure. Comparison with available experimental results is also shown.

### 1. INTRODUCTION

Radio-frequency (RF) discharge is of importance for various applications such as biomedicine [1], microelectronics [2] and other plasma-based technologies [3]. It is crucial to establish operating conditions which can be determined from the breakdown voltage curve, known as Paschen curve. A necessary condition for a self sustained discharge and consequently formation of plasma is to have feedback between the electron growth towards instantaneous anode and their initialization at the cathode. Hence, the purpose of this paper is to introduce a model for RF breakdown in electron dominated regime and to try to explain basic phenomenology by employing kinetic representation.

### 1. RESULTS AND DISCUSSION

Monte Carlo (MC) code was developed and tested in our group [4]. The code follows transport of electrons across the gap between electrodes. Background gas argon is represented by four cross-sections for electrons: momentum-transfer, two excitation and ionization cross-section. For each value of gas pressure and voltage, the time dependence of electron density, electron energy distribution, ionization rate and many additional properties were sampled. Depending on whether electron density is increasing or decreasing, the breakdown voltage (pressure) could be found by appropriate changes of pressure (voltage).

The rf breakdown voltage curve has a U-shape shown in Figure 1. Under certain circumstances, there is a region to the left of the minimum where a

single gas pressure corresponds to two breakdown voltages (multi-valued nature of the RF Paschen curve [5]). Figure 1 also shows comparison with published experimental data [5]. Our results are in a reasonably good agreement with experiment.

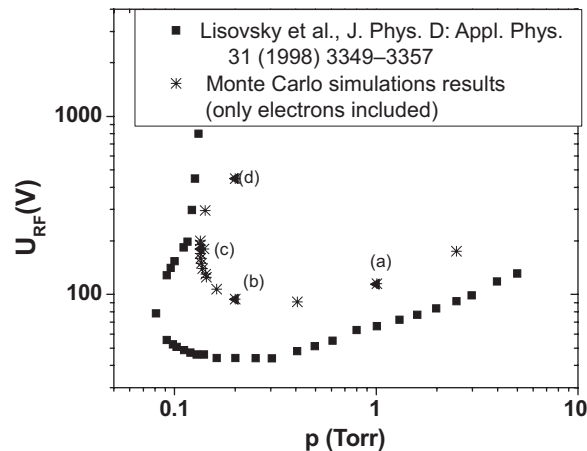


**Figure 1.** Paschen curve obtained by MC collision code including electrons only presented by (\*). Published experimental results [5] presented by (▪) as a comparison to our results. Gap size is  $d=23\text{mm}$  and frequency is  $f=13.56\text{MHz}$ , background gas is argon.

Figure 2 shows the spatial profiles of the swarm properties (electron density, electron energy and ionization rate) along the Paschen curve from the Figure 1. Calculations were carried out for the following conditions: (a)  $p=1\text{Torr}$   $U=114\text{V}$ , (b)  $p=0.2\text{Torr}$   $U=94\text{V}$ ; (c)  $p=0.14\text{Torr}$   $U=180\text{V}$ ; (d)  $p=0.2\text{Torr}$   $U=447\text{V}$ . In RF discharges, electrons can attain oscillatory energy from the AC field. When an electron suffers a collision, its oscillatory motion is disturbed and its momentum is randomized and mean energy increases. At higher pressures (points *a* and *b*) large number of collisions takes place within one wave period, so electrons cannot travel far from the cathode and are unable to gain enough energy to perform ionization. At lower pressure, however (points *c* and *d*), one or fewer collisions occur per cycle, so electrons gain enough energy from the field leading to a higher probability for ionization. As expected, in both cases most of electrons are produced in proximity of electrodes. For the higher breakdown voltage (point *d*) electron production is pushed right into the electrode. Hence losses are increased sufficiently to compensate excessive production by ionization. Any further increase of voltage will make losses greater than production.

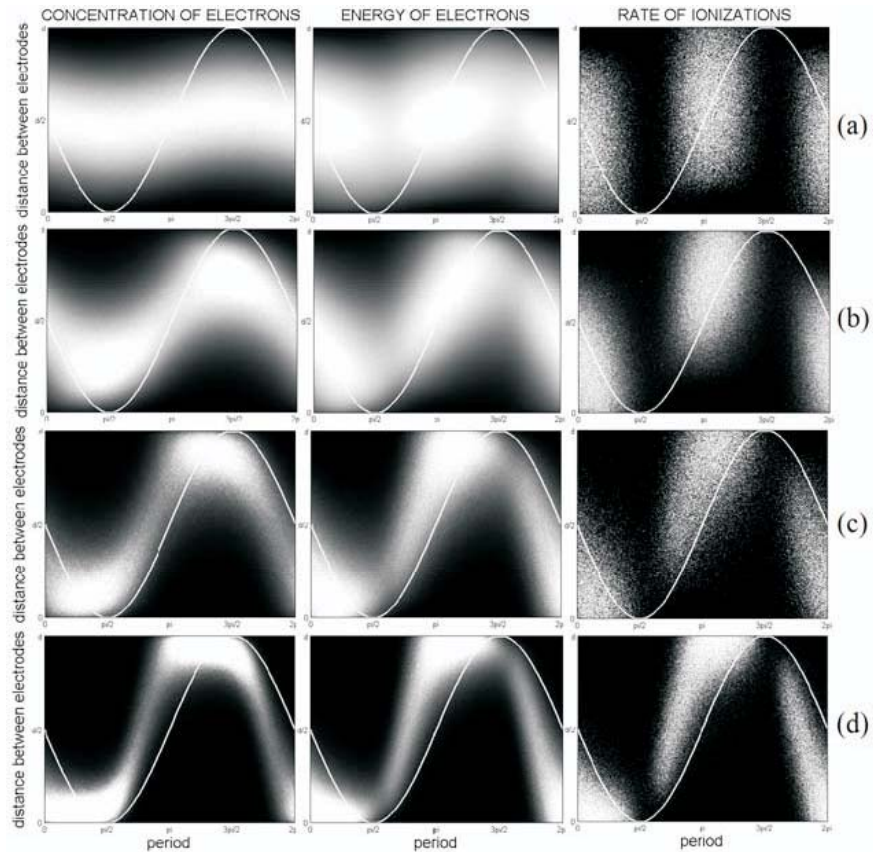


**Figure 2.** Electron density, electron energy and ionization, respectively, for different conditions along the Paschen curve. Calculations were carried out in argon at 13.56MHz and (a)  $p=1\text{Torr}$   $U=114\text{V}$ , (b)  $p=0.2\text{Torr}$   $U=94\text{V}$ ; (c)  $p=0.14\text{Torr}$   $U=180\text{V}$ ; (d)  $p=0.2\text{Torr}$   $U=447\text{V}$ .

Simulation results, presented here, confirm that there is a low-pressure region where a multi-valued dependence of the RF breakdown voltage on the gas pressure exists which is in agreement with previous experimental observations [5]. It was found that the multi-valued nature of the left hand branch of the RF breakdown voltage curve can be explained by the effect of electrons only. The two different regimes of operation, each satisfying the breakdown condition are illustrated in contour plots of electron concentration, electron energy and ionization rate.

### Acknowledgements

The present work has been supported by Ministry of Education and Science, Republic of Serbia project O171037project.

### REFERENCES

- [1] S. Lazović, N. Puač, M. Miletić, D. Pavlica, M. Jovanović, D. Bugarski, S. Mojsilović, D. Maletić, G. Malović, P. Milenković and Z.Lj. Petrović *New Journal of Physics* 12, 083037 2010.
- [2] T. Makabe and Z.Lj. Petrović, *Plasma Electronics: Applications in Microelectronic Device Fabrication*, (Taylor&Francis Group, 2006) ISBN 0-7503-0976-8
- [3] Z. Lj. Petrović, P. Maguire, M. Radmilović-Radjenović, M. Radetić, N. Puač, D. Marić, C. Mahony, G. Malović, “On Application of Plasmas in Nanotechnologies” in *Nanotechnology for Electronics, Photonics, and Renewable Energy*, Springer Series Nanostructure Science and Technology, (Springer, New York, 2010), p.85
- [4] M. Šuvakov, Z. Ristivojević, Z.Lj. Petrović, S. Dujko, Z.M. Raspopović, N.A. Dyatko, A.P. Napartovich, *IEEE Trans. Plasma Sci.* 33, 532- 533 2005.
- [5] A. V. Lisovskiy, V. D. Yegorenkov , *J. Phys. D: Appl. Phys.*, vol. 31, pp. 3349–3357, 1998

## COLLISION-DRIVEN POSITRON CLOUD EXPANSION – EXPERIMENT AND SIMULATION

Srđan Marjanović<sup>1</sup>, Ana Banković<sup>1</sup>, Milovan Šuvakov<sup>1</sup>, Tim Mortensen<sup>2</sup>,  
Adam Deller<sup>2</sup>, C. Aled Isaac<sup>2</sup>, Dirk P. van der Werf<sup>2</sup>, Michael Charlton<sup>2</sup>,  
Zoran Lj. Petrović<sup>1</sup>

<sup>1</sup>*Institute of Physics, University of Belgrade, Pregrevica 118 11080 Zemun,  
Serbia*

<sup>2</sup>*Department of Physics, College of Science, Swansea University, Singleton  
Park, Swansea SA2 8PP, United Kingdom*

**Abstract.** The rotating wall technique is commonly used for compression of particles in positron accumulator devices including those employing buffer gases to effect trapping and cooling. Upon deactivation of the rotating wall the positron cloud expands, in the axial magnetic field, linearly over time ( $t$ ), which is not expected according to the  $\sim\sqrt{t}$  diffusion. This linear behavior is reproduced qualitatively in our simulation of positrons in a cooling gas. In this communication we present preliminary results from both experiment and simulation which indicate that the behavior of trapped clouds can give insight into low energy positron scattering physics.

### 1. INTRODUCTION

The Penning-Malmberg-Surko trap is the most commonly used tool for cooling and accumulating positrons in sufficient numbers for a variety of experimental purposes (see e.g., [1, 2]). In some instances (see e.g., [1, 3]) the positrons are dense and cold enough to form a plasma. However, this is not the case in the present work, which is confined to the so-called single particle, or cloud regime. Recently it has become feasible to compress the accumulated positron cloud by applying the rotating wall technique in the last stage of the accumulator [4, 5] using a rotating dipolar or quadrupolar electric field in the presence of an efficient cooling gas such as SF<sub>6</sub> or CF<sub>4</sub>.

If the rotating field is switched off after compressing, the positron cloud will expand with the rate of expansion dependant on the buffer gas pressure and the strength of axial magnetic field. The time dependence of the cloud width exhibits a clear linear behaviour, as opposed to the expected behavior of  $\sim\sqrt{t}$  for diffusive processes. As the number of trapped particles is relatively small [6], space charge will not significantly influence the expansion. While the

prevalent cause of expansion is the scattering of positrons by the buffer gas, the time dependence indicates that this stage of the development of the ensemble is non-hydrodynamic in nature such that a full kinetic representation is required.

In the attempt to investigate the nature of the expansion we have performed a Monte Carlo simulation [7, 8] of positrons contained by an axial magnetic field in a gas mixture that is typically used for cooling in positron accumulators. A Monte Carlo simulation developed for swarms of charged particles is suitable when space charge effects can be neglected. Due to the lack of cross-section data for SF<sub>6</sub> (the experiment at Swansea was performed using SF<sub>6</sub> as a cooling gas) a CF<sub>4</sub> - N<sub>2</sub> gas mixture which, is often used for positron trapping and cooling [2], was simulated.

## 2. EXPERIMENT

The expansion experiments were performed inside our two-stage trap [6] by accumulating positrons for a ~100ms and then compressing the cloud using a rotating dipole field. N<sub>2</sub> gas at high pressure ( $6 \times 10^{-4}$  mbar) is used in the first stage for promoting trapping. SF<sub>6</sub> was used in the accumulation region at varying pressures to promote cooling. After compressing for ~20ms the rotating dipole was switched off and the cloud was dumped and imaged using a micro-channel plate and phosphor system viewed using a CCD camera. From the imaged cloud the width,  $\sigma$ , of the positron swarm was determined. Note that this parameter is characteristic of a Gaussian profile [8]

## 3. SIMULATION

The positrons were initialized with near a thermal energy of ~100 meV in a Maxwell-Boltzmann distribution and a Gaussian spatial distribution. As the initial ensemble is near thermal equilibrium an exact representation of thermal effects [7] was included.

Due to the fact that there are no comprehensive cross-sections available for positron interaction with SF<sub>6</sub> we used a mixture of equal parts of CF<sub>4</sub> and N<sub>2</sub> with cross-sections that were used in our previous simulations of positron traps [8]. Although CF<sub>4</sub> is commonly used as a cooling gas [2], its total cross-section at thermal energies is significantly smaller than that of SF<sub>6</sub> [9]. Therefore it should be expected that the simulated expansion rates would be smaller than those measured. Furthermore, the ratio of cooling to buffer gases is different from that employed in the experiment.

The total pressures that were used are within the scope of the experiment ( $4-14 \times 10^{-5}$  mbar) and the starting width of the cloud is several millimeters. The particle motion is guided by the axial magnetic field which can have values in range 100 – 400 Gauss. Typically the simulation was run with 100 000 initial particles without external electric field.

#### 4. RESULTS

Results of the simulation for  $14 \times 10^{-5}$  mbar and the experiment with the notional corresponding pressure are given in figure 1. As expected, the expansion in the simulation is slower than that measured, but both are linear in time. As such both can be fitted well with a straight line and the slopes of these fits represent the expansion rate and are given in figure 1, though strictly the experiment and the simulation cannot be compared directly.

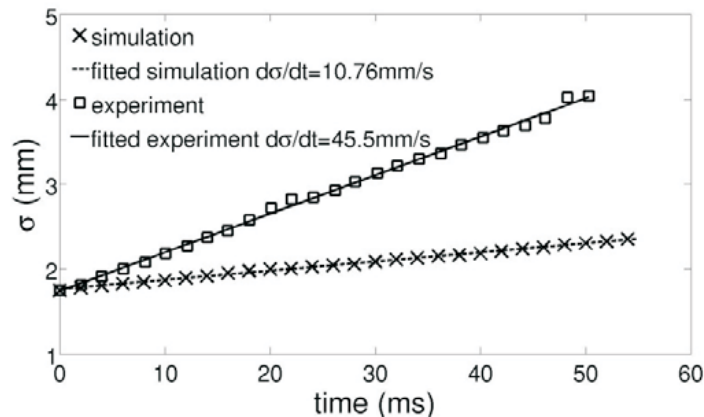


**Figure 1.** Simulation for  $14 \times 10^{-5}$  mbar total pressure in 200 Gauss axial magnetic field and the expansion experiment. The full and slashed lines are linear fits to the experiment and simulation respectively.

#### 4. CONCLUSION

The results of the simulations show good qualitative agreement with our preliminary experimental results but in order to obtain accurate predictions of the expansion rates, detailed cross-sections for appropriate gases are required. Also, it is necessary to know the precise pressures and composition of the gas. The simulated results for individual pressure points show linear expansion, which is slower than those measured, presumably due to smaller cross-sections for  $\text{CF}_4$ .

The present preliminary investigations show that it should be possible to model the behaviour of positron clouds in accumulation devices which rely upon the use of gases for capture and cooling. Furthermore, it may be possible to derive information on positron scattering processes by comparing experiment with detailed simulations. It should be possible to use the accumulator to trap electrons and perform similar expansion-mode measurements. Since accurate cross-section data sets exist for the relevant molecules, it should be possible to fully calibrate the apparatus to allow absolute comparison with the simulations.

## Acknowledgements

This work is supported by MNPRS Projects ON171037 and III41011, and by the EPSRC (UK). T. M. and A. D. are grateful for the provision of EPSRC studentships.

## REFERENCES

- [1] C. M. Surko and R. G. Greaves, *Phys. Plasmas* 11, 2333 (2004)
- [2] J. P. Sullivan, A. Jones, P. Caradonna, C. Makochekanwa, and S. J. Buckman, *Rev. Sci. Instrum.* 79, 113105 (2008)
- [3] L. V. Jørgensen et al. (ATHENA Collaboration), *Phys. Rev. Lett.* 95, 025002 (2005)
- [4] R. G. Greaves and J. M. Moxom, *Phys Plasmas* 15, 072304 (2008)
- [5] C.A.Isaac,C.J.Baker,T.Mortensen,D.P.vanderWerf,andM. Charlton, *Phys. Rev. Lett.* 107, 033201 (2011)
- [6] J. Clarke, D. P. van der Werf, B. Griffiths, D. C. S. Beddows, M. Charlton, H. H. Telle, and P. R. Watkeys, *Rev. Sci. Instrum* 77, 063302 (2006)
- [7] Z. Ristivojevic and Z. Lj. Petrovic, *Plasma Sources Sci. Technol.* 21, 035001 (2012)
- [8] S. Marjanovic, M. Suvakov, A. Bankovic, M. Savic, G. Malovic, S. J. Buckman, Z. L. Petrovic, *IEEE T. Plasma Sci.* 39, 2614 (2011)
- [9] R. G. Greaves and C. M. Surko, *Phys. Rev. Lett.* 85, 1883 (2000)

## MONTE CARLO SIMULATION OF POSITRON TRAPPING EFFICIENCY

Srđan Marjanović, Milovan Šuvakov and Zoran Lj. Petrović

*Institute of physics, University of Belgrade, Pregrevica 118, 11080 Zemun, Serbia*

**Abstract.** Positron trapping efficiency could be improved in two ways: shortening the thermalization time for trapped particles and increasing the percentage of particles trapped. Using a well tested and Monte Carlo code, we examine both approaches and give an overview of the processes involved. We examine temporal and spatial distribution of energy and show a gradual transition of a beam into a thermal swarm of positrons. The simulated trap model is a classic three stage potential well design using  $N_2$  as a buffer gas in the first two stages and a  $N_2/CF_4$  mixture in the third. It was found that including cross sections for rotational  $e^+-N_2$  excitation is essential to achieve final stages of thermalization. Different trapping experiments use different sources and moderators, and depending on the properties of the moderated beam the trap can be optimized by changing its parameters (geometry, electrode potentials, gas composition, magnetic field, etc.).

### 1. INTRODUCTION

Gas filled Penning Malberg positron trap (or Surko trap) is the main tool for studying positron interaction with matter [1] and has seen a lot of improvement in the recent years [2, 3]. A typical trap consists of three stages of different lengths, different gas pressures and composition, electrode diameters and applied voltages. Each subsequent stage has lower potential, thus forming a potential well in which particles are confined as they lose energy in collisions with the background gas. For radial confinement, there is an axial magnetic field. The most commonly used trapping gas is  $N_2$  due to its high and conveniently placed cross sections for electronic excitation of a1Π level. This collision is used as the basic trapping mechanism as positrons lose  $\sim 8.8eV$  of energy and cannot leave the trap. On the other hand the trapping window is narrow as the positronium formation cross section becomes stronger after  $\sim 10eV$  and over that energy the probability that the particle is lost becomes much higher. There are additional losses that come from radial transport and losses to the walls or particles that do not lose enough energy through collisions and escape over the

gate electrode. A negligible amount of particles is also lost to direct annihilation over times required for thermalization.

## 2. MODEL AND SIMULATION

The code we are using has been developed and used previously for exact treatment of charged particle transport [4] and heavy particle collisions [5]. Also in order to calculate thermalization times correctly we had to include thermal effects in the simulation [6]. Cross-section sets have been compiled for  $N_2$ [6,7] and  $CF_4$ [8-12].

The trap is divided into three segments, with different geometries and different pressures of  $N_2$  and  $CF_4$ . The particles are moving independent of each other in the axial magnetic field. When the particle reaches the end of the segment it is either reflected, if its axial energy is lower than the potential barrier that the electrodes form, or it is transferred to the next stage and is either accelerated or decelerated by the appropriate potential difference.

We usually run a simulation with 100 000 – 1 000 000 particles, and it runs from a couple of hours to a couple of days. A general scheme for the simulation setup is given in Figure 1.

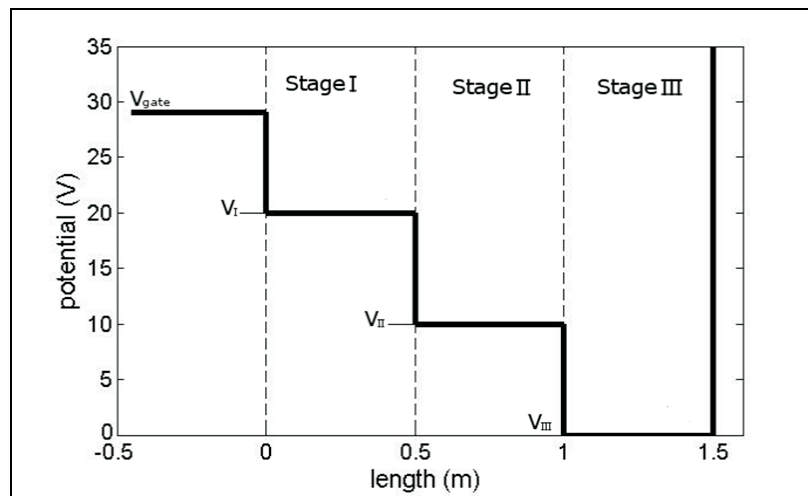


**Figure 1.** A general model of a three stage buffer gas positron trap.

## 3. RESULTS

Results of the simulation are given in figures 2 and 3. Figure 2 shows mean kinetic energy of particles in each segment and mean energy total over time. It turns out that, rotational levels of  $N_2$  are essential in achieving the last stages of thermalization, and that increasing the percentage of  $CF_4$  in the second and third stage shortens the time required for thermalization. Noise features

appearing for mean energy in the first and second stage are due to low statistic as the last particles are leaving the stage.

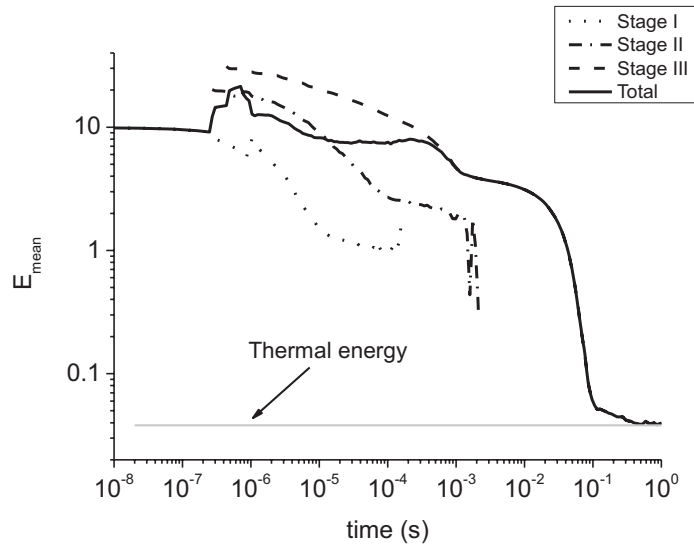


**Figure 2.** Mean kinetic energy for separate stages and total.

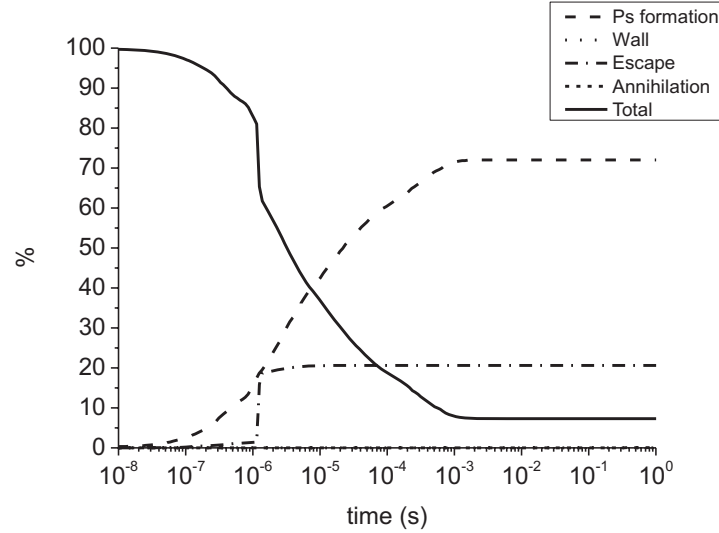


**Figure 3.** Trapping efficiency and contribution of loss processes.

Figure 3 shows the trapping efficiency and the contribution of individual processes to the total particle loss. It can be seen that on the relevant timescales direct annihilation is negligible and the main loss process is actually positronium formation.

#### 4. CONCLUSION

A Monte Carlo simulation gives us insight into processes occurring inside a positron trap. Using this knowledge we can improve the operating parameters of the trap. For instance we can increase the pressure in the first stage to reduce the number of escaping particles. Also, because annihilation is negligible on this timescale increasing the pressure in the last stage or adding more  $\text{CF}_4$  will reduce thermalization time without impacting trapping efficiency. Trapping efficiency is strongly limited by the positronium formation as its threshold is close to that of a  $^1\Pi$  electronic excitation of  $\text{N}_2$ .

The positrons that start out as a beam with narrow and well defined energy distribution, after crossing the stages and having high energy loss collisions, quickly split into several beams that combine together as they cool down and turn into a swarm of particles. For this reason Monte Carlo codes are more suitable for dealing with this problem than beam based simulations.

#### Acknowledgements

This work is supported by MNPRS Projects ON171037 and III41011.

#### REFERENCES

- [1] C. M. Surko, M. Leventhal and A. Passner, Phys. Rev. Letters 62, 901 (1989)
- [2] C. M. Surko and R. G. Greaves, Phys. Plasmas 11, 2333 (2004)
- [3] J. P. Sullivan, A. Jones, P. Caradonna, C. Makochekanwa, and S. J. Buckman, Rev. Sci. Instrum. 79, 113105 (2008)
- [4] A. Banković, Z. Lj. Petrović, R. E. Robson, J. P. Marler, S. Dujko and G. Malović, Nucl. Instrum. Methods Phys. Res. B 267, 350 (2008)
- [5] Z. Ristivojevic and Z. Lj. Petrovic, Plasma Sources Sci. Technol. 21, 035001 (2012)
- [6] A. Banković, J. P. Marler, M. Šuvakov, G. Malović and Z. Lj. Petrović, Nucl. Instrum. Methods Phys. Res. B 266, 462 (2008)
- [7] E. Guerjoy and S. Stein, Phys. Rev. 97, 1671 (1955)
- [8] M. Kurihara, Z. Lj. Petrović and T. Makabe, J. Phys. D: Appl. Phys 33, 2146 (2000)
- [9] J. P. Marler and C. M. Surko, Phys. Rev. A 72, 062702 (2005)
- [10] L. D. Barnes, S. J. Gilbert and C. M. Surko, Phys. Rev. A 67, 032706 (2003)
- [11] J. P. Marler, J. P. Sullivan and C. M. Surko, Phys. Rev. A 71, 022701 (2005)
- [12] T. Nishimura and F. A. Gianturco, J. Phys. B: At. Mol. Opt. Phys. 37, 215 (2004)

## TRANSPORT OF F<sup>-</sup> IONS IN F<sub>2</sub>

V. Stojanović<sup>1</sup>, Z. Raspopović<sup>1</sup>, J. Jovanović<sup>2</sup>, Ž. Nikitović<sup>1</sup>, Z. Lj. Petrović<sup>1</sup>

<sup>1</sup>

<sup>1</sup> *Institute of Physics, University of Belgrade, Pregrevica 118, 11080 Belgrade, Serbia*

<sup>2</sup> *Faculty of Mechanical Engineering, University of Belgrade, Kraljice Marije 16, 11000 Belgrade, Serbia*

**Abstract.** Transport properties of F<sup>-</sup> ions in F<sub>2</sub> in DC fields were calculated using Monte Carlo simulation technique assuming the scattering cross section set assembled on the basis of Nanbu's technique separating elastic from reactive collisions. In this work we present reaction rate coefficients and drift velocity for the conditions of low and moderate reduced electric fields  $E/N$  ( $N$ -gas density) accounting for the non-conservative collisions.

### 1. INTRODUCTION

F<sub>2</sub> gas and more usually fluorine molecule formed in the process are frequently present in numerous processing plasmas. For example, pulsed plasma doping system is technology of choice for low-energy ion implantation. In such a system uniform plasma is necessary to create over the entire wafer that could be more than 500 mm wide. Complicated chemistry and poor understanding for range of processes of particles interacting with gas and surface forced to further insights of such plasmas. Time resolved measurements of ion energy distributions in cathode boundary [1] showed possible role of charge-transfer collisions between singly charged ions of various masses. In this work our intention is to study energy dependent scattering probabilities of F<sup>-</sup> ions in F<sub>2</sub> gas and to explore effects of non-conservative processes on transport properties of the F<sup>-</sup> ions.

### 2. TECHNIQUE

The cross sections for scattering of F<sup>-</sup> on F<sub>2</sub> molecule are calculated by using Nanbu's theory [2,3] separating elastic from reactive endothermic collisions. In

Nanbu's theory reactive collision is treated by accounting for thermodynamic threshold energy and branching ratio according to the Rice-Rampersperger-Kassel (RRK) theory [2]. In the RRK theory of unimolecular reaction rates excited molecular complex is treated as excited activated complex where internal energy is distributed among equivalent oscillators-vibrational modes of the complex.

Our procedure is an implementation of this theory and approximation. We have used value  $1.2611 \cdot 10^{-30} \text{ m}^3$ , for polarizability of  $\text{F}_2$  recommended by Spelsberg and Meyer [4], ionization potentials for  $\text{F}_2$  and  $\text{F}$  from [5], and the bond values between atoms in Ref. [6]. The usually applied procedure would be to unfold the cross sections from the measured transport coefficients and thermo-chemical data in a separate drift tube experiment but to our knowledge no such data are available.

The Monte Carlo technique was applied to perform calculations of transport parameters as well as rate coefficients in DC electric fields. In this paper we have used a Monte Carlo code that properly takes into account the thermal collisions [7,8]. The code has passed all the tests and the benchmarks that were covered in our earlier studies [8,9]. Bulk and flux values of the drift velocity [10] are presented for a range of reduced electric fields  $E/N$  ( $E$ -electric field,  $N$ -gas density) including the range where effects of the charge transfer collisions take place.

### 3. DISCUSSION AND RESULTS

Most probable reaction paths, based on thermochemical data [4-6] are shown in Table 1. We found them relevant for the selected domain of low  $\text{F}^-$  energies in  $\text{F}_2$ .

**Table 1.**  $\text{F}^- - \text{F}_2$  endothermic reaction paths considered in the model and the corresponding thermodynamic threshold energies [4-6].

<i>No</i>	<i>reaction</i>	$\Delta$ (eV)
1	$\text{F}_2^- + \text{F}$ (CT)	-0.38
2	$\text{F} + 2\text{F}$ (DIS)	-1.602
3	$\text{F} + \text{F}_2 + \text{e}^-$ (DET)	-3.4012
4	$\text{F} + 2\text{F} + \text{e}^-$ (DD)	-5.0032

In Fig. 1 we show calculated cross sections for  $\text{F}^-$  scattering on  $\text{F}_2$ . Cross section for charge transfer (CT) producing  $\text{F}_2^-$  ion measured by Chupka *et al.* [11] is shown in the same figure.

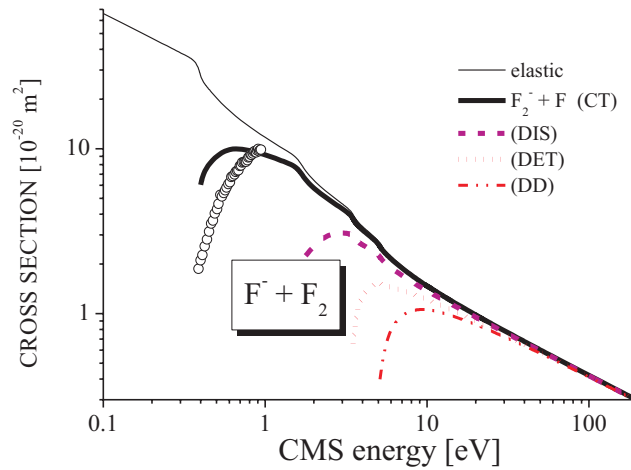


**Figure 1.** Cross section set for  $F^-$  ions in  $F_2$ . Open circles denote the data of Chupka *et al.* [11] placed on absolute scale by assuming maximum value as obtained by Nanbu's theory.

Transport parameters were calculated for gas temperature  $T=300$  K. Calculated rate coefficients for processes presented in Table 1 are shown in Fig 2 a). Flux and bulk drift velocities [10] as a function of  $E/N$  are given in Fig. 2 b). Effect of reactive collisions affecting splitting of flux and bulk drift velocity components is observable above 40 Td.

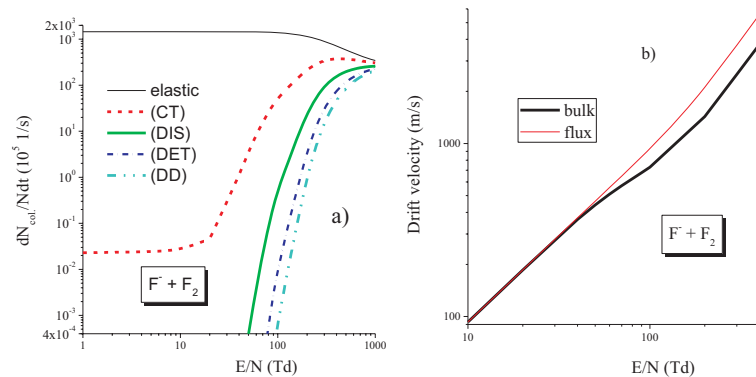


**Figure 2.** a) Rate coefficients, and b) bulk and flux values of drift velocity, for  $F^-$  ions in  $F_2$  as a function of  $E/N$ .

### Acknowledgements

This work is partly supported by our Ministry under the grant NO 171037 and 410011.

### REFERENCES

- [1] S. Radovanov, L. Godet, R. Dorai, Z. Fang, B.W. Koo, C. Carinaud, G. Cartry, D. Lenoble, and A. Grouillet, *J. Appl. Phys.* **98** (2005) 113307.
- [2] K. Denpoh and K. Nanbu, *J. Vac. Sci. Technol. A* **16** (1998) 1201.
- [3] Z.Lj. Petrović, Z.M. Raspopović, V.D. Stojanović, J.V. Jovanović, G. Malović, T. Makabe, J. De Urquijo, *Appl. Surf. Sci.* **253** (2007) 6619.
- [4] D. Spelsberg and W. Meyer, *J.Chem.Phys.* **101**(2) (1994) pp.1282-1288
- [5] E.W. Mc Daniel, *Atomic Collisions -Electron and Photon Projectiles*, John Willey & Sons, New York, 1989.
- [6] J.A. Stockdale, D.R. Nelson, F.J. Davis and R.N. Compton, *J. Chem. Phys.* **56** (1972) 3336.
- [7] Z. Ristivojević and Z.Lj. Petrović, arXiv:0806.0401v1 [physics.plasm-ph], 2 June, 211 2008. Available from: <<http://arxiv.org/abs/0806.0401v1>>.
- [8] Z.Lj. Petrović, J.V. Jovanović, V. Stojanović, Z.M. Raspopović, Z. Ristivojević, *Eur. Phys. J. D* **48** (2008) 87.
- [9] Z.Lj. Petrović, V.D. Stojanović, *J. Vac. Sci. Technol. A* **16** (1998) 329.
- [10] K. Kumar, H.R. Skullerud, R.E. Robson, *Aust. J. Phys.* **33** (1980) 343; R.E. Robson, *Aust. J. Phys.* **44** (1991) 685; K. Ness, R.E. Robson, *Phys. Rev. A* **34** (1986) 2185; R.E. Robson, R.D. White, Z.Lj. Petrović, *Rev. Mod. Phys.* **77** (2005) 1303.
- [11] W.A. Chupka, J. Berkowitz and D. Gutman, *JCP*, **55**(6) (1971) 2724-2733.

## HIGH ORDER FLUID MODEL FOR STREAMER DISCHARGES

S. Dujko<sup>1,2</sup>, A. Markosyan<sup>2</sup>, R. D. White<sup>3</sup>, U. Ebert<sup>2,4</sup>

<sup>1</sup>*Institute of Physics, University of Belgrade, P.O. Box 68, 11080, Serbia*

<sup>2</sup>*Centrum Wiskunde & Informatica (CWI), P.O. Box 94079, 1090 GB Amsterdam, The Netherlands*

<sup>3</sup>*ARC Centre for Antimatter-Matter Studies, James Cook University, Townsville 4810, Australia*

<sup>4</sup>*Department of Applied Physics, Eindhoven University of Technology,  
P.O. Box 513, 5600 MB Eindhoven, The Netherlands*

**Abstract.** A high order fluid model for streamer discharges is developed and used to investigate propagation of negative streamer fronts in N<sub>2</sub>. Momentum transfer theory is employed to evaluate the collision terms and close the system of moment/balance equations. The results of simulations are compared with those obtained by a PIC/MC method and by the classical first order fluid model based on the drift-diffusion and local field approximations. The comparison clearly validates the theoretical basis of the high order fluid model, while the first order fluid model underestimates many aspects of streamer dynamics.

### 1. INTRODUCTION

When a strong electric field is applied to non-ionized or lowly ionized matter, filaments of weakly ionized non-equilibrium plasma, called streamers can grow. They can be observed in different kinds of high-pressure discharges, for example in corona discharges, but they also appear in the form of plasma bullets observed in plasma jets [1]. Streamers have applications in diverse areas of science and technology ranging from their role in creating lightning and transient luminous events in the upper atmosphere [2] to industrial applications such as the treatment of polluted gases and water [3].

During the last three decades, the prevalent opinion has been that streamer dynamics could be described adequately by the so-called first order fluid model based on the drift-diffusion and local field approximations for all species in the plasma-including the electrons. However, recent modeling [5] suggests that we should revise this opinion. In typical situations (e.g., in the pure gases and little explicit effects of photo-ionization) the local field approximation is generally insufficient to represent the electron dynamics as the electron energy depends upon the electric field in a wider spatial range. One way to deal with this issue has been recently demonstrated by Li *et al.* [6] through the development of the so-called extended fluid

models. These models involve a density gradient expansion of the source term to approximate the spatial non-locality of the ionization processes at the streamer front. The alternative way to incorporate the complex electron dynamics in the streamer front is to consider the energy balance equation. In this work we illustrate that this is not a straightforward process and we show how to derive a consistent set of fluid equations beyond the equation of continuity and the momentum balance equation.

## 2. THEORY

The starting point of our formalism is a set of moment/balance equations which is found by multiplying the Boltzmann equation by an arbitrary function  $\Phi(\mathbf{c})$  of the charged particle velocity, and integrating over all velocities

$$\frac{\partial}{\partial t} [n\Phi(\mathbf{c})] + \nabla \cdot [n\langle \mathbf{c}\Phi(\mathbf{c}) \rangle] - n\frac{q}{m} \langle \mathbf{E} \cdot \frac{\partial}{\partial \mathbf{c}} \Phi(\mathbf{c}) \rangle = - \int \Phi(\mathbf{c}J(f))d\mathbf{c}, \quad (1)$$

where  $\langle \rangle$  represents the average over particle velocity  $\mathbf{c}$ ,  $q$  and  $m$  are the charge and mass of the charge particle,  $\mathbf{E}$  is the electric field vector and  $J$  is the collision operator accounting for elastic and inelastic collisions. If one takes  $\Phi(\mathbf{c})$  equal to 1,  $m\mathbf{c}$ ,  $\frac{1}{2}m\mathbf{c}^2$  and  $\frac{1}{2}m\mathbf{c}^2\mathbf{c}$ , etc., one generates an infinite series of equation, a full solution of which would be equivalent to calculating the phase space distribution function  $f(\mathbf{r}, \mathbf{c}, t)$ . In practice, however, one must truncate the chain, and in this work we propose that the energy flux equation is crucial for the success of the fluid model of streamer discharge:

$$\frac{\partial n}{\partial t} + \nabla \cdot n\mathbf{v} = C_0, \quad (2)$$

$$\frac{\partial}{\partial t} [nm\mathbf{v}] + \nabla \cdot [nm\langle \mathbf{c}\mathbf{v} \rangle] = C_{m\mathbf{c}}, \quad (3)$$

$$\frac{\partial}{\partial t} (n\varepsilon) + \nabla \cdot (n\xi) - n\mathbf{m}\mathbf{a} \cdot \mathbf{v} = C_{\frac{1}{2}m\mathbf{c}^2}, \quad (4)$$

$$\frac{\partial}{\partial t} (n\xi) + \nabla \cdot [n\langle \frac{1}{2}nm\mathbf{c}^2\mathbf{c}\mathbf{v} \rangle] - n\mathbf{m}\mathbf{a} \langle \frac{\partial}{\partial \mathbf{c}} (\frac{1}{2}m\mathbf{c}^2\mathbf{c}) \rangle = C_{\frac{1}{2}m\mathbf{c}^2\mathbf{c}}, \quad (5)$$

where  $\mathbf{v} = \langle \mathbf{c} \rangle$ ,  $\mathbf{a}$  is the acceleration due to the electric field force,  $\varepsilon$  is the mean energy and  $\xi$  is the energy flux.

The fluid equations (2)-(5), obtained as velocity moments of the Boltzmann equation are closed in the local mean energy approximation and coupled to the Poisson equation for the space charge electric field. The high order tensors appearing in the energy flux equation are specified in terms of lower order moments. The collision terms are evaluated using the momentum transfer theory, and are given by:

$$C_0 = -n(\nu_A - \nu_I), \quad (6)$$

$$C_m \mathbf{c} = \frac{mm_0}{m+m_0} n \nu_m \mathbf{v} - nm \mathbf{v} [\nu_A - \zeta \nu'_A], \quad (7)$$

$$C_{\frac{1}{2}mc^2} = -n \nu_e \left( \varepsilon - \frac{3}{2} kT \right) - \frac{m_0}{m+m_0} \sum_i (\nu_i - \nu_i^s) \epsilon_i - n \varepsilon \nu_A - n \nu_i^{(i)} \Delta \varepsilon_i, \quad (8)$$

$$C_{\frac{1}{2}mc^2} \mathbf{c} = -n \nu_m \boldsymbol{\xi}, \quad (9)$$

where  $\nu_m$  and  $\nu_e$  are the average collision frequencies for momentum and energy transfer,  $\nu_A$  and  $\nu_I$  are the attachment and ionization rates, while  $\zeta$  is given by

$$\zeta = \frac{2}{3} \frac{m_0}{m_0 + m} \left[ \frac{1}{2} m \langle c^2 \rangle - \frac{1}{2} m \mathbf{v}^2 \right]. \quad (10)$$

Likewise,  $\nu_i$  and  $\nu_i^s$  are inelastic and superelastic collision frequencies for inelastic channel  $i$  while  $\epsilon_i$  and  $\Delta \varepsilon_i$  are the thresholds for inelastic and ionization processes, respectively.

### 3. RESULTS AND DISCUSSION

The finite volume method is used to spatially discretize the system (2)-(5) on a uniform grid with 1000 points. To approximate the spatial derivative we use the second-order central difference discretization while the time derivatives are approximated with the Runge-Kutta 4 method. The continuity equation for the electron and ion densities has a second order spatial derivative, and therefore requires two boundary conditions for each direction in space. For  $x = 0$  we use Neumann boundary condition, so that electrons that arrive at those boundaries may flow out of the system. For  $x = L$  we employ Dirichlet boundary condition to ensure that there is no outflow of electrons from the system. In all calculations we set  $L = 1.2$  mm.

The average collision frequencies for momentum and energy transfer in elastic and inelastic collisions required as an input in the fluid equations are calculated using a multi term Boltzmann equation solution [7]. The cross sections for the electron scattering in  $N_2$  detailed by Stojanović and Petrović [8] are used in this work. The results of simulations are compared with those obtained by a PIC/MC method [5, 6] and by the classical first order fluid model based on the drift-diffusion and local field approximations.

In figure 1 we show the electron density and mean energy for electrons after 1 ns. Our results and those obtained by a PIC/MC method agree very well. High-order fluid profiles are slightly faster than those obtained by the PIC/MC method but the agreement is much better than between the PIC/MC results and those obtained by the first order fluid model based on the drift-diffusion approximation, particularly for the ionization level behind the front.

Perhaps one of the most striking properties is the behavior of the mean energy in the streamer channel. Although the electric field is entirely screened inside of the channel, the mean energy significantly exceeds thermal energy. This is a typical non-local effect as the mean energy does not have enough time to be fully thermalized in the streamer interior on the time

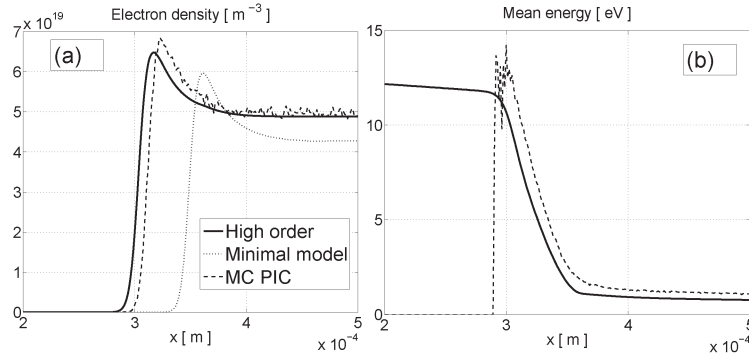


**Figure 1.** Electron density (a) and mean energy (b) after 1 ns. The simulation is started with the same initial Gaussian distribution for electrons and ions with a maximum density of  $2 \times 10^{18} \text{ m}^{-3}$  at the position  $x = 8 \times 10^{-4}$  m from the left boundary.

scale relevant for streamer formation under conditions considered in this work. The lower ionization density behind the front in the classical fluid model is also the effect of too low electron energies, this time in the streamer head.

**Acknowledgements** The authors thank to J. Teunissen for helpful discussions about the PIC/MC simulations of streamer discharges.

## REFERENCES

- [1] G. Naidis, *J. Phys. D: Appl. Phys.* 45, 135202 (2012).
- [2] U. Ebert, S. Nijdam, C. Li, A. Luque, T.M.P. Briels and E.M. van Veldhuizen, *J. Geophys. Res.* 115, A00E43 (2010).
- [3] E.M. van Veldhuizen, *Electrical Discharges for Environmental Purposes: Fundamentals and Applications*, (Huntington, NY: Nova Science) (2000).
- [5] C. Li, U. Ebert and W. Hundsdorfer, *J. Comp. Phys.* 229, 200 (2010)
- [6] C. Li, W.J.M. Brok, U. Ebert and J.J.A.M. van der Mullen, *J. Appl. Phys.* 101, 123305 (2007).
- [7] S. Dujko, R.D. White, Z.Lj. Petrovic and R.E. Robson, *Phys. Rev. E* 81, 046403 (2010).
- [8] V.D. Stojanovic and Z.Lj. Petrovic, *J. Phys. D: Appl. Phys.* 31, 834 (1998).

## PROGRESS OF STARK-B DATABASE AND SERBIAN VIRTUAL OBSERVATORY

Milan S. Dimitrijević<sup>1,2</sup>, Sylvie Sahal-Bréchet<sup>2</sup>, Darko Jevremović<sup>1</sup>  
Veljko Vujčić<sup>1</sup> and Andjelka Kovačević<sup>3</sup>

<sup>1</sup>*Addresses: Astronomical Observatory, Volgina 7, 11060 Belgrade, Serbia*

<sup>2</sup>*Observatoire de Paris, 92195 Meudon, France*

<sup>3</sup>*Department of Astronomy, Faculty of Mathematics, Studentski Trg 15, 11000  
Belgrade, Serbia*

**Abstract.** Progress of the work on development of STARK-B database for Stark broadening parameters of isolated non-hydrogenic lines and of Serbian Virtual Observatory – SerVO is presented. STARK-B database enters in the Virtual Atomic and Molecular Data Center – VAMDC.

### 1. INTRODUCTION

According to the idea formulated at the end of 2000, Virtual observatories are created to retrieve and analyze astronomical data obtained in various observatories and cosmic missions. At Belgrade Astronomical Observatory the work on Serbian Virtual Observatory [1-4] (<http://www.servo.aob.rs/~darko>) started at 2008, after long lasting interest for organization of our scientific results in databases.

As a first trace in documents we can cite de letter of one of the authors (MSD) to Mr Del Bigio in UNESCO in Paris, of 4. 11. 1992, asking to obtain CDS/ISIS software for creation of a database and the corresponding Agreement signed the same day in UNESCO Headquarters in Paris by MSD and Giampaolo Del Bigio, Programme Manager, Division of the General Information Programme of UNESCO. After, at the end of nineties, we created database BELDATA [5-10] containing Stark broadening parameters, which, after the changement of management at Observatory in 2002, was transferred in Paris, where was further developed and named STARK-B [11]. This database enters also in Virtual Atomic and Molecular Data Center (VAMDC – [12-15]), an FP7 founded project. Project leader is Marie-Lise Dubernet from Observatoire de Paris and core consortium is made of 15 institutions with 24 scientific groups from France, Serbia, Russia, England, Austria, Italia, Germany, Sweden and Venezuela.

The participants of AOB (Astronomical Observatory – Belgrade) VAMDC Node are: Milan S. Dimitrijević, Luka Č. Popović, Andjelka

Kovačević, Darko Jevremović, Zoran Simić, Edi Bon and Nenad Milovanović. Recently, in this activity is also included Veljko Vujičić.

In this contribution we discuss the project of Serbian Virtual Observatory (SerVO), and STARK-B database, their actual state and recent developments.

## 2. STARK-B DATABASE

The database STARK-B is available on line at the web address <http://stark-b.obspm.fr/> and is further developing by Laboratoire d'Etude du Rayonnement et de la Matière en Astrophysique of the Observatoire de Paris-Meudon (Sylvie Sahal-Bréchet and Nicolas Moreau) and the Astronomical Observatory of Belgrade (Milan S. Dimitrijević). This database contains Stark line broadening parameters (widths and shifts) for isolated lines, obtained within the impact approximation using the semiclassical perturbation approach. STARK-B is currently developed in Paris, and a mirror site is under construction in Belgrade. STARK-B is one of databases of the european FP7 project: Virtual Atomic and Molecular Data Center – VAMDC.

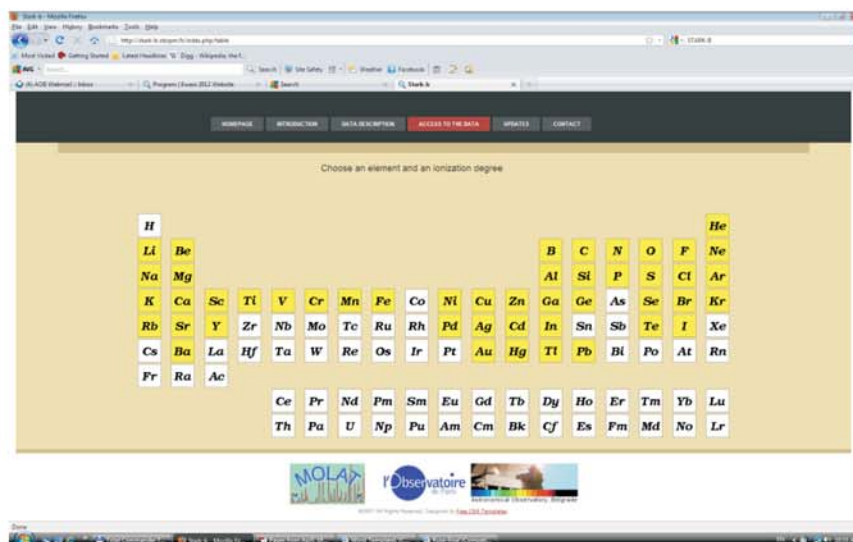


**Figure 1.** “Access to data” page of STARK-B.

## 3. SERBIAN VIRTUAL OBSERVATORY - SerVO

SerVO - Serbian virtual observatory (<http://www.servo.aob.rs/~darko>) was founded as the project TR13022 financed by the Ministry of Science and Technological Development of Republic of Serbia from April 1<sup>st</sup> 2008 till December 31<sup>st</sup> 2010. From the 1<sup>st</sup> January of 2011, SerVO is financed by the Ministry of Education and Science of Republic of Serbia through the project III44002 "Astroinformatics and virtual observatories". Main objectives are to

publish data obtained by Serbian astronomers as well as to provide astronomers in Serbia with VO tools for their research.

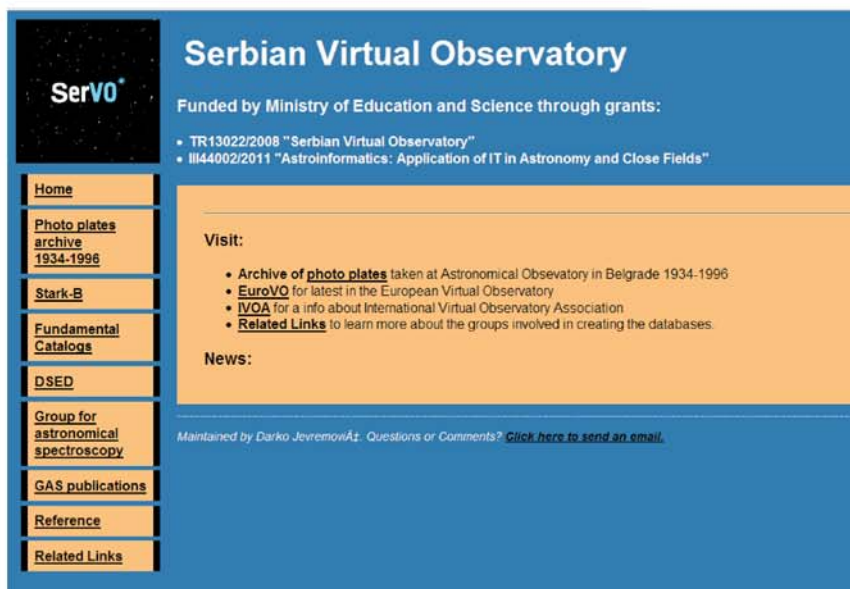


**Figure 2.** Homepage of Serbian Virtual Observatory.

Now, SerVO has five different collections:

1. Archive of photo-plates from the 1934-1996 period.
2. Link to, and the mirror site in construction of the STARK-B database.
3. Fundamental Catalogues
4. Link to, and the mirror site in construction of the DSED (Dartmouth Stellar Evolution Database) database.
5. Electronic editions of the GAS – Group for Astrophysical Spectroscopy.

Work on SerVO is in progress and we hope to enter soon in IVOA. We plan also to further develop and improve STARK-B database, and to enlarge and complete all mentioned collections of SerVO. We also plan to develop further the Serbian VAMDC node with an aim to become a regional center in South Eastern Europe

## REFERENCES

- [1] M. S. Dimitrijević, S. Sahal-Bréchet, A. Kovačević, D. Jevremović, L. Č. Popović, VAMDC Consortium (P.I. M.-L. Dubernet), Proceedings of the VII Bulgarian-Serbian Astronomical Conference, 1- 4 June, 2010, Chepelare, Bulgaria, eds. M. K. Tsvetkov, M. S. Dimitrijević, K. Tsvetkova, O. Kounchev, Ž. Mijajlović, Publ. Astron. Soc. »Rudjer Bošković 11, 13 (2012).

- [2] D. Jevremović, M. S. Dimitrijević, L. Č. Popović, et al., *New Astronomy Review* 53, 222 (2009).
- [3] M. S., Dimitrijević, S. Sahal-Bréchet, A. Kovačević, D. Jevremović, L. Č. Popović, In *Computer Systems and Technologies, Proceedings of the 12<sup>th</sup> International Conference CompSysTech'11*, eds. B. Rachev, A. Smrikarov, ACM (Association for Computing Machinery) ICPS (International Conference Proceedings Series), ACM Press, New York 578, 23 (2011).
- [4] D. Jevremović, M. S. Dimitrijević, L. Č. Popović, M. Dačić, V. Protić-Benišek, E. Bon, N. Gavrilović, J. Kovačević, V. Benišek, A. Kovačević, D. Ilić, S. Sahal-Bréchet, K. Tsvetkova, Z. Simić, M. Malović. *Proceedings of the VII Bulgarian-Serbian Astronomical Conference, 1-4 June, 2010, Chepelare, Bulgaria*, eds. M. K. Tsvetkov, M. S. Dimitrijević, K. Tsvetkova, O. Kounchev, Ž. Mijajlović, *Publ. Astron. Soc. »Rudjer Bošković«* 11, 55 (2012).
- [5] L. Č. Popović, M. S. Dimitrijević, N. Milovanović, N. Trajković, *Publications of Astronomical Observatory of Belgrade* 65, 225 (1999).
- [6] L. Č. Popović, M. S. Dimitrijević, N. Milovanović, N. Trajković, *Journal of Research in Physics* 28, 307 (1999).
- [7] N. Milovanović, L. Č. Popović, M. S. Dimitrijević, *Publications of the Astronomical Observatory of Belgrade* 68, 117 (2000).
- [8] N. Milovanović, L. Č. Popović, M. S. Dimitrijević, *Baltic Astronomy* 9, 595 (2000).
- [9] M. S. Dimitrijević, L. Č. Popović, E. Bon, V. Bajčeta, P. Jovanović, N. Milovanović, *Publications of the Astronomical Observatory of Belgrade* 75, 129 (2003).
- [10] M. S. Dimitrijević, L. Č. Popović, in *Virtual Observatory; Plate Content Digitization, Archive Mining, Image Sequence Processing*, eds. M. Tsvetkov, V. Golev, F. Murtagh, R. Molina, p. 115 (Heron Press Science Series, Sofia, 2006).
- [11] S. Sahal-Bréchet, Case studies on recent Stark broadening calculations and STARK-B database development in the framework of the European project VAMDC (Virtual Atomic and Molecular Data Centre). *Journal of Physics Conference Series* 257, 012028 (2010).
- [12] M. L. Dubernet, V. Boudon, J. L. Culhane, et al., *Journal of Quantitative Spectroscopy and Radiative Transfer* 111, 2151 (2010).
- [13] G. Rixon, et al., 7<sup>th</sup> International Conference on Atomic and Molecular Data and their Applications - ICAMDATA - 2010, Vilnius, Lithuania 21-24 September 2010, eds. A. Bernotas, R. Karazija, Z. Rudzikas, *American Institute of Physics Conference Proceedings* 1344, 107 (2011).
- [14] M. S. Dimitrijević, S. Sahal-Bréchet, A. Kovačević, D. Jevremović, L. Č. Popović, *Journal of Physics: Conference Series* 257, 012032 (2010).
- [15] M. S. Dimitrijević, S. Sahal-Bréchet, A. Kovačević, D. Jevremović, L. Č. Popović, *Journal of Physics: Conference Series* 257, 012032 (2010).
- [16] F. Kupka, F. and the VAMDC collaboration, *Balt. Astron.* 20, 503 (2011).

## **SECTION 4.**

### **General Plasmas**

- 4.1 Fusion Plasmas
- 4.2 Astrophysical Plasmas
- 4.3 Collective Phenomena

### **ABSTRACTS OF INVITED LECTURES**



**ION-DRIFT ACCELERATION OF  
MAGNETIZED PLASMA IN  
QUASI-STATIONARY PLASMA  
ACCELERATORS**

V. M. Astashinski

*National Academy of Sciences of Belarus, Republic of Belarus*

**PLASMA SIMULATIONS FOR  
LASER FUSION**

G. Ferland

*University of Kentucky, USA*

**INTGRATED SIMULATIONS FOR  
LASER FUSION**

H. Nagatomo

*Institute for Laser Engineering, Osaka University, Japan*

## **ELECTRON IMPACT EXCITATION IN PLANETARY AND COMETARY ATMOSPHERES**

Laurence Campbell and Michael J. Brunger

*ARC Centre for Antimatter-Matter Studies, Flinders University,  
GPO Box 2100, Adelaide, SA 5000, Australia*

**Abstract.** Sunlight produces photoionization and hence a low-density plasma in upper planetary atmospheres and in the coma around comets. Electrons in the solar wind, accelerated in magnetospheric processes, produce localised ionisation and thus aurora. In both cases a flux of secondary electrons is produced, leading to further ionization, plus dissociation and excitation, before the electrons recombine with the ions. The excited atoms and molecules can release energy in radiative decay, or by taking part in chemical reactions. Hence plasma processes drive energy transfer and the composition of minor constituents in cometary and planetary atmospheres.

In order to model these processes, it is necessary to know the composition and temperature of the neutral atmosphere, the electron impact cross sections for the ionization, dissociation, and excitation processes, recombination rates and the plasma conditions. The latter are usually characterised by a differential electron flux spectrum. We describe four computational studies, of which the aim was to investigate the application of new or updated electron impact excitation cross sections, but that could not proceed without the assembly of an appropriate model of the plasma:

- Calculations of electron cooling in the atmosphere of Mars, using new electron impact cross sections for vibrational modes of CO<sub>2</sub>.
- Predictions of infrared radiation from CO in the atmospheres of Mars and Venus, using new measurements of absolute cross sections for electron impact vibrational excitation of CO.
- Predictions of fourth positive emissions from comet Hale-Bopp, based on new measurements of electron impact excitation of the  $A^1\Pi$  state of CO, indicating that a previous study overestimated the abundance of CO in the comet by 40%.
- Application of new measurements of electron impact excitation of the higher energy states of molecular oxygen, leading to identification of an intensity ratio that should provide a sensitive indicator for remote sensing of the atmosphere of Europa.

**AB INITIO DETERMINATION OF STARK  
BROADENING PARAMETERS AND  
APPLICATION IN ASTROPHYSICS**

N. B. Nassib

*INSAT, Univeristy of Carhage, Tunisia*

## **EVALUATION OF PLASMA POTENTIAL AND ELECTRON ENERGY DISTRIBUTION FUNCTION BY LANGMUIR PROBES IN MAGNETIZED PLASMA**

Tsv K Popov<sup>1</sup>, M Dimitrova<sup>2,3</sup>, P Ivanova<sup>3</sup>, J Horacek<sup>2</sup>, J Stöckel<sup>2</sup>, R Dejarnac<sup>2</sup>  
and COMPASS tokamak team<sup>2</sup>

<sup>1</sup> *Faculty of Physics, St. Kliment Ohridski University of Sofia,  
5, J. Bourchier Blvd., 1164 Sofia, Bulgaria*

<sup>2</sup> *Institute of Plasma Physics, Academy of Sciences of the Czech Republic v.v.i.,  
Za Slovankou 3, 182 00 Prague 8, CR*

<sup>3</sup> *Emil Djakov Institute of Electronics, Bulgarian Academy of Sciences, 72,  
Tsarigradsko Chaussee, 1784 Sofia, Bulgaria*

Among the contact methods of plasma diagnostics, the electric probes are the most reliable diagnostic tools allowing one to measure edge plasma parameters with sufficiently high temporal and spatial resolution. In non-magnetized, low density plasmas Langmuir probes (LP) allow local measurements of the plasma potential, the charged particles density and the electron energy distribution functions,  $f(\mathcal{E})$  (EEDF).

In magnetized plasma, the interpretation of the electron part of current-voltage (IV) characteristics above the floating potential,  $U_{fl}$ , remains till now problematic - the electron part of the IV characteristics is distorted due to the influence of the magnetic field. For this reason, in the strongly magnetized tokamak plasmas the ion saturation branch of the IV and the part around the floating potential are usually used when retrieving the plasma parameters. This method only assumes a Maxwellian EDF for the electrons but in fact does not measure the real one. However, some experimental evidences of non-Maxwellian distributions in tokamak edge plasmas are confirmed. The knowledge of the real EEDF is of great importance to understand the underlying physics of processes occurring at the plasma edge in tokamaks, such as the formation of transport barriers, plasma-wall interactions, edge plasma turbulence, etc.

In this work the recently published first derivative probe method for evaluation of the electron energy distribution function based on the kinetic theory in non-local approach is reviewed and results from measurements with vertical reciprocating probe in tokamak COMPASS, Prague, IPP, CR are presented.

Data of radial distribution of the plasma potential, EEDF (respectively electron temperatures and densities are presented and compared with first results from Thomson scattering.

Experimental results obtained on the COMPASS tokamak by 39 LPs embedded in the divertor tiles and processed using the first derivative probe method are also presented.

The results obtained demonstrate that the first derivative probe method uses electron part of the measured IV probe characteristic allow one to acquire the main plasma parameters in tokamak edge plasma.

**Acknowledgements:** This research is in implementation of Work Plan 2012 of the Association EURATOM/INRNE.BG in collaboration with the Association EURATOM/IPP.CR, Prague, Czech Republic; JOINT RESEARCH PROJECT between Institute of Electronics, Bulgarian Academy of Sciences and Institute of Plasma Physics v.v.i., AS CR, 2011, bilateral Bulgaria-Slovenia contract BI-BG/11-12-011 and CEEPUS III, network AT-0063-01-0506 2011, mobility program.

## PLASMA SPECTROSCOPY IN THE CONDITIONS OF THE ITER TOKAMAK

J. Rosato<sup>1</sup>, Y. Marandet<sup>1</sup>, V. Kotov<sup>2</sup>, D. Reiter<sup>2</sup>, H. Capes<sup>1</sup>, L. Godbert-Mouret<sup>1</sup>,  
R. Hammami<sup>1</sup>, M. Koubiti<sup>1</sup> and R. Stamm<sup>1</sup>

<sup>1</sup>*Laboratoire PHIM, UMR 7345 Université d'Aix-Marseille / CNRS, Centre de  
Saint-Jérôme, Case 232, F-13397 Marseille Cedex 20, France*

<sup>2</sup>*IEK-4 Plasma Physics, Forschungszentrum Jülich GmbH, Trilateral Euregio  
Cluster, Euratom Association, D-52425 Jülich, Germany*

**Abstract.** The ITER tokamak, presently under construction in Cadarache (France), will be equipped with an extensive set of plasma diagnostics [1,2]. Passive spectroscopy of the hydrogen Balmer lines with a low upper principal quantum number  $n$  (in particular the H $\alpha$  transition:  $n = 3 \rightarrow 2$ ) is presently considered to measure fluxes of the hydrogen isotopes and to determine the isotopic proportion of the fuelling gas ( $N_T/N_D, N_H/N_D$ ) in the divertor region. Furthermore, information on the electron density  $N_e$  will be available through the analysis of the Stark broadening of high- $n$  lines. Such lines are already observed in present divertor plasmas in the so-called “detached regime”, e.g. in JET [3] and Alcator C-Mod [4]. A well-known difficulty that occurs in the interpretation of an observed spectrum is provided by the non-uniformity of the plasma along the line-of-sight. In a recent work [5], this issue has been investigated numerically for plasma conditions relevant to ITER, by using a line shape code and the transport code B2-EIRENE [6]. The possibility for a line shape-based diagnostic has been demonstrated, at least for H $\alpha$  in one typical plasma background. In this presentation, we report on this result and we extend this investigation to other lines. The line shape and the plasma models are presented in details. We examine the possibility for a diagnostic by performing fittings of simulated spectra to recover plasma parameters from the line shape. Opacity effects, which are important on the Lyman lines, will also be addressed.

### REFERENCES

- [1] A. J. H. Donné et al., Nucl. Fusion 47, S337 (2007)
- [2] V. S. Lisitsa et al., Plasma Phys. Rep. 38, 138 (2012)
- [3] M. Koubiti et al., J. Quant. Spectrosc. Radiat. Transfer 81, 265 (2003)
- [4] B. L. Welch et al., Phys. Plasmas 2, 4246 (1995)
- [5] J. Rosato, V. Kotov, and D. Reiter, J. Phys. B: At. Mol. Opt. Phys. 43, 144024 (2010)
- [6] V. Kotov, D. Reiter, and A. S. Kukushkin. “Numerical Study of the ITER Divertor Plasma with the B2-EIRENE Package, Forschungszentrum Jülich Report Jül-4257 (2007)

## **KINETIC TRANSPORT SIMULATION STUDIES FOR NON-AXISYMMETRIC HELICAL PLASMA CONFINEMENT**

T.-H. Watanabe<sup>1,2</sup>, H. Sugama<sup>1,2</sup>, M. Nunami<sup>1,2</sup>, and A. Ishizawa<sup>1</sup>

<sup>1</sup>*National Institute for Fusion Science, Toki, Gifu 509-5292, Japan*

<sup>2</sup>*The Graduate University for Advanced Studies (Sokendai), Toki, Gifu 509-5292, Japan*

**Abstract.** Heat transport in toroidal plasmas is one of the critical issues in magnetic confinement fusion research. Density and temperature gradients of high temperature torus plasma cause the drift wave turbulence that enhances the transport fluxes to a much higher level than that given by a classical estimate based on binary collisions of particles. Gyrokinetic simulations solving a reduced kinetic equation for the particle distribution function in a five-dimensional phase space have been carried out towards quantitative prediction of the turbulent (say, ‘anomalous’) transport.

Confinement field configuration of tokamak devices, such as ITER, is well approximated by a torus with the toroidal symmetry around the central axis, while non-axisymmetric helical systems, such as the Large Helical Device (LHD), have more degrees of freedom for designing the confinement field structure. It has recently been recognized by novel theoretical and numerical investigations that improvement of collisionless particle orbits by optimizing the helical field components contributes not only to reduction of the neoclassical transport but also to regulation of the plasma turbulence and transport.

Gyrokinetic simulations of LHD plasmas have demonstrated that an  $E \times B$  plasma flow with poloidal and toroidal symmetry (which is driven by the turbulent stress and is known as ‘zonal flows’) is more strongly generated in the neoclassically optimized confinement field than the non-optimized case. The enhanced zonal flows suppress the turbulence, and lead to the anomalous transport regulation.

The recent developments of the gyrokinetic simulations of LHD plasmas are presented in the conference.

**Acknowledgments.** This work is partly supported by grants-in-aid of the Ministry of Education, Culture, Sports, Science and Technology (No. 21560861, 22760660, and 24561030), and by the National Institute for Fusion Science (NIFS) Collaborative Research Program (KNTT006, KNST006, UNTT002, and KEIN1201). Numerical simulations are carried out by use of the Plasma Simulator system at NIFS.

## **THE STRUCTURE OF Si IV REGION IN Be STARS; A STUDY OF Si IV SPECTRAL LINES IN 68 Be STARS**

A. Antoniou<sup>1,4</sup>, E. Danezis<sup>1</sup>, E. Lyratzi<sup>1,2</sup>, L. Č. Popović<sup>3</sup>, M. S. Dimitrijević<sup>3</sup>  
and D. Stathopoulos<sup>1</sup>

<sup>1</sup> *Address: University of Athens, Faculty of Physics Department of Astrophysics, Astronomy and Mechanics, Panepistimioupoli, Zographou 157 84, Athens, Greece*

<sup>2</sup> *Address: Eugenides Foundation, 387 Sygrou Av., 17564, Athens, Greece*

<sup>3</sup> *Address: Astronomical Observatory of Belgrade, Volgina 7, 11160 Belgrade, Serbia*

<sup>4</sup> *Address: University of Peloponnese, Faculty of Science and Technology, Department of Telecommunications Science and Technology, Karaiskakis Str. 22100 Tripolis, Greece*

**Abstract.** In this paper, using the GR model, we analyze the UV Si IV resonance lines in the spectra of 68 Be stars of different spectral subtypes, in order to detect the structure of Si IV region. We study the presence and behavior of absorption components and analyze their characteristics. From this analysis we can calculate the values of a group of physical parameters, such as the apparent rotational and radial velocities, the random velocities of the thermal motions of the ions, the Full Width at Half Maximum (FWHM), the optical depth, as well as the absorbed energy and the column density of the independent regions of matter which produce the main and the satellites components of the studied spectral lines. Finally, we present the relations between these physical parameters and the spectral subtypes of the studied stars and we give our results about the structure of the Si IV region in their atmosphere.

## STELLAR POPULATION IN TYPE 2 ACTIVE GALACTIC NUCLEI

Nataša Gavrilović-Bon<sup>1</sup>, Edi Bon<sup>1</sup>, Philippe Prugniel<sup>2,3</sup>  
and Luka Č. Popović<sup>1</sup>

<sup>1</sup>*Astronomical Observatory, Volgina 7, Belgrade, Serbia*

<sup>2</sup>*Observatoire de Lyon, 9 avenue Charles André, Saint-Genis Laval cedex,  
F-69561, France Ecole Normale Supérieure de Lyon, Lyon, France*

<sup>3</sup>*Université Lyon1, Villeurbanne, F-69622, France Centre de Recherche  
Astronomique de Lyon*

**Abstract.** To analyse simultaneously stellar populations (SPs) in active galactic nuclei (AGN), AGN featureless continuum and emission lines, we used ULYSS code, adopted to fit total spectra of an active galaxy. In this paper we present the investigations of the accuracy, limitations and applications of the code in a research of stellar populations in narrow emission line galaxies (type 2). To validate the method, we have simulated several thousands of line-of-sight integrated spectra of type 2 galaxies. We fitted simulated spectra with ULYSS and found that code can extract SP and AGN parameters with a high precision. Additionally, we used the method to investigate SP and AGN spectral parameters of a sample of type 2 AGNs. Especially we investigate the properties of stellar population in the first kiloparsec.

## THE PROPERTIES OF THE EMISSION LINES AND THEIR CORRELATIONS IN SPECTRA OF ACTIVE GALACTIC NUCLEI

Jelena Kovačević<sup>1</sup> and Luka Č. Popović<sup>1</sup>

<sup>1</sup>*Astronomical Observatory, Volgina 7, 11060 Belgrade, Serbia*

**Abstract.** Active Galactic Nuclei (AGNs) are the most luminous objects in the Universe. It is assumed that an AGN consists of a supermassive black hole in the center, surrounded by accreting gas. In that process, a large amount of energy is produced, resulting in a very complex spectrum that shows a number of strong emission lines, which arise in plasma located close to the supermassive black hole.

Here we analyze the shapes, the flux ratios of the AGN lines, as well as their shifts and widths, which are signature of the geometry, physical and kinematical properties of the emission gas. We specially analyzed the optical Fe II lines, in order to answer on some unexplained questions about their origin, and mechanism of excitation. Additionally, we investigated some correlations between line properties which physical background is still not explained, with focus on Fe II lines, Balmer lines and forbidden [O III] lines in spectra of AGNs.

## **LABORATORY STUDIES OF CHARGING PROPERTIES OF DUST GRAINS IN ASTROPHYSICAL/PLANETARY ENVIRONMENTS**

Authors: D.Tankosic<sup>1</sup>, M.M. Abbas<sup>2</sup>

<sup>1</sup>*NASA Postdoctoral Program/NASA-MSFC, Huntsville, AL, USA,*

<sup>2</sup>*NASA-MSFC, Huntsville, AL, USA*

**Abstract.** Dust grains in various astrophysical environments are generally charged electrostatically by photoelectric emissions with UV/X-ray radiation, as well as by electron/ion impact. Knowledge of physical and optical properties of individual dust grains is required for understanding of the physical and dynamical processes in space environments and the role of dust in formation of stellar and planetary systems.

In this paper we focus on charging of individual micron/submicron dust grains by processes that include: (a) UV photoelectric emissions involving incident photon energies higher than the work function of the material and b) electron impact, where low energy electrons are scattered or stick to the dust grains, thereby charging the dust grains negatively, and at sufficiently high energies the incident electrons penetrate the grain leading to excitation and emission of electrons referred to as secondary electron emission (SEE).

It is well accepted that the charging properties of individual micron/submicron size dust grains are expected to be substantially different from the bulk materials. However, no viable models for calculation of the charging properties of individual micron size dust grains are available at the present time. Therefore, the photoelectric yields, and secondary electron emission yields of micron-size dust grains have to be obtained by experimental methods. Currently, very limited experimental data are available for charging of individual micron-size dust grains. Our experimental results, obtained on individual, micron-size dust grains levitated in an electrodynamic balance facility (at NASA-MSFC), show that: (1) The measured photoelectric yields are substantially higher than the bulk values given in the literature and indicate a particle size dependence with larger particles having order-of-magnitude higher values than for submicron-size grains; (2) dust charging by low energy electron impact is a complex process. Also, our measurements indicate that the electron impact may lead to charging or discharging of dust grains depending upon the grain size, surface potential, electron energy, electron flux, grain composition, and configuration (e.g. Abbas et al, 2010).

Laboratory measurements on charging of analogs of the interstellar dust as well as Apollo 11 dust grains conducted at the NASA-MSFC Dusty Plasma Lab. are presented here.



## **SECTION 4.**

### **General Plasmas**

- 4.1 Fusion Plasmas
- 4.2 Astrophysical Plasmas
- 4.3 Collective Phenomena

### **CONTRIBUTED PAPERS**



# GRAVITO-ACOUSTIC WAVES TRANSMISSION

Gordana Jovanović

*University of Montenegro, Natural-Science Faculty, POB 211, 21000 Podgorica, Montenegro*

**Abstract.** In this paper is discussed the transmission of gravito-acoustic waves at a horizontal interface separating two isothermal regions of a gravitationally stratified non-magnetized plasma.

## 1. INTRODUCTION

Wave modes propagate in a two region model, solar interior (photosphere) and solar atmosphere (corona). This regions, assumed quasi-isothermal and without magnetic field, are separated by a boundary  $z = 0$  where considered gravito-acoustic waves suffer reflection and transmission. Taking typical values of physical parameters for this simplified two-region model of the solar photosphere and corona, I analyzed the conditions for gravito acoustic waves to cross the boundary  $z = 0$ .

## 2. BASIC EQUATIONS

Standard set of hydrodynamic equations describe the dynamics of adiabatic processes in a fully ionized hydrogen plasma in presence of gravity with constant acceleration:

$$\begin{aligned} \frac{\partial \rho}{\partial t} + \nabla \cdot (\rho \vec{v}) &= 0, \\ \rho \frac{\partial \vec{v}}{\partial t} + \rho \vec{v} \cdot \nabla \vec{v} &= -\nabla p + \rho \vec{g}, \\ \frac{\partial p}{\partial t} + \vec{v} \cdot \nabla p &= \gamma \frac{p}{\rho} \left( \frac{\partial \rho}{\partial t} + \vec{v} \cdot \nabla \rho \right). \end{aligned} \quad (1)$$

The unperturbed gas is initially in hydrostatic equilibrium and assumed to be stepwise isothermal  $T_0 = \text{const}$ , i.e. with constant speed of sound  $v_s$  in each of the two regions separated by the boundary  $z = 0$ . The basic state is thus described by:

$$\frac{d}{dz} \ln \rho_0 = -\frac{\gamma g}{v_s^2}, \quad (2)$$

with  $v_s^2 = \gamma RT_0$ ,  $\gamma = c_p/c_v$  being the ratio of specific heats:  $R = R_0/\bar{M}$  where  $R_0 = 8.31 \text{ JK}^{-1}\text{mol}^{-1}$  is the universal gas constant and  $\bar{M} = 0.5\text{kgmol}^{-1}$  is the mean particle molar mass of the considered e-p plasma. Eq. (2) now yields the solution for density profile:

$$\rho_0(z) = \rho_{00}e^{-z/H}, \quad (3)$$

where  $H = v_s^2/\gamma g$  is constant scale height. The basic state quantities  $\Psi_0$  are subject to small adiabatic perturbations  $\Psi_1(x, y, z, t)$  that are harmonic in time  $t$  and in coordinates  $x$  and  $y$ , whose amplitudes  $\hat{\Psi}$  satisfy the condition  $|\hat{\Psi}| \ll |\Psi_0|$  and depend on the vertical coordinate  $z$ :  $\Psi_1(x, y, z, t) = \hat{\Psi}(K_x, K_y, \Omega; z)e^{i(K_x x/H + K_y y/H - \Omega t v_s/H)}$ . Here,  $K_x = k_x H$ ,  $K_y = k_y H$  are dimensionless wave-number components and  $\Omega = \omega H/v_s$  is dimensionless frequency. Eqs.(1) for such perturbations can be reduced to a sistem of two coupled ordinary differential equations:

$$\begin{aligned} \frac{d\hat{\xi}_{1z}}{dz} &= \frac{1}{\gamma H} \hat{\xi}_{1z} - \frac{(\Omega^2 - K_p^2)}{\rho_0(z)v_s^2\Omega^2} \hat{p}_1 \\ \frac{d\hat{p}_1}{dz} - \frac{v_s^2}{\gamma H} \frac{d\rho_0}{dz} \hat{\xi}_{1z} &= \rho_0(z) \frac{v_s^2}{H^2} \left( \Omega^2 + \frac{1}{\gamma^2} \right) \hat{\xi}_{1z} - \frac{1}{\gamma H} \hat{p}_1, \end{aligned} \quad (4)$$

where  $\hat{\xi}_{1z} = iv_{1z}/\Omega$  is z-component of the Lagrangian displacement,  $\hat{p}_1$  is pressure perturbation,  $\rho_0(z)$  is density distribution given by (3),  $K_p = \sqrt{K_x^2 + K_y^2}$  is the horizontal dimensionless wave-number. Eqs.(4) allow the following solutions for the vertical displacement  $\hat{\xi}_{1z}$  and the pressure perturbation  $\hat{p}_1$ :

$$\hat{\xi}_{1z}(z) = \xi_{1z}(0)e^{z/2H} e^{iK_z z/H}, \quad (5)$$

$$\hat{p}_1(z) = p_1(0)e^{-z/2H} e^{iK_z z/H}. \quad (6)$$

which can be transformed to a system of equations with constant coefficients if expressions:  $\hat{\xi}_{1z}e^{-z/2H}$  and  $\hat{p}_1e^{z/2H}$  are introduced as new unknowns. This finally yield dimensionless dispersion equation:

$$K_p^2 = \frac{\Omega^2(\Omega^2 - K_z^2 - \Omega_{co}^2)}{\Omega^2 - \Omega_{BV}^2}, \quad (7)$$

with  $K_z = k_z H$  dimensionless vertical wavenumber,  $\Omega_{co} = \frac{1}{2}$  dimensionless acoustic wave cut-off frequency and  $\Omega_{BV} = \sqrt{\frac{\gamma-1}{\gamma^2}}$  dimensionless Brunt-Väisälää frequency. Eq. (7) is fourth-order in  $\Omega$  and it corresponds to the gravito-acoustic wave equation known from the literature [1],[2].

### 3. TRANSMISSION COEFFICIENT

Harmonic wave, which propagates throught regions (1) and (2), does not change its frequency  $\Omega$  and horizontal wavevector component  $K_p$

parallel to the boundary  $z = 0$  [3]. Normal wavevector component  $K_z$  has a discontinuity at  $z = 0$ , where it changes from  $K_{z1}$  to  $K_{z2}$  according to the dispersion equation (7). An incident wave with a unit amplitude in region (1) is partially reflected at the boundary  $z = 0$  with amplitude  $A_r$  and partially transmitted into the region (2) with amplitude  $A_t$ . The solutions for the displacement  $\hat{\xi}_{1z}$ , according to equation (5), could be written as:

$$\hat{\xi}_{1z} = e^{[iK_{z1} + \frac{1}{2}] \frac{z}{H_1}} + A_r e^{[-iK_{z1} + \frac{1}{2}] \frac{z}{H_1}}, z < 0 \quad (8)$$

and

$$\hat{\xi}_{1z} = A_t e^{[iK_{z2} + \frac{1}{2}] \frac{z}{H_2}}, z > 0. \quad (9)$$

The solutions for pressure perturbation  $\hat{p}_1$ , according to equation (6), are:

$$\hat{p}_1 = G_{(1,1)} e^{[iK_{z1} - \frac{1}{2}] \frac{z}{H_1}} + A_r G_{(1,2)} e^{[-iK_{z1} + \frac{1}{2}] \frac{z}{H_1}}, z < 0 \quad (10)$$

$$\hat{p}_1 = A_t G_{(2,1)} e^{[iK_{z2} - \frac{1}{2}] \frac{z}{H_2}}, z > 0, \quad (11)$$

$$G_{(1,1)} = \frac{g\rho_{01}V_h^2}{V_h^2 - 1} \left( 1 - \frac{\gamma}{2} - \frac{i\gamma\Omega}{V_{v1}} \right),$$

$$G_{(1,2)} = \frac{g\rho_{01}V_h^2}{V_h^2 - 1} \left( 1 - \frac{\gamma}{2} + \frac{i\gamma\Omega}{V_{v1}} \right), \quad (12)$$

$$G_{(2,1)} = \frac{g\rho_{02}sV_h^2}{sV_h^2 - 1} \left( 1 - \frac{\gamma}{2} - \frac{i\gamma\Omega}{sV_{v2}} \right),$$

with dimensionless horizontal phase velocity  $V_h = \Omega/K_p$  and dimensionless vertical phase velocities  $V_{v1} = \Omega/K_{z1}$  and  $V_{v2} = \Omega/K_{z2}$ . Parameter  $s$  can be derived from the equality of unperturbed pressures at  $z = 0$ :

$$\rho_{01}v_{s1}^2 = \rho_{02}v_{s2}^2. \quad (13)$$

Here,  $s = \rho_{02}/\rho_{01} = v_{s1}^2/v_{s2}^2 = T_1/T_2$  is constant because photosphere (1) and corona (2) are assumed isothermal with temperatures  $T_1 = 6 \cdot 10^3 K$  and  $T_2 = 10^6 K$ . Applying continuity of the Lagrangean displacement  $\hat{\xi}_{1z}$  and the pressure perturbation  $\hat{p}_1$  at the boundary  $z = 0$ , the following set of equations for complex amplitudes  $A_r$  and  $A_t$  can be obtained:

$$A_t - A_r = 1$$

$$[G_{(2,1)} - g\rho_{02}]A_t - [G_{(1,2)} - g\rho_{01}]A_r = G_{(1,1)} - g\rho_{01}, \quad (14)$$

whose solutions are:

$$A_r = \frac{G_{(1,1)} - G_{(2,1)} + g[\rho_{02} - \rho_{01}]}{G_{(2,1)} - G_{(1,2)} - g[\rho_{02} - \rho_{01}]}, \quad (15)$$

$$A_t = \frac{G_{(1,1)} - G_{(1,2)}}{G_{(2,1)} - G_{(1,2)} - g[\rho_{02} - \rho_{01}]}. \quad (16)$$

These are general equations for reflection and transmission amplitudes of gravito-acoustic waves. For large but finite parameters  $\Omega$ ,  $V_h$ ,  $V_{v1}$  and  $V_{v2}$ , gravitational effects becomes important. They are given by a small term  $\alpha$  as a first order correction of the pure acoustic case. Now the transmission coefficient  $T = |A_t|^2$  has a form:

$$T = \frac{4(sV_h^2 - 1)}{\left(s\sqrt{V_h^2 - 1} + \sqrt{sV_h^2 - 1}\right)^2}(1 + \alpha). \quad (17)$$

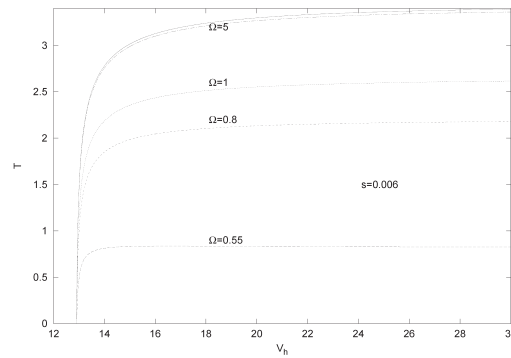


**Figure 1.** Solid line represents transmission coefficient of the pure acoustic waves. Gravity has a stronger influence on waves with frequencies near  $\Omega_{co}$  and it reduces value of transmission coefficient  $T$ . For the frequencies higher than one gravity influence is weaker and coefficient  $T$  has the values little bit smaller than in the pure acoustic case. These waves have a bigger chance to get from photosphere to corona than waves with frequencies in the range  $\Omega_{co} < \Omega < 1$ .

### Acknowledgements

This work is done in the framework of montenegrin national project "Physics of Ionized Gases and Ionized Radiation".

### REFERENCES

- [1] Mihalas, D.:1984, Foundations of Radiation Hydrodynamics, Oxford University Press
- [2] Goedbloed, H., Poeds, S.:2004, Principles of Magnetohydrodynamics, Cambridge University Press, Cambridge, UK
- [3] L.D.Landau and E.M.Lifshitz, Fluid Mechanics, Volume 6 of Course of Theoretical Physics, Second English Edition

## A STUDY OF THE C IV BALs IN HiBALQSO SPECTRA

D. Stathopoulos<sup>1,2</sup>, E. Lyratzi<sup>1,2</sup>, E. Danezis<sup>1</sup>, A. Antoniou<sup>1</sup>, D. Tzimeas<sup>1</sup>

<sup>1</sup>*University of Athens, Faculty of Physics Department of Astrophysics,  
Astronomy and Mechanics, Athens, Greece*

<sup>2</sup>*Eugenides Foundation, Athens, Greece*

**Abstract.** This paper is the second part of the study of Lyratzi et al. 2011, in which we calculated the rotational and radial velocities of the clouds that construct the BLR and the velocities of the random motions of the ions of each cloud (kinematical parameters) through the UV C IV Broad Absorption Lines (BALs) in the spectra of 30 Hi BALQSOs. In this paper we calculate some other physical parameters such as the absorbed energy and the FWHM of the C IV resonance lines created in BLR clouds.

### 1. INTRODUCTION

Most of Broad Absorption Line Regions (BALRs) in Quasars present very complex spectral line profiles because they are not homogenous but consist of a number of dense regions or ion populations (BLR clouds) that present different physical parameters (Dietrich et al. 1999; Bottorff and Ferland 2001). Each of these clouds gives an independent classical absorption line. If these clouds rotate with large velocities and move radially with small velocities, the produced lines have large widths and small shifts. As a result, they are blended among themselves and thus they are not discrete and we have the misimpression of a spectral line with complex profile (Lyratzi et al. 2007; Danezis et al. 2007).

The reason that these complex profiles cannot be fitted is that the radiative transfer equation, for a complex atmosphere, is not solved. This means that it is impossible to extract the values of many important parameters of the BLR clouds that produce these spectral lines. These are the kinematical parameters, the optical depth, the column density, the FWHM, the absorbed or emitted energy etc. Our scientific group solved for the first time the radiative transfer equation for a very complex atmospherical structure and found the line function that is able to fit the simple and the complex profile of the absorption and the emission spectral lines (GR model, Danezis et al. 2006, 2007; Lyratzi et al. 2009). As a result, we calculated the previously mentioned important parameters.

Danezis, et al. (2006), indicated the similarity between the broad asymmetric line profiles in the spectra of hot emission stars and the BALs and BELs of broad line QSOs. Using the GR model, our scientific group through fitting 30 AGN spectra calculated a number of important physical parameters (such as the ones mentioned before) of the clouds that construct the BLR.

Lyratzi et al. (2011), calculated the kinematical parameters of the UV C IV Broad Absorption Lines (BALs) in the spectra of 30 Hi BALQSOs. This poster paper is the second part of the study of Lyratzi et al. (2011). We continue by using the same data (30 BALQSOs), in order to study the absorbed energy and the FWHM of the studied spectral lines.

## 2. DATA AND SPECTRAL ANALYSIS

In order to study the UV CIV resonance lines we apply the GR model to the spectra of 30 BALQSOs, taken from SDSS Data Release 7. In Figure 1 we give some examples of the fitted spectra. The black line corresponds to the observed spectra and the grey line corresponds to the theoretical line profiles given by the GR model. The lower lines present the residuals, i.e., the differences between the observed spectrum and the theoretical profile. We studied all the absorption lines that follow the Balnicity Index criteria (Weymann et al. 1991). Finally, from all these lines we accepted as BALs only those which follow the rest Balnicity Index criteria. We found that 25 of the 30 quasars of our sample have Broad Absorption Lines.

## 3. RESULTS AND CONCLUSIONS

Using the GR model, we were able to fit the complex profiles of the studied CIV lines with 1 to 5 absorption components. For them we calculated the absorbed energy and the FWHM. The values of these parameters are presented in Table 1.

The absorption lines which follow the BI criteria satisfy the following conclusions: (1) the absorbed energies are between  $3.51 \pm 3.38$  eV and  $7.42 \pm 3.27$  eV; (2) the FWHM lies between  $9.80 \pm 0.61$  Å and  $32.58 \pm 17.17$  Å. In this point we have to note that the calculated absorbed energies and the FWHM are the mean values of the respective components of the resonance lines.

**Table 1.** Absorbed Energy (eV) and FWHM (Å)

Object name (SDSS)	E1	E2	E3	E4	E5	FW1	FW2	FW3	FW4	FW5
J001025.90 +005447.6	3.32	5.98				17.46	15.76			3.32
J001438.28 -010750.1	8.71					65.14				
J001502.26 +001212.4	5.90					64.62				
J002127.88 +010420.1	5.33					64.51				

26th Summer School and International Symposium on the Physics of Ionized Gases

---

J003551.98			3.90	3.32				8.95	
+005726.4									
J004041.39	4.21					51.02			
-005537.3									
J004118.59	7.79		1.75			27.39		19.16	
+001742.4									
J004323.43	3.69	5.45				34.19	35.11		
-001552.4									
J004732.73	4.15					45.47			
+002111.3									
J005355.15	3.88	3.88				10.21	10.21		
-000309.3									
J005419.99	4.84		3.86			30.95		22.14	
+002727.9									
J010241.04	1.75	1.75			4.97	19.15	19.15		
-004208.9									
J010336.40	5.75				5.58	36.36			17.58
-005508.7									
J011227.60	2.73	2.17	5.41	3.65		17.27	13.73	11.13	9.63
-011221.7									
J015024.44			5.16		13.04			17.90	21.87
+004432.99									
J015048.83	3.93					43.08			
+004126.29									
J021327.25				2.98	6.09			10.01	11.01
-001446.92									
J023908.99	3.02		11.31			24.09		25.87	
-002121.42									
J025747.75			10.65					25.72	
-000502.91									
J031828.91	2.10	3.48				16.24	16.71		
-001523.17									
J102517.58	3.40					26.20			
+003422.17									
J104109.86			3.95					9.08	
+001051.76									
J104152.62	2.12	2.12	4.00			12.16	12.16	12.55	
-001102.18									
J104841.03	1.58					21.47			
+000042.81									
J110041.20	6.08	9.09	5.65			24.69	25.34		10.65
+003631.98									

---

### Acknowledgements

This research project is in progress at the University of Athens, Department of Astrophysics, Astronomy and Mechanics; we are thankful to the Special Account for Research Grants for the financial support.

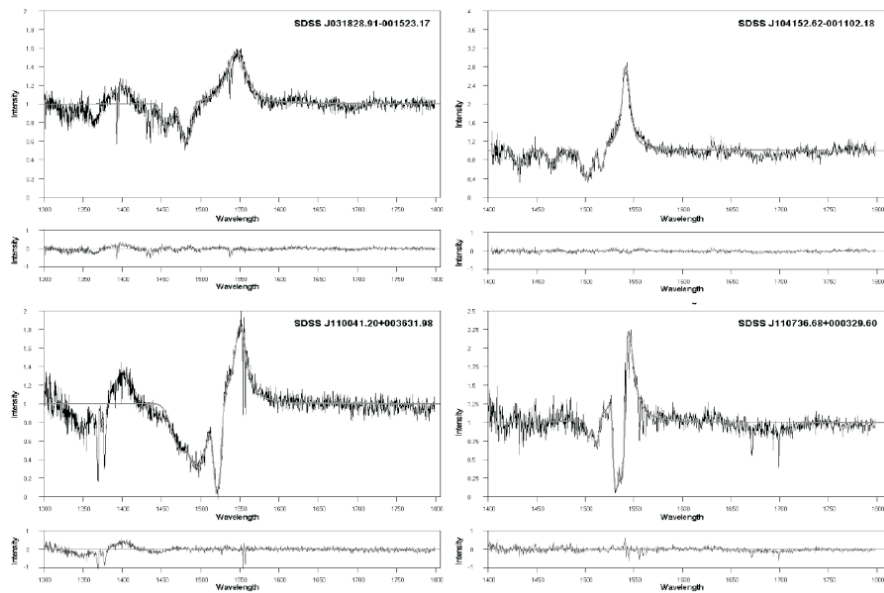


**Figure 1.** Four examples of fitted spectra. Black lines show the observed spectra and grey lines are the theoretical line profiles given by the GR model. The lower panels show differences between the observed spectra and the corresponding theoretical profiles.

## REFERENCES

- [1] E. Lyratzi, E. Danezis, L. C. Popovic, A. Antoniou, M. S. Dimitrijevic, D. Stathopoulos, *BaltA*, 20, 448L (2011)
- [2] M. Dietrich, S. J. Wagner, J. – L. Courvoisier, H. Bock, P. North, *A&A*, 351, 31D (1999)
- [3] M. Bottorff, and G. Ferland, *ApJ*, 549, 118B (2001)
- [4] E. Lyratzi, E. Danezis, M. S. Dimitrijevic, L. C. Popovic, D. Nikolaidis, A. Antoniou, *AIPC*, 938, 176L (2007)
- [5] E. Danezis, A. Antoniou, E. Lyratzi, L. C. Popovic, M. S. Dimitrijevic, D. Nikolaidis, *AIPC*, 938, 119D (2007)
- [6] E. Danezis, L. C. Popovic, E. Lyratzi, M. S. Dimitrijevic, *AIPC*, 876, 373D (2006)
- [7] E. Lyratzi, L. C. Popovic, E. Danezis, M. S. Dimitrijevic, A. Antoniou, *NewAR*, 53, 179L (2009)
- [8] R. J. Weymann, S. L. Morris, C. B. Foltz, P. C. Hewett, *ApJ*, 273, 23W (1991)

## MODAL FREQUENCIES OF IONOSPHERIC PERTURBATIONS INDUCED BY SOLAR X-FLARES

Aleksandra Nina<sup>1</sup> and Vladimir M. Čadež<sup>2</sup>

<sup>1</sup>*Institute of Physics, University of Belgrade, P.O. Box 57, Belgrade, Serbia*

<sup>2</sup>*Astronomical Observatory, Volgina 7, 11060 Belgrade, Serbia*

**Abstract.** In this paper, we analyze the amplitude time variation of very low frequency (VLF) signal being emitted by the DHO transmitter in Germany and recorded by the AWESOME receiver located in Institute of Physics in Belgrade at a solar X-flare occurrence on May 5, 2010. Energy released during solar X-flare events causes transient changes in the ionospheric electron concentration which further results into a specific time behavior of the recorded radio wave amplitude. The presented study starts from the fast Fourier transform (FFT) of such time dependent signal amplitude in search for characteristic frequencies of eigen-mode oscillations excited in the perturbed ionosphere. We obtain peaks in the computed oscillation spectrum at frequencies falling within ranges of ionospheric type Pc1-Pc5 pulsations.

### 1. INTRODUCTION

The terrestrial atmosphere is under permanent influences of different origins from outer space. The variations in intensity of their affects perturb the topology of the magnetosphere and the adjacent ionosphere. The resulting effects are various types of oscillations with eigen-frequencies typical of physical properties of the local plasma such as magnetic field and charged particle concentration. It was shown that modal frequencies can be deduced from spectral analyses of registered real time variations of VLF radio-wave amplitude [1] and they can further be utilized as a useful tool for diagnosing the lower ionosphere. Namely, during propagation between the transmitter and receiver, the waves are being deflected from the low ionosphere at some reflection height  $H(n_e)$  that depends on local time dependent electron concentration  $n_e(t)$  which results into time varying wave trajectory and, consequently, the amplitude and phase of the registered VLF signal become time dependent too. As a result, study of such signal time variations can also be used to estimate some parameters [2,3], relevant to local atomic processes of electron production in the ionosphere at height  $H$ .

## 2. RESULTS AND DISCUSSIONS

In what follows, we analyze a particular ionospheric perturbation caused by a solar X-flare (class C8.8) that erupted at around noon on May 5, 2010. At that time, GOES-15 satellite registered an increase of radiation intensity in the wavelength range between 0.1 and 0.8 nm as shown in Fig. 1, the top panel while the bottom panel in Fig. 1 shows the resulting rise in the VLF signal amplitude  $A(t)$  due to the increased electron concentration caused by the intensified photo-ionization. The considered VLF signal was taken to be the one emitted from the DHO transmitter in Germany operating at frequency 23.4 kHz.

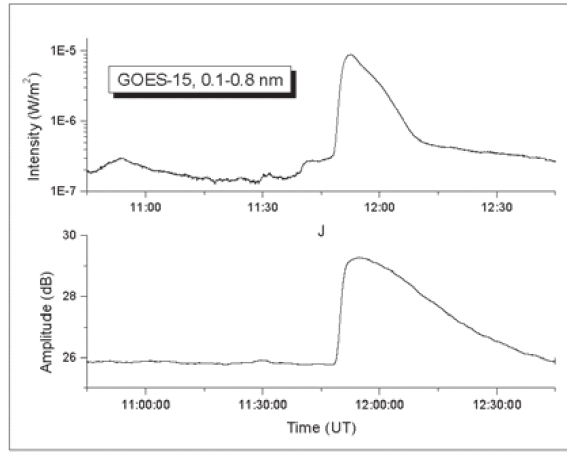


**Figure 1.** Time variation of the radiation intensity registered by the GOES-15 satellite (top panel) and signal amplitude recorded by AWESOME receiver located in the Institute of Physics in Belgrade.

The time dependence of the observed amplitude  $A(t)$  of the signal can now be Fourier decomposed which yields the oscillation spectrum  $A_F(T)$  according to:

$$A_F(T) = \frac{1}{\sqrt{2\pi}} \int_{-\infty}^{\infty} e^{-2\pi i t/T} A(t) dt, \quad (1)$$

where  $T$  is the oscillation period.

The external perturber of the ionosphere, the considered solar X-flare in our case, thus induces a spectrum of harmonic oscillations with different time periods  $T$  whose amplitude  $A_F(T)$  is given by Eq. (1). The main aim of this work is to filter out periods  $T=T_m$  of local maxima for  $A_F(T)$  which can be attributed to a discrete set of characteristic eigen-oscillations of the perturbed system.

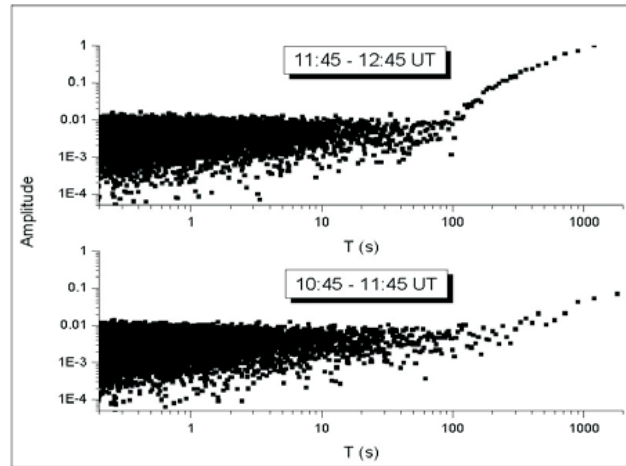


**Figure 2.** Fourier spectra for two time intervals: 1 h before the solar X-flare occurred at  $t=10:45$  UT (bottom panel), and 1 h during the perturbation period (top panel).

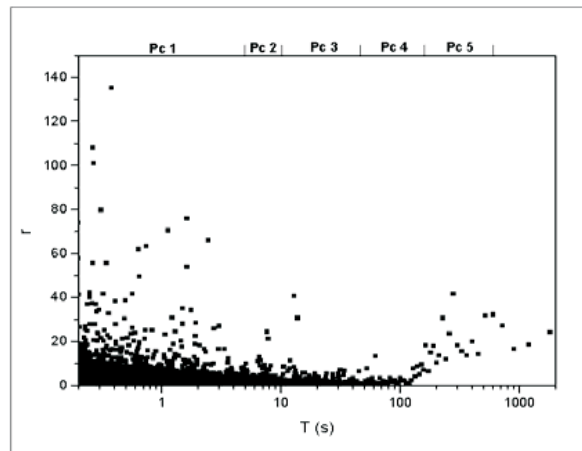


**Figure 3.** Increase of the Fourier spectra amplitude in the perturbed period  $A_F(T; t > t_0)$  relate to the period of unperturbed ionosphere  $A_F(T; t < t_0)$  ( $r = A_F(T; t > t_0) / A_F(T; t < t_0)$ ).

According to Fig. 1, the signal amplitude undergoes a sharp rise at about  $t = t_0 \equiv 11:45$  UT and the perturbation lasts for about one hour. The spectral analysis is now applied to two separate time intervals. The first one is between 10:45 UT and 11:45 UT when the ionosphere is still unperturbed, and the second one falls between 11:45 and 12:45 UT when the ionosphere is perturbed by the solar flare radiation. Fig. 2 shows numerical computations of

Fourier transforms of the signal amplitude  $A_F(T)$  versus oscillation period  $T$  for the two time intervals. It is evident that the amplitude  $A_F(T)$  grows for periods  $T$  exceeding 100 s while it remains within the range  $10^4 - 10^2$  s for smaller  $T$ .

The effect of the perturbation is visualized in Fig. 3 by plotting the ratio of the Fourier amplitudes for the two time domains:

$$r = r(T) \equiv \frac{A_F(T; t > t_0)}{A_F(T; t < t_0)} \quad (2)$$

As can be seen in Fig. 3, the most pronounced values of  $r$  occur for periods of about  $T = 0.2$  s, somewhat smaller are grouped around  $T = 1$  s,  $T = 10$  s, and  $T = 200-600$  s.

### 3. CONCLUSIONS

**Table 1.** Pulsation classes

	Continuous pulsations					Irregular pulsations	
	Pc1	Pc2	Pc3	Pc4	Pc5	Pi1	Pi1
T (s)	0.2-5	5-10	10-45	45-150	150-600	1-40	40-150
f (mHz)	200	100-200	22-100	7-22	2-7	25-1000	2-25

According to Table 1 which gives classification of typical ionospheric pulsations, and taking into account Fig. 3, we conclude that the dominant disturbance caused by the considered solar flare are the class Pc1 pulsations in addition to somewhat less intense Pc2-Pc3 and Pc5 pulsations.

### Acknowledgements

This work was financed by the Ministry of Education and Science of the Republic of Serbia through projects III 44002, 176002 and 176004.

### REFERENCES

- [1] V. Čadež, D. Šulić and V. Srećković, Pub. Astro. Obs. Belgr. 86, 39 (2009).
- [2] A. Nina, V. Čadež, V. Srećković, D. Šulić, Nucl. Instrum. Meth. B 279, 110 (2012).
- [3] A. Nina, V. Čadež, D. Šulić, Srećković, V. Žigman, Nucl. Instrum. Meth. B 279, 106 (2012).

## THE NON-SYMMETRIC ION-ATOM ABSORPTION PROCESSES IN THE STELAR ATMOSPHERES

A.A. Mihajlov<sup>1</sup>, V.A. Srećković<sup>1</sup>, L.J.M. Ignjatović<sup>1</sup> M.S. Dimitrijević<sup>2</sup> and A. Metropoulos<sup>3</sup>

<sup>1</sup>*University of Belgrade, Institute of physics, P.O. Box 57, 11001, Belgrade, Serbia*

<sup>2</sup>*Astronomical Observatory, Volgina 7, 11060 Belgrade 74 Serbia*

<sup>3</sup>*Theoretical and Physical Chemistry Institute, National Hellenic Research Foundation, Athens, Greece*

**Abstract.** The aim of this work is to draw attention to the processes of absorption charge-exchange and photo-association in non-symmetric ion-atom collisions together with the processes of the photo-dissociation as a factor of influence on the opacity of solar and some DB white dwarfs atmospheres in UV and VUV region. In all considered cases the absorption processes with  $A = He$  and  $B = H$  are taken into account. In the case of the solar atmosphere the absorption processes with  $A = H$  and  $B = Mg, Si$  and  $Al$  are also included in the considerations. On chosen examples it has been established that the examined processes generate rather wide molecular absorption bands in the UV and VUV region, which should be taken into account for the interpretation of data obtained from laboratory measurements or astrophysical observations.

### 1.INTRODUCTION

In a series of previous papers the influence of the processes of radiative charge exchange in symmetric  $H(1s) + H^+$  and  $He(1s^2) + He^+(1s)$  collisions and corresponding photo-association/dissociation processes on the opacity of stellar atmospheres was studied. It was shown that in the hydrogen case these processes are important for the atmospheres of the Sun and of some DA white dwarfs [1], and in the helium case - for the atmospheres of some DB and DA white dwarfs [1, 2]. The mentioned papers made it clear that at least symmetric ion-atom radiative collisions play a significant role in the stellar atmospheres. But the question, whether some non-symmetric ion-atom radiative processes can also influence the optical characteristics of the considered stellar atmospheres, is still open. A detailed study of such non-symmetric processes in connection with the stellar atmospheres would require a very extensive research, and it remains a task for the future. The aim of this article is to point out at least some objects where such processes could be of interest, and to show the possible ways of describing their influence. For this purpose it was natural to start from the same DB

white dwarfs and the solar atmosphere (which were considered in previous papers, since adequate models exist for them). In the case of DB white dwarfs we mean models presented in [3], as well as in [4]. The necessary

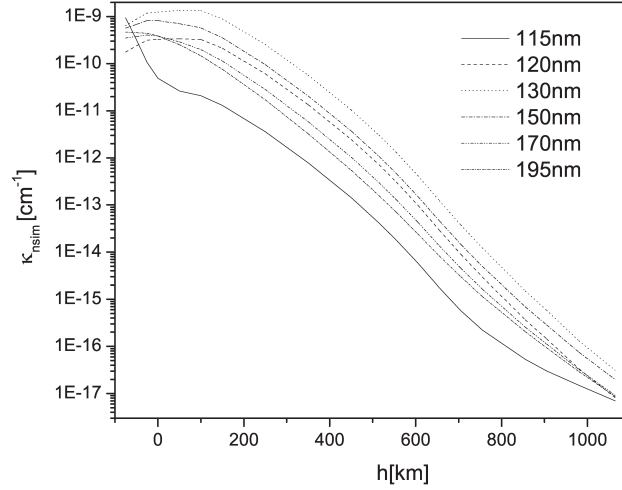
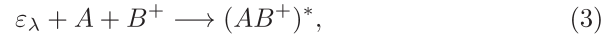
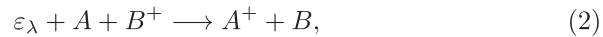
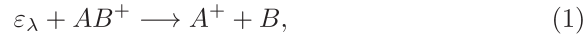


**Figure 1.** Quiet Sun. Spectral absorption coefficient  $\kappa_{nsim}(\lambda, T)$ , for  $115 \text{ nm} \leq \lambda \leq 195 \text{ nm}$ .

models of the solar atmosphere were described in [5, 6]. A composition of the mentioned models and the previous results for the ion-atom symmetric radiative process suggest that, in the considered atmospheres the following non-symmetric absorption processes have to be taken into account



where  $B$  is the ground state atom with the ionization potential  $I_B$  which is less than the ionization potential  $I_A$  of the atom  $A$ ,  $AB^+$  - the corresponding molecular ion. In the general case, apart from these absorption processes, the corresponding inverse emission processes should also be considered. However, it can be shown that, under the conditions of plasma taken from the models mentioned above, the significance of such emission processes can be neglected in comparison with other relevant emission processes. In accordance with models, in the both cases (Sun and DB white dwarfs) is possible that  $A = He(1s^2)$  and  $B = H(1s)$ , and in the case of the Sun, it is additionally possible that  $A = H(1s)$ , and that  $B$  is the atom of a

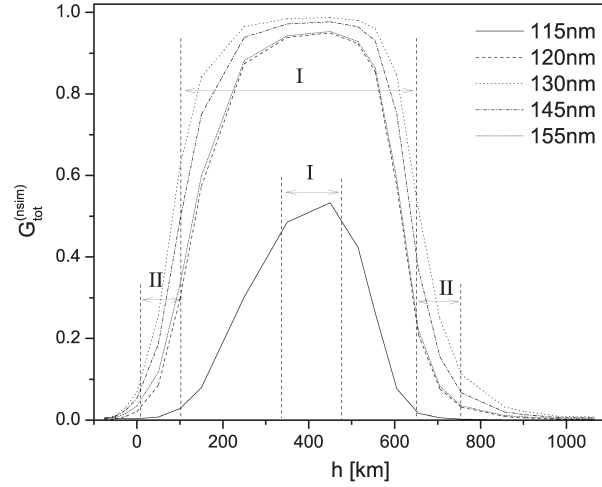


**Figure 2.** The behavior of the quantity  $G_{tot}^{(nsim)}(\lambda)$  as the function of  $h$  for the Solar atmosphere for  $115\text{nm} \leq \lambda \leq 155\text{nm}$ .

metal. The contribution of the considered non-symmetric ion-atom absorption processes is described here by the spectral absorption coefficients in the UV and VUV region as the function of the local temperature  $T$ , wavelength  $\lambda$ , and the particle densities.

## 2.RESULTS AND DISCUSSION

The contribution of the considered non-symmetric ion-atom absorption processes (1)-(3) to the opacity of the solar atmosphere is described here by the spectral absorption coefficient  $\kappa_{nsim}(\lambda, T)$ . The behavior of  $\kappa_{nsim}(\lambda, T)$  for several values of  $\lambda$  is illustrated by Fig.1, where  $h$  is the distance of considered layer from the referent one ( $h=0$ ) in accordance with [5]. The calculated values of the quantity  $G_{tot}^{(nsim)}(\lambda) = \kappa_{ia;nsim}(\lambda; T) / \kappa_{ia;tot}(\lambda; T)$ , where  $\kappa_{ia;tot}(\lambda; T)$  characterize the total contribution of all ion-atom absorption processes, i.e. symmetric and non-symmetric (1)-(3), is shown in Fig.2. From this figure one can see that around the temperature minimum ( $T \lesssim 5000$  K,  $150 \text{ km} \lesssim h \lesssim 705$  km) the contribution of non-symmetric processes are dominant in respect to the symmetric processes. Such region of the non-symmetric processes domination is denoted in these figures as the region "I". In the case of the DB white dwarfs atmospheres the results of the calculations of the spectral absorption coefficients  $\kappa_{ia;nsim}(\lambda)$ , as function of Rosseland optical depth  $\tau$  for  $-5.6 \leq$

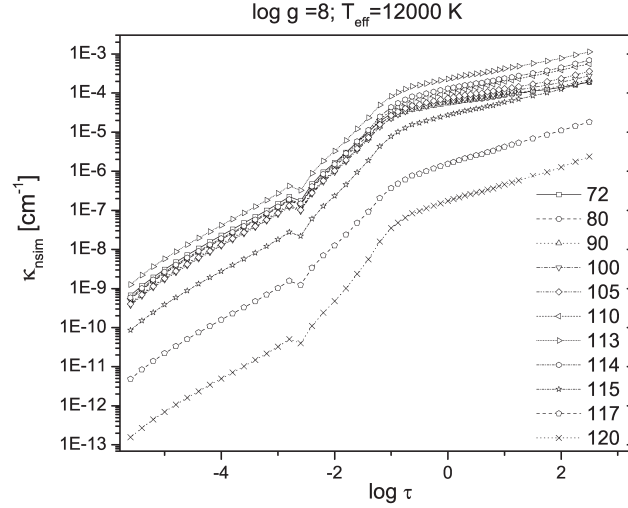


**Figure 3.** The spectral absorption coefficients, as function of Rosseland optical depth  $\tau$  for the DB white dwarf atmosphere model with  $\log g = 8$  and  $T_{\text{eff}} = 12000$  K.

$\log \tau \leq 2.6$ , are presented in Fig. 3 which relate to the model with  $\log g = 8$  and  $T_{\text{eff}} = 12000$  K. The quantity  $G_{\text{sim}}^{(\text{tot})}(\lambda) = \kappa_{\text{ia;tot}}(\lambda)/\kappa_{\text{ia;sim}}(\lambda)$ , where  $\kappa_{\text{ia;tot}}(\lambda; T)$  characterize the total contribution of all ion-atom absorption processes, i.e. symmetric and non-symmetric (1) - (3), is shown in Fig. 4. Our results presented in [7] and here shows that the neglecting of the contribution of the non-symmetric processes to the opacity of the stellar atmospheres, in respect to the contribution of symmetric processes would caused noticeable errors. All mentioned facts suggest that the considered non-symmetric ion-atom absorption processes should be *ab initio* included in the stellar atmospheres models.

From the presented material it follows that the considered non-symmetric ion-atom absorption processes can not be treated only as one of the channel among many equal channels of the influence on the opacity of the stellar atmospheres. Namely, in the case of the solar atmosphere these nonsymmetric processes so increase the absorption of EM radiation around the temperature minimum, that this absorption caused by all (symmetric and non-symmetric) ion-atom absorption processes becomes almost uniform in the whole solar photosphere. Moreover, the presented results show that further investigations of these processes promise to demonstrate that they are so important as the known process of the photo-detachment of ion H-, which was treated until recently as the absolutely dominant.

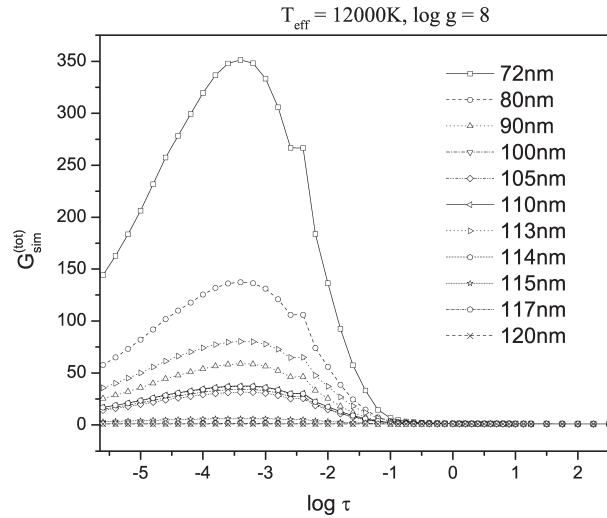


**Figure 4.** The quantity  $G_{sim}^{(tot)}$ , for the DB white dwarf atmosphere model with  $\log g = 8$  and  $T_{eff} = 12000$  K.

#### Acknowledgements

This work was supported by the Ministry of Education and Science of the Republic of Serbia as a part of the projects 176002, III4402.

#### REFERENCES

- [1] P. C. Stancil, ApJ 430, 360 (1994).
- [2] A. A. Mihajlov and M. S. Dimitrijević, A&A 256, 305 (1992).
- [3] D. Koester, A&AS 39, 401 (1980).
- [4] P. Bergeron, F. Wesemael and A. Beauchamp, PASP 107, 1047 (1995).
- [5] J. Vernazza, E. Avrett and R. Loser, ApJS 45, 635 (1981).
- [6] J. M. Fontenla, W. Curdt, M. Haberreiter, J. Harder and H. Tian, ApJ 707, 482 (2009).
- [7] V. A. Srećković et al., JENAM Saint-Petersburg, Russia, Contrib. Papers p.84. (2011).



# STARK EFFECT FOR A CONFINED HYDROGEN ATOM WITH DEBYE SCREENING POTENTIAL

Lj. Stevanović and D. Milojević

*Department of Physics, Faculty of Sciences and Mathematics, University of Niš  
Višegradska 33, 18000 Niš, Serbia*

**Abstract.** Effect of the static electric field on energy levels of the hydrogen atom with Debye potential and confined by impenetrable sphere is considered. Variations of Stark energy and splitting for lowest  $s$  and  $p$  states with the radius of the confining sphere, screening parameter and electric field strength are discussed.

## 1. INTRODUCTION

Investigation of the properties of atoms in plasma environment and under different conditions is of significant interest for astrophysics. These conditions often imply the high electron density of plasma, high pressure and temperature and presence of electric or magnetic (or both) fields. In order to study interaction between the atom and plasma with such parameters, the model of compressed or confined atom is adopted [1-4]. Here, we study the influence of the weak static electric field on the hydrogen atom embedded in plasma. In section 2 of the paper, we give the outline of the theoretical model and numerical Lagrange-mesh method for solving Schrödinger equation. In section 3 the results and discussion with the conclusions are presented.

## 2. MODEL

The non-relativistic Hamiltonian of the hydrogen atom, embedded in plasma and under the stationary electric field directed along the  $z$  axis, in spherical coordinates is given by

$$H = -\frac{1}{2}\Delta^2 - \frac{1}{r} e^{-\mu r} + V_c(r) + Fr\cos\vartheta \quad . \quad (1)$$

Here,  $F$  is the electric field strength, potential  $V_c$  reflects the confinement by impenetrable sphere of radius  $r_c$

$$V_c(r) = \begin{cases} 0, & r < r_c \\ \infty, & r \geq r_c \end{cases} \quad (2)$$

and  $\mu$  is the screening parameter related with temperature and number density of the plasma (one can simulate different plasma conditions from a given value of  $\mu$ ). All the quantities in Eq. (1) are given in atomic units ( $\hbar = m_e = |e| = 1$ ).

Lagrange-mesh method is a variational method coupled with Gauss quadrature associated with the mesh. The basis functions  $f_i(x)$  on interval  $[a, b]$  are Lagrange functions satisfying the cardinality condition

$$f_i(x_j) = \frac{1}{\sqrt{w_i}} \delta_{ij}, \quad (i, j = 1, 2, \dots, N) \quad (3)$$

where  $x_i$  and  $w_i$  are the points and weights, appearing in Gauss quadrature formula

$$\int_a^b g(x) dx \approx \sum_{i=1}^N w_i g(x_i). \quad (4)$$

The simplicity of the method is that it does not require any explicit evaluation, analytical or numerical, of matrix elements of the potential, but only the values of this potential at mesh points.

In order to numerically solve Schrödinger equation

$$H\psi(r, \theta) = E\psi(r, \theta) \quad (5)$$

with Hamiltonian (1), it is required two-dimensional basis set with elements

$$G_{ij}(x, y) = f_i(x)g_j(y), \quad (6)$$

where dimensionless coordinates  $x = r/R_0$  and  $y = \cos\theta$  ( $0 \leq x \leq 1$ ,  $-1 \leq y \leq 1$ ) were introduced. The problem is now reduced to eigenvalue problem of the Hamiltonian matrix with elements

$$H_{ij,kl} = \frac{1}{R_0^2} (T_x)_{ik} \delta_{jl} + \frac{1}{R_0^2 x^2} (T_y)_{jl} \delta_{ik} + V_{ij,kl}(x, y) \delta_{ik} \delta_{jl}, \quad (7)$$

where

$$T_x = -\frac{1}{2} \frac{d^2}{dx^2}, \quad T_y = -\frac{1}{2} \frac{d}{dy} (1 - y^2) \frac{d}{dy} + \frac{m^2}{1 - y^2}, \quad (8)$$

$$V(x, y) = -\frac{e^{-\mu R_0 x}}{R_0 x} + F R_0 x y. \quad (9)$$

The functions  $f_i$  ( $i = 1, \dots, N_x$ ) from (6) are Lagrange functions constructed from shifted Legendre polynomial of order  $N_x$  and regularized through multiplication by  $x(1-x)$  in order to deal with singularity at the origin and to satisfy Dirichlet boundary condition at  $x = 1$ . The functions  $g_j$  ( $j = 1, \dots, N_y$ ) are given in terms of associated Legendre polynomials  $(1-y^2)^{m/2} P_{N_y+m}^m$ . The matrix elements of the operators in (8) are calculated at the zeros of corresponding Legendre and associated Legendre polynomials [5].

### 3. RESULTS AND DISCUSSION

The numerical method, described in the pervious section, is used to calculate the energies of the  $1s$ ,  $2s$ ,  $2p$  and  $3p$  states for different values of  $r_c$ ,  $\mu$  and  $F$ . Here we report the energies and splitting only for  $r_c = 2$  and  $8$ ,  $\mu = 0.1$  and  $0.5$  and  $F \leq 0.1$ . Results are generated using the bases with dimensions  $N_x = 50$ ,  $N_y = 50$ . Validity of the method was checked by comparing the computed ground state energy for zero-field case with the data available in literature [1] and an excellent match was found.

Figure 1 presents the energies of  $1s$  and  $2s$  states as a function of electric field strength when  $r_c = 2$  and  $\mu = 0.5$ . Ground state energy decreases, and energy of the  $2s$  state increases with increasing field strength. This is the situation which takes place in unconfined hydrogen atom, also. Our extended calculations show that changing of the  $1s$  and  $2s$  energies in opposite directions with increasing electric field is valid for all confining radii and screening parameters.

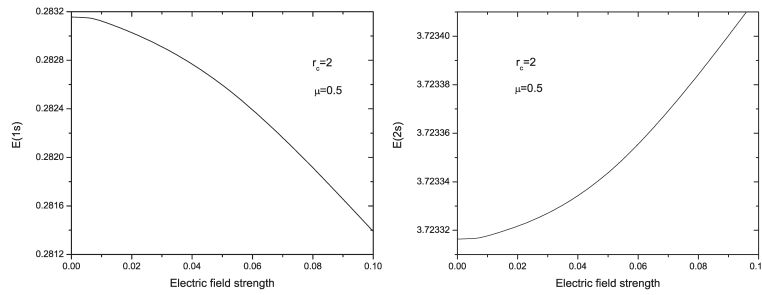


Figure 1: Energies of  $1s$  and  $2s$  states as a function of electric field strength at given values of confining radius and screening parameter.

Energy levels with  $l \neq 0$  split into a number of sublevels depending of possible  $m$  values (levels with  $|m|$  and  $-|m|$  are degenerated). Figure 2 represents the variations in energy splitting of  $2p$  and  $3p$  levels (difference between the levels with  $m = 0$  and  $m = \pm 1$ ) with electric field strength for specific values of confining radius and screening parameter, as labelled in the figure. Energy splitting of both levels are increasing function in electric field strength when  $r_c = 2$  (left panel in Fig. 2), meaning that levels with  $m = 0$  are higher than the ones with  $m = 1$ . With the larger value of confining radius  $r_c = 8$ , energy splitting of  $2p$  level has negative values and is decreasing function in  $F$  only when  $\mu = 0.1$ . In other words,  $2p_0$  level is always below  $2p_1$  level. Concerning the splitting of  $3p$  level, it has the negative values at all the field strengths only for  $\mu = 0.1$  and takes the positive values at stronger fields when  $\mu = 0.5$ .

In conclusion we can summarize the results: 1)  $2p$  splitting is larger than the one for  $3p$  level since the higher lying  $3p$  level is less affected

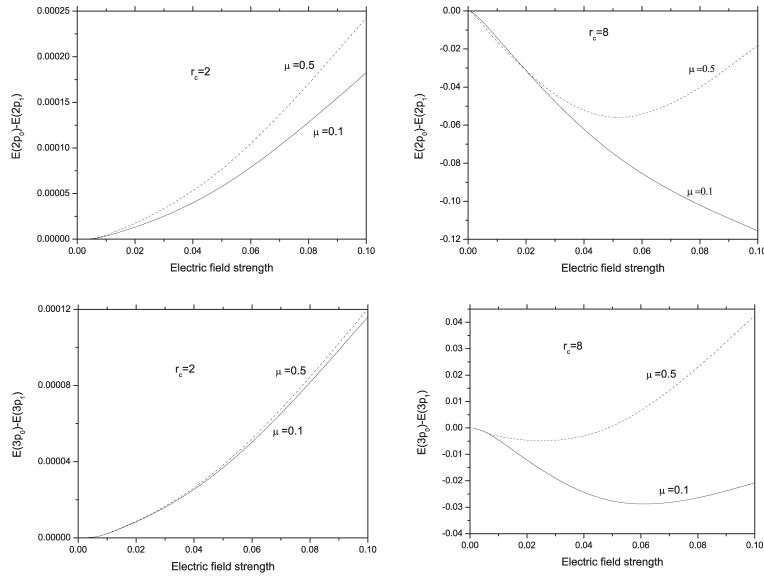


Figure 2: Stark splitting of  $2p$  and  $3p$  levels as a function of electric field strength at different values of confining radius and screening parameter.

by the field; 2) the absolute value of the splitting is decreasing function with decreasing  $r_c$  since for smaller radii there is a smaller difference in the potential between the two sides of the confining sphere.

### Acknowledgements

The authors acknowledge the financial support by the Serbian Ministry of Education and Science under the grant OI 171028.

### REFERENCES

- [1] B. Saha, P. K. Mukherjee and G. H. F. Dierksen, *Astron. Astrophys.* 396, 337 (2002).
- [2] Y. P. Varshni, *Can. J. Phys.* 81, 1243 (2003).
- [3] S. Bhattacharyya, A. N. Sil, S. Fritzsche and P. K. Mukherjee, *Eur. Phys. J. D* 46, 1 (2008).
- [4] Lj. Stevanović and D. Milojević, XVI NCAS, Book of Abstracts, pp. 16 (Belgrade, Serbia 2011).
- [5] M. Vincke, L. Malegat and D. Baye, *J. Phys. B* 26, 811 (1993).

## COLLISIONAL-RADIATIVE MODELS APPLIED TO ENTRY SITUATIONS IN EARTH OR MARS ATMOSPHERE

Julien Annaloro and Arnaud Bultel

*UMR CNRS 6614 CORIA, Université de Rouen,  
76801 Saint-Etienne du Rouvray, FRANCE*

**Abstract.** In order to understand the underlying dynamics resulting from the crossing of the shock front of a molecular mixture in the conditions of a planetary atmospheric entry, we elaborated a time-dependent Collisional-Radiative (CR) model. For the moment, this CR model cannot be yet implemented in an aerodynamic code owing to its complexity. Our approach is vibrational and electronic specific, which means that vibrational and electronic states are considered as independent. This CR model can work in the case of either Earth or Mars planetary atmospheric entries and allows a thorough examination of the dissociation and excitation mechanisms. As an illustration, only the case of the air dynamics will be treated in the present communication.

### 1. INTRODUCTION

During the atmospheric entry of a spacecraft, the hypersonic flow is converted into a high enthalpy flow through a shockwave: the temperature reached during this phase induces the dissociation of the molecules and the ionization of the gas [1]. The gas is therefore converted into plasma. The related complex chemistry involves a lot of radicals and ionized species. In the case of an Earth's atmospheric entry, the species produced are  $N_2$ ,  $O_2$ , Ar, NO, N, O,  $N_2^+$ ,  $O_2^+$ ,  $Ar^+$ ,  $NO^+$ ,  $N^+$ ,  $O^+$ , and  $e^-$ , whereas they are  $CO_2$ ,  $N_2$ , Ar,  $O_2$ , NO, CO, CN,  $C_2$ , C, N, O,  $N_2^+$ ,  $Ar^+$ ,  $O_2^+$ ,  $NO^+$ ,  $CO^+$ ,  $CN^+$ ,  $C_2^+$ ,  $C^+$ ,  $N^+$ ,  $O^+$ , and  $e^-$  in the case of a Martian atmospheric entry. The behavior of these mixtures is complex and is now far from being completely understood. In addition, the characteristic hydrodynamic times scales are short, which prevents a complete relaxation of the flow: this flow is therefore in thermal and chemical non-equilibrium [2]. In this context, the chemistry of the flow plays a key role, for example in the radiative flux transferred to the spacecraft and in the recombination processes taking place on the fuselage. To avoid any damaging of the vehicle, a thermal protection system is used. Its sizing and its characteristics depend on the chemistry of the flow: this chemistry has therefore to be well understood.

Understanding this complex chemistry is one of the main objectives of the works reported in this communication. We elaborated a model able to give us detailed information on the behavior of the mixture in thermodynamic non equilibrium for different situations. This model is based on the specific treatment of the balance equation of each species on excited states considered as independent in a simplified case corresponding to constant pressure and temperature. Collisional and radiative elementary processes are taken into account. The state-to-state collisional-radiative (CR) model thus developed can be used to estimate the chemical characteristic time scales.

## 2. PHYSICAL MODEL

The species observed in the case of a re-entry in the Earth atmosphere are in part those observed during a Martian entry, except that no carbonated compound is encountered. We have therefore elaborated our model in order to work either in Mars or Earth case. The considered species are listed in Table 1. Molecules, molecular ions, atoms and atomic ions are involved. The model is electronic specific and vibrational specific only for the ground electronic state of neutral molecules except for CO<sub>2</sub> owing to the weak energy of dissociation and to the strong dissociation rate coefficients of this molecule.

**Table 1.** List of the species considered in the present CR model.

<i>Species</i>	<i>States</i>
CO <sub>2</sub>	X <sup>1</sup> Σ <sub>g</sub> <sup>+</sup>
N <sub>2</sub>	X <sup>1</sup> Σ <sub>g</sub> <sup>+</sup> (v = 0 → 67), A <sup>3</sup> Σ <sub>u</sub> <sup>+</sup> , B <sup>3</sup> Π <sub>g</sub> , W <sup>3</sup> Δ <sub>u</sub> , B <sup>1</sup> Σ <sub>u</sub> <sup>-</sup> , a <sup>1</sup> Σ <sub>u</sub> <sup>-</sup> , a <sup>1</sup> Π <sub>g</sub> , w <sup>1</sup> Δ <sub>u</sub> , G <sup>3</sup> Δ <sub>g</sub> , C <sup>3</sup> Π <sub>u</sub> , E <sup>3</sup> Σ <sub>g</sub> <sup>+</sup>
O <sub>2</sub>	X <sup>3</sup> Σ <sub>g</sub> <sup>-</sup> (v = 0 → 46), a <sup>1</sup> Δ <sub>g</sub> , b <sup>1</sup> Σ <sub>g</sub> <sup>+</sup> , c <sup>1</sup> Σ <sub>u</sub> <sup>-</sup> , A <sup>3</sup> Δ <sub>u</sub> , A <sup>3</sup> Σ <sub>u</sub> <sup>+</sup> , B <sup>3</sup> Σ <sub>u</sub> <sup>-</sup> , f <sup>1</sup> Σ <sub>u</sub> <sup>+</sup>
C <sub>2</sub>	X <sup>1</sup> Σ <sub>g</sub> <sup>+</sup> (v = 0 → 36), a <sup>3</sup> Π <sub>u</sub> , b <sup>3</sup> Σ <sub>g</sub> <sup>-</sup> , A <sup>1</sup> Π <sub>u</sub> , c <sup>3</sup> Σ <sub>u</sub> <sup>+</sup> , d <sup>3</sup> Π <sub>g</sub> , C <sup>1</sup> Π <sub>g</sub> , e <sup>3</sup> Π <sub>g</sub> , D <sup>1</sup> Σ <sub>u</sub> <sup>+</sup>
NO	X <sup>2</sup> Π (v = 0 → 39), a <sup>4</sup> Π, A <sup>2</sup> Σ <sup>+</sup> , B <sup>2</sup> Π, b <sup>4</sup> Σ <sup>-</sup> , C <sup>2</sup> Π, D <sup>2</sup> Σ <sup>+</sup> , B <sup>2</sup> Δ, E <sup>2</sup> Σ <sup>+</sup> , F <sup>2</sup> Δ
CO	X <sup>1</sup> Σ <sup>+</sup> (v = 0 → 70), a <sup>3</sup> Π, a <sup>3</sup> Σ <sup>+</sup> , d <sup>3</sup> Δ, e <sup>3</sup> Σ <sup>-</sup> , A <sup>1</sup> Π, I <sup>1</sup> Σ <sup>-</sup> , D <sup>1</sup> Δ <sup>-</sup> , b <sup>3</sup> Σ <sup>+</sup> , B <sup>1</sup> Σ <sup>+</sup>
CN	X <sup>2</sup> Σ <sup>+</sup> (v = 0 → 41), A <sup>2</sup> Π, B <sup>2</sup> Σ <sup>+</sup> , D <sup>2</sup> Π, E <sup>2</sup> Σ <sup>+</sup> , F <sup>2</sup> Δ
N <sub>2</sub> <sup>+</sup>	X <sup>2</sup> Σ <sub>g</sub> <sup>+</sup> , A <sup>2</sup> Π <sub>u</sub> , B <sup>2</sup> Σ <sub>u</sub> <sup>+</sup> , a <sup>4</sup> Σ <sub>u</sub> <sup>+</sup> , D <sup>2</sup> Π <sub>g</sub> , C <sup>2</sup> Σ <sub>u</sub> <sup>+</sup>
O <sub>2</sub> <sup>+</sup>	X <sup>2</sup> Π <sub>g</sub> , a <sup>4</sup> Π <sub>u</sub> , A <sup>2</sup> Π <sub>u</sub> , b <sup>4</sup> Σ <sub>g</sub> <sup>-</sup>
C <sub>2</sub> <sup>+</sup>	X <sup>4</sup> Σ <sub>g</sub> <sup>-</sup> , I <sup>2</sup> Π <sub>u</sub> , <sup>4</sup> Π <sub>u</sub> , I <sup>2</sup> Σ <sub>g</sub> <sup>+</sup> , 2 <sup>2</sup> Π <sub>u</sub> , B <sup>4</sup> Σ <sub>u</sub> <sup>-</sup> , I <sup>2</sup> Σ <sub>u</sub> <sup>+</sup>
NO <sup>+</sup>	X <sup>1</sup> Σ <sup>+</sup> , a <sup>3</sup> Σ <sup>+</sup> , b <sup>3</sup> Π, W <sup>3</sup> Δ, b <sup>3</sup> Σ <sup>-</sup> , A <sup>1</sup> Σ <sup>+</sup> , W <sup>1</sup> Δ, A <sup>1</sup> Π
CO <sup>+</sup>	X <sup>2</sup> Σ <sup>+</sup> , A <sup>2</sup> Π, B <sup>2</sup> Σ, C <sup>2</sup> Δ
CN <sup>+</sup>	X <sup>1</sup> Σ <sup>+</sup> , a <sup>3</sup> Π, <sup>1</sup> Δ, c <sup>1</sup> Σ <sup>+</sup>

N	$^4S^o, ^2D^o, ^2P^o, \dots$
O	$^3P, ^1D, ^1S, \dots$
C	$^3P, ^1D, ^1S, \dots$
Ar	$^1S, [3/2]_2, [1/2]_0, \dots$
$N^+$	$^3P, ^1D, ^1S, \dots$
$O^+$	$^4S^o, ^2D^o, ^2P^o, \dots$
$C^+$	$^2P^o, ^4P, ^2D, \dots$
$Ar^+$	$^2P^o, ^2S, ^4D, \dots$

---

The coupling between these different states is due to the elementary collisional and radiative processes.

- *Collisional processes.* Vibrational processes (VV, VT, Ve), excitation, dissociation, ionization by electron or heavy particle impact, dissociative recombination, neutral and charge exchange, and excitation transfer are taken into account,
- *Radiative processes.* Atomic lines and main molecular systems are accounted for, with a possible self-absorption governed by escape factors.

The rate coefficient of each backward process is calculated from that of the forward process using the detailed balance.

### 3. RESULTS

The general implementation of the CR model in aerodynamics equations is tricky because the coupling with the energy balance equation requires the calculation of the temperature-dependent rate coefficient at each step. However, the entry-induced plasma leads sometimes to the formation of a shock layer corresponding to a Heaviside-like distribution for the thermodynamic parameters such as pressure and temperature, therefore density. Behind the shock front, their values are uniform, which justifies the resolution of the species balance equations only.

This is the case of the well-known FIRE II flight conditions into the Earth's atmosphere, at the altitude  $z = 54$  km [3]. Figure 1 illustrates in this case the behavior of the different species when the cold mixture in the upstream conditions is suddenly put at  $p = 80000$  Pa and  $T = 10000$  K. Owing to the important value of the collision frequency, the mixture is assumed in thermal equilibrium. The mixture is in chemical non-equilibrium, which is illustrated by the relaxation of its composition until a steady-state is reached. Since the (radiative) exchanges play a minor role (self-absorption of the main radiative systems), equilibrium is obtained at long time, i.e. for  $t > 70 \mu s$  in the present conditions.

One can note the quick formation of N and O due to the dissociation of  $N_2$  and  $O_2$ , which leads to the formation of NO by the Zeldovich processes

[ $N_2(v) + O \rightarrow NO(v') + N$  and  $O_2(v) + N \rightarrow NO(v') + O$  with a weaker rate]. The first electrons are produced through associative ionization and electroneutrality is firstly given by the  $O_2^+$  molecules, then by the  $NO^+$  molecules. Afterwards, electroneutrality is given by the  $N^+$  ions owing to the global density ratio between nitrogen and oxygen. Since no electrons exist at the beginning, only collisions between heavy particles can produce atoms by dissociation. The specific vibrational dynamics allows such dissociation. Figure 2 illustrates the vibrational dynamics of the main molecules  $N_2$ ,  $O_2$  and  $NO$ .

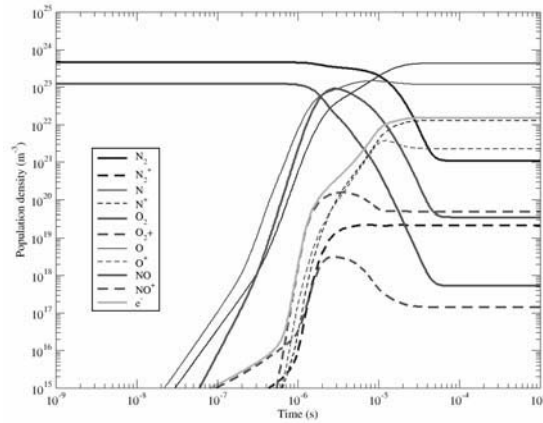


**Figure 1.** Population densities of the species behind a shock front for the FIRE II flight conditions entering into Earth's atmosphere ( $z = 54$  km).

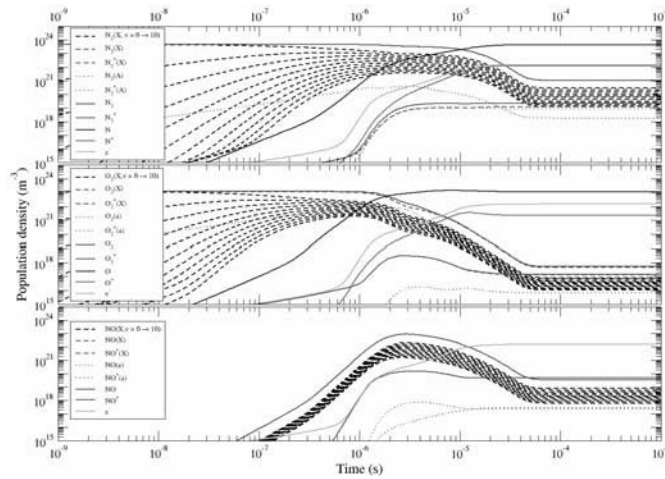


**Figure 2.** In the conditions of Figure 1, focus on the vibrational distributions of  $N_2$ ,  $O_2$  and  $NO$  on their ground electronic state. The evolution of some electronic excited states is also displayed.

Figure 2 shows that the initial vibrational temperature of  $N_2$  and  $O_2$ , initially small because of the coupling with the upstream conditions, increases. Indeed, the excited vibrational states population density increase. Then a good coupling is observed, when the dissociation degree is high. Afterwards, the global dissociation process continues with a very good vibrational coupling until the dissociation degree reaches its equilibrium value. Conversely, NO presents a different behavior. This is due to the absence of NO in the upstream mixture. The formation of NO on the different vibrational states takes place during their excitation: the apparent coupling is then very strong and leads to a very high vibrational temperature.

The dynamics of the excited states cannot be developed there, but it will be developed during the conference. The study will be also performed in the case of  $CO_2$ ,  $N_2$ , Ar mixtures related to Martian entries.

#### 4. CONCLUSION

A time dependent Collisional-Radiative model is elaborated in the purpose of describing thoroughly the dissociation – ionization of the molecular mixture involved during the hypersonic entries into Earth or Mars planetary atmosphere. This model is vibrational and electronic specific: the dissociation of the main molecules and the particles storage in radiative states is therefore calculated realistically. This model can also work in recombination situations such as those observed in boundary layers. During the conference, results related to these situations will be also illustrated.

#### REFERENCES

- [1] Ya.B Zel'dovich, Yu P. Raizer *Physics of shock waves and high-temperature hydrodynamic phenomena* (Dover Publications, N. Y., 2002)
- [2] S.C. Lin (1961) *Planetary and Space Science* **6** 94
- [3] A. Bultel, J. Annaloro (2012) *Plasmas de rentrée atmosphérique: problématique et enjeux* (in French), in press in CNRS Cold Plasmas French Network

## AUTHOR INDEX

<b>A</b>		Burger M.	281, 285
Abbas M. M.	367		
Acid H.	130	<b>C</b>	
Aerts R.	121	Campbell L.	358
Allan M.	14, 75	Canon F.	55
Andric L.	9	Capes H.	362
Annaloro J.	128, 393	Carniato S.	9
Antoniou A.	364, 375	Charlton M.	4, 333
Aparicio J. A.	127, 143	Coreno M.	11
Astashinski V. M.	355	Cvejić M.	151, 155, 175, 289
Aubrecht V.	139	Cvelbar U.	63, 305
Axente E.	64	Cvetanović N.	132
Azharonok V.	203	Cvetić J.	159, 163
<b>B</b>			
Banković A.	333	<b>Ć</b>	
Bartlova M.	139	Ćirišan M.	64, 151
Batani D.	61		
Beldžilali S.	64	<b>Č</b>	
Belić D. S.	12	Čadež V.	379
Belmonte M. T.	127, 143	Čurik R.	8
Berezcky R. J.	79		
Berndt J.	130	<b>D</b>	
Bibić N.	111, 115	Danezis E.	364, 375
Bizau J.-M.	6	Dejarnac R.	360
Bogaerts A.	121	Deller A.	333
Bogatyreva N.	139	Deshmukh P. C.	39
Bojarov A.	147	Dimitrijević M. S.	349, 364, 383
Borka D.	87, 107	Dimitrova M.	360
Borka Jovanović V.	107	Dojčilović R. J.	99, 103
Bošnjaković D.	265	Dojčinović I. P.	215, 245, 249, 261
Boufendi L.	130		
Božanić D. K.	103	Dudchik N. V.	321
Brandenburg R.	195	Dujko S.	265, 345
Brunger M. J.	358		
Bukvić S.	281, 285		
Bultel A.	128, 219, 393		
Burgdörfer J.	74		

<b>Dj</b>		<b>I</b>	
Djeniže S.	281, 285	Ignjatović Lj. M.	383
Djulgerova R.	269	Ikeda T.	65
Djurić R.	159, 163	Isaac C. A.	333
Djurović S.	127, 143, 167, 171, 317	Ishizawa A.	363
Djordjević A.	309	Ito K.	9
		Ivanova P.	360
		Ivković M.	183
<b>E</b>		<b>J</b>	
Ebert U.	122, 345	Jevremović D.	349
Epstein I. L.	191	Jevtić D.	245
		Jose J.	39
		Jovanović A. P.	253, 257, 301
		Jovanović G.	371
		Jovanović J.	341
		Jovičević S.	151, 155, 175, 179, 289
		Jovović J.	187, 191
		Jureta J. J.	47
<b>F</b>		<b>K</b>	
Ferland G.	356	Kilibarda F. G.	103
Filatova I.	203	Kirillov A. A.	321
		Kobilarov R.	167, 171, 313, 317
		Konjević N.	151, 175, 179, 183, 187, 191, 289
		Koperski J.	269
		Kotov V.	362
		Koubiti M.	362
		Kovačević A.	349
		Kovačević E.	130
		Kovačević J.	366
		Kovačević M.	79
		Kovačević V. V.	195, 207, 235
		Krčma F.	199
		Krstić I. B.	207, 235
		Kubala D.	14
<b>G</b>			
Gadzhieva G.	203		
Gajo T.	313		
Galijaš S. M. D.	69, 70, 91, 95		
Gavanski L.	167, 317		
Gavrilovic M.	155, 175, 179		
Gavrilović-Bon N.	365		
Gerlich D.	3		
Gervasoni J. L.	67		
Gigosos M. A.	183		
Giuliani A.	55		
Gocić S. R.	253, 301		
Godard G.	219		
Godbert-Mouret L.	362		
Gogolides E.	231		
Goncharik S.	203		
González M. Á.	183		
Grozdanov T. P.	9, 23		
Gruden-Pavlović M.	75		
<b>H</b>			
Hammami R.	362		
Hermann J.	64, 151		
Hikosaka Y.	9		
Horacek J.	360		

Kuraica M. M.	195, 207, 235	Mihelič A.	134
Kushner M.	123	Mijatović Z.	167, 171, 313, 317
<b>L</b>		Mijović S.	293, 297
Lablanquie P.	9	Miladinović T. M.	51
Lara N.	183	Milojević D.	389
Lazović S.	133, 305, 309	Milojević N.	19
Lebedev Yu. A.	191	Milosavljević A. R.	47, 55, 79
Lemell C.	74	Milosavljević M. K.	261
Lieb K. P.	111	Milosavljević V.	66
Lyratzi E.	364, 375	Mirković M. A.	69, 91
<b>M</b>		Mišković Z. L.	87
Maho Th.	130	Morel V.	128, 219
Majkić M. D.	69, 70, 91, 95, 99	Mortensen T.	333
Majstorović G. Lj.	211	Mothe E.	64
Maletić D.	309	Mozetič M.	305
Maljković J. B.	55	<b>N</b>	
Malović G.	273, 305, 309	Nađ Z.	167
Mančev I.	19	Nagatomo H.	357
Manson S. T.	39	Nahon L.	55
Mao M.	121	Nakano M.	9
Mar S.	127, 143	Nassib N. B.	359
Marandet Y.	362	Nedeljković N. N.	69, 70, 91, 95, 99, 103
Marić D.	35, 273, 329	Nenadović M.	83
Marinković B. P.	47, 79, 227	Neyts E.	121
Marjanović S.	333, 337	Nezhvinskaya O. E.	321
Markosyan A.	345	Nikitović Ž.	223, 341
Marković V. Lj.	253, 257, 301	Nikolić N. D.	301
Martinović M. M.	215	Nikolić Z.	281
May O.	14, 75	Nina A.	379
Mazankova V.	199	Novaković M.	111, 115
McCarroll R.	23	Nunami M.	363
Mercadier L.	64	<b>O</b>	
Metropoulos A.	383	Obradović B. M.	195, 207, 235
Mihailov V.	269	Obradović M. B.	99
Mihajlov A. A.	383	<b>P</b>	
		Pajović J.	103

Palaudoux J.	9	<b>S</b>	
Peláez R. J.	127, 143	Safronau Y. A.	321
Penent F.	9	Sahal-Bréchet S.	349
Petrović S.	71	Savić I.	171, 313, 317
Petrović Z. Lj.	35, 147, 223, 265, 269, 273, 305, 309, 329, 333, 337, 341	Savić M.	325, 329
Ponjavić M.	159, 163	Selaković N.	309
Poparić G. B.	12, 27, 43	Selles P.	9
Popov Tsv. K.	360	Shigemasa E.	9
Popović L. Č.	364, 365, 366	Simonchik L. V.	321
Popović M.	27, 111, 115	Simonović N.	31
Popović M. P.	43	Sivoš J.	35, 273
Potočnik J.	83	Skočić M.	281, 285
Pouvesle J.-M.	124	Soejima K.	9
Prlina I. P.	95	Somers W.	121
Prugniel P.	365	Spasić K.	305
Puač N.	305, 309	Spasojević Dj.	131
Purić J.	215, 245, 249, 261	Srećković V. A.	383
<b>R</b>		Sretenović G. B.	195, 207, 235
Rabasović M.	227	Stamenković S. N.	253, 257, 301
Radjenović B.	325	Stamm R.	362
Radmilović-Radjenović M.	147, 325, 329	Stankov M. N.	253, 257, 301
Radojević V.	39	Stathopoulos D.	364, 375
Radović I.	87	Stefanović J. S.	51
Radović M.	73	Steflekova V.	239
Radulović M. M.	51	Stevanović Lj.	389
Rakočević Z.	83	Stöckel J.	360
Raspopović Z.	341	Stockli M.	5
Reiter D.	362	Stojadinović S.	187
Ristić M. M.	12, 27, 43	Stojanović V.	35, 223, 341
Ristić V. M.	51	Sugama H.	363
Rosato J.	362	Sumarac D.	159, 163
		Suzuki I. H.	9
		<b>Š</b>	
		Šćepanović M.	249, 261, 293, 297
		Šević D.	227
		Šiljegović M.	115
		Šišović N. M.	135, 187, 191, 211

Škoro N.	35, 136, 231, 273	Ž	
Štrbac S.	83	Žitnik M.	9
Šuvakov M.	329, 333, 337		
<b>T</b>			
Tankosić D.	367		
Tapalaga I.	245, 249, 261		
Tatarinov A. V.	191		
Teslikova I.	199		
Tókési K.	79		
Tošić S. D.	13		
Traverse A.	111		
Trifković Z.	159, 163		
Tzimeas D.	375		
<b>V</b>			
Van der Werf D. P.	333		
Van Gaens W.	121		
Varma H. R.	39		
Vičić M.	27, 43		
Vojnović M. M.	27, 43		
Vučeljić M.	293, 297		
Vučić S.	277		
Vujčić V.	349		
<b>W</b>			
Wachter G.	74		
Wagner H.-E.	125		
Watanabe T.-H.	363		
White R. D.	345		
<b>Y</b>			
Yip W. L.	64		
Yusupov M.	121		
<b>Z</b>			
Zhang K.	111		
Zhechev D.	239		
Zhukovsky A.	203		
Zlatar M.	75		

## **APPLICATION OF LOW TEMPERATURE PLASMAS FOR THE TREATMENT OF ANCIENT ARCHAEOLOGICAL OBJECTS**

Frantisek Krcma, Vera Sazavska, Petra Fojtikova, Lucie Radkova,  
Adam Kujawa, Radek Prikryl, Michal Prochazka, Radka Balastikova,  
Premysl Mencik, Lucie Blahova, Jakub Horak, Martin Zmrzly,  
Drahomira Janova

*Brno University of Technology, Faculty of Chemistry, Purkynova 118, 612 00  
Brno, Czech Republic*

**Abstract.** The plasma chemical removal of the corrosion layers from archaeological artifacts by RF hydrogen low pressure plasma is a relatively new technique discovered at mid 80's. Because each object is original with the unique composition of corrosion layers as well corrosion history the model corroded samples were used for the presented study. The different duty cycles were applied to keep low temperature of samples. The second plasma application in the conservation is deposition of thin layers protecting the objects from the secondary corrosion. The organosilicone and parylene thin films were applied.

### **1. INTRODUCTION**

Reduction of corrosion layers using hydrogen plasma is a relatively new method, which should be used for conservation and restoration of archaeological artifacts. The conservation of artifacts represents a serious problem because of post-corrosion which occurs after excavation [1]. At the first, Daniels used a glow discharge in hydrogen gas to reduce silver tarnish back to silver [2]. He used it for Daguerreotype too, and his process was successful [2]. The method of plasma treatment for metallic artifacts was developed at the end of the 20 century at Institute of Inorganic Chemistry, University of Zürich. The method was successfully applied to the treatment of more than 13 000 historical objects from various periods (400 B.C. until 19<sup>th</sup> Century) and places of excavation [3]. This technology is used mainly for iron objects, because the optimal conditions for the corrosion removal of other metals are not known yet [3].

Because each archaeological object is original with the unique composition of corrosion layers as well corrosion history it is necessary to study the influence of processes and discharge conditions using the model corroded samples. Samples of the most frequent ancient metallic materials (iron, bronze,

copper, brass) were prepared using anorganic acid vapors (HCl, ammonia) or by dipping into the acid solution ( $\text{H}_2\text{SO}_4$ ,  $\text{HNO}_3$ ) and after that they were stored in dessicator for 2-4 weeks. The longer time storage was realized in polyethylene ziplock bags up to application of plasma.

## 2. EXPERIMENTAL

The corrosion removal is realized by low pressure RF hydrogen plasma where different duty cycles are applied to keep low temperature of samples. The treatment was carried out in a Quartz cylindrical reactor (length 90 cm, i.d. 9.5 cm). Radio-frequency electric field (13.56 MHz) was applied by two external copper electrodes using automatic matching network and capacitively coupled RF discharge was generated. The reactive hydrogen particles (atoms, ions, molecules) were formed in plasma and reacted with the corrosive layer containing oxygen. This reaction leads to sputtering of corrosion layer and creates the OH radical, which emits light in the region of 305–320 nm that is used as process monitoring quantity [4], example of results is given in Fig. 1. The data were not recalculated with respect to the discharge on time.

## 3. RESULTS

Rotational temperatures and integral intensity of OH radicals were determined from obtained data. The sample temperature was measured by thermocouple installed inside the sample volume. Temperature was readed out when discharge was stopped for 5 s to eliminate RF field influence on this measurement. The corroded samples were usually less warm in pulsed mode than in continuous mode (see at Figure 2). The sample temperature is one of the critical treatment parameters because elevated temperatures (even over about  $120^\circ\text{C}$  depending on material) can initiate the metallographic or composition changes in objects.

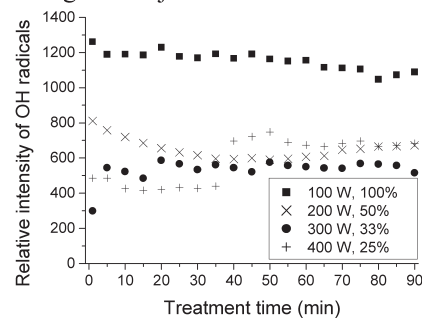


**Figure 1:** Relative intensity of OH radicals (brass, ammonia atmosphere).

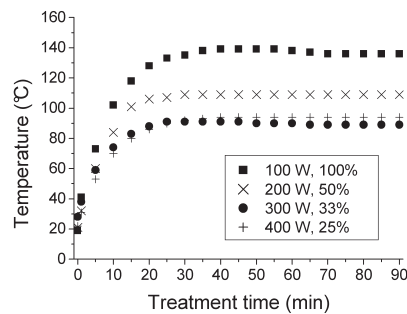


**Figure 2:** Temperature of samples during treatment (brass, ammonia atmosphere).

XRD pattern has shown that the corrosion layer in case of brass corroded in ammoniac atmosphere was formed by zinc chloride hydroxide ( $\text{ZnOHCl}$ ), ammonium chloride ( $\text{NH}_4\text{Cl}$ ) and zinc hydroxyl chloride hydrate ( $\text{Zn}_5(\text{OH})_8\text{Cl}_2 \cdot \text{H}_2\text{O}$ ). The corrosion layer was redish brown with black crystals on the surface. The same compounds were observed after the plasma treatment, but their abundance was different and the samples color was brown with white cover on the surface.

After the plasma chemical corrosion layers removal, the surface is highly reactive and inclines to secondary oxidation. To prevent this process, it is necessary to protect the surface with a barrier film preventing the penetration of oxygen a humidity (as well as the other corrosion agents) to the surface.

We tested possibilities of the archaeological artefacts model samples protection by a thin film deposition of  $\text{SiO}_x$  and Parylene (poly-para-xylylene) thin films. Parylene coatings are chemically inert, conformal and transparent with excellent barrier properties [5] but relatively small adhesion. These all properties determine parylene to be a perfect material for protection of archaeological artefacts. Parylene coatings are prepared by the standard chemical vapor deposition (CVD) method [6].  $\text{SiO}_2$ -like high density films were prepared by PECVD in a low pressure reactor with capacitively coupled plasma discharge (13.56 MHz). Mixture of Hexamethyldisiloxane with oxygen was used as a precursor of plasmachemical reactions.

The coatings were characterized by various methods in order to obtain information about their thickness (ellipsometry), chemical structure (FTIR) and elemental composition (XPS), surface morphology (LCSM, SEM) and barrier properties (OTR) - examples of results see in Figs. 3 and 4. To verify applicability of our prepared thin protective layers, the standard corrosion tests were performed. Example of such test is shown in Fig. 5 where standard protected brass samples (protected by Paraloid B44 varnish) and parylene coated samples were exposed in salt chamber according to the ISO 9227 norm.

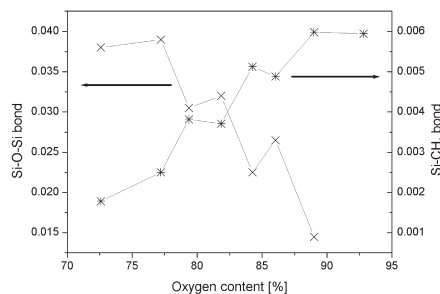


**Figure 3:** Content of Si-O and Si-CH<sub>3</sub> in dependence on oxygen content in HMDSO-O<sub>2</sub> reacting gas mixture.

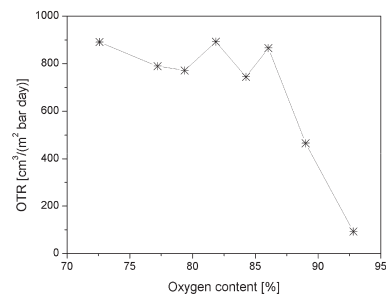


**Figure 4:** Oxygen transmission rate on  $\text{SiO}_x$  thin films (substrate has value of about 600).

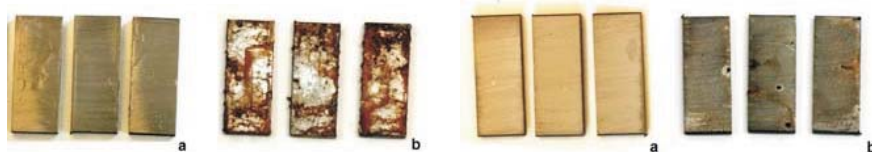


**Figure 5** Comparison of classically protected brass samples (left) and parylene coated samples (right) before (a) and after (b) 300 hours test in salt chamber.

#### 4. CONCLUSION

The presented contribution clearly demonstrated the applicability of pulsed RF hydrogen plasma for the removal of surface corrosion from ancient archaeological objects. The decrease of the mean applied energy led to the significant decrease of the samples temperature, on the other hand the plasma process was nearly the same effective at all cases. This result is very important mainly for the treatment of temperature sensitive objects made from bronze or for objects with broken structure (nearly fully corroded objects). The application of both  $\text{SiO}_x$  and parylene thin films showed very good barrier properties in contrary with classical conservation procedure. The possibility to protect more objects at the same time is the main advantage of their application but their removal must be studied because all protecting procedures must be reversible.

#### Acknowledgements

This work has been supported by the Ministry of Culture of the Czech Republic, project No. DF11P01OVV004.

#### REFERENCES

- [1] J. Patscheider, S. Veprek, *Studies Conserv.* 31, 29 (1986)
- [2] V.D. Daniels, L. Holland, M.W. Pascoe, *Studies Conserv.* 24, 85 (1979)
- [3] S. Vepřek, J. Patscheider, J. Elmer, *Plasma Chem. Plasma Process.* 8, 445 (1988)
- [4] Z. Raskova, F. Krcma, M. Klima, J. Kousal, *Czech. J. Phys.* 52, D927 (2002)
- [5] E. Meng, P.-Y. Li, Y.-C. Tai, *J. Micromech. Microeng.* 18, 045004 (2008)
- [6] J.B. Fortin, T.-M. Lu, *Chemical Vapor Deposition Polymerization – The Growth and Properties of Parylene Thin Films*, Kluwer Academic Publishers, New York 2004.

## **INVESTIGATION OF DC BREAKDOWN IN NITROGEN: INFLUENCE OF PRESSURE AND ELECTRODE GAP VARIATION**

Nikola Škoro<sup>1</sup>, Saša Gocić<sup>2</sup>, Dragana Marić<sup>1</sup> and Zoran Lj. Petrović<sup>2</sup>

<sup>1</sup> *Institute of Physics, University of Belgrade, Pregrevica 118,  
11080 Belgrade, Serbia*

<sup>2</sup> *Department of Physics, University of Niš, P.O.Box 224, 18001 Niš, Serbia*

**Abstract.** Paschen curves in nitrogen have been measured in a discharge chamber with parallel-plate copper electrodes. Measurements of breakdown voltage were done in two ways: (i) by fixing the electrode gap and varying the pressure and (ii) by keeping the pressure constant while changing electrode distance. Electrical measurements were supported by recording of axial discharge profiles, to verify the regime of discharge after the breakdown. Obtained results provided information on possible processes responsible for discrepancies in breakdown voltages at low and high  $pd$  values.

### **1. INTRODUCTION**

Breakdown is the fundamental process for all types of artificially produced plasmas and it has been investigated since very beginning of plasma research [1]. Studies of breakdown are important both for laboratory discharges [2,3] and applications [4] Low pressure DC breakdown in nitrogen has been studied by many authors [5,6]. The main point of the present contribution is to illustrate deviations from the standard shape of Paschen curves by using breakdown measurements performed in nitrogen. Influence of diffusion losses to the scaling of Paschen curves at different electrode gaps has already been studied in [6]. In this paper, we will discuss additional factors that can influence the breakdown results, such as long path breakdown and effective path of the discharge.

### **2. EXPERIMENTAL SETUP**

We studied DC breakdown in nitrogen, in parallel-plate electrode system. Both electrodes were cylinders made of copper, with the diameter of flat polished bases of  $D = 2.2$  cm positioned against each other and placed in a glass tube with the connection to a vacuum system. Distance between electrodes could be changed. The discharge tube was pumped down to a low pressure and

filled with research grade nitrogen at a desired pressure. During measurements, very small flow was kept in a system in order to remove impurities. Details about electrical circuit are described elsewhere [7-8].

In order to obtain breakdown voltages, the discharge was ignited in low-current regime and then by continuously changing operating voltage, the lowest possible current was reached. Breakdown voltage is then determined by extrapolation of discharge voltage to zero current. In this way, long breakdown time delays were avoided as well as overvoltage. For the lowest possible currents ( $\sim 1 \mu\text{A}$ ), 2D side-on profiles of emission integrated in visual spectra were recorded by an ICCD camera.

### 3. RESULTS AND DISCUSSION

In Fig. 1 two Paschen curves measured in  $\text{N}_2$  are shown. One curve is obtained by varying the pressure at fixed electrode gap (squares), while another is recorded with changing electrode gap at the constant pressure (circles).

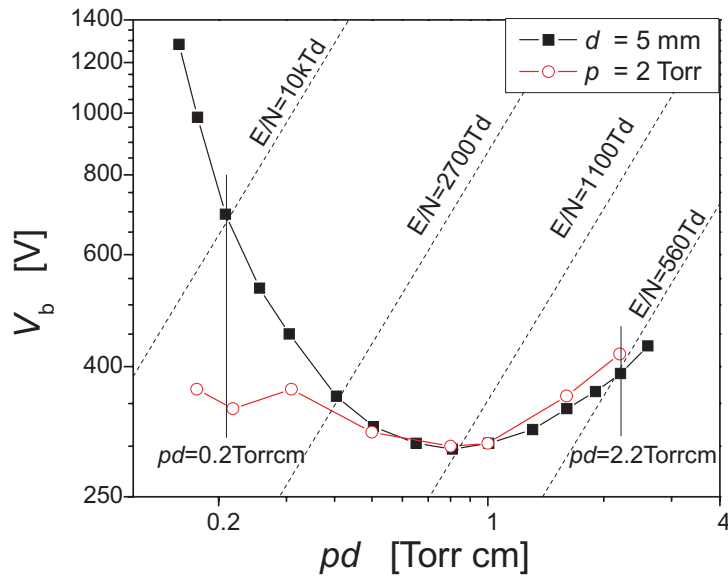


**Figure 1.** Paschen curves in low-pressure  $\text{N}_2$  obtained at: (i) fixed electrode gap ( $d = 5 \text{ mm}$ ) – squares and (ii) at constant pressure ( $p = 2 \text{ Torr}$ ) – circles. Dashed lines mark values of reduced electric field at characteristic points. Solid lines at selected  $pd$  values correspond to images in Fig. 2.

Curves agree well around the minimum voltage of  $300 \text{ V}$  at  $pd = 0.8 \text{ Torr cm}$ . In this case, for both measurement approaches used, since pressure and electrode gap are similar, the agreement is expected.

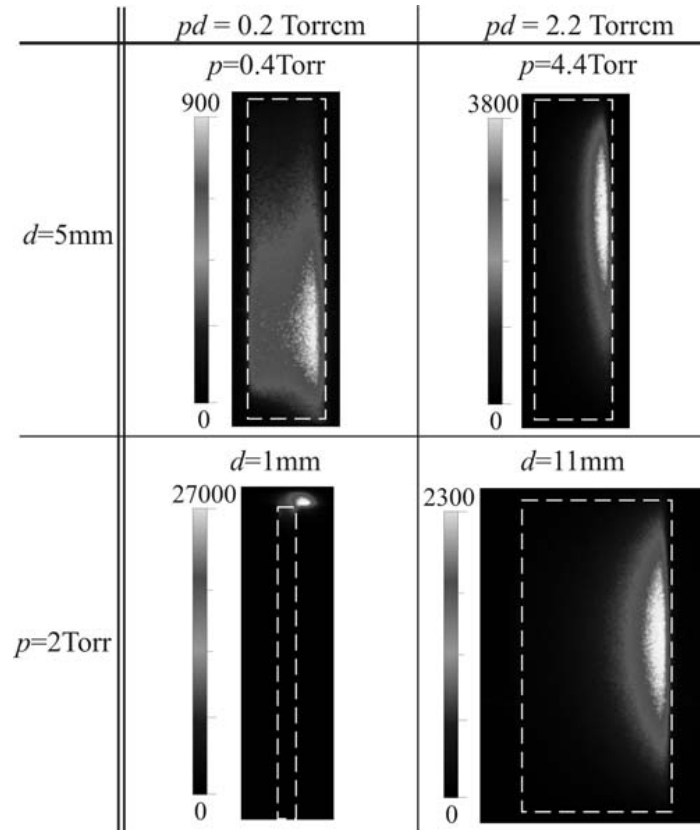


**Figure 2.** 2D profiles of low-current  $N_2$  discharge recorded at  $pd = 0.2$  Torr $\cdot$ cm and  $pd = 2.2$  Torr $\cdot$ cm (columns). Profiles in upper row are obtained for fixed  $d$ , in lower row for fixed  $p$ . Dashed lines enclose discharge volume. The cathode is on the left hand side.

However, in the left hand branch of the curve, around  $pd = 0.2$  Torr $\cdot$ cm, large discrepancy in breakdown voltages is evident. Fixed-pressure Paschen curve exhibits a plateau to the left from the minimum. The profile in Fig. 2 reveals that in this case ( $p = 2$  Torr $\cdot$ cm;  $d = 1$  mm) the discharge is running in a small space between electrodes' outer sides and the glass wall. The long-path breakdown effectively extends electrode distance allowing the discharge to breakdown at lower voltages [8]. On the other hand, at the same  $pd$ , for the fixed-gap case ( $p = 0.4$  Torr;  $d = 5$  mm), the discharge remains inside the volume between electrodes. Apparently, even though  $pd$  is the same in those two cases, higher pressure is more favorable for the long-path breakdown to occur. In this case, mean free path of electrons is small enough for electrons to perform collisions in narrow gaps between electrode sides and surrounding glass wall [8].

In the right hand branch of the curve, breakdown voltages for the fixed-pressure case are somewhat higher than those for the fixed-gap case. One

of the possible causes could be increased diffusion losses at larger gap/diameter ratios, which would require higher voltage to breakdown [6]. Another possible cause becomes obvious from images of discharge at high and low pressures for  $d=5$  mm. These profiles reveal that electrodes were not ideally parallel, as at lower  $pd$ -s axis of the discharge is shifted towards lower part of the discharge volume (larger effective gap), while at higher  $pd$ -s it is shifted towards upper part of the volume (shorter effective gap) [8]. Differences in Paschen curves at high  $pd$ -s would correspond to 0.5 mm shorter effective gap due non-parallel electrodes. It is most likely that both of the stated effects contribute to observed discrepancies in results.

To summarize, we have illustrated some of the issues that can influence the results of breakdown measurements. Results emphasize importance of simultaneous measurements of breakdown potentials and spatial structure of the discharge. Without clear connection between electrical properties and spatial emission distributions, results can lead to misinterpretations. In some cases, it is possible to avoid stated problems, e.g. diffusion losses at lateral walls can be reduced by increasing electrode diameter, to keep gap/diameter ratio small. However, it is difficult to avoid long path breakdown at high pressures (short mean free paths), even with tight fitting walls [8].

### Acknowledgements

This work is supported by MESRS, projects ON171037 and III41011.

### REFERENCES

- [1] F. Paschen, Ann. Phys. Chem. 37, 69 (1889)
- [2] A. V. Phelps and Z. Lj. Petrović, Plasma Sources Sci. Technol. 8 R21 (1999)
- [3] G. Malović, A. Strinić, S. Živanov, D. Marić and Z. Lj. Petrović, Plasma Sources Sci. Technol. 12, S1 (2003)
- [4] J. Beckers, F. Manders, P. C. H. Aben, W. W. Stoffels and M. Haverlag, J. Phys. D: Appl. Phys. 41 144028 (2008).
- [5] V. Lj. Marković, S. R. Gocić, S. N. Stamenković, Z. Lj. Petrović and M. Radmilović, Eur. Phys. J. AP 14 171 (2001).
- [6] V. A. Lisovskiy, S. D. Yakovin and V. D. Yegorenkov J. Phys. D: Appl. Phys. 33, 2722 (2000).
- [7] D. Marić, K. Kutasi, G. Malović, Z. Donko and Z. Lj. Petrović, Eur. Phys. J. D 21, 73 (2002).
- [8] D. Marić, N. Škoro, P. D. Maguire, C. M. O. Mahony, G. Malović and Z. Lj. Petrović, Plasma Sources Sci. Technol. 21, 035016 (2012)